AAAS

Science

PROTEIN SHAKE

Generative deep learning powers emulation of protein ensembles p. 700

14 AUGUST 2025

Can synthetic organs and AI replace animal testing? p. 676

Plant volatiles enhance pathogen defense through soil feedback pp. 680 & 698

Diamond is not the only carbon allotrope in rings p. 708

Scientists' role in defending democracy

Gretchen Goldman and **Erica Chenoweth**

The United States' democratic leadership, commitment to freedom of expression, and investment in the pursuit of knowledge have long enabled its preeminence in science and technology. Yet today we are witnessing what happens to a nation's science and technology enterprise when democratic principles and the rule of law are ignored. The US scientific community is well-suited to play a leading role in pushing back, drawing inspiration from historical cases that have been effective. Building alternative institutions outside of government that reduce reliance on the authoritarian regime, lessen its power and relevance over day-to-day life, and preserve sites of independent thought can be vital both in preserving science and in defending democracy.

The people and processes that provided a check on the Trump administration's attacks on science and scientists during his first term—federal scientific integrity policies, inspectors general, and Congress, for example—are now gone, severely diminished, or complicit in the actions the executive branch is pursuing. Despite court orders and congressional mandates, scientists committed to publishing nonpartisan data are being summarily fired, federal science agencies and external advisory bodies are being hollowed out or dismantled, scientific research grants are being severed, and public scientific resources—such as websites containing public health information—have been removed.

The ability to tell the truth... is an essential prerequisite for a free society.

We know from other countries and contexts that aspiring authoritarians often target scientists, elevate loyalists, and suppress or sideline any who might have the knowledge, expertise, or power to challenge government transgression and failures to make science-based policy decisions. In response to such threats, the US scientific community can work to rebuild critical elements of the federal science enterprise now being dismantled or compromised, including science advisory committees and scientific assessments, which for decades have helped ensure that the best available science informs policy decisions.

There are several promising models for success. For example, when the first Trump administration disbanded a scientific panel charged with advising the Environmental Protection Agency on air pollution standards, the disbanded panel convened independently to review the evidence and advise the agency on the science of the health effects of particulate matter. This work supported successful legal challenges and faster progress when the next administration arrived. Following this model, fired federal science advisers are now organizing an alternative version of the Centers for Disease Control and Prevention Advisory Committee on Immunization Practices, and the Union of Concerned Scientists has released a toolkit providing guidance on independent science committees.

These efforts to develop independent science advice may not match the reach and respect of a formal government body, but they preserve scientific truth in the public record, which can prove useful both for the public's awareness and, when relevant, in legal proceedings. They can also effectively counter misinformation coming from government officials and help hold them accountable. Even if the federal context doesn't improve in the coming years, independent science infrastructure provides reliable science advice for other levels of government and for the public. The US scientific community now has the chance to apply this strategy at scale.

The ability to tell the truth, especially when it does not suit any particularly partisan aims, is an essential prerequisite for a free society. Scientists can leverage their substantial social standing and trustworthiness to preserve this vital ingredient. Under authoritarian conditions in the Soviet Union, many dissident leaders were prominent scientists, circulating underground writings that criticized the pseudoscience that the communist state approved and promoted. These materials helped to break through the wall of invincibility that the government tried to create—even when the dissidents themselves paid a price. Indeed, the US government used to prioritize breaking down autocrats' control of information throughout countries behind the Iron Curtain, by supporting dissident and alternative news sources that could break barriers to truth.

Every would-be dissident scientist has a different tolerance for risk, and efforts to reestablish public sources of trusted scientific information can't fully recreate the US science apparatus now being dismantled. But alternative institutions offer a promising pathway for preserving an essential role of science in public life, while maintaining democratic principles that enable a free society. Those in the science community who are willing and able to be more visible can step up. Acting together will be more impactful than going it alone. □

Gretchen Goldman is president of the Union of Concerned Scientists, Washington, DC, USA. ggoldman@ucs.org **Erica Chenoweth*** is the Frank Stanton Professor of the First Amendment at the John F. Kennedy School of Government, Harvard University, Cambridge, MA, USA. erica_chenoweth@hks.harvard.edu
*E.C. writes this piece in their personal capacity. The views expressed in this editorial reflect the authors' alone.

10.1126/science.aea9328

Check for

INFECTIOUS DISEASES

NIH weighs controversial overhaul of HIV budget

Scientists worry $1 billion push for "implementation science" will harm basic research

JON COHEN

In a push to end the HIV/AIDS epidemic in the United States, leaders at the National Institutes of Health (NIH) are discussing the possibility of a massive shift in investment away from basic research and toward "implementation science"—studies of the most effective way to use existing treatment and prevention tools, such as the breakthrough drug lenacapavir. *Science* has learned the agency may devote $1 billion—roughly one-third of the agency's budget for HIV—to the approach. NIH Director Jayanta "Jay" Bhattacharya has said a major push is needed to exploit the promise of lenacapavir, which provides 6 months of protection with a single shot.

The idea has alarmed scientists both inside and outside NIH because basic research that drives HIV treatment, prevention, and cure advances would lose about $800 million annually. Scientists also question whether so much money can be spent responsibly on HIV-related implementation science. The proposal received a critical reception at a 30 July ad hoc meeting of the NIH HIV/AIDS Executive Committee (NAEC), according to minutes of the meeting obtained by *Science*. NAEC advises the agency's Office of AIDS Research (OAR).

Bhattacharya has in several public venues voiced enthusiasm about preexposure prophylaxis (PrEP) using lenacapavir, which came to market in June. He discussed the topic at length in a 25 July "Director's Desk" interview with Geri Donenberg, OAR's acting director. Donenberg, a clinical psychologist who founded and ran an implementation science program at the University of Illinois, called lenacapavir PrEP a "game changer" in HIV prevention. "Why is there any reason to wait?" Bhattacharya asked her. "Why don't we just really commit to ending the HIV epidemic, actually doing it with the toolkit we have now?"

According to the NAEC minutes, Donenberg, who attended the meeting, was asked to write a memo to NIH's parent agency, the Department of Health and Human Services (HHS), that spells out a "strategic plan to end the AIDS epidemic." She suggested NIH increase its implementation science budget from $216 million to $441 million. HHS rejected that as too low, leading OAR to raise the proposed amount to $1 billion by fiscal year 2027. "This number has NOT been approved or finalized by leadership," the minutes state in bold type, noting it will "likely be significantly adjusted" if NIH's budget is cut. President Donald Trump's administration has pushed for reducing NIH's budget by 40%, but the Senate Committee on Appropriations flatly rejected this proposal and approved a bill that would instead slightly increase funding for the agency.

"Implementation science" evaluates programs to connect people to biomedical advances—such as a truck offering HIV services.

NAEC members, mainly representatives from NIH institutes and centers that fund HIV research, "expressed multiple concerns" about the push for implementation science, the minutes show. These include "eliminating important areas of science," having to rescind promised funding for research that's already in the works, and "the possible absence of strong scientific proposals" in implementation science.

Donenberg countered that NIH branches will still have 70% of their HIV research budget to spend on other types of research. Some institute and center representatives conceded that they have had to reject "strong scientific proposals in implementation science" in the past for a lack of money. NIH did not respond to *Science*'s request to speak with Bhattacharya or Donenberg.

High-ranking HIV/AIDS scientists at NIH who asked not to be identified for fear of retribution shared NAEC's concerns. Bhattacharya and OAR "are very naïve about how to do this in a reasonable way at a reasonable pace that would allow for funding meritorious implementation science research and avoid ending other streams of important HIV research, such as vaccines," one says. (HHS Secretary Robert F. Kennedy Jr. claimed at a June congressional hearing that HIV vaccine research "accomplishes nothing.")

The scientist notes that lenacapavir's manufacturer, Gilead Sciences, already finances implementation studies of the drug. Gilead says it is funding 16 investigators exploring implementation in the U.S., as well as providing the drug for studies "to inform sustainable access" in

South Africa and Brazil. It also plans to sponsor a multisite study in the U.S. "to evaluate implementation in multiple settings."

A second NIH scientist is "very, very worried" about the proposal. "The strength of the NIH is in biomedical research," says the scientist, who notes that lenacapavir's discovery owes a great deal to NIH-funded research into the capsid protein that the drug targets. In his talk with Donenberg, Bhattacharya acknowledged this. "The DNA of the NIH is basic biomedical research, lab work," he said. "But this is a science, too."

Implementation science is "a worthwhile area because we do have this opportunity to get it right," says Kenneth Mayer, medical research director at the Fenway Institute, a veteran of HIV implementation science studies. Getting lenacapavir to people at high risk of HIV infection won't be easy, he says, as many who could benefit from it "are not necessarily middle class, well-regimented, well-insured people who are going to show up every 6 months on time for their appointments."

It may help to have vans in underserved communities offer lenacapavir PrEP as one of several health services, for example. A phone app might help remind people of their appointments, or clinics can change their hours to better suit their communities. These types of approaches should be studied, Mayer says. "Some of these things seem mundane, and it may seem intuitively obvious, but ... you can't always anticipate what the results are going to be."

Still, Mayer worries the budget shift will harm "categories of research" the Trump administration dislikes, including vaccine research. "I hope they are putting thought into exactly what they would be funding and not just playing around with numbers," he says. "There's too much at stake."

He also notes that other administration policies may undermine access to lenacapavir PrEP, including the One Big Beautiful Bill, which the Congressional Budget Office estimates may cause nearly 11 million people in the U.S. to lose their health insurance. The administration's hostility toward transgender people—who have disproportionately high HIV infection rates—and its aversion to any program focusing on minority groups will also hamper any effort to end the epidemic, he says. "Certainly some of the implementation has to do with communities and cultures that they've not been necessarily very fond of recently." □

IN FOCUS

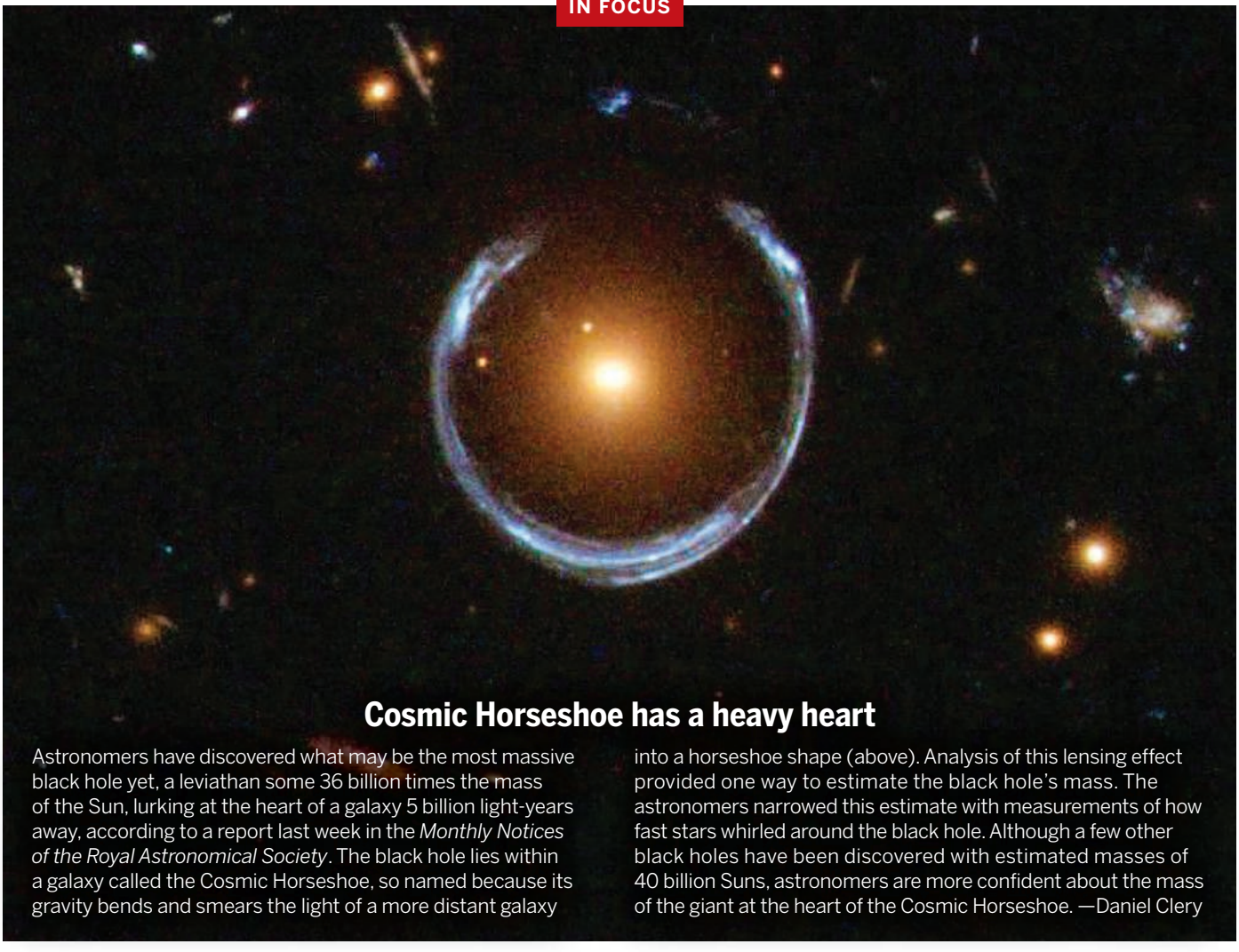

PHOTO: NASA/ESA

Cosmic Horseshoe has a heavy heart

Astronomers have discovered what may be the most massive black hole yet, a leviathan some 36 billion times the mass of the Sun, lurking at the heart of a galaxy 5 billion light-years away, according to a report last week in the *Monthly Notices of the Royal Astronomical Society*. The black hole lies within a galaxy called the Cosmic Horseshoe, so named because its gravity bends and smears the light of a more distant galaxy into a horseshoe shape (above). Analysis of this lensing effect provided one way to estimate the black hole's mass. The astronomers narrowed this estimate with measurements of how fast stars whirled around the black hole. Although a few other black holes have been discovered with estimated masses of 40 billion Suns, astronomers are more confident about the mass of the giant at the heart of the Cosmic Horseshoe. —Daniel Clery

Ewa Stępień (left) and Paweł Moskal seen through their plastic-based PET scanner.

MEDICAL PHYSICS

Twist on PET unlocks hidden signals

Overlooked emissions from exotic positronium atoms open unexpected window for diagnosing cancer and other diseases

ZACK SAVITSKY, in Kraków, Poland

Paweł Moskal opens a closet in the corner of his lab and looks back with a grin. "This is something very special since the communistic times," he says, reaching for a rustic, lead-walled safe designed to hold nuclear materials. From the safe, he pulls out a small, yellow wafer with a single black dot of radioactive sodium-22 at its center. Later, he will inject the sodium into human tissues, where the glow from its decay will be captured by a positron emission tomography (PET) scan.

For 50 years, physicians have used PET scanners to detect diseases such as cancer and Alzheimer's. But Moskal, a physicist here at Jagiellonian University, has quietly pioneered a technique to squeeze additional information out of the devices. By probing the lifetime of an exotic atom called positronium that forms within the body during PET scans, Moskal thinks he can use this new information to better identify different types of cancer, monitor disease progression, and guide treatment plans.

The technique is catching on with several other labs around the world. If Moskal and those colleagues can convince the medical industry to buy in, "it could really open up a new dimension in nuclear medical imaging," says Katia Parodi, a physicist at the Ludwig Maximilian University of Munich who collaborates with a group in Japan that does positronium imaging. "Now I think many people are appreciating the huge potential."

Traditional PET scans rely on radioactive tracers that decay in minutes to hours by emitting a positron (the antimatter counterpart of an electron). When the positron encounters an electron in the body, the two annihilate in a flash, sending two photons flying in opposite directions. Detected by sensors in the PET scanner, they are traced back to their origin in the patient. By binding the tracers to molecules the body naturally processes, such as glucose, scientists can monitor the rate of metabolism in different tissues to look for hallmarks of disease. For instance, cancer cells metabolize glucose much faster than normal cells. As a result, diseased regions eat up more tracer and glow more brightly on the scan.

Because PET scans trace biological function rather than structure, they can provide earlier warnings than other imaging techniques. But they aren't perfect. Because of their limited resolution and ambiguous factors that influence metabolism rates, they must be confirmed with biopsies. Furthermore, access to PET scanners is limited. Seventy countries have none at all, and most—including Poland—have fewer than one device per million people. Struck by this disparity, Moskal hunted for a way to democratize the machines, which cost a few million dollars.

About half of that cost comes from rare-earth crystals used to register photons. Moskal realized he could replace those crystals with less sensitive but cheaper plastic detectors. To the surprise of his colleagues, by 2016, Moskal and collaborators had stacked the plastic detectors in layers to build a prototype PET scanner with sufficient sensitivity. Moskal says their latest version, expected in 2028, should cost just 10% to 20% as much as commercial machines and have even higher sensitivity.

Moskal sought a way to put the additional light-gathering power of his plastic PET sensors to use. From his background in nuclear physics, Moskal knew of a process traditional scans overlook. Positrons and electrons don't always instantly annihilate—about 40% of the time, they instead bind to form a temporary, atomlike state called positronium. Within a few nanoseconds, the positronium collapses and annihilates itself, giving off a delayed pair of photons.

Working with Jagiellonian medicinal physicist Ewa Stępień, Moskal began to investigate physiological features that control the speed of that positronium decay. Positronium forms in the gaps between molecules in tissues, where it can hide from stray electrons that cause it to decay. Its lifetime is shorter in denser tissues with smaller pores and in voids with reactive molecules such as oxygen. As some tissues become cancerous, their pores shrink and oxygen levels fall, and Stępień and Moskal wondered how these factors would affect positronium lifetimes.

Measuring those lifetimes with their machine required some tweaks. PET scans usually detect only the two photons given off by annihilation. But by turning to a tracer that emits an additional photon at the time a positronium atom forms, Moskal and Stępień could clock the elapsed time between this "prompt" photon and the annihilation photons to calculate the positronium lifetime. They designed

their scanner specifically to look for the prompt photon, which is typically disregarded as noise.

Over the past few years, the team has demonstrated the potential medical value of positronium imaging. In 2021, they reported the first positronium image, comparing heart cancer cells and healthy fat cells extracted from patients. The study showed the cancer cells had significantly shorter positronium lifetime than the healthy ones. Last year, they imaged a brain cancer patient and found that positronium lifetimes in the tumor were shorter than those in healthy brain tissues.

These in vivo images were relatively fuzzy and weak, because the tracer they relied on, gallium-68, emits a prompt photon only in about 1% of its decays. Using a tracer such as scandium-44, which emits an initial photon 100% of the time, would increase the number of registered events and boost the sensitivity by a factor of 100, Moskal says.

With the promise of heightened sensitivity, Stępień dreams of using positronium to do "virtual biopsies," reconstructing tissue composition without the need for surgery. Parodi imagines using positronium not only to monitor how cancer patients respond to radiation therapies, but also to investigate the efficacy of experimental ones.

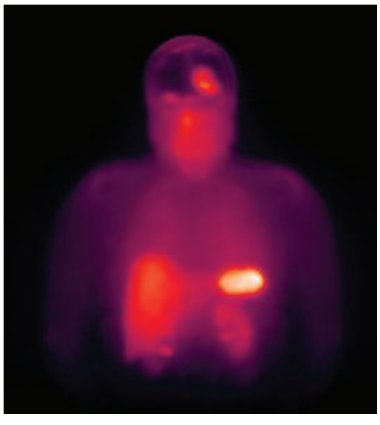

An image made from triple-photon events is a step toward measuring positronium lifetimes.

The excitement is spreading to other labs. A team at the University of Pennsylvania has used its PET scanner to practice measuring positronium lifetimes in small inanimate objects in preparation for human imaging. In Switzerland, a collaboration between the University of Bern and Siemens Medical Solutions, which sells PET scanners, recently measured positronium lifetimes in the organs of three patients. And at the National Institute of Radiological Sciences in Japan, researchers investigated how positronium could be used to image hypoxia, or oxygen deficiency, which often corresponds with cancer progression and drug-resistance.

The field has been boosted by a wave of full-body PET scanners, which are sensitive enough to register all three positronium photons with minimal upgrades. "Almost by accident, they are able to perform these measurements," says Adrien Hourlier, a physicist at Strasbourg University who led a review of positronium imaging last year. "The advent of full-body scanners really helped buy some credit into the idea."

But the technique still faces hurdles. Chief among them will be untangling the different factors that control positronium lifetime in a given tissue. "It could reveal something meaningful, but at the moment … it's not clear what the signal really corresponds to," says Robert Seifert, a nuclear physician working with the Bern team.

Getting the medical industry on board will be another challenge, because large-scale adoption would require upgrading detectors and retraining staff. It's a battle all too familiar to Moskal, who struggled to commercialize his plastic PET detectors with companies that told him the devices wouldn't raise their bottom line. But he thinks the promise of positronium imaging will eventually carry the day—and maybe help him sell his cheaper detectors, too.

"We are not losing the hope," Moskal says. He and Stępień are currently developing a full-body version of their PET scanner as well as a mobile version. They've also just taken their first images of human tissues with the promising scandium-44 tracers, and they are now racing the groups in Pennsylvania, Switzerland, and Japan to gain regulatory approval for the tracer in live patients.

"We are basically seeing the birth of a new type of imaging," Hourlier says. He likens it to the gradual embrace of the first digital cameras. "Progressively, they're going to get better and better, and then people will see the actual gain." □

RESEARCH BRIEFS

TEETH FILL GAP IN HUMAN HISTORY

Ancient teeth from between 2.6 million and 2.8 million years ago show early members of our genus *Homo* coexisted with a newly discovered species of *Australopithecus*, according to a report this week in *Nature*. In eastern Africa, *Australopithecus afarensis*—the 1-meter-tall upright walking apes whose members included the famous Lucy skeleton—disappeared about 3 million years ago. By 2 million years ago, early *Homo* species were well established. What happened in between is now clearer thanks to 13 fossil teeth found in 2015 and 2018 from a site called Ledi-Geraru in northern Ethiopia. Three teeth belonged to *Homo* species. The rest, the researchers say, came from a previously unknown and still unnamed species of *Australopithecus*. —Bridget Alex

GENETIC CLUES FOUND FOR ME/CFS

The largest genetic study of myalgic encephalomyelitis/chronic fatigue syndrome (ME/CFS) has identified clues about the condition, which afflicts millions with extreme exhaustion and difficulty thinking clearly. By analyzing DNA from more than 15,000 people diagnosed with the illness, U.K. researchers identified eight genomic regions associated with the disorder, including some that are linked to immune responses to infection. Although treatments and diagnostics for ME/CFS remain distant, the findings, posted in a preprint last week, will help direct future research and validate ME/CFS as a biological condition, says University of Amsterdam biopsychologist Jos Bosch. It's "an important corrective to psychologizing 'all in the mind' perspectives on the disease," he says. —Catherine Offord

DEVICES LEVITATE IN THIN AIR Researchers have made featherweight devices that could levitate in sunlight indefinitely to probe an understudied region of the upper atmosphere. The centimeter-scale aircraft, made from two thin membranes connected by tiny struts, absorb light on one side and reflect it on the other. That results in temperature differences across the device that are big enough to propel the thin, high-altitude air around and through it, keeping it aloft. Although the devices have only been tested in the lab, their inventors report this week in *Nature* that swarms of them could be outfitted with sensors and deployed to explore the mesosphere, a layer of air 50 to 80 kilometers up that's too thin for planes or balloons and too thick for space-based satellites. —Annika Inampudi

IMAGE: P. MOSKAL *ET AL.*, *IEEE TRPMS* (2025) DOI: 10.1109/TRPMS.2025.3583554/CC BY

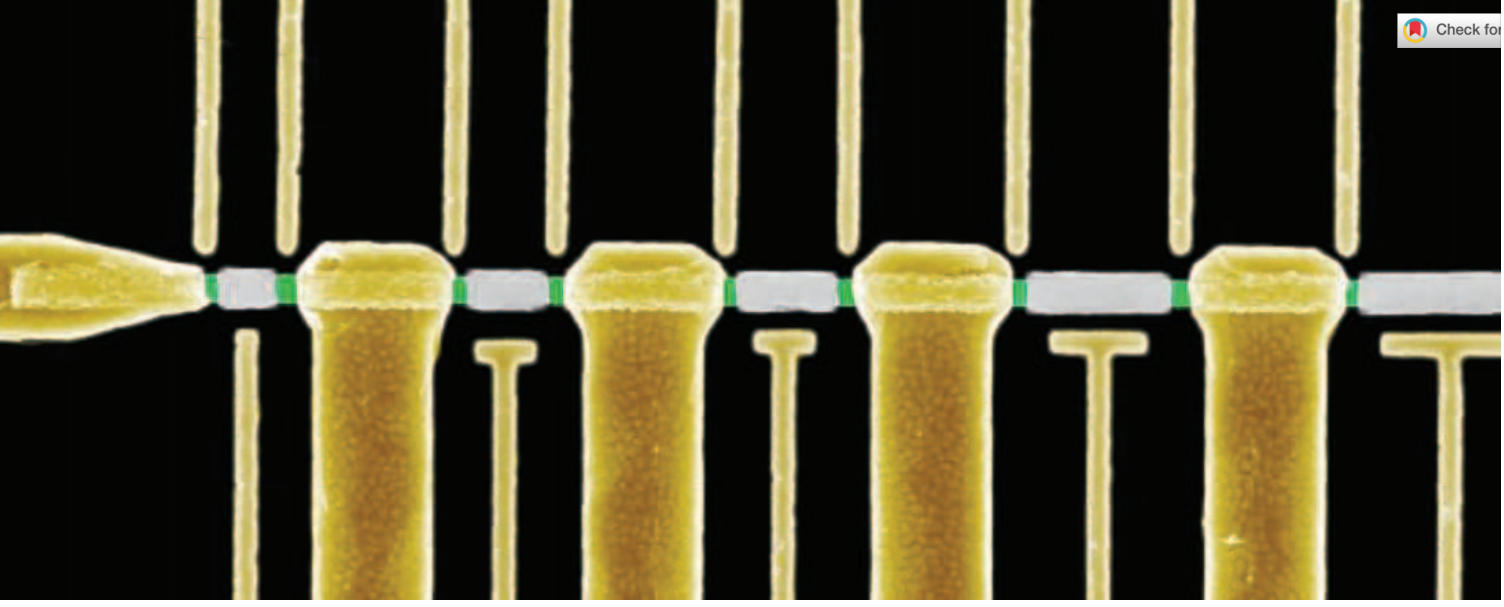

PHYSICS

Correction in *Science* rekindles debate over Microsoft's quantum computing research

Disputes over elusive Majorana particles—the hoped-for key to robust quantum chips—continue to divide the field

ADAM MANN

Like Schrödinger's famously dead-and-alive cat, the qubits that underpin quantum computers can exist in two states at once. It seems that one corner of quantum computing research—a quest to fashion qubits out of mysterious Majorana quasiparticles—also trundles along in a kind of dual reality: both believed and not believed.

After years of dispute, *Science* this week added a correction to a 2020 paper by Microsoft-sponsored researchers who claimed to have conjured up Majorana particles within tiny "nanowires"—an important step toward building a more resilient kind of quantum computer. But the journal's decision, which follows the recommendations of a university investigation that found no scientific misconduct, seems unlikely to end the tug of war between the authors and their critics, who still want the work retracted because of alleged data cherry-picking.

The correction is also unlikely to calm the broader debate surrounding ongoing Majorana research sponsored by Microsoft, which has poured more than $1 billion into the field. In February, when the company announced what it billed as the first Majorana-based quantum processing chip, it was met with skepticism by independent experts and downright scorn from a group of committed critics. "This is a result of overheatedness from the confluence of science, social media, and corporations," says Jay Sau, a condensed matter theorist at the University of Maryland. "There is definitely a toxic cloud around the word 'Majorana' because of all this."

Unlike classical bits, which must be set to either 0 or 1, qubits can inhabit a "superposition" of coexisting 0 and 1 states. Devices that harness this capability should in theory be able to outperform classical computers in certain fields, such as codebreaking and advanced chemical simulations.

But qubits are fragile, and any slight disturbance can collapse their carefully crafted superposition states. That's why Microsoft and others have pursued so-called topological qubits, which spatially spread out the quantum states to protect them from local noise. For instance, if researchers can align electrons and positively charged "holes" in just the right way within the atomic lattice of a superthin nanowire, individual electrons can appear to be torn in half, with the halves moving to opposite ends of the wire. This sundering trick should make these half-electron qubits behave like their own antiparticles, a property named after the early 20th century Italian physicist Ettore Majorana, and fortify them against disruption. "It's kind of like splitting the bit of information and storing it in two separate locations, like Voldemort's horcruxes," says Sergey Frolov, a physicist at the University of Pittsburgh.

The problem is proving that any Majorana qubits exist. Researchers scan through the voltage of their devices looking for a particular quantized signature in the electrical conductance, but the inherent complexity of most materials can confound such probing. "The disorder can basically create the same signatures that you would expect from the Majorana," says Henry Legg, a quantum physicist at the University of St. Andrews.

Because a number of high-profile Majorana qubit claims have been retracted over the years, new findings receive a lot of scrutiny. That was the case with the 2020 paper, which was led by researchers at the University of Copenhagen (KU) and supported by Microsoft. Soon after publication, Frolov and Vincent Mourik of the Jülich Research Center flagged problems in the paper that led *Science* to place an editorial expression of concern on it. "The essential question was: 'Did the authors plot noise and claim that it was signal by obscuring the rest of the noise?'" says Jake Yeston, an editor at *Science* who oversees physical sciences research papers. (*Science*'s News team operates independently from the journal's research arm.)

Majorana quasiparticles may exist at the ends of thin wires (gray and green materials).

In 2023, KU examined the team's procedures and practices and concluded that, although the researchers sometimes used subjective judgment in data selection, the excluded data didn't undermine the paper's main conclusions. It found that the authors' behavior did not constitute negligence or scientific misconduct. As a result, *Science* has replaced the expression of concern with the correction, which clarifies several terms and protocols and expands a catalog of experimental data.

The study's main experimentalists, Charles Marcus, now at the University of Washington, and his former KU graduate student, Saulius Vaitiekėnas, welcome the outcome. "Personally, it was very emotional," says Vaitiekėnas, now an associate professor at KU. "It wasn't very nice to have this thing, which now has been shown not to be true, hanging above our heads all of these years." Frolov and Mourik continue to say the work is shoddy and anything other than full retraction is inadequate.

For their part, members of the Microsoft team, some of whom are also co-authors on the 2020 *Science* paper, are carrying on with the quest. The Majorana 1 chip announced in February is based not on nanowires, but on an indium arsenide wafer in which electrons and holes on the atomic checkerboard are supposed to collectively create up to eight Majorana particles acting as two qubits. Last month, its creators posted a preprint on the arXiv describing experiments purporting to show that one of the qubits functioned correctly for a few fractions of a second. They say they have developed protocols to tell true Majorana signals from imposters. "We understand our devices very well," says Microsoft Technical Fellow Chetan Nayak. "The presence of those fake signatures is a very modelable and understandable phenomenon."

Yet the doubts seem unlikely to dissipate any time soon. "There's no evidence for even the basic physics existing in these devices," Legg says. "Let alone that you can build a qubit from it." □

Adam Mann is a science journalist in Oakland, California.

POLICY

Europe eyes civilian science funding for defense research

Worried about regional security, the EU wants to allow major grants to fund "dual-use" projects for the first time **ELISE CUTTS**

At a new interdisciplinary center for marine research in France, researchers are figuring out how to get swarms of autonomous floating robots to work together to form a vast, underwater antenna. The research could unlock new ways for civilian scientists to study ocean currents or track marine mammals. It could also help the military keep tabs on what's going on above and below the waves.

Many European institutions have traditionally shied away from the kind of "dual-use" research taking place at the Polytechnic Institute of Paris (IP Paris) center, which receives support from both France's civil research agency and the Ministry of Armed Forces. But as the war in Ukraine rages on and U.S. President Donald Trump's mercurial stance toward Europe crumbles faith in the trans-Atlantic alliance, EU leaders are looking for ways to boost the bloc's defense capabilities—and they are eyeing the billions in funding that now go to civilian science.

A striking pivot toward defense came last month, when the European Commission announced its proposal for the next iteration of Horizon Europe, the European Union's key science funding scheme. Breaking with 4 decades of precedent, the next 7-year program, set to begin in 2028 with a proposed €175 billion budget, would allow funds to go to research with both civilian and military applications.

Traditionally, the scheme has exclusively funded civilian research, excluding any projects that investigate potential defense applications. "There were just steel walls—you could not do things that had a military purpose," says Katherine Richardson, a University of Copenhagen earth system scientist who chairs the EU's expert advisory group on science policy.

Hints that this approach might change have been bubbling up in Brussels for a few years, says Mattias Björnmalm, secretary general of CESAER, a nonprofit representing European science and tech universities. Last year, the Commission proposed allowing one part of Horizon Europe, the European Innovation Council (EIC), to fund dual-use technologies. EIC, which supports startups and high-risk, high-reward research, receives €10 billion under the current program. The new plans go much further. If the European Parliament approves them, they would open the entirety of Horizon Europe to dual-use projects, including basic science grants funded through the European Research Council.

Many in the research community are uneasy. "A lot of academics and students oppose dual-use and military research—even if the university leadership and the national political leadership in their country would be willing to embark on it," says Kurt Deketelaere, secretary general of the League of European Research Universities, an association of 24 universities. He says when the Commission consulted the research community on plans to open EIC to dual-use projects last year, nearly all supported retaining the existing arrangement, in which Horizon Europe only funds civilian research, with a completely separate European Defence Fund for dual-use and military research.

Some scientists are worried a focus on military research will bring tighter security measures that may compromise academic freedom. For instance, the 21 "affiliate countries" that participate in Horizon Europe but are not members of the EU could be excluded from certain schemes for security or political reasons.

Others oppose dual-use research on ethical grounds. The Science4Peace Forum, an advocacy group of antiwar scientists, published a position paper against dual-use research last year. They say scientists should prevent their work from being used for war and argue that dissolving clear boundaries will compromise international collaboration and "create only anger, mistrust, and further conflicts" that could slow progress on urgent problems such as climate change.

The case of Israel, an affiliate country, is already bringing such concerns to a head. Motivated by the ongoing humanitarian catastrophe in Gaza, the Commission recently proposed blocking Israel from receiving funds from EIC's startup scheme, mentioning the potential for such money to go to dual-use applications such as cybersecurity and drones. In a recent vote, the sanctions failed to garner enough support from member states to pass.

For the Commission, however, opening Horizon Europe up to dual-use research has practical upsides. The EU's executive branch has promised to drastically up its defense spending, and Horizon Europe "is a big pot of money that the European Commission has quite a lot of control over," Björnmalm says. Other EU programs can't be reshaped to serve their policy priorities as easily.

Europe's shift to dual-use research is also playing out at a national level. Germany, for instance, has long drawn a sharp distinction between military and civilian research: Many German universities have civil clauses, or *zivilklauseln*, that ban research for military purposes. But the Federal Ministry of Research, Technology, and Space last year called for civil clauses to be re-evaluated and federal agencies to pour more money into civil-military research collaborations.

Thomas Klapötke, a chemist who studies explosives and propellants at the Ludwig Maximilian University of Munich—one of a handful of German research universities without a civil clause—says he's already seen Germany's shift play out in funding for his work. "In the past, my funding was 80% from the U.S. Army and Navy," he says, but these days, the German military funds most of his research. Still, his work remains controversial. Klapötke says he's received death threats, and many of his colleagues have openly criticized his military work.

In France, defense research at universities is nothing new, says Thierry Coulhon, president of IP Paris. Two IP Paris member institutes are military schools, and it hosts a 25-lab-strong interdisciplinary center dedicated to defense and security funded by the research arm of the French Ministry of Armed Forces. Ongoing projects aim to develop everything from algorithms for controlling robot swarms to methods for detecting biological and chemical threats.

Similar examples can be found across the continent. Denmark's Aalborg University conducts defense research. The Delft University of Technology in the Netherlands has collaborated with defense industry and military partners for decades and is exploring ways to work with the Dutch Ministry of Defense in areas such as artificial intelligence, drones, and quantum technologies. Farther east, Estonia's Tallinn University of Technology has supported military research for a quarter-century, studying topics including sensors, armor, maritime defense, and camouflage, and just this year established a new center for defense and security technologies.

Institutions like these show that it's possible for military and civil research to coexist, Björnmalm says. "We should learn from them."

There's no universal formula for successfully balancing research security and academic openness, Coulhon says. "This is a tension, an interesting tension," he says, "but it's not an obstacle." IP Paris employs measures including having separate secure spaces for sensitive research and placing certain restrictions on researchers who've worked at universities linked to foreign militaries. But staying competitive means recruiting the best minds from around the world, too, Coulhon says. IP Paris is the most international university in France: More than 40% of its staff and students hail from abroad.

For now, the details of the Commission's push toward dual-use research remain fuzzy. The proposed budget needs to pass through negotiations in the European Parliament and could still change. But for good or ill, the era of "steel walls" between military and civilian research in Europe appears to be ending. As Richardson puts it, "We're making baby steps into a gray zone right now." □

Elise Cutts is a science journalist based in Graz, Austria.

IN FOCUS

Ants show strength in numbers

More than a century ago, tug-of-war experiments found people tend to exert themselves less as teams get bigger, perhaps because of loss of motivation. But ants actually work harder in teams, according to a report this week in *Current Biology*. The researchers studied weaver ants (*Oecophylla smaragdina*), which build nests in trees by bending leaves and gluing them together. In experiments with artificial leaves (left), they showed that single ants pulled on leaves with a force nearly 60 times their body weight. But in groups of 15, the ants each pulled 103 times their body weight. By clamping their jaws onto neighbors' waists, the ants form chains in which they can store more force than they alone could generate, the researchers say. —Erik Stokstad

Check for

SCIENCE POLICY

Trump moves to politicize decisions on science grants

Researchers say plan would enable political operatives to overrule peer reviewers **JEFFREY MERVIS**

Last week, President Donald Trump moved to tighten his administration's control over what science agencies decide to fund, alarming research advocates. A new White House directive would require political appointees to sign off on new grant solicitations, allow them to overrule advice from peer reviewers on what to fund, and make it easier for them to terminate grants already awarded.

Some changes described in the order are already underway at research agencies like the National Institutes of Health (NIH) and National Science Foundation (NSF). But its existence could strengthen the hand of Trump appointees in ensuring that science conforms to the president's political agenda, says Carrie Wolinetz, a former senior administrator at NIH.

"We've already seen this administration take steps to exert its authority that have resulted in delays, freezes, and termination of billions of dollars in grants," says Wolinetz, now a lobbyist for Lewis-Burke Associates. "This would codify those actions in a way that represents the true politicization of science, which would be a really bad idea."

The new executive order promises "to strengthen oversight and coordination of agency grantmaking … while ending [the] offensive waste of tax dollars." It would install a noncareer political appointee at every agency to oversee agency announcements about funding opportunities and decisions on what to fund and whether to cut off a grant. "The Trump Administration has already terminated many wasteful grants," the order asserts. "[This] helps ensure that bureaucrats can't make the same mistakes in the future."

The top Democrat on the science committee in the U.S. House of Representatives sees it differently. "This Executive Order is nothing short of obscene," Representative Zoe Lofgren (CA) said in a statement. "In what world does Donald Trump think that Americans want political appointees—who, need I remind the President, are unelected bureaucrats—making decisions on what science gets funded?"

The order builds on moves Trump has made since he returned to office and named Elon Musk to lead the so-called Department of Government Efficiency (DOGE). Musk has left, but DOGE staffers remain in place at most agencies and are exerting varying degrees of control over grantmaking decisions, according to reporting by *Science* and other media.

The new order would expand that control. In one major change, it would give the White House Office of Management and Budget (OMB) the ability to terminate a grant "for convenience." Agencies can already revoke a grant "for cause," Wolinetz says, which covers improper use of government funds or work that deviates significantly from the intended focus. But federal judges this year have repeatedly sided with NSF- and NIH-funded scientists who have sued to stop the administration from unilaterally killing grants without spelling out adequate reasons and for ignoring statutory requirements for spending in some areas.

President Donald Trump's directive asserts new control over federal science spending.

Science advocates fear the executive order, once implemented, would allow the Trump administration to evade those court orders and terminate any research project it doesn't like at any point. The executive order could also bolster OMB's campaign to drive down what agencies spend on indirect costs—reimbursement to universities for the facilities and administrative support they provide to carry out federally funded research.

Institutions now negotiate individually with the government to set reimbursement rates, which vary widely. But the order says agencies should favor institutions with lower indirect cost rates, making indirect costs a major factor in the decision on what science to fund.

That's another bad idea, says Matt Owens, president of COGR, one of 10 scientific organizations that are urging Congress and OMB to adopt an alternative reimbursement method they say accounts for how much universities actually spend to support research. "The administration refuses to acknowledge and pay for the true costs of research critical to the security of the nation and the health of its people," Owens says.

The order touches on several other long-running issues in grantmaking. For example, it urges agencies to fund "a broad range of recipients rather than a select group of repeat players" and says grantees should spell out and meet "clear benchmarks for measuring success." It also doubles down on some controversial recent stances by the Trump administration, among them a demand that all awards "demonstrably advance the president's policy priorities" and that none of them promote the "notion that sex is a chosen or mutable characteristic."

Science advocates hope Congress will block some provisions with language in pending bills on next year's federal budget. Senate and House spending panels have already objected to earlier White House proposals for a low, flat rate on indirect costs. □

PHOTO: JULIA DEMAREE NIKHINSON/AP

BEYOND LAB ANIMALS

With a boost from the Trump administration, organ chips, AI, and other technologies bid to replace animals for drug and chemical testing

SARA REARDON

Organ chips allow researchers to measure how drugs, toxins, and other factors affect human cells.

The small plastic chip etched with channels is a synthetic human organ—and one vision of future drug safety testing. Inside, layers of human liver, epithelial, and immune cells line the tiny conduits, which feed them with blood-like fluid and remove waste. The chip, made by the Boston-based biotech company Emulate Inc., could one day help researchers and pharmaceutical companies screen out candidate drugs that cause a condition known as drug-induced liver injury (DILI)—one of several types of liver toxicity that together scuttle 22% of all clinical trials.

DILI often doesn't show up when drugs are tested in animals. But in a recent study, Emulate's chip was 87% accurate in identifying compounds known to cause DILI—and 100% accurate in flagging those that don't. The chip is now undergoing further testing as part of a new U.S. Food and Drug Administration (FDA) pilot program to evaluate alternatives to animal testing. If it performs well, drug developers will be able to use data it generates to show a new drug is likely safe before they apply to begin human trials.

Animal rights activists see organ chips and similar technologies as a potential means to replace the tens of millions of lab animals used annually in the United States to test the safety of drugs, foods, and chemicals and to do basic research. And, increasingly, U.S. agencies seem to agree. In April, both FDA and the Environmental Protection Agency (EPA) announced they plan to move away from requiring animal tests for certain drug candidates and chemicals such as pesticides. Both agencies will now encourage—but not yet require—researchers to use organ chips and other new approach methodologies (NAMs) to determine whether a drug is safe enough for human testing or a new chemical can be safely marketed. In July, the National Institutes of Health (NIH) followed suit, announcing it would no longer seek proposals for research performed exclusively in animal models.

Animal welfare concerns, shared by a rising fraction of the public, are not the only motivation. FDA said NAMs could accelerate drug evaluation and, eventually, lower research costs. EPA cited a need for better and more cost-effective ways to evaluate new chemicals. And although President Donald Trump's administration has ignored scientific consensus in many areas, particularly vaccination policy and climate change, many in the scientific community call the move to NAMs a good idea, at least if the technologies are used to complement rather than replace animal studies. "I don't see this as antiscientific or superradical," says Megan LaFollette, executive director at the 3Rs Collaborative, a nonprofit that works with academic and industry researchers to reduce animal testing.

LaFollette and others point to advances that have already made animal replacement methods more effective. These next-generation NAMs include machine learning algorithms that can predict how drugs or other

chemicals will affect health based on their molecular structures, as well as 3D cell culture techniques such as organ chips and organoids—balls of stem cells that can be coaxed to form miniature organ models. Because these approaches use human data and human cells, they may be better stand-ins for people than animals are. Cell-based methods such as the DILI chip—collectively known as microphysiological systems (MPS)—"are reflecting the architecture and functionality of an organ," says Thomas Hartung, a pharmacologist at the Johns Hopkins Bloomberg School of Public Health.

Lured by this promise, dozens of companies have sprung up in recent years to develop such systems, and drugmakers have raced to adopt them. "At this point, I'm not aware of any large pharma company that's not working with MPS technologies or machine learning tools," says Szczepan Baran, a veterinarian and former animal compliance training officer at the pharmaceutical company Novartis.

Nevertheless, scientific, regulatory, and cultural hurdles still stand in the way of widespread acceptance. Academic scientists who have always studied a certain species are unlikely to quickly shift their methods. Many fear that one clinical trial gone wrong could set the entire NAM movement back, especially if it is driven by a premature switch to unvalidated technologies. And in an era of unprecedented threats to biomedical research, the funding to develop and validate the new methods is far from assured. "It's the science that has to drive it, but you have to invest in those tools for them to evolve," Baran says.

SINCE 1938, the year after more than 100 people died from an inadequately tested drug, FDA has required all drugs be tested in animals—usually two different species—before they can enter human trials. Animal testing has been considered so reliable that the agency has sometimes trusted in animal data alone to approve drugs in emergency situations (vaccines for smallpox and anthrax, for example). Historically, EPA has also relied on animals to determine whether chemicals, such as pesticides and the plastic component bisphenol A, are harmful enough to regulate.

But the limitations of animal testing have long been apparent. Some 90% of drugs that appear safe in preclinical testing end up failing in human trials, often because of unforeseen side effects. Researchers have suspected that in at least some of these cases, a disconnect between animal models and human physiology is to blame. To supplement animal testing, the U.S. government has long maintained a list of dozens of cell-based assays, in vitro tests, and models of human skin that certain agencies allow as supplements to animal testing for some products, such as pesticides and other chemicals.

A shift to greater use of NAMs is now gathering speed. In a major policy change, then-President Joe Biden's administration in 2022 removed FDA's long-standing requirement that all drugs must be tested in animals, although FDA did not issue a final rule to that effect. EPA has also tried to move away from animal testing, in fits and starts. In 2020, during Trump's first term, the agency said it would reduce testing in mammals by 30% by this year and eliminate it entirely by 2035. At the time, many scientists called this timeline too aggressive, worrying that evaluating compounds based only on NAM data would end up harming both humans and the environment, and EPA reversed its decision during Biden's administration.

But in April, EPA Administrator Lee Zeldin revived plans to phase out animal testing, telling *The Washington Times* the agency needed to "get back on track," although he hasn't reinstated the deadlines. The same day as Zeldin's announcement, FDA Commissioner Martin Makary said his agency would also move toward abandoning animal models, at least in some cases. Animals simply don't predict human reactions well, the agency said, especially in cancer, immunology, and brain diseases. "This initiative marks a paradigm shift in drug evaluation," Makary said in a statement. "It is a win-win for public health and ethics."

FDA says it will start "encouraging" companies to include NAM data when they apply for the agency's approval to test a new therapy in humans. Initially it will focus on therapies based on monoclonal antibodies, immune system proteins engineered to attack highly specific molecular targets. In a pilot program, FDA will allow select companies to rely primarily on NAMs to screen new monoclonal antibodies for human trials. "It's a very good choice because most [monoclonal antibodies] have no effect on animals," Hartung says. What's more, an antibody that appears safe in one species can cause a dangerous immune response in another, as happened in 2006, when a candidate drug for leukemia and rheumatoid arthritis called TGN1412 that appeared safe in mice and monkeys caused life-threatening autoimmune effects in every person who took it in a small trial.

Similarly, EPA already allows certain in vitro tests, such as assays that measure how human enzymes interact with chemicals, to be used when determining whether a compound is toxic. The agency is in the process of replacing the "six-pack" of animal tests it conducts for skin irritation, toxic inhalation, and other measures with NAM alternatives, such as skin samples reconstructed from human cells and statistical predictions based on human epidemiological data.

Now, NIH is joining the push for

Gaining momentum

Investment by the National Institutes of Health (NIH) in alternatives to animal research has increased steadily in recent years. Projects using nonanimal systems accounted for 1.1% of all new and renewed NIH research grants awarded in 2000 and grew to 8% in 2024.

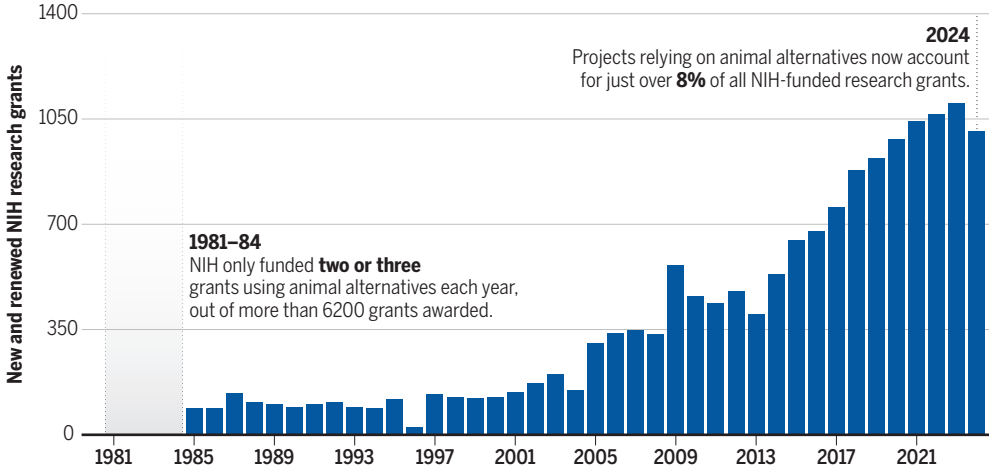

CREDITS: (GRAPHIC) V. PENNEY/*SCIENCE*; (DATA) NATIONAL INSTITUTES OF HEALTH ADVISORY COMMITTEE TO THE DIRECTOR WORKING GROUP ON HUMAN RESEARCH ALTERNATIVES AND ALTERNATIVES TO ANIMALS IN RESEARCH AND TESTING

A bone marrow organ chip contains all the types of immune and structural cells found in the real tissue, allowing it to be used to model diseases or study cells' reactions to drugs.

NAMs. Just days after the other agencies' announcements this spring, NIH announced it would create a new Office of Research Innovation, Validation, and Application to "expand funding and training in nonanimal approaches and awareness of their value" in turning basic research into treatments. The agency said the office will work with peer-review panels to address "animal bias" among grant reviewers who might favor work with the traditional model organisms they're familiar with, although it's not yet clear what this will involve. And on 7 July, NIH announced that calls for grant applications across the agency will emphasize NAMs.

The momentum is global. Early next year, the European Commission plans to release a road map for phasing out animal testing in chemical safety assessments, and the European Medicines Agency is considering whether to accept NAM data in decisions on clinical trials and drug approvals. The United Kingdom's Health and Safety Executive also declared that no pesticide testing "shall be conducted in vertebrate animals where validated alternative methods are available" and that animals should only be used "as a last resort" for skin and eye irritation tests. "There's definitely a drive to find better ways of doing the safety assessments across all sectors," says Fiona Sewell, head of toxicology at the U.K.'s National Centre for the Replacement, Refinement and Reduction of Animals in Research (NC3Rs), which aims to foster those technologies.

ORGANOIDS, organ chips, and other complex cell cultures are looking increasingly able to meet the challenge. Clive Roper, a toxicology consultant based in Edinburgh, Scotland, points to Emulate's DILI chip as a case in point. Even if the accuracy isn't perfect, the chip's results could help companies decide whether to push ahead with an expensive clinical program, he says—and gauge the risk to participants. Spotting DILI risks early "would have a massive impact on those patients who are going through clinical trials and getting sick," he says. In September 2024, FDA accepted Emulate's DILI chip as the first entry into its pilot program to fund NAMs for drug development.

Other companies are developing similar technologies. LaFollette says her organization is currently testing nine companies' liver models, including organoids and organ chips, by exposing them to a set of drugs known to either cause or not cause liver toxicity. They plan to submit the data to FDA to help the agency develop guidelines for NAMs. "It's going to hopefully build confidence, as well as highlight what sort of variability might be expected across the different platforms," she says.

Researchers envision many other kinds of chips, tailored to specific organs and diseases. A brain on a chip with neurons taken from a person with a neurodegenerative disorder, for instance, could show how the disease progresses and what therapies might slow it.

But no single NAM can fully capture the complexity of human biology. "We do not have replacements for all of [our] organs, especially how they work in coordination," LaFollette says. Instead, she says, future drug testing might involve combinations of MPS and artificial intelligence (AI) models, each representing a specific organ or a specific endpoint, such as toxicity to a developing fetal brain.

Although in vitro tests have already reduced animal use, some hope AI systems could become the new standard for toxicology testing. Trained on scientific publications and available toxicology data, their algorithms can look at a molecule's structure, determine which proteins and cellular products it is likely to interact with, and predict whether those interactions could be toxic to the human body.

Hartung's lab, for instance, has created an AI prediction tool called OPERA, which is trained on about 10 million known chemical structures

from a database called PubChem and information from dossiers submitted by companies to U.S. and EU regulators about the chemicals' properties and known health risks. By performing trillions of comparisons between the chemicals, the algorithm learned to predict how new chemicals would perform on nine tests traditionally done with animals, such as evaluations for eye irritation and genetic mutations. Its predictions aligned with animal test results 87% of the time—more often, Hartung says, than animal tests themselves can be reproduced. He says a newer version of the tool, which has not yet been published, was trained on 260 million data points and predicts 4000 properties of novel chemicals with 91% accuracy. Such insights could show whether the chemicals would cause liver toxicity or affect fetal brain development, for instance.

That accuracy could probably be improved even further with more data. "Our AI models are based on what we know, and there's so many unknowns," says Sally Thompson-Iritani, a veterinary scientist at the University of Washington and a member of the Interagency Coordinating Committee on the Validation of Alternative Methods, an independent panel that assesses NAMs across government agencies. Those include both gaps in scientific knowledge as well as data that pharmaceutical companies keep under lock and key, such as why past drug candidates have failed.

With the new push for NAMs, some companies are starting to open up their data troves. A Virtual Dog project funded by NC3Rs and seven major pharmaceutical companies, for instance, is developing a machine learning model designed to predict whether a given chemical would be toxic to a dog. The algorithm, which could be available in a few years, is being trained on the companies' proprietary data about how various compounds interact with dog tissues and organs. Its creators hope this "virtual second species" could eventually fulfill some countries' requirements for drug testing in two species, allowing human trials to be approved with only actual testing on rodents.

Baran and others say machine learning models are becoming de rigueur at many pharmaceutical companies. Such an approach can go beyond simply labeling compounds as toxic or nontoxic, as traditional animal tests do, Hartung says. "What science delivers is gray, not black and white." AI can capture that nuance, but Hartung notes its predictions still need to be validated. "I would not take a decision based on these systems yet."

Terry van Vleet, head of investigative toxicology and pathology at AbbVie, adds that animal models are still better at revealing health effects caused by the small molecule drugs that are a mainstay of medicine. Unlike a highly targeted monoclonal antibody, such molecules typically interact with six to 12 different targets and are broken down into smaller chemicals that interact with still more targets—a prediction challenge AI can't yet handle. "At this time, it is challenging to envision completely eliminating the need for animal testing," Van Vleet says.

THE RUSH to embrace NAMs worries some experts. Matthew Bailey, president of the National Association for Biomedical Research, which advocates for humane animal research, is especially skeptical of deadlines like those set by EPA. Not every physiological response can be simulated by AI and MPS technologies, he says. And he notes that research institutions already have systems in place to ensure that only necessary animal research is conducted. "I don't think there ever will be a situation where there's a magic bullet and we don't need animals for any reason anymore," he says.

The stakes of moving prematurely into clinical trials could be high. Thompson-Iritani notes that the 1999 death of a teenager in a gene therapy trial cast a pall over that entire field for decades. "If there's a bad outcome like that, and people can identify that that bad outcome is because we didn't test it in an animal model, that's going to set us back," she says.

Meanwhile, some Asian, European, and South American countries still require drugs be tested in animals, which could dissuade multinational companies from abandoning animals altogether. "If they know that one country will require animal testing, then they're going to do that," Thompson-Iritani says. But Sewell is hopeful these disconnects will disappear soon, because most countries follow FDA's lead. "These announcements are a really key signal to make a shift," she says.

For NAMs to move forward, education and training for the people who evaluate new drugs and chemicals will be key. "What I'm excited to see is [government agencies] really giving their staff the time and the support that they need to get familiar with and understand the methods," says Amy Clippinger, president of PETA Science Consortium International, noting that she has seen more employees from federal regulatory agencies attending meetings and publishing papers on NAMs in recent years.

Bailey, however, worries concerns about animal rights are eclipsing the scientific mission of NIH and other agencies. "Oftentimes people lose sight of what the real goals are supposed to be," he says. "Is the goal of the NIH to communicate to the public how few animals they're using in research, or to improve human health with new discoveries and new treatments?"

Roper says a consensus around the idea that NAMs are—or eventually will be—better models for human health will be far more effective at persuading researchers to abandon animal testing than an argument about the ethics of animal research. "When we focus on generating something to support human health, that objective is actually much easier to achieve," he says. "It becomes a scientific discussion." □

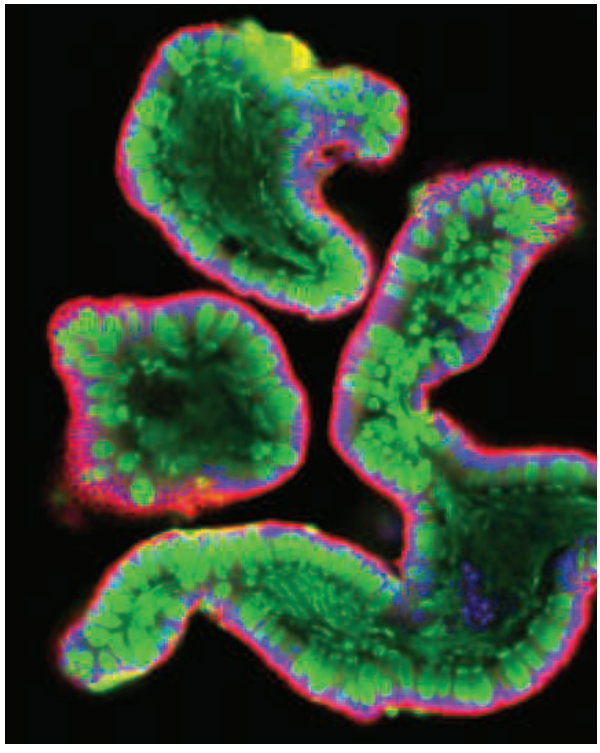

Organoids such as this mini-intestine can be grown from human stem cells, providing models of the full-size organ.

IMAGE: STEMCELL

Sara Reardon is a science journalist based in Cambridge, Massachusetts.

COMMENTARY

PERSPECTIVES

PLANT SCIENCE

The scent of a crowd

Maize plants recruit immunity-modulating soil microbes in response to high-density planting

Niklas Schandry *and* **Claude Becker**

Plants have evolved complex systems to perceive and integrate information about their environment, such as light intensity, nutrient availability, and attacks by pathogens. They also respond to the density of the local plant community, that is, the number of individuals growing per area. However, it remains unknown how density is perceived and translated into a physiological response. On page 698 of this issue, Guo *et al.* (*1*) report that linalool, a volatile compound that many plants release into the air, acts at the top of a density signaling cascade. Above a threshold concentration, linalool triggers a chemical response in the root of maize plants (*Zea mays*). This ultimately leads to alterations to the microbial community in the soil—the microbiome—which has a lasting effect on plant growth and defense. These findings could help develop plants specifically adapted to modern agriculture.

Plants respond not only to the presence of neighboring plants but also to the density and the relatedness of the surrounding vegetation (*2*, *3*). The canonical pathway for neighbor perception is through shading, which causes changes in the spectral composition of light reaching the plant. Neighbor proximity can also be conveyed through air- or soil-borne chemical signals that are released by plants. These compounds increase in concentration in high-density environments and can carry information not only on the presence but also on the physiological condition of neighboring plants (*4*).

Maximizing plant density is a hallmark of modern agriculture and has been a decisive factor in increasing food production over the past century (*5*). However, although high planting density generally increases yield, it also produces conditions that are favorable for pathogens and insect herbivores, such as caterpillars, which can spread more easily and in higher numbers when many (genetically identical) hosts are available and when air circulation is decreased and humidity is high. At higher density, plants tend to shift their resources from growth to defense to anticipate attacks by predators and herbivores. In the absence of an attack, however, putting up defenses comes at a cost with no benefits (*6*).

Guo *et al.* studied this fitness-defense trade-off in fields of maize (see the photo). In the inner section of the field (low airflow, more

In the center of a densely planted field of maize, the concentration of the signaling compound linalool in the air is high.

shading), plants grew smaller and were resistant to herbivore attack than those growing at the same density on the field outskirts (higher airflow, less shading). In controlled greenhouse experiments, the authors observed what is known as plant-soil feedback: Plants growing in soil from prior high-density planting showed decreased biomass but increased defenses against pathogens, viruses, and above- and below-ground herbivores. By combining chemical with physiological and genetic analyses, the authors reconstituted the chain of events that translates plant density into long-term plant-soil feedback. They identified the leaf volatile linalool as the first signal: Its release is constitutive, and therefore its concentration in low-airflow conditions correlates with plant density. Once linalool reached a certain threshold concentration in the air, it caused the maize to increase production of the hormone jasmonate, which in turn led to higher exudation of another class of specialized metabolites, benzoxazinoids, from maize roots into the soil.

Benzoxazinoids are multifunctional compounds in many grass species, including major crops such as wheat and maize. They act as herbivore repellents (*7*), prevent growth of other nearby plants (*8*), and improve iron uptake from soil (*9*). Notably, benzoxazinoid exudation also results in lasting changes to the soil microbiome. In a previous study, maize plants grown in soil that had initially been used to grow benzoxazinoid-producing maize showed stronger defenses and less growth than plants grown in soil collected from benzoxazinoid-deficient maize. These changes were not directly linked with the effect of the chemical composition of the soil on the plant but with the effects of benzoxazinoids on the soil microbiome (*10*).

In line with these reports, Guo *et al.* found that linalool-triggered benzoxazinoid release from maize plants altered the composition of the soil microbiome, which influenced the next generation of plants to grow in that soil.

Most surprising was the speed at which the effects mediated by the linalool-jasmonate-benzoxazinoid cascade set in: After only 3 days of growth in high-density conditions, Guo *et al.* detected increased defense against caterpillars on maize subsequently planted in that soil. Plants thus act as efficient relays that translate volatile above-ground signals into soil-borne below-ground signals through jasmonate signaling. The finding also demonstrates that microbial communities can change rapidly and lastingly in response to the plant-derived chemical triggers and that, ultimately, what causes the fitness-defense trade-off response of the plant to high-density planting resides in the soil microbiome, not in the originally perceived linalool signal.

Although benzoxazinoid-dependent plant-soil feedback is well described phenomenologically, the molecular mechanisms that drive the restructuring of the microbiome remain unknown. Benzoxazinoids exist in different forms in the plant and can be further modified upon exudation into the soil and contact with the root and soil microbiomes, which contributes to the molecular complexity of plant-soil feedback (*11*). Conversely, how microbiome restructuring results in increased defenses in the perceiving plants remains to be resolved. Preliminary findings from two recent studies on benzoxazinoid-mediated plant-soil feedback in the non–benzoxazinoid-producing model species *Arabidopsis thaliana* have provided some initial indications of a role for plant immune receptors in this process (*12*, *13*).

The research presented by Guo *et al.* highlights the importance of balancing defense and growth in response to a combination of environmental factors, in this case, neighbor density and the associated higher risk of infection and herbivory. This bet-hedging by the plant has implications for agriculture, because high-density planting, despite its inherent risks, generally results in higher yield (*5*). Linalool production could therefore be a promising breeding target: Plants with higher baseline linalool production might be better suited for dense growth in areas with a higher risk of pathogen or herbivore attacks because they would allocate more resources into primed defenses. Conversely, low linalool production would allow higher resource allocation for growth and seed production when pathogen and herbivore pressures are low. Extensive field trials with different crop genotypes and in different field settings will be necessary before these findings can be translated into targeted guidelines for agricultural practices. □

REFERENCES AND NOTES

1. D. Guo *et al.*, *Science* **389**, eadv6675 (2025).
2. R. Zhang, K. Tielbörger, *Nat. Commun.* **11**, 2532 (2020).
3. C. Becker *et al.*, *Trends Plant Sci.* **28**, 31 (2023).
4. L. Hu, *New Phytol.* **233**, 618 (2022).
5. J. Deng *et al.*, *Proc. Natl. Acad. Sci. U.S.A.* **109**, 15823 (2012).
6. Z. He, S. Webster, S. Y. He, *Curr. Biol.* **32**, R634 (2022).
7. L. Hu *et al.*, *Proc. Natl. Acad. Sci. U.S.A.* **118**, e2109602118 (2021).
8. S. Venturelli *et al.*, *Plant Cell* **27**, 3175 (2015).
9. L. Hu *et al.*, *Science* **361**, 694 (2018).
10. L. Hu *et al.*, *Nat. Commun.* **9**, 2738 (2018).
11. L. Thoenen *et al.*, *Nat. Commun.* **15**, 6535 (2024).
12. H. Janse van Rensburg *et al.*, bioRxiv 10.1101/2025.02.25.640125 (2025).
13. K. Stengele *et al.*, bioRxiv 10.1101/2024.10.21.619081 (2024).

ACKNOWLEDGMENTS

The authors acknowledge support from the Ludwig-Maximilians-Universität München and from the Deutsche Forschungsgemeinschaft (DFG) in the frame of TRR356 project A05 (project no. 491090170 to N.S.).

10.1126/science.adz7633

LMU Biocenter, Faculty of Biology, Ludwig-Maximilians-Universität München, Munich, Germany. Email: claude.becker@lmu.de

PHYSICS

Seeing with atoms

A beam of neutral atoms penetrates a solid material to probe its properties **Bodil Holst**

Throughout history, new scientific methods have led to breakthroughs that themselves have contributed to further technological development and progress. Indeed, this has been the case for techniques that enable the diffraction of x-rays, photons, subatomic particles, and atoms by crystalline materials. The evolution of these approaches has underpinned fundamental discoveries in the physical and chemical properties of materials, up to the nanoscale. On page 724 of this issue, Kanitz *et al.* (*1*) report another advance in the field—a new method that diffracts neutral atoms through a solid material. Until now, the transmission and diffraction of atoms through the inside (bulk) of materials have been elusive. The advance paves the way for direct probing of the outermost electron density distribution of crystalline materials, which is critical for understanding of, for example, superconductivity.

The diffraction of subatomic particles (electrons and neutrons) has been a powerful means to explore the surface and bulk of matter. These technologies provide high-resolution information at the atomic level. However, the physical dimensions of these particles are very small, and the interaction is mainly with the atom core. In the experiments of Kanitz *et al.*, the atom in its entirety is used where dominating interaction is with the outermost electrons of a material. This corroborates the notion that electrons probe the "bones" of a material and atoms probe the "skin."

Kanitz *et al.* break new ground by demonstrating the diffraction of neutral atoms that have penetrated a material. The authors sent either helium or hydrogen through a sheet of graphene—a one-atom-thick layer of carbon atoms arranged in a hexagonal lattice (commonly referred to as a honeycomb structure). The extreme thinness of graphene makes it a suitable choice for the first demonstration experiment of transmission atom diffraction. The energy of the atoms was increased to a point at which they would penetrate the material rather than being reflected (the way low-energy atoms that are used for surface diffraction studies would). In the experiment, each helium or hydrogen atom behaves as a matter wave that can interfere with itself. The wavelike nature of the atom allows it to explore multiple paths at the same time, and the wave paths interfere with each other. This creates a diffraction pattern as the atom "goes through" several openings in the honeycomb simultaneously. In principle, this is a similar process to transmission diffraction of subatomic particles through a crystalline material, but with atoms.

Transmission diffraction experiments with neutral matter waves have been performed previously to explore the wave nature of matter. The most famous experiment was conducted in 1999 when a beam of C60 molecules was sent through a 100-nm period diffraction grating made of silicon nitride to obtain a diffraction pattern (*2*). Later, a diffraction grating of roughly the same period was made by carving slits into graphene and used to diffract phthalocyanin molecules (*3*). The big difference and breakthrough achieved by Kanitz *et al.* is that they suceeded in performing diffraction directly through a solid material. This was possible because the neutral atom beams were tuned by using an elegant ionization-acceleration-deionization configuration, which was developed originally for grazing incidence surface scattering experiments (*4, 5*). This multistep technique takes advantage of the ability to easily manipulate charged particles with electric fields, as compared with neutral atoms. The generated ions are accelerated to a desired kinetic energy, followed by a step to neutralize the ions into energetic atoms. The authors thus obtained coherent beams with an energy that is large enough to penetrate the openings of the graphene honeycomb structure while keeping a wavelength long enough that they could resolve a diffraction pattern (the higher the energy of a matter wave, the smaller the wavelength according to the de Broglie equation).

So why is this such an important scientific advance? Nature, despite all its variety, has only a limited number of ways in which beams of subatomic particles, atoms, molecules, or photons can interact with solid materials so that their wave properties are exploited in imaging and sensing. Consider the techniques of diffraction, microscopy, and interferometry. Transmission and reflection diffraction and microscopy that use light, electrons, or ions, as well as neutral atom reflection diffraction, are all established experimental techniques. Neutral atom reflection microscopy is under development (*6*). Collectively, these methods in their many configurations make up an incredibly versatile set of tools with applications that extend from biological to material sciences.

The method demonstrated by Kanitz *et al.* is one of the last missing pieces of this powerful arsenal: transmission diffraction of neutral atoms. This may eventually lead to the development of the atom transmission microscope, which could be a new tool for investigation of, for example, the influence of defects on the outermost electron density distribution. In addition, transmission atom diffraction could be used not only as a sensitive probe of the outermost electron density distribution of materials but also to obtain further information about how this electron density distribution responds to perturbations by conducting systematic measurements with different energies of the incident atom beam and changing the interaction of the beam with the sample. Sample preparation will be a challenge because the material needs to be so thin that the atoms can penetrate with an energy (wavelength) that allows the diffraction pattern to be resolved. Thus, potential areas of investigation could include lipid membranes and two-dimensional porous protein crystals.

Kanitz *et al.* also discuss potential applications of transmission diffraction of neutral atoms in interferometry. A large momentum transfer between the atoms and the crystalline sample can be obtained because the crystalline sample (such as graphene) has such a small lattice constant (short distance between atoms). However, an equally small lattice constant can also be achieved by reflection diffraction of neutral atoms from a crystalline surface. A monolithic interferometer configuration based on this idea was recently proposed (*7*). Thus, the potential for new interferometry experiments seems less compelling than the potential material science applications and remains to be seen.

Lord Kelvin is credited with the quote, "You only know what you can measure." Kanitz *et al.* have provided the world with a new way to measure. Now it is up to the scientific community to formulate research questions and exploit this new tool. □

REFERENCES AND NOTES

1. C. Kanitz *et al.*, *Science* **389**, 724 (2025).
2. M. Arndt *et al.*, *Nature* **401**, 680 (1999).
3. C. Brand *et al.*, *Nat. Nanotechnol.* **10**, 845 (2015).
4. P. Rousseau, H. Khemliche, A. G. Borisov, P. Roncin, *Phys. Rev. Lett.* **98**, 016104 (2007).
5. A. Schüller, S. Wethekam, H. Winter, *Phys. Rev. Lett.* **98**, 016103 (2007).
6. A. S. Palau, S. D. Eder, G. Bracco, B. Holst, *Ultramicroscopy* **251**, 113753 (2023).
7. J. Fiedler, K. Lefmann, W. von Klitzing, B. Holst, *Phys. Rev. A* **108**, 023306 (2023).

10.1126/science.adz7660

Department of Physics and Technology, University of Bergen, Bergen, Norway.
Email: bodil.holst@uib.no

Check for

CANCER

The ins and outs of circulating DNA

DNA sequestered in circulating platelets could inform early tumor diagnosis

W. H. Adrian Tsui[1,2,3] and Y. M. Dennis Lo[1,2,3,4]

Circulating DNA refers to fragmented DNA molecules found in bodily fluids such as blood plasma. These fragments arise from the breakdown of nucleated cells through programmed cell death (apoptosis), necrosis, and active release. Over the past three decades, diagnostics relying on circulating DNA have moved to the forefront of minimally invasive liquid biopsies for cancer detection, prenatal testing, and monitoring of graft rejection (*1*). Early approaches used the analysis of genetic variants to identify circulating DNA of tumor, fetal, or donor origin. However, the proportion of fragments in the plasma that harbor these informative genetic markers is often small. Thus, much emphasis has been placed on characterizing new features and populations of circulating DNA to maximize its clinical utility. On page 702 of this issue, Murphy *et al.* (*2*) report that some circulating DNA is sequestered within platelets. This source could improve sensitivity in monitoring for genetic abnormalities across tissues.

Platelets are small, anucleate cell fragments derived from the cytoplasm of bone marrow megakaryocytes and are a constituent of circulating blood. They are classically considered mediators of vascular homeostasis and maintenance. Platelets also internalize nucleic acids and viral particles, and trigger inflammatory responses to microbial infection through nucleic acid–sensing receptors (Toll-like receptors 7 and 9) (*3*). It also has been proposed that "tumor-educated" platelets harbor cancer cell–derived mRNA and proteins and can associate with circulating tumor cells (*4*). To determine whether platelets might also capture circulating DNA, Murphy *et al.* used fluorescence in situ hybridization to show that platelets from human mothers harboring male fetuses—a classic model system (*5*)—contain Y chromosome–derived DNA, likely picked up in the placenta. After inducing acute depletion of platelets in mice using anti-platelet antibodies, the authors found that the concentration of circulating DNA in plasma increased, suggesting a potential new role for platelets as a sink for circulating DNA. However, whether circulating DNA concentration correlates with platelet count under normal hemostatic conditions remains an unanswered question.

There is a variety of DNA molecules in circulating blood. These can be ultrashort (~50 bases) single- or double-stranded (*6*, *7*), long (>500 bases) (*8*), histone-bound (*9*), or encapsulated within extracellular vesicles (*10*). Murphy *et al.* designed a series of in vitro experiments to assess whether platelets can capture circulating DNA molecules of different properties. By coincubating platelets with live cells, DNA-loaded vesicles, or synthetic naked DNA fragments of varying sizes [but lacking binding proteins (histones)], the authors showed that platelets could internalize histone-bound DNA, extracellular vesicles, and naked DNA of 128 to 657 base pairs in length (see the figure). Newly captured platelet DNA proved resistant to degradation by nucleases added in vitro. These observations suggest that platelet DNA may also be protected from nuclease activity in the blood, and that platelet DNA may exhibit fragmentation patterns distinct from those of DNA circulating in plasma (the liquid component of blood). For example, the latter exhibits a characteristic DNA end motif (a 5′-CC preference; C is cytosine) that reflects the involvement of deoxyribonuclease 1–like 3, whereas the end motif is different in newly generated circulating DNA (*11*), and potentially in platelet DNA as well. Apart from nucleases, there are at least two other pathways for clearing circulating DNA: passive filtration into the urine in the kidney, and active uptake by macrophages of the reticuloendothelial system, immune cells that remove cellular debris and foreign matter from the bloodstream and tissues (*12*). Intuitively, platelet DNA might be protected from clearance through a transrenal route, as platelets should be too large to traverse a healthy glomerular barrier in the kidney to exit the body in urine. However, because old platelets are removed by resident macrophages in the liver and spleen, their DNA content might be cleared in the same way. The specific effects that platelet capture of circulating DNA has on these pathways is worth exploring.

If platelets sequester circulating DNA under normal hemostatic conditions, it is possible that tumor-derived DNA could be enriched in platelets relative to the plasma, where such potential cancer signals are often hugely diluted by the background circulating DNA, especially in patients with early-stage tumors. Accordingly, Murphy *et al.* found that in colorectal carcinoma mouse models and human patients with premalignant colon lesions, cancer-associated mutant alleles were sometimes more abundant in copy number in platelet DNA than in plasma DNA. This valuable in-

Platelets as carriers of circulating DNA

Different populations of DNA circulating in the blood have distinct structural properties, biological features, and potential clinical applications. Platelets can internalize histone-bound DNA, DNA contained in extracellular vesicles, and naked DNA. DNA released from cancer cells can also be detected in the DNA sequestered by platelets. Increasing the amount of DNA in platelets for diagnostic purposes can be achieved with inhibitors of platelet activation such as aspirin and the small molecule ibrutinib.

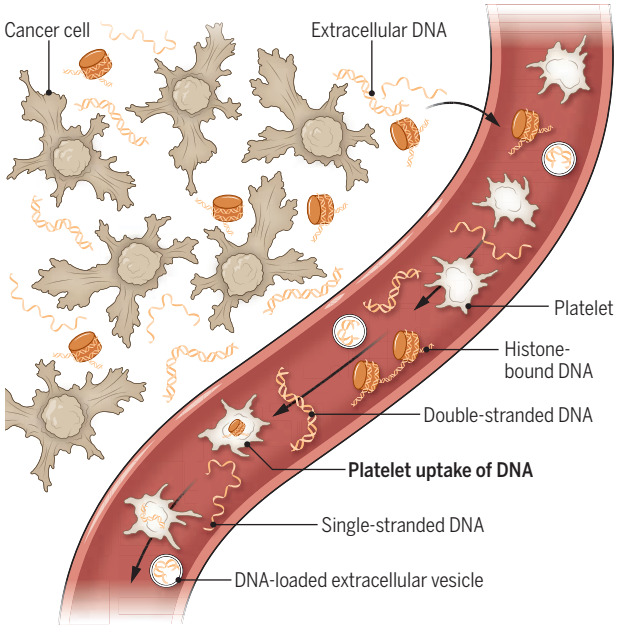

Circulating DNA-based cancer assays

Plasma DNA liquid biopsies
Isolating plasma from blood is a minimally invasive approach for detecing cancer, prenatal testing, and monitoring graft rejection.

Platelet DNA liquid biopsies
Platelets obtained from purified plasma, apheresis, or cell sorting may improve the sensitivity for detecting circulating DNA.

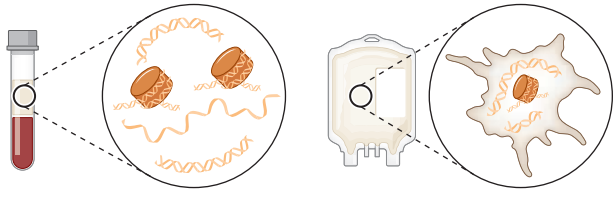

GRAPHIC: A. FISHER/*SCIENCE*

formation would likely have been overlooked by standard circulating DNA analysis protocols, which only analyze the plasma contents and not that of platelets. Nevertheless, whether combining plasma with platelet DNA analysis confers diagnostic advantages remains to be seen.

One potential approach to increase the recovery of circulating tumor DNA in the blood is by transiently inhibiting circulating DNA clearance. For example, the use of liposome- and antibody-based "priming agents" has been proposed to block liver macrophage uptake and nuclease degradation, respectively (*13*), and hence potentially increase the sensitivity of liquid biopsy. Similarly, Murphy *et al.* surveyed a variety of drugs that could modulate platelet activation and its cargo trafficking. Blocking platelet activation with aspirin and ibrutinib (a small-molecule drug used to treat B cell cancers) led to an increase in DNA sequestered in platelets, which also supports the hypothesis that platelet activation is associated with DNA release from platelets. Whether aspirin and other antiplatelet drugs, which are widely used to treat and prevent ischemic heart diseases, affect the circulating DNA concentration and thus the performance of liquid biopsies is an open question.

Although Murphy *et al.* did not investigate the relative superiority of platelet versus plasma DNA for detecting cancer-derived variants, their study raises interesting questions, with potential biological and clinical implications for liquid biopsies, many of which relate to the mechanistic underpinnings of circulating DNA clearance. Addressing these fundamental issues and evaluating potential platelet DNA–based cancer detection approaches in larger multicenter studies should yield some answers. □

REFERENCES AND NOTES

1. Y. M. D. Lo, D. S. C. Han, P. Jiang, R. W. K. Chiu, *Science* **372**, eaaw3616 (2021).
2. L. Murphy *et al.*, *Science* **389**, eadp3971 (2025).
3. Y. Tian *et al.*, *Signal Transduct. Target. Ther.* **10**, 159 (2025).
4. S. G. J. G. In 't Veld, T. Wurdinger, *Blood* **133**, 2359 (2019).
5. Y. M. D. Lo *et al.*, *Lancet* **350**, 485 (1997).
6. I. Hudecova *et al.*, *Genome Res.* **32**, 215 (2022).
7. J. Müller *et al.*, *Genome Res.* **34**, 1185 (2024).
8. S. C. Y. Yu *et al.*, *Proc. Natl. Acad. Sci. U.S.A.* **118**, e2114937118 (2021).
9. R. Sadeh *et al.*, *Nat. Biotechnol.* **39**, 586 (2021).
10. E. Z. Malkin, S. V. Bratman, *Cell Death Dis.* **11**, 584 (2020).
11. D. S. C. Han *et al.*, *Am. J. Hum. Genet.* **106**, 202 (2020).
12. D. S. C. Han, Y. M. D. Lo, *Trends Genet.* **37**, 758 (2021).
13. C. Martin-Alonso *et al.*, *Science* **383**, eadf2341 (2024).

ACKNOWLEDGMENTS

The authors acknowledge support from the Innovation and Technology Fund under the InnoHK Initiative from the Hong Kong Special Administrative Region Government, and from the State Key Laboratory of Translational Oncology with the Innovation and Technology Commission. Y.M.D.L. acknowledges support from the Li Ka Shing Foundation. Y.M.D.L. holds equities in DRA, Take2, and Insighta and receives patent royalties from Grail, Illumina, LabCorp, DRA, Take2, Insighta, and Xcelom.

10.1126/science.aea0555

[1]Centre for Novostics, Hong Kong Science Park, Pak Shek Kok, New Territories, Hong Kong SAR, China. [2]Li Ka Shing Institute of Health Sciences, The Chinese University of Hong Kong, Shatin, New Territories, Hong Kong SAR, China. [3]Department of Chemical Pathology, The Chinese University of Hong Kong, Shatin, New Territories, Hong Kong SAR, China. [4]State Key Laboratory of Translational Oncology, The Chinese University of Hong Kong, Shatin, New Territories, Hong Kong SAR, China. Email: loym@cuhk.edu.hk

IMMUNOLOGY

Setting the table for immune tolerance

Interaction between breast milk antibodies and gut microbes shape immune responses during weaning

Michael Silverman[1,2] and **Kathryn Knoop**[3]

From birth, newborn babies become colonized with trillions of microbes, creating the daunting challenge of rapidly and accurately discerning which ones are beneficial or harmful for human health. Neonates must develop tolerance to beneficial or commensal microbiota while mounting effective immune responses against pathogens. Maternal antibodies transferred in utero and through breast milk have roles in protecting newborns from pathogenic microbes, yet whether they shape other immunological responses has been unclear. On page 703 of this issue, Shenoy *et al.* (*1*) report that during the first week of life, immunoglobulin G (IgG) antibodies in maternal milk of mice interact with nonpathogenic members of the mouse microbiota to regulate immune responses in pups to microbial and dietary antigens in the gut encountered later during the weaning transition to solid food. Providing microbiota-reactive maternal antibodies could potentially prevent human infants from developing colitis, as well as dangerous allergic responses to food antigens.

Newborn mice lacking maternal antibodies were previously shown to develop increased amounts of an activated immune cell population in the gut called T follicular helper cells (T_{FH} cells) (*2*). These cells are important for the development of high-quality antibody responses to vaccination and to pathogenic and nonpathogenic microbes. To investigate how maternal antibodies affect early-life immune development in mice, Shenoy *et al.* used antibody-sufficient and antibody-deficient females bred with wild-type males. By cross-fostering the offspring at different ages to control the timing of exposure to maternal antibodies, the authors discovered that the first week of life is a crucial period during which maternal antibodies restrain the development of T_{FH} cells. In addition, the authors demonstrate that this depends on the binding of maternal IgG antibodies to nonpathogenic microbes in the gut to form immune complexes specifically during this developmental window. Mechanistically, these IgG-microbe complexes are sensed by the neonatal immune system through Fc gamma chain receptors and antibody-dependent complement activation, which ultimately restrain T_{FH} cells.

The ingestion of milk-derived IgA but not IgG during this early life developmental window in mice establishes a homeostatic amount of peripheral regulatory T cells in the gut (*3*). These cells suppress excessive inflammatory responses in the gut. Thus, exposure to different classes of maternally derived antibody can shape distinct aspects of immune development. Furthermore, early cessation of breastfeeding in humans correlates with an increased risk of developing asthma later in life, suggesting that the benefits of maternal antibodies in breast milk go beyond dietary antigens (*4*). Taken together, these studies provide compelling evidence that the ingestion of maternal antibodies in milk is a crucial regulatory mechanism during the neonatal window of immune development.

Weaning provides a second window of immune system development in mammals because the transition from milk to solid food brings the new challenge of developing tolerance to a wide range of food antigens and to a dramatically diversified gut microbiota (*5*, *6*). Disrupting the gut microbiome with antibiotics during weaning, or interfering with the ability of the immune system to detect gut

microbes during this period, has long-term effects on immune homeostasis in mice, including decreased tolerance of gut microbes and increased susceptibility to colitis later in life (*7*, *8*). Similarly, colonization of the intestine by a defined consortium of early-life microbes can suppress autoimmunity in diabetes-susceptible mice, albeit only if the mice are colonized with these species before weaning (*9*). Thus, microbes present in the gut at weaning, and the corresponding immune cells that interact with them, represent distinct components that are both crucial for the development of a healthy immune system during this second age-dependent window (*10*).

It is conceivable that maternal antibodies are required to "set the table" in the first developmental window by shaping the immune responses in a manner that readies the immune system for the blitz of new dietary and microbial antigens that come with weaning. In support of this notion, Shenoy *et al.* showed that exposure of newborn mice to maternal IgG was associated with decreased diet-specific IgE antibodies, suggesting that maternal IgG complexed to nonpathogenic gut microbes can regulate responses to food antigens. Similarly, complexes of maternal IgG and dietary antigens can induce long-term tolerance toward dietary antigens through the activation of regulatory T cells (*11*, *12*). The distinct complexes of IgG-bacteria and IgG–dietary antigen could together limit T_{FH} cells and promote tolerance to solid foods and the changing microbiota.

Shenoy *et al.* provide a mechanistic basis for how maternal IgG antibodies in milk can shape the immune system in mice during a discrete developmental window to tune the immune responses to foreign antigens. How do the findings relate to host-microbe interactions in humans? In contrast to mice, humans have much more IgA than IgG in breast milk (*13*). Because IgA does not engage the complement system, it is unclear whether this mechanism would be applicable to humans. Alternatively, because even low concentrations of IgG-microbe immune complexes can trigger immune responses, boosting the amount of specific IgG in maternal milk by exposing, or potentially immunizing, mothers to specific antigens could promote tolerance of gut microbes and dietary antigens in infants. Translating these findings to human infants will require studies that integrate information on the timing of exposure to maternal antibodies and on the development of key immune components and intestinal microbiota. This could improve the immune system trajectories in infants and children as well as lead to therapies that prevent immune-mediated diseases. □

REFERENCES AND NOTES

1. M. K. Shenoy *et al.*, *Science* **389**, eado5294 (2025).
2. M. A. Koch *et al.*, *Cell* **165**, 827 (2016).
3. D. Ramanan *et al.*, *Cell* **181**, 1276 (2020).
4. L. Shenhav *et al.*, *Cell* **187**, 5431 (2024).
5. N. Torow, T. W. Hand, M. W. Hornef, *Immunity* **56**, 485 (2023).
6. T. R. Cheifetz, K. A. Knoop, *Immunol. Rev.* **326**, 17 (2024).
7. Z. Al Nabhani *et al.*, *Immunity* **50**, 1276 (2019).
8. K. A. Knoop *et al.*, *Sci. Immunol.* **2**, eaao1314 (2017).
9. J. Green *et al.*, bioRxiv 580579 [Preprint] (2024); https://doi.org/10.1101/2024.02.15.580579.
10. J. A. Brown, H. Bashir, M. Y. Zeng, *Mucosal Immunol.* **18**, 509 (2025).
11. A. Ohsaki *et al.*, *J. Exp. Med.* **215**, 91 (2018).
12. E. Mosconi *et al.*, *Mucosal Immunol.* **3**, 461 (2010).
13. K. Donald, C. Petersen, S. E. Turvey, B. B. Finlay, M. B. Azad, *Cell Host Microbe* **30**, 650 (2022).

ACKNOWLEDGMENTS

The authors thank L. Eisenlohr for discussions. M.S. acknowledges support from the National Institutes of Health (R01DK133453) and Breakthrough T1D (CDA-2020-946-S-B).

10.1126/science.adz8687

[1]Division of Infectious Diseases, Children's Hospital of Philadelphia, Philadelphia, PA, USA. [2]Perelman School of Medicine, University of Pennsylvania, Philadelphia, PA, USA. [3]Department of Immunology, Mayo Clinic, Rochester, MN, USA. Email: silvermam1@chop.edu

MICROBIOLOGY

Mitochondria hoard folate to starve a parasite

Metabolic immunity contributes to cells' defenses against *Toxoplasma gondii*

Anu Suomalainen[1,2,3] and **Joni Nikkanen**[4]

Toxoplasma gondii is a common human parasite—30 to 50% of the world population have been infected at some point in their lives. Although most infections are asymptomatic, in pregnant individuals, transmission of the parasite can cause fetal death. Additionally, immunocompromised individuals, such as those living with an organ transplant or HIV infection, can develop severe symptoms. Mechanistic understanding of *Toxoplasma*-host interaction is essential for developing targeted therapies for this global health concern (*1*). On page 701 of this issue, Medeiros *et al.* (*2*) report that the mitochondria in the host cell sense *T. gondii* infection and initiate a cascade of protective metabolic stress responses. One of the main effectors of these responses is folate, also known as vitamin B9, which is needed to synthesize nucleotides, the building blocks of DNA. The findings suggest that the host cell siphons folate into mitochondria, restricting parasites' access to nucleotides, thereby slowing down the infection.

Over the course of evolution, the constant push and pull between host cells and *T. gondii* has sculpted host metabolism to help eliminate the pathogen (see the photo), giving rise to metabolic immunity (*3*). In this process, the host limits the pathogen's access to nutrients to restrict pathogen growth. Alternatively, the host can increase the amounts of metabolites to cause damage to the invading pathogen (*3*). Together, these strategies rewire host metabolism to eradicate or stall the growth of the parasite. Mitochondria are cellular organelles that are essential, versatile contributors to metabolism in living organisms. Early in evolution, these organelles were independent bacteria, then potentially intracellular parasites, which eventually shifted in allegiance to favor collaboration (endosymbiosis) over competition with the host. Mitochondria transform nutrient energy into cellular energy—adenosine triphosphate—and contribute to a wide range of biosynthetic reactions for cellular growth and repair. Furthermore, increasing evidence indicates that mitochondria have essential roles in immunity and host defense mechanisms (*4*). For example, the mitochondrial outer membrane serves as a signaling platform for antiviral pathways, and the organelle can release nucleic acids to the cytoplasm to enhance antiviral immunity (*4*).

The study by Medeiros *et al.* explores how immune signaling integrates with mitochondrial responses to shape metabolic immunity. The authors show that infection with *T. gondii* initiates a signaling cascade in the host cell that involves the mitochondria and culminates in the activation of the mitochondrial integrated stress response (ISR).

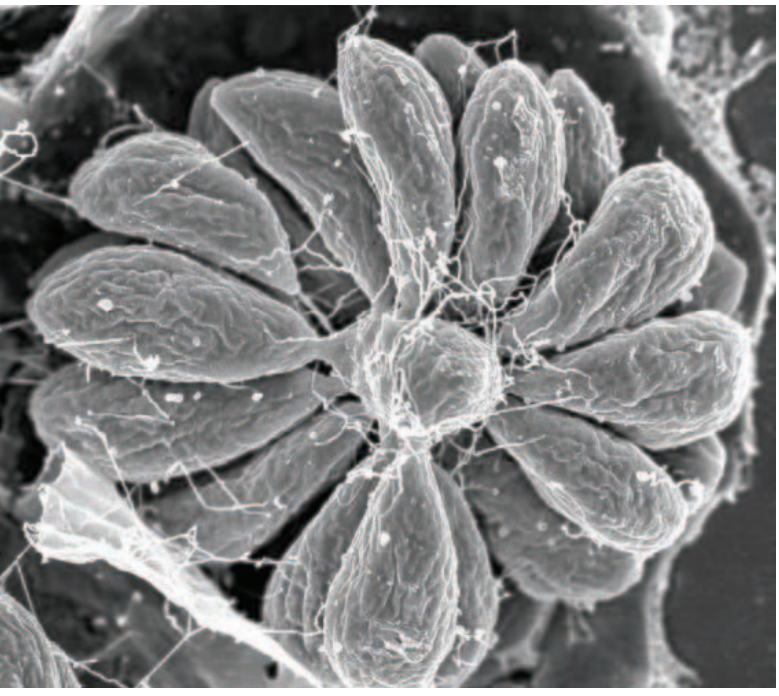

The parasite *Toxoplasma gondii* lives and replicates in host cells, forming rosette-like structures.

Mitochondrial ISR is initiated by mitochondrial stress and involves activation of transcription programs in the nucleus and remodeling of the metabolome that together promote anabolic repair and growth pathways (*5*). Medeiros *et al.* report that in response to *T. gondii* infection, OMA1 (overlapping activity with m-AAA protease 1), a mitochondrial inner membrane protease, is activated by mitochondiral membrane stress (*6*) and cleaves the effector molecule DELE1 (DAP3-binding cell death enhancer 1) (*7*), leading to transcriptional activation of ISR genes (*8*). In theory, the parasite residing in the host cytosol could cause stress in the endoplasmic reticulum or other cellular compartments, initiating the ISR. However, when Medeiros *et al.* abolished OMA1 expression, ISR activation by *T. gondii* was blunted, demonstrating that the stress signal came from mitochondria. Mitochondrial ISR is a well-known response in mammals, induced especially in the context of mitochondrial DNA expression defects (*5*, *8*–*11*). Therefore, the observations of Medeiros *et al.* indicate that *T. gondii* infection produces a conserved stress response, which is similar to that induced by primary mitochondrial DNA expression defects.

A key feature of ISR is up-regulation of activating transcription factors (ATFs) (*12*). Medeiros *et al.* report that the ISR triggered by *T. gondii* resulted in activation of ATF4. Experimental inhibition of ATF4 in cultured cells or in living mice favored *T. gondii* replication, indicating that ATF4 activity is protective for the host. To understand more about how ATF4 might be having this protective effect, the authors explored the genes that are regulated by ATFs and are involved in the mitochondrial ISR (*5*, *8*–*11*) and identified mitochondrial folate metabolism as a potential effector. Most organisms obtain folate from the diet. This folate is then modified within organs to generate different forms that facilitate the transfer of glucose-derived one-carbon units that are used for the synthesis of amino acids, glutathione, creatine, and phospholipids (*13*). Notably, the synthesis of nucleotides also relies on folate metabolism, and *T. gondii* needs to synthesize nucleotides for DNA replication. Medeiros *et al.* introduced serine labeled with deuterium (a heavy isotope of hydrogen) into uninfected cells and those infected with *T. gondii*. When examining the incorporation of deuterium into cellular metabolites, the authors found low amounts of thymidine labeling, suggesting that the host cells inhibited synthesis of thymidine (a nucleoside). They speculate that the host cells activate mitochondrial folate metabolism to sequester folate in mitochondria and deplete the cytoplasmic folate pools, which decreases folate-dependent thymidine synthesis and restricts parasite growth. The authors show that pathogen burden increases after exogenous folate addition, indicating that folate can promote pathogen growth. Experiments that involve measuring the amount of folates in cytosolic and mitochondrial compartments and modifying the mitochondrial folate pathway will further clarify the mechanisms that link mitochondrial ISR, folate metabolism, and parasite growth.

Previous studies have identified roles for mitochondria in cellular defense against *T. gondii*. For example, infection with *T. gondii* causes shedding of the mitochondrial outer membrane, which depletes anti-inflammatory components that reside on that membrane and benefits the parasite (*14*). *T. gondii* infection also increases the fusion of mitochondria, thus limiting the parasite's access to fatty acids and protecting the host (*15*). This observation is particularly relevant to the findings of Medeiros *et al.* because it supports the concept that the cell siphons metabolites to the mitochondria to prevent the parasite from accessing them. The two observations might also be mechanistically linked: A reduction in cytoplasmic folate forms would decrease both nucleotide synthesis and phospholipid synthesis, with the latter altering membrane dynamics and lipid metabolism.

Modifying folate metabolism is an optimal choice for an antipathogen metabolic response because folate is required for the major biosynthesis reactions in all cells—both in the host and the parasite. The mitochondrial capacity to secure essential growth components may have been a major benefit for host survival during parasite infection and an important benefit in evolution. Mitochondria are emerging as frontline guardians of precious metabolites during infection, but whether the purpose of siphoning these metabolites is to secure mitochondrial fitness during cellular stress remains to be explored. The findings of Medeiros *et al.* raise folate metabolism as an interesting target to treat *T. gondii* infection. Notably, the mechanisms of host immunity against *T. gondii* are likely to be shared by an array of parasitic infections. □

REFERENCES AND NOTES

1. P. R. Torgerson, P. Mastroiacovo, *Bull. World Health Organ.* **91**, 501 (2013).
2. T. C. Medeiros *et al.*, *Science* **389**, eadr6326 (2025).
3. S. Kreimendahl, L. Pernas, *Trends Cell Biol.* **34**, 496 (2024).
4. L. E. Newman, G. S. Shadel, *Annu. Rev. Biochem.* **92**, 299 (2023).
5. J. Nikkanen *et al.*, *Cell Metab.* **23**, 635 (2016).
6. U. Richter, T. Lahtinen, P. Marttinen, F. Suomi, B. J. Battersby, *J. Cell Biol.* **211**, 373 (2015).
7. X. Guo *et al.*, *Nature* **579**, 427 (2020).
8. H. Tyynismaa *et al.*, *Hum. Mol. Genet.* **19**, 3948 (2010).
9. X. R. Bao *et al.*, *eLife* **5**, e10575 (2016).
10. I. Kühl *et al.*, *eLife* **6**, e30952 (2017).
11. S. Forsström *et al.*, *Cell Metab.* **30**, 1040 (2019).
12. K. Pakos-Zebrucka *et al.*, *EMBO Rep.* **17**, 1374 (2016).
13. A. S. Tibbetts, D. R. Appling, *Annu. Rev. Nutr.* **30**, 57 (2010).
14. X. Li *et al.*, *Science* **375**, eabi4343 (2022).
15. L. Pernas, C. Bean, J. C. Boothroyd, L. Scorrano, *Cell Metab.* **27**, 886 (2018).

ACKNOWLEDGMENTS

A.S. acknowledges support from the Jane and Aatos Erkko Foundation, the Sigrid Jusélius Foundation, the Research Council of Finland, the Chan Zuckerberg Initiative, and the PolG Foundation. J.N. acknowledges support from National Institutes of Health grant DP2AI184813.

10.1126/science.aea0875

[1]Stem Cells and Metabolism Research Program, Faculty of Medicine, University of Helsinki, Helsinki, Finland. [2]Helsinki Institute of Life Science (HiLIFE), University of Helsinki, Helsinki, Finland. [3]Diagnostic Center, Helsinki University Hospital, Helsinki, Finland. [4]Department of Nutritional Sciences and Toxicology, University of California Berkeley, Berkeley, CA, USA. Email: anu.wartiovaara@helsinki.fi

Check for

POLICY FORUM

AGRICULTURE

Climate-smart biofuel policy as a pathway to decarbonize agriculture

A policy that relies on farm-specific carbon-intensity scores can promote climate-smart agricultural practices.

Madhu Khanna[1,2], Bruno Basso[3], Jeff O'Hara[4], David Zilberman[5], Gal Hochman[1]

Strategies for achieving net-zero emissions climate goals have emphasized an important role for bioenergy to displace fossil fuels and for carbon-dioxide (CO_2) removal from the atmosphere. Soil carbon sequestration is one of the key approaches for using the vast potential of land as a sink for atmospheric carbon. Carbon mitigation could be as high as 4 billion to 8 billion tonnes of CO_2 per year with near complete deployment globally of practices that enhance soil carbon sequestration with crop production (*1*). However, there is a disconnect between renewable energy policies to promote the production of low-carbon biofuels and conservation policies that promote soil carbon sequestration practices. We propose that any "climate-smart" biofuel policy should consider farm-specific values of emissions from biofuel feedstock production and soil carbon sequestration and incentivize the adoption of climate-smart practices. This could provide lessons and develop capacity that may help expand policies and practices to agriculture more broadly.

We define climate-smart practices as those that reduce direct life-cycle emissions and/or increase soil carbon sequestration. Farming practices that enhance soil carbon sequestration include both proven best-management practices—such as no-tillage, crop rotation, and cover-cropping—as well as frontier technologies such as biochar, enhanced rock weathering, and perennial crops that are still under research and development (*2*). Policies to promote renewable fuels in the transportation sector in the United States, such as the Renewable Fuel Standard (RFS) and the Low Carbon Fuel Standard (LCFS), differentiate across different types of biofuel feedstocks and the resulting carbon intensity (CI) of the biofuel (the life-cycle greenhouse gas emissions per unit of energy when a biofuel is produced). However, they use default assumptions about on-farm practices and do not distinguish CI scores according to the method of feedstock production (such as the use of fertilizer inputs, cover crops, rotation, and tillage methods), which affect its life-cycle emissions and soil carbon sequestration. Biofuel policies in other countries, such as the European Union's Renewable Energy Directive and the Canadian Clean Fuels Regulation, also do not account for farm-specific production practices and soil carbon sequestration.

The CIs used in US biofuel policies account for soil carbon emissions from indirect land-use change (ILUC) attributed to feedstock production (for example, if increased demand for crops for biofuels raises crop prices, creating incentives for the conversion of grasslands and forestland to crop production). But the ILUC estimate is also based on the default assumption that after this conversion to cropland, the land will be farmed with business-as-usual practices. State and national policymakers, as well as international agencies, establishing biofuel policies should modify current CI accounting methods to avoid over- or underestimating the CI of biofuels by disregarding the carbon effects of crop management practices implemented in the field.

Practices to promote soil carbon sequestration by the agricultural sector in the United States have been promoted separately from the biofuel-specific context: through conservation payment programs and numerous voluntary carbon-offset programs that pay farmers to provide offsets for carbon emissions to the private sector. The effectiveness of programs in promoting adoption of climate-smart practices has been limited by low payment rates, high transaction costs, and for carbon offset protocols, the need to demonstrate the additionality of soil carbon sequestration practices (*3*). The latter requirement entails showing that the practice would not have been undertaken in the absence of the carbon credit revenues. This penalizes early adopters of climate-smart practices and can even create perverse incentives to disadopt or delay adoption to qualify for carbon credits in the future.

Despite these programs, the adoption rate for cover cropping has risen to only about 6% of harvested crop acreage and 35% for no-till practice, whereas precision farming was practiced by by 12% of farms by 2022 (*4*). An alternative market-based mechanism to incentivize low carbon crop production practices would be through the development of commodity markets that would pay a premium price for a low-carbon food or feed product. Lack of regulatory requirements and policy or market incentives for labeling products as low carbon has made it challenging to scale this approach for decarbonizing agriculture.

In contrast to traditional markets for agricultural commodities, biofuel markets that are willing to pay a carbon-based price premium for low-CI biofuels exist already because of policies such as a LCFS. The "40B" Sustainable Aviation Fuel (SAF) tax credit (offered in the United States in 2023–2024) was new in accounting for differences in the CI of SAF from feedstocks produced with climate-smart practices; the magnitude of the tax credit increased as the CI score of SAF decreased. In January 2025, the US Department of the Treasury announced guidance for the 45Z Clean Fuels Production Credit for all transportation fuels and an intent to incorporate the carbon benefits from feedstocks produced with climate-smart practices when the 45Z rule is finalized. Concurrently, the US Department of Agriculture (USDA) has adapted the Argonne National Laboratory's Feedstock Carbon Intensity Calculator (USDA FD-CIC) to develop protocols for climate-smart practices. The FD-CIC determines a feedstock's CI at a county-level on the basis of the farming practices adopted from a specified list (*5*). Changes in soil carbon stocks are calculated as the difference between scenarios with full adoption of a climate-smart practice in the county and a business-as-usual level of adoption as the baseline. The International Civil Aviation Organization's Carbon Offsetting Reduction Scheme for International Aviation (CORSIA) is developing a soil organic carbon accounting methodology. These biofuel protocols are at various stages of development and vary in the extent and approaches for accounting for farm-specific adoption of climate-smart practices.

CLIMATE-SMART BIOFUEL POLICY

The climate-smart biofuel policy proposed here provides a more comprehensive incentive structure than that of existing policies to incentivize low carbon biofuels. Unlike existing low-carbon biofuels policies (such as the RFS and LCFS), the CI scores of a biorefinery would be based on farm-specific feedstock production life-cycle emissions and include soil carbon sequestration, in addition to refinery conversion emissions and ILUC-related emissions (see the figure). Studies show that by optimizing fertilizer application through precision agriculture

Components of the carbon intensity and premium for climate-smart biofuels

Existing biofuel policies, in addition to including biorefinery process emissions and indirect land use change (ILUC)–related emissions, include a representative value for feedstock production life-cycle emissions (for all farms and irrespective of method of production) in the biofuel carbon intensity (CI) score. Under a climate-smart policy CI score, feedstock production life-cycle emissions, and soil carbon sequestration, would be farm-specific components, differentiated by method of production (darker green). The climate-smart biofuel price premium will include credits for lowering feedstock production and biorefinery process emissions and for soil carbon sequestration, as well as a penalty for ILUC emissions.

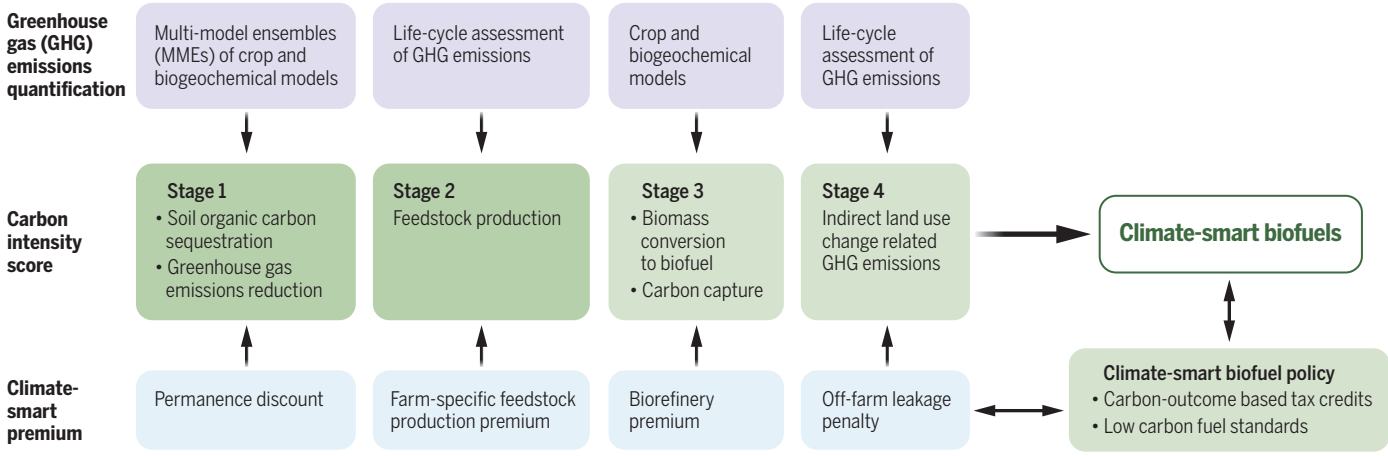

and digital technologies, electrifying farm vehicles and equipment, and improving crop genetics, the life-cycle CI of corn production could be reduced by as much as 71% (*6*). Cover cropping and no-till can more than reverse the depletion of soil carbon stocks from conventional tillage to lower the CI of corn ethanol (*7*).

Unlike conservation programs, the scale for incentivizing climate-smart practices under a biofuel policy need not be limited by program budgets; for example, the acreage converted to producing climate-smart feedstocks and the payments for it under a LCFS would be market-driven and depend on the stringency of policy targets. Although a climate-smart biofuel policy would affect only the feedstock production–related emissions in a biofuel's CI, these emissions are a substantial component. So it offers an opportunity for developing supply chains and protocols that could support broader implementation of mechanisms for promoting climate-smart practices for food, feed, and fiber.

Furthermore, unlike offset programs, a climate-smart biofuel policy would not require that a farmer demonstrate that a practice would not have been undertaken in the absence of carbon credit revenues. Instead, a climate-smart biofuel policy would incentivize carbon reduction beyond business-as-usual levels through the quantification of the additional soil carbon sequestered and/or reduction in life-cycle emissions generated by a practice each year, relative to a counterfactual emissions baseline at the farm level. This baseline can include practices previously adopted for any reason. This is because a reduction in a feedstock's CI score is a mechanism for the biorefinery to reduce its internal supply-chain emissions through low-carbon producton practices. Such a policy could lower the barriers for farmers to obtain credit for their carbon sequestration by bundling the market value of the crop with its CI and being sold into a single market for a carbon-differentiated biofuel feedstock rather than in two separate markets (feedstock and carbon).

POLICY AND IMPLEMENTATION CONSIDERATIONS

There are various policy and implementation considerations with promoting climate-smart biofuels. A key concern with relying on soil carbon sequestration for lowering the CI scores of biofuels is that an increase in soil carbon sequestration could be reversible if the practice is discontinued. Studies report that adoption of conservation practice, such as no-till and cover cropping, is often intermittent for various agronomic, cost, and other reasons (*5*). However, intermittent tillage does not reverse all the soil carbon gains from no-till (*8*), and even temporary sequestration has climate benefits (*9*). One way to address dynamic soil carbon fluxes in ILUC and soil carbon crediting calculations is through equivalency factors that relate tonne-years of temporary storage to 1 tonne of permanent abatement based on the climate response (*10*, *11*). An equivalency factor together with the assessment of the extent of carbon sequestration with alternative durations of adoption of a climate-smart practice can be determined to discount the carbon sequestered.

Studies also note that climate-smart practices have the potential to generate off-farm leakages of emissions (*12*); for example, cover cropping practices that lower cash crop yield can raise crop prices, leading to ILUC. However, research evidence of this is inconclusive and unverified. Although some climate-smart practices may reduce agricultural yields in some regions, and during early stages of the adoption process, they can increase yield in the long run owing to improvements in soil health. There exists substantial potential to optimize climate-smart practices to increase crop yields and soil carbon sequestration by altering crop management practices and nutrient application rates (*13*).

Four key components of implementing a climate-smart biofuel policy must be considered to address the issues raised above. First, implementation of this policy will require collection of on-farm data and verification of crop-management practices adopted. Emerging digital twin technologies can enable documentation of feedstock production practices and ease accurate quantification of feedstock life-cycle emissions intensity (*14*). International standards such as the International Sustainability and Carbon Certification have been developed for verifying and providing third-party certifications to show that feedstocks have been sustainably produced and allow refiners to have chain-of-custody systems to track feedstocks back to the farms; these can be adapted for a climate-smart biofuel policy.

Second, farm-specific estimates of life-cycle emissions intensity and changes in soil carbon stocks relative to a baseline will be needed. Assessing the additional soil carbon sequestered as the result of a climate-smart practice at a farm scale is complicated because it varies substantially at fine spatial resolutions owing to climatic factors (such as temperature and precipitation), soil conditions (such as initial carbon stocks and texture), land management history, and the specific combination of practices implemented. Annual changes in soil carbon stocks from sequestration practices are often <1% of existing stocks. Differentiating these small changes from background noise requires rigorous, stratified, and costly sampling over long intervals, making annual-scale policy implementation based on soil carbon measurement costly (*1*). Process-based ecosystem models provide a cost-effective alternative for assessing

additional soil carbon changes at fine spatial and temporal resolutions. These models can simulate counterfactual baselines (without adopting the climate-smart practice) and calculate with high precision changes that result from adopting the practice for various durations (*7*).

Recent advancements in ecosystem modeling and computational speed now enable the deployment of multimodel ensembles (MMEs) to assess soil carbon changes under various mixes and durations of adoption of climate-smart practices and the range in these outcomes. A MME demonstrated superior performance in predicting soil carbon compared with individual models when tested against 52 experimental treatments across 17 long-term research sites (*7*). The ensemble achieved the highest accuracy and lowest uncertainty when predicting soil carbon changes across diverse management systems. MMEs reduce prediction uncertainty from 99% with individual models to just 36% when eight models are combined. These models also enable inclusion of the effects of these practices on nitrous-oxide emission reductions in the CI score of the feedstock. This substantial uncertainty reduction provides the confidence needed for using MMEs to assess the effect of climate-smart practices on feedstock CI scores. These models can also enable creation of lookup tables for practical policy implementation. These MMEs can also be applied to determine the impact of climate-smart practices on cash crop yields and the potential for positive or negative leakage effects from effects on commodity prices with various levels of adoption.

Third, contractual agreements will be needed between a biorefinery and a farmer to set the duration and mix of climate-smart practices that will be adopted. This information, once verified, can be combined with MMEs and appropriate equivalency factors to obtain a composite CI score that ensures equivalence of soil carbon sequestered with a reduction in direct life-cycle emissions (that represents permanent carbon abatement). This can be used to design payment plans that reward longer contracts, as in carbon credit programs offered in Canada and Australia that relate carbon payment discount rates to the duration of the contract for carbon sequestration (*1*).

Fourth, chain-of-custody tracking requirements from the farm to the biorefinery (which will be comingling feedstock with differing CI scores) will be needed to determine the average CI of its feedstock mix and to trace the contributions of a farmer to the CI of the biofuel through the supply chain, so that a farmer can be paid for their share in lowering the CI of the biofuel produced by that biorefinery. Tracking feedstocks with different CI scores as they move along the supply chain by physically segregating (otherwise functionally equivalent) feedstocks would be prohibitively expensive. Instead, a "book and claim" approach or a "mass-balance" approach provides low-cost alternatives. A mass-balance approach allows mixing feedstocks with different CI scores but tracking the ownership rights to the CI score reduction through the supply chain and back to the farm that produced the climate-smart feedstock. In a book-and-claim system, the credit for the CI reduction is detatched from the feedstock and is tradeable. This would allow farms to sell certificates to refiners without having to trace the CI reductions throughout the supply chain. Such an approach would need infrastructure, such as a certificate registry, to support a marketplace. It would have high set-up costs but lower costs of tracking and bookkeeping and a lower administrative burden than that of other chain-of-custody approaches (*15*).

Implementing a cost-effective climate-smart biofuel policy will depend on technological advances and sound science to guide the design of a performance-based climate-smart premium (see the figure). This premium will implicitly vary with the farm-specific CI score of the biofuel, defined to account for the four types of emissions in the figure: feedstock production emissions (including soil carbons sequestration), refinery emissions, transportation emissions, and indirect emissions.

OPPORTUNITY TO SCALE UP

The agricultural sector offers low-cost options for carbon-dioxide removal through adopting climate-smart practices. However, current approaches to promote their adoption have had limited success. Biofuel markets with their well-developed mechanisms for CI accounting and transferring payments from energy markets to biofuel producers offer an opportunity to rely on performance-based policy incentives and market-based mechanisms to induce low-carbon biofuels and to scale up adoption of climate-smart practices in agriculture.

Several policy aspects are still in need of refinement. Given the pressing need for net-zero solutions, delaying action while waiting for scientific uncertainty about policy design and its impacts to be fully resolved will be costly. Instead, evidence-based policies that can be adapted on the basis of unanticipated unintended outcomes and observed behavioral responses can enable learning by doing and lead to more efficient policy designs. Last, to use the full potential of cropland to sequester and store soil carbon, a climate-smart policy should go beyond biofuels to include crops produced for food, feed, and fiber as well. Current food crop–based biofuels use only a portion of the crop as feedstock. Implementation of a climate-smart biofuel policy, together with a scientific evaluation of its effectiveness and potential unintended consequences, can inform the design of approaches for extending it to induce broader adoption of climate-smart practices. A climate-smart biofuel policy, currently focused on food crop–based biofuels, could also pave the path for policy incentives to induce the production of advanced biofuels from energy crops that have even greater potential to sequester carbon and produce biofuels with negative CI scores. □

REFERENCES AND NOTES

1. K. Paustian, E. Larson, J. Kent, E. Marx, A. Swan, *Front. Clim.* **1**, 8 (2019).
2. NASEM, *Negative Emissions Technologies and Reliable Sequestration: A Research Agenda* (National Academies Press, 2018); http://www.ncbi.nlm.nih.gov/books/NBK541442.
3. C. T. Barbato, A. L. Strong, *npj Clim. Action* **2**, 26 (2023).
4. USDA, "U.S. Census of Agriculture" (2022); https://www.nass.usda.gov/AgCensus.
5. USDA, "Documentation of literature, data, and modeling analysis to support the treatment of CSA practices that reduce agricultural soil carbon dioxide emissions and increase carbon storage (Office of Energy and Environmental Policy, Office of the Chief Economist, 2025); https://www.usda.gov/sites/default/files/documents/USDA_Durability_WhitePaper_01_14.pdf
6. D. L. Northrup, B. Basso, M. Q. Wang, C. L. S. Morgan, P. N. Benfey, *Proc. Natl. Acad. Sci. U.S.A.* **118**, e2022666118 (2021).
7. B. Basso *et al.*, *Sci. Rep.* **15**, 24881 (2025).
8. H. Blanco-Canqui, C. S. Wortmann, *Soil Tillage Res.* **198**, 104534 (2020).
9. H. D. Matthews, K. Zickfeld, A. Koch, A. Luers, *Nat. Commun.* **14**, 5485 (2023).
10. Z. Parisa, E. Marland, B. Sohngen, G. Marland, J. Jenkins, *For. Policy Econ.* **144**, 102840 (2022).
11. B. Minasny, A. B. McBratney, *Soil Secur.* **15**, 100153 (2024).
12. T. Searchinger, R. Waite, C. Hanson, J. Ranganathan, *Creating a sustainable food future: A Menu of Solutions to Feed Nearly 10 Billion People by 2050* (World Resources Institute, 2019).
13. T. Qiu *et al.*, *Nat. Commun.* **15**, 10617 (2024).
14. S. Cesco *et al.*, *Eur. J. Agron.* **146**, 126809 (2023).
15. J. Pechstein, N. Bullerdiek, M. Kaltschmitt, *Energy Policy* **136**, 111014 (2020).

ACKNOWLEDGMENTS

The findings and conclusions of this article are those of the authors and should not be construed to represent any official USDA or US government determination or policy. The authors acknowledge support from a cooperative agreement from the USDA Office of the Chief Economist; the US Department on Energy (DOE) Center for Advanced Bioenergy and Bioproducts Innovation (DOE, Office of Science, Biological and Environmental Research Program under award DE-SC0018420) (M.K.); Great Lakes Bioenergy Research Center, DOE, Office of Science, Biological and Environmental Research Program under award DE-SC0018409 (B.B.); National Science Foundation Long-term Ecological Research Program (DEB 2224712) at the Kellogg Biological Station, USDA National Institute of Food and Agriculture, award 2020-67021-32799 (B.B.); USDA Office of the Chief Economist (M.K., B.B., and G.H.); Michigan State University AgBioResearch (B.B.); USDA multistate hatch project S1075 (G.H.); USDA/NIFA grant 2022-67023-36404 (G.H. and M.K.); and by the Council On Food, Agricultural And Resource Economics (C-FARE) (G.H., M.K., B.B., J.O'H., and D.Z.). B.B. is cofounder of CIBO Technologies and The Soil Inventory Project.

10.1126/science.adw6739

[1]Department of Agricultural and Consumer Economics, University of Illinois, Urbana-Champaign, IL, USA. [2]Institute for Sustainability, Energy and Environment, University of Illinois, Urbana-Champaign, IL, USA. [3]Department of Earth and Environmental Sciences, Michigan State University, East Lansing, MI, USA. [4]Office of the Chief Economist, US Department of Agriculture, Washington, DC, USA. [5]Department of Agricultural and Resource Economics, University of California, Berkeley, CA, USA. Email: khanna1@illinois.edu

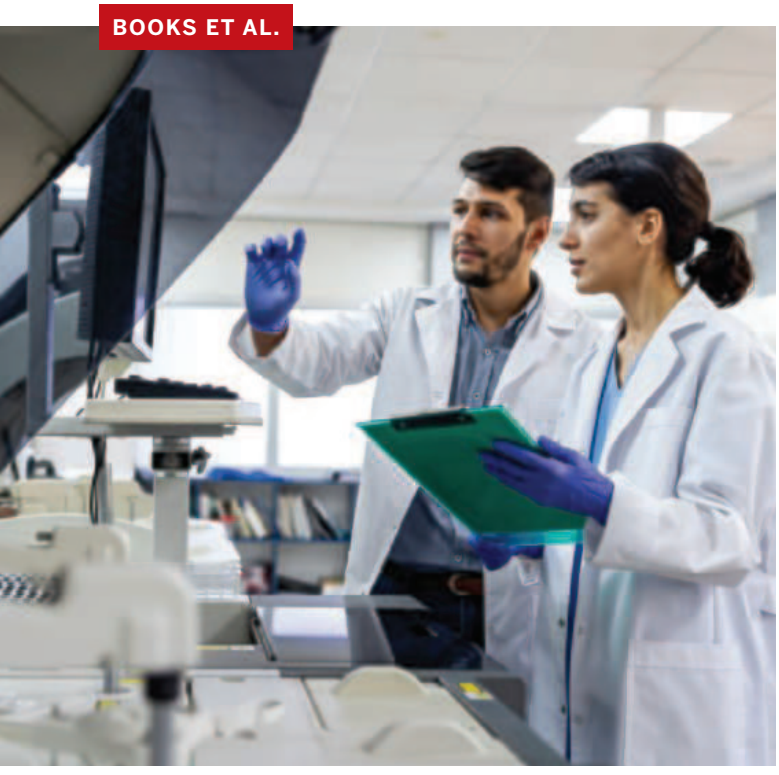

Lab leaders must aim to create environments where all can thrive.

PROFESSIONAL DEVELOPMENT

Leading a lab, and all it entails

A chemist offers actionable leadership advice to principal investigators **Jonathan Wai**

Jen Heemstra
Harvard University Press, 2025. 328 pp.

LABWORK TO LEADERSHIP | Being good at benchwork can give a scientist a chance at a tenure-track faculty appointment, but what is she to do once she has actually won the position and now must lead a research group? In *Labwork to Leadership*, chemist Jen Heemstra provides tips for how to develop the leadership skills needed to actually do the job.

The book has three sections: self-leadership, leading others, and coaching future leaders. The self-leadership section reviews many of the strategies summarized in popular business and leadership books, but Heemstra also points out the importance of personality and individual differences, namely understanding one's own strengths and weaknesses as well as those of the people working under one's leadership. Here, it might have helped to point the reader to a reliable, valid, and free measure of personality developed by research psychologists (*1*) or to a research-based book on career development (*2*).

This section also has actionable advice on time management, leadership strengths and styles, goals, motivation, resilience, and receiving feedback. Heemstra reminds readers, for example, that because time is finite, everything a lab leader says "yes" to is a "no" to something else and that with whom we surround ourselves can affect our goals. She also argues that "leveraging your natural strengths" can help principal investigators find creative ways to lead their labs. On failure, she shares this advice that she received from a colleague: "The people who are ultimately successful aren't necessarily those who succeed on the first try, but rather those who just keep trying." However, one aspect not discussed in this section is how senior scholars can often lose touch with the daily lab work, whether as part of the natural evolution to leadership or otherwise.

In the second section, on leading others, Heemstra introduces the idea of giving more ownership to those working under one's leadership: "I want to encourage you to set aside your own ideas and preferences, hand over control to the people in your research group, and see where that takes you." This is because "leadership is not about getting things done; it's about getting things done through other people." A large focus of this section is on creating a lab environment where everyone can thrive.

Heemstra has specific suggestions for creating such an environment, which center on cultivating an encouraging approach: "In a healthy environment, feedback doesn't have to lack candor, but it should be delivered in a way that seeks to build up each individual and help them do their best." She gives her own lab group awards, basing them on "qualities such as perseverance, kindness, collegiality, drive, inclusivity, and courage." These themes flow into the other recommendations for giving feedback, conflict resolution, ethical leadership, and communication.

In the third section, on coaching future leaders, Heemstra integrates parts 1 and 2 of the book to help readers teach their current students to become future leaders in whatever professions they choose to pursue. Here, she focuses a lot on what she calls "mindset" or appropriate mental orientation. In the section on vulnerability, she reminds principal investigators that they have enormous privilege and should coach others with that in mind, and she encourages them to openly admit to mistakes and insecurities as a way to help their mentees be more open about their own.

Near the end of the book, Heemstra provides some case studies, or "coaching contexts," in which she walks the reader through common research lab conflict situations and provides ideas on how to resolve them appropriately. Examples include a situation where two prospective coauthors, a postdoc and a graduate student, are having an author order dispute. The graduate student in the scenario has been placed second in the author order by the postdoc but believes she should be first. Heemstra suggests encouraging the student to think through all the possibilities of what might be going on, such as whether there has been a miscommunication during the process, and providing advice to the postdoc about how they might resolve authorship disagreements in the future.

Overall, *Labwork to Leadership* fills a hole in the career training literature for scientists and researchers, joining other recent career resources (*3*–*7*) and guides for improving academic writing (*8*) and science communication (*9*). It is important to remember, however, that leadership skills are not substitutes for learning to conduct solid and replicable science. □

REFERENCES AND NOTES

1. The SAPA Project; https://www.sapa-project.org/.
2. D. P. Campbell, *If You Don't Know Where You're Going, You'll Probably End Up Somewhere Else: Finding a Career and Getting a Life* (Sorin Books, 2007).
3. MyIDP: Science Careers Individual Development Plan; https://myidp.sciencecareers.org/.
4. ImaginePhD; https://www.imaginephd.com/.
5. A. De Los Reyes, *The Early Career Researcher's Toolbox: Insights Into Mentors, Peer Review, and Landing a Faculty Job* (CREATE, 2020).
6. J. Brennan, *Good Work If You Can Get It: How to Succeed in Academia* (Johns Hopkins Univ. Press, 2020).
7. P. A. Schwartzkroin, *So You Want to Be a Scientist?* (Oxford Univ. Press, 2009).
8. L. Cassuto, *Academic Writing as if Readers Matter* (Princeton Univ. Press, 2024).
9. N. Baron, *Escape from the Ivory Tower: A Guide to Making Your Science Matter* (Island Press, 2010).

10.1126/science.ady7700

The reviewer is at the Department of Education Reform and Department of Psychology, University of Arkansas, Fayetteville, AR, USA. Email: jwai@uark.edu

Check for

SCIENTIFIC INTEGRITY

The Sisyphean quest for scientific certainty

An epidemiologist calls for humility and triangulation to converge on truth **Sorin M. S. Krammer**

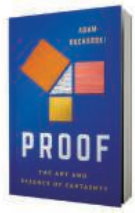

Proof: The Art and Science of Certainty
Adam Kucharski
Basic Books, 2025. 368 pp.

Adam Kucharski's latest book, *Proof: The Art and Science of Certainty*, offers an expansive exploration of certainty in science, from geometry and jurisprudence to randomized trials and neural networks. Across eight sections, the book examines how we seek and find truth, often conflating confidence with correctness in the process. This conflation, in turn, seems to undermine science's reputation in tackling some of the world's current and most pressing problems. In an era grappling with algorithmic bias, scientific misinformation, and postpandemic epistemic aftershocks, *Proof*'s objective is to critically assess the scaffolding of scientific research rather than reassure us of its superiority.

Kucharski, an epidemiologist at the London School of Hygiene and Tropical Medicine who gained prominence during the COVID-19 pandemic, argues that our methods of establishing truth are as fallible as the institutions wielding them. His thesis cuts against the grain of both scientific triumphalism (*1*) and postmodern relativism (*2*) by suggesting that the tools we have constructed to pursue certainty—logic, statistics, experimentation, and artificial intelligence—systematically embed the very biases and constraints they originally sought to transcend. Through vivid examples such as the Monty Hall problem, Gödel's incompleteness theorems, and Lincoln's geometric reasoning for political arguments, Kucharski demonstrates that even mathematics, often seen as the bastion of certainty, harbors philosophical fault lines.

Kucharski discusses several particularly timely themes in the book. First, he problematizes our increasing reliance on automated inference, from risk algorithms in criminal justice to black box artificial intelligence models in health care and science. These systems, he argues, embed existing societal biases under a veneer of objectivity. Fairness, as he puts it, is often mathematically incompatible: An algorithm calibrated equally across racial groups may still yield disproportionate outcomes when structural inequalities persist. Thus, whereas Kucharski is sympathetic to algorithmic advances, he warns of their seductive opacity. However, proponents of algorithmic systems may see these deficiencies as part of a transitional learning curve rather than a reason for permanent dismissal (*3*).

A second major thread is the fragility of public trust in scientific evidence, particularly in the wake of COVID-19. Here, the book becomes personal as Kucharski revisits early pandemic communication failures, including his own hesitancy to cite internal death toll projections before they were public. Despite superior data and models, scientific persuasion faltered during the pandemic because truth had become politically fractured. Kucharski contends that transparent and timely evidence is no longer enough; proof must engage with the cognitive and social lenses through which people construct their beliefs.

This insight is powerful but perhaps underdeveloped in terms of institutional critique. Kucharski diagnoses some well-known academic failures of science (e.g., the ivory tower syndrome, communication breakdown, and credibility deficits) but offers less on how to tackle them successfully, particularly in the current environment characterized by media sensationalism, political polarization, and increasing international competition (*4*, *5*).

The book's most valuable insight is its treatment of epistemic humility. Through recurring examples, from Janet Lane-Claypon's breastfeeding trials to the AlphaFold protein predictions, Kucharski illustrates that actionable certainty rarely comes with absolute proof. Instead, good science accepts uncertainty, triangulates methods, and builds slowly from provisional belief. He draws an elegant contrast between "proof beyond reasonable doubt" and "proof beyond delay," urging action without the paralyzing demand for perfection (*6*).

A contrary view might suggest that some of today's science communication failures stem not from excessive certainty but from excessive caveating. For instance, in the case of vaccines or climate change, overly cautious hedging coupled with social media's impact as an information source has sometimes allowed denialism to flourish unchallenged.

Kucharski ends with a call to embrace methodological pluralism and to acknowledge that proof is a social, dynamic, and often contested act. Rather than searching for ultimate, irrefutable arguments, he advocates for triangulation by using independent, sometimes imperfect methods to converge on truth. This insight is likely the book's most enduring contribution.

Proof arrives at a moment when faith in expertise faces unprecedented strain worldwide. Can science maintain authority while acknowledging its limitations? Should algorithms be trusted more than human judgment, or does their opacity make them more dangerous? Kucharski's answer is characteristically nuanced: Proof is not a static achievement but a dynamic, social process of negotiation that requires both intellectual rigor and social awareness to navigate our fractured epistemic landscape. □

REFERENCES AND NOTES

1. J. D. Trout, *Wondrous Truths: The Improbable Triumph of Modern Science* (Oxford Univ. Press, 2016).
2. G. Andrade, *Philosophia* **20**, 197 (2019).
3. F. Mohr, J. N. van Rijn, *Mach. Learn.* **113**, 8371 (2024).
4. B. Huber, M. Barnidge, H. Gil de Zúñiga, J. Liu, *Public Underst. Sci.* **28**, 759 (2019).
5. V. Cologna *et al.*, *Nat. Hum. Behav.* **9**, 713 (2025).
6. R. Hoekstra, S. Vazire, *Nat. Hum. Behav.* **5**, 1602 (2021).

10.1126/science.aea4594

The reviewer is at the University of Southampton Business School, University of Southampton, Southampton, UK. Email: s.krammer@soton.ac.uk

ILLUSTRATION: JOZEF MICIC/SHUTTERSTOCK

EDITOR'S NOTE

On 27 March 2020, *Science* published the Research Article "Flux-induced topological superconductivity in full-shell nanowires" by S. Vaitiekėnas *et al.* (*1*). After readers expressed concerns about whether the authors selected data for publication that were not representative of the entirety of the data collected in association with the project (*2*), *Science* published an Editorial Expression of Concern (*3*) and contacted the authors' institution (University of Copenhagen), which convened an external expert panel to conduct an investigation. In February 2024, the panel released a detailed report, to which *Science* directed readers in an Editor's Note (*4*). The report concluded in part that "[t]he presented data do, for the most part, represent the outcome of the experiments: the authors have exercised scientific judgement in selecting which data to share using criteria whose application was partially subjective. Although data selection did, in our view, result in conclusions that did not adequately capture the variability of outcomes, the excluded data did not undermine the paper's main conclusions" (*5*). The matter was then referred to the Danish Board on Research Misconduct, which formally concluded in October 2024 that the authors did not commit misconduct. In December 2024, the Practice Committee of the University of Copenhagen concluded that the authors did not engage in questionable research practices.

Science accepts and respects the conclusions of the expert panel, the Danish Board, and the Practice Committee that the authors' actions neither constituted misconduct nor undermined the paper's main conclusions. Therefore, we have replaced the Editorial Expression of Concern with an Erratum (*6*) that addresses the concerns highlighted in the panel report.

H. Holden Thorp, Editor-in-Chief, *Science*

REFERENCES AND NOTES

1. S. Vaitiekėnas *et al.*, *Science* **367**, eaav3392 (2020).
2. S. Frolov, V. Mourik, "Post-publication review of 'Flux-tuned topological superconductivity in full-shell nanowires' Vaitiekenas et al. *Science* 2020," Zenodo (2022); https://doi.org/10.5281/zenodo.6344446.
3. H. H. Thorp, *Science* **373**, 500 (2021).
4. H. H. Thorp, *Science* **383**, 837 (2024).
5. S. Guéron, P. Hakonen, A. MacDonald, "*Science* paper 'Flux-induced topological superconductivity in full-shell nanowires,' report from expert panel," Zenodo (2024); https://doi.org/10.5281/zenodo.10647079.
6. "Erratum to the RA "Flux-induced topological superconductivity in full-shell nano-wires," *Science* **389**, aea6837 (2025).

10.1126/science.aea4953

Risks of ending US science-policy training

Training scientists to engage with policy-makers and pursue careers in public service is among the most effective ways to turn research strength into real-world impact. However, in February, the Trump administration eliminated key science-policy training programs, including the Presidential Management Fellowship (*1*), the Donald M. Payne International Development Fellowship (*2*), and the newly formed Science for Development Fellowship at the US Agency for International Development (USAID) (*3*). It also abruptly terminated fellows in the Laboratory Leadership Service at the Centers for Disease Control and Prevention (*4*) and the Presidential Innovation Fellowship at the General Services Administration (*5*). As alumni of the AAAS Science & Technology Policy Fellowship (AAAS is the publisher of *Science*), which places hundreds of scientists in federal agencies each year, we urge the US government to preserve science-policy training programs and recognize their role in sustaining American scientific leadership and global competitiveness.

Scientists are trained to solve complex problems, challenge assumptions, and think laterally—skills the government urgently needs. These fellowships teach scientists to communicate with policy-makers, industry, and the public and equip them to address the country's most pressing issues (*6*, *7*), such as achieving energy independence, strengthening national security, preventing future pandemics, and guiding the rise of artificial intelligence (AI) and biotechnology.

In addition to training scientists to serve in government, science-policy training programs help reshape academic science to better serve the public interest. Many fellows return to academia with a deeper understanding of how research can inform real-world challenges and continue to engage in the policy process. They also teach and mentor more effectively, drawing on a clearer sense of how science contributes to the bigger picture (*6*–*8*).

Many scientists want to serve the public and make a tangible difference. Science-policy training programs offer them critical pathways from academia into public service (*6*, *7*, *9*). Eliminating these opportunities wastes potential and risks driving talented individuals to other countries or out of public service entirely. These cuts come amid a broader erosion of federal support for science, prompting other countries to ramp up efforts to attract scientists working in the US (*10*). Some states are stepping up to fill the gap (*11*, *12*), but it will be difficult to match the scale, reach, and coordination that national programs provide. The US government must protect the programs that train the people who can translate the US research engine into real progress for health, national security, and the economy.

Scott Glaberman[1] and Cynthia Wei[2]

[1]Centre for Environmental Research and Justice, School of Biosciences, University of Birmingham, Birmingham, UK. [2]Science, Technology, and International Affairs Program, Walsh School of Foreign Service, Georgetown University, Washington, DC, USA. Email: s.glaberman@bham.ac.uk

REFERENCES AND NOTES

1. O. George, "Trump ends federal leadership program, cutting off key talent pipeline," *Washington Post*, 20 February 2025.
2. C. Boudreau, "Meet the grad students who lost prestigious career paths to DOGE cuts: 'This is something I've been working toward for years,'" *Business Insider*, 4 April 2025.
3. S. Imbler, "An interview with a fired Science For Development Fellow at USAID," *Defector*, 5 May 2025.
4. M. Wadman, "Ax falls on elite group of Ph.D.s training to lead U.S. public health labs," *Science*, 19 February 2025.
5. M. Kelly, "DOGE has started gutting a key US technology agency," *Wired*, 12 February 2025.
6. B. Alberts, B. D. Gold, L. L. Martin, M. E. Maxon, *Proc. Natl. Acad. Sci. U.S.A.* **115**, 1952 (2018).
7. Science & Technology Policy Fellowships, "A retrospective evaluation of the STPF program (American Association for the Advancement of Science, 2020).
8. A. Sponberg, L. Nanayakkara, B. Voss, *Limnol. Oceanogr. Bull.* **28**, 149 (2019).
9. E. Linos, B. Sciepura, A. Wall, "Getting your foot in the door: The impact of public sector fellowships on career trajectories" (The People Lab, Harvard Kennedy School, 2025).
10. N. Gaind, R. Fieldhouse, M. Naddaf, G. Guglielmi, "US brain drain: *Nature*'s guide to the initiatives drawing scientists abroad," *Nature*, 16 May 2025.
11. National Conference of State Legislatures (NCSL), Integrating evidence and data in the policymaking process through science policy fellowships; https://www.ncsl.org/center-for-results-driven-governing/science-policy-fellowships.
12. A. Mace, J. Bando, "States as laboratories for science policy innovation," *Issues in Science and Technology*, 25 January 2022.

10.1126/science.adz0737

NEWS FROM
Science
AAAS

Subscribe to **News from Science** for unlimited access to authoritative, up-to-the-minute news on research and science policy.

bit.ly/NewsFromScience

West Philippine Sea dispute threatens sea life

Dominion over the South China Sea and the recently declared West Philippine Sea has been under dispute for decades (*1*). To claim ownership, China has built artificial islands in the sea (*1*), and multiple nations, including the Philippines, Vietnam, Malaysia, Brunei, and Taiwan, have increased naval patrols, established military outposts, and installed defense infrastructure (*2*). This geopolitical conflict threatens marine ecosystems, the sustainability of fisheries, and the livelihoods of coastal communities. Scientists should advocate for global agreements and the establishment of marine reserves to help ease conflicts and safeguard marine life.

The South China Sea and West Philippine Sea are renowned for their rich marine biodiversity, particularly diverse coral reefs (*1*, *2*), but large-scale land reclamation has severely degraded these vital ecosystems. China's artificial island–building activities, particularly in the Spratly Islands and Paracel Islands, involve dredging, which smothers coral ecosystems with sediment, destroying the habitats of numerous species (*3*, *4*). Sediment plumes cover more than 250 km^2 and affect an area exceeding 1200 km^2 (*3*). Reduced levels of chlorophyll a—a key indicator of marine productivity—suggest a decline in biological health (*3*).

Many coastal communities in the Philippines, particularly in Palawan and the Zamboanga Peninsula, rely on fishing as their primary source of income (*5*, *6*). However, the construction of military outposts, the encroachment of foreign fishing vessels, and the destruction of marine habitats have led to a decline in fish production, forcing many fishers to seek alternative livelihoods (*7*). The military spending by claimant states has also diverted resources away from social and economic development programs, exacerbating poverty and inequality in the region (*5*, *8*).

In some areas, fishers have shifted to tourism-related activities. Although this transition provides financial relief, it increases competition for resources and comes with the risk of being displaced by large-scale tourism companies (*6*, *7*). The shift to tourism also increases pollution and causes further reef degradation (*9*).

Marine research has been shown to promote international cooperation and address transboundary challenges, which makes it a valuable tool for managing disputed marine regions (*10*). For example, the Mediterranean Action Plan (*11*) under the Barcelona Convention coordinates 22 countries in managing Specially Protected Areas of Mediterranean Importance, and the Gulf of Mexico Marine Protected Area Network (*12*) was established in 2017 among Mexico, Cuba, and the US amid political turmoil. These agreements demonstrate that marine conservation networks can act as instruments of ocean science diplomacy by establishing neutral grounds for international collaboration on common marine resources (*12*).

Adrian A. Mabalay

Department of Management and Organization, De La Salle University, Manila, Philippines.
Email: adrian.mabalay@dlsu.edu.ph

REFERENCES AND NOTES

1. K. A. Gwiazdon, in *The Role of Integrity in the Governance of the Commons: Governance, Ecology, Law, Ethics*, L. Westra, J. Gray, F.-T. Gottwald, Eds. (Springer, 2017), pp. 105–122.
2. N. C. Hoi, V. H. Dang, *Int. J. Law Public Admin.* **1**, 8 (2018).
3. L. Smith, P. Cornillon, D. Rudnickas, C. B. Mouw, *Sci. Rep.* **9**, 5295 (2019).
4. J. W. McManus, *Int. J. Mar. Coast. Law* **32**, 199 (2017).
5. A.-G. D. S. Mohammad, *Int. J. Multidiscip. Res.* **6**, 10.36948/ijfmr.2024.v06i03.23063 (2024).
6. M. J. J. Buncag, *Asian J. Resilience* **1**, 15 (2019).
7. M. Fabinyi, *Marit. Stud.* **19**, 29 (2020).
8. R. U. Mendoza, C. Siriban, T. J. Ty, *J. Econ. Surv.* **33**, 1028 (2019).
9. F. Culhane *et al.*, *J. Appl. Ecol.* **61**, 2897 (2024).
10. A. Polejack, L. F. Coelho, *Front. Res. Metr. Anal.* **6**, 637127 (2021).
11. United Nations Environment Programme, Mediterranean Action Plan, Barcelona Convention, "Convention for the Protection of the Marine Environment and the Coastal Region of the Mediterranean and its Protocols" (2022); https://www.vliz.be/imisdocs/publications/265691.pdf.
12. K. R. Thompson, F. Bretos, P. Canals, C. Besancon, *Mar. Policy* **178**, 106709 (2025).

10.1126/science.adx9555

EDITOR'S NOTE

On 27 March 2020, *Science* published the Research Article "Flux-induced topological superconductivity in full-shell nanowires" by S. Vaitiekėnas *et al.* (*1*). After readers expressed concerns about whether the authors selected data for publication that were not representative of the entirety of the data collected in association with the project (*2*), *Science* published an Editorial Expression of Concern (*3*) and contacted the authors' institution (University of Copenhagen), which convened an external expert panel to conduct an investigation. In February 2024, the panel released a detailed report, to which *Science* directed readers in an Editor's Note (*4*). The report concluded in part that "[t]he presented data do, for the most part, represent the outcome of the experiments: the authors have exercised scientific judgement in selecting which data to share using criteria whose application was partially subjective. Although data selection did, in our view, result in conclusions that did not adequately capture the variability of outcomes, the excluded data did not undermine the paper's main conclusions" (*5*). The matter was then referred to the Danish Board on Research Misconduct, which formally concluded in October 2024 that the authors did not commit misconduct. In December 2024, the Practice Committee of the University of Copenhagen concluded that the authors did not engage in questionable research practices.

Science accepts and respects the conclusions of the expert panel, the Danish Board, and the Practice Committee that the authors' actions neither constituted misconduct nor undermined the paper's main conclusions. Therefore, we have replaced the Editorial Expression of Concern with an Erratum (*6*) that addresses the concerns highlighted in the panel report.

H. Holden Thorp, Editor-in-Chief, *Science*

REFERENCES AND NOTES

1. S. Vaitiekėnas *et al.*, *Science* **367**, eaav3392 (2020).
2. S. Frolov, V. Mourik, "Post-publication review of 'Flux-tuned topological superconductivity in full-shell nanowires' Vaitiekenas et al. *Science* 2020," Zenodo (2022); https://doi.org/10.5281/zenodo.6344446.
3. H. H. Thorp, *Science* **373**, 500 (2021).
4. H. H. Thorp, *Science* **383**, 837 (2024).
5. S. Guéron, P. Hakonen, A. MacDonald, "*Science* paper 'Flux-induced topological superconductivity in full-shell nanowires,' report from expert panel," Zenodo (2024); https://doi.org/10.5281/zenodo.10647079.
6. "Erratum to the RA "Flux-induced topological superconductivity in full-shell nano-wires," *Science* **389**, aea6837 (2025).

10.1126/science.aea4953

Risks of ending US science-policy training

Training scientists to engage with policy-makers and pursue careers in public service is among the most effective ways to turn research strength into real-world impact. However, in February, the Trump administration eliminated key science-policy training programs, including the Presidential Management Fellowship (*1*), the Donald M. Payne International Development Fellowship (*2*), and the newly formed Science for Development Fellowship at the US Agency for International Development (USAID) (*3*). It also abruptly terminated fellows in the Laboratory Leadership Service at the Centers for Disease Control and Prevention (*4*) and the Presidential Innovation Fellowship at the General Services Administration (*5*). As alumni of the AAAS Science & Technology Policy Fellowship (AAAS is the publisher of *Science*), which places hundreds of scientists in federal agencies each year, we urge the US government to preserve science-policy training programs and recognize their role in sustaining American scientific leadership and global competitiveness.

Scientists are trained to solve complex problems, challenge assumptions, and think laterally—skills the government urgently needs. These fellowships teach scientists to communicate with policy-makers, industry, and the public and equip them to address the country's most pressing issues (*6*, *7*), such as achieving energy independence, strengthening national security, preventing future pandemics, and guiding the rise of artificial intelligence (AI) and biotechnology.

In addition to training scientists to serve in government, science-policy training programs help reshape academic science to better serve the public interest. Many fellows return to academia with a deeper understanding of how research can inform real-world challenges and continue to engage in the policy process. They also teach and mentor more effectively, drawing on a clearer sense of how science contributes to the bigger picture (*6*–*8*).

Many scientists want to serve the public and make a tangible difference. Science-policy training programs offer them critical pathways from academia into public service (*6*, *7*, *9*). Eliminating these opportunities wastes potential and risks driving talented individuals to other countries or out of public service entirely. These cuts come amid a broader erosion of federal support for science, prompting other countries to ramp up efforts to attract scientists working in the US (*10*). Some states are stepping up to fill the gap (*11*, *12*), but it will be difficult to match the scale, reach, and coordination that national programs provide. The US government must protect the programs that train the people who can translate the US research engine into real progress for health, national security, and the economy.

Scott Glaberman[1] and Cynthia Wei[2]

[1]Centre for Environmental Research and Justice, School of Biosciences, University of Birmingham, Birmingham, UK. [2]Science, Technology, and International Affairs Program, Walsh School of Foreign Service, Georgetown University, Washington, DC, USA. Email: s.glaberman@bham.ac.uk

REFERENCES AND NOTES

1. O. George, "Trump ends federal leadership program, cutting off key talent pipeline," *Washington Post*, 20 February 2025.
2. C. Boudreau, "Meet the grad students who lost prestigious career paths to DOGE cuts: 'This is something I've been working toward for years,'" *Business Insider*, 4 April 2025.
3. S. Imbler, "An interview with a fired Science For Development Fellow at USAID," *Defector*, 5 May 2025.
4. M. Wadman, "Ax falls on elite group of Ph.D.s training to lead U.S. public health labs," *Science*, 19 February 2025.
5. M. Kelly, "DOGE has started gutting a key US technology agency," *Wired*, 12 February 2025.
6. B. Alberts, B. D. Gold, L. L. Martin, M. E. Maxon, *Proc. Natl. Acad. Sci. U.S.A.* **115**, 1952 (2018).
7. Science & Technology Policy Fellowships, "A retrospective evaluation of the STPF program (American Association for the Advancement of Science, 2020).
8. A. Sponberg, L. Nanayakkara, B. Voss, *Limnol. Oceanogr. Bull.* **28**, 149 (2019).
9. E. Linos, B. Sciepura, A. Wall, "Getting your foot in the door: The impact of public sector fellowships on career trajectories" (The People Lab, Harvard Kennedy School, 2025).
10. N. Gaind, R. Fieldhouse, M. Naddaf, G. Guglielmi, "US brain drain: *Nature*'s guide to the initiatives drawing scientists abroad," *Nature*, 16 May 2025.
11. National Conference of State Legislatures (NCSL), Integrating evidence and data in the policymaking process through science policy fellowships; https://www.ncsl.org/center-for-results-driven-governing/science-policy-fellowships.
12. A. Mace, J. Bando, "States as laboratories for science policy innovation," *Issues in Science and Technology*, 25 January 2022.

10.1126/science.adz0737

Volunteers collect plastic waste from a river in Bali, Indonesia.

PHOTO: VICTOR LOCHON/GETTY IMAGES

Addressing Southeast Asia's plastic pollution

As some of the largest producers and emitters of plastic waste (*1*), member states of the Association of Southeast Asian Nations (ASEAN) play a critical role in tackling the global plastic crisis. At the 44th and 45th ASEAN Summits held in October 2024, the organization issued the ASEAN Declaration on Plastic Circularity (*2*), signaling the bloc's commitment to address the plastic crisis using a full–life cycle approach. Although the document indicates a step forward, ASEAN countries must do more to overcome the region's challenges.

More than 55% of the ocean's plastic debris originated from ASEAN countries; the Philippines, Malaysia, Indonesia, and Myanmar are ranked as top emitters (*3*). Waste management in Southeast Asia is characterized by underdeveloped infrastructure, unsustainable practices, and unregulated activities (*4*). Out of the 150 million tonnes of solid waste generated annually in Southeast Asia between 2010 and 2014 (*5*), only 47% was collected, and 34% of this material was illegally dumped after collection (*6*). Most ASEAN members recycle 5 to 28% of their plastic waste, and private and unregulated ("informal") sectors are the primary drivers in collection, sorting, and recycling (*4*, *5*). Southeast Asia's fast-growing market for consumer goods, potentially reaching USD 4 trillion by 2030 (*7*), will undoubtedly intensify the plastic crisis in the region, prompting urgent need for sustainable solutions.

Despite mounting challenges, Southeast Asia is well positioned to drive far-reaching regional and global sustainability efforts. The demand for green alternatives to conventional plastics and the region's strong agricultural output have propelled ASEAN's bioplastic sector; Thailand has emerged as the world's second-largest bioplastics manufacturer, and Indonesia and Malaysia are expected to gain substantial market share (*8*). Southeast Asia is also experiencing a surge in multisectoral and transnational collaborative efforts in research, innovation, and capacity building (*6*). Many such efforts are supported by foreign governments, such as Australia's Indo-Pacific Plastics Innovation Network (*9*).

Although ASEAN's sustainable initiatives are poised to drive change, many lack support from domestic markets and primarily rely on exporting their products to developed countries (*10*). To increase domestic commitment to sustainability, ASEAN countries' governments should promote plastics alternatives and innovative approaches for plastic waste management. All ASEAN countries should also incorporate and strengthen Extended Producer Responsibility (EPR) policies, which require producers to take responsibility for the treatment and disposal of end-of-life plastic products (*11*). This approach enhances the value of postconsumer plastic materials and incentivizes traceability and recycling (*12*). Indonesia, Singapore, Vietnam, and the Philippines have already implemented EPR policies, and other ASEAN members are developing or considering the framework (*12*).

Tu Xayachak[1], Nawshad Haque[2], Biplob Kumar Pramanik[1]

[1]School of Engineering, RMIT University, Melbourne, VIC, Australia. [2]Commonwealth Scientific and Industrial Research Organisation (CSIRO), Clayton South, Melbourne, VIC, Australia. Email: biplob.pramanik@rmit.edu.au

REFERENCES AND NOTES

1. J. R. Jambeck *et al.*, *Science* **347**, 768 (2015).
2. The ASEAN Secretariat, "ASEAN Declaration on Plastic Circularity" (ASEAN, 2024).
3. L. J. J. Meijer, T. van Emmerik, R. van der Ent, C. Schmidt, L. Lebreton, *Sci. Adv.* **7**, eaaz5803 (2021).
4. C. H. Ng *et al.*, *Front. Environ. Sci.* **11**, 1142071 (2023).
5. United Nations Environment Programme (UNEP), "Waste Management in ASEAN Countries" (UNEP, 2017).
6. The ASEAN Secretariat, "ASEAN Regional Action Plan for Combating Marine Debris in the ASEAN Member States (2021-2025)" (ASEAN, 2021).
7. World Economic Forum, "Future of Consumption in Fast-Growth Consumer Markets: ASEAN" (World Economic Forum, 2020).
8. "Southeast Asia bioplastics market size & share analysis - growth trends & forecasts (2025 - 2030)" (Mordor Intelligence, 2024).
9. S.-J. Stevenson, A. Claridge-Chang, "Our sustainability soundtrack in Southeast Asia" (CSIRO, 2024); https://www.csiro.au/en/news/All/Articles/2024/December/Southeast-Asia-innovation-science.
10. P. Kerdlap, J. Baker, "Is There a Case for Bioplastics? Experience from Thailand" (Asian Development Bank, 2023).
11. Organisation for Economic Co-operation and Development (OECD), "Extended Producer Responsibility: Basic facts and key principles" (OECD Publishing, 2024).
12. M. Kojima, A. S. Suwarno, "Extended Producer Responsibility on Plastics in Southeast Asian Countries" (Economic Research Institute for ASEAN and East Asia, 2025).

10.1126/science.adx7543

RESEARCH

IN *SCIENCE* JOURNALS

Edited by Michael Funk

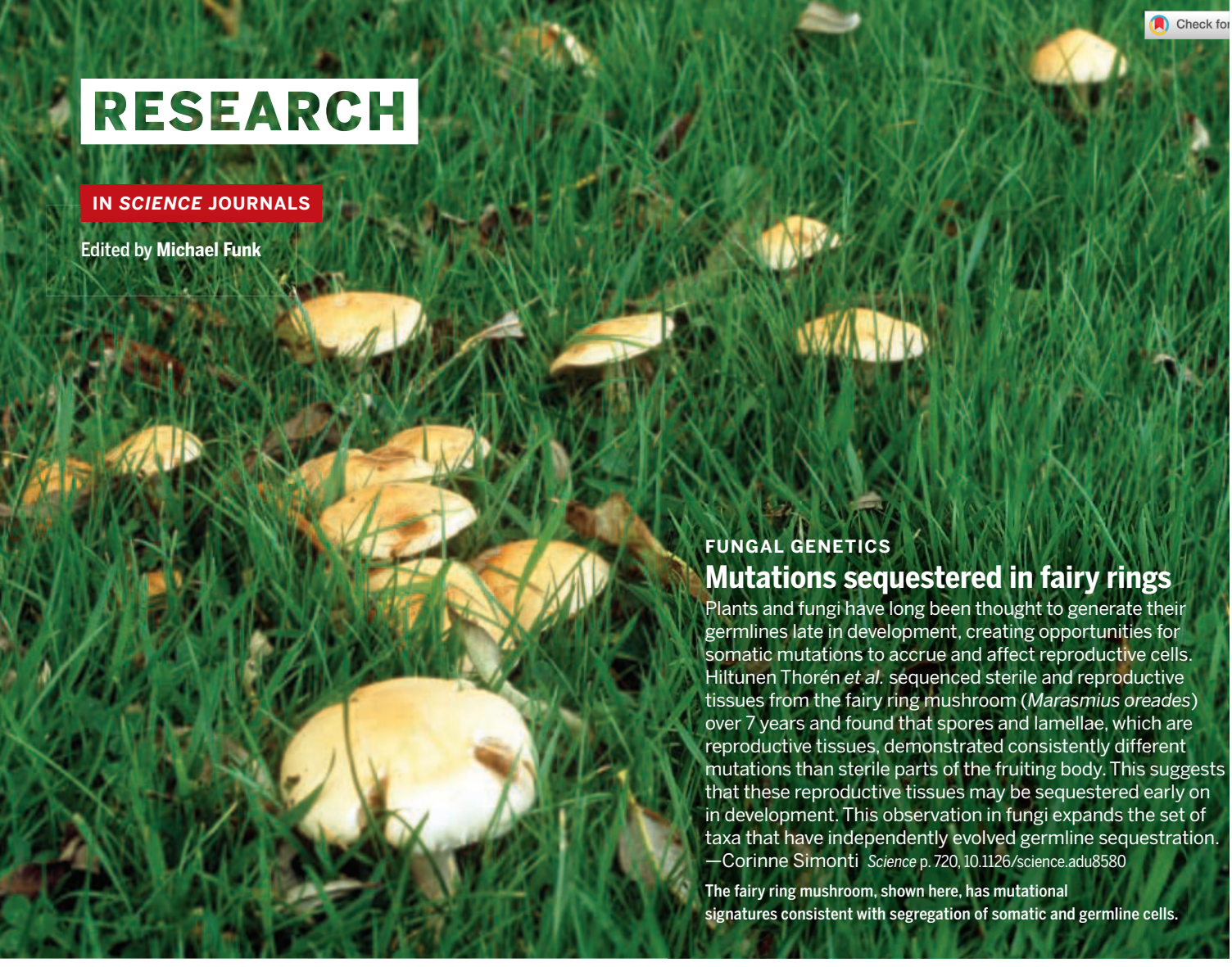

FUNGAL GENETICS

Mutations sequestered in fairy rings

Plants and fungi have long been thought to generate their germlines late in development, creating opportunities for somatic mutations to accrue and affect reproductive cells. Hiltunen Thorén *et al.* sequenced sterile and reproductive tissues from the fairy ring mushroom (*Marasmius oreades*) over 7 years and found that spores and lamellae, which are reproductive tissues, demonstrated consistently different mutations than sterile parts of the fruiting body. This suggests that these reproductive tissues may be sequestered early on in development. This observation in fungi expands the set of taxa that have independently evolved germline sequestration. —Corinne Simonti *Science* p. 720, 10.1126/science.adu8580

The fairy ring mushroom, shown here, has mutational signatures consistent with segregation of somatic and germline cells.

PHOTO: NIGEL CATTLIN/MINDEN PICTURES

CARBON ALLOTROPES

Ring protection

The discovery of C_{60} and related three-dimensional fullerenes introduced a molecular class of carbon allotropes more discrete than diamond and graphite. Recently, scanning probe microscopy has enabled the synthesis of two-dimensional molecular carbon rings, but these could only be assembled one by one on surfaces. Gao *et al*. now report a method to prepare macroscopic quantities of a ring comprising 48 carbons in solution phase. The key was to protect the backbone by threading it through three macrocycles during preparation of the precursor. —Jake S. Yeston

Science p. 708, 10.1126/science.ady6054

MANY-BODY DYNAMICS

Persisting localization

Interactions in a many-body system often lead to thermalization. However, it has recently been theoretically predicted that an interacting one-dimensional bosonic gas subject to periodic "kicks" localizes instead of thermalizing. Guo *et al*. realized such a system using quantum-degenerate samples of cesium atoms and tuned the interaction strength from noninteracting to strongly interacting, finding localization in both limits. —Jelena Stajic

Science p. 716, 10.1126/science.adn8625

NUCLEAR FUSION

Modeling ignition

The inertial confinement fusion experiment uses powerful lasers to induce nuclear reactions and produce fusion energy. The design of the experiment is complex, and computer simulations are routinely used to optimize it. Typically, these simulations require manual tuning, which limits their predictive power. Spears *et al*. built a generative machine learning, physics-informed model that successfully predicted the initial ignition shot and the statistics of subsequent experiments with the same design. —Jelena Stajic

Science p. 727, 10.1126/science.adm8201

EVOLUTIONARY BIOLOGY

Evolutionary courtship

In the fruit fly *Drosophila subobscura*, courtship behavior includes nuptial gift giving, in which the male feeds the female a regurgitated food gift. The same behavior is not observed in related species, including the common lab animal *D. melanogaster*. Tanaka *et al*. studied the genetics of nuptial gift giving in male animals and showed that expression of the gene *FruitlessM* (*FruM*) in insulin-like peptide-producing cells (IPCs) was both necessary and sufficient for triggering this behavior in *D. subobscura*. Overexpression of *FruM* in *D. melanogaster* IPCs induced neurite outgrowth in these cells and increased regurgitation behavior. These results unveil the genetic and neuronal basis of an evolutionary important species-specific behavior. —Mattia Maroso

Science p. 747, 10.1126/science.adp5831

Edited by **Michael Funk**

PLANT COMMUNICATION

Plants communicate through soil microbes

Maize plants emit a volatile gas called linalool, which can influence the growth and development of neighboring plants. Guo *et al*. found that at high planting densities, high linalool concentrations triggered neighboring plants to release benzoxazinoids into the soil (see the Perspective by Schandry and Becker). These compounds cause the soil microbiota to change composition, with knock-on effects for plants that are subsequently grown there. The altered microbiome enhances defense responses to herbivores but reduces plant growth. These findings demonstrate the implications of high planting density on multiple facets of the plant growth environment. —Madeleine Seale

Science p. 698, 10.1126/science. adv6675; see also p. 692, 10.1126/science.adz7633

OPTICAL MATERIALS

Full-color circularly polarized luminescence

Hierarchical supramolecular materials assembled from achiral amphiphilic polymer micelles and chiral additives have high chiroptical activity across the visible spectrum. Kim *et al*. synthesized nanoscopic micelles with inner hydrophilic and outer hydrophobic blocks that hydrogen bonded to R- (or S-) mandelic acid to create nanobelts and ultimately chiral microfibers. Incorporating achiral fluorescent dyes and nanocrystals into these assemblies could produce circularly polarized emission with dissymmetry factors of about 0.1. —Phil Szuromi

Science p. 699, 10.1126/science.adu0296

PROTEIN SIMULATIONS

Going deep on molecular dynamics

Proteins can typically adopt a range of conformations in solution. Molecular dynamics simulations have been used to generate ensembles with realistic probabilities, but the required computational resources are large even for simple problems. Lewis *et al*. developed a generative deep learning protein dynamics emulator called BioEmu that is trained on extensive molecular dynamics results, protein structures, and experimental data. Using a tiny fraction of the power used in traditional simulations, BioEmu generates accurate conformational ensembles for medium-sized soluble proteins. The ability to quickly, cheaply, and accurately generate such data will enable researchers to generate and test many more hypotheses and shift computational resources to validation and investigation of more difficult problems. —Michael A. Funk

Science p. 700 10.1126/science.adv9817

CELL BIOLOGY

Mitochondria versus microbe

Mitochondria consume nutrients that are also needed by invading pathogens. Whether cells exploit this overlap for host defense has been unclear. Medeiros *et al*. found that cells harness mitochondrial metabolism to restrict access of the intracellular parasite *Toxoplasma gondii* to the essential B vitamin folate (see the Perspective by Suomalainen and Nikkanen). When host cells detect intracellular parasite effectors, they activate the integrated stress response and its key effector, ATF4. ATF4 induces one-carbon metabolism processes in host mitochondria that use folate. Because *Toxoplasma* requires folate to generate thymidine for DNA synthesis, ATF4 activation restricts parasite replication. Thus, infected cells can weaponize mitochondrial metabolism to defend against pathogens. —Stella M. Hurtley

Science p. 701, 10.1126/science.adr6326; see also p. 697, 10.1126/science.aea0875

PLATELETS

Added value to platelet purpose

Although platelets are best known for their role in blood clotting, they also contribute to host defense and homeostasis. Murphy *et al*. found that platelets could acquire DNA from nucleated cells by internalizing extracellular vesicles and taking up DNA not enclosed in a membrane, called cell-free DNA (cfDNA) (see the Perspective by Tsui and Lo). In mice, depletion of platelets increased the concentration of cfDNA within blood plasma, indicating that platelets may help to remove cfDNA that has the potential promote inflammation. Human platelets isolated from pregnant individuals contain fetal DNA, and those from cancer patients contain DNA with tumor-associated mutations. Because there is a relatively low concentration of cfDNA in blood plasma, platelets might be an additional source to help overcome a current limitation in clinical diagnostics. —Sarah H. Ross

Science p. 702, 10.1126/ science.adp3971; see also p. 695, 10.1126/science.aea0555

IMMUNOLOGY

Maternal antibodies aid gut homeostasis

Mammals must initiate regulatory mechanisms to limit inflammatory responses to components of food and the microbiome. Shenoy *et al*. found that antibodies ingested by mice from breast milk in the first week after birth regulated immune responses in the gut (see the Perspective by Silverman and Knoop). These antibodies restrained the formation of immune structures, known as germinal centers, within the gut tissue, helped limit T cell responses to food antigens during weaning, and provided protection against experimentally induced colitis. The maternal antibodies could recognize the microbiota in the pups. Complexes comprising bacteria and antibodies could bind to antibody receptors (FcRs) in neonatal life and attenuate the activation of adaptive immune cells. — Sarah H. Ross

Science p. 703, 10.1126/science.ado5294; see also p. 696, 10.1126/science.adz8687

STRUCTURAL METHODS

Diffracting atoms through crystals

High-energy hydrogen and helium atoms have been shown to diffract through graphene without damaging its lattice. Kanitz *et al*. were able to observe diffraction with atoms having kinetic energies normal to the lattice of up to 1.6 kiloelectron volts despite the expected detrimental effects of decoherence and lattice damage (see the Perspective by Holst). Unlike electron diffraction, this method could enable studies of diffraction of matter waves prepared in specific internal states in transmission experiments. —Phil Szuromi

Science p. 724, 10.1126/science.adx5679; see also p. 694, 10.1126/science.adz7660

METHANOGENESIS

Slow down and equilibrate

The isotopic composition of methane is an important signal indicating whether the molecules were produced by biological or geological processes. However, there are

many factors in natural environments that are not reflected in laboratory culture conditions, and caution is necessary when making assumptions about the isotope signatures of biological methanogenesis. Gropp *et al*. used a CRISPR-edited model methanogen with an inducible version of methyl-CoM reductase, the key enzyme of methanogenesis. Lowered expression of this enzyme resulted in a pathway blockage that increased reversibility in the oxidative branch of methanol and acetate metabolism, resulting in an overall shift of isotopic composition in intermediates leading to methane. —Michael A Funk

Science p. 711, 10.1126/science.adu2098

2D MATERIALS

Revealing supermoiré effects

Moiré superlattices formed by stacking two layers of van der Waals materials have characteristic length scales much longer than the lattice constants of the constituent layers. If another layer is then added on top, a supermoiré lattice can form with an even longer wavelength. Xie *et al*. studied the influence of this supermoiré potential on the electronic structure of magic-angle twisted trilayer graphene. The researchers used a local probe, a scanning single-electron transistor microscope, that revealed strongly correlated phases caused by the supermoiré potential and not accessible to transport measurements. —Jelena Stajic

Science p. 736, 10.1126/science.adl2544

HIV

An autoreactive reservoir

A subset of individuals living with HIV-1 harbor persistent plasma HIV-1 RNA despite antiretroviral therapy. Wu *et al*. investigated the potential cause for this and found that HIV-infected $CD4^+$ T cells from individuals with nonsuppressible viremia could produce viral RNA after stimulation ex vivo with autologous cell lysates, indicating that the cells were autoreactive. Moreover, the RNA produced by these cells matched plasma viral RNA from the same individual. These data suggest that autoreactive HIV-1–infected $CD4^+$ T cells may serve as a source of viral RNA in individuals with nonsuppressible viremia. —Courtney Malo

Sci. Transl. Med. (2025) 10.1126/scitranslmed.adu4643

CANCER

Going retro to kill tumors

Cytoplasmic double-stranded RNAs (dsRNAs), such as those derived from endogenous retroviruses, stimulate type I interferon production to promote antitumor responses. Pattarayan *et al*. found that the long noncoding RNA EPIC1, which interacts with the epigenetic regulator EZH2, limited antitumor immunity by repressing the expression of EZH2-regulated retroelements. Loss of EPIC1 in cancer cell lines increased cytoplasmic dsRNA amounts, stimulated interferon-β production, and promoted immune cell activation. In humanized mice bearing breast cancer xenografts, reduction of EPIC1 levels reduced tumor growth and enhanced the efficacy of immunotherapy. —Annalisa M. VanHook

Sci. Signal. (2025) 10.1126/scisignal.adr9131

BIOCATALYSIS

An enabling switch to copper

Copper-catalyzed radical aminations are an important tool for organic chemists, but there has so far not been an enzymatic parallel for use in biocatalytic reactions. Shen *et al*. adapted a nonheme iron enzyme for this purpose by substituting the iron for copper and strategically testing amino acid variations around the active site. The reaction starts with excitation of an organic photocatalyst, which can then oxidize the active-site copper ion bound to the desired amine substrate and reduce an *N*-hydroxyphthalimide ester substrate. The two fragments can then combine to form the product. —Michael A. Funk

Science p. 741, 10.1126/science.adt5986

DROUGHT

What will you do when the well runs dry?

As society grapples with the growing impact of climate change on water resources, researchers are turning to the past to understand how our ancestors dealt with water-related stress. James *et al*. developed a new take on a classic case study for climate-driven societal change: transformation of the Mayan culture near the end of the first millennium CE. The authors used ultra-high-resolution chemical records from a cave formation in Mexico to pinpoint multiple megadroughts within this period of societal change. Different Mayan cultural centers exhibited contrasting responses to these events, highlighting the importance of agricultural and economic systems as a filter on the societal impacts of climate change. —Gabriel Bowen

Sci. Adv. (2025) 10.1126/sciadv.adw7661

CLIMATE MODELING

Predicting ocean state far in advance

Predictions of weather and climate are crucial to making plans, from weddings to emergency responses. Guo *et al.* introduce ORCA-DL, a global, three-dimensional, data-driven ocean forecasting model. Trained on CMIP6 climate model ocean data, ORCA-DL outperforms traditional dynamical modeling in predicting the ocean state, including accompanying variability such as El Niño and extremes such as marine heat waves, using a deep learning approach. An international team of data scientists, oceanographers, and climatologists worked together to extract the most predictive signals within ocean physical variables. The system may still be improved, e.g., by including atmospheric variables, but ORCA-DL is a key step forward in climate prediction, resembling, but distinct from, recent leaps in predicting weather 10 days in advance. —Baylor Fox-Kemper

Sci. Adv. (2025)
10.1126/sciadv.adu2488

ANCIENT PROTEINS

Was the Harbin individual a Denisovan?

Ancient DNA has revealed a great deal about our history, especially admixture events with archaic hominins. However, DNA degrades much faster than other biomolecules such as proteins. Ancient proteomics may enhance our ability to study remains that are older and in environments inhospitable to DNA. Fu *et al*. analyzed ancient proteomic data from a 146,000-year-old cranium from Harbin, China. They identified 95 proteins with sufficient peptides and found that the amino acid variants were consistent with this individual being most closely related to Denisovans. Given the paucity of confirmed Denisovan remains, ancient proteomics may allow the increased identification of such individuals, enabling further study of these enigmatic hominins. —Corinne Simonti

Science p. 704, 10.1126/science.adu9677

VACCINES

Same target, different response

Effective immunity after vaccination depends upon coordinated immune and stromal interactions within the draining lymph nodes. Whether specific vaccine formulations differentially affect the stroma to produce altered immune responses is unknown. Fair-Mäkelä *et al*. functionally assessed how immunizations with different gene-based mRNA, adenovirus vector, and protein-based severe acute respiratory syndrome coronavirus 2 (SARS-CoV-2) vaccine formulations controlled cellular responses in the draining lymph nodes. Although all vaccine types targeted the SARS-CoV-2 spike protein, their specific formulations produced distinct effects on lymph node priming, stromal cell behavior, antigen transfer, and immune migration within draining lymph nodes. —Leoma Bere

Sci. Immunol. (2025)
10.1126/sciimmunol.adr6787

BIOCATALYSIS

An enzyme entry to cyclic terpenoids

Terpenoids are a large class of natural products that derive from enzymatic modification of terpenes. Wang *et al*. developed a combined enzymatic and traditional synthetic chemistry approach to generating meroterpenoid compounds. The authors used directed evolution to generate an epoxidase enzyme that is highly selective for the internal olefin of farnesol. The product of this reaction can then be used as an entry point for further modification and cyclization, often cutting synthetic schemes down considerably.—Michael A. Funk

Science p. 732, 10.1126/science.adt2096

IN OTHER JOURNALS

Edited by **Corinne Simonti** and **Jesse Smith**

DEMENTIA

Soothing tunes

Severe distress puts dementia patients at an increased risk of self-harm or harm to others. UK mental health wards of the National Health Service (NHS) rely on medications to manage distress among dementia patients. However, some evidence suggests that psychosocial interventions may be effective and less costly. Thompson *et al.* designed a pilot intervention for two NHS dementia wards that involved licensed therapists who provided music therapy for patients with advanced dementia, the group least receptive to verbal communication. The music therapy sessions involved both recorded and live music with caretakers, patients, and families present. There were slight improvements in patients' distress and no adverse effects. Although exploratory, findings call for more attention to compassionate alternatives for dementia care. —Ekeoma Uzogara

Front. Psychiatry (2025)
10.3389/fpsyt.2025.1618324

PHYSICS

Friend or foe

Quantum computers are expected to be able to tackle tasks that are too difficult for their classical counterparts. Especially challenging for classical computers are problems where entanglement accumulates over time. Zhao *et al.* explored the influence of quantum entanglement on algorithm error associated with product formula methods for quantum simulation. In contrast to classical computing, they found that entanglement was beneficial to quantum simulation because it resulted in smaller error bounds. These findings could lead to more efficient quantum algorithms that adapt to growing entanglement. —Jelena Stajic

Nat. Phys. (2025)
10.1038/s41567-025-02945-2

PROTEIN EVOLUTION

Simulating random emergence of folds

Globular proteins typically fold into compact domains composed of well-packed secondary structural elements. Such folded proteins likely emerged very early in biology, but it is not clear how or from what starting point. To study this puzzle, Sahakyan *et al.* developed a computational simulation for protein fold evolution starting from random amino acid sequences. They observed that the emergence of simple folded

HUMAN GENETICS

Adapting to the Himalayas

Living at high altitude poses health risks for humans, leading to studies of populations that have lived multiple generations in Tibet and the Andes. Arciero *et al.* sequenced 87 individuals from 16 Himalayan populations from China, Nepal, Bhutan, and India. Although these groups clustered together genetically, they showed differing admixture levels between South Asian and East Asian populations, as well as differing divergence times, including some as deeply diverged as 10,000 years ago. All populations carried the high-altitude Denisovan EPAS1 haplotype originally identified in Tibetan populations, in addition to novel selection signals. This study expands our understanding of high-altitude adaptation in humans and the demographic history of these populations. —Corinne Simonti

Curr. Biol. (2025) 10.1016/j.cub.2025.06.048

Genetic study of expanded Himalayan populations reveals new potential signs of selection for high-altitude living.

proteins required, on average, several mutations per site over many generations. Whether this simulation reflects how protein folds truly emerged is a matter of speculation, but it at least suggests that it is a plausible mechanism. —Michael A. Funk

Proc. Natl. Acad. Sci. U.S.A. (2025) 10.1073/pnas.2509015122

MATERIALS SCIENCE

Encoding tiny structures

Inverse design methods start with a specific target and work backward to determine the characteristics of individual constituents that need to be tuned to obtain the desired outcome. These approaches allow designing complex hierarchical structures that were unobtainable by traditional methods. Kahn *et al.* used sequence-specific DNA bonds to direct assemblies of three-dimensional nanostructures with long-range orders. The authors minimized the amount of encoded information by using a set of voxels, which served as a conceptual motif to guide the design process. Several exemplary structures were demonstrated, including a nanoscale analog of a face-centered perovskite and a distributed Bragg reflector. —Sumin Jin

Nat. Mater. (2025) 10.1038/s41563-025-02263-1

SLEEP

Good morning, brain

The process of transitioning from sleep to wakefulness (awakening) in humans has been shown to occur over several minutes. However, how the awakening process occurs at the level of brain activity remains to be fully elucidated. Stephan *et al.* analyzed more than 1000 awakening events in humans using high-density electroencephalography (EEG) and revealed distinct spatiotemporal EEG signatures associated with awakening from non–rapid eye movement (non-REM) and REM sleep. When present before waking up from non-REM sleep, this distinct EEG pattern was associated with feeling less sleepy. These results might have implications for sleep disorders associated with abnormal sleepiness during wakefulness. —Mattia Maroso

Curr. Biol. (2025) 10.1016/j.cub.2025.06.064

METABOLISM

Weighing energy expenditure

As human societies have urbanized and become more internationally connected, obesity has followed. However, it is not clear what the main contributor to body size is or if obesity is a cause or outcome of correlated disease risks. McGrosky *et al.* measured energy expenditures in populations across the economic development spectrum. Despite common beliefs around decreased activity in industrialized societies, total energy expenditure differed very little between groups, suggesting that energy intake may explain differences in body size (although this was not measured directly). Increasing affluence has led to reductions in pathogen burdens, which might mean that less energy is spent on immune responses. Alternatively, excess energy intake could originate in easy access to calories in industrial food products. —Caroline Ash

Proc. Natl. Acad. Sci. U.S.A. (2025) 10.1073/pnas.2420902122

Check for

RESEARCH ARTICLE SUMMARY

IMMUNOLOGY

Breast milk IgG engages the mouse neonatal immune system to instruct responses to gut antigens

Meera K. Shenoy, Diane M. Rico†, Alina K. Lorant†, Hamadoun Touré, Shannon Gordon, Luke J. Milburn, Jeanette S. Schwensen, Madelyn E. Cabán, Meghan A. Koch*

Full article and list of author affiliations: https://doi.org/10.1126/science.ado5294

INTRODUCTION: In mammals, the early-life period after birth is a time of profound immune development during which the generation of appropriate responses to newly encountered commensal and environmental antigens is crucial for maintaining health. Breast milk is positioned to regulate nascent mucosal immune responses through the delivery of live microbes, commensal-selecting oligosaccharides, maternal cells, and immunomodulatory factors, such as antibodies, directly to the infant gut. By defining the beneficial components of breast milk and the mechanisms by which they function, we may advance strategies to boost healthy immunity in early life and beyond.

RATIONALE: Numerous studies in mice and humans support a central function for breast milk antibodies in establishing healthy gut immunity, yet the mechanisms underlying this process are not clear. Existing models, largely based on lumenal immunoglobulin A (IgA) in adults, overlook critical physiological features of early life, including an immature gut barrier, dynamic microbiota, and the presence of multiple breast milk–derived antibody isotypes (IgA, IgG, and IgM) in the infant lumen. We developed a strategy to dissect the specific contributions, timing, and function of breast milk antibodies during the postnatal period.

RESULTS: Using an established mouse model of maternal antibody deficiency in which offspring were cross-fostered at various postnatal time points, we found that ingestion of breast milk antibodies in the first week of life served to restrain germinal center T follicular helper cell (T_{FH} cell) and B cell responses weeks later, after weaning. This elevated immune response was specific to gut-associated lymphoid tissues and was attenuated in sterile animals lacking a gut microbiota. Feeding mouse pups during the first 7 days of life with IgG purified from milk or serum was sufficient to restrain later immune dysregulation. Although the ability of ingested IgG to bind neonatal gut bacteria was linked with its protective functions, it did not cause changes in microbiota composition or gut barrier function. Unlike IgA, mouse IgG can directly engage with the immune system through antibody (Fc) receptors and the complement pathway. Neonatal immune cells in the intestinal lamina propria and epithelium expressed multiple Fc and complement receptors, and oral IgG administration was unable to dampen aberrant immunity in offspring deficient in these IgG-sensing systems. Last, we found that feeding pups microbiota-reactive IgG in the first week of life served to limit offspring susceptibility to colitis and prevent aberrant allergic responses to food antigens during the weaning transition.

CONCLUSION: Breast milk antibodies play a vital role in shaping early-life intestinal homeostasis. Our data support a model in which breast milk IgG interacts with gut bacteria and antibody-sensing systems in young mice to dampen subsequent immune responses to gut microbial and dietary antigens encountered during weaning. This broad, protective effect of maternal IgG may represent an evolutionary strategy by which mammals promote tolerogenic responses to the diverse antigens introduced during this developmental period. □

*Corresponding author. Email: mkoch@fredhutch.org †These authors contributed equally to this work. Cite this article as M. K. Shenoy *et al.*, *Science* **389**, eado5294 (2025). DOI: 10.1126/science.ado5294

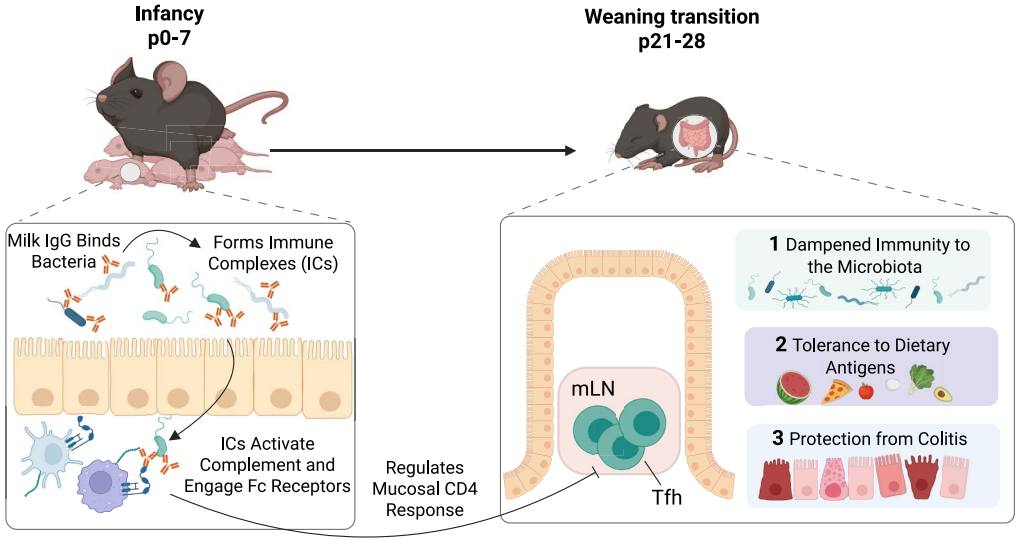

Breast milk IgG orchestrates adaptive immune responses to gut antigens. Maternal IgG, orally acquired through breastfeeding in the first week of life, binds to commensal bacteria in the neonatal gut and forms immune complexes. These immune complexes engage neonatal IgG sensors, thus regulating subsequent adaptive immune responses to gut bacteria and dietary antigens and reducing susceptibility to colonic wounding. [Figure created with BioRender.com]

IMMUNOLOGY

Breast milk IgG engages the mouse neonatal immune system to instruct responses to gut antigens

Meera K. Shenoy[1,2], Diane M. Rico[1]†, Alina K. Lorant[1]†, Hamadoun Touré[1], Shannon Gordon[1]‡, Luke J. Milburn[1], Jeanette S. Schwensen[3,4,5], Madelyn E. Cabán[1,6], Meghan A. Koch[1,6]*

Maternal antibodies fundamentally regulate gut immunity in the developing infant, yet the mechanisms underlying this process remain elusive. We found that maternal immunoglobulin G (IgG), ingested in the first week of life, restrained microbiota-dependent adaptive immune responses weeks later, after weaning. This activity was linked to maternal antibodies that could bind bacteria in the neonatal gut and the ability of microbe-IgG complexes to engage Fc and complement-dependent effector functions in offspring. Ingestion of microbiota-specific maternal IgG also limited aberrant neonatal responses to dietary antigens encountered at weaning. These discoveries suggest that maternal IgG engages the immune system of offspring in early postnatal life to tune mucosal responses and reinforce intestinal homeostasis in the face of dynamic shifts in food and bacterial antigens during development.

A fundamental function of the immune system is to promote mutualism between the host and resident microbiota. In the gut, this process enables the host to harness numerous benefits from microbes, including expanded nutrient assimilation, immune education, and resistance to pathogen colonization, while mitigating risks such as toxin exposure, chronic inflammation, and pathobiont invasion (*1*–*3*). In early life, establishing immune tolerance toward the microbiota while avoiding harmful inflammation is complicated by the dynamic nature of the neonatal period—marked by rapid changes in microbiota and food antigen composition. Studies linking perturbations in infant microbiota exposure or assembly with increased risk of metabolic and/or inflammatory diseases underscore the importance of this process (*4*–*8*). Ingested immediately after birth, breast milk is poised to regulate nascent host-microbiota interactions. Along with nutrients, breast milk provides offspring with live bacteria, maternal immune cells, and immunomodulatory molecules, including cytokines and immunoglobulins (*9*, *10*).

Multiple antibody isotypes, including immunoglobulin A (IgA) and IgG, are readily detectable in breast milk, although the relative abundance of these isotypes differs according to species. For example, mouse milk contains proportionately higher levels of IgG compared with that of humans (*11*). Pioneering work by Kramer and Cebra revealed that young mice reared by dams lacking B and T cells exhibit increased T cell–dependent germinal center (GC) reactions in gut-associated lymphoid tissues, including Peyer's patches (PPs) and mesenteric lymph nodes (mLNs), indicating that maternal antibodies regulate homeostatic gut immunity (*12*). In subsequent studies, we solidified the importance of breast milk antibodies (rather than maternal T cells) in this process by using mothers with a targeted disruption of the mu heavy chain gene ($\mu MT^{-/-}$). These mice lack mature B cells and are deficient in antibodies. Wild-type (WT) C57Bl/6 (B6) offspring reared by $\mu MT^{-/-}$ dams exhibit similar immune dysregulation, characterized by heightened GC T follicular helper cell (T_{FH} cell) and GC B cell frequencies and numbers in the mLNs and PPs (*13*). This response is transient, with elevated T_{FH} cell responses peaking around postnatal days 25 to 26 (p25 to p26) and normalizing to WT levels at later time points. Additional studies in humans and mice have shown that breast milk antibodies readily bind infant gut microbes and can help shape the assembly of the microbiome, promote barrier function, restrain inflammatory responses to commensal microbes, and guide the abundance of mucosal T cell subsets (*9*, *10*, *12*–*16*).

The prevailing model of immune instruction mediated by maternal antibodies is largely based on studies of IgA-directed regulation of enteric pathogens and certain gut commensal strains in adult mice (*17*–*23*). However, this model does not account for substantial differences in gut physiology, such as increased barrier permeability in early life, altered microbiota composition, and the presence of other antibody isotypes—such as breast milk–derived IgG—in the infant gut (*13*, *24*–*27*). As such, the mechanisms underlying antibody function at the maternal-offspring interface remain unclear. In this work, we developed a mouse model that enabled precise control over the timing and composition of breast milk antibodies, the microbiota, and the infant immune system to delineate the mechanisms by which breast milk antibodies tune offspring immunity to newly encountered mucosal antigens.

Results

Early-life acquisition of breast milk antibodies restrains mucosal adaptive immune responses after weaning

Mucosal immunity is heavily influenced by the microbiota, which can vary substantially between different housing conditions and physical locations (*28*, *29*). Thus, to confirm that T_{FH} cell–driven immune dysregulation is a common feature of breast milk antibody deficiency, we assessed responses in mice maintained at the Fred Hutchinson Cancer Center in Seattle, Washington. Mirroring our prior findings with neonates housed at the University of California, Berkeley in Berkeley, California (*13*), we found that the acquisition of breast milk antibodies during the entire preweaning period, from birth to 21 days (p0 to p21), prevented mucosal immune dysregulation. Four days after weaning (p25), the offspring of $\mu MT^{-/-}$ dams and B6 sires had elevated T_{FH} cell numbers and frequencies in the mLNs (marked as $CD4^+Foxp3^-CD44^+PD\text{-}1^+CXCR5^{hi}Bcl6^+$) (fig S1A) compared with that of control pups of B cell–sufficient, $\mu MT^{+/-}$ dams (Fig. 1, A and B). These differences were also observed in the PPs and corresponded with elevated GC B cell responses, as distinguished by the number and frequency of $CD19^+IgD^{lo}B220^+PNA^+GL7^+$ cells (fig. S1, B to D). We performed similar experiments with a distinct model of B cell deficiency by using $Jh^{-/-}$ dams, which are completely devoid of mature B cells and antibodies owing to a targeted deletion of JH gene segments. Further, to rule out strain-specific effects in maternal antibody function, we used $Jh^{-/-}$ on the Balb/c background, which is genetically distinct from the C56Bl/6 background of $\mu MT^{-/-}$ mice. We observed similar immune dysregulation in p25 offspring of B cell–deficient $Jh^{-/-}$ dams and WT sires (fig. S1, E and F). Having established that heightened mLN T_{FH} cell abundance was consistently observed in neonates lacking maternal antibodies, we focused on this response as a "readout" to decipher the mechanisms involved in breast milk antibody function.

Establishing intestinal homeostasis relies on a series of coordinated events occurring during distinct developmental phases, such as

[1]Basic Sciences Division, Fred Hutchinson Cancer Center, Seattle, WA, USA. [2]Singapore Immunology Network (SIgN), Agency for Science, Technology and Research (A*STAR), Singapore, Republic of Singapore. [3]Translational Science and Therapeutics Division, Fred Hutchinson Cancer Center, Seattle, WA, USA. [4]Molecular and Cellular Biology Graduate Program, University of Washington, Seattle, WA, USA. [5]Medical Scientist Training Program, University of Washington, Seattle, WA, USA. [6]Department of Immunology, University of Washington, Seattle, WA, USA. ***Corresponding author. Email: mkoch@fredhutch.org**
†These authors contributed equally to this work. ‡Present address: Department of Medicine, University of Chicago, Chicago, IL, USA.

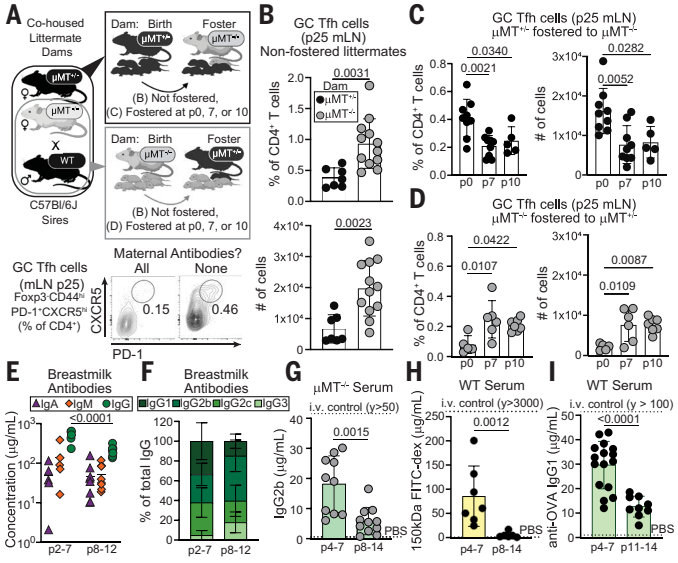

Fig. 1. Acquisition of breast milk antibodies in early life prevents immune dysregulation after weaning. (**A**) (Top) Timed breedings were performed by using cohoused, littermate $\mu MT^{+/-}$ and $\mu MT^{-/-}$ dams and B6 sires. Offspring were maintained with their birth mother or cross-fostered at p0, p7, or p10 and analyzed at p25. (Bottom) Representative flow cytometric analysis of GC T_{FH} cells ($CD4^+Foxp3^-CD44^{hi}PD\text{-}1^+CXCR5^{hi}Bcl6^+$) isolated from the mLNs of p25 offspring born to and reared by the indicated dams. Numbers in flow plots indicate percentage of T_{FH} cells of total $CD4^+$ T cells. Cells were gated according to the schematic in fig. S1A (**B**) (Top) Proportions and (bottom) numbers of mLN GC T_{FH} cells in p25 offspring born to and reared by the indicated dams. (**C**) (Left) Proportions and (right) numbers of mLN GC T_{FH} cells in p25 offspring born to $\mu MT^{+/-}$ dams and fostered to $\mu MT^{-/-}$ dams at the indicated postnatal time points. (**D**) Similar to (C), comparing $\mu MT^{-/-}$ born offspring fostered to $\mu MT^{+/-}$ dams. (**E**) IgA, IgM, and IgG titers and (**F**) IgG subclass distribution in breast milk from wild-type (WT) B6 dams sampled at the indicated time periods after parturition. All dams were 12 to 16 weeks of age. (**G**) Serum IgG2b levels in $\mu MT^{-/-}$ pups of the indicated age 2 hours after gavage with 10 mg/kg monoclonal mouse IgG2b antibodies. Bottom and top dotted lines indicate detected IgG2b levels in mice gavaged with PBS or injected intravenously (i.v.) with IgG2b, respectively. (**H**) Serum FITC-dextran (FITC-dex) titers in WT pups of the indicated age 2 hours after gavage with 10 mg/kg FITC-dex (150 kDa). Bottom and top dotted lines indicate detected FITC-dex levels in mice gavaged with PBS or injected intravenously with FITC-dex, respectively. (**I**) Serum OVA-specific IgG1 levels in WT pups of the indicated age 2 hours after gavage with 10 mg/kg monoclonal mouse IgG1 antibodies to OVA. Bottom and top dotted lines indicate detected OVA-specific IgG1 levels in mice gavaged with PBS or injected intravenously with antibodies to OVA IgG1, respectively. Error bars indicate the mean ± SD; symbols indicate individual mice. Data are representative of three to four independent experiments with five or more mice per group. Statistical significance was determined by using one-way analysis of variance (ANOVA) and Tukey post-hoc tests, except (B) and (G) to (I), for which unpaired two-tailed Student's *t* tests were used.

microbiota seeding and diversification, innate immune hyporesponsiveness, and controlled transport of luminal antigens (*30*). To determine whether breast milk antibody transfer during a specific postnatal window was required to regulate mucosal immunity, we cross-fostered the offspring of $\mu MT^{+/-}$ and $\mu MT^{-/-}$ dams and B6 sires at different ages (Fig. 1A). The microbiome can vary markedly between noncohoused, nonlittermate animals, driving intestinal alterations that are independent of genetically encoded immune factors, such as maternal antibodies (*31*). Thus, to maximally homogenize the microbiota between birth mothers, offspring, and foster mothers, we used littermate, cohoused $\mu MT^{+/-}$ and $\mu MT^{-/-}$ dams that were only separated briefly: first for breeding with sires, and then again before parturition and through offspring weaning. Progeny of $\mu MT^{+/-}$ dams fostered to antibody-deficient $\mu MT^{-/-}$ dams after the first week of life (p7 or later) harbored reduced frequencies and numbers of T_{FH} and GC B cells compared with those of pups fostered at birth (p0) (Fig. 1C and fig. S1, G and H). Additionally, $\mu MT^{-/-}$ dam-born pups fostered to antibody-sufficient $\mu MT^{+/-}$ dams at p0 did not exhibit immune dysregulation, whereas elevated mucosal T_{FH} and GC B cell responses were apparent in littermate counterparts fostered after p7 (Fig. 1D and fig. S1, G and I). These findings indicated that antibody ingestion during the first week of life regulates homeostatic immune development in the gut.

Maternal antibodies have been described to promote intestinal barrier function in offspring at weaning (*15*). However, we found no difference in the accumulation of type 3 innate lymphoid cells (ILC3s) or the amount of interleukin-22 (IL-22) in the lamina propria, factors important for maintaining gut barrier function (fig. S2, A to C). Direct tests of barrier function by means of gavage of the nondigestible substrate fluorescein isothiocyanate (FITC)–dextran or a laboratory strain of *Escherichia coli* (K-12) also revealed no difference in the translocation of these substances between young maternal antibody–sufficient and –deficient mice (fig. S2, D and E).

A network of antigen-presenting cells (APCs) directs the differentiation of effector T cells in gut-draining lymphoid tissues. Thus, we considered that differences in mLN APC composition could precede the T_{FH} cell immune dysregulation in mice lacking maternal antibodies (*32*, *33*). Analysis at p21, before the elevated T_{FH} and GC B cell responses observed in these offspring, revealed only modest alterations in mLN APCs, including type-1 and -2 conventional dendritic cells (cDC1 and cDC2), $F4/80^+$ macrophages, and CX_3CR1^+ mononuclear phagocytes (MNPs) (fig. S2, F and G) (*34*). These findings demonstrated that the absence of maternal antibodies did not impair intestinal barrier function nor broadly alter the distribution of mLN APC subsets.

Kinetics of mouse antibody consumption and gut permeability during development

To understand how breast milk antibodies regulated intestinal homeostasis, we assessed breast milk consumption and composition over time (fig. S3A). Breast milk intake increased as a function of age (fig. S3B), and the total immunoglobulin concentration in milk (the sum of IgG, IgA, and IgM; IgE was not detected) was largely stable during the first 2 weeks of lactation. Milk from dams 0 to 7 days postpartum contained more IgG than from those sampled later, consisting of approximately 30% IgG1, 30% IgG2b, 35% IgG2c, and 5% IgG3 (Fig. 1, E and F). Extrapolating data on milk intake and antibody concentrations, we estimate pups in our mouse colony consumed 244 μg/day of IgG and 17 μg/day IgA on average in the first week of life (fig. S3C).

The gastrointestinal tract undergoes developmentally regulated physiological changes characterized by alterations in antimicrobial peptides, mucus, nutrient transporters, and barrier permeability (*35*, *36*). In healthy human infants, gut permeability to small sugars is increased during the first week of life (*37*), and one study reported translocation of IgA dimers (~300 kDa) in term babies orally administered IgA within 24 hours after birth (*38*). These observations prompted us to assess whether the window of breast milk antibody acquisition required to dampen offspring immunity correlated with gut barrier permeability to ingested IgG. To directly evaluate IgG translocation in the absence of cognate antigens or endogenous maternal- or offspring-derived IgG, we orally administered an isotype-control IgG2b (normalized mg/kg) to $\mu MT^{-/-}$ progeny of $\mu MT^{-/-}$ dams. Two hours after treatment, we detected higher levels of (total) serum IgG2b in p0 to p7 pups as compared with older offspring (Fig. 1G). We observed a similar heightened translocation of ovalbumin (OVA)–specific IgG1 or 150 kDa fluorescein-conjugated dextran (similar molecular weight to that of IgG) in young (p0 to p7) WT B6 pups (Fig. 1, H and I), ruling out the possibility that the increase in barrier permeability resulted from

developmental defects in μMT$^{-/-}$ animals. Thus, the mouse gut was more permeable to luminal substrates during the first week of life, the same window during which maternal antibodies must be ingested to establish intestinal homeostasis.

Oral IgG can prevent mucosal immune dysregulation in offspring

To define the maternal antibody isotypes required to prevent immune dysregulation, we fractionated IgG from IgA, IgM, and other milk proteins using Protein A purification (Fig. 2A). We confirmed the efficient isolation of IgG subclasses and overall purity of fractionated milk IgG (>98%), whereas the flow-through (mΔIgG) was enriched for IgA (Fig. 2B).

We then performed "add-back" experiments in which we fed littermate, maternal antibody–deficient offspring fractionated milk antibodies, thus allowing a direct comparison of cohoused littermates born to and reared by the same mother and avoiding potential confounding variables introduced by maternal microbiota, antibody concentrations, or housing conditions (*31*). We fed maternal antibody–deficient offspring 0.5 μg of milk IgG (mIgG), 1 μg milk IgA (mΔIgG; also harboring other proteins), or 1 μg bovine serum albumin (BSA; irrelevant protein antigen) daily from p0 to p7 (Fig. 2A). At p25, neonates fed mIgG exhibited reduced mLN T_{FH} cell responses compared with that of pups administered BSA or mΔIgG (Fig. 2C and fig. S4A). Low pregnancy rates from timed breedings and unanticipated pup attrition due to natural behaviors (such as cannibalism) made it difficult to generate large numbers of offspring for each experimental group (*39*, *40*). Thus, for this experiment and others in which obtaining a high number of mice (*n*) was difficult, we show two or more combined replicates. We obtained similar results to mIgG using IgG purified from sera of WT C57Bl/6 mice in our mouse colony (sIgG), in which administration of sIgG—but not serum depleted of IgG (sΔIgG; of which IgM was the dominant isotype), BSA, or phosphate-buffered saline (PBS)—resulted in fewer mLN T_{FH} cells in p25 progeny of μMT$^{-/-}$ dams and B6 sires (Fig. 2, D and E, and fig. S4B).

Although the magnitude of the immune dysregulation varied between litters, mLN T_{FH} cell responses were consistently lower in pups fed sIgG as compared with littermate controls given sΔIgG (Fig. 2F and fig. S4C). Administration of sIgG to offspring reared by μMT$^{-/-}$ dams did not affect the accumulation of other differentiated mLN CD4 T cell populations that serve important functions in mucosal immunity, including T-bet^{+} [T helper type 1 cell (T_H1 cell)] and retinoid-related orphan receptor–γt^{+} (RORγt^{+}) (T_H17 cell) effector subsets nor Foxp3^{+} regulatory T cell (T_{reg} cell) subsets (fig. S4, D and E) (*41*, *42*).

Oral IgG was also able to dampen mLN T_{FH} cell responses through use of a distinct model of maternal antibody deficiency achieved by breeding C57/Bl6 B cell–deficient Jh$^{-/-}$ dams with B6 sires (fig. S4F). The ability of IgG to prevent mucosal immune dysregulation indicated that the absence of antibodies, rather than an unrelated perturbation in the milk or the behavior of B cell–deficient mothers, triggered aberrant intestinal immunity. Dose-response experiments revealed that as little as 1 μg/day sIgG during p0 to p7 was sufficient to fully restrain mesenteric T_{FH} cell responses in p25 offspring of μMT$^{-/-}$ dams and B6 sires (Fig. 2G and fig. S4G). Because mouse serum is more plentiful than milk, and milk lipoproteins impede the efficient purification of IgG, we used sIgG for the remaining studies.

The interplay between maternal antibodies, the postnatal microbiome, and homeostatic intestinal immunity

The selective elevation of T_{FH} cell responses at mucosal (such as mLNs and PPs) but not systemic sites [such as the spleen (*13*)] prompted us to examine the role of the gut microbiota in driving immune dysregulation in offspring lacking maternal antibodies. We first analyzed "sterile" mice maintained under germ-free (GF) conditions and thus devoid of gut bacteria. Offspring of GF B6.Jh$^{-/-}$ dams and WT sires harbored equivalent, low frequencies and numbers of mucosal T_{FH} cells, regardless of maternal antibody acquisition (Fig. 3A and fig. S5A). As a complementary approach, we treated mice with a cocktail of broad-spectrum antibiotics composed of ampicillin, vancomycin, neomycin, and metronidazole (AVNM) to reduce gut microbial density immediately before the height of the T_{FH} response (p17 to p24) (fig. S5B) (*43*). Consistent with the data from GF mice, AVNM reduced T_{FH} cell frequencies and numbers in maternal antibody–deficient offspring. However, the response in these animals was still elevated compared with maternal antibody–sufficient progeny that received antibiotics (fig. S5, C and D). This increase could result from incomplete microbial elimination or changes in microbial composition after AVNM treatment (*43*, *44*). Alternatively, it is possible that other mucosal antigens, such as dietary components, contributed to immune dysregulation in mice lacking maternal antibodies. Weaning pups earlier (p18) or later (p25) than the standard of p21 resulted in similar immune dysregulation, indicating that this response was not controlled by the cessation of breastfeeding (Fig. 3B and fig. S5E). Together, these observations suggested that the microbiota triggered a homeostatic T_{FH} cell response after weaning and that maternal antibodies controlled the magnitude of this response.

Antibodies are key regulators of gut microbiota diversity and composition (*16*, *45*–*47*), which led us to explore whether alterations in microbiome assembly correlated with immune dysregulation in maternal antibody–deficient offspring. 16*S* ribosomal RNA (rRNA) gene sequencing of ileal and colonic contents (fig. S6A) did not reveal substantial differences in the diversity of microbes in each sample (alpha diversity) nor between-group distances (beta diversity) between age-matched offspring of μMT$^{+/-}$ or μMT$^{-/-}$ littermate dams and B6 sires (fig. S6, B to E). However, the abundance of a small subset of taxa differed between p7 offspring of μMT$^{+/-}$ and μMT$^{-/-}$ dams, and this variation increased with age (Fig. 3, C and D, and fig. S6, F to H). Thus, the absence of all breast milk antibodies correlated with minor alterations in the assembly of the postnatal microbiome. Analysis of p20 progeny of μMT$^{-/-}$ dams and B6 sires fed sIgG or BSA during the first week of life similarly failed to reveal differences in alpha or beta diversity as a function of feeding (Fig. 3E and fig. S7, A to C). Instead, litter was a driving factor (Fig. 3F and fig. S7D). The provision of IgG resulted in the differential abundance of only a single ileal taxon and two colonic taxa (Fig. 3G and fig. S7E), which were distinct from those identified in p21 offspring of μMT$^{+/-}$ and μMT$^{-/-}$ dams. Taken together with results from littermate mice (Fig. 2F and fig. S4C), these data demonstrated that the ability of early-life IgG to regulate neonatal immunity was robust to natural microbiome variation between litters. Additionally, the similarity in microbiota community structure between IgG- and BSA-fed littermates indicates that breast milk IgG could regulate neonatal immunity without altering the composition of the developing microbiome.

Early-life IgG-microbe immune complexes prevent intestinal immune dysregulation

The acquisition of maternal antibodies through breastfeeding, rather than placental transfer, was required to prevent T_{FH} cell–driven immune dysregulation (Fig. 1, B to D) (*13*). Serum analysis of p7 offspring of μMT$^{+/-}$ or μMT$^{-/-}$ dams and B6 sires cross-fostered at birth revealed that mice receive a substantial amount of maternal IgG through breastfeeding as opposed to during gestation (Fig. 4A and fig. S8A). We found that maternal antibody–deficient pups fed sIgG harbored even lower serum IgG titers as compared with that of offspring that only received maternal antibodies in utero (Fig. 4A and fig. S8A). Because feeding pups sIgG was sufficient to reduce mucosal T_{FH} responses, these findings rule out the possibility that the immune dysregulation observed in pups nursed by antibody-deficient dams resulted from insufficient amounts of circulating IgG and indicated that the route of acquisition (oral) underlies the immunoregulatory function of maternal IgG.

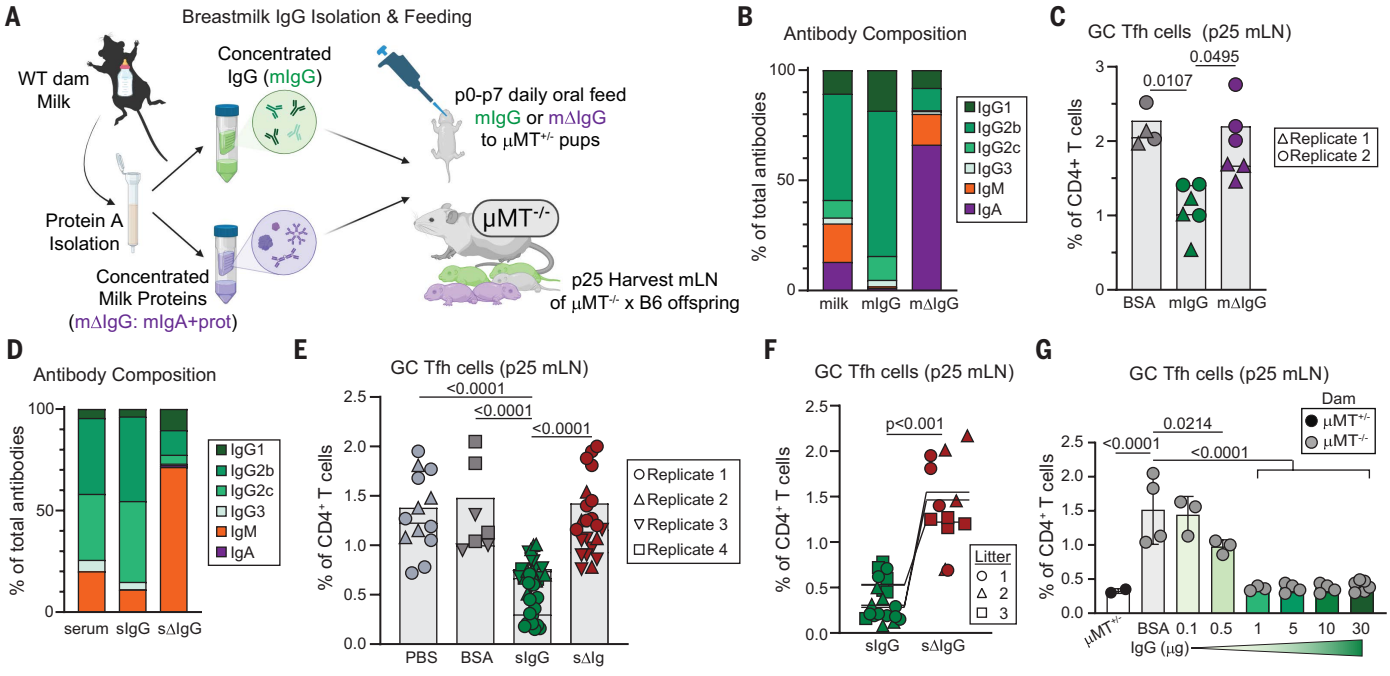

Fig. 2. Oral IgG is sufficient to restrain T_{FH} immune dysregulation in offspring lacking maternal antibodies. (**A**) Milk IgG was fractionated from other proteins by using Protein A columns; fractions were concentrated then fed to offspring of $\mu MT^{-/-}$ dams and B6 sires during the first week of life. Control pups were fed BSA. (**B**) Immunoglobulin distribution in milk (input) and after Protein A fractionation into purified milk (mIgG) and eluate (mΔIgG) components. Milk was isolated from B6 dams at 12 to 16 weeks of age. (**C**) Proportions of mLN GC T_{FH} cells in p25 offspring fed 0.5 μg mIgG, 1 μg mIgA (plus other proteins), or 1 μg BSA daily from p0 to p7. (**D**) Immunoglobulin distribution in serum (input) and after Protein A fractionation into purified serum (sIgG), and eluate (sΔIgG). Serum was isolated from WT mice at 10 to 16 weeks of age. (**E**) Proportions of mLN GC T_{FH} cells in p25 offspring of $\mu MT^{-/-}$ dams and B6 sires fed 10 μg serum-purified IgG (sIgG), IgG-depleted serum (sΔIgG), PBS, or BSA daily during p0 to p7 as indicated. (**F**) Similar to (E), comparing proportions of mLN GC T_{FH} cells in littermate, cohoused pups given 10 μg sIgG or sΔIgG between p0 to p7. Littermate animals are indicated by symbols, and lines connect the mean of cohoused littermates. (**G**) Similar to (E), comparing p25 mLN GC T_{FH} frequencies in offspring of $\mu MT^{+/-}$ dams or of $\mu MT^{-/-}$ dams fed the indicated concentrations of sIgG or BSA between p0 and p7. For (B), milk was pooled from approximately two dozen dams, each with four or more pups aged between 4 and 10 days. Pooled milk was separated by means of Protein A chromatography, and the antibody composition was determined with enzyme-linked immunosorbent assay (ELISA). The indicated fractions from pooled milk were used for all independent experiments. Data are representative of three to four independent experiments with three or more mice per group, except for (C) and (E), in which data were combined from two to four replicate experiments and representative of four or more independent experiments. Lines on bar graphs indicate the mean of each replicate, and symbols indicate individual mice. For (F), error bars indicate the mean of each litter, and diagonal lines connect the means of cohoused littermates. For (G), error bars indicate the mean ± SD; symbols indicate individual mice. Statistical significance was determined by using two-way ANOVA with Sidak post-hoc tests for (C) and (E), one-way ANOVA and Tukey post-hoc tests for (G), and an unpaired two-tailed Student's *t* test for (F).

These observations prompted us to hypothesize that maternal IgG must bind to neonatal gut microbes to regulate mucosal immunity. We assessed the antibody binding profiles of milk and serum using microbiota–flow cytometry (mFLOW) (fig. S8B) (*13*). To avoid precoating of infant bacteria by maternal antibodies, we used gut contents from $\mu MT^{-/-}$ pups (p6 to p8). IgG antibodies from either milk or serum bound a substantial fraction of the neonatal microbiota (Fig. 4, B to D). Although all IgG subclasses were detectable in breast milk, the IgG response to pup-derived microbiota in both milk and serum was largely composed of IgG2b and IgG3 subclasses (Fig. 4E and fig. S8C), which is consistent with our previous report that used serum and microbiota from adult animals (*13*). When matched for concentration, milk IgG tended to bind a larger fraction of infant gut bacteria, whereas paired serum IgG bound a larger proportion of bacteria derived from 3-month-old $\mu MT^{-/-}$ adult mice (fig. S8D). Additionally, we confirmed that fractionated IgG used for feeding studies retained the ability to bind to neonatal gut microbes (fig. S8E).

We queried whether efficient binding to intestinal microbes was required for oral IgG to prevent neonatal mucosal immune dysregulation. Using serum IgG from GF mice (GF-sIgG), which harbor reduced titers of microbiota-reactive antibodies, including to the infant microbiota (Fig. 4F) (*13*, *48*), we fed progeny of $\mu MT^{-/-}$ dams and B6 sires 1 μg/day GF-sIgG, specific pathogen–free (SPF)–sIgG, or BSA between p0 and p7. Although normalized by concentration, GF-sIgG was unable to restrain mucosal immune dysregulation, as evidenced by the heightened mLN T_{FH} cell responses in these animals compared with pups fed SPF-sIgG (Fig. 4G and fig. S8F).

Because IgG from GF mice retained some ability to bind the microbiota, it is possible that higher amounts of GF-sIgG would be sufficient to limit subsequent T cell responses. Thus, we attempted complementary experiments by administering commercially available "nonspecific" monoclonal antibodies. We identified IgG1 and IgG2a (allelic variant of IgG2c) clones that did not react to the infant microbiota; however, all IgG2b and IgG3 clones we tested exhibited some amount of binding (fig. S8G). The commensal-reactive IgG antibody response is largely comprised of IgG2b and IgG3 responses (Fig. 4E). Because IgG subclass composition is a core determinant of antibody function (*49*, *50*), we opted to administer a cocktail of IgG antibodies that included IgG2b and IgG3 clones even though they demonstrated low-level binding to the microbiota, in addition to nonspecific IgG1 and IgG2a. Compared with mice given sIgG, mucosal T_{FH} cell responses tended to be higher in pups given the IgG isotype cocktail, yet this difference was not statistically significant (fig. S8, H and I). This partial effect could be ascribed to the non-negligible microbiota binding by IgG2b

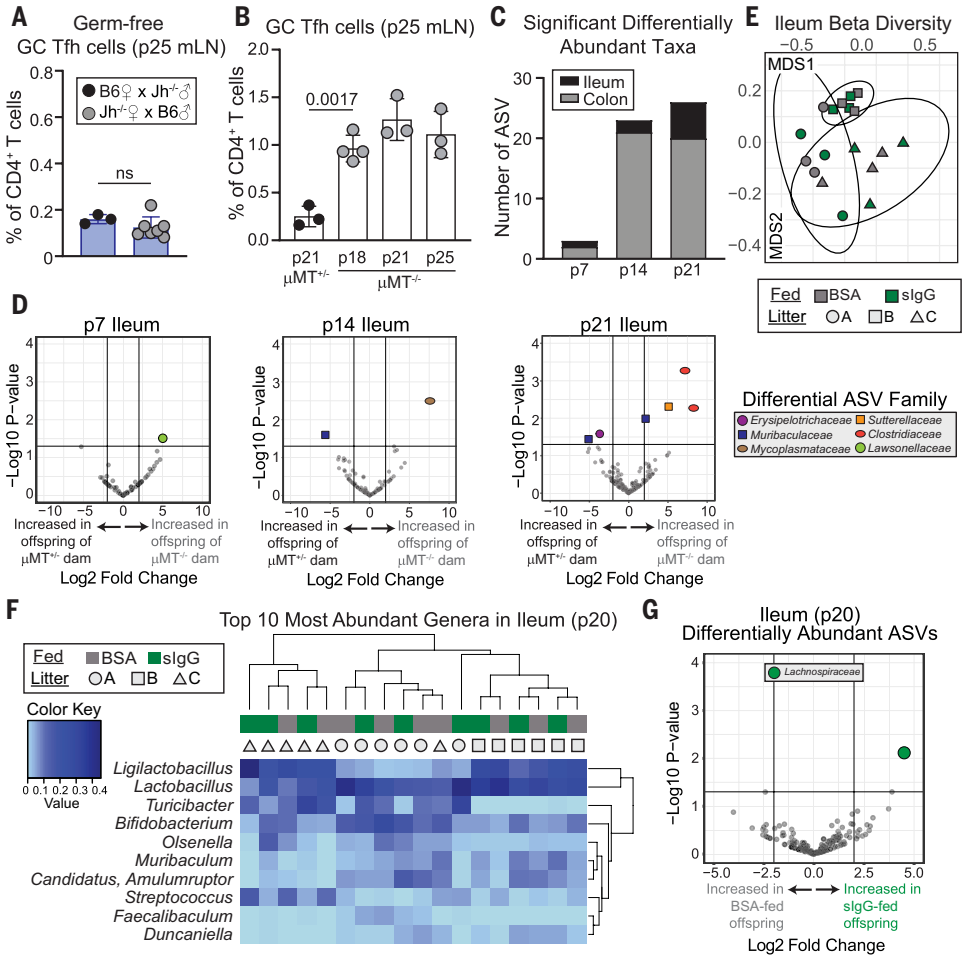

Fig. 3. Impact and assembly of the microbiota in maternal antibody–deficient offspring. (**A**) Proportions of mLN GC T_{FH} cells in GF p25 offspring born to and reared by the indicated B6.Jh$^{-/-}$ or B6 dams bred with the indicated B6.Jh$^{-/-}$ or B6 sires. (**B**) Proportions of mLN GC T_{FH} cells in p25 offspring born to the indicated dams and weaned on the indicated postnatal days. (**C**) Number of significant differentially abundant taxa (sequence variants) between maternal antibody–sufficient and –deficient offspring isolated from the indicated intestinal sites at the indicated postnatal time points. (**D**) Volcano plots of ileal microbiota taxa (sequence variants) at the indicated postnatal time points of mice described in (C). The taxonomic families of significantly altered taxa are indicated by symbols and colors. (**E**) Nonmetric multidimensional scaling plot displaying the Bray-Curtis distances between ileal bacteria from p20 littermate offspring of μMT$^{-/-}$ dams and B6 sires fed 10 μg/day sIgG or BSA in the first week of life. The PERMANOVA analysis results were litter, P = 0.001, coefficient of determination (R^2) = 0.482, and F = 6.98; IgG feeding group, P = 0.929, R^2 = 0.013, and F = 0.218. (**F**) Heatmap of (rows) genus-level ileal taxa isolated from (columns) individual p20 offspring described in (E) and ordered by complete linkage clustering. Feed and litter status of each mouse is indicated at the top of the heatmap by colors and symbols, respectively. (**G**) Volcano plot of p20 ileal microbiota species (sequence variants) in mice described in (E). The taxonomic family of the single significantly altered taxa is indicated. For (A) to (B), error bars indicate the mean ± SD; symbols indicate individual mice. Data are representative of three independent experiments with three or more mice per group. Statistical significance was determined by using an unpaired two-tailed Student's t test (A) or one-way ANOVA and Tukey post-hoc tests (B). For (C) and (D), data were combined from two independent experimental cohorts with samples harvested >1 year apart, totaling $n \geq 10$/group. For (E) to (G), data were generated from three separate litters with $n = 9$ per group. Symbols in (E) and (G) and columns in (F) indicate individual mice.

and IgG3 antibodies in the cocktail. Nevertheless, the equivalent immune dysregulation in offspring administered BSA or the isotype cocktail suggested that antigen binding in the postnatal gut is important for breast milk IgG to shape mucosal T cell responses in offspring.

We investigated whether antibody-bacteria immune complexes were sufficient to prevent immune dysregulation in pups that did not receive breast milk antibodies. To recapitulate the homeostatic T cell–independent, anticommensal IgG responses observed in mice (*13*), we immunized mice genetically deficient in all T cell subsets (TCRβδ$^{-/-}$) with *E. coli* strain BL21 (BL21). Although not substantially altering the distribution of serum IgG subclasses, immunization elicited a modest increase in IgG1, IgG2c, and IgG2b and a substantial increase in IgG3 titers (fig. S9, A and B). Flow cytometry analysis of antibody binding to bacterial cells (bFLOW) (fig. S9C) (*13*, *51*) revealed that the BL21-specific response was dominated by IgG2b and IgG3 isotypes, which stably bound to BL21 for up to 1 week (fig. S9, D and E). Immunization did not elicit BL21-specific IgG1, whereas a slight IgG2c response was generated. Serum from antibody-deficient μMT$^{-/-}$ and naive TCRβδ$^{-/-}$ mice exhibited similar IgG binding profiles, demonstrating that naïve TCRβδ$^{-/-}$ mice in our colony did not harbor "natural" IgG capable of binding this strain (fig. S9, D and E).

Like administration of sIgG, feeding pups BL21 coated or "complexed" with IgG from immune mice (Immune-BL21) during the first week of life reduced mucosal T_{FH} cell responses in maternal antibody–deficient offspring at p25 (Fig. 4, H and I, and fig. S9F). By contrast, T_{FH} cell numbers and frequencies remained elevated in mice given BL21 incubated with sera from naïve mice (naïve-BL21). Because IgG from naïve TCRβδ$^{-/-}$ mice did not bind to BL21 (fig. S9, D and E), these data indicated that early-life encounter of IgG-bacteria immune complexes was sufficient to restrain T cell immune dysregulation after weaning. Mucosal T_{FH} cell responses tended to be lower in pups given polyclonal sIgG as compared with those given BL21-IgG immune complexes, perhaps reflecting that breast milk IgG must bind multiple types of infant gut bacteria to maximally dampen immune dysregulation (Fig. 4I and fig. S9F). Collectively, these data indicate that maternal IgG binds to and forms immune complexes with microbes in the infant gut to tune neonatal immunity.

Maternal IgG engages neonatal IgG sensors to restrain microbiota-dependent adaptive immunity

The Fc domain of mouse IgG immune complexes allows them to shape immune responses by triggering IgG-sensing systems, including binding Fc receptors (FcRs) and activating complement (*52*). Analysis of WT pups at p6 revealed broad expression of FcRs and complement receptors by gut myeloid cells (Fig. 5A and fig. S10, A to D). To define the molecular basis by which maternal IgG restrained neonatal immune dysregulation, we fostered FcRγ$^{-/-}$ offspring, which lack the common FcRγ chain required for the expression and signaling of activating FcRs (FcγRI, FcγRIII, and FcγRIV) (*53*), to antibody-deficient μMT$^{-/-}$ dams at p0 and fed them sIgG or BSA daily for the first week of life (Fig. 5B).

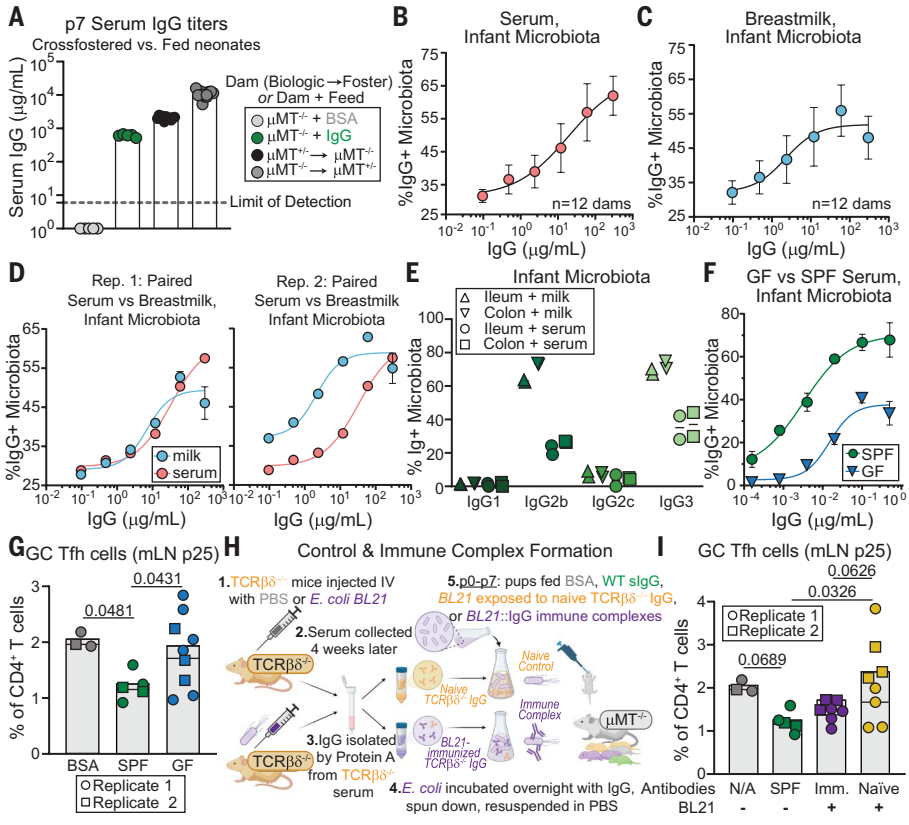

Fig. 4. Efficient binding to mucosal antigens is required for early-life IgG to restrain mucosal T_{FH} responses. (**A**) Serum IgG titers of p7 offspring of the indicated dams that were cross-fostered or fed proteins as indicated. (**B** to **D**) Proportion of SYBR$^+$ bacteria bound by IgG as assessed by means of mFLOW. Microbiota were pooled from the small intestine and colon of p6 μMT$^{-/-}$ neonates and incubated with [(B) and (D)] sera or [(C) and (D)] milk. For (B) and (C), graphs depict the mean proportion of IgG bound microbiota from 12 independent (B) serum or (C) breast milk samples. (D) Graphs depict IgG-bound microbiota after incubation with matched sera and milk from two replicate dams. IgG$^+$ SYBR$^+$ bacteria were gated according to the schematic in fig. S8B. (**E**) Proportion of SYBR$^+$ bacteria bound by IgG subclasses after incubation of milk or sera isolated from adult (10+ weeks) mice with small intestinal or colonic microbiota isolated from p6 μMT$^{-/-}$ neonates. (**F**) Similar to (B) but comparing IgG-bound SYBR$^+$ bacteria after incubation with sera of adult (10+ weeks) SPF or GF animals. (**G**) Proportions of mLN GC T_{FH} cells in p25 offspring of μMT$^{-/-}$ dams and B6 sires fed 1 μg sIgG purified from SPF or GF mice, or BSA, as indicated. (**H**) Serum was collected from TCRβδ$^{-/-}$ mice 4 weeks after intravenous injection of BL21 or PBS, and IgG was purified by means of Protein A fractionation. Timed breedings were performed by using cohoused littermate μMT$^{-/-}$ dams and B6 sires, and resulting offspring were fed sIgG, BSA, or BL21 preincubated with serum from BL21-immunized (Imm.) or PBS-immunized (Naïve) mice daily in the first week of life. (**I**) Proportions of mLN GC T_{FH} cells in p25 offspring of μMT$^{-/-}$ dams and B6 sires fed the indicated proteins with or without bacteria. For (B) to (D) and (F), graphs depict the relative median ± SD. For (A), (G), and (I), error bars indicate the mean ± SD; symbols indicate individual mice. Data are representative of two to four independent experiments with two or more mice per group. For (G) and (I), data were combined from two replicate experiments, representative of three independent experiments, and indicated with symbols. Bars indicate the mean of each replicate experiment, and statistical significance was determined by using two-way ANOVA and Holm-Sidak post-hoc tests.

Administration of sIgG decreased mLN T_{FH} cell frequency and trended toward reduced numbers in p25 FcRγ$^{-/-}$ offspring (Fig. 5C and fig. S10E). IgG also activates complement through C1q, and oral administration of sIgG triggered elevated intestinal C5a levels, a downstream product of complement activation, in infant mice in a C1q-dependent manner (fig. S10F). However, sIgG was able to attenuate mLN T_{FH} cell responses in offspring lacking this pathway (C1qa$^{-/-}$ pups) (Fig. 5D and fig. S10G).

Because neither IgG-sensing pathway in isolation was necessary for maternal IgG to restrain mucosal T_{FH} cell responses, we generated C1qa$^{-/-}$FcRγ$^{-/-}$ mice that lack both pathways. IgG administration to C1qa$^{-/-}$FcRγ$^{-/-}$ offspring fostered to lactating μMT$^{-/-}$ dams was unable to prevent adaptive immune dysregulation in these animals, which phenocopied control μMT$^{-/-}$-born offspring that did not receive IgG (Fig. 5E and fig. S10H). Thus, IgG sensing by the neonatal immune system was required for maternal IgG to calibrate offspring mucosal immunity.

Early-life acquisition of oral IgG broadly regulates infant gut immunity after weaning

The temporal difference between maternal IgG activity, required in the first week of life, and subsequent impact on mucosal immunity after weaning suggested a regulatory mechanism by which early postnatal immune engagement by maternal IgG served to temper later responses to gut antigens. Consistent with this model, we found that the provision of oral IgG in early life protected mice from experimental colitis induced during the weaning transition. Compared with BSA-treated littermates, sIgG supplementation of progeny of μMT$^{-/-}$ dams and B6 sires resulted in greater weight gain, longer colon lengths, and reduced inflammatory cytokine levels induced with oral administration of dextran sodium sulfate (DSS) (fig. S11, A to C).

To further explore this idea of immune instruction, we assessed whether maternal IgG regulated infant adaptive immune responses to newly encountered food antigens using a well-established protocol of dietary OVA administration (*54*, *55*). During the first week of life, we fed maternal antibody-deficient offspring BSA or purified sIgG isolated from naïve mice that did not harbor OVA-reactive IgG (fig. S11D). At weaning, we adoptively transferred naïve OVA-specific CD4$^+$ T cells into neonates and fed them dietary OVA (Fig. 5F). Analysis 1 week later revealed the expected increase in OVA-specific Foxp3$^+$ T_{reg} cells in the mLNs of mice given dietary OVA. This expansion did not differ between pups given IgG or BSA, indicating that the absence of maternal antibodies did not impair peripheral T_{reg} cell induction to food antigens (Fig. 5G and fig. S11, E and F) (*55*). Food antigens have been shown to elicit the differentiation of a small subset of T_{FH} cells, as well as a distinct population of FR4$^+$CD73$^+$CD44^{hi} activated cells that lack expression of other key transcription factors such as RORγt and T-bet (termed Th^{lin-}) (*56*). We observed an increased accumulation of OVA-specific T_{FH} cells and a concomitant decrease in Th^{lin-} cells in the mLNs of OVA-treated pups that did not receive IgG (Fig. 5, H to J, and fig. S11, G and H). Elevated food-specific T_{FH} cell responses also correlated with an increase in intestinal titers of OVA-specific IgE, a key T_{FH} cell–dependent mediator of allergic disease, as well as circulating OVA-specific IgG1 titers (Fig. 5K and fig. S11I). These data demonstrated that oral acquisition of maternal IgG in the first week of life dampens the differentiation of T_{FH} cell and associated IgE responses to food antigens. Because the IgG fed to pups did not bind the dietary antigen used in this model, our results indicated that ingestion of microbiota-reactive, maternal IgG broadly shapes infant adaptive

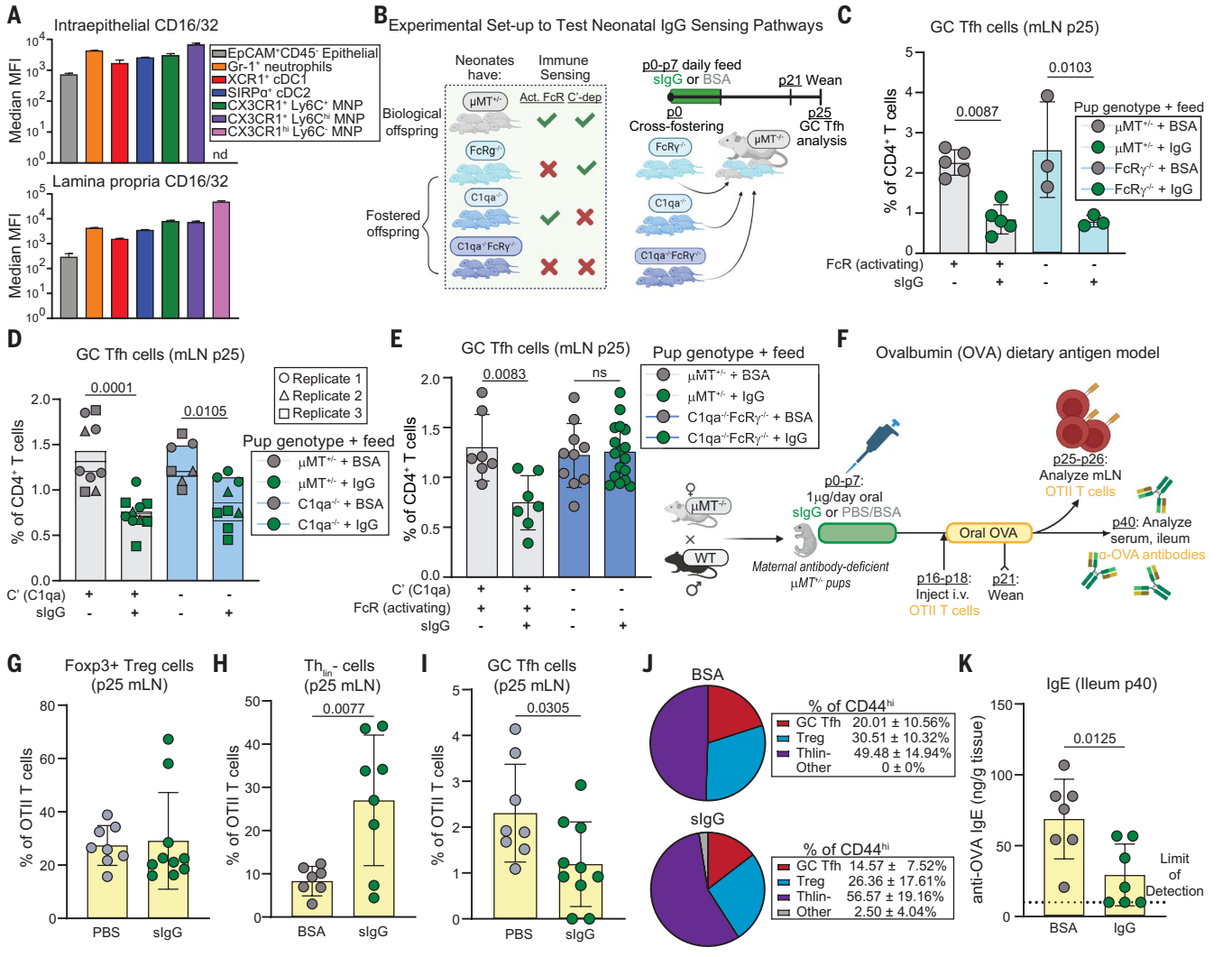

Fig. 5. Oral IgG engages Fc-dependent effector functions in the neonate to regulate intestinal homeostasis. (**A**) Median fluorescence intensity (MFI) expression of FcγRII/FcγRIII (CD16/32) by small intestinal cell subsets isolated from WT p7 neonates. Cell subsets comprised epithelial cells ($EpCAM^+CD45^-$) and myeloid $CD45^+B220^-CD90.2^-NK1.1^-SiglecF^-$ populations, including cDC1 ($MHCII^{hi}CD11C^{hi}XCR1^+$), cDC2 ($MHCII^{hi}CD11C^{hi}SIRP\alpha^+$), neutrophils ($Gr\text{-}1^+$), and CX_3CR1^+ MNPs ($MHCII^+CD11c^+CX_3CR1^+Ly6C^{var}$). nd, cell population not detected in the indicated tissue. Cells were gated according to the schematic provided in fig. S10A. (**B**) Timed breedings were performed with $\mu MT^{-/-}$ dams and B6 sires and IgG sensor-deficient dams and sires, including $FcR\gamma^{-/-}$, $C1qa^{-/-}$, and $C1qa^{-/-}FcR\gamma^{-/-}$ pairs. At birth, a portion of offspring of $\mu MT^{-/-}$ dams and B6 sires were replaced with age-matched IgG sensor-deficient offspring. All offspring were fed 10 μg purified sIgG or BSA daily in the first week of life. (**C**) Proportions of mLN GC T_{FH} cells in p25 $FcR\gamma^{-/-}$ or $\mu MT^{+/-}$ offspring fed the indicated proteins in the first week of life. (**D**) Similar to (B), comparing $C1qa^{-/-}$ and $\mu MT^{+/-}$ offspring. (**E**) Similar to (B), comparing $C1qa^{-/-}FcR\gamma^{-/-}$ and $\mu MT^{+/-}$ offspring. (**F**) Offspring of $\mu MT^{-/-}$ dams and B6 sires were fed 10 μg purified sIgG or BSA daily in the first week of life. At p16 to p18, offspring were given 1×10^5 to 10×10^5 $CD45.1^+CD4^+$ OVA-specific OTII transgenic T cells and administered OVA in drinking water until analysis at p25 or p26. Controls were given regular drinking water. (**G** to **J**) Cells were gated according to the schematics provided in figs. S4D and S11E. (G) Proportions of mLN OVA-specific $CD45.1^+V\alpha2^+V\beta5.1^+CD4^+Foxp3^+$ pT_{reg} cells in p25 offspring given the indicated treatments as described in (F). (H) Similar to (G), but comparing proportions of mLN OVA-specific $CD45.1^+V\alpha2^+V\beta5.1^+Foxp3^-CD44^{hi}FR4^+CD73^+$ Th^{lin-} cells. (I) Similar to (G), but comparing proportions of mLN OVA-specific $CD45.1^+V\alpha2^+V\beta5.1^+$ GC T_{FH} cells. (J) Pie chart depicting fraction of GC T_{FH} cells, T_{reg} cells, Th^{lin-} cells, and "other" subsets of total activated $CD44^{hi}CD45.1^+V\alpha2^+V\beta5.1^+$ OVA-specific T cells of offspring described in (F). Numbers in legends indicate the mean percentage of events (±SD) of all samples within the experiment. (**K**) Ileal OVA-specific IgE titers of p40 offspring given the indicated treatments as described in (F). For (A), (C) to (E), (G) to (I), and (K), error bars indicate the mean ± SD; symbols indicate individual mice. Data are representative of two to four independent experiments with two or more mice per group. For (A), data are representative of two independent experiments, with two or more samples per group, and three or four mice pooled per sample. For (D), data are combined from three replicate experiments indicated by symbols. For (C) and (E), statistical significance was determined by using one-way ANOVA and Tukey post-hoc tests. For (D), statistical significance was determined by using two-way ANOVA and Holm-Sidak post-hoc tests. For (G) to (I) and (K), statistical significance was determined by using an unpaired, two-tailed Student's *t* test.

immune responses to newly encountered mucosal antigens during the weaning transition.

Discussion

Breast milk antibodies are critical for establishing intestinal homeostasis, yet the mechanisms underlying this process remain elusive. We have demonstrated that neonatal sensing of breast milk IgG-microbiota immune complexes in early postnatal life was sufficient to guide subsequent mucosal immune responses after weaning, including dampening T_{FH} responses to microbiota-derived and dietary antigens and alleviating disease severity during experimental colitis. Because our work focused on early life, how breast milk IgG influences long-term health outcomes remains an open question. Nevertheless, our discovery of a temporal difference between maternal IgG activity in the first

week of life and the subsequent impact on intestinal immunity after weaning provides a regulatory mechanism compatible with dynamic and sometimes unpredictable changes in microbiota assembly and food antigen exposure typical of the weaning transition (*57*–*59*).

The immunoregulatory activity of oral IgG correlated with binding to the infant microbiota. IgG with reduced reactivity to gut microbes failed to completely restrain immune dysregulation, suggesting that microbial recognition is essential. However, future studies using truly non–microbiota-reactive IgG are warranted to confirm this result. Although the milk- and serum-purified IgG used in our studies contained all IgG subclasses, the mouse commensal-reactive IgG response is largely composed of IgG2b and IgG3 subclasses (*13*, *48*). It is possible that these two isotypes are required for breast milk IgG to dampen immunity—an idea supported by the reduced mLN T_{FH} cell responses observed in offspring fed *E. coli* primarily coated with IgG2b and IgG3. Prior work has indicated that the transfer of maternal IgG1-food antigen complexes through breastfeeding induce food antigen–specific T_{reg} cells and protect offspring from allergic disease (*60*). Whether IgG binding to dietary antigens (food-IgG complexes) can also broadly limit mucosal T cell responses to other microbiota and dietary-derived antigens remains unknown.

Although maternal IgA also binds offspring microbiota, milk IgA did not restrain adaptive immune responses in maternal antibody–deficient offspring as effectively as IgG. This result may reflect differences in necessary concentration or in microbial targeting breadth because IgG can target a more expansive proportion of the microbiota compared with IgA (*13*). Additionally, the engagement of IgG-sensing systems in offspring, including activating Fc receptors and complement components, further distinguishes oral IgG from other isotypes abundant in milk. Although activating FcγRs do not bind IgA or IgM, IgM effectively triggers complement. However, previous work indicates that milk IgM alone is unable to prevent mucosal immune dysregulation in mouse offspring (*13*). Engagement of IgG-sensing systems provides contextual cues to APCs that guide diverse downstream effects such as increasing phagocytosis, expression of costimulatory molecules, and antigen presentation to T cells (*52*, *61*, *62*). Considering the breadth of FcγR and complement receptor expression by infant gut myeloid populations, future studies investigating how breast milk IgG shapes the function of these cells to regulate T cell–dependent mucosal immunity are warranted.

Although our feeding approach demonstrated that IgG was sufficient to attenuate immune activation in maternal antibody–deficient pups, our findings do not preclude contributions from other milk isotypes in regulating host-microbiota interactions in the natural setting. Breast milk IgA can facilitate postnatal microbiota assembly, support intestinal epithelial cell function, and limit microbial translocation and immune activation (*16*, *27*, *47*, *63*, *64*). IgM, although less studied, may augment complement-mediated lysis of milk bacteria, thus shaping the composition of microbes that seed the infant gut (*65*). Coupled with our work, these observations suggest that breast milk antibody isotypes operate through distinct, yet potentially complementary, mechanisms to establish intestinal homeostasis.

IgG is also readily detectable in human breast milk (*66*, *67*), albeit at substantially lower concentrations than in mice. Despite this low abundance, several reports have described functions of human milk IgG in regulating infant immunity at both mucosal and systemic sites (*22*, *68*–*70*). Like mice, healthy humans generate circulating microbiota-reactive IgG antibodies (*66*, *67*), yet their transfer from breastfeeding and function in guiding mucosal immunity remain unknown. Moreover, humans encode a receptor for IgA [Fc alpha receptor (FcaR1)] (*71*), which may allow breast milk IgA to promote intestinal homeostasis through mechanisms parallel with those of mouse IgG. Dissecting the specific features of breast milk microbiota-reactive IgG that contribute to immune instruction—and how these features differ from other antibody isotypes and across species—remain important areas of investigation.

Although our work centers on T cell–dependent responses to dietary antigens and the microbiota, breast milk IgG may also restrain responses to other gut antigens acquired in early life, including vaccines or enteric pathogens (*72*). Mucosal T_{FH} cells and associated GC-derived antibodies can shape microbiota composition and function; cross-react with enteric pathogens and dietary antigens; and influence pathological responses in the contexts of barrier breach, cancer, and inflammatory disease (*24*, *64*, *73*–*75*). A substantial proportion of the adult intestinal B cell pool in mice originates from precursors activated during the weaning period, suggesting that perturbations to B cell responses during this window could have durable impacts (*76*). The exaggerated T_{FH} cell and GC responses in mice not receiving oral IgG could serve as a compensatory mechanism to restore intestinal homeostasis or, conversely, contribute to adverse health outcomes in certain contexts. For example, heightened generation of food-specific IgE in the absence of oral IgG could increase susceptibility to allergic diseases among nonbreastfed individuals (*77*, *78*).

Our findings reveal a function of maternal IgG in directing tolerogenic mucosal immune responses through neonatal recognition of IgG-microbe immune complexes, expanding the scope of maternal IgG beyond its traditional function in providing passive defense to infants against virulent microorganisms (*23*). Further understanding the maternal-offspring interactions that shape immune education will advance strategies to promote beneficial responses to innocuous microbes and environmental antigens and prevent pathological responses throughout life.

Materials and methods

Mice Specific pathogen-free (SPF) C57Bl/6J (Jax000664), $\mu MT^{-/-}$ (B6.129S2-*Ighm*^{tm1Cgn}/J, Jax002288), *C1qa*$^{-/-}$ (B6(Cg)-*C1qa*$^{tm1d(EUCOMM)Wtsi}$/TennJ, Jax031675), and TCRβδ$^{-/-}$ (B6.129P2-*Tcrb*^{tm1Mom} *Tcrd*^{tm1Mom}/J, Jax002122) mice were purchased from the Jackson Laboratory. $Jh^{-/-}$ mice on the Balb/c background were purchased from Taconic (1147). *Fcrg*$^{-/-}$ mice generated using C57Bl/6 embryonic stem cells by T. Saito were obtained through a materials transfer agreement (RIKEN). GF C57Bl/6 mice were purchased from Taconic (Tac-B6), and GF and SPF colonized C57Bl/6 $Jh^{-/-}$ mice were provided by A. Macpherson (Bern, Switzerland).

All mice were bred and maintained at an American Association for the Accreditation of Laboratory Animal Care (AAALAC)-accredited animal facility at the Fred Hutchinson Cancer Center (SPF animals) or UC Berkeley (GF animals) and housed in accordance with the procedures outlined in the *Guide for the Care and Use of Laboratory Animals*. All experiments with mice were performed in accordance with the guidelines of the Institutional Animal Care and Use Committee at the Fred Hutchinson Cancer Center (protocol # 51030) or UC Berkeley (protocol # 2015-02-7222-3). All mice were maintained under a 12-hours light-dark cycle (7 a.m. to 7 p.m.) and given a standard chow diet (Teklad 2918) and neutral water (pH 6.5 to 7.5) ad libitum unless otherwise indicated.

For cohousing experiments, mice were combined at 3 to 4 weeks of age until breeding age. For breeding of littermate or cohoused dams, females were separated into individual cages and bred for 2 to 3 nights. Dams were then "re-cohoused" for approximately 18 days. Pregnant females were separated and housed individually until parturition. Age-matched offspring of both sexes were used in experiments. In some cases, pups were tattooed at birth using a 25G needle (Ketchum).

Tissue processing

Mice were euthanized with CO_2, and the mLNs and PPs were collected and placed into 0.5 ml cold complete media (RPMI 1640 supplemented with 2 mM L-glutamine, 1 mM sodium pyruvate, 100 U/ml penicillin, 100 mg/ml streptomycin; all from Gibco) supplemented with 5% or

3% (v/v) fetal calf serum (FCS) (Cytiva) in a 6 well plate. Lymphoid tissues were digested by adding 5 ml complete media (without FCS) containing 0.5 mg/ml DNAseI (Sigma-Aldrich) and 1 mg/ml Collagenase III (Stem Cell Technologies) to each well and incubating plates for 20 to 30 min at 37°C. Small intestinal tissues were cut into 1-inch pieces, placed into 5 mM EDTA (Sigma-Aldrich) with 0.15 mg/ml DTT (Sigma-Aldrich) in complete media, and stirred at 37°C. Small intestine tissue suspensions were strained through kitchen strainers (Amazon.com) and shaken for 30 s by hand in 5 mM EDTA in complete media three times to remove epithelial cells, then digested by incubating tissues with 0.5 mg/ml DNAseI and 0.2 mg/ml Liberase Blendzyme TL (Millipore Sigma) for 30 min at 37°C. The enzymatic reaction was stopped with the addition of 10 ml cold complete media containing 3% FCS and tissues were passed through 70 μm (mLN, small intestine) or 100 μm (PP) cell strainers. The rubber end of 1 ml syringe plungers was used to gently mash remaining tissue pieces through the filter, after which the filter was rinsed with complete media to enhance cell recovery. Cells were pelleted at 475x*g*, the supernatant was aspirated, and the pellet was resuspended in complete media containing 3% FCS prior to downstream analysis. The pellet from small intestine prep was resuspended in 37.5% Percoll (Cytivia), centrifuged at 690x*g* for 20 min without brake. The cell pellet was washed once in complete media containing 3% FCS, cells were then pelleted at 475x*g*, the supernatant was aspirated, and the pellet was resuspended in complete media containing 3% FCS prior to downstream analysis.

Flow cytometry

For microbiota flow cytometry, intestinal contents were dissected out, placed in 1 ml sterile PBS in a microfuge tube and vortexed vigorously. Contents were centrifuged at 200x*g* and supernatant containing bacteria transferred to a separate tube. Bacteria were pelleted at 3210x*g*, rinsed with sterile PBS, pelleted again at 3210x*g* and OD_{600} was measured. Bacteria were resuspended at approximately 5×10^7 bacteria/ml in sterile-filtered bacterial staining buffer (BSB; PBS with 1% bovine serum albumin (BSA; Fisher) and 0.05% sodium azide (Sigma-Aldrich)]. Bacterial concentration was estimated as an OD of $1 = 5 \times 10^8$ bacteria/ml. 25 μl of diluted serum or breastmilk antibodies was mixed with 25 μl microbial suspension in a v-bottom plate and incubated for 30 min at 4°C. 100 μl of BSB was added to each well, and cells were pelleted by centrifugation at 3210x*g* for 5 min. Secondary staining with fluorochrome-conjugated or biotinylated antibodies diluted in BSB followed by streptavidin-PE-Cy7 diluted in BSB was performed (20 min each at 4°C). Cells were centrifuged at 3210x*g* for 5 min and resuspended in sterile-filtered PBS with SYBR Green (Invitrogen) and analyzed by FACS. A similar protocol was used for bacterial flow cytometry, except that an overnight culture of *E. coli* (BL21) was used as a source of microbes, rather than intestinal contents, and resuspended at 5×10^7 bacteria/ml, then plated at 2.5×10^5 bacteria/ well. A list of antibody clones/fluorophores and concentrations used is provided in table S1.

For flow cytometry of leukocytes, approximately 2×10^6 to 5×10^6 cells were incubated in 40 μl of fixable viability dye (Tonbo Biosciences) diluted in PBS. This and all subsequent steps were performed in the dark at room temperature unless otherwise stated. After 10 min, 10 μl of Fc block diluted in FACS buffer (PBS supplemented with 2% (v/v) FCS and 2 mM EDTA; Sigma-Aldrich) was added to cells. After 5 min, 50 μl of the extracellular antibody stain diluted in FACS buffer was added. After 30 min, 100 μl FACS buffer was added to each well, cells were centrifuged at 475x*g* for 5 min, and fixed and permeabilized using the Foxp3/Transcription Factor Staining Buffer Set (ThermoFisher Scientific) for 20 min at 4°C. Cells were centrifuged at 685x*g* for 5 min, and 100 μl of the intracellular antibody stain diluted in Perm Wash (ThermoFisher Scientific) was added. After 30 to 45 min at 4°C, cells were washed with 150 μl PermWash, centrifuged at 685x*g* for 5 min, and resuspended in 200 μl of PermWash. Analysis was performed no later than 18 hours post-staining using a BD FACSymphony A5 High-Parameter Cell Analyzer. Beads (UltraComp eBeads, Invitrogen) stained with individual antibodies were used for compensation, except for the viability dye control, wherein compensation was performed with leftover cells incubated with the viability dye alone. A list of antibody clones/dyes and concentrations used is provided in table S1. To obtain cell counts, a separate aliquot of cells was mixed with beads (Accucheck Counting Beads, Invitrogen) and diluted in 4′,6-diamidino-2-phenylindole (DAPI, Sigma Aldrich) and analyzed immediately on a BD FACSymphony A5 High-Parameter Cell Analyzer or BD Canto. All data were analyzed in FlowJo, version 10.

Dietary OVA administration

$CD4^+$ T cells were isolated by magnetic bead separation (Miltenyi; L3T4). Mice were given 1×10^5 to 10×10^5 CD45.1 OTII $CD4^+$ T cells via retro-orbital injection between p16 and p18. The next day, animals were given drinking water containing 1.5 mg/ml OVA (grade III) until p25/26. For some experiments, the day after OTII injection, 50 mg of OVA (grade III; A5378; Sigma) was administered in 200 μl PBS by oral gavage. Animals were harvested on p25/p26 or p40 to p45 for analysis of T cell and antibody responses, respectively.

DSS-induced colitis

Offspring were cohoused at p20 and provided drinking water with 2% DSS (w/v) (molecular weight 36-50 kDa; Thermo-Fisher Scientific) for 7 days. Body weight and physical appearance were monitored approximately every other day until time of sacrifice. Mice that appeared moribund or experienced ≥25% weight loss were euthanized.

Measurement of intestinal permeability

Mice were given 100 mg/kg FITC-dextran (4 kDa or 150 kDa, Sigma), 10 mg/kg monoclonal IgG2b (Bioxcel), or 5 mg/kg monoclonal ReadyTag anti-ova IgG1 (Bioxcell) diluted in PBS via pipet feeding (p0 to p13) or oral gavage (p14 to p18). As a positive control, some animals were given substances i.v. 2 hours later, blood was isolated by decapitation (p0 to p10) or cardiac puncture (p10 to p28) and allowed to clot for 30 min at room temperature. Samples were centrifuged at 1300x*g* for 15 min and serum collected. For FITC-dextran, serum was diluted 1:5 in PBS and measured with excitation and emission wavelengths of 435 and 538 nm, respectively, using an Epoch microplate reader (Biotek). Serum IgG2b and anti-OVA IgG1 titers were assessed via enzyme-linked immunosorbent assay (ELISA). Fluorescence or antibody levels were interpolated from a standard curve generated via nonlinear 4 parametric logistic regression (Prism, GraphPad).

For bacterial gavage experiments, mice were administered 1×10^{10} to 10×10^{10} *E. coli* K12 MG155 containing a plasmid encoding for ampicillin resistance (pTrc-HisC; Invitrogen #V36020) in 150 μl PBS via oral gavage at p21. Mice were gavaged with metal animal feeding needles, 22 gauge, 1" (Cadence Scientific). *E. coli K12* cultures were grown overnight in Luria-Bertani (LB) broth (Research Products International) at 37°C, cultures were centrifuged at 4000x*g* and washed with PBS twice, and OD was attained by spectrophotometer. OD600 = 1.0 was estimated as 1×10^8 bacteria/ml and colony-forming units (CFU) was confirmed by plate count. 16 to 18 hours post-gavage, animals were euthanized, mLN collected into 2 ml microtubes containing 0.5 ml PBS, and homogenized (Polytron). 250 μl of homogenate was plated on LB agar per mouse, plates were incubated at 37°C, and colonies were counted 18 to 36 hours later. Plate counts were multiplied by 2 to estimate CFU/mLN.

Mouse antibody feeding experiments

Pups were fed daily from p0 to p7 (8 days) of life with up to 10 μg purified antibodies diluted in PBS, with the exception of the IgG titration feed (Fig. 2G and fig. S4F). Pups were administered up to 2 μl of diluted antibodies per day via pipet. For isotype cocktail experiments (fig. S8, F to H), each pup was given a cocktail comprised of 1 μg of IgG1 (BioXcell, RT0267), 5 μg of IgG2a (BioXcell, BP0085), 3 μg of IgG2b

(Sydlabs, PA007130), and 1 μg of IgG3 (Biolegend, 401329), reflecting the distribution of subclasses observed in Protein A–purified sIgG (10% IgG1, 50% IgG2b, 30% IgG2a/c, 10% IgG3 as per Fig. 2D).

ELISA

Approximately 3 cm of the terminal ileum was homogenized at 100 mg/ml in PBS containing protease inhibitor (Roche). Serum, milk, or homogenized ileal tissue was centrifuged 13,000x*g* for 10 min and supernatant was used to assay immunoglobulin levels or complement proteins by ELISA. Briefly, Nunc Hi Affinity ELISA plates (Thermo Scientific) were coated with isotype-specific antibodies or 50 μg/ml OVA (grade VI, Sigma A2512) overnight at 4°C or C5a coating antibody overnight at room temperature. C5a ELISA was performed by following the manufacturer instructions (Biotechne DY2150) using Duoset reagents kit (DY008B). For isotype and OVA-specific ELISA, plates were washed 5X with Wash Buffer [PBS containing 1%BSA (w/v; Fisher) and 0.05% Tween-20 (v/v; Fisher)] and blocked with PBS with 1% BSA (w/v) and 2% goat serum diluted in PBS (Gibco; v/v) for 1 hour at 22° to 25°C. Plates were washed 5X with Wash Buffer, serial dilutions of samples diluted in PBS with 1% BSA were added, and plates were incubated for up to 2 hours at 22° to 25°C. Plates were washed 5X with Wash Buffer and peroxidase-conjugated secondary antibodies specific to mouse isotypes and diluted in PBS containing 1% BSA were added. After up to 2 hours at 22° to 25°C, plates were washed 5X with Wash Buffer, and developed using 1-Step Turbo TMB (Thermo Fisher) followed by 2N H_2SO_4 Stop solution. Absorbance at 450 nm was measured on an Epoch microplate reader (Biotek) within 10 min of adding Stop solution. A list of antibody clones and concentrations used is provided in table S1. Antibody titers were interpolated from a standard curve generated via nonlinear 4 parametric logistic regression (Prism, GraphPad).

IL-22 detection

Approximately 3 cm of the terminal ileum was homogenized at 100 mg/ml in PBS containing protease inhibitor (Roche). Homogenate was centrifuged at 13,000x*g* for 10 min and supernatant was used to assay IL-22 levels via Bio-Plex Mouse IL-22 kit (Biorad) according to the manufacturer's instructions.

Antibody purification from serum and milk

For milk collection, dams were separated from pups for 2 hours at 3 to 18 days post-parturition and anesthetized via nose-cone with isoflurane. Dams were injected intraperitoneally with 250 μL of 2 IU oxytocin diluted in 1 ml PBS (Thermo-Fisher Scientific), and milk expression was encouraged with hand massage. Milk was collected using microhematocrit capillary tubes, transferred to a microfuge tube and stored at −80°C for subsequent analysis.

For serum collection from adult mice, blood was collected via retro-orbital bleed or cardiac puncture of mice at the time of euthanasia. For neonates, blood was collected after decapitation. To collect serum, blood was allowed to clot at room temperature for up to 60 min, centrifuged at 10°C, 13,000x*g* for 15 min, and the serum supernatant was transferred to a separate microfuge tube and kept at −80°C for subsequent analysis.

Pooled serum or milk antibodies were purified over a Protein A column according to the manufacturer's instructions with minor modifications as described below (Pierce; Thermo Scientific). For milk antibodies, milk was thawed on ice, diluted 1:2 in PBS, centrifuged at 21,000x*g* for 15 min, and the top (fat) layer was removed by aspiration. The milk supernatant was transferred to a new tube, diluted a subsequent time 1:2 in PBS and centrifuged again at 21,000x*g* for 15 min. The supernatant (minus fat layer) was used for Protein A fractionation. To ensure recovery of all IgG isotypes, including IgG3, IgG was eluted via 2 sequential washes in Elution Buffer pH = 2.8, followed by 1 wash with Elution Buffer modified to pH = 4.5. IgG was neutralized immediately following each elution and all fractions were combined. IgG-enriched and -depleted protein fractions were concentrated using a 100,000 MWCO protein concentrator (Pierce; Thermo Scientific). Antibody purity and concentration were assessed by isotype and/or subclass specific ELISA (for example, IgA, IgG1, IgG2b) and nanodrop protein absorption.

Milk consumption

Pups were fasted for 4 hours by separating them from lactating dams. Pups were then weighed, returned to dams to nurse for one hour, and weighed a second time. Latching was confirmed by visual confirmation and milk consumption was estimated by the difference in weight gain before and after 1 hour of suckling. To maintain pup health and encourage suckling upon return to dam, pups were kept on a heating pad during the fasting period and maintained in a darkened hood. We note that as weight loss due to urination and defecation were not accounted for, reported values may slightly underestimate total milk consumption.

Antibiotic administration

Microbiota depletion was performed as described (*43*). Briefly, animals were gavaged once per day with a cocktail of antibiotics consisting of ampicillin (20 mg/kg; Fisher), vancomycin (10 mg/kg; Sigma-Aldrich), neomycin (20 mg/kg; ThermoFisher), and metronidazole (20 mg/kg; Alfa Aesar) between p17 to p24. Microbiota depletion was confirmed via stool culture on Luria-Bertani and blood agar plates, as well as visual confirmation of enlarged cecums.

Immune complex generation and administration

Serum was collected from TCRβδ$^{-/-}$ mice four weeks after i.v. injection of 1×10^6 *E.coli* (BL21, Thermo Fisher Cat no. C600003) or PBS, and incubated with BL21 overnight at 4°C at a ratio of 1 μl serum per 1.25×10^6 bacteria in 50 μl PBS. Bacteria were washed in BSB to remove unbound antibodies, resuspended at 5×10^6 CFU/μl, and kept at 4°C for 8 days. Immune complex formation and stability was confirmed using bacterial flow cytometry on the first and last day of treatment.

Pups were fed daily between p0 to p7 of life with 5×10^7 bacteria preincubated with sera from immune or naïve animals.

16S rRNA gene sequencing and microbial community analysis

Amplification and MiSeq Illumina Sequencing of the V4 region of the 16*S* gene was performed by the Alkek Center for Metagenomics and Microbiome Research (CMMR) at Baylor College of Medicine. Reads were demultiplexed, trimmed, and quality checked with bbduk (*79*). Paired-end reads were then merged using bbmap (*79*) and run through the MaLiAmPi workflow to generate amplicon sequence variants (ASVs) using DADA2 (*80*, *81*). The Bayesian classifier Pplacer (*82*) was used to estimate taxonomic classification of ASVs using phylogenetic placement with a likelihood cutoff of 90%. This analysis method does not use strict sequence similarity, which is often not sufficient to distinguish between closely related reference sequences with differing taxonomic assignments. Sequences that could not be assigned unambiguously to a single genus were instead assigned at a higher taxonomic level. The degree of taxonomic resolution provided by 16*S* amplicon sequencing is generally reported in the field at the genus level, with any lower-level results (species) generally viewed with a level of skepticism. This conservative approach led us to report genus level results in our analysis.

Alpha diversity estimates were generated by MaLiAmPi and Bray-Curtis dissimilarity was calculated using the R package *vegan* (v2.6-4) (DOI: 10.32614/CRAN.package.vegan) (*83*)), to determine beta diversity estimates. A pseudocount was applied prior to calculating differences in the relative abundance of taxonomic groups and ASVs with fewer than 10 reads across all samples were removed from the dataset.

Differential abundance was determined using DESeq2 (*84*), and data was normalized using the "poscounts" size estimator.

Statistics

Statistical significance was determined as indicated in the figure legends with Prism 10 (GraphPad Software Inc). Significance of beta diversity comparisons was determined using permutational multivariate analysis of variance (PERMANOVA), which was conducted using the adonis2 function in the R package *vegan*.

REFERENCES AND NOTES

1. Y. Belkaid, T. W. Hand, Role of the microbiota in immunity and inflammation. *Cell* **157**, 121–141 (2014). doi: 10.1016/j.cell.2014.03.011; pmid: 24679531
2. D. Zheng, T. Liwinski, E. Elinav, Interaction between microbiota and immunity in health and disease. *Cell Res.* **30**, 492–506 (2020). doi: 10.1038/s41422-020-0332-7; pmid: 32433595
3. J. L. Round, S. K. Mazmanian, The gut microbiota shapes intestinal immune responses during health and disease. *Nat. Rev. Immunol.* **9**, 313–323 (2009). doi: 10.1038/nri2515; pmid: 19343057
4. L. M. Cox *et al.*, Altering the intestinal microbiota during a critical developmental window has lasting metabolic consequences. *Cell* **158**, 705–721 (2014). doi: 10.1016/j.cell.2014.05.052; pmid: 25126780
5. M. P. Kronman, T. E. Zaoutis, K. Haynes, R. Feng, S. E. Coffin, Antibiotic exposure and IBD development among children: A population-based cohort study. *Pediatrics* **130**, e794–e803 (2012). doi: 10.1542/peds.2011-3886; pmid: 23008454
6. T. Olszak *et al.*, Microbial exposure during early life has persistent effects on natural killer T cell function. *Science* **336**, 489–493 (2012). doi: 10.1126/science.1219328; pmid: 22442383
7. K. A. Knoop *et al.*, Microbial antigen encounter during a preweaning interval is critical for tolerance to gut bacteria. *Sci. Immunol.* **2**, eaao1314 (2017). doi: 10.1126/sciimmunol.aao1314; pmid: 29246946
8. J. Cahenzli, Y. Köller, M. Wyss, M. B. Geuking, K. D. McCoy, Intestinal microbial diversity during early-life colonization shapes long-term IgE levels. *Cell Host Microbe* **14**, 559–570 (2013). doi: 10.1016/j.chom.2013.10.004; pmid: 24237701
9. K. P. Gopalakrishna, T. W. Hand, Influence of maternal milk on the neonatal intestinal microbiome. *Nutrients* **12**, 823 (2020). doi: 10.3390/nu12030823; pmid: 32244880
10. J. D. Thai, K. E. Gregory, Bioactive Factors in Human Breast Milk Attenuate Intestinal Inflammation during Early Life. *Nutrients* **12**, 581 (2020). doi: 10.3390/nu12020581; pmid: 32102231
11. W. L. Hurley, P. K. Theil, Perspectives on immunoglobulins in colostrum and milk. *Nutrients* **3**, 442–474 (2011). doi: 10.3390/nu3040442; pmid: 22254105
12. D. R. Kramer, J. J. Cebra, Early appearance of "natural" mucosal IgA responses and germinal centers in suckling mice developing in the absence of maternal antibodies. *J. Immunol.* **154**, 2051–2062 (1995). doi: 10.4049/jimmunol.154.5.2051; pmid: 7868882
13. M. A. Koch *et al.*, Maternal IgG and IgA antibodies dampen mucosal T helper cell responses in early life. *Cell* **165**, 827–841 (2016). doi: 10.1016/j.cell.2016.04.055; pmid: 27153495
14. D. Ramanan *et al.*, An immunologic mode of multigenerational transmission governs a gut Treg setpoint. *Cell* **181**, 1276–1290.e13 (2020). doi: 10.1016/j.cell.2020.04.030; pmid: 32402238
15. M. Gomez de Agüero *et al.*, The maternal microbiota drives early postnatal innate immune development. *Science* **351**, 1296–1302 (2016). doi: 10.1126/science.aad2571; pmid: 26989247
16. E. W. Rogier *et al.*, Secretory antibodies in breast milk promote long-term intestinal homeostasis by regulating the gut microbiota and host gene expression. *Proc. Natl. Acad. Sci. U.S.A.* **111**, 3074–3079 (2014). doi: 10.1073/pnas.1315792111; pmid: 24569806
17. T. C. Cullender *et al.*, Innate and adaptive immunity interact to quench microbiome flagellar motility in the gut. *Cell Host Microbe* **14**, 571–581 (2013). doi: 10.1016/j.chom.2013.10.009; pmid: 24237702
18. G. P. Donaldson *et al.*, Gut microbiota utilize immunoglobulin A for mucosal colonization. *Science* **360**, 795–800 (2018). doi: 10.1126/science.aaq0926; pmid: 29724905
19. S. Okai *et al.*, High-affinity monoclonal IgA regulates gut microbiota and prevents colitis in mice. *Nat. Microbiol.* **1**, 16103 (2016). doi: 10.1038/nmicrobiol.2016.103; pmid: 27562257
20. O. Pabst, V. Cerovic, M. Hornef, Secretory IgA in the coordination of establishment and maintenance of the microbiota. *Trends Immunol.* **37**, 287–296 (2016). doi: 10.1016/j.it.2016.03.002; pmid: 27066758
21. T. Rollenske *et al.*, Parallelism of intestinal secretory IgA shapes functional microbial fitness. *Nature* **598**, 657–661 (2021). doi: 10.1038/s41586-021-03973-7; pmid: 34646015
22. C. Atyeo, G. Alter, The multifaceted roles of breast milk antibodies. *Cell* **184**, 1486–1499 (2021). doi: 10.1016/j.cell.2021.02.031; pmid: 33740451
23. S. N. Langel, M. Blasi, S. R. Permar, Maternal immune protection against infectious diseases. *Cell Host Microbe* **30**, 660–674 (2022). doi: 10.1016/j.chom.2022.04.007; pmid: 35550669
24. J. J. Bunker, A. Bendelac, IgA responses to microbiota. *Immunity* **49**, 211–224 (2018). doi: 10.1016/j.immuni.2018.08.011; pmid: 30134201
25. Y. Yang, N. W. Palm, Immunoglobulin A and the microbiome. *Curr. Opin. Microbiol.* **56**, 89–96 (2020). doi: 10.1016/j.mib.2020.08.003; pmid: 32889295
26. H. Renz *et al.*, The neonatal window of opportunity-early priming for life. *J. Allergy Clin. Immunol.* **141**, 1212–1214 (2018). doi: 10.1016/j.jaci.2017.11.019; pmid: 29247715
27. K. P. Gopalakrishna *et al.*, Maternal IgA protects against the development of necrotizing enterocolitis in preterm infants. *Nat. Med.* **25**, 1110–1115 (2019). doi: 10.1038/s41591-019-0480-9; pmid: 31209335
28. A. C. Ericsson, C. L. Franklin, The gut microbiome of laboratory mice: Considerations and best practices for translational research. *Mamm. Genome* **32**, 239–250 (2021). doi: 10.1007/s00335-021-09863-7; pmid: 33689000
29. C. A. Thomson, S. C. Morgan, C. Ohland, K. D. McCoy, From germ-free to wild: Modulating microbiome complexity to understand mucosal immunology. *Mucosal Immunol.* **15**, 1085–1094 (2022). doi: 10.1038/s41385-022-00562-3; pmid: 36065057
30. M. W. Hornef, N. Torow, 'Layered immunity' and the 'neonatal window of opportunity'—Timed succession of non-redundant phases to establish mucosal host-microbial homeostasis after birth. *Immunology* **159**, 15–25 (2020). doi: 10.1111/imm.13149; pmid: 31777069
31. K. D. McCoy, M. B. Geuking, F. Ronchi, Gut microbiome standardization in control and experimental mice. *Curr. Protoc. Immunol.* **117**, 1.1, 13 (2017). doi: 10.1002/cpim.25; pmid: 28369684
32. T. Sun, A. Nguyen, J. L. Gommerman, Dendritic cell subsets in intestinal immunity and inflammation. *J. Immunol.* **204**, 1075–1083 (2020). doi: 10.4049/jimmunol.1900710; pmid: 32071090
33. R. Kedmi, D. R. Littman, Antigen-presenting cells as specialized drivers of intestinal T cell functions. *Immunity* **57**, 2269–2279 (2024). doi: 10.1016/j.immuni.2024.09.011; pmid: 39383844
34. T. Joeris, K. Müller-Luda, W. W. Agace, A. M. Mowat, Diversity and functions of intestinal mononuclear phagocytes. *Mucosal Immunol.* **10**, 845–864 (2017). doi: 10.1038/mi.2017.22; pmid: 28378807
35. B. Mihi *et al.*, Interleukin-22 signaling attenuates necrotizing enterocolitis by promoting epithelial cell regeneration. *Cell Rep. Med.* **2**, 100320 (2021). doi: 10.1016/j.xcrm.2021.100320; pmid: 34195684
36. C. S. Pohl, J. E. Medland, A. J. Moeser, Early-life stress origins of gastrointestinal disease: Animal models, intestinal pathophysiology, and translational implications. *Am. J. Physiol. Gastrointest. Liver Physiol.* **309**, G927–G941 (2015). doi: 10.1152/ajpgi.00206.2015; pmid: 26451004
37. C. Catassi, A. Bonucci, G. V. Coppa, A. Carlucci, P. L. Giorgi, Intestinal permeability changes during the first month: Effect of natural versus artificial feeding. *J. Pediatr. Gastroenterol. Nutr.* **21**, 383–386 (1995). doi: 10.1002/j.1536-4801.1995.tb11955.x; pmid: 8583288
38. S. S. Ogra, D. Weintraub, P. L. Ogra, Immunologic aspects of human colostrum and milk. III. Fate and absorption of cellular and soluble components in the gastrointestinal tract of the newborn. *J. Immunol.* **119**, 245–248 (1977). doi: 10.4049/jimmunol.119.1.245; pmid: 577500
39. S. Brajon *et al.*, All the pups we cannot see: Cannibalism masks perinatal death in laboratory mouse breeding but infanticide is rare. *Animals* **11**, 2327 (2021). doi: 10.3390/ani11082327; pmid: 34438784
40. M. Dorsch, I. Wittur, W. Garrels, Efficiency of timed pregnancies in C57BL/6 and BALB/c mice by mating one male with up to four females. *Lab. Anim.* **54**, 23677219897687 (2020). doi: 10.1177/0023677219897687; pmid: 32046590
41. C. Ohnmacht *et al.*, The microbiota regulates type 2 immunity through RORgammat(+) T cells. *Science* **349**, 989–993 (2015). doi: 10.1126/science.aac4263; pmid: 26160380
42. E. Sefik *et al.*, Individual intestinal symbionts induce a distinct population of RORgamma(+) regulatory T cells. *Science* **349**, 993–997 (2015). doi: 10.1126/science.aaa9420; pmid: 26272906
43. D. H. Reikvam *et al.*, Depletion of murine intestinal microbiota: Effects on gut mucosa and epithelial gene expression. *PLOS ONE* **6**, e17996 (2011). doi: 10.1371/journal.pone.0017996; pmid: 21445311
44. P. Ray, S. Chakraborty, A. Ghosh, P. Aich, Effects of treatment with three antibiotics, vancomycin, neomycin, and AVNM on gut microbiome in C57BL/6 mice. bioRxiv, 430372 [Preprint] (2021); https://doi.org/10.1101/2021.02.08.430372.
45. J. Fadlallah *et al.*, Microbial ecology perturbation in human IgA deficiency. *Sci. Transl. Med.* **10**, eaan1217 (2018). doi: 10.1126/scitranslmed.aan1217; pmid: 29720448
46. K. Suzuki *et al.*, Aberrant expansion of segmented filamentous bacteria in IgA-deficient gut. *Proc. Natl. Acad. Sci. U.S.A.* **101**, 1981–1986 (2004). doi: 10.1073/pnas.0307317101; pmid: 14766966
47. A. M. Weis, J. L. Round, Microbiota-antibody interactions that regulate gut homeostasis. *Cell Host Microbe* **29**, 334–346 (2021). doi: 10.1016/j.chom.2021.02.009; pmid: 33705705
48. M. Y. Zeng *et al.*, Gut microbiota-induced immunoglobulin G controls systemic infection by symbiotic bacteria and pathogens. *Immunity* **44**, 647–658 (2016). doi: 10.1016/j.immuni.2016.02.006; pmid: 26944199
49. G. Vidarsson, G. Dekkers, T. Rispens, IgG subclasses and allotypes: From structure to effector functions. *Front. Immunol.* **5**, 520 (2014). doi: 10.3389/fimmu.2014.00520; pmid: 25368619

50. P. Bruhns, F. Jönsson, Mouse and human FcR effector functions. *Immunol. Rev.* **268**, 25–51 (2015). doi: 10.1111/imr.12350; pmid: 26497511
51. K. Moor *et al.*, Analysis of bacterial-surface-specific antibodies in body fluids using bacterial flow cytometry. *Nat. Protoc.* **11**, 1531–1553 (2016). doi: 10.1038/nprot.2016.091; pmid: 27466712
52. L. L. Lu, T. J. Suscovich, S. M. Fortune, G. Alter, Beyond binding: Antibody effector functions in infectious diseases. *Nat. Rev. Immunol.* **18**, 46–61 (2018). doi: 10.1038/nri.2017.106; pmid: 29063907
53. C. Ra, M. H. Jouvin, U. Blank, J. P. Kinet, A macrophage Fc gamma receptor and the mast cell receptor for IgE share an identical subunit. *Nature* **341**, 752–754 (1989). doi: 10.1038/341752a0; pmid: 2529442
54. U. Hadis *et al.*, Intestinal tolerance requires gut homing and expansion of FoxP3$^+$ regulatory T cells in the lamina propria. *Immunity* **34**, 237–246 (2011). doi: 10.1016/j.immuni.2011.01.016; pmid: 21333554
55. D. Mucida *et al.*, Oral tolerance in the absence of naturally occurring Tregs. *J. Clin. Invest.* **115**, 1923–1933 (2005). doi: 10.1172/JCI24487; pmid: 15937545
56. S. W. Hong *et al.*, Immune tolerance of food is mediated by layers of CD4$^+$ T cell dysfunction. *Nature* **607**, 762–768 (2022). doi: 10.1038/s41586-022-04916-6; pmid: 35794484
57. Z. Al Nabhani *et al.*, A weaning reaction to microbiota is required for resistance to immunopathologies in the adult. *Immunity* **50**, 1276–1288.e5 (2019). doi: 10.1016/j.immuni.2019.02.014; pmid: 30902637
58. T. Yatsunenko *et al.*, Human gut microbiome viewed across age and geography. *Nature* **486**, 222–227 (2012). doi: 10.1038/nature11053; pmid: 22699611
59. H. J. Ku, Y. T. Kim, J. H. Lee, Microbiome study of initial gut microbiota from newborn infants to children reveals that diet determines its compositional development. *J. Microbiol. Biotechnol.* **30**, 1067–1071 (2020). doi: 10.4014/jmb.2002.02042; pmid: 32270658
60. A. Ohsaki *et al.*, Maternal IgG immune complexes induce food allergen-specific tolerance in offspring. *J. Exp. Med.* **215**, 91–113 (2018). doi: 10.1084/jem.20171163; pmid: 29158374
61. S. Bournazos, A. Gupta, J. V. Ravetch, The role of IgG Fc receptors in antibody-dependent enhancement. *Nat. Rev. Immunol.* **20**, 633–643 (2020). doi: 10.1038/s41577-020-00410-0; pmid: 32782358
62. E. E. West, M. Kolev, C. Kemper, Complement and the regulation of T cell responses. *Annu. Rev. Immunol.* **36**, 309–338 (2018). doi: 10.1146/annurev-immunol-042617-053245; pmid: 29677470
63. G. P. Donaldson *et al.*, Suppression of epithelial proliferation and tumorigenesis by immunoglobulin A. bioRxiv 561290 [Preprint] (2023); https://doi.org/10.1101/2023.10.06.561290.
64. O. Pabst, E. Slack, IgA and the intestinal microbiota: The importance of being specific. *Mucosal Immunol.* **13**, 12–21 (2020). doi: 10.1038/s41385-019-0227-4; pmid: 31740744
65. D. Xu *et al.*, Complement in breast milk modifies offspring gut microbiota to promote infant health. *Cell* **187**, 750–763.e20 (2024). doi: 10.1016/j.cell.2023.12.019; pmid: 38242132
66. H. Akhter, F. Aziz, F. R. Ullah, M. Ahsan, S. N. Islam, Immunoglobulins content in colostrum, transitional and mature milk of Bangladeshi mothers: Influence of parity and sociodemographic characteristics. *J. Mother Child* **24**, 8–15 (2021). pmid: 33548166
67. M. Czosnykowska-Łukacka, J. Lis-Kuberka, B. Królak-Olejnik, M. Orczyk-Pawiłowicz, Changes in human milk immunoglobulin profile during prolonged lactation. *Front Pediatr.* **8**, 428 (2020). doi: 10.3389/fped.2020.00428; pmid: 32850542
68. N. I. Mazur *et al.*, Breast milk prefusion F immunoglobulin G as a correlate of protection against respiratory syncytial virus acute respiratory illness. *J. Infect. Dis.* **219**, 59–67 (2019). pmid: 30107412
69. J. Mabuka, R. Nduati, K. Odem-Davis, D. Peterson, J. Overbaugh, HIV-specific antibodies capable of ADCC are common in breastmilk and are associated with reduced risk of transmission in women with high viral loads. *PLOS Pathog.* **8**, e1002739 (2012). doi: 10.1371/journal.ppat.1002739; pmid: 22719248
70. G. G. Fouda *et al.*, HIV-specific functional antibody responses in breast milk mirror those in plasma and are primarily mediated by IgG antibodies. *J. Virol.* **85**, 9555–9567 (2011). doi: 10.1128/JVI.05174-11; pmid: 21734046
71. R. C. Monteiro, J. G. Van De Winkel, IgA Fc receptors. *Annu. Rev. Immunol.* **21**, 177–204 (2003). doi: 10.1146/annurev.immunol.21.120601.141011; pmid: 12524384
72. P. L. F. Rippey, F. Aravena, J. P. Nyonator, Health impacts of early complementary food introduction between formula-fed and breastfed infants. *J. Pediatr. Gastroenterol. Nutr.* **70**, 375–380 (2020). doi: 10.1097/MPG.0000000000002581; pmid: 31834112
73. D. Sterlin, J. Fadlallah, E. Slack, G. Gorochov, The antibody/microbiota interface in health and disease. *Mucosal Immunol.* **13**, 3–11 (2020). doi: 10.1038/s41385-019-0192-y; pmid: 31413347
74. K. E. Huus, C. Petersen, B. B. Finlay, Diversity and dynamism of IgA-microbiota interactions. *Nat. Rev. Immunol.* **21**, 514–525 (2021). doi: 10.1038/s41577-021-00506-1; pmid: 33568782
75. K. Chen, G. Magri, E. K. Grasset, A. Cerutti, Rethinking mucosal antibody responses: IgM, IgG and IgD join IgA. *Nat. Rev. Immunol.* **20**, 427–441 (2020). doi: 10.1038/s41577-019-0261-1; pmid: 32015473
76. S. Vergani *et al.*, A self-sustaining layer of early-life-origin B cells drives steady-state IgA responses in the adult gut. *Immunity* **55**, 1829–1842.e6 (2022). doi: 10.1016/j.immuni.2022.08.018; pmid: 36115337
77. Z. Koukou *et al.*, The effect of breastfeeding on food allergies in newborns and infants. *Children* **10**, 1046 (2023). doi: 10.3390/children10061046; pmid: 37371277
78. A. Stuebe, The risks of not breastfeeding for mothers and infants. *Rev. Obstet. Gynecol.* **2**, 222–231 (2009). pmid: 20111658
79. B. Bushnell, J. Rood, E. Singer, BBMerge—Accurate paired shotgun read merging via overlap. *PLOS ONE* **12**, e0185056 (2017). doi: 10.1371/journal.pone.0185056; pmid: 29073143
80. S. S. Minot *et al.*, MaLiAmPi enables generalizable and taxonomy-independent microbiome features from technically diverse 16S-based microbiome studies. *Cell Rep. Methods* **3**, 100639 (2023). doi: 10.1016/j.crmeth.2023.100639; pmid: 37939711
81. B. J. Callahan *et al.*, DADA2: High-resolution sample inference from Illumina amplicon data. *Nat. Methods* **13**, 581–583 (2016). doi: 10.1038/nmeth.3869; pmid: 27214047
82. F. A. Matsen, R. B. Kodner, E. V. Armbrust, pplacer: Linear time maximum-likelihood and Bayesian phylogenetic placement of sequences onto a fixed reference tree. *BMC Bioinformatics* **11**, 538 (2010). doi: 10.1186/1471-2105-11-538; pmid: 21034504
83. J. Oksanen *et al.*, Vegan: Community Ecology Package (2025); https://cran.r-project.org/package=vegan.
84. M. I. Love, W. Huber, S. Anders, Moderated estimation of fold change and dispersion for RNA-seq data with DESeq2. *Genome Biol.* **15**, 550 (2014). doi: 10.1186/s13059-014-0550-8; pmid: 25516281
85. M. K. Shenoy *et al.*, Breastmilk IgG engages the murine neonatal immune system to instruct responses to gut antigens, dataset. Dryad (2025); https:/doi.org/10.5061/dryad.z8w9ghxrf.

ACKNOWLEDGMENTS

We thank the Fred Hutchinson Comparative Medicine Facility; the Fred Hutchinson Flow Cytometry Core; and H. Wynd, L. Hueffed, N. Huber, and S. Minot for technical support. We thank G. Barton, G. Reiner, A. Stanbery, and L. Kreuk for providing GF sera and technical assistance regarding GF experiments. We thank E. Tait-Wojno, O. Harrison, J. Talbot, and P. Mitchell for critical reading of the manuscript. We thank Y. Wu, V. O'Brien, and M. Headley for constructive feedback on this project. This research was supported by the Comparative Medicine Shared Resource (RRID:SCR 022610) and the Flow Cytometry Shared Resource (RRID:SCR 022613) of the Fred Hutchinson/University of Washington/Seattle Children's Cancer Consortium (P30 CA015704). Some figure panels were created using BioRender, for which the Koch lab has been granted a license to publish in a journal. **Funding:** M.K.S. was supported by the Fred Hutchinson Cancer Center's Immunotherapy Integrated Research Center Award. H.T. and A.K.L. are Washington Research Foundation Postdoctoral Fellows. M.A.K. is a Pew Scholar in the Biomedical Sciences, supported by The Pew Charitable Trusts. R01A1173199 and grants from the Hartwell Foundation, Rita Allen Foundation, Fred Hutchinson Cancer Center's Microbiome Research Initiative Integrated Research Center and the Kenneth Rainin Foundation to M.A.K. also supported this work. The content is solely the responsibility of the authors and does not necessarily represent the official views of the National Institutes of Health. **Author contributions:** Conceptualization: M.K.S., M.A.K. Formal analysis: M.K.S., D.M.R., M.A.K. Methodology: M.K.S., M.A.K. Investigation: M.K.S., D.M.R., A.K.L., H.T., S.G., L.J.M., J.S.S., M.E.C., M.A.K. Visualization: M.K.S., D.M.R., M.A.K. Funding acquisition: M.K.S., M.A.K. Project administration: M.K.S., M.A.K. Writing – original draft: M.K.S., M.A.K. Writing – review & editing: M.K.S., A.K.L., H.T., S.G., J.S.S., M.E.C., M.A.K. **Competing interests:** The authors declare that they have no competing interests. **Data and materials availability:** All data needed to evaluate the conclusions in the paper are present in the paper or the supplementary materials. 16S sequencing data are available on Dryad (*85*). *Fcrg*$^{-/-}$ mice are available from T. Saito under a materials transfer agreement with RIKEN. **License information:** Copyright © 2025 the authors, some rights reserved; exclusive licensee American Association for the Advancement of Science. No claim to original US government works. https://www.science.org/about/science-licenses-journal-article-reuse

SUPPLEMENTARY MATERIALS

science.org/doi/10.1126/science.ado5294
Figs. S1 to S11; Table S1; MDAR Reproducibility Checklist

Submitted 9 February 2024; resubmitted 25 January 2025; accepted 9 June 2025
10.1126/science.ado5294

Check for

RESEARCH ARTICLE SUMMARY

PLATELETS

Platelets sequester extracellular DNA, capturing tumor-derived and free fetal DNA

Lauren Murphy *et al.*

Full article and list of author affiliations: https://doi.org/10.1126/science.adp3971

INTRODUCTION: Platelets are the smallest and second most abundant cell type in our blood, contributing to a range of physiological processes, including hemostasis, vascular maintenance, and innate immunity. Whereas megakaryocytes, the platelet-producing cells in the bone marrow, have a large, highly polyploid nucleus, platelets have no nucleus at all and have traditionally been assumed to be devoid of DNA. Platelets have a distinct cellular physiology with a series of surface-connected membrane channels, called the open canalicular system, mediating efficient internalization and release of biomolecules, including nucleic acids such as viral RNA and DNA, within the circulation.

RATIONALE: Given their known ability to sense and internalize exogenous nucleic acids, we hypothesized that platelets may sequester endogenous extracellular DNA during circulation. Conceivably, this process might contribute to physiological mechanisms that limit the abundance of cell-free DNA (cfDNA) in plasma, which is immunostimulatory. This phenomenon would be relevant to liquid biopsy approaches, many of which focus on cfDNA isolated from platelet-depleted plasma, in which platelet nucleic acids are discarded. cfDNA contained within platelets may offer an untapped, additional reservoir of clinically relevant genetic material to, for example, increase sensitivity in cancer screening to detect low–tumor burden disease.

RESULTS: By using high resolution imaging and flow cytometry, we confirmed that platelets contain fractional quantities of DNA. To test whether platelets can acquire DNA after their release from megakaryocytes, we performed live cell imaging and coculture experiments, demonstrating transfer of mutant DNA from malignant cells to healthy donor platelets in vitro. We confirmed that cfDNA sequestration by platelets occurs in vivo, corroborating both visually (with fluorescence in situ hybridization) and molecularly (with droplet digital polymerase chain reaction) that platelets from healthy pregnant females carrying male babies contained fragments of the Y chromosome.

Whole-genome sequencing of platelet DNA revealed a fragmentation pattern and nucleosome footprint that mirrored the attributes of cfDNA isolated from platelet-depleted plasma. The DNA fragments in platelets were histone-associated chromatin, with DNA methylation marks suggesting a similar cellular composition to cfDNA with contributions from blood leukocytes and megakaryocytes and a minor contribution from hepatocytes in healthy individuals.

Given our hypothesis that platelets clear cfDNA from plasma, we reasoned that plasma cfDNA would increase in the setting of thrombocytopenia. Indeed, acute platelet depletion in an immune thrombocytopenic purpura (ITP) mouse model led to a rise in plasma cfDNA, and patients with ITP and severely low platelet counts exhibited significantly higher plasma cfDNA levels than individuals with normal platelet counts.

We found that platelets could acquire DNA by internalizing both DNA-loaded extracellular vesicles released by apoptotic cells and membrane-free DNA fragments. Uptake and release of DNA could be pharmacologically manipulated. Platelet-encapsulated DNA was protected from external deoxyribonuclease (DNase) degradation, and inhibiting platelet exocytosis increased the abundance of DNA obtained from platelets.

Lastly, we demonstrated that tumor-derived DNA was present in platelets of patients with advanced cancer, where cfDNA was in high abundance; in low–tumor burden disease; and also in those with premalignant colonic polyps.

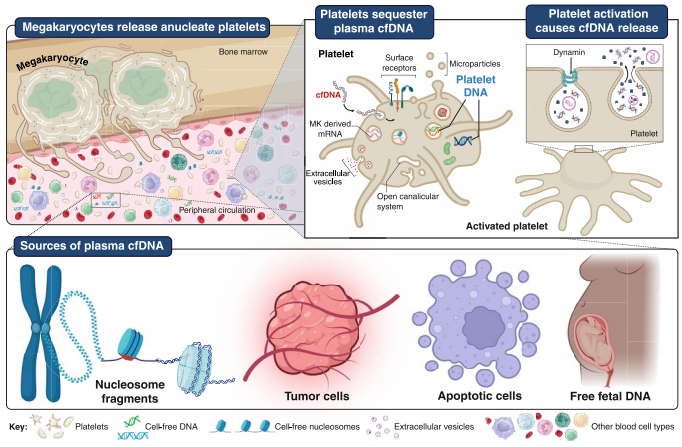

Platelets sequester cfDNA during circulation. Bone marrow megakaryocytes release platelets into the bloodstream. During circulation, platelets encounter extracellular DNA—histone-bound nucleosome fragments—released by cells undergoing physiological apoptosis, including tumor cells and free fetal DNA. Platelets protect internalized DNA from external DNase degradation and release their DNA cargo in a dynamin-dependent manner upon platelet activation. [Figure created with BioRender.com]

CONCLUSION: Platelets can acquire a repertoire of DNA fragments that map across the nuclear genome, including DNA derived from tumor cells and free fetal DNA. Prior work has shown that tumor cell–derived RNA is detectable within circulating platelets. Given their abundance, ease of isolation, and tissue-wide perfusion, platelets are ideally positioned to serve as biosensors for genetic perturbations across tissues. This finding has broad clinical relevance and sets the stage for future work to clarify the role of platelets in cfDNA homeostasis as well as the fate and physiological consequences of DNA fragments released at sites of platelet activation. □

*Corresponding author. Email: bethan.psaila@ndcls.ox.ac.uk (B.P.); benjamin.schuster-boeckler@ludwig.ox.ac.uk (B.S.-B.) Cite this article as L. Murphy *et al.*, *Science* **389**, eadp3971 (2025). DOI: 10.1126/science.adp3971

PLATELETS

Platelets sequester extracellular DNA, capturing tumor-derived and free fetal DNA

Lauren Murphy[1], Jeanne Inchauspé[1,2], Giampiero Valenzano[3], Pamela Holland[4], Nikolaos Sousos[1,5], Hayley L. Belnoue-Davis[6], Rong Li[1], Natalie J. Jooss[1], Camelia Benlabiod[1], Eleanor Murphy[1], Zohar Etzioni[2], Emelie Shepherd[2], Lucy Denly[2], Sujata Biswas[5], Lin Chen[2], Jennifer O'Sullivan[1], Michael P. Rimmer[4], Abdullah O. Khan[1], Christina Simoglou Karali[1], Nadia Nasreddin[6], Ian S. Hitchcock[7], Milka Koupenova[8], Skirmantas Kriaucionis[2], Jim R. Hughes[1], Eric O'Neill[3], Manu Vatish[9], Paul Rees[10,11], Simon Leedham[6], Michael Desborough[1,5], Adam J. Mead[1,5], Benjamin Schuster-Böckler[2]*, Christopher D. Gregory[4], Bethan Psaila[1,2,5]*

Platelets are anucleate blood cells vital for hemostasis and immunity. During cell death and aberrant mitosis, nucleated cells release DNA, resulting in "cell-free" DNA in plasma (cfDNA). An excess of cfDNA is deleterious. Given their ability to internalize pathogen-derived nucleic acids, we hypothesized that platelets may also clear endogenous cfDNA. We found that, despite lacking a nucleus, platelets contained a repertoire of DNA fragments mapping across the nuclear genome. We detected fetal DNA in maternal platelets and cancer-derived DNA in platelets from patients with premalignant and cancerous lesions. As current liquid biopsy approaches utilize platelet-depleted plasma, important genetic information contained within platelets is being missed. This study establishes a physiological role for platelets that has not previously been highlighted, with broad translational relevance.

Platelets are fundamental to hemostasis, vascular maintenance, and both innate and adaptive immunity. Platelets inherit RNAs from their parent megakaryocytes together with translational and splicing machinery. As part of their role in immunity, platelets sense pathogen-derived nucleic acids and internalize DNA and RNA viruses, triggering inflammatory responses (*1*–*4*). Notably, in addition to pathogen-derived nucleic acids, RNAs originating from solid tumor cells and inhaled pine tree pollen have also been detected in human platelets (*5*, *6*), indicating that platelets internalize RNA from a range of cellular sources during peripheral circulation. Although platelet RNA has emerging utility as a liquid biopsy approach for hematological (*7*) and solid malignancies (*8*, *9*), whether platelets contain any form of DNA—and if so, its genomic origin—has not been extensively investigated.

During cell death and aberrant mitosis, nucleated cells release chromosomal DNA, resulting in "cell-free" DNA in plasma (cfDNA). Analysis of cfDNA from blood plasma is currently implemented in a wide range of clinical settings, including cancer care (*10*–*16*) and prenatal testing (*17*). A major obstacle to clinical utility is the low sensitivity in scenarios where the abundance of target DNA is low. We hypothesized that in addition to internalizing pathogen-derived exogenous DNA, platelets may clear endogenous cfDNA from plasma, including DNA fragments released by healthy cells as well as those bearing oncogenic mutations. As conventional methods isolate cfDNA from platelet-depleted plasma, any DNA fragments that are sequestered within platelets would be missed. We therefore also hypothesized that including DNA captured by platelets may add value in diagnostic pathways.

Results

Platelets contain DNA

To determine whether DNA is present within human platelets, platelets were purified from three sources: whole peripheral blood, isolated plasma, and "plateletpheresis" concentrates, clinical-grade platelet pools isolated from healthy donors for transfusion purposes (Fig. 1A). We examined platelets by fluorescence microscopy after labeling purified platelets with NUCLEAR-ID Red DNA, a highly specific, cell-permeable dye that intercalates with double-stranded DNA (dsDNA). A proportion of platelets showed a clear signal for the DNA probe (Fig. 1B). To verify that this represented nuclear DNA, we confirmed the presence of a nuclear genomic region of the *TP53* gene in platelet DNA (pDNA) (fig. S1, A and B). Immunofluorescence staining of a peripheral blood smear also showed a clear signal for the DNA stain Hoechst in platelets, confirming that the DNA was not acquired by platelets during purification from whole blood (fig. S1C).

To quantify the proportion of platelets that contained DNA we used flow cytometry, examining positivity for DRAQ5, a dsDNA-specific dye. Most platelets showed low-level DRAQ5 positivity, whereas around 8% were strongly positive (DRAQ5^{hi}) (Fig. 1C and fig. S1D). Prior studies have shown that newly produced or "younger" platelets can be distinguished from "older" platelets by their higher content of RNA and that younger platelets also have higher expression of markers of platelet receptor activation or degranulation (*18*–*20*). Costaining for RNA and DNA showed that the majority of DRAQ5^{hi} platelets were low or negative for RNA (Fig. 1D and fig. S1E), indicating that DNA is present in both newly produced (RNA-high) and older (RNA-low) platelets. Comparing DRAQ5^{hi} and DRAQ5^{lo} platelets showed that DRAQ5^{hi} platelets contained more RNA and had higher expression of markers of activation than DRAQ5$^{lo/neg}$ platelets, implying that the DNA content of platelets also decreased during platelet lifespan and after platelet activation, in parallel with RNA content (Fig. 1, D and E).

To investigate platelet content of DNA in a larger cohort, we extracted pDNA from peripheral blood of 76 adult donors (tables S1 to S4). The extremely high purity of the platelet pellets was confirmed by flow cytometry analysis and cytospin preparations (fig. S1, A, F, and G). DNA was obtained from both the platelet pellet and platelet-depleted plasma (cfDNA) in all cases, with a higher yield of DNA from platelet pellets than from matched platelet-depleted plasma (i.e., a conventional cfDNA preparation). In this cohort, a median abundance of 7.18 genomic copies was isolated from platelets per microliter of blood plasma, which equates to approximately 0.000012 genomic equivalents of DNA per platelet (fig. S1H).

Platelets sequester DNA during circulation

To determine whether the DNA detected in platelets was captured during peripheral circulation or solely derived from parent megakaryocytes (*21*), we collected antenatal blood samples and looked for fragments

[1]MRC Molecular Haematology Unit, MRC Weatherall Institute of Molecular Medicine, Radcliffe Department of Medicine and National Institute of Health Research (NIHR), Oxford Biomedical Research Centre, University of Oxford, Oxford, UK. [2]Ludwig Institute for Cancer Research, Nuffield Department of Medicine, University of Oxford, Oxford, UK. [3]Department of Oncology, University of Oxford, Old Road Campus Research Building, Roosevelt Drive, Oxford, UK. [4]Centre for Inflammation Research, Institute for Regeneration and Repair, University of Edinburgh, Edinburgh BioQuarter, 4-5 Little France Drive, Edinburgh, UK. [5]Oxford University Hospitals NHS Foundation Trust, Oxford, UK. [6]Wellcome Centre for Human Genetics, University of Oxford, Oxford, UK. [7]York Biomedical Research Institute and Department of Biology, University of York, Heslington, York, UK. [8]Division of Cardiovascular Medicine, Department of Medicine, University of Massachusetts Chan Medical School, 368 Plantation Street, Worcester, Massachusetts, USA. [9]Nuffield Department of Women's and Reproductive Health, University of Oxford, John Radcliffe Hospital, Oxford, UK. [10]Department of Biomedical Engineering, Faculty of Science and Engineering, Swansea University, Swansea, Wales, UK. [11]Imaging Platform, Broad Institute of MIT and Harvard, Cambridge, MA, USA. ***Corresponding author. Email: bethan.psaila@ndcls.ox.ac.uk (B.P.); benjamin.schuster-boeckler@ludwig.ox.ac.uk (B.S.-B.)**

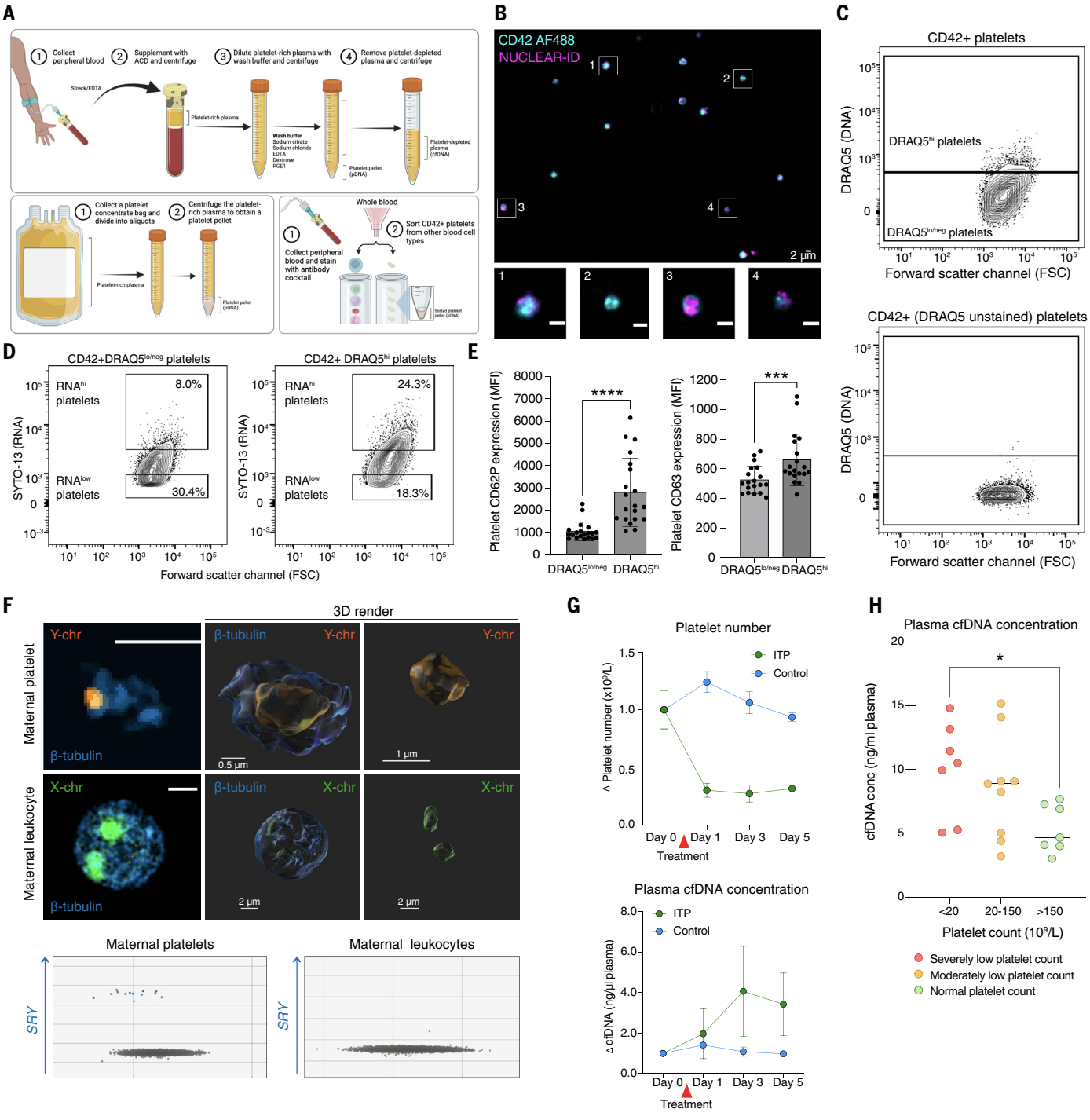

Fig. 1. Platelets sequester DNA during circulation. (**A**) Schematic showing sources of purified platelets. (Top) Sequential centrifugation of peripheral blood to simultaneously extract pDNA and cfDNA. (Bottom left) Centrifugation of healthy donor plateletpheresis concentrates to obtain a platelet pellet. (Bottom right) FACS of whole blood. (**B**) Healthy donor–derived platelets identified by CD42 AF488 (cyan) show an internal fluorescent signal for NUCLEAR-ID, a cell-permeable dye that intercalates with dsDNA (magenta). White boxes mark magnified regions; representative images are shown below. Scale bars, 2 µm. (**C**) Flow cytometric analysis of $CD42^{+}$ healthy donor–derived platelets stained with and without the DNA marker DRAQ5. (Top) Eight percent of circulating platelets stain strongly positive for DRAQ5; $n = 20$ healthy donors concatenated into a single FCS file. (Bottom) Single $CD42^{+}$-stained platelets show no DRAQ5 autofluorescence; $n = 10$ healthy donors; concatenated data shown. (**D**) Flow cytometric analysis quantifying RNA content (SYTO-13 positivity) of $CD42^{+}$, $DRAQ5^{hi}$, and $DRAQ5^{lo/neg}$ platelets ($n = 10$ healthy donors; concatenated data shown). (**E**) Platelets with a higher DNA content ($DRAQ5^{hi}$) showed higher levels of activation as determined by P-selectin (CD62P) and CD63 expression. Each dot represents an individual healthy donor. $n = 19$ and 20 donors for CD63 and CD62P, respectively. Bars show mean ± SD. $^{***}P < 0.001$; $^{****}P < 0.0001$; as determined by a Wilcoxon signed-rank test. (**F**) FISH and ddPCR show detection of the Y-chromosome gene *SRY* in maternal platelets but not in leukocytes sampled from mothers of male offspring prior to delivery. Platelets and leukocytes were counterstained with β-tubulin (blue) and imaged using a ZEISS LSM900, 63× magnification. Representative images and ddPCR data are shown; 3D rendering was performed using ImarisViewer. $n = 5$ and 25 female donors for FISH and ddPCR, respectively. (**G**) Rise in cfDNA following acute depletion of platelets in healthy mice following administration of an antiplatelet antibody. $n = 5$ mice per day; $n = 20$ mice per condition. Each dot shows

mean ± SEM fold change at days 1, 3, and 5 compared with baseline (day 0, untreated mice). (**H**) Plasma cfDNA concentrations (nanograms per milliliter) for patients with ITP and severely ($<20 \times 10^9$/L, $n = 7$) or moderately (20×10^9 to 150×10^9/L, $n = 9$) low platelet counts or counts in the normal range ($\geq 150 \times 10^9$/L, $n = 7$). *$P < 0.05$; for a Mann- Whitney *U* test, each point shows data from one individual, with line at the median. MFI, mean fluorescence intensity.

of the Y chromosome in platelets of mothers with uncomplicated pregnancies carrying male offspring (table S5). Using Y chromosome fluorescence in situ hybridization, Y chromosome fragments were visualized in the platelets of mothers carrying a male fetus (Fig. 1F and movie S1). In 100% of samples ($n = 30$), we correctly ascertained the sex of the fetus by the presence or absence of the Y chromosome gene sex-determining region Y (*SRY*) alleles in maternal platelets (Fig. 1F). *SRY* remained detectable in platelets at 24 and 48 hours after delivery of the baby (fig. S1I) and was not detected in mononuclear cells (MNCs) (Fig. 1F) or red blood cells (RBCs) (fig. S1J) from the same blood samples, indicating that free fetal DNA could be detected exclusively in maternal platelets. This suggested that the detection of *SRY* in maternal platelets was not due to "contaminating" cfDNA in the cell pellets nor the presence of fetal blood cells in the maternal circulation. Although cross-placental transfer of fetal platelets cannot be fully excluded, this observation confirmed the presence of nuclear DNA within platelets.

Platelets "clear" cfDNA from plasma

We reasoned that if platelets were clearing cfDNA from plasma, then the abundance of cell- or platelet-free DNA in plasma would increase if the platelet count was reduced. To test this, we induced acute and specific antibody-mediated depletion of platelets in mice. In accordance with our hypothesis, induction of immune thrombocytopenia led to an acute rise in plasma cfDNA concentration (Fig. 1G). Similarly, we found higher concentrations of plasma cfDNA in patients with immune thrombocytopenic purpura (ITP) who had severely low platelet counts ($<20 \times 10^9$/L) as compared to those with normal platelet counts (Fig. 1H and table S6; $P < 0.05$, $n = 23$).

Together, these data indicate a biological role for platelets in the clearance of cfDNA from plasma.

Platelets rapidly capture DNA from nucleated cells

To confirm that platelets sequestered chromosomal fragments released from nucleated cells, we used live cell imaging to visualize DNA uptake in vitro. Colorectal adenocarcinoma cells (COLO205) were labeled with DNA probes and washed twice to remove any noninternalized probe prior to coincubation with platelets. Rapid acquisition of COLO205 cell-derived DNA by platelets was observed (Fig. 2, A and B; fig. S2, A to C; and movies S2 and S3). The average DNA fluorescence intensity of the 168 platelets imaged plateaued at ~6 min, suggestive of saturation of DNA uptake (Fig. 2C).

DNA is internalized and released on platelet activation

To determine the localization of pDNA, we performed high-resolution Airyscan imaging of healthy donor platelets spread on collagen-coated glass coverslips. During spreading, platelets evaginate the membranes of their open canalicular system (OCS), an internal surface-connected system of channels, to increase their surface area (*22*). This process extrudes materials captured within the OCS and pushes intracellular contents to the center (*22*). Imaging of spread platelets costained for P-selectin (CD62P), a marker of platelet activation and degranulation, and DRAQ5 revealed that DNA was located at the center of spread platelets (Fig. 2D). Calculation of the DRAQ5 staining intensity during progressive computational erosion of the CD62P mask from the edge of the platelet to the center further confirmed that DNA was internalized within the body of the platelet and not held within the OCS (fig. S2D).

We next performed colocalization analyses by costaining platelets for DNA (DRAQ5), the different types of platelet storage granules (alpha and dense granules), and other organelle markers. We observed strong colocalization between DNA and membrane-bound internal vesicles (CD81 and LAMP-2), with no correlation with mitochondria (TOM20) (Fig. 2, E to H), confirming that the DNA content of platelets was largely contained within membrane-bound vesicles and not stored in granules or restricted to mitochondrial DNA.

Platelets internalize DNA-loaded extracellular vesicles

DNA-loaded extracellular vesicles (EVs) are released during cellular apoptosis, and viable cells also remove excess cytoplasmic DNA created during aberrant cycles of mitosis by the release of DNA-loaded EVs (*23*–*27*). Platelets internalize EVs through their OCS and endocytosis (*28*), and platelet uptake of tumor cell-derived EVs has previously been shown to transfer cancer cell–derived protein cargo and mRNA transcripts (*29*).

We therefore investigated whether EVs may mediate DNA transfer to platelets. Platelets isolated from female donors were incubated with EVs derived from male Burkitt's lymphoma (BL2) cells or isogenic BL2 cells engineered to overexpress the apoptosis-suppressing gene *BCL2* (BL2-Bcl-2 cells). This system enabled us to also explore whether DNA loading of EVs occurred during apoptosis. EVs were isolated from BL2 and BL2-Bcl-2 cells after ultraviolet irradiation, generating apoptotic EVs (apo EVs) from BL2 cells or nonapoptotic (nonapo EVs) from BL2-Bcl-2 cells. The EVs were treated with deoxyribonuclease (DNase) to remove any noninternalized DNA (Fig. 2I). DNA-loaded EVs were visible adherent to, as well as within, platelets following coincubation (Fig. 2, J and K; movies S4 and S5; and fig. S2, E and F). Copies of *SRY* were detectable in platelets from female donors only following incubation with BL2-derived EVs as well as in higher abundance following coincubation with apo EVs than with nonapo EVs (Fig. 2L and fig. S2G). Similarly, by using whole chromosome X and Y fluorescence in situ hybridization (FISH) probes, fragments of both X and Y chromosomes were visualized in female platelets following coincubation with HEL cells that also derive from a male donor (Fig. 2M).

Platelets internalize membrane-free DNA fragments

To test whether platelets could also internalize "free" DNA fragments that were not contained within EVs, we exposed healthy donor platelets to synthetic DNA fragments ranging from 128 to 657 base pairs (bp) in length. Platelets efficiently internalized all tested DNA fragments, confirming that platelets sequestered non–membrane-bound DNA of varying lengths in addition to DNA-loaded EVs (Fig. 2N).

Pharmacological modulation of DNA trafficking

To explore whether DNA uptake and release by platelets could be pharmacologically manipulated, we tested the impact of agonists and inhibitors known to block platelet activation and/or specific components of cargo trafficking. Activation of platelets with the canonical platelet agonist thrombin receptor activating peptide (TRAP) decreased their DNA content (Fig. 3A), indicating that DNA is released by platelets upon activation. In keeping with this, the yield of DNA isolated from platelets was higher when platelets were treated with two potent inhibitors of platelet activation:- aspirin and ibrutinib, a Bruton's tyrosine kinase (BTK) inhibitor (Fig. 3, B and C, and fig. S3A).

We next tested a range of inhibitors known to block specific components of cargo trafficking by platelets, including inhibitors of actin (cytochalasin D), membrane ruffling (imipramine), clathrin (Pitstop 2), caveolae-dependent endocytosis (nystatin), dynamin (Dynole) and Na^+/H^+ exchange or micropinocytosis (amiloride). In keeping with previous literature suggesting that platelets "engulf" EVs through endocytosis

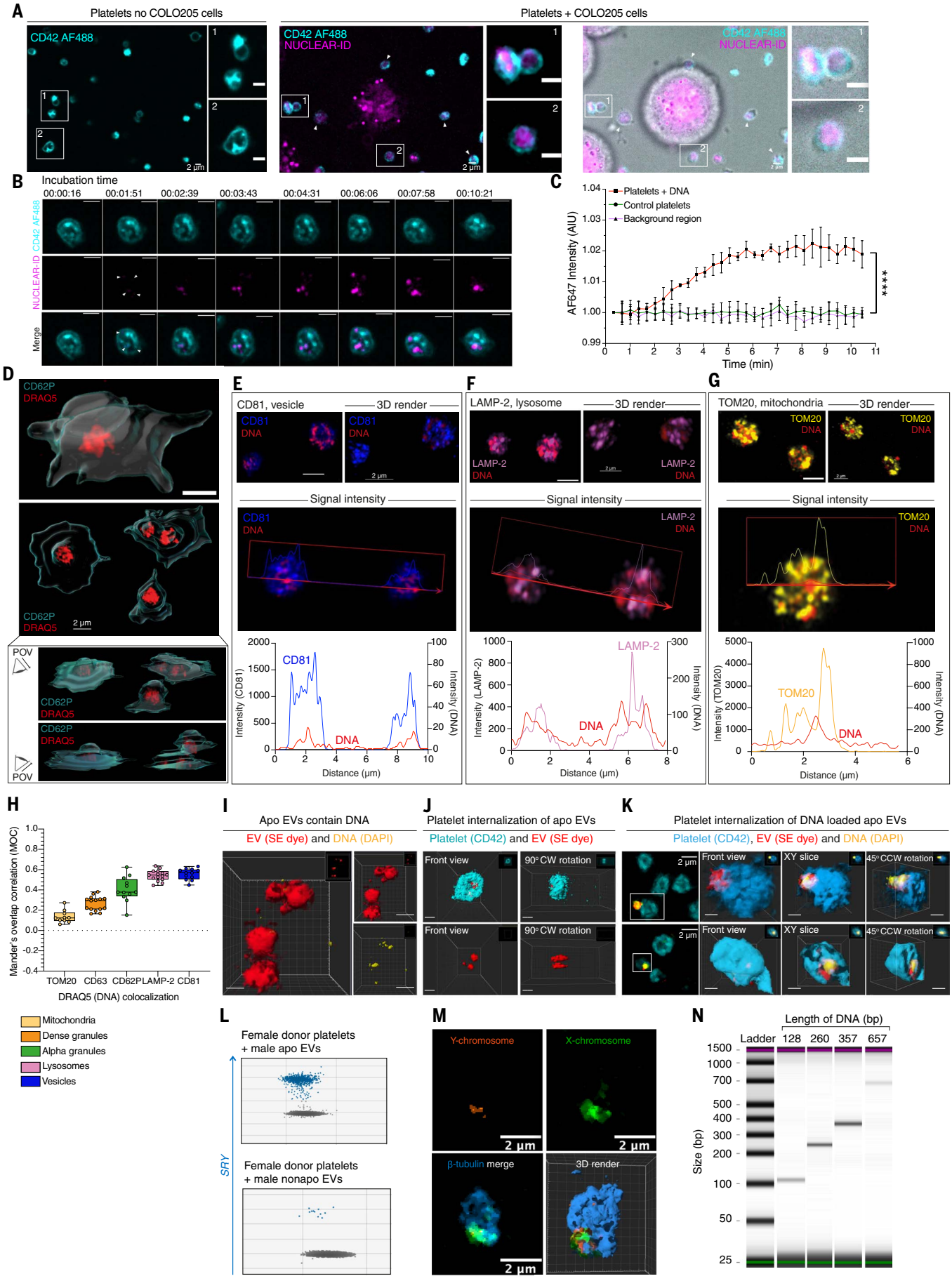
A
Platelets no COLO205 cells
Platelets + COLO205 cells
CD42 AF488
NUCLEAR-ID
2 µm
B
Incubation time
00:00:16
00:01:51
00:02:39
00:03:43
00:04:31
00:06:06
00:07:58
00:10:21
CD42 AF488
NUCLEAR-ID
Merge
C
Platelets + DNA
Control platelets
Background region
AF647 Intensity (AIU)
Time (min)
****
D
CD62P
DRAQ5
POV
E
CD81, vesicle
3D render
CD81
DNA
Signal intensity
Intensity (CD81)
Intensity (DNA)
Distance (µm)
F
LAMP-2, lysosome
LAMP-2
G
TOM20, mitochondria
TOM20
H
Mander's overlap correlation (MOC)
TOM20 CD63 CD62P LAMP-2 CD81
DRAQ5 (DNA) colocalization
Mitochondria
Dense granules
Alpha granules
Lysosomes
Vesicles
I
Apo EVs contain DNA
EV (SE dye) and DNA (DAPI)
J
Platelet internalization of apo EVs
Platelet (CD42) and EV (SE dye)
Front view
90° CW rotation
K
Platelet internalization of DNA loaded apo EVs
Platelet (CD42), EV (SE dye) and DNA (DAPI)
XY slice
45° CCW rotation
L
Female donor platelets
+ male apo EVs
Female donor platelets
+ male nonapo EVs
SRY
M
Y-chromosome
X-chromosome
β-tubulin merge
3D render
N
Length of DNA (bp)
Ladder 128 260 357 657
Size (bp)

Fig. 2. Platelets rapidly internalize DNA released by nucleated cells through uptake of DNA-loaded EVs and non–membrane-encapsulated DNA fragments. (**A**) Healthy donor–derived, CD42 AF488 (cyan)–labeled platelets before (left) and after (middle and right) coincubation with COLO205 cells labeled with NUCLEAR-ID (magenta) to track DNA transfer. White boxes show magnified regions; arrows highlight platelet uptake of COLO25-derived DNA. Scale bars, 2 μm. Middle (fluorescence) and far right (bright field) are the same image. (**B**) Live-cell time-lapse imaging of a representative platelet showing internalization of DNA. Scale bars, 3 μm. (**C**) Time-course quantification of pDNA fluorescence intensity; data points show mean ± SD. AF647 signal was measured in background regions to detect fluctuations. ****$P < 0.0001$, as determined by a Wilcoxon signed-rank test. Tracking shown for platelets incubated with control media ($n = 168$ platelets) or media conditioned by NUCLEAR-ID–labeled COLO205 cells ($n = 173$ platelets). (**D** to **G**) Representative images acquired using the Airyscan detector of a ZEISS LSM980 as well as 3D rendering performed using ImarisViewer. (D) Healthy donor platelets spread on collagen and stained with CD62P, to create a translucent cell surface mask (turquoise), and DRAQ5 (DNA, red). Four representative platelets are shown. (Bottom) Alternate views of the same platelets from above and below; scale bars, 2 μm. [(E) to (G)] (Top) Representative images and 3D renders of two healthy donor platelets showing colocalization of pDNA (DRAQ5, red) with (E) CD81 (vesicles, blue), (F) LAMP-2 (lysosomes, pink), and (G) TOM20 (mitochondria, yellow). (Bottom) Pixel intensity (*y* axis) along defined lines (distance in micrometers; *x* axis) was analyzed using ZEISS Zen software. (**H**) Manders' correlation coefficients were calculated for DNA with mitochondria (TOM20), dense granules (CD63), alpha granules (CD62P), lysosomes (LAMP-2), and vesicles (CD81). Box plots show the median, first quartile, and third quartile, with whiskers extending to minimum and maximum values. Platelets analyzed per marker: TOM20 ($n = 10$), CD63 ($n = 15$), CD62P ($n = 12$), LAMP-2 ($n = 15$), and CD81 ($n = 12$). (**I**) A representative 3D reconstruction of EV clusters released by apoptotic BL2 cells labeled with an amine-reactive membrane dye (CF658, red) and DNA stain (DAPI, yellow), revealing internalized DNA. Imaged using a ZEISS LSM900, 63X magnification. Scale bars, 2 μm. (**J**) Platelets stained with CD42 AF488 (cyan) following incubation with labeled EVs (red) showing three EVs within a single representative platelet. 3D modeling shows 90° clockwise rotation. Scale bar, 1.4 μm. (**K**) 3D reconstruction showing platelet internalization of DNA-loaded apo EVs (DNA, yellow; EVs, red). Two representative platelets are shown: one with surface-bound DNA-loaded EVs (top) and one with internalized EVs (bottom). Scale bars, 0.5 μm unless stated otherwise. (**L**) ddPCR quantification of the Y-chromosome gene *SRY* in DNA derived from platelets of a female donor after incubation with apo EVs and nonapo EVs. Representative data from $n = 3$ independent experiments. (**M**) Representative FISH and 3D render demonstrating fragments of X and Y chromosomes in female donor platelets following incubation with male HEL cells. Platelets were counterstained with β-tubulin (blue). Imaged using a ZEISS LSM900, 63× magnification; 3D render was created using ImarisViewer. (**N**) Electrophoresis data showing recovery of 128- to 657-bp synthetic DNA fragments from washed healthy donor platelets after overnight incubation. Representative data from $n = 5$ independent experiments. AIU, arbitrary intensity units; BL2, Burkitt's lymphoma cells; chr, chromosome; CCW, counterclockwise; CW, clockwise; POV, perspective of view; SE, succinimidyl ester.

at the OCS membrane, we found that platelet uptake of DNA-loaded apo EVs was reduced by the dynamin inhibitor Dynole, indicating that DNA-loaded apo EVs were internalized by clathrin-mediated endocytosis (Fig. 3, E and F).

These inhibitors did not reduce the uptake of free DNA fragments by platelets, suggesting that this occurs through an alternative, clathrin-independent mechanism (Fig. 3G). Rather, we found that Dynole and amiloride substantially increased the amount of DNA obtained from the platelets exposed to synthetic DNA fragments (Fig. 3, H and I). Dynole and amiloride also block platelet exocytosis and the release of intracellular contents (*30*, *31*). Accordingly, we found that Dynole reduced pDNA release (Fig. 3, J to L).

Together, these data indicated platelet activation was not required for DNA uptake, but that DNA was released by platelets upon activation. Furthermore, platelet content of DNA can be pharmacologically modulated to increase the abundance of DNA preserved within platelets (fig. S3B).

Detecting cancer mutations in platelets

Given the growing importance of cfDNA detection in cancer screening and molecular profiling, we sought to determine whether platelets may take up tumor-derived DNA fragments that conferred cancer-specific genetic variants.

Platelets from healthy donors were incubated with a variety of human cancer cell lines harboring common cancer-associated gene mutations, including colorectal cells and erythroleukemia cells (Fig. 4A). Analysis of DNA isolated from platelets following coincubation with cancer cell lines detected all relevant oncogenic mutations, including $KRAS^{G12D}$, $BRAF^{V600E}$, $PIK3CA^{H1047R}$, and $JAK2^{V617F}$ (Fig. 4, B and C). No cancer-specific gene mutations were identified in healthy donor platelets incubated alone, but wild-type alleles were detected (Fig. 4C), indicative of DNA sequestered by platelets prior to blood sampling.

To determine whether the ability to capture extracellular DNA was specific to platelets or shared by other blood cell types, we tested whether $BRAF^{V600E}$ derived from COLO205 cells was also sequestered in vitro by peripheral blood MNCs and RBCs. Although mutant *BRAF* ($BRAF^{V600E}$) was readily detectable in pDNA (Fig. 4D), fewer copies of $BRAF^{V600E}$ were detected in MNCs and RBCs (Fig. 4D and fig. S3, C to E), where they were of negligible abundance in comparison to wild-type alleles (fig. S3, D and E).

pDNA is protected from nucleases

To test whether pDNA was protected from external nuclease digestion, conditioned media (analogous to cfDNA) and platelets were treated with DNase following conditioning by HEL cells that carry the $JAK2^{V617F}$ mutation. Detection of $JAK2^{V617F}$ in HEL cell–conditioned media was completely abrogated by DNase treatment (Fig. 4E). By contrast, there was no reduction in the abundance of $JAK2^{V617F}$ in platelets following DNase treatment (Fig. 4E), indicating that the majority of DNA was encapsulated by the platelet outer membrane and protected from enzymatic degradation. This was verified by using synthetic DNA fragments and target-specific primers (fig. S3F).

Genomic distribution and origin of pDNA

We then set out to explore the genomic characteristics of pDNA and validate its utility for detection of cancer gene aberrations in vivo.

cfDNA has a classical fragmentation profile with a periodicity reflecting nucleosomal footprints (*12*). Electrophoretic analysis of pDNA showed fragments of around 12,000 to 16,000 bp, and many samples also showed shorter fragments of around 120 to 500 bp with nucleosome footprints, similar to the nucleosome footprint of cfDNA (fig. S4, A and B). Low-input chromatin immunoprecipitation (ChIP) for H3k27 histone acetylation of DNA isolated from platelet pellets and live-cell imaging of platelets coincubated with H2B-mCherry–labeled HEL cells confirmed that the DNA sequestered by platelets was associated with nucleosomes and that histone modifications are preserved in pDNA (fig. S4, C and D, and movie S6).

To compare the genomic origin of pDNA and cfDNA, whole-genome sequencing (WGS) was performed on matched pDNA and cfDNA extracted from the peripheral blood of 15 donors—of whom 10 had active malignancy, and 5 had undergone surgery and/or chemoradiotherapy—to screen for residual disease (table S4). Size selection was performed on the pDNA to separate the shorter (<600 bp) "s-pDNA," which were similar in length to cfDNA fragments, from the longer fragments ("l-pDNA").

We performed low-pass WGS (mean target coverage of 1X) on s-pDNA, l-pDNA, and paired cfDNA ($n = 15$). Platelets contain a small number of mitochondria, estimated at four to six mitochondria per cell (*32*, *33*). The majority of fragments from both s- and l-pDNA mapped to the nuclear genome (97.0 to 99.9% for s-pDNA and 69.9 to 99.1% for l-pDNA) (Fig. 4F). As expected, given that the mitochondrial

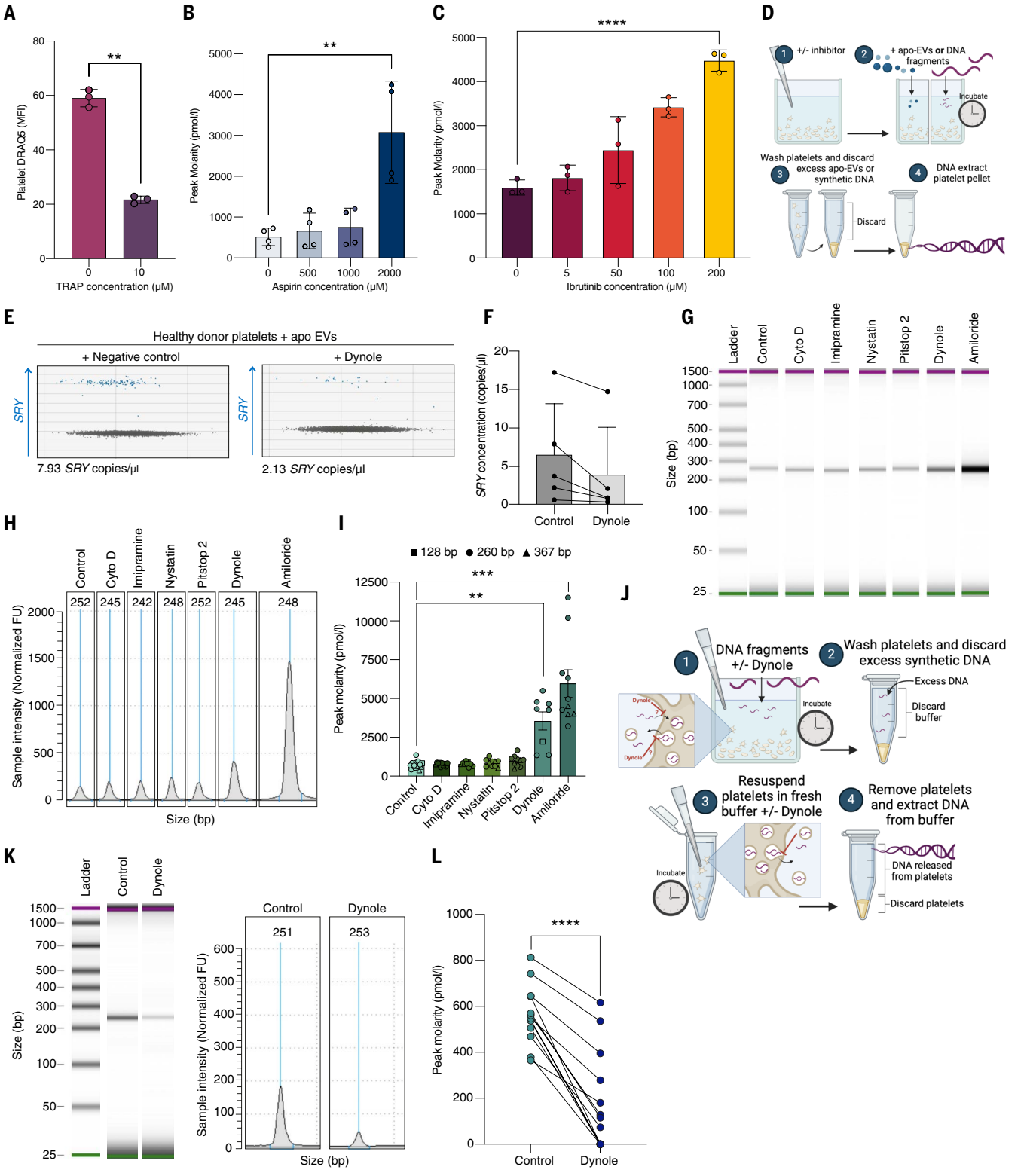

Fig. 3. pDNA content can be pharmacologically modulated. (**A**) Flow cytometric analysis of DNA (DRAQ5) content in healthy donor–derived platelets, with and without activation using 10 μM TRAP-6. $n = 3$; points represent data from individual healthy donors; bars show mean ± SD; $^{**}P < 0.01$, as determined by a paired t test. (**B** and **C**) Inhibition of platelet activation with (B) aspirin or (C) ibrutinib increases the yield of DNA from platelet pellets. $n = 3$ to 4 independent experiments; plots show mean ± SD peak molarity corresponding to DNA TapeStation peaks for synthetic DNA fragments coincubated with platelets prior to washing and DNA extraction. $^{**}P < 0.01$; $^{****}P < 0.0001$; as determined by an unpaired t test. (**D**) Schematic of the method for investigating DNA uptake. Platelets were pretreated with inhibitors, incubated with DNA-loaded apo EVs or synthetic DNA fragments, then washed, pelleted, and subjected to DNA extraction. (**E** and **F**) ddPCR quantification of *SRY* in platelet-derived DNA from female donors after incubation of platelets with apo EVs treated with or without Dynole. Fewer *SRY* copies were detected in dynamin-inhibited platelets compared with controls. (E) Representative ddPCR plot and (F) $n = 5$ independent experiments, paired line plot shows mean ± SD, with lines connecting data points before and after

inhibition. (**G** and **H**) Representative electrophoresis showing recovery of 260-bp synthetic DNA fragments from platelets treated with inhibitors known to block components of cargo trafficking. More DNA was extracted from platelets treated with Dynole and amiloride. (**I**) Summary plot showing mean ± SD for all DNA fragment lengths (128 to 367 bp) following treatment with inhibitors [(G) and (H)]. Data from four independent experiments ($n = 4$) with two to five replicate wells per condition. $^{**}P < 0.01$; $^{***}P < 0.001$; as determined by a paired *t* test. (**J**) Schematic of the method for investigating pDNA release. Platelets were treated with or without Dynole, incubated with synthetic DNA, washed, resuspended in fresh buffer, and incubated for 3 hours. DNA was then extracted from platelet-depleted buffer. (**K**) Representative electrophoresis and (**L**) a paired-line plot showing significant inhibition of pDNA release following Dynole treatment, with lines connecting data points before and after inhibition. Data from five independent experiments ($n = 5$), with two to three replicate wells per condition. $^{****}P < 0.0001$; as determined by a paired *t* test. cyto D, cytochalasin D; FU, fluorescence units.

genome is ~16,500 bp, a higher subfraction (0.9 to 30.1%) of l-pDNA mapped to the mitochondrial genome versus 0.081 to 2.968% of the shorter fragments (Fig. 4F).

Mapping across the genome revealed that pDNA fragments covered the entire nuclear genome (fig. S4E), mirroring cfDNA and demonstrating that sampling of pDNA would enable genetic variants across the genome to be detected. Compared with cfDNA, the s-pDNA fragments showed more even coverage, as indicated by a lower Gini index (*34*) (fig. S4F).

pDNA maps to the nuclear genome, and coverage mirrors cfDNA

We then obtained deeper sequencing (mean sequencing depth 15× ± 3 versus 12× ± 1 for cfDNA and s-pDNA, respectively) of paired cfDNA and s-pDNA, including five from donors after therapy (samples 1 to 5) and two from donors with active, untreated pancreatic and colorectal carcinoma (table S4). No notable differences were detected in sequencing quality (base quality, 3′ bias, mapping rate) between s-pDNA and cfDNA, except for a higher estimated polymerase chain reaction (PCR) duplication rate (cfDNA, 3.2% ± 0.6%; pDNA, 11.3% ± 7.2%), indicating lower complexity of short pDNA libraries, presumably due to the size selection.

Nucleosome-bound cfDNA is more protected from degradation than nucleosome-free DNA. This leads to a characteristic fragment-length distribution of cfDNA, with mono- and dinucleosome length peaks at approximately 167 and 320 bp, respectively (*35*). The peak mean fragment length for s-pDNA was 166 bp ± 0.8, with a second, dinucleosome peak at approximately 328 bp. The dinucleosome peak was, by a fraction, larger in s-pDNA than cfDNA (fig. S5A), likely reflecting the increased protection of pDNA from nuclease digestion, as observed in our in vitro experiments (Fig. 4E and fig. S3F).

cfDNA fragments of tumor cell origin are shorter than wild-type fragments (*36*, *37*). In accordance with this, we observed that both mono- and dinucleosome fragment lengths were notably shorter in both pDNA and cfDNA in sample 6, derived from a patient with an inoperable pancreatic tumor and containing readily detectable tumor-derived cfDNA, indicating that fragmentomic analysis may be applied to pDNA to detect the presence of cancer (*38*) and that platelets capture DNA fragments that resemble those found in cfDNA in vivo (Fig. 4G and table S4).

To confirm the capture of circulating tumor cell–derived DNA (ctDNA) by platelets in vivo, we used ichorCNA (*39*) to look for copy number alterations (CNAs) and estimate the fraction of tumor-derived DNA. Clonal amplifications and deletions in chromosomes 6 and 7 as well as subclonal amplifications in chromosome 2 were detected in both cfDNA and s-pDNA from sample 6 (from the patient with pancreatic cancer), with an estimated tumor fraction of 25% (Fig. 4H). CNAs detected in s-pDNA mirrored those present in cfDNA, and the estimated proportion of tumor-derived DNA was highly correlated between s-pDNA and cfDNA (fig. S5, B and C). Selecting DNA fragments smaller than 150 bp increased the estimated tumor content of s-pDNA from 25 to 30%, in parallel to the increase seen in cfDNA (fig. S5D). No CNAs were detected in the l-pDNA from sample 6 (fig. S5E), in line with previous reports that ctDNA is enriched in shorter fragments (*37*), nor in either the cfDNA or pDNA from patients after therapy.

Matched tumor and healthy tissue biopsy samples were available for sample 7 from a patient with colorectal carcinoma, enabling us to look deeper for low-level ctDNA by screening for tumor-specific mutations not present in matched healthy tissue. We compared the detection rate of tumor-specific mutations from the relevant donor with detection of random samples of mutations taken from other patients with colorectal carcinoma (*40*). The matched tumor mutations were detected at a higher rate than the random mutations in the cfDNA and s-pDNA and at similar frequency (likelihood rate of 8.92×10^{-11} for cfDNA and 2.30×10^{-7} for s-pDNA), with lower-level detection in the l-pDNA ($P < 0.0004$; Fig. 4I), confirming the presence of ctDNA in platelets.

These data indicated that ctDNA was present within platelets in similar abundance to cfDNA, both in patients with high levels of ctDNA and clear CNAs (>20%, sample 6; Fig. 4H) and in those with extremely low levels (<0.5%, sample 7; Fig. 4I), where targeted analysis and matched tumor tissue was required. Overall, ctDNA was identified in both platelets and cfDNA in 20% of the pretreatment samples either by detecting CNAs or known tumor mutations, in keeping with the sensitivity of WGS for ctDNA detection reported in large clinical cohorts (*41*).

The enrichment for nucleosome-bound DNA in cfDNA has previously been used to gain insight into gene expression patterns and cell-of-origin, with prior reports showing that a depletion of reads occurs over transcriptional start sites (TSSs) with periodicity in coverage relative to the TSS (*42*). In addition, DNA methylation studies have shown that the majority (>90%) of cfDNA in both healthy individuals and in those with cancer is of blood cell origin, including neutrophils, monocytes, erythroblasts (*43*), and megakaryocytes (*44*). We found very similar depletion in sequencing coverage and periodicity around TSS for genes that are highly expressed in peripheral blood MNCs in both pDNA and cfDNA, suggesting a shared cellular origin of pDNA and cfDNA (Fig. 4J and fig. S5F). Notably, the depletion in coverage for high-expression MNC genes was less marked for the sample that had an estimated ctDNA fraction of 25% than for the other samples (Fig. 4J).

To orthogonally validate the cell-of-origin of pDNA, whole-genome methylation analysis was performed using the bisulfite-free sequencing method, TET-assisted pyridine borane sequencing (TAPS) (*45*). The data was then deconvoluted using a published atlas of cell-specific methylation patterns (*46*). This confirmed a similar cellular origin of pDNA and cfDNA, with the majority originating from blood leukocytes and a minor contribution from hepatocytes. Of note, a higher proportion of l-pDNA than s-pDNA mapped to megakaryocyte-specific loci (35.9 versus 16.8%), suggesting that more l-pDNA may derive from parent megakaryocytes (fig. S5G).

High abundance of mutant alleles in platelets in colorectal and pancreatic carcinoma

To test whether including an analysis of pDNA would add value to plasma cfDNA in the setting of cancer diagnostics, we used a mouse model of colorectal carcinoma in which expression of *KRAS*^{G12D} and *TP53* mutations are induced by the villin promoter, resulting in locally invasive colorectal adenocarcinoma with a low incidence of metastases

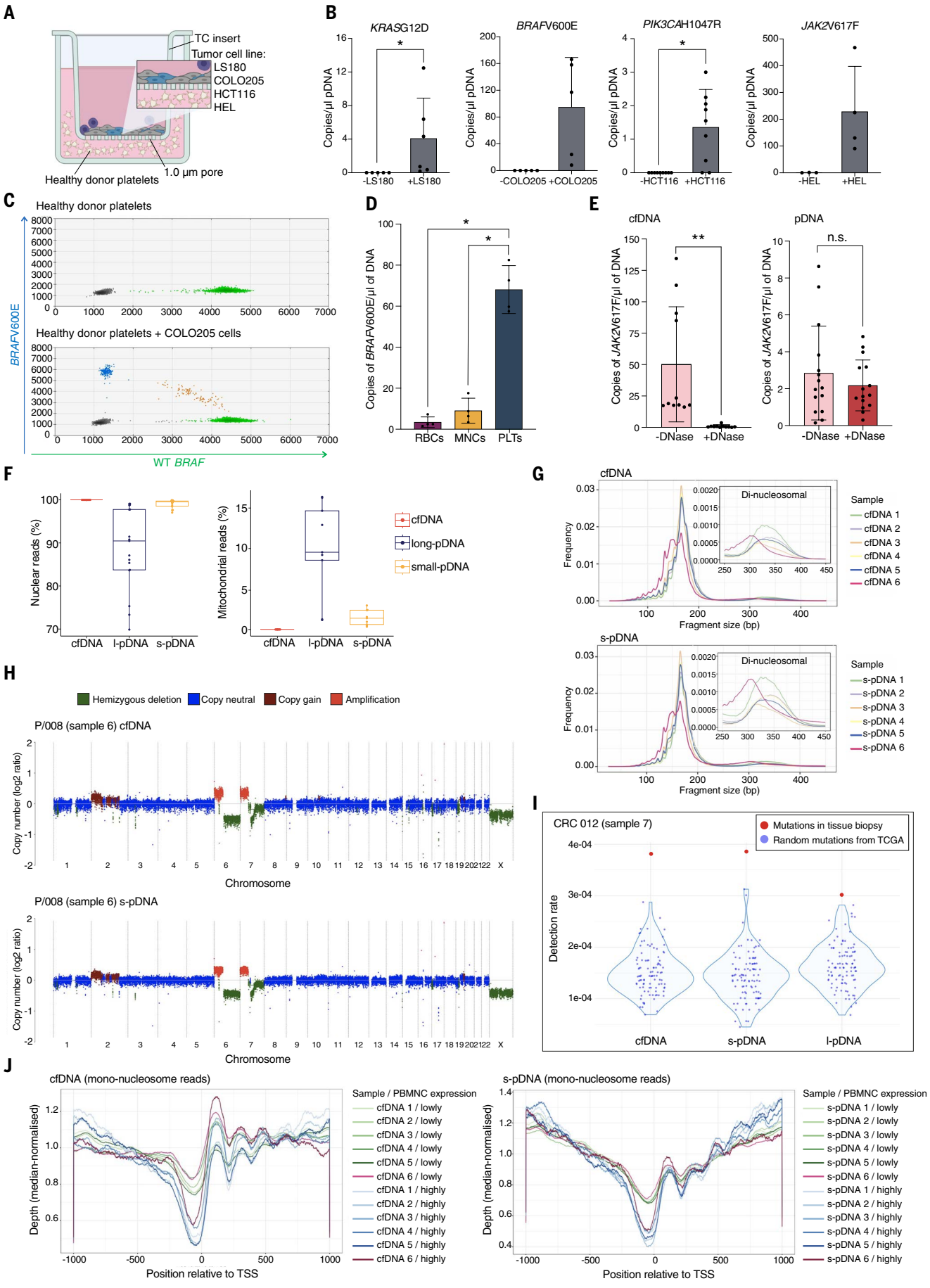
A
TC insert
Tumor cell line:
LS180
COLO205
HCT116
HEL
Healthy donor platelets
1.0 µm pore
B
KRASG12D
BRAFV600E
PIK3CAH1047R
JAK2V617F
Copies/µl pDNA
-LS180 +LS180
-COLO205 +COLO205
-HCT116 +HCT116
-HEL +HEL
C
Healthy donor platelets
Healthy donor platelets + COLO205 cells
BRAFV600E
WT BRAF
D
Copies of BRAFV600E/µl of DNA
RBCs MNCs PLTs
E
cfDNA
pDNA
Copies of JAK2V617F/µl of DNA
n.s.
-DNase +DNase
F
Nuclear reads (%)
Mitochondrial reads (%)
cfDNA l-pDNA s-pDNA
cfDNA
long-pDNA
small-pDNA
G
cfDNA
s-pDNA
Frequency
Fragment size (bp)
Di-nucleosomal
Sample
cfDNA 1
cfDNA 2
cfDNA 3
cfDNA 4
cfDNA 5
cfDNA 6
s-pDNA 1
s-pDNA 2
s-pDNA 3
s-pDNA 4
s-pDNA 5
s-pDNA 6
H
Hemizygous deletion
Copy neutral
Copy gain
Amplification
P/008 (sample 6) cfDNA
P/008 (sample 6) s-pDNA
Copy number (log2 ratio)
Chromosome
I
CRC 012 (sample 7)
Mutations in tissue biopsy
Random mutations from TCGA
Detection rate
cfDNA s-pDNA l-pDNA
J
cfDNA (mono-nucleosome reads)
s-pDNA (mono-nucleosome reads)
Depth (median-normalised)
Position relative to TSS
Sample / PBMNC expression
cfDNA 1 / lowly
cfDNA 2 / lowly
cfDNA 3 / lowly
cfDNA 4 / lowly
cfDNA 5 / lowly
cfDNA 6 / lowly
cfDNA 1 / highly
cfDNA 2 / highly
cfDNA 3 / highly
cfDNA 4 / highly
cfDNA 5 / highly
cfDNA 6 / highly
s-pDNA 1 / lowly
s-pDNA 2 / lowly
s-pDNA 3 / lowly
s-pDNA 4 / lowly
s-pDNA 5 / lowly
s-pDNA 6 / lowly
s-pDNA 1 / highly
s-pDNA 2 / highly
s-pDNA 3 / highly
s-pDNA 4 / highly
s-pDNA 5 / highly
s-pDNA 6 / highly

Fig. 4. Platelets contain a repertoire of DNA fragments that map over the human nuclear genome, including tumor-derived DNA-bearing cancer-associated gene mutations. (**A**) Schematic of the experimental system for coincubating healthy donor platelets with malignant cells, separated by 1 μm membrane inserts to allow extracellular biomolecule and small EV exchange while preventing cell transfer. After coincubation, platelets were removed, washed three times, and subjected to DNA extraction. (**B**) Number of copies of mutant alleles detected per microliter of DNA extracted from platelets incubated with (+) or without (−) colorectal (LS180, COLO205, and HCT116) and erythroleukemia (HEL) cell lines. Data were collected from one to three independent experiments, with three to five replicate wells per condition. Each point represents one coculture experiment per condition. Replicates per condition were as follows: LS180 ($n = 2$ experiments, 3 replicates each), COLO205 ($n = 1$ experiment, 4 and 5 replicates), HCT116 ($n = 3$ experiments, 3 replicates each), and HEL ($n = 1$ experiment; 3 and 4 replicates). Bars represent mean ± SD; $^{*}P < 0.05$, as determined by a Wilcoxon paired signed-rank test. (**C**) Representative ddPCR analysis showing quantification of wild-type (WT) *BRAF* and $BRAF^{V600E}$ alleles in pDNA extracted from healthy donor platelets before (top) and after coincubation with COLO205 colorectal cancer cells (bottom). (**D**) Quantification of $BRAF^{V600E}$ in RBCs, MNCs, and platelets (PLTs) following incubation in media conditioned by COLO205 cells. Data are presented as mean ± SD; individual points represent $n = 2$ independent experiements, each with 2 replicates. $^{*}P < 0.05$; as determined by a Mann-Whitney *U* test. (**E**) Impact of DNase treatment on the detection of *JAK2* mutant alleles in pDNA and cfDNA (media) following coincubation of healthy donor platelets with HEL cells. Data are presented as mean ± SD; individual points represent $n = 5$ independent experiments, each with 3 replicates. n.s., not significant; $^{**}P < 0.01$; determined by a Wilcoxon signed-rank test. (**F**) Percentage of fragments mapping to the nuclear and mitochondrial genomes from cfDNA, short (>100 and <600 bp) and long (>600 bp) pDNA fragments. In the box plot, the center line shows the median, whiskers indicate the minimum and maximum values, and each data point represents one patient; $n = 15$ donors with gastrointestinal carcinoma. (**G**) Fragment length distribution of paired, aligned reads for cfDNA (top) and s-pDNA (bottom). $n = 6$ donors with gastrointestinal carcinoma; samples 1 to 5 show a primary peak at ~165 bp (mononucleosomal) and a smaller secondary peak at ~325 bp (dinucleosomal; inset). Sample 6 (red line), from a patient with untreated pancreatic adenocarcinoma, has shorter mono- and dinucleosomal fragments than samples 1 to 5 (post–anticancer therapy patients). (**H**) Deviation from median coverage in 100-kbp windows across all chromosomes for cfDNA (top) and s-pDNA (bottom) for P/008 (sample 6), revealing chromosomal aberrations in chromosomes 2, 6, and 7 (copy number gains and amplifications shown in red; deletions shown in green). (**I**) Detection rates of mutations in cfDNA, s-pDNA, and l-pDNA for sample 7 where matched tumor biopsy was available. The red dot indicates mutations detected in the tumor biopsy; blue dots indicate 100 random samples of mutations from other patients with colorectal carcinoma from The Cancer Genome Atlas (TCGA) dataset. (**J**) Read-depth distribution around transcription start sites (TSSs) of genes highly [transcripts per million (TPM) >15, blue] and lowly (TPM <15, green) expressed in peripheral blood MNCs for cfDNA (left) and s-pDNA (right) mononucleosome reads. $n = 6$ donors with gastrointestinal carcinoma. Depth per position per sample was normalized to the median read depth across all genes in that expression category. Single-letter abbreviations for the amino acid residues referenced throughout the paper and figures are as follows: G, Gly; D, Asp; V, Val; E, Glu; H, His; R, Arg; F, Phe.

and mice with $KRAS^{G12D/+}$, $TP53^{fl/fl}$, plus $NOTCH^{fl/+}$, with more aggressive and metastatic disease (*47*) (Fig. 5A). pDNA and cfDNA were extracted simultaneously from the same blood sample (Fig. 5A).

Mutant $KRAS^{G12D}$ as well as wild-type *KRAS* alleles were readily detectable in both cfDNA and platelets of mice with colorectal carcinoma. In more than half of the mice (13/20, 65%), copies of $KRAS^{G12D}$ per microliter of DNA were in higher abundance in pDNA than cfDNA, both in mice with locally invasive and metastatic disease (Fig. 5, B to E).

To corroborate these findings in a second model and examine an early stage during tumorigenesis prior to tumor dissemination, we used an orthotopic pancreatic cancer model, where pancreatic cancer cells were inserted within a Matrigel plug into the body of the pancreas (*48*). Fourteen days after implantation and prior to local tumor invasion, $KRAS^{G12D}$ alleles were readily detected in murine platelets (Fig. 5C and fig. S6, A and B) and were not reduced in mice receiving low-dose systemic aspirin therapy (fig. S6C).

$BRAF^{V600E}$ in platelets of patients with precancer

Improving the sensitivity for liquid biopsy screening is crucial in the setting of low–tumor burden disease and in patients with premalignant lesions, where the abundance of ctDNA is low. Sessile serrated lesions (SSLs) are high-risk, premalignant colon polyps driven by mutations in *BRAF* that account for around one-quarter of colorectal cancers (CRCs) (*49*). To explore the utility of pDNA for detecting premalignant lesions, we collected platelets and cfDNA from patients found to have SSLs at colonoscopy ($n = 31$) versus controls ($n = 14$).

Mutant $BRAF^{V600E}$ alleles were detected in either the cfDNA and/or pDNA in 16.1% of the patients with serrated polyps (5/31) (Fig. 5F), consistent with previous reports of the frequency of detectable ctDNA in SSL cohorts (*50*, *51*). Mirroring our findings in the CRC mouse model, around half (3/5) of the patients with detectable ctDNA had a higher number of $BRAF^{V600E}$ copies in pDNA than in cfDNA (Fig. 5, F to H, and fig. S6D). $BRAF^{V600E}$ was not detected in any of the pDNA samples from 14 controls (Fig. 5F), demonstrating high specificity of targeted mutational analysis of pDNA in this setting and that at least half of the relevant ctDNA is sequestered by blood platelets.

Discussion

Prior studies of platelet nucleic acid content have only focused on RNA (*8*, *52*–*54*), although the presence of DNA in platelets has been noted by other groups (*3*, *4*, *21*, *55*). For example, a study examining the presence of histone proteins in platelets during sepsis showed that 5 to 35% of platelets were positive for the DNA-specific marker, DRAQ5 (*55*), and the presence of megakaryocyte-derived DNA in platelets was recently corroborated by an independent group (*21*). In this work, we have performed a detailed interrogation of pDNA content, demonstrating a biological role for platelets that was previously unappreciated: as scavengers of endogenous extracellular cfDNA, including tumor-derived and free fetal DNA.

We show that platelet uptake of DNA can occur by multiple mechanisms: endocytosis of DNA-loaded EVs from apoptotic cells and uptake of membrane-free DNA fragments. Previous reports indicated that DNA can bind to the platelet surface (*56*, *57*). We found that DNA was also internalized by platelets and held in membrane-bound vesicles, where it was protected from exogenous DNase degradation and subsequently released upon platelet activation. DNA release could be prevented by using pharmacological inhibitors, thereby preserving the DNA within platelets where it is protected from degradation, increasing the yield of DNA obtained from platelet pellets.

Several physiological mechanisms exist to limit the abundance of cfDNA, as excess extrachromosomal DNA in the cytosol and plasma is proinflammatory (*58*, *59*). We demonstrated higher and more variable levels of cfDNA in plasma in the setting of severe thrombocytopenia in both a mouse model and in patients. This supports a role for platelets in regulating the cfDNA content of plasma, although we cannot exclude that the higher level of cfDNA observed was due to other consequences of antibody-mediated platelet clearance.

Further work is required to ascertain whether platelets deploy their DNA content at sites of activation. An attractive hypothesis is that platelet clearance may control the nonspecific immunostimulatory activity of cfDNA in plasma, and that platelets may release DNA cargo to evoke an immune response in a targeted fashion at sites of platelet activation. Platelets have also been shown to mediate horizontal transfer of RNAs and transcription factors (*60*), either through uptake of

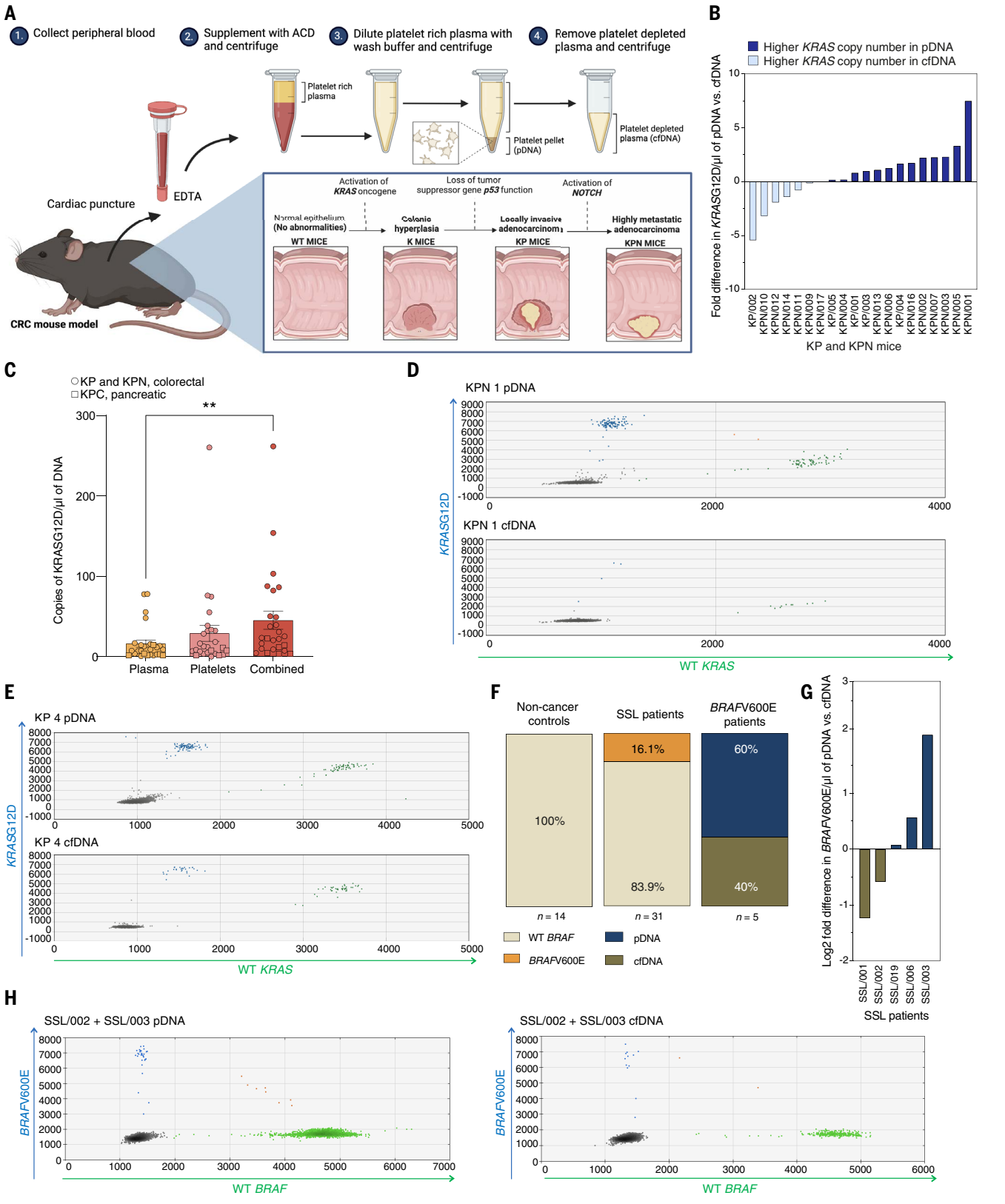

Fig. 5. Detection of driver mutations in pDNA and cfDNA from mice with localized and metastatic colorectal adenocarcinoma and patients with premalignant colonic lesions. (**A**) Schematic showing isolation of pDNA and cfDNA from C57BL/6 mice expressing *KRAS*^{G12D} and *TP53* (KP) mutations through the villin promotor resulting in locally invasive colorectal adenocarcinoma as well as mice with *KRAS*^{G12D}, *TP53*, and *NOTCH* (KPN) mutations with aggressive, metastatic disease. (**B**) Waterfall plot showing fold difference in copies of *KRAS*^{G12D} detected using ddPCR per microliter of DNA extracted from the plasma (cfDNA) and platelets (pDNA) of KP and KPN mice, two weeks after tumor cell implantation. $n = 5$ KP and 15 KPN mice. (**C**) *KRAS*^{G12D} copies detected by ddPCR, shown as copies per microliter of DNA extracted from plasma (cfDNA) and platelets (pDNA) of KP, KPN (circle), and KPC (square) mice compared with the total number of copies from plasma and platelets. $n = 5$ KP, 15 KPN, and 6 KPC mice; datapoints

correspond to individual mice; mean ± SEM is shown. $^{**}P < 0.01$, as determined by a paired *t* test. (**D** and **E**) Representative ddPCR plots showing *KRAS*^{G12D} (blue) in higher abundance in pDNA (top) than in cfDNA (bottom) in two representative mice, (D) a KPN mouse and (E) a KP mouse. (**F**) Pie charts showing *BRAF*^{V600E} detection in high-risk colonic lesion patients (SSL, $n = 31$) and colonoscopy-screened controls ($n = 14$). Mutant *BRAF* (more than three positive events) was found in 16.1% (5/31) of SSL patients and 0% (0/14) of controls. (**G**) Relative *BRAF*^{V600E} copy number in pDNA versus cfDNA for five SSL patients with detectable mutant *BRAF*. Data are log2-transformed with a pseudo count of 1. (**H**) ddPCR plot showing *BRAF*^{V600E} (blue) in pDNA (left) and cfDNA (right) for two representative SSL patients. Data are combined.

whole platelets by phagocytes, endothelial cells, and smooth muscle cells or by the release of platelet-derived microvesicles (*59*). Whether platelets can similarly act as a vector for the horizontal transfer of DNA fragments, including potentially extrachromosomal DNA (*59*), and whether platelets modify sequestered DNA prior to release remain unknown.

Detection and analysis of cfDNA is rapidly being implemented in several clinical settings, including cancer screening, molecular profiling, and detection of residual disease as well as in prenatal diagnosis (*61*–*63*). Currently, a major limitation is the poor sensitivity for low–tumor burden disease. Preanalytical approaches to increase capture of ctDNA would be of interest. Anucleate RBCs have also been shown to contain DNA fragments, including cancer cell–derived DNA (*64*). In our studies, we did not detect *SRY* in red cell pellets of pregnant women, and a substantially lower ratio of mutant–to–wild-type alleles was observed in red cells than platelets in our coculture experiments, suggesting a superiority of platelets over red cells for liquid biopsy–based screening approaches. Our data suggest that a substantial proportion of ctDNA is contained within platelets and that this information is currently missed from standard sampling protocols that extract cfDNA from platelet-depleted plasma. This study paves the way for validation in larger clinical cohorts to test whether combining cfDNA with pDNA adds value as well as for future research to further establish a role for platelets in cfDNA homeostasis.

Materials and methods

Ethical approval, banking, and processing of samples

All procedures were performed in accordance with the ethical standards of the Declaration of Helsinki. Patient samples were collected by the Oxford Translational Gastroenterology Unit (TGU) and the Oxford Radcliffe Biobank (ORB). All patients provided informed consent, and procedures were approved by Yorkshire & The Humber - Sheffield Research Ethics Committee (REC reference number: 16/YH/0247), ORB research tissue bank ethics (REC reference 19/SC/0173) and Oxford GI Cohort ethics (REC reference 21\YH\0206).

Ten to 20 ml of peripheral blood was drawn into EDTA-coated (Fisher Scientific, cat # 367839) or cfDNA (Streck, cat # 218997) blood collection tubes from patients presenting with colorectal, esophageal, or pancreatic cancer. Ten ml of peripheral blood was collected into Streck tubes, from patients with sessile serrated lesions and from those on the bowel cancer screening pathway or those with inflammatory bowel disease undergoing colonoscopy.

For healthy controls, fully anonymised blood samples were collected from the Oxford Biomedical Research Laboratory under The INForMeD Study (REC reference 16/LO/1376). All donors provided informed consent, and blood was drawn into EDTA-coated tubes. Healthy donor platelet apheresis samples were provided by Oxford NHS Blood and Transplant (NHSBT) through the Non-Clinical Issue (NCI) service.

The usage and collection of healthy human donor blood samples in Edinburgh was authorised under the project "21-EMREC-041 – The Role of Inflammation in Human Immunity". Freshly drawn blood from healthy human donors was collected into 50 ml BD Falcon tubes containing 4 ml of CPD buffer (16 mM citric acid, 90 mM sodium citrate, 16 mM NaH_2PO_4, 142 mM dextrose, pH 7.4).

For obstetric samples, 10 ml of blood was collected from mothers at the time of delivery, and postnatally at 24 and 48 hours after delivery into Streck blood collection tubes. Samples were taken at the Department of Women's and Reproductive Health at the John Radcliffe Hospital Oxford and approved by the Oxfordshire Research Ethics Committee (07/H0607/74). Sex of the neonate was confirmed after delivery and all mothers provided written informed consent.

Patients with immune thrombocytopenic purpura (ITP) were consented under the INForMeD Study (REC reference 16/LO/1376) and 10 ml of peripheral blood was collected into Streck tubes.

Animal models

All mice were bred and maintained in accordance with UK Home Office regulations. All experiments were performed under Project Licenses P2FF90EE8, P0B63BC4D and PP6460882 and approved by the University of Oxford Animal Welfare and Ethical Review Body. All mice were housed in individually ventilated cages at the animal unit either at Functional Genetics Facility (Wellcome Centre for Human Genetics, University of Oxford) or the Biomedical Services Facility at the John Radcliffe Hospital (The MRC Weatherall Institute of Molecular Medicine, University of Oxford), in a specific-pathogen-free (SPF) facility, with unrestricted access to food and water, and were not involved in any previous procedures.

For the immune thrombocytopenia model, CD45.2 female, wild-type mice were injected intra-venously with either an anti-platelet antibody to reduce platelet count (Emfret, cat # R300) or an IgG control that had no cytotoxic effects on platelets in mice (Emfret, cat # C301). Mice were humanely culled and blood collected via cardiac puncture into EDTA coated microvettes (Sarstedt, cat # 20.1288) at 24, 72 and 120 hours post treatment. Platelet counts were determined using an automated blood cell counter. cfDNA was extracted from plasma and quantified.

For the CRC model, murine blood was drawn from KPN (*villin*Cre^{ER} *Kras*$^{G12D/+}$ *Trp53*$^{fl/fl}$ *R26*$^{Nlicd/+}$) and KP (*villin*Cre^{ER} *Kras*$^{G12D/+}$ *Trp53*$^{fl/fl}$) mice via cardiac puncture into EDTA coated microvettes (Sarstedt, cat # 20.1288). All strains used in this model were maintained on C57BL/6J background. Both male and female KP and KPN mice were used.

For the orthotopic pancreatic cancer model, a total of 500 KPC-F cells (passages 9-11) were injected in a volume of 10 µl in a mixture of 50% Matrigel and 50% DMEM (Gibco) using a 0.5 ml Micro-fine insulin syringe (BD). Following anesthesia of the mice using 4% isoflurane/oxygen and clipping of hair, an incision of 1 cm was made in the left abdominal site. The spleen and pancreas were exteriorized using forceps and KPC-F cells were injected in the tail of the pancreas. Successful injection was verified by the appearance of a wheal at the injection site with no leakage through the pancreatic capsule. Spleen and pancreas were gently moved back into the peritoneal cavity; the abdominal wall was sutured with absorbable 4.0 Vicryl suture (Ethicon) and the skin was closed using a 7 mm wound clip. Two weeks post-surgery, after the mice had recovered, blood was drawn via cardiac puncture into EDTA-coated microtainer tubes (BD).

For the cohort of KPC mice treated with aspirin, aspirin (NSC 27223; Selleck Chemicals, cat #. S3017) was administered via intraperitoneal injection on alternate days at a dose of 10 mg/kg. Treatment began on day 4 after tumor cell implantation and continued every other day until day 14. Control animals received intraperitoneal injections of vehicle (2% DMSO in PBS) on the same schedule.

Blood cell isolation and nucleic acid extraction

Blood tubes were kept at room temperature and handled gently to avoid platelet activation. For human samples, platelets were isolated within 4 or 24 hours of blood sampling (depending on blood tube) using a modified previously published protocol (*3*). Briefly, whole

blood was supplemented with citrate-dextrose solution (ACD) (Sigma Aldrich, cat # C3821-50ML) and centrifuged at 180 × g for 20 min at room temperature. Eighty % of the supernatant was removed using a Pasteur pipette, diluted with platelet wash buffer and centrifuged at 600 × g for 20 min at room temperature. The resulting platelet pellet was resuspended in pre-warmed HEPES-modified Tyrode's buffer. The remaining platelet poor plasma was centrifuged at 16'000 × g for 10 min at 4°C to ensure the pelleting of all cellular components and the isolation of pure plasma cfDNA. For the collection of platelets from healthy donor platelet apheresis bags, samples were pelleted at 600 × g for 20 min at room temperature. Platelet numbers were determined using an automated blood cell counter (Horiba, Pentra ES 60 Cell Counter).

Human MNCs were isolated from freshly drawn venous blood into EDTA coated tubes. Whole blood was supplemented with ACD and centrifuged at 180 × g for 20 min at room temperature. The supernatant was removed and the remaining layer diluted with wash buffer (PBS pH 7.4 0.5% FBS, 2mM EDTA). Diluted blood was layered onto density gradient media (GE Healthcare, cat # 5442-03) and centrifuged for 20 min at 600 × g, low brake. MNCs were collected from the white inter-phase 'buffy coat' using a Pasteur pipette and transferred to a Falcon tube. Human RBCs were sampled from the upper layer of the RBC/granulocyte pellet and diluted with wash buffer. The remaining RBC/granulocyte pellet was resuspended with chilled RBC Lysis Buffer (eBioscience, cat # 00-4300-54) and incubated at 4°C for 5 min. The lysed sample was centrifuged at 1000 × g for 5 min, the supernatant discarded and the granulocyte pellet diluted with wash buffer. The remaining white granulocyte pellet was washed, centrifuged and stored at -80°C until required. Purity studies using an automated cell counter provided no evidence of MNC or RBC contamination in the granulocyte pellet.

DNA was extracted from equal volumes of fresh platelets (resuspended in modified Tyrode's buffer) and 'platelet poor plasma' using the QIAamp cfDNA kit (Qiagen, cat # 55114), as per the manufacturer's instructions. Genomic DNA was extracted from nucleated cells using the DNeasy Blood & Tissue Kit (Qiagen, cat # 51104). Extracted DNA was quantified using a Qubit fluorometer (Thermofisher Scientific) and stored at -80°C until required.

Mouse platelets were isolated within four hours of blood collection via cardiac puncture. Whole blood was supplemented with ACD and centrifuged at 100 × g for 10 min at room temperature. The plasma was removed and collected into a 1.5 ml Eppendorf tube. The plasma was then diluted with platelet wash buffer and centrifuged at 3500 × g for 11 min to pellet the platelets. The platelet pellet was resuspended in pre-warmed HEPES-modified Tyrode's buffer. The platelet poor plasma was removed and centrifuged at 1300 to 16'000 × g for 10 min at 4°C to remove all cells and debris, and the final supernatant collected for cfDNA isolation.

Cell lines

The following cancer cell lines were used as positive and negative controls for common cancer-associated mutations; HCT116 (CVCL S744) *PIK3CA*^{H1047R}, LS180 (CVCL 0397) *KRAS*^{G12D}, COLO205 (CVCL 0218) *BRAF*^{V600E}, HEL (CVCL_0001) *JAK2*^{V617F}. All cell lines were purchased from American Type Culture Collection (cat # CCL-247, CL-187, CCL-222 and TIB-180 for HCT116, LS180, COLO205 and HEL cells respectively). All cells were cultured according to American Type Culture Collection recommendations and tested monthly for mycoplasma contamination.

NKPCB-NBC12.1F (KPC-F) cells, derived from a KPC mouse (LSL-*Kras*^{G12D}; LSL-*Trp53*^{R172H}; *Pdx1*Cre) were cultured in DMEM (Gibco) supplemented with 10% FBS, 2 mM glutamine, 100 U/ml penicillin, 100 µg/ ml streptomycin and maintained at 37°C with 5% CO_2.

The human Burkitt's lymphoma cell line, BL2 [CVCL 1966, cat # CRL-2959) was used to generate tumor cell-derived EVs]. Both standard BL2 cells and BL2 cells stably transfected with the apoptosis-suppressing gene *BCL2* were used, to obtain apo EVs from BL2 cells and nonapo EVs from apoptosis-resistant BL2-Bcl-2 cells. Protein expression was regularly tested by flow cytometry, confirming that 98% of the BL2-Bcl-2 cells expressed BCL2. Both cell lines were maintained in 50% X-VIVO medium (50% Gibco RPMI-1640, 50% X-VIVO-20 medium; Lonza, Basel, Switzerland), supplemented with 50 U/ml penicillin and 50 µg/ml streptomycin at 37°C with 5% CO_2.

Generation of EVs from BL2 and BL2-Bcl-2 cells

BL2 and BL2-Bcl-2 cells were cultured at 20×10^6/ml in 0.1 µm filtered 50% X-vivo 20 and irradiated with ultraviolet light to induce apoptosis with 6 doses at 50mJ/cm^2, for a total of 300mJ/cm^2. Apoptosis was monitored hourly by Annexin V and Sytox Blue staining. To isolate EVs, the culture supernatant was centrifuged at 25 × g for 1 hour followed by sequential filtering through a 5 µm mesh filter and a 1.2 µm syringe filter.

Purification and labeling of apo and nonapo EVs

The EVs were purified from soluble factors and proteins from the cell culture by size exclusion chromatography using in-house prepared sepharose columns (Thermofisher, cat # 45-000-067 and Sigma Aldrich, cat # CL6B200-100ML). After purification, EV concentration and size profile was measured by Nanoparticle Tracking Analysis using a NanoSight LM10 and Malvern NanoSight software (v3.3). The software analyzed each sample five times to give the average concentration, mean and modal size of each sample. EV size ranged between 150-200 nm and the concentration was between 100×10^8 to 200×10^8/ml. The number of EVs added to platelets was standardized across experiments, using a ratio of 50×10^8 EVs with 1×10^7 healthy donor platelets. For imaging experiments, prior to incubation with platelets, the purified EVs were resuspended in 0.1 µm filtered HBSS and were stained with Biotium CF568 NHS ester with a covalent attachment of the dye to EV proteins, according to the manufacturer's protocol (Biotium, cat # NC1542764). To remove unbound dye, the EVs were purified again by size exclusion chromatography through sepharose columns.

Flow cytometry and fluorescence-activated cell sorting (FACS)

All experiments were carried out using an LSRFortessa X-20 flow cytometer (Becton, Dickinson and Company). Platelets and paired plasma were prepared as previously described, pelleted and resuspended in HEPES-modified Tyrode's buffer. The samples were stained with a cocktail of antibodies for 20 min at room temperature in the dark, prior to being washed and resuspended in fresh buffer for flow cytometric analysis. The antibodies used are as follows, CD42 FITC, CD41 PE-Cy7, CD3 PE, CD11b and CD33 APC, CD19 APC-Cy7 and CD235a BV650. To assess the nucleic acid content of platelets, healthy donor blood was drawn into EDTA-coated tubes and platelets were isolated as previously described. The platelets were stained with the antibody CD42 PeCy7 and nucleic acid stains DRAQ5 (DNA) and Syto-13 (RNA) for 20 min at room temperature in the dark. After incubation, the platelets were washed and resuspended in fresh HEPES-modified Tyrode's buffer for analysis. Compensation beads (were stained and analyzed in parallel, as an additional negative control to fluorescence minus one (FMO) controls to confirm no non-specific binding of the nucleic acid stains (BD Invitrogen, cat # 01-1111-42). To assess platelet activation, platelets were isolated from healthy donor blood drawn into citrate tubes. Following isolation, platelets were maintained at a physiological concentration of ~300×10^6/ml.

To evaluate the activation status and DNA content of healthy donor platelets, after isolation, platelets were stained with CD42 FITC, and antibodies for activation; CD63 PB and CD62P BV857. The DNA content was simultaneously assessed by the inclusion of the DNA marker, DRAQ5. After a 20-min incubation at room temperature, the platelets were washed and resuspended in HEPES-modified Tyrode's buffer.

To determine changes in pDNA content upon activation, 10 µl of platelets were added to Eppendorf tubes containing the antibodies

CD42 FITC, CD63 PB and CD62P BV857 and the DNA stain DRAQ5. The platelets were then treated with 3 µl of either a 'resting' or an 'activation' buffer, both comprising HEPES-modified Tyrode's buffer supplemented with 20 mM calcium (Sigma-Aldrich, cat. # 21115-100ML). For the activation buffer, the agonist TRAP-6 was added at concentrations of 5, 10, 50, or 100 µM (10x the final concentration, Bachem AG, cat. # 4031274.0025). After a 15-min incubation at room temperature, the platelets were washed twice prior to resuspension in HEPES-modified Tyrode's buffer and analyzed.

The BD FACSymphony S6 was used for cell sorting. 30 µl of healthy donor blood was diluted with an antibody cocktail to a final volume of 100 µl. The platelets were incubated for 20 min at room temperature in the dark, washed and resuspended in fresh buffer. The staining solution included the following antibodies, CD42 FITC, CD3 BV421, CD11b and CD33 APC, CD19 APC-Cy7 and CD235a FITC. Platelets ($CD42^+$, $CD3^-$, $CD11b^-$, $CD33^-$, $CD19^-$ and $CD235a^-$) were sorted into 15 ml falcon tubes containing HEPES-modified Tyrode's buffer. The platelets were centrifuged at 600 × g for 20 min, the supernatant removed, and pellet frozen at -20°C.

Single color-stained controls and FMO controls were used for all experiments. FACS data were collected using BD FACSDiva software (v9.0) and gates were set using FMO controls and negative populations. All antibodies and nucleic acid stains are listed in table S7.

Droplet digital PCR

Droplet digital PCR (ddPCR) assays were ordered from Bio-Rad. All ddPCR assays were conducted on a QX200 Droplet Digital PCR System using the manufacturer's recommended protocol and reagents (Bio-Rad Laboratories). Positive and negative controls were included in every assay. Analysis was performed using the QuantaSoft software (Bio-Rad Laboratories, Watford UK).

To detect mouse $KRAS^{G12D}$, a ddPCR assay was designed for the detection of the *KRAS* p.G12D c.35G>A point mutation. Primers for the detection of *KRAS* were as follows: forward 5′-GCCTGCTGAAAATGACTGAG-3′ and reverse 5′-CGTAGGGTCATACTCATCCAC-3′. Two dual labeled probes were also used to target the wild-type and mutant sequences.

Wild-type 5′-HEX- ACGCC[+A][+C]CAG[+C]TCCAA-BHQ1-3′ and mutant 5′-6FAM-AC[+G]CC[+A][+T][+C]AG[+C]TCCAA-BHQ1-3′. Square brackets indicate LNA bases (Merck Life Sciences).

Synthetic DNA oligo generation

Single stranded DNA oligos were designed to include the mouse $KRAS^{G12D}$ genetic marker and synthesized by Integrated DNA Technologies (IDT, Iowa USA). Synthesized DNA was reconstituted according to the manufacturers protocol. PCR assays for the detection of *KRAS* were performed using the KAPA2G Fast HotStart PCR Kit (Roche, cat # KK5512) and primers were as follows: forward 5′-GCCTGCTGAAAATGACTGAG-3′ and reverse 5′-CGTAGGGTCATACTCATCCAC-3′. Fragmentation profiles of DNA oligos were analyzed using an Agilent Tapestation 2200 system (Agilent Technologies). Electrophoresis data was analyzed using the Tapestation Analysis Software (Agilent).

In vitro coculture of platelets, tumor cells, EVs, and synthetic DNA oligos

To explore uptake of DNA shed from tumor cells, platelets (3×10^5/µl), MNCs (0.075×10^5/µl) and RBCs (3×10^5/µl) from healthy donors were added to individual wells within a 24-well plate and a 1.0 µm TC Insert (Sartstedt, cat # 83.3932.101) placed into the well. Cancer cells (0.03×10^5/µl) were carefully placed in the inserts and the plate incubated for approximately eight hours at 37°C. Control samples were incubated simultaneously but without the addition of tumor cells. After incubation, the inserts were removed and the blood cells transferred to Eppendorfs. To ensure complete removal of any contaminating cfDNA in the media, all cells/platelets were washed and centrifuged at 600 × g for 10 min. The supernatant was removed and the pelleted blood cells re-suspended in fresh buffer. The cells were washed for a total of three times and finally resuspended in 1 ml of fresh pre-warmed HEPES-modified Tyrode's buffer prior to DNA extraction using the QIAamp cfDNA kit. Following DNA extraction, the samples were quantified and ddPCR was used to identify the presence of mutant alleles.

To investigate platelet uptake of DNA-containing EVs, 50×10^8 labeled, purified apo and nonapo EVs resuspended in Tyrode's buffer were incubated with 0.1×10^8 platelets for three hours at 37°C with gentle inversion every 30 min. Following incubation, the samples were centrifuged for 20 min at 800 × g. The supernatant was discarded, and the platelets resuspended in 300 µl of PBS. EV and platelet pellets were treated with DNase as per manufacturer's protocol (Sigma Aldrich, cat # AMPD1) and then DNA extracted using the QIAamp cfDNA kit. Following DNA extraction, the samples were quantified and assayed for the male *SRY* gene using ddPCR.

To understand whether platelets also take up "free" DNA fragments, platelets were incubated with synthetic DNA fragments ranging from 128 to 657 bp. Healthy donor human platelets were aliquoted into Eppendorf tubes and spiked with reconstituted synthetic DNA oligos for a final concentration of 10 ng/ml. The platelets were mixed gently by pipetting and incubated at 37°C overnight. Following incubation, the platelets were centrifuged for 10 min at 600 × g. The supernatant (containing excess DNA oligo) was discarded, and the platelets resuspended in fresh buffer. The platelets were washed for a total of two times and finally resuspended in 1ml of fresh pre-warmed HEPES-modified Tyrode's buffer prior to DNA extraction using the QIAamp cfDNA kit. Eluted DNA was PCR amplified using the KAPA2G Fast HotStart PCR Kit (Roche, cat # KK5512) and fragment length was confirmed using the Agilent Tapestation.

DNase treatment to investigate pDNA internalization

Platelets were incubated with HEL erythroleukemia cells as previously described. Following coincubation, platelets were treated with DNase according to the manufacturers protocol (Ambion DNA-free Kit, cat # AM1906). To confirm catalytic activity of the enzyme, DNase was also added to conditioned media. Following DNase treatment, the platelet samples were washed with 500 µl of 5mM EDTA and centrifuged at 600 × g for 10 min. The supernatant was removed and the wash repeated. After the second centrifugation, the supernatant was discarded and the platelet pellet resuspended in 1 ml of fresh pre-warmed HEPES-modified Tyrode's buffer. Following DNase inactivation of the conditioned media, 900 µl of HEPES buffer was added to a final volume of 1 ml in preparation for DNA extraction. For control samples, no DNase was added and 10 µl of 1M tris-HCL was added in replacement of 10X DNase I Buffer for the platelet samples.

In a separate experiment, healthy donor platelets or an equal volume of HEPES-modified Tyrode's buffer (to mimic plasma) was spiked with a 260 bp synthetic DNA oligo and incubated overnight. The samples were then treated with DNase according to the manufacturers protocol (Life technologies, RapidOut DNA Removal Kit, cat # K2981). Following DNase treatment, the platelet samples were washed and centrifuged at 600 × g for 10 min. The supernatant was removed and platelet pellet wash repeated. After the second centrifugation, the supernatant was discarded and the platelet pellet resuspended in 1 ml of fresh pre-warmed HEPES-modified Tyrode's buffer. For 'cfDNA' (buffer) samples, DNase was inactivated and 900 µl of HEPES buffer was added to a final volume of 1 ml. DNA was extracted from all samples using the QIAamp cfDNA kit. Eluted DNA was PCR amplified and the fragment length confirmed as previously described. For control samples, no DNase was added and 10 µl of 1M tris-HCL was added in replacement of 10X DNase I Buffer for the platelet samples.

Inhibition of cargo trafficking by platelets

Healthy donor human platelets were treated with the following inhibitors or appropriate negative control molecules; Dynole 34-2 (Abcam, cat # ab120463, 30 µM), Dynole 31-2, Negative control (Abcam, cat #

ab120464-5mg, 30 μM), Pitstop (Abcam, cat # ab120687, 25 μM), Pitstop 2 Negative control, (Abcam, cat # ab120688, 25 μM), Cytochalasin D (Santa Cruz Biotechnology, cat # CAS 22144-77-0, 5 μM), Nystatin (Merck Life Science UK, cat # N9150-20ML, 30 units/ml), Amiloride (Abcam cat # ab120281, 500 μM), Imipramine (Abcam, cat # ab141046, 5 μM). After treatment, platelets were spiked with a 260 bp synthetic DNA oligo for a final concentration of 10 ng/ml and incubated at 37°C overnight. Following incubation, the platelets were centrifuged for 10 min at 600 × g. The supernatant (containing excess inhibitor/negative control and DNA oligo) was discarded, and the platelets re-suspended in fresh buffer. The platelets were washed for a total of two times and finally resuspended in 1 ml of fresh pre-warmed HEPES-modified Tyrode's buffer prior to DNA extraction using the QIAamp cfDNA kit. Eluted DNA was PCR amplified and the fragment length confirmed as previously described.

To assess the impact of platelet activation inhibition on pDNA uptake, platelets were treated with 500, 1000 or 2000 μM aspirin (Merck Life Sciences, cat # A2093-500G) or 5, 50, 100 or 200 μM ibrutinib (PCI-32765) (Stratech Scientific Ltd, cat # S2680-SEL-5mg). Following treatment, a 260 or 367 bp synthetic DNA oligo was added to resting platelets for a final concentration of 10 ng/ml DNA and incubated at 37°C overnight. Following incubation, the platelets were centrifuged for 10 min at 600 × g. The supernatant (containing excess inhibitor/negative control and DNA oligo) was discarded, and the platelets re-suspended in fresh buffer. The platelets were washed for a total of two times and finally resuspended in 1 ml of fresh pre-warmed HEPES-modified Tyrode's buffer prior to DNA extraction. Eluted DNA was amplified by PCR and the Agilent TapeStation was used to confirm fragment length.

To assess the impact of dynamin inhibition on platelet secretion, platelets were treated with Dynole or paired negative control, exposed to the 260 bp synthetic DNA oligo and incubated overnight. Following incubation, the platelets were pelleted, resuspended in fresh buffer, re-treated with the inhibitor or negative control and incubated for 3 hours at 37°C. After the second incubation, the platelets were pelleted and discarded, and the supernatant (platelet 'releasate') was collected. The supernatant was centrifuged at 16'000 × g for 5 min to ensure complete removal of any contaminating platelets and subject to DNA extraction, PCR amplification and fragment analysis.

To understand the impact of dynamin inhibition on platelet EV internalization, 0.1×10^8 healthy donor platelets were incubated with either the dynamin inhibitor, paired negative control or DMSO for 30 min at 37°C. After incubation, 50×10^8 labeled, purified apo EVs resuspended in Tyrode's buffer were added to the treated platelets and incubated as previously described prior to DNase treatment, DNA extraction and *SRY* ddPCR.

H3k27ac ChIPmentation of platelet chromatin

Platelets were isolated from plateletpheresis samples from 3 independent healthy donors. 13 ml of each sample was centrifuged at 600 × g for 30 min at room temperature, the supernatant was removed and platelet pellets were immediately used for H3K27ac ChIPmentation using a protocol tailored for low-DNA input samples from a published protocol (*65*), using the H3k27ac antibody (Diagenode, cat # C15410196). In brief, bead-bound chromatin underwent a one-step adaptor insertion via Tn5 tagmentation and only one post-PCR DNA purification was performed to reduce sample loss.

For each reaction, 5 μl A-Dynabeads (Invitrogen cat # 10001D) were coated with the H3K27ac antibody (Diagenode, cat # C15410196) (150 μl PBS, 0.5% BSA, 1x Proteinase inhibitor). The antibody-bound beads were then washed in PBS and 0.5% FBS, before being added to samples for overnight incubation.

Platelet pellets were incubated in 600 μl lysis buffer (50 mM Tris pH 8, 10 mM EDTA, 0.5% SDS, 1x Protease Inhibitor) for 20 min on ice. Then, 1% Triton-X100 was added, and the samples centrifuged to pellet insoluble material. The supernatant was split into three 200 μl sub-samples, and the samples were incubated overnight with the H3k27ac antibody coated beads. Before incubation, 5% of the sample was kept aside for input control tagmentation.

After overnight incubation, the beads were washed three times with RIPA wash buffer (50 mM HEPES pH 7.6, 500 mM LiCl1, 1 mM EDTA, 1% NP-40 / IGEPAL CA-630, 0.7% Na-Deoxycholate), followed by one wash with TE and then 10 mM Tris pH8. Beads and input control samples were then tagmented in tagmentation buffer (50 mM Tris pH 8, 25 mM MgCl2, 50% Dimethylformamide) with Tn5 transposase (Illumina, cat # 20034197) for 10 min at 37°C and immediately cooled down. Beads were immediately washed. Library preparation was then conducted with Nextera-based sequencing primers (*66*). qPCR and fragmentation analysis were performed.

Immunofluorescence microscopy

Live: To visualize pDNA uptake in vitro, washed human platelets were stained with anti-CD42 AF488 (BioLegend, cat # 303914) for 30 min at room temperature. Separately, COLO205 cells or H2B-mCherry HEL cells were labeled using either the highly specific live cell DNA stain, SiR-DNA (Spirochrome, cat # CHF260.00), NUCLEAR-ID Red DNA stain or 4′,6-diamidino-2-phenylindole (DAPI) (HEL only) as per the manufactures' protocols (Enzo Life Sciences, cat # ENZ-52406). Stained COLO205 or H2B-mCherry HEL cells were then washed and added to collagen type-1 (Corning, cat # 354236)-coated microscopy slides (Greiner Bio-One, cat # 543079). CD42 stained platelets were added to the wells containing tumor cells immediately before imaging. To analyze endogenous wild-type DNA within healthy donor platelets, platelets were co-stained with anti-CD42 AF488 and NUCLEAR-ID Red DNA and imaged alone.

Regarding platelet uptake of tumor derived DNA from conditioned media, COLO205 cells were labeled with NUCLEAR-ID Red. Following staining, the cells were washed with MEM Alpha 5% FCS, pelleted and the supernatant removed. The cells were washed a further two times to ensure complete removal of the DNA stain and resuspended in 200 μl of fresh media. The cells were incubated at 37°C and vortexed periodically to encourage cell death and DNA release. After two hours, the COLO205 cells were centrifuged at 16'000 × g for 10 min at 4°C. Supernatant was removed from the pelleted cells, transferred to a fresh Eppendorf and the cell pellet discarded. Healthy donor platelets were stained with anti-CD42 AF488 and added to wells of Poly-L-lysine coated slides (Ibidi, cat # 81201). DNA labeled COLO205 cell conditioned media was added to the platelets immediately before imaging. All live imaging was performed using the Zeiss Spinning Disk Confocal with a 63X oil immersion objective.

Fixed: BL2 cell-derived apo EVs were isolated, labeled with an amine-reactive fluorescent dye (Biotium, cat # 92131) and frozen as previously described. Prior to imaging, the EVs were thawed and co-stained with DAPI for 30 min at room temperature. The EVs were washed twice, pelleted at 20'000 × g for 30 min at 4°C and resuspended in HBSS buffer. Labeled EVs were then added to Poly-L-lysine coated chamber slides and incubated overnight at 4°C. Following incubation, the supernatant was carefully removed and the EVs fixed with 4% formaldehyde at room temperature for 30 min. The fixative was then removed and the EVs gently washed three times with PBS. To confirm imaging of EVs and not auto-fluorescent debris, PBS was stained with DAPI, incubated overnight, and fixed onto slides alongside the EV preparations. The slides were mounted and the EVs and PBS controls resolved by fluorescence microscopy using a Zeiss LSM900 with a 63X oil immersion objective.

To visualize platelet sequestration of EVs, 5×10^9 apo EVs labeled with an amine-reactive fluorescent dye were thawed and added to 1 ml of 10×10^6 washed healthy donor platelets and incubated for three hours at 37°C. To ensure adequate mixing, the cells were inverted

gently every 30 min. Following incubation, the cells were centrifuged at 800 × g for 20 min, low brake. The supernatant (containing the EVs) was removed, and the platelets resuspended in PBS. Platelets were centrifuged onto a Poly-L-lysine coated chamber slide at 600 × g for 20 min and fixed in 2% formaldehyde/PBS for 10 min at room temperature. The fixative was removed and the platelets washed twice with PBS. The platelets were then labeled with anti-CD42 AF488 for 20 min at room temperature. After labeling, the slides were washed, mounted with ProLong Gold Antifade Mountant (Thermofisher, cat # P36930) and imaged using the Zeiss LSM900.

Histology, immunohistochemistry, and imaging of peripheral blood films

Cell contamination was assessed after cytospin of the resuspended platelet pellet onto a glass slide (5 min at 500 r.pm.) and May–Grünwald Giemsa staining, according to standard protocols. Images were obtained using an Olympus BX60 Microscope.

KPC mice were sacrificed, and pancreatic tissue was taken for p53 immunohistochemical staining. Briefly, a total of 24 hours post fixation in 10% neutral buffered formalin at 4°C, tissues were transferred to 70% ethanol and stored overnight at 4°C. Fixed tissues were processed overnight using the STP120 Spin Tissue Processor (Thermo Fisher Scientific) and embedded the next day in paraffin wax. Tissues were cut into 4 μm sections using a Leica RM215 microtome and adhered onto SuperFrost Ultra Plus Adhesion slides (Thermo Fisher Scientific) before drying overnight in a 37°C incubator. After deparaffinization, rehydration in an ethanol gradient (100%, 70%, 50%), and antigen retrieval with Citrate Buffer Antigen Retriever (Sigma-Aldrich), slides were incubated with Dual Endogenous Enzyme-Blocking Reagent (Dako) for 1 hour, washed in PBS, incubated with 5% goat serum for 30 min, washed in PBS again, and incubated with the primary antibody, p53 (Cell Signaling Technologies, cat # 2524) diluted 1:2000 for 2 hours at room temperature. Slides were then washed in PBS with 0.05% Polysorbate 20 and incubated with the secondary antibody, horse anti-mouse IgG (Cell Signaling Technologies, cat # 7076), diluted 1:100 for 45 min at room temperature, washed in PBS with 0.05% Polysorbate 20 again, and incubated with 3,3′-Diaminobenzidine (DAB) chromogen for 3 min at room temperature. After staining, slides were dehydrated in an ethanol gradient (50% 70%, 100%), followed by tissue clearing in xylene (ThermoFisher). Slides were mounted with dibutylphthalate polystyrene xylene (DPX; Sigma-Aldrich), dried for 24 hours and scanned using an Aperio ScanScope CS digital slide scanner (Leica Biosystems) at 20X magnification.

Healthy donor blood was used to prepare a peripheral blood film. The blood smear was fixed with 100% methanol for 30 s and stained with CD42 AF488 (BioLegend, cat # 303914) to identify platelets and the DNA stain Hoechst (Invitrogen, cat # H3570), to identify nucleated cells. The slide was mounted with a coverslip and imaged using the Leica SPE.

FISH

Platelets in suspension were centrifuged onto Poly-L-lysine coated chamber slides and fixed in 2% formaldehyde/PBS for 10 min at room temperature. The platelets were then permeabilized in 0.5% Triton X-100/PBS for 10 min at room temperature and washed twice in 0.05% Triton-X 100/PBS. The platelets were washed in 0.02% Tween20/PBS (PBST) and incubated with the primary anti-β-tubulin antibody (Sigma Aldrich, cat # T5201) diluted in blocking buffer for 30 min at 37°C in a humid box. Following primary labeling, the platelets were washed with PBST and incubated with the secondary donkey anti-mouse IgG H&L AF405 antibody (Abcam, cat # ab175658) diluted in blocking buffer for 30 min at 37°C. The labeled platelets were then washed with PBST, fixed and washed with PBS for 10 min at room temperature. FISH staining was carried out according to the manufacturer's protocol. Briefly, slides were incubated in 0.1N HCL, washed with 2x SSC and dehydrated in 70% ethanol for 3 min. Equal volumes of X- and Y-chromosome probes (Metasystems, cat # D-0323-050-FI and D-0324-100-OR) were added to the slide and covered with a 22 × 22 mm^2 coverslip. The slides were incubated at 85°C for 5 min, sealed with rubber cement and incubated in a humidified chamber at 37°C overnight. Following hybridization, the rubber seal was removed, and the slides washed in 0.1X SSC at 60°C. Slides were mounted and imaged using the Zeiss LSM900 with a 63X oil immersion objective. Control cells (HEL cells and MNCs) were fixed onto slides, permeabilized and labeled with the X- and Y- chromosome paints. Following overnight hybridization, the cells were washed and counterstained with DAPI.

Airyscan imaging of platelet ultrastructure

Glass coverslips (VWR, cat # 631-0150) were coated with 5 μg/ml fibrillar collagen-I (Horm), (Nycomed) and incubated at 4°C overnight in a 24 well plate. The coverslips were blocked with 5 mg/ml BSA for 1 hour at room temperature. After blocking, the BSA was removed and 300 μl of washed healthy donor platelets diluted to 1×10^7/ml was added to the wells. The platelets were left to spread for 45 min in a humidified chamber at 37°C. Following incubation, the liquid was carefully removed and washed with PBS. The platelets were fixed with 5% formalin for 10 min at room temperature, washed with PBS and permeabilized with 0.1% Triton-X 100/PBS (Sigma, cat # SLCF5969) for 5 min. The slides were washed with PBS and blocked for 30 min with blocking buffer (1% BSA + 2% goat + 2% donkey serum). The primary antibodies: mouse anti- human CD63, mouse anti-human LAMP2, rabbit anti- human TOM20, rabbit anti- human CD81 and mouse anti-human CD62P were diluted in blocking buffer and incubated with the platelets at 4°C overnight. Following primary incubation, the coverslips were washed three times with PBS and incubated with the DNA stains (DRAQ5, NUCLEAR-ID Red, Hoechst) and the secondary antibodies; goat anti- mouse IgG H&L AF568 and goat anti- rabbit IgG H&L AF488 for 45 min at 37°C. Following incubation, the coverslips were washed and mounted onto imaging slides using Hydromount (Scientific Laboratory Supplies Ltd, cat # NAT1324). The slides were imaged using the Airyscan function of a Zeiss LSM 980 confocal microscope (63X objective lens, NA 1.4).

Quantitative analysis of imaging data and image analysis software

Images were analyzed using ImageJ (v2.1.0) (National Institute of Health, US-MD) and 3D reconstructions were generated in Imaris Viewer v9.7.0 (Oxford Instruments, Abingdon). CellProfiler (v4.0.7) (Broad Institute, US-MA) was used to quantitatively analyze platelet-tumor cell interaction. In brief, cells were segmented using the 'Identify Primary/Secondary Object' module. Thresholding strategies were employed to accurately mask cells for segmentation. Platelets were tracked using the 'Track Objects' module. Finally, AF647 intensity was measured using 'Measure Object Intensity' and data 'Exported to Spreadsheet'. This image-analysis pipeline, as well as others can be recreated in Cell Profiler tool (freely available from the Broad Institute at www.cellprofiler.org).

For colocalization analysis, we calculated the Pearson's correlation coefficient, r and Mander's overlap coefficient, *R* for each platelet by manually defining a cuboid region (90 × 90 pixels; 3.8 × 3.8 μm), enclosing fluorescence from all three channels. The equations used to calculate fluorescence correlation coefficients are described in the Supplementary Text, with calculations performed using MATLAB as described by Jung *et al.* (*67*).

To assess the location of the DNA fluorescence within the platelet we developed a simple algorithm in MATLAB to calculate the total intensity of the DNA marker in a three-dimensional (3D) platelet mask that was subsequently eroded away from the surface to the center. First, we generated a 3D platelet mask by applying a one level Otsu thresholding algorithm to the CD62P fluorescence signal. The DNA intensity within the platelet was obtained by integrating the DRAQ5 fluorescence signal from pixels within the 3D platelet mask. To determine

the position of the DNA fluorescence within the platelet, we used a series of one pixel erosion operations on the original 3D mask. After each erosion step, a convex hull was applied to ensure there were no 'holes' in the mask. The integrated DNA fluorescence intensity was then obtained within this new eroded mask. This procedure was repeated until a single pixel of the 3D platelet mask remained i.e., the center of the platelet had been reached.

Whole-genome sequencing (WGS)

WGS was performed on paired pDNA and cfDNA isolated simultaneously from the same peripheral blood samples of 15 patients with a recent diagnosis of gastrointestinal adenocarcinoma. Libraries were prepared from samples that were confirmed (using the Agilent Tapestation) to have both short DNA fragments of approximately 160 bp in addition to longer peaks of ~12'000 bp. l-pDNA was fragmented prior to library preparation. Briefly, 15 µl of DNA diluted in TE buffer (1mM Tris-HCl, pH 8.0, 0.1 mM EDTA) was added to a Covaris microtube-15 (Covaris, cat # 520145) and briefly centrifuged at 3000 × g for 1 min. The microtube was loaded onto the Covaris ME220 Focused-ultrasonicator and the protocol run using the treatment conditions required for a 150 bp target peak. Fragment size was determined using the Agilent Tapestation 2200 system (Agilent Technologies) and the sonication was repeated if DNA fragments were > 150 bp.

DNA-Seq libraries were prepared using the NEBNext Ultra II DNA Sample Preparation Kit for Illumina (New England BioLabs, Ipswich, MA, USA) according to the manufacturer's protocol. pDNA was size selected into 2 groups: short fragments (s-pDNA; under 600 bp) and long fragments (l-pDNA; over 600 bp). The short fragments were further cleaned to remove <100 bp fragments and large platelet fragments were fragmented via sonication as previously described. Following end repair and adapter ligation, adapter-ligated DNA fragments were amplified in enrichment PCR to generate final libraries. Cleaned up libraries were then multiplexed, and 1.5 pM libraries analyzed on an Illumina NextSeq 500 (300 cycle PE) at low-pass (0.1X) for all samples, and 10X for the cfDNA and s-pDNA, using four lanes in each sample with 4% PhiX to monitor sequencing performance. This amounted to 240 fastq files.

Data preprocessing

Quality control of all fastq files was conducted by running FastQC (v0.11.8) (*68*). Reads were adaptor- and quality-trimmed using Trim Galore! (*69*) (v0.6.5) and aligned to the GATK Genome Reference Consortium Human Build 38 (GRCh38) (*70*) using bwa-mem (v0.7.17) (*71*). Reads were aligned to alternate contigs to represent common complex variation using bwa_postalt.js (https://github.com/lh3/bwa/blob/master/bwakit/README.md) (*71*). Resulting BAM files were merged, sorted and indexed with samtools (v1.13.0) (*72*).

GATK toolkit (v4.1.7.0) was used to mark optical and PCR duplicates, estimate library complexity, and calculate summary metrics on insert sizes (*73*). Mapping rate was evaluated with samtools flagstat and the number of reads mapped to each chromosome and the mitochondrial genome with idxstats. Repetitive elements in the ENCODE blacklist (*74*) were excluded using bedtools intersect (v2.30.0) (*75*).

Insert size distribution

For all uniquely mapped, nonduplicated, and properly paired read pairs, the frequency of insert size values was counted across all autosomes and chromosome X using samtools (*72*) and R. The distributions were plotted using ggplot2 (*76*).

Read depth around transcription start sites

Transcription start sites were defined by refTSS (v3.3) (*77*). We used the nearest refTSS entry to the 5′ coding sequence of all protein coding genes. Coverage per base in a 2 kilobase pair (kbp) region around each TSS was extracted with Rsamtools, counting only uniquely mapped, non-duplicate, correctly paired reads with insert sizes between 150 and 170 bp ("mono-nucleosome") or between 280 and 350 bp ("di-nucleosome"). Peripheral blood mononuclear cell (PBMC) gene expression values were taken from Blueprint Epigenome experiment:

EGAX00001327129 (http://dcc.blueprint-epigenome.eu/#/experiments/ERX1123729).

Briefly, genes with posterior mean estimates of transcripts per million > 15 were defined as "highly expressed" in PBMCs.

Dinucleosome peak difference quantification

A χ^2test of independence was performed in R with a simulated p-value to examine the relation between DNA type (cfDNA and s-pDNA) and the proportion of di-nucleosome fragments. We separated the fragments in (i) fragments below 250 bp representing mono-nucleosome fragments and (ii) fragments above 250 bp representing di-nucleosome fragments. The proportion of di-nucleosome fragments was higher in s-pDNA than in cfDNA ($P < 0.0005$ in all samples).

Chromosome coverage

Coverage was calculated using samtools bedcov, using a bed file of 10 kbp non-overlapping windows for all main chromosomes, but excluding reads with mapQ <1. Position with mappability (as defined by umap: https://bismap.hoffmanlab.org/) in the lowest 8 percentile were removed (*78*). The Coverage was then corrected for mappability and GC content bias using a linear regression model and visualized with karyoplotR (*79*).

Gini index

After filtering for reads that were in pair, uniquely mapped, mapped in proper pairs, primary alignments, and non-duplicates, (samtools view parameters: -f 2 -F 3972 -q 1), we calculated the coverage with samtools depth. Evenness of coverage was evaluated by calculating the Gini index (*80*) on the short pDNA and cfDNA's coverage, which was previously binned into adjacent 10 kbp bins.

ichorCNA

Copy number alterations in the 10X and low-pass WGS were evaluated using ichorCNA (v0.2.0) (*39*) (github: https://github.com/broadinstitute/ichorCNA/releases/tag/v0.2.0).

Tumor tissue DNA sequencing and analysis

DNA from resected tumor tissue and adjacent tumor-free colonic mucosa was extracted using the Monarch Genomic DNA Purification Kit (Monarch, cat # T3010S). For sequencing, gDNA was prepared as follows: 500 ng per sample at a concentration of 25 ng/µl. The tumor samples were sequenced at 75X and the normal samples at 30X by Novogene UK Ltd. The complete NextFlow pipeline for processing sequencing output to mutation calls is provided in the Zenodo code repository. Briefly, reads were trimmed using Trim Galore! (*69*) (v0.6.5), requiring >= 2 bp adapter overlap and quality-trimming bases with Phred score below 20, and aligned against the complete hg38 genome, including alt alleles, using bwa-mem2 using default parameters. Mutations were called independently using Mutect2 (v4.1.7.0), Strelka (v2.9.10) and Octopus (v0.7.0). Mutations called by only one caller were excluded.

Estimation of observed and expected tumor fragments

Ninety-nine sets of random single-base mutations, each matching the unique mutation count identified in the tumor tissue of patient CRC_012, were generated by sampling from all SNVs detected in any WGS-sequenced colorectal cancer from TCGA. Any SNV overlapping a SNP (dbSNP v155) with > 0.5% allele frequency in 1000Genomes, HapMap, dbGaP_PopFreq, GnomAD_exomes, TOPMED or GnomAD were excluded, as well as variants identified as SNPs in the non-cancer control sample for patient CRC_012. Together with the original

CRC_012 mutation set, this amounted to 100 mutation sets. For each set, reads covering the mutation positions were extracted, excluding improperly paired reads or reads with mapQ < 25. Detection rate was then calculated by dividing the count of reads containing the variant allele (min base quality: 10) by the total number of reads covering the mutation sites. Positions that exhibited an allele fraction of > 20% in plasma or platelet derived DNA were excluded as potential SNPs. The likelihood of observing a detection rate as high or higher than that of CRC_012 tissue mutations in that patient's plasma and platelet-derived DNA was calculated using a normal distribution parameterized to the observed mean and standard deviation of detection rates for random mutation sets. Code and intermediate files are deposited in the publication's Zenodo repository.

TAPS sample preparation

s-pDNA (<600 bp) and l-pDNA (>600 bp) was separated using 0.55X AMPure beads, followed by a 1.8X clean-up of the s-pDNA. Genomic TAPS was carried out on l-pDNA and cfDNA TAPS was carried out on s-pDNA, as previously described (*45*, *81*). Briefly, l-pDNA was mixed with spike-ins of 0.1% CpG-methylated lambda phage DNA and 0.01% unmodified 2 kbp plasmid DNA and was sonicated and size-selected to 300-500 bp prior to library construction. s-pDNA was mixed with pre-fragmented spike-ins of the same ratio and used directly in library construction. DNA was ligated with KAPA Unique Dual-Indexed Adapter Kit using KAPA HyperPrep Kit according to the manufacturer's protocol. The ligated DNA was subjected to mTet1-mediated oxidation and borane reduction. Converted DNA was then amplified with short primers ordered from IDT (FW-5′-AATGATACGGCGACCACCGAGATCTACAC-3′, RV-5′-CAAGCAGAAGACGGCATACGAGAT-3′) using KAPA HiFi HotStart Uracil+ ReadyMix PCR Kit for four cycles according to the manufacturer's protocol. The PCR product was purified with AMPure XP beads. Finally, libraries were sequenced for 300 cycles in paired-end mode on the NextSeq 2000 with XLEAP-SBS chemistry P4 cartridge.

TAPS data processing and analysis

Raw sequencing reads were trimmed from adapter sequences and low-quality bases using Trim Galore! (*69*) (v0.6.5) and assessed for quality with FastQC (*68*) (v0.11.9). Reads were aligned to the reference genome using BWA-MEM2 (*71*) (v2.2.1) and duplicates were marked with Picard (*73*) (gatk, v4.4.0.0). BAM files were indexed and merged using samtools (*72*) (v1.16.1). TAPS conversion efficiency and methylation bias were estimated by analyzing sequencing spike-ins. Methylation levels were called using rastair (v0.8.1).

Sample cellular deconvolution was performed using WGBStools and UXM deconv as described in Loyfer *et al.* (2023) (*46*). A custom cellular atlas was built using the Loyfer *et al.* (2023) pat files for B cells, T cells, NK (natural killer) cells, blood granulocytes, monocytes, erythrocyte progenitors, hepatocytes and vascular endothelium, and an in-house megakaryocyte TAPS dataset. Lymphoid (B cells, T cells, and NK cells) and Myeloid (blood granulocytes, monocytes and erythrocyte progenitors) cells contributions were summed for visualization purposes. All code is available in the Zenodo repository.

Code availability

The code used in these studies is available from Zenodo (*82*).

Statistical analysis

Parametric tests, such as the paired Student's t test, were used for comparisons within the same group when the data appeared normally distributed based on visual inspection. When data were paired but not normally distributed, nonparametric tests such as the Wilcoxon signed-rank test were applied. For comparisons between independent groups, the Mann-Whitney U test was used to assess statistical significance.

REFERENCES AND NOTES

1. C. Deppermann, P. Kubes, Start a fire, kill the bug: The role of platelets in inflammation and infection. *Innate Immun.* **24**, 335–348 (2018). doi: 10.1177/1753425918789255; pmid: 30049243
2. J. N. Thon *et al.*, T granules in human platelets function in TLR9 organization and signaling. *J. Cell Biol.* **198**, 561–574 (2012). doi: 10.1083/jcb.201111136; pmid: 22908309
3. M. Koupenova *et al.*, The role of platelets in mediating a response to human influenza infection. *Nat. Commun.* **10**, 1780 (2019). doi: 10.1038/s41467-019-09607-x; pmid: 30992428
4. M. Koupenova, J. E. Freedman, Platelets and Immunity: Going Viral. *Arterioscler. Thromb. Vasc. Biol.* **40**, 1605–1607 (2020). doi: 10.1161/ATVBAHA.120.314620; pmid: 32579477
5. M. Koupenova *et al.*, Pollen-derived RNAs Are Found in the Human Circulation. *iScience* **19**, 916–926 (2019). doi: 10.1016/j.isci.2019.08.035; pmid: 31518900
6. R. J. A. Nilsson *et al.*, Blood platelets contain tumor-derived RNA biomarkers. *Blood* **118**, 3680–3683 (2011). doi: 10.1182/blood-2011-03-344408; pmid: 21832279
7. Z. Shen *et al.*, Platelet transcriptome identifies progressive markers and potential therapeutic targets in chronic myeloproliferative neoplasms. *Cell Rep. Med.* **2**, 100425 (2021). doi: 10.1016/j.xcrm.2021.100425; pmid: 34755136
8. M. G. Best *et al.*, RNA-Seq of Tumor-Educated Platelets Enables Blood-Based Pan-Cancer, Multiclass, and Molecular Pathway Cancer Diagnostics. *Cancer Cell* **28**, 666–676 (2015). doi: 10.1016/j.ccell.2015.09.018; pmid: 26525104
9. S. G. J. G. In 't Veld *et al.*, Detection and localization of early- and late-stage cancers using platelet RNA. *Cancer Cell* **40**, 999–1009.e6 (2022). doi: 10.1016/j.ccell.2022.08.006; pmid: 36055228
10. C. Bettegowda *et al.*, Detection of circulating tumor DNA in early- and late-stage human malignancies. *Sci. Transl. Med.* **6**, 224ra24 (2014). doi: 10.1126/scitranslmed.3007094; pmid: 24553385
11. A. J. Bronkhorst, V. Ungerer, S. Holdenrieder, The emerging role of cell-free DNA as a molecular marker for cancer management. *Biomol Detect. Quantif.* **17**, 100087 (2019). doi: 10.1016/j.bdq.2019.100087; pmid: 30923679
12. S. Cristiano *et al.*, Genome-wide cell-free DNA fragmentation in patients with cancer. *Nature* **570**, 385–389 (2019). doi: 10.1038/s41586-019-1272-6; pmid: 31142840
13. A. Dasari *et al.*, ctDNA applications and integration in colorectal cancer: An NCI Colon and Rectal-Anal Task Forces whitepaper. *Nat. Rev. Clin. Oncol.* **17**, 757–770 (2020). doi: 10.1038/s41571-020-0392-0; pmid: 32632268
14. F. Diehl *et al.*, Circulating mutant DNA to assess tumor dynamics. *Nat. Med.* **14**, 985–990 (2008). doi: 10.1038/nm.1789; pmid: 18670422
15. C. Fiala, E. P. Diamandis, Utility of circulating tumor DNA in cancer diagnostics with emphasis on early detection. *BMC Med.* **16**, 166 (2018). doi: 10.1186/s12916-018-1157-9; pmid: 30285732
16. J. C. M. Wan *et al.*, Liquid biopsies come of age: Towards implementation of circulating tumour DNA. *Nat. Rev. Cancer* **17**, 223–238 (2017). doi: 10.1038/nrc.2017.7; pmid: 28233803
17. Y. M. Lo *et al.*, Presence of fetal DNA in maternal plasma and serum. *Lancet* **350**, 485–487 (1997). doi: 10.1016/S0140-6736(97)02174-0; pmid: 9274585
18. L. Hille *et al.*, Evaluation of an Alternative Staining Method Using SYTO 13 to Determine Reticulated Platelets. *Thromb. Haemost.* **119**, 779–785 (2019). doi: 10.1055/s-0039-1681101; pmid: 30934103
19. P. C. Armstrong *et al.*, Temporal in vivo platelet labeling in mice reveals age-dependent receptor expression and conservation of specific mRNAs. *Blood Adv.* **6**, 6028–6038 (2022). doi: 10.1182/bloodadvances.2022007099; pmid: 36037520
20. H. E. Allan *et al.*, Proteome and functional decline as platelets age in the circulation. *J. Thromb. Haemost.* **19**, 3095–3112 (2021). doi: 10.1111/jth.15496; pmid: 34390534
21. J. Moss *et al.*, Megakaryocyte- and erythroblast-specific cell-free DNA patterns in plasma and platelets reflect thrombopoiesis and erythropoiesis levels. *Nat. Commun.* **14**, 7542 (2023). doi: 10.1038/s41467-023-43310-2; pmid: 37985773
22. G. Escolar, E. Leistikow, J. G. White, The fate of the open canalicular system in surface and suspension-activated platelets. *Blood* **74**, 1983–1988 (1989). doi: 10.1182/blood.V74.6.1983.1983; pmid: 2804343
23. L. Balaj *et al.*, Tumour microvesicles contain retrotransposon elements and amplified oncogene sequences. *Nat. Commun.* **2**, 180 (2011). doi: 10.1038/ncomms1180; pmid: 21285958
24. C. Kahlert *et al.*, Identification of double-stranded genomic DNA spanning all chromosomes with mutated KRAS and p53 DNA in the serum exosomes of patients with pancreatic cancer. *J. Biol. Chem.* **289**, 3869–3875 (2014). doi: 10.1074/jbc.C113.532267; pmid: 24398677
25. A. Takahashi *et al.*, Exosomes maintain cellular homeostasis by excreting harmful DNA from cells. *Nat. Commun.* **8**, 15287 (2017). doi: 10.1038/ncomms15287; pmid: 28508895
26. Z. Hu, H. Chen, Y. Long, P. Li, Y. Gu, The main sources of circulating cell-free DNA: Apoptosis, necrosis and active secretion. *Crit. Rev. Oncol. Hematol.* **157**, 103166 (2021). doi: 10.1016/j.critrevonc.2020.103166; pmid: 33254039
27. B. K. Thakur *et al.*, Double-stranded DNA in exosomes: A novel biomarker in cancer detection. *Cell Res.* **24**, 766–769 (2014). doi: 10.1038/cr.2014.44; pmid: 24710597
28. D. Jerez-Dolz *et al.*, Internalization of microparticles by platelets is partially mediated by toll-like receptor 4 and enhances platelet thrombogenicity. *Atherosclerosis* **294**, 17–24 (2020). doi: 10.1016/j.atherosclerosis.2019.12.017; pmid: 31945614

29. R. J. Nilsson *et al.*, Rearranged EML4-ALK fusion transcripts sequester in circulating blood platelets and enable blood-based crizotinib response monitoring in non-small-cell lung cancer. *Oncotarget* **7**, 1066–1075 (2016). doi: 10.18632/oncotarget.6279; pmid: 26544515
30. S. Koseoglu *et al.*, Dynamin-related protein-1 controls fusion pore dynamics during platelet granule exocytosis. *Arterioscler. Thromb. Vasc. Biol.* **33**, 481–488 (2013). doi: 10.1161/ATVBAHA.112.255737; pmid: 23288151
31. Y. Yatomi *et al.*, Separable function of platelet release reaction and clot retraction. *Biochem. Biophys. Res. Commun.* **140**, 329–334 (1986). doi: 10.1016/0006-291X(86)91094-6; pmid: 3022719
32. H. Melchinger, K. Jain, T. Tyagi, J. Hwa, Role of Platelet Mitochondria: Life in a Nucleus-Free Zone. *Front. Cardiovasc. Med.* **6**, 153 (2019). doi: 10.3389/fcvm.2019.00153; pmid: 31737646
33. L. H. Boudreau *et al.*, Platelets release mitochondria serving as substrate for bactericidal group IIA-secreted phospholipase A2 to promote inflammation. *Blood* **124**, 2173–2183 (2014). doi: 10.1182/blood-2014-05-573543; pmid: 25082876
34. S. O'Hagan, M. Wright Muelas, P. J. Day, E. Lundberg, D. B. Kell, GeneGini: Assessment via the Gini Coefficient of Reference "Housekeeping" Genes and Diverse Human Transporter Expression Profiles. *Cell Syst.* **6**, 230–244.e1 (2018). doi: 10.1016/j.cels.2018.01.003; pmid: 29428416
35. M. W. Snyder, M. Kircher, A. J. Hill, R. M. Daza, J. Shendure, Cell-free DNA Comprises an In Vivo Nucleosome Footprint that Informs Its Tissues-Of-Origin. *Cell* **164**, 57–68 (2016). doi: 10.1016/j.cell.2015.11.050; pmid: 26771485
36. F. Mouliere *et al.*, Enhanced detection of circulating tumor DNA by fragment size analysis. *Sci. Transl. Med.* **10**, eaat4921 (2018). doi: 10.1126/scitranslmed.aat4921; pmid: 30404863
37. H. R. Underhill *et al.*, Fragment Length of Circulating Tumor DNA. *PLOS Genet.* **12**, e1006162 (2016). doi: 10.1371/journal.pgen.1006162; pmid: 27428049
38. Y. M. D. Lo, D. S. C. Han, P. Jiang, R. W. K. Chiu, Epigenetics, fragmentomics, and topology of cell-free DNA in liquid biopsies. *Science* **372**, eaaw3616 (2021). doi: 10.1126/science.aaw3616; pmid: 33833097
39. V. A. Adalsteinsson *et al.*, Scalable whole-exome sequencing of cell-free DNA reveals high concordance with metastatic tumors. *Nat. Commun.* **8**, 1324 (2017). doi: 10.1038/s41467-017-00965-y; pmid: 29109393
40. C. Kandoth *et al.*, Mutational landscape and significance across 12 major cancer types. *Nature* **502**, 333–339 (2013). doi: 10.1038/nature12634; pmid: 24132290
41. A. Jamshidi *et al.*, Evaluation of cell-free DNA approaches for multi-cancer early detection. *Cancer Cell* **40**, 1537–1549.e12 (2022). doi: 10.1016/j.ccell.2022.10.022; pmid: 36400018
42. M. S. Esfahani *et al.*, Inferring gene expression from cell-free DNA fragmentation profiles. *Nat. Biotechnol.* **40**, 585–597 (2022). doi: 10.1038/s41587-022-01222-4; pmid: 35361996
43. J. Moss *et al.*, Comprehensive human cell-type methylation atlas reveals origins of circulating cell-free DNA in health and disease. *Nat. Commun.* **9**, 5068 (2018). doi: 10.1038/s41467-018-07466-6; pmid: 30498206
44. R. Sadeh *et al.*, ChIP-seq of plasma cell-free nucleosomes identifies gene expression programs of the cells of origin. *Nat. Biotechnol.* **39**, 586–598 (2021). doi: 10.1038/s41587-020-00775-6; pmid: 33432199
45. Y. Liu *et al.*, Bisulfite-free direct detection of 5-methylcytosine and 5-hydroxymethylcytosine at base resolution. *Nat. Biotechnol.* **37**, 424–429 (2019). doi: 10.1038/s41587-019-0041-2; pmid: 30804537
46. N. Loyfer *et al.*, A DNA methylation atlas of normal human cell types. *Nature* **613**, 355–364 (2023). doi: 10.1038/s41586-022-05580-6; pmid: 36599988
47. R. Jackstadt *et al.*, Epithelial NOTCH Signaling Rewires the Tumor Microenvironment of Colorectal Cancer to Drive Poor-Prognosis Subtypes and Metastasis. *Cancer Cell* **36**, 319–336.e7 (2019). doi: 10.1016/j.ccell.2019.08.003; pmid: 31526760
48. S. Go *et al.*, Tissue-resident NK cells support survival in pancreatic cancer through promotion 1 of cDC1-CD8T activity. bioRxiv 2023.10.14.562332 [Preprint] (2024); https://doi.org/10.1101/2023.10.14.562332.
49. J. E. East *et al.*, British Society of Gastroenterology position statement on serrated polyps in the colon and rectum. *Gut* **66**, 1181–1196 (2017). doi: 10.1136/gutjnl-2017-314005; pmid: 28450390
50. A. Junca *et al.*, Detection of Colorectal Cancer and Advanced Adenoma by Liquid Biopsy (Decalib Study): The ddPCR Challenge. *Cancers* **12**, 1482 (2020). doi: 10.3390/cancers12061482; pmid: 32517177
51. M. Galanopoulos *et al.*, Comparative Study of Mutations in Single Nucleotide Polymorphism Loci of *KRAS* and *BRAF* Genes in Patients Who Underwent Screening Colonoscopy, With and Without Premalignant Intestinal Polyps. *Anticancer Res.* **37**, 651–657 (2017). doi: 10.21873/anticanres.11360; pmid: 28179313
52. M. G. Best, P. Wesseling, T. Wurdinger, Tumor-Educated Platelets as a Noninvasive Biomarker Source for Cancer Detection and Progression Monitoring. *Cancer Res.* **78**, 3407–3412 (2018). doi: 10.1158/0008-5472.CAN-18-0887; pmid: 29921699
53. S. A. Joosse, K. Pantel, Tumor-Educated Platelets as Liquid Biopsy in Cancer Patients. *Cancer Cell* **28**, 552–554 (2015). doi: 10.1016/j.ccell.2015.10.007; pmid: 26555171
54. D. C. Calverley *et al.*, Significant downregulation of platelet gene expression in metastatic lung cancer. *Clin. Transl. Sci.* **3**, 227–232 (2010). doi: 10.1111/j.1752-8062.2010.00226.x; pmid: 21500395
55. G. H. Frydman *et al.*, Megakaryocytes contain extranuclear histones and may be a source of platelet-associated histones during sepsis. *Sci. Rep.* **10**, 4621 (2020). doi: 10.1038/s41598-020-61309-3; pmid: 32165642
56. L. Clejan, H. Menahem, Binding of deoxyribonucleic acid to the surface of human platelets. *Acta Haematol.* **58**, 84–88 (1977). doi: 10.1159/000207812; pmid: 409023
57. C. A. Dorsch, Binding of single-strand DNA to human platelets. *Thromb. Res.* **24**, 119–129 (1981). doi: 10.1016/0049-3848(81)90037-2; pmid: 7330833
58. C. Vanpouille-Box, S. Demaria, S. C. Formenti, L. Galluzzi, Cytosolic DNA Sensing in Organismal Tumor Control. *Cancer Cell* **34**, 361–378 (2018). doi: 10.1016/j.ccell.2018.05.013; pmid: 30216189
59. Y. Wang *et al.*, eccDNAs are apoptotic products with high innate immunostimulatory activity. *Nature* **599**, 308–314 (2021). doi: 10.1038/s41586-021-04009-w; pmid: 34671165
60. I. Hawwari *et al.*, Platelet-derived transcription factors licence human monocyte inflammation. bioRxiv 2022.08.10.503291 (2023); https://doi.org/10.1101/2022.08.10.503291.
61. E. S. Kim *et al.*, Blood-based tumor mutational burden as a biomarker for atezolizumab in non-small cell lung cancer: The phase 2 B-F1RST trial. *Nat. Med.* **28**, 939–945 (2022). doi: 10.1038/s41591-022-01754-x; pmid: 35422531
62. D. G. Rothwell *et al.*, Utility of ctDNA to support patient selection for early phase clinical trials: The TARGET study. *Nat. Med.* **25**, 738–743 (2019). doi: 10.1038/s41591-019-0380-z; pmid: 31011204
63. J. D. Merker *et al.*, Circulating Tumor DNA Analysis in Patients With Cancer: American Society of Clinical Oncology and College of American Pathologists Joint Review. *J. Clin. Oncol.* **36**, 1631–1641 (2018). doi: 10.1200/JCO.2017.76.8671; pmid: 29504847
64. N. Liang *et al.*, Mature Red Blood Cells Contain Long DNA Fragments and Could Acquire DNA from Lung Cancer Tissue. *Adv. Sci. (Weinh.)* **10**, 2206361 (2023). doi: 10.1002/advs.202206361; pmid: 36599687
65. C. Schmidl, A. F. Rendeiro, N. C. Sheffield, C. Bock, ChIPmentation: Fast, robust, low-input ChIP-seq for histones and transcription factors. *Nat. Methods* **12**, 963–965 (2015). doi: 10.1038/nmeth.3542; pmid: 26280331
66. J. D. Buenrostro, B. Wu, H. Y. Chang, W. J. Greenleaf, ATAC-seq: A Method for Assaying Chromatin Accessibility Genome-Wide. *Curr. Protoc. Mol. Biol.* **109**, 29.1, 9 (2015). doi: 10.1002/0471142727.mb2129s109; pmid: 25559105
67. Y. Jung, L. Wen, A. Altman, K. Ley, CD45 pre-exclusion from the tips of T cell microvilli prior to antigen recognition. *Nat. Commun.* **12**, 3872 (2021). doi: 10.1038/s41467-021-23792-8; pmid: 34162836
68. S. Andrews, FastQC (Babraham Bioinformatics, Babraham Institute, 2010).
69. F. Krueger, F. James, P. Ewels, E. Afyounian, B. Schuster-Boeckler, FelixKrueger/TrimGalore: v0.6.7, Zenodo (2021); https://zenodo.org/record/5127899.
70. V. A. Schneider *et al.*, Evaluation of GRCh38 and de novo haploid genome assemblies demonstrates the enduring quality of the reference assembly. *Genome Res.* **27**, 849–864 (2017). doi: 10.1101/gr.213611.116; pmid: 28396521
71. H. Li, Aligning sequence reads, clone sequences and assembly contigs with BWA-MEM. arXiv:1303.3997 [q-bio.GN] (2013).
72. H. Li *et al.*, The Sequence Alignment/Map format and SAMtools. *Bioinformatics* **25**, 2078–2079 (2009). doi: 10.1093/bioinformatics/btp352; pmid: 19505943
73. G. Van der Auwera, B. O'Connor, *Genomics in the cloud: using Docker, GATK, and WDL in Terra* (O'Reilly Media, 2020).
74. H. M. Amemiya, A. Kundaje, A. P. Boyle, The ENCODE Blacklist: Identification of Problematic Regions of the Genome. *Sci. Rep.* **9**, 9354 (2019). doi: 10.1038/s41598-019-45839-z; pmid: 31249361
75. A. R. Quinlan, I. M. Hall, BEDTools: A flexible suite of utilities for comparing genomic features. *Bioinformatics* **26**, 841–842 (2010). doi: 10.1093/bioinformatics/btq033; pmid: 20110278
76. H. Wickham, *ggplot2: Elegant Graphics for Data Analysis* (Springer, 2016), pp. 189–201. doi: 10.1007/978-3-319-24277-4_9
77. I. Abugessaisa *et al.*, refTSS: A reference data set for human and mouse transcription start sites. *J. Mol. Biol.* **431**, 2407–2422 (2019). doi: 10.1016/j.jmb.2019.04.045; pmid: 31075273
78. M. Karimzadeh, C. Ernst, A. Kundaje, M. M. Hoffman, Umap and Bismap: Quantifying genome and methylome mappability. *Nucleic Acids Res.* **46**, e120–e120 (2018). doi: 10.1093/nar/gky677; pmid: 30169659
79. B. Gel, E. Serra, karyoploteR: An R/Bioconductor package to plot customizable genomes displaying arbitrary data. *Bioinformatics* **33**, 3088–3090 (2017). doi: 10.1093/bioinformatics/btx346; pmid: 28575171
80. C. Gini, On the measure of concentration with special reference to income and statistics. *Colorado College Publication: General Series* **208**, 73–79 (1936).
81. P. Siejka-Zielińska *et al.*, Cell-free DNA TAPS provides multimodal information for early cancer detection. *Sci. Adv.* **7**, eabh0534 (2021). doi: 10.1126/sciadv.abh0534; pmid: 34516908
82. B. Schuster-Boeckler, J. Inchauspe, Scripts and Outputs for Murphy et al. Zenodo (2022).

ACKNOWLEDGMENTS

We thank J. Koth and C. Lagerholm from the MRC WIMM Imaging Facility; H. Gersen, K. Meissner, F. Roseman, J. Brown, N. Hayder, M. Jacobs, and D. Moralli for ideas and support with experiments; the COMBATcancer consortium; and the CRUK Oxford Centre. We thank the patients and healthy donors for their participation in the research and the Oxford COMBATcancer Consortium and CRUK Oxford Centre for helping with recruitment and sample banking. We also acknowledge BioRender for figure creation. **Funding:** Funding was provided by Cancer Research UK Early Detection Project Grant EDDCPJT/100003 (B.P., C.D.G., P.R.); CRUK Advanced Clinical Scientist Fellowship C67633/A29034 (B.P.); Senior Fellowship RCCSCF-May24/100001 funded by Cancer Research UK in partnership with the Rosetrees Trust (B.P.); Ludwig Institute for Cancer Research Associate Member Program (B.P., B.S.-B.); Medical Research Council Grant MR/T04490X/1 (B.S.-B.); Kidani Memorial Trust (E.O.N.); CRUK Oxford Centre Clinical Research Training Fellowship C130623/A249471 (N.S.); and an unrestricted research grant from Emerson Health (now Yosemite) (B.P.). We also acknowledge support from the National Institute for Health Research (NIHR), Oxford Biomedical Research Centre (BRC), and CRUK Oxford Centre Grant CTRQQR-2021\100002. **Author contributions:** Conceptualization: L.M., B.P., C.D.G.; Methodology: L.M., J.I., N.S., H.L.B.-D., P.H., G.V., R.L., N.J.J., C.B., E.M., Z.E., L.C., E.S., L.D., S.K., I.H., M.K., E.O.N., M.V., P.R., S.L., B.S.-B., C.D.G., B.P.; Software: J.I., B.S.-B., J.R.H.; Validation: L.M., J.I., P.R., C.D.G., B.P., B.S.-B., C.B., N.J.J.; Formal analysis: L.M., J.I., B.S.B., P.R.; Investigation: L.M., J.I., N.S., H.L.B.-D., P.H., G.V., R.L., N.J.J., C.B., S.B., Z.E., L.C., J.O.S., M.P.R., A.O.K., C.S.K., N.N., E.M., E.S., L.D.; Resources: L.M., N.S., B.S.-B., C.D.G., P.R., S.L., M.D., M.V., E.O.N., N.N.; Data curation: L.M., J.I., B.S.-B., J.R.H., Z.E., S.B., L.C., P.R.; Writing - original draft: L.M., B.P.; Writing - review and editing: all authors; Visualization: L.M., J.I., Z.E., L.C., B.S.-B.; Supervision: B.P., A.J.M., P.R., C.D.G., B.S.-B., J.R.H.; Project administration: L.M., B.P., C.D.G., B.S.-B.; Funding acquisition: B.P., C.D.G., B.S.-B. **Competing interests:** B.P., A.J.M., C.D.G., L.M., and N.S. are listed as inventors on patent GB2203947.3 (CRUK Ref: CR/2021-069), submitted in 2022 by the University of Oxford, which covers the detection of disease-associated gene mutations in nucleic acids derived from purified platelets. B.P., A.J.M., and L.M. are also inventors on patent P45651W01 (GB2314848.9), filed in 2023 by the University of Oxford, relating to the recovery of cell-free nucleic acids from platelets. B.P. is a cofounder and major shareholder of Alethiomics; has received honoraria for speaking engagements and/or advisory work for Incyte, BMS, Constellation Therapeutics, GSK, Blueprint Medicines, Novartis, and Alethiomics; and has received research funding from Incyte, Galecto, and Alethiomics. A.J.M. is a cofounder and shareholder of Alethiomics; has received honoraria or served on advisory boards for Alethiomics, Novartis, CTI, Gilead, and Shire; and has received research funding from Alethiomics and Galecto. L.M. has consulted for Alethiomics. All other authors declare that they have no competing interest. **Data and materials availability:** All data needed to evaluate the conclusions in the paper are present in the paper or the supplementary materials. Raw whole-genome sequencing data has been deposited in the European Genome-phenome Archive (EGA) under accession number EGAS00001006854 (study: EGA00001006854; dataset: EGAD00001009856; data access committee: EGAC00001003034). Code is available on Zenodo (*82*). **License information:** Copyright © 2025 the authors, some rights reserved; exclusive licensee American Association for the Advancement of Science. No claim to original U.S. Government Works. This work is licensed under a Creative Commons Attribution 4.0 International (CC BY 4.0) license, which permits unrestricted use, distribution, and reproduction in any medium, provided the original work is properly cited. To view a copy of this license, visit https://creativecommons.org/licenses/by/4.0/. This license does not apply to figures/photos/artwork or other content included in the article that is credited to a third party; obtain authorization from the rights holder before using such material.

SUPPLEMENTARY MATERIALS

science.org/doi/10.1126/science.adp3971
Supplementary Text; Figs. S1 to S6; Tables S1 to S7; MDAR Reproducibility Checklist; Movies S1 to S6

Submitted 24 March 2024; resubmitted 1 January 2025; accepted 13 June 2025

10.1126/science.adp3971

Check for

RESEARCH ARTICLE SUMMARY

CELL BIOLOGY

Mitochondria protect against an intracellular pathogen by restricting access to folate

Tânia Catarina Medeiros, Jana Ovciarikova, Xianhe Li, Patrick Krueger, Tim Bartsch, Silvia Reato, John C. Crow, Michelle Tellez Sutterlin, Bruna Martins Garcia, Irina Rais, Kira Allmeroth, Matías D. Hartman, Martin S. Denzel, Martin Purrio, Andrea Mesaros, Kit-Yi Leung, Nicholas D. E. Greene, Lilach Sheiner, Patrick Giavalisco, Lena Pernas*

Full article and list of author affiliations: https://doi.org/10.1126/science.adr6326

INTRODUCTION: Mitochondria are key hubs of cellular metabolism. This means that in addition to generating a range of metabolites, these organelles also use and consume many nutrients that invading pathogens rely on. Although mitochondria number in the hundreds to up to the thousands in mammalian cells—in contrast to few invading pathogens—it remains unclear whether host cells leverage mitochondria to restrict pathogen access to essential metabolites.

RATIONALE: We reasoned that mitochondrial processes that rely on diverse cytosolic metabolites might reveal competing metabolic demands between mitochondria and intracellular pathogens. We focused on the replication of mitochondrial DNA (mtDNA), which requires nutrients including those that maintain one-carbon metabolism processes required for nucleotide biosynthesis. We found that infection with the intracellular parasite *Toxoplasma gondii* increased mtDNA copy number. This response was independent of mitochondrial biogenesis but required activating transcription factor 4 (ATF4), which was activated through the integrated stress response (ISR) kinase HRI in response to parasite effector–induced mitochondrial stress.

RESULTS: Having identified that *Toxoplasma* infection led to an increase in mtDNA in an ATF4-dependent manner, we next investigated the underlying mechanism. During infection, ATF4 induced the mitochondrial one-carbon enzymes MTHFD2 and SHMT2, which use folate to provide carbon units for biosynthetic pathways, such as nucleotide synthesis. Both ATF4 and MTHFD2 were required for the increase in mtDNA and for restricting parasite growth. We pinpointed this restriction to competition for folate, an essential cofactor that *Toxoplasma* requires to produce deoxythymidine monophosphate (dTMP) and to proliferate. Disrupting mitochondrial one-carbon metabolism—through ATF4 loss or methotrexate treatment—led to increased parasite dTMP synthesis and replication. In vivo, preventing ATF4 activation through pharmacological inhibition of the ISR similarly elevated parasite burden.

CONCLUSION: We discovered a host defense strategy rooted in metabolic competition between mitochondria and an intracellular pathogen. This defense was mediated by the ISR effector ATF4, which was activated in response to the detection of parasite effector–induced mitochondrial stress. ATF4 enhanced mitochondrial one-carbon metabolism, thereby depriving *Toxoplasma gondii* of host folate(s) and limiting its ability to synthesize dTMP and proliferate. Thus, mitochondria execute a noncanonical metabolic defense against an intracellular pathogen. We propose that these organelles are positioned to compete with other intracellular pathogens for nutrients, such as folate, that are essential for their replication. □

*Corresponding author. Email: lfpernas@mednet.ucla.edu Cite this article as T. C. Medeiros *et al.*, *Science* **389**, eadr6326 (2025). DOI: 10.1126/science.adr6326

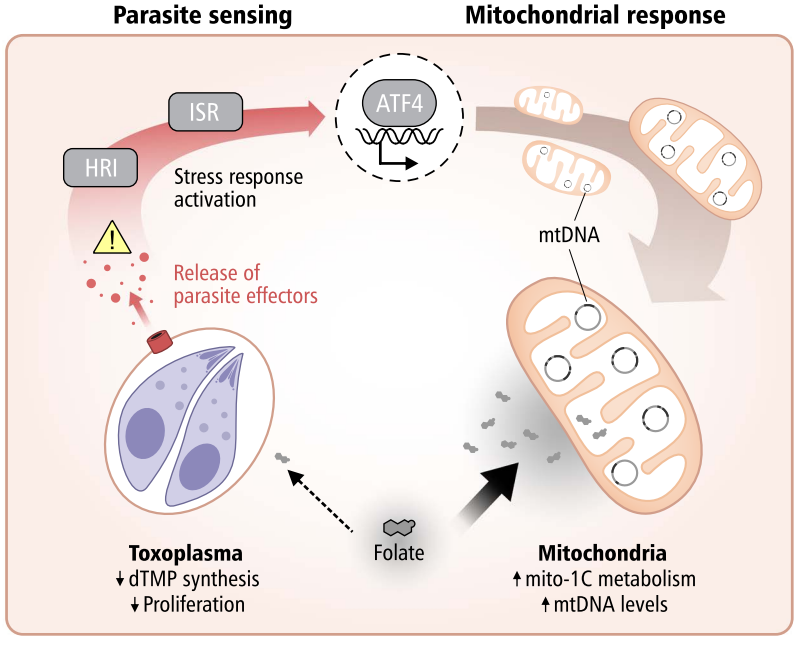

Host cells weaponize mitochondrial metabolism. Upon detection of secreted parasite effectors, host cells activate the ISR. The ISR effector ATF4 increases mtDNA levels and induces mitochondrial one-carbon (mito-1C) metabolism, thereby restricting *Toxoplasma* access to the folate(s) that it requires for dTMP synthesis and growth.

CELL BIOLOGY

Mitochondria protect against an intracellular pathogen by restricting access to folate

Tânia Catarina Medeiros[1], Jana Ovciarikova[2], Xianhe Li[1], Patrick Krueger[1], Tim Bartsch[3], Silvia Reato[3,4], John C. Crow[3], Michelle Tellez Sutterlin[1], Bruna Martins Garcia[1], Irina Rais[1], Kira Allmeroth[5], Matías D. Hartman[5], Martin S. Denzel[5], Martin Purrio[6], Andrea Mesaros[6], Kit-Yi Leung[7], Nicholas D. E. Greene[7], Lilach Sheiner[2], Patrick Giavalisco[8], Lena Pernas[1,3,4]*

As major consumers of cellular metabolites, mitochondria are poised to compete with invading microbes for the nutrients that they need to grow. Whether cells exploit mitochondrial metabolism to protect from infection is unclear. In this work, we found that the activating transcription factor 4 (ATF4) activates a mitochondrial defense based on the essential B vitamin folate. During infection of cultured mammalian cells with the intracellular pathogen *Toxoplasma gondii*, ATF4 increased mitochondrial DNA levels by driving the one-carbon metabolism processes that use folate in mitochondria. Triggered by host detection of mitochondrial stress induced by parasite effectors, ATF4 limited *Toxoplasma* access to folates required for deoxythymidine monophosphate synthesis, thereby restricting parasite growth. Thus, ATF4 rewires mitochondrial metabolism to mount a folate-based metabolic defense against *Toxoplasma*.

A mammalian cell can contain hundreds to up to thousands of mitochondria (*1*). In a healthy cell, mitochondria are viewed as powerhouses that produce adenosine 5′-triphosphate (ATP) and anabolic precursors and as signaling hubs that regulate diverse cellular programs (*2*). To carry out these functions, these organelles consume large amounts of cellular nutrients (*3*). But in an infected cell, mitochondria are perceived as targets for intracellular microbes. However, mitochondria can function as nutrient competitors during infection, thereby depriving intracellular pathogens of access to key nutrients required for growth (*4*, *5*).

To investigate the cellular programs that rewire mitochondrial metabolism during infection, we focused on mitochondrial DNA (mtDNA). Unlike other organelles, mitochondria have their own genome, a vestige of their prokaryotic origin (*6*). To replicate their genome, mitochondria depend on cytosolic resources, such as those sustained by the B vitamin folate (*7*). This essential cofactor is required for a broad set of reactions known as one-carbon (1C) metabolism that occur in the cytosol and mitochondria and are crucial for biochemical processes, including the synthesis of purines and deoxythymidine monophosphate (dTMP), both of which are used to generate deoxynucleotide triphosphates (dNTPs) for DNA replication (*7*). Thus, mtDNA levels reflect mitochondrial use of various cellular resources, and dysregulated 1C metabolism and aberrant dNTP pools are linked to mtDNA replication defects (*8*–*10*).

[1]Metabolism of Infection Group, Max Planck Institute for Biology of Ageing, Cologne, Germany. [2]Centre for Parasitology, University of Glasgow, Glasgow, Scotland, UK. [3]Department of Microbiology, Immunology and Molecular Genetics, University of California Los Angeles, Los Angeles, CA, USA. [4]Howard Hughes Medical Institute, University of California Los Angeles, Los Angeles, CA, USA. [5]Metabolic and Genetic Regulation of Ageing, Max Planck Institute for Biology of Ageing, Cologne, Germany. [6]Phenotyping Core Facility, Max Planck Institute for Biology of Ageing, Cologne, Germany. [7]Developmental Biology and Cancer Department, UCL Great Ormond Street Institute of Child Health, University College London, London, UK. [8]Metabolomics Core Facility, Max Planck Institute for Biology of Ageing, Cologne, Germany.
***Corresponding author. Email: lfpernas@mednet.ucla.edu**

Several intracellular pathogens also require host products downstream of 1C metabolism for their growth. Host cells have thus evolved defense mechanisms to limit 1C metabolite availability, such as through the degradation of dNTPs during viral infection (*5*, *11*). However, whether cells actively reprogram mitochondria to restrict pathogen access to 1C metabolism–linked nutrients is unknown. We used the intracellular human parasite *Toxoplasma gondii*, which salvages host resources that depend on 1C metabolism, to investigate the dynamics of mitochondrial metabolism during infection (*12*, *13*).

ATF4 regulates mtDNA levels during infection and infection-independent stress

To determine whether infection leads to changes in host mtDNA copy number, we measured mtDNA levels in human ES-2 ovarian cancer cells infected with type I *Toxoplasma* parasites. We examined levels of *DLOOP*, the regulatory region of mtDNA, and four genes at different locations on the mitochondrial genome: *mt-ND1*, *mt-ND6*, *mt-CYTB*, and *mt-CO1* (Fig. 1A). At 24 hours postinfection (hpi), the copy number of each gene was increased by ~30% (Fig. 1B). Similar results were obtained in HeLa cells and human fibroblasts (fig. S1). To test whether *Toxoplasma* infection increased mtDNA synthesis, we incubated uninfected and infected cells with the thymidine analog 5-ethynyl-2-deoxyuridine (EdU), which is incorporated into newly synthesized DNA, and compared the abundance of EdU foci per mtDNA nucleoid. Infection increased the number of EdU foci per mtDNA foci (fig. S2, A and B). However, we did not detect cytosolic mtDNA nor the consequent activation of innate immune genes, including *ISG15* and *IRF7* (fig. S2, C and D) (*14*, *15*). Thus, *Toxoplasma* infection drives an increase in intramitochondrial DNA levels.

We noted that infection increased the expression of promoters of mitochondrial biogenesis, including nuclear factor erythroid 2–related factor 2 (NRF2) and peroxisome proliferator–activated receptor-γ coactivator 1α (*PGC1α*) (fig. S3, A and B) (*16*). To determine whether the increase in mtDNA was due to infection-induced mitochondrial biogenesis, we compared nuclear and mitochondrially encoded transcripts' levels, including *SDHB* and *mt-ND1*, in uninfected and *Toxoplasma*-infected cells. Infection did not increase their levels (fig. S3, C and D). Consistent with these results, flow cytometry–based analysis of mitochondrial mass revealed minimal differences between uninfected and infected cells at 6, 12, and 24 hpi (fig. S3E). Furthermore, the expression of enzymes involved in host novo nucleotide synthesis and cytoplasmic nucleotide salvage were mostly unchanged (fig. S3, F and G). Thus, mtDNA copy number is increased during infection independently of global changes in mitochondrial abundance.

How do *Toxoplasma*-infected cells increase mtDNA levels? We noted that infection also induced the expression of the mtDNA transcription factor *TFAM* and mtDNA helicase *TWNK*, whose mild overexpression increases mtDNA levels by ~1.5-fold, comparable to changes that we observed during infection (fig. S4 and Fig. 1B) (*17*, *18*). We posited that the increase in mtDNA was regulated by an infection-induced transcription factor upstream of *TFAM* and *TWNK*. To address this possibility, we compared the protein abundance in whole-cell extracts from uninfected cells and *Toxoplasma*-infected cells using mass spectrometry (table S1). Infection with *Toxoplasma* caused an increase in the abundance of several transcription factors, including c-MYC, JUN, and FOS, in line with previous observations (Fig. 1C) (*19*–*21*). However, the activating transcription factor 4 (ATF4) was the highest induced host transcription factor with an ~16-fold enrichment in the proteomes of infected cells (Fig. 1C).

ATF4 is the main effector of the integrated stress response (ISR), which promotes cellular recovery during various stresses, including endoplasmic reticulum (ER) stress and viral infection (*22*). Recently ATF4 has been recognized as a key regulator of mitochondrial stress responses (*23*). Furthermore, the ISR promotes mtDNA recovery in cells with mtDNA double-stranded breaks (*24*). The treatment of cells with tunicamycin, an inhibitor of N-linked glycan biosynthesis that

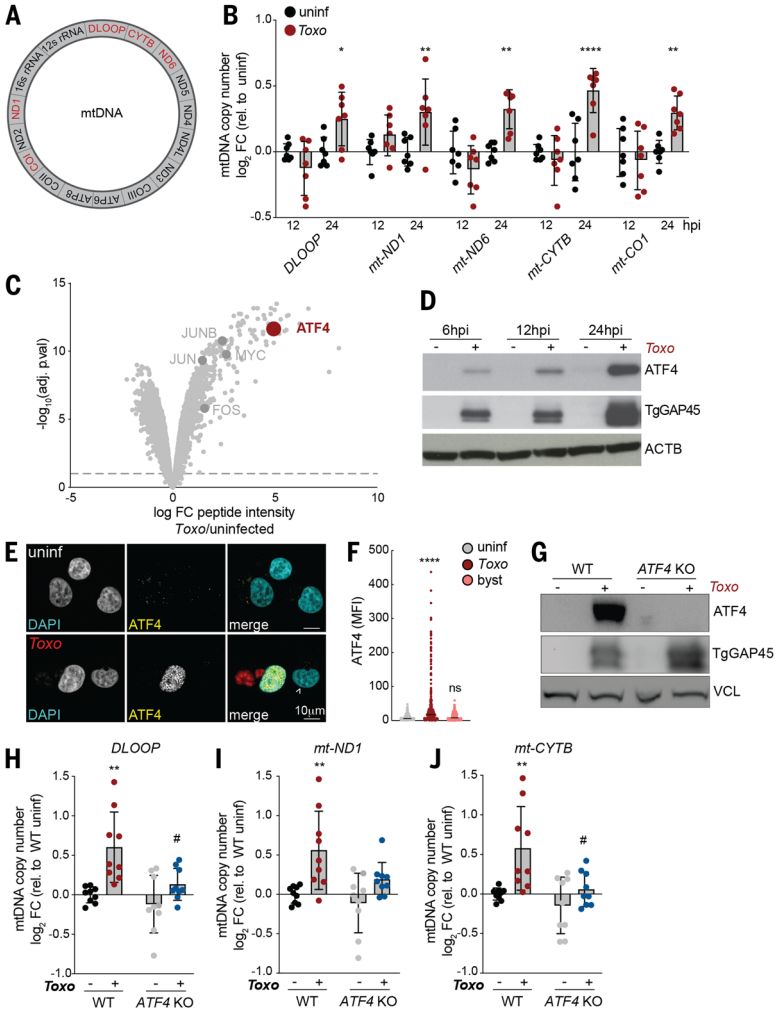

Fig. 1. ATF4 increases mtDNA levels during *Toxoplasma* infection. (**A**) Schematic of human mitochondrial genome, with genes analyzed by qPCR shown in red. rRNA, ribosomal RNA. (**B**) mtDNA levels monitored by qPCR (normalized to *RUNX2*) in ES-2s cells that were uninfected (uninf) or infected with *Toxoplasma* (*Toxo*) at an MOI of 4 at 12 and 24 hpi. Data are means ± SDs of $n = 7$ independent cultures. *$P < 0.05$; **$P < 0.01$; ****$P < 0.0001$ for uninfected versus infected by means of two-way ANOVA analysis. (**C**) Volcano plot of whole-cell lysates from uninfected and infected HeLa cells at 24 hpi and analyzed by means of mass spectrometry with highlighted transcription factors. FC, fold change. (**D**) ES-2 cells were uninfected or *Toxo*-infected (MOI: 4) for 6, 12, and 24 hours and analyzed by means of immunoblotting for ATF4, ~50 kDa; β-Actin (ACTB), ~45 kDa; and *Toxoplasma* GAP45 (TgGAP45), ~45 kDa. (**E**) Immunofluorescence images of uninfected cells and cells infected with mCherry-expressing *Toxoplasma* at 24 hpi. Arrowhead indicates an uninfected bystander cell that is proximal to an infected cell. Scale bar, 10 µm. DAPI, 4′,6-diamidino-2-phenylindole. (**F**) Quantification of mFI of ATF4 in the nuclei of cells in images as in (E). byst, bystander cell. ****$P < 0.001$ for comparison with uninfected by means of one-way ANOVA analysis. (**G**) Immunoblot analyses of lysates from uninfected and *Toxoplasma*-infected (MOI: 4) WT and *ATF4* KO ES-2 cells at 24 hpi: ATF4, ~50 kDa; vinculin (VCL), ~124 kDa; and *Toxoplasma* GAP45 (TgGap45), ~45 kDa. (**H** to **J**) mtDNA levels monitored by qPCR of *DLOOP*, *mt-ND1*, and *mt-CYTB* (normalized to *RUNX2*) in uninfected and *Toxoplasma*-infected (MOI: 4) ES-2 cells at 12 at 24 hpi. Data are means ± SDs of $n = 9$ independent cultures. **$P < 0.01$; ***$P < 0.001$ for uninfected versus infected. #$P < 0.05$; ##$P < 0.01$ for WT versus *ATF4* KO by means of two-way ANOVA analysis. [(B) to (J)] ES-2 cells used for all experiments.

activates the ISR and thus ATF4, was sufficient to increase mtDNA levels independently of infection (fig. S5). We thus sought to address the role of ATF4 in mtDNA dynamics during infection. To first confirm our proteomics results, we analyzed uninfected cells and *Toxoplasma*-infected cells by immunoblot analysis. Infection induced ATF4 as early as 6 hpi and maximally at 24 hpi, and ATF4 nuclear translocation was only evident in infected cells (Fig. 1, D to F). Similar results were obtained in cells infected with the less virulent type II strain of *Toxoplasma*, which indicates that ATF4 activation is a general consequence of *Toxoplasma* infection (fig. S6, A to C). To test the role of ATF4 in increasing mtDNA levels during infection, we generated ATF4 knockout (KO) ES-2 cells using CRISPR-Cas9 technology (Fig. 1G). The loss of ATF4 prevented the increase in mtDNA copy number during both *Toxoplasma* infection or tunicamycin treatment in wild-type (WT) cells (Fig. 1, H to J, and fig. S5). Thus, ATF4 activation regulates mtDNA levels during infection and infection-independent stress.

ATF4 increases mtDNA levels in a mitochondrial 1C metabolism–dependent manner

How does ATF4 regulate mtDNA during infection? Because infection induced the expression of *TFAM* and *TWNK*, we posited that ATF4 regulated mtDNA levels in a TFAM- and TWNK-dependent manner (fig. S4). To address this possibility, we examined their expression in uninfected and *Toxoplasma*-infected WT and ATF4 KO cells. Contrary to our expectation, the loss of ATF4 did not block the increase in *TFAM* and *TWNK* transcripts during infection (fig. S4). In fact, ATF4 KO cells had higher expression of *TWNK* relative to WT uninfected and *Toxoplasma*-infected cells (fig. S4A). These results indicated that ATF4 increases mtDNA levels independently of TFAM and TWNK.

Because gene targets of ATF4 vary depending on its mechanism of activation, we next sought to define the host pathway upstream of ATF4 during infection (*25*). During the ISR, diverse cellular stresses are sensed by the so-called ISR kinases, which subsequently phosphorylate eukaryotic translation initiation factor 2α (eIF2α) at serine-51 (*22*). The consequent attenuation of translation leads to the translation of ISR effectors, such as ATF4 (*22*). Alternatively, ATF4 can be activated by progrowth signals that stimulate mechanistic target of rapamycin complex 1 (mTORC1), the anabolic regulator of the cell (*26*). To determine whether the ISR or mTORC1 mediated ATF4 activation during infection, we generated mouse embryonic stem cells (mESCs) deficient for eIF2α phosphorylation ($eIF2\alpha^{S51A}$). In WT mESCs, both *Toxoplasma* infection and tunicamycin treatment drove eIF2α phosphorylation and ATF4 induction, as in ES-2 cells (Fig. 2A and fig. S7A). However, neither induced ATF4 in $eIF2\alpha^{S51A}$ mESCs or in ES-2 cells treated with ISRIB, a small-molecule inhibitor of the ISR (Fig. 2A and fig. S7A). Consistent with this result, rapamycin- or torin1-based inhibition of mTORC1, as assessed by phosphorylation of its target ribosomal protein S6 kinase 1 (S6K1), did not block ATF4 activation during *Toxoplasma* infection (fig. S7B). Thus, infection activates ATF4 in an ISR-dependent manner.

To identify the ATF4 targets common to infection and ISR activation that mediated the increase in mtDNA levels, we compared the expression of a panel of ATF4 targets in uninfected cells, *Toxoplasma*-infected cells, and cells treated with tunicamycin (table S2) (*27*). ATF4 targets induced by both *Toxoplasma* infection and tunicamycin treatment included the transcription factor *ATF3* and asparagine synthase (*ASNS*) (Fig. 2B). Of particular interest were *MTHFD2* and *SHMT2*, enzymes of the mitochondrial arm of the 1C metabolism processes that use folate as cofactor to activate and transfer 1C groups for the biosynthesis of nucleotide precursors (Fig. 2B) (*7*, *23*, *27*, *28*). Furthermore, MTHFD2 has been linked to mtDNA deficiencies (*8*, *28*). As expected, infection induced *MTHFD2* and *SHMT2* in an ATF4-dependent manner (Fig. 2, C and D). To test the importance of mitochondrial 1C (mito-1C)

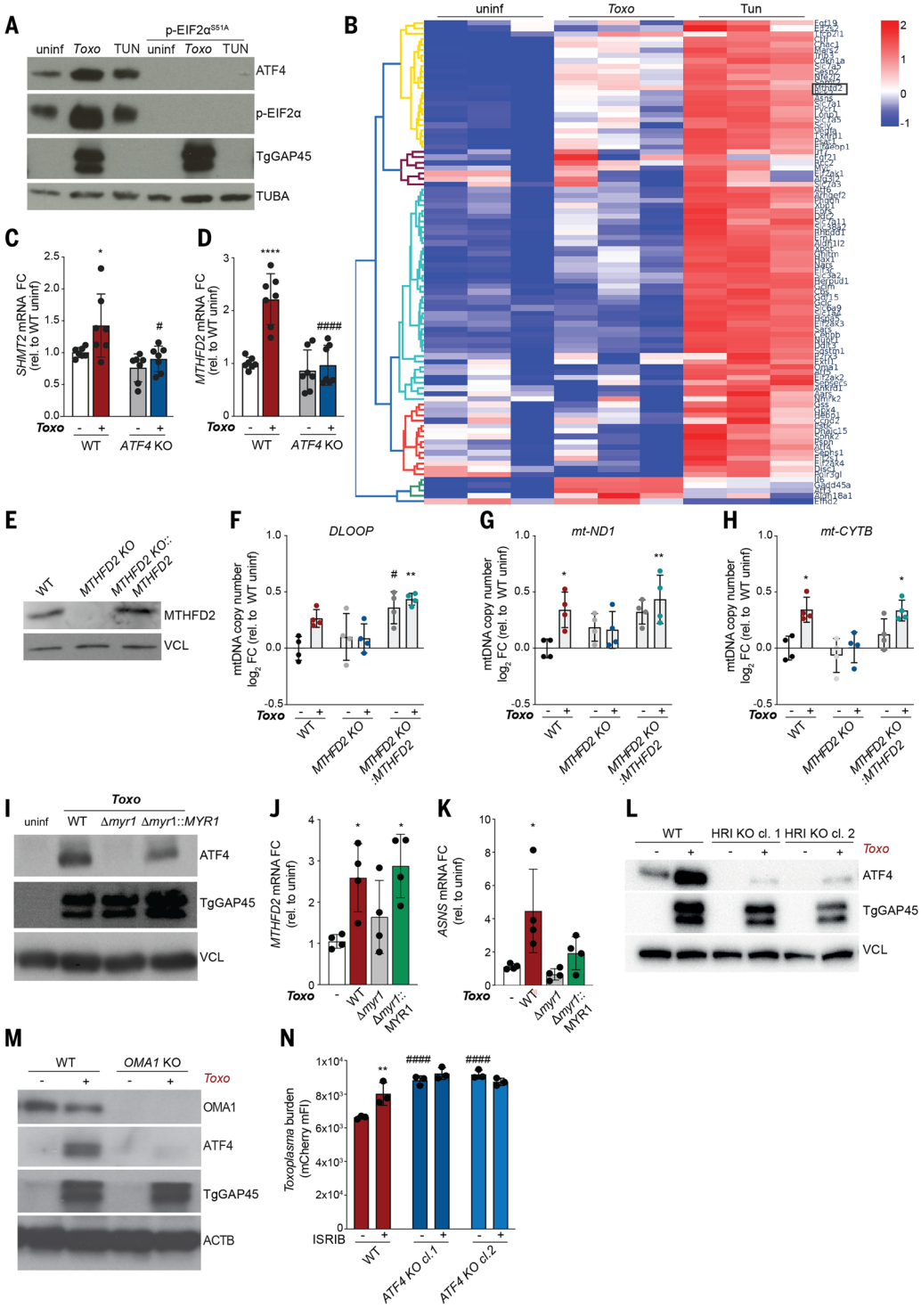

Fig. 2. ATF4 requires mito-1C metabolism to increase mtDNA levels. (**A**) Immunoblot (IB) analyses of WT and eIF2α^{S51A} AN3-12 cells that were uninfected (uninf), infected with *Toxoplasma* (*Toxo*), or tunicamycin (TUN)–treated (3 μg/ml) for 24 hours (h): ATF4; phospho-EIF2α (Ser51), ~38 kDa; α-Tubulin (TUBA), ~55 kDa; and TgGAP45. (**B**) Heatmap of mRNA levels of *ATF4* target genes in uninfected, *Toxo*, and TUN (3 μg/ml)–treated ES-2 cells. $n = 3$ independent cultures. (**C** and **D**) WT and *ATF4* KO ES-2 cells were uninfected or *Toxo* for 24 hours and analyzed by qPCR for *SHMT2* and *MTHFD2*. Transcripts were normalized to *ACTB* and are relative to WT uninfected. Data are means ± SDs of $n = 7$ independent cultures. *$P < 0.05$; ****$P < 0.0001$ for uninfected versus *Toxo* by two-way ANOVA analysis. (**E**) IB of ES-2 cells as indicated: MTHFD2, ~32 kDa and TUBA. (**F** to **H**) ES-2 cells as indicated were analyzed for mtDNA by qPCR for *DLOOP*, mt-*ND1*, and mt-*CYTB* normalized to *RUNX2* levels and relative to WT uninfected. Data are means ± SDs of $n = 4$ independent cultures. *$P < 0.05$; **$P < 0.01$ for uninfected versus *Toxo*. #$P < 0.05$; ##$P < 0.01$ for WT versus *MTHFD2* KO by two-way ANOVA analysis. (**I**) IB analysis of ES-2 cells as indicated at 24 hpi (MOI: 4 for *Toxo*): ATF4, VCL, and TgGAP45. (**J** and **K**) Cells treated as in (I) were analyzed by qPCR as in (C) and (D). Data are means ± SDs of $n = 4$ independent cultures. *$P < 0.05$; **$P < 0.01$ by one-way ANOVA analysis. (**L**) IB analysis of WT and HRI KO ES-2 cells that were uninfected or *Toxo* at 24 hpi; *Toxoplasma* GRA7 (TgGRA7), ~32 kDa. (**M**) IB analysis of uninfected and *Toxo* WT and OMA1 KO MEFs at 24 hpi: OMA1, ~35 kDa, ATF4, ACTB, and TgGAP45. (**N**) *Toxo* WT and *ATF4* KO ES-2 cells were treated ± ISRIB (200 nM) and analyzed 24 hpi using flow cytometry for *Toxoplasma* burden (mCherry mFI). Data are means ± SEMs of $n = 3$ biological experiments. **$P < 0.01$ for DMSO versus ISRIB; ####$P < 0.0001$ for WT versus ATF4 KO by two-way ANOVA analysis.

metabolism in the changes in mtDNA during infection, we generated cells deficient for MTHFD2 (Fig. 2E). Infection did not increase mtDNA levels in MTHFD2 KO cells, unlike in WT cells (Fig. 2, F to H). The overexpression of *MTHFD2* cDNA in MTHFD2 KO cells rescued the increase in mtDNA levels in infected cells and even increased mtDNA levels in uninfected cells (Fig. 2, F to H). Thus, mito-1C metabolism is required for ATF4 to increase mtDNA levels during infection.

Host cells activate ATF4 in response to mitochondrial stress induced by parasite effectors

Because ATF4 regulated mtDNA dynamics in a mito-1C metabolism–dependent manner, we hypothesized that the activation of ATF4 was a defensive host response to *Toxoplasma*. However, the possibility remained that the ISR was activated by metabolic stress caused by the siphoning of nutrients by replicating parasites, as previously suggested (*19*). To distinguish between these possibilities, we first tested whether the induction of ATF4 required parasite effector proteins that are secreted into the host cell. To do so, we examined ATF4 activation in cells infected with Δ*myr1* parasites that lack the translocon apparatus required for the secretion of a class of effector proteins but are competent for replication and thus nutrient siphoning (*29*, *30*). Host cells infected with Δ*myr1* parasites did not induce ATF4 nor its targets *MTHFD2* and *ASNS* (Fig. 2, I to K, and fig. S6D). In line with this result, infection similarly induced ATF4 activation in cells deficient for the nutrient-sensing ISR kinase GCN2 and its WT counterparts (fig. S8, A and B). Thus, host cells activate ATF4 in response to a secreted parasite effector.

How are *Toxoplasma* effectors sensed by the ISR? Having excluded a role for GCN2, we next investigated whether the ISR kinases (PKR)–like endoplasmic reticulum kinase (PERK), protein kinase R (PKR), or eukaryotic translation initiation factor 2α kinase 1 (HRI) mediated ISR activation during infection (*22*). Infection did not induce levels of BiP, a canonical marker of ER stress that is sensed by PERK, unlike the ER stressor tunicamycin (fig. S7A). PKR is mainly activated by double-stranded RNA during viral infection (*22*). We thus focused on HRI, which relays mitochondrial stress to the ISR (*31*). To this end, we generated HRI KO cells, which, as expected, had impaired ATF4 induction after treatment with the ATP synthase inhibitor oligomycin (fig. S8C). HRI was required for the induction of ATF4 during infection (Fig. 2L). To further understand how infection induces the ISR, we tested the role of OMA1, a stress-activated mitochondrial protease that mediates HRI activation through its cleavage of the inner mitochondrial membrane protein DELE1 (*31*). As with HRI KO cells, OMA1 KO cells were deficient for the activation of ATF4 during infection (Fig. 2M). Thus, HRI activates the ISR in response to parasite effector–induced mitochondrial stress.

Having established that host cells activate the ISR in response to effector-induced mitochondrial stress, we next asked whether the ISR benefited host cells or *Toxoplasma*. Both the pharmacological suppression of the ISR using ISRIB and the genetic ablation of ATF4 led to significant increases in parasite replication (Fig. 2N). Furthermore, the expression of WT ATF4, but not a DNA binding ATF4 mutant, was sufficient to restrict *Toxoplasma* growth in ATF4 KO cells (fig. S9). Thus, the activation of ATF4 in response to host detection of *Toxoplasma* effectors restricts parasite growth.

ATF4 drives mito-1C metabolism and limits parasite dTMP synthesis and proliferation

How does ATF4 affect mitochondrial metabolism and parasite growth? To address this question, we first assessed the contribution of mito-1C metabolism to dTMP and dTTP biosynthesis during *Toxoplasma* infection. Because serine is the predominant donor of carbons to 1C pathways in cultured cells, we cultured uninfected and *Toxoplasma*-infected WT cells with deuterium-labeled serine [2,3,3-^{2}H-serine] and examined the resulting incorporation of ^{2}H into dTMP or dTTP (Fig. 3A) (*7*, *32*). The contribution of mito-1C–derived folates leads to dTMP and dTTP with 1 deuterium and a mass shift of 1 Da (M+1); the contribution of cytosolic-1C (cyto-1C)–derived folates will instead lead to the incorporation of 2 deuteriums and results in M+2 dTMP or dTTP (Fig. 3A) (*32*). In uninfected WT cells, M+1 dTMP and M+1 dTTP were the dominant isotopologs at 100% and >98% of their respective isotope-labeled pools (Fig. 3, B and C). This result is in line with previous observations that mito-1C predominately supplies 1C units in most cultured cell lines (*32*). However, *Toxoplasma* infection of WT cells led to a 10-fold increase in M+2 dTTP levels. M+2 dTMP was not detected, likely owing to the lower abundance of intracellular dTMP pools (Fig. 3B). We next assessed the effect of ATF4 ablation on mito-1C metabolism during infection. The loss of ATF4 led to a significant increase in the contribution of non–mito-1C metabolism to dTMP and dTTP synthesis. M+2 dTMP, which was not detected in WT infected cells or uninfected ATF4 KO cells, made up ~20% of labeled dTMP in infected ATF4 KO cells, whereas M+2 dTTP was approximately twofold higher than infected WT cells (Fig. 3, B and C). Thus, ATF4 maintains host mito-1C metabolism during infection.

We reasoned that the observed increase in M+2 dTMP and dTTP in infected WT and ATF4 KO cells could result from a shift to host reliance on host cyto-1C. Alternatively, because *Toxoplasma* expresses a single cytosolic SHMT and can synthesize pyrimidines de novo, parasite-derived dTMP and dTTP synthesis could also contribute to the increase in M+2 dTMP and dTTP isotopologs (Fig. 3A) (*33*, *34*). To distinguish between these possibilities, we first assessed levels of pyrimidines in uninfected and *Toxoplasma*-infected cells treated with or without leflunomide, a small-molecule inhibitor of host dihydroorotate dehydrogenase and thus pyrimidine synthesis (*35*). Infection led to ~10-fold and ~2-fold increases in total dTMP and dTTP, even in the presence of leflunomide, despite the expected accumulation of the pyrimidine precursors carbamoyl aspartic acid and dihydroorotic acid (fig. S10, A and B). Thus, the increases observed during infection were, in part, driven by *Toxoplasma*-derived dTMP and dTTP.

We next addressed whether the increase in M+2 dTMP and dTTP in ATF4 KO cells was due to their synthesis by host cells or *Toxoplasma*. To do so, we examined M+1 and M+2 isotopologs of dTMP and dTTP during infection with parasites that are deficient for their de novo synthesis owing to the loss of carbamoyl phosphate synthetase II (CPSII) and thus only replicate if supplemented with exogenous uracil (*33*). Infection with Δ*cpsII* parasites led to ATF4 activation but, unlike in the case of WT parasites, failed to drive the increases in M+2 dTMP and M+2 dTTP observed in ATF4 KO cells (Fig. 3, B to D). Thus, the M+2 dTMP and M+2 dTTP detected in infected ATF4 KO cells were parasite derived, and ATF4 loss enhances parasite dTMP synthesis. Consistent with this, parasites isolated from ATF4 KO cells had higher total dTMP and dTTP levels compared with those in WT cells but similar levels of host-derived dTMP (Fig. 3E and fig. S11). Moreover, blocking host 1C metabolism with the dihydrofolate reductase (DHFR) inhibitor methotrexate (MTX) led to the expected loss of host M+1 dTMP and dTTP synthesis but drove approximately twofold increases in parasite M+2 dTMP and dTTP levels (fig. S12). Thus, ATF4-induced mito-1C restricts parasite dTMP synthesis.

How does ATF4 activation regulate parasite dTMP levels? Unlike in mammals, in *Toxoplasma*, the synthesis of dTMP is catalyzed by the bifunctional enzyme dihydrofolate reductase–thymidylate synthase (DHFR-TS) (fig. S13A) (*36*). This means that parasites couple the generation of dTMP, the rate-limiting step in DNA synthesis, to the reduction of dihydrofolate (DHF) to tetrahydrofolate (THF). To synthesize dTMP, *Toxoplasma* requires 5,10-methylene–THF (CH2-THF) and the ability to reduce DHF, a by-product of this reaction, back to THF—the form capable of carrying 1C units and that is necessary for regenerating CH2-THF (fig. S13A). Because ATF4 activation induced increased mito-1C cycle activity that uses 1C-carrying folates, we reasoned that ATF4 restricted *Toxoplasma* access to the folates required for dTMP synthesis and parasite growth. We thus assessed levels of folates in uninfected and infected cells using mass spectrometry. Infection caused a marked reduction in CH3-THF—the main circulating form of folate—and total

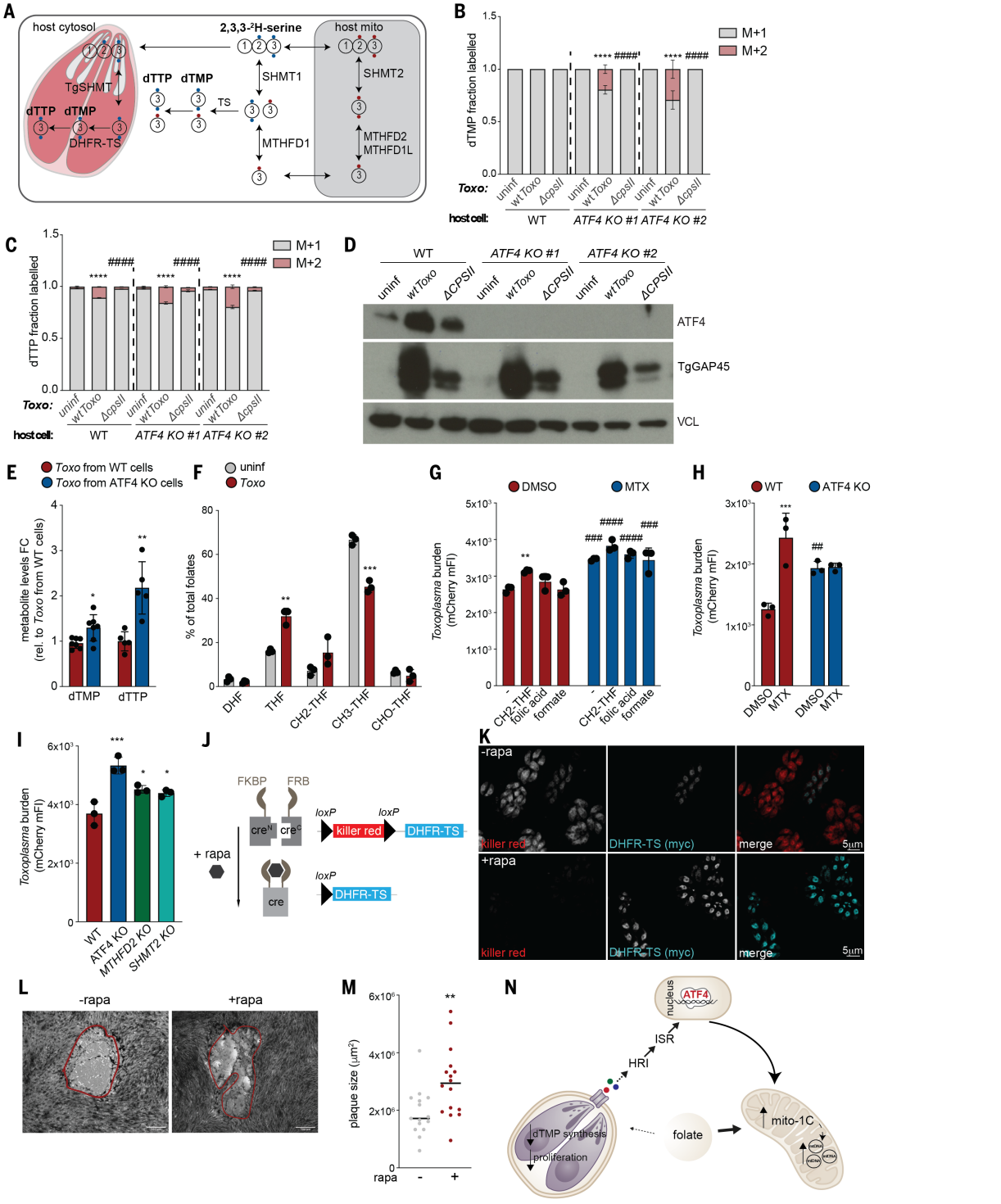

Fig. 3. Mito-1C metabolism restricts parasite dTMP synthesis and replication. (**A**) M+2 ^{2}H–labeled dTMP from cyto-1C (two blue dots), M+1 ^{2}H–labeled dTMP from mito-1C (one red dot). (**B** and **C**) Labeled dTMP and dTTP in WT and *ATF4* KO ES-2 cells uninfected (uninf) or infected (inf) with WT *Toxo* and Δ*cpsII* parasites. Data are means ± SDs of $n = 3$. ****$P < 0.0001$ for uninfected versus infected; ####$P < 0.0001$ for WT versus ATF4 KO clones by two-way ANOVA. (**D**) ATF4, VCL, and TgGAP45 in ES-2 cells as indicated. (**E**) dTMP levels in *Toxo* from WT and *ATF4* KO cells. Data are means ± SDs of $n = 7$. dTTP not detected in two cultures. *$P < 0.05$; **$P < 0.01$ for WT versus *ATF4* KO by unpaired *t* test. (**F**) Total folate species (percentage) in uninfected and infected ES-2 cells in MEM, normalized to cell number. DHF, dihydrofolate; CH2-THF, 5,10-methylene-tetrahydrofolate; CH3-THF, 5-methyl-tetrahydrofolate; CHO-THF, 10-formyl-tetrahydrofolate. Data are means ± SDs of $n = 4$. **$P < 0.01$; ***$P < 0.001$ for uninfected versus infected by multiple unpaired *t* test. (**G**) Infected WT ES-2 cells treated ± MTX (200 nM) and either 68 µM folic acid, 2 mM formate, or 25 µM CH3-THF, and analyzed by flow cytometry for *Toxoplasma* mCherry mFI. Data are means ± SEMs of $n = 3$. **$P < 0.001$ for untreated versus folate(s). ## $P < 0.001$; ####$P < 0.0001$ for DMSO versus MTX by two-way ANOVA. (**H**) ES-2 cells treated ± MTX (200 nM) and analyzed as in (G). Data are means ± SEMs of $n = 3$. ***$P < 0.001$ for DMSO versus MTX; ##$P < 0.01$ for WT versus ATF4 KO by two-way ANOVA analysis. (**I**) ES-2 cells as indicated, analyzed as in (G). [(B) to (I)] Harvested at 24 hpi. Data are means ± SEMs of $n = 3$. *$P < 0.05$; ***$P < 0.001$ by one-way ANOVA. (**J**) Inducible DHFR-TS system. (**K**) Immunofluorescence images of HFFs infected with Di-Cre parasites expressing killer-red (−rapa) or DHFR-TS (+rapa). (**L** and **M**) Plaque assays and quantification of Di-Cre parasites ± rapa (50 nM) in HFFs at 7 dpi. $n = 15$. **$P < 0.01$ by unpaired *t* test. (**N**) Model of ATF4-drived folate-based immunity.

folate levels, which indicates that 1C cycle activity is disrupted during infection and may restrict the availability of key folates (Fig. 3F and fig. S13, B and C). In fact, supplementation with CH2-THF, which is required for *Toxoplasma* dTMP synthesis but not its precursor folate nor derivative formate, promoted parasite growth regardless of host 1C activity (Fig. 3G and fig. S13A). Thus, ATF4 restricts *Toxoplasma* access to folates required for dTMP synthesis.

To test whether ATF4 restricted parasite growth in a folate-dependent manner, we treated WT and ATF4 KO cells with MTX. MTX is not taken up by *Toxoplasma* and thus does not inhibit *Toxoplasma* DHFR-TS (*37*). MTX treatment increased parasite proliferation in WT cells but not in ATF4 KO cells (Fig. 3H). Furthermore, impairing mito-1C metabolism through ablation of the ATF4 targets, MTHFD2 or SHMT2, or knock down of the reduced folate carrier SLC19A1 rendered cells permissive to *Toxoplasma* replication and increased dTMP levels (Fig. 3I and fig. S14) (*38*). Thus, ATF4 restricts parasite growth in a mito-1C–dependent manner.

If dTMP is rate-limiting for *Toxoplasma* growth, we expected that increasing its synthesis should promote *Toxoplasma* growth. To test this possibility, we turned to *Toxoplasma* DiCre (dimerizable Cre recombinase) parasites for the inducible overexpression of DHFR-TS (*39*). In these parasites, Cre recombinase is expressed as two inactive fragments that are fused to rapamycin binding proteins FRB and FKBP (Fig. 3J) (*39*). DiCre parasites were engineered to constitutively express killer red unless cre-mediated recombination occurs, in which case myc-tagged DHFR-TS is expressed (Fig. 3, J and K). In monolayers of human fibroblasts, rapamycin-induced DHFR-TS–expressing parasites formed significantly larger plaques compared with killer red–expressing parasites; notably, rapamycin did not affect the growth of WT parasites (Fig. 3, K to M, and fig. S13, D and E). Thus, dTMP synthesis is rate-limiting for *Toxoplasma* growth. Furthermore, ATF4 rewires mitochondrial metabolism to sequester 1C-carrying folates from *Toxoplasma* (Fig. 3N).

ATF4 activates a host-protective response in vivo

We next investigated whether ATF4 activated a host-protective response in vivo. To address this question, we first asked whether ATF4 was activated in a mouse model of *Toxoplasma* infection. We injected mice intraperitoneally with vehicle, tunicamycin, or mCherry-expressing *Toxoplasma* and measured the levels of ATF4 target transcripts in peritoneal exudate cells (PECs) isolated at 5 days postinfection (dpi), near the peak of acute infection (*40*). Infection drove increases in the levels of ATF4 targets *Atf3*, *Shmt2*, and *Mthfd2*, similar to our results in cultured cells (Fig. 2B and fig. S15, A to D). To determine whether the observed increases during infection were due to the ISR, mice were injected with vehicle or the ISR inhibitor ISRIB before infection and after every other day (Fig. 4A). ISRIB treatment blunted the induction of ATF4 targets *Atf3*, *Mthfd2*, and *Shmt2* levels observed in PECs isolated from infected mice (Fig. 4, B to D). We next tested whether blocking the ISR affected *Toxoplasma* proliferation in vivo. To this end, we examined the progression of *Toxoplasma* infection by examining peritoneal exudate of ISRIB- versus vehicle-treated mice at 3 dpi and 5 dpi. ISRIB treatment led to higher intracellular *Toxoplasma* levels as assessed at 3 dpi, which corresponded with an approximately threefold increase in extracellular parasites at 5 dpi (Fig. 4, E to L). Similar results were obtained at 5 dpi and 7 dpi with type II parasites (fig. S16). Thus, activation of the ISR restricts parasite proliferation in vivo.

Conclusions

We have shown that ATF4 effects a folate-based metabolic defense against *Toxoplasma* that involves increased activity of mito-1C metabolism. This raises several questions, beginning with how does HRI sense *Toxoplasma* effectors to activate the ISR? Both OMA1 and HRI were required for the secretion of effector proteins to trigger ATF4 induction. A *Toxoplasma* effector (or effectors) could thus directly activate OMA1 or induce a mitochondrial stress that drives OMA1 cleavage of DELE1 and its subsequent activation of HRI in the cytosol.

How is mito-1C metabolism host protective? Although *Toxoplasma* is capable of folate synthesis, it also scavenges exogenous folate, which suggests that this metabolite is required in abundance for parasite proliferation (*41*). Unlike in mammals, in *Toxoplasma*, folate availability is tied to the production of dTTP, the rate-limiting step in DNA synthesis. Because *Toxoplasma* is deficient for thymidine salvage, it likely that the parasite depends on DHFR-TS for dTTP synthesis and thus DNA replication (*12*). Compartmentalization of 1C metabolism processes within the mitochondria might block parasite access to the 1C-carrying folates required for dTMP synthesis. Indeed, supplementation with CH2-THF increased parasite growth, whereas the loss of ATF4 led to an increase in parasite dTMP synthesis and proliferation. Furthermore, impairing host use of folate for 1C metabolism processes using MTX, a drug that is widely used in anticancer therapies, led to increased growth in WT cells but not ATF4 KO cells. Although these results support a role for mito-1C metabolism in limiting parasite access to folate, we cannot exclude the possibility that ATF4 activates other 1C effectors that contribute to *Toxoplasma* restriction.

Can enhancing host mito-1C suppress the growth of *Toxoplasma* in vivo or other human pathogens that require folate for dTMP synthesis, such as *Plasmodium falciparum*, the causative agent of malaria? Conversely, does increasing folate availability through dietary supplementation without a parallel modulation of mito-1C metabolism enhance replication of these pathogens? High dietary folate increased parasite replication in a murine malaria model, and increased folate concentrations were associated with an increase in malaria infection in humans (*42*, *43*). These observations hint at a key role for folate competition in certain host-pathogen interactions.

Finally, do mitochondria more broadly compete with intracellular pathogens for metabolites? Emerging evidence shows that the microbiota protect against gut infections by consuming nutrients also used by pathogens (*44*). Analogously, mitochondria may contribute to cellular resistance to infection by competing with intracellular pathogens for shared cytosolic resources beyond 1C-carrying folates, such as nucleotides. Although the demand to replicate a single 16-kb mitochondrial genome may seem minimal, each of the estimated ~880 mitochondria per cell contains on average three genomes—adding up to ~42 Mb of total mtDNA (*1*). During chronic mito-1C activation resulting from mtDNA deficiency, mitochondria even limited the availability of nucleotides for nuclear DNA replication (*9*, *10*).

Our discovery of ATF4 as an effector of a folate-driven metabolic defense response reveals a role for mitochondrial metabolism in defense against the human pathogen *Toxoplasma*. These findings establish a framework for exploring the role of folate metabolism during infection and noncanonical mitochondrial defenses against intracellular pathogens.

Materials and methods

Cell culture and cell lines

HeLa adenocarcinoma cells, ES-2 ovary clear cell carcinoma, and human foreskin fibroblasts (HFFs) were obtained from ATCC (CCL-2, CRL-1978, and SCRC-1041, respectively); ES-2 cells stably expressing pMXs-eGFP-OMP25 (referred to as OMM-GFP; Addgene no. 83356) were generated through lentiviral transduction. Unless stated otherwise, cell lines were cultured in Dulbecco's modified Eagle's medium (DMEM) containing 10% heat-inactivated fetal bovine serum (FBS) and maintained at 37°C and 5% CO_2. AN3-12 mESCs were obtained from J. Penninger (*45*) and were cultured in DMEM high glucose supplemented with glutamine, 15% FBS, penicillin/streptomycin, nonessential amino acids, sodium pyruvate, β-mercaptoethanol, and leukemia inhibitory factor (LIF), as previously described (*46*). *ATF4* KO ES-2s were cultured in DMEM high glucose, 10% FBS, β-mercaptoethanol, and nonessential amino acids. Cells were tested every 2 weeks for *Mycoplasma* infection by means of polymerase chain reaction (PCR). Immortalized WT and *Oma1* KO murine embryonic fibroblasts (MEFs)

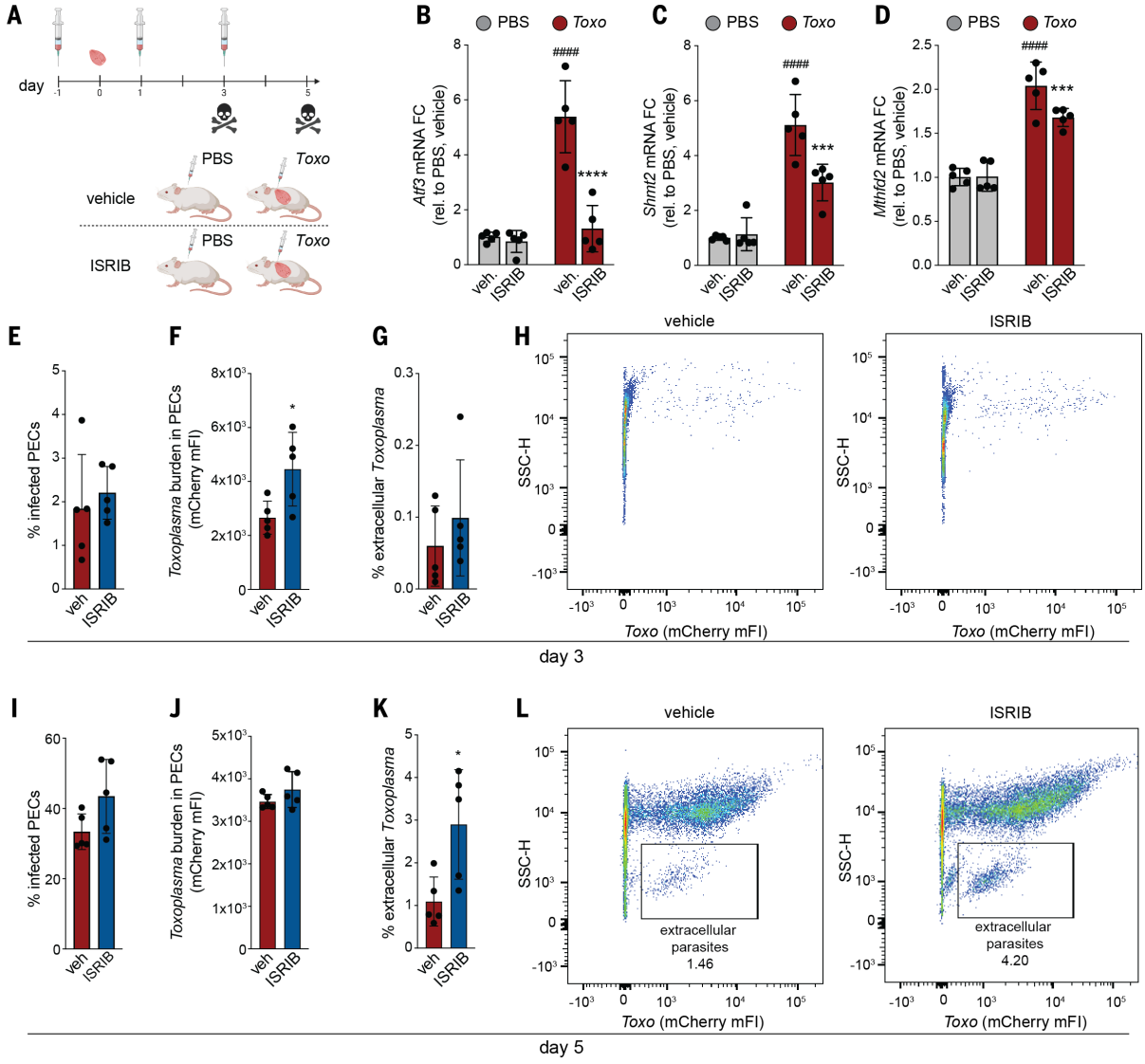

Fig. 4. ATF4 protects against *Toxoplasma* infection in vivo. (**A**) Schematic of infection and ISRIB administration. Mice ($n = 5$) where injected with ISRIB 1 day before infection with 50 tachyzoites or 1x PBS injection and every other day after. (**B** to **D**) PECs were isolated from mice treated as in (A) at 5 dpi and analyzed for the indicated ATF4 target genes by qPCR. Transcripts were normalized to *Hprt* and relative to uninfected PECs mice ($n = 5$). ***$P < 0.001$; ****$P < 0.0001$ for vehicle versus ISRIB. #$P < 0.05$; ###$P < 0.001$; ###$P < 0.0001$ for PBS versus *Toxoplasma* by means of two-way ANOVA analysis. (**E** to **G**) Peritoneal exudate was isolated 3 dpi from mice treated as in (A) and analyzed by means of flow cytometry for (E) percentage of infected PECS (E), *Toxoplasma* parasite burden in infected PECs (mCherry mFI) (F), percentage of extracellular parasites (G). Data are means ± SDs of $n = 5$ mice. *$P < 0.05$ by unpaired *t* test analysis (vehicle versus ISRIB). (**H**) Representative scatter plots of peritoneal exudate isolated from mice treated as in (A). (**I** to **L**) Same as (E) to (H), except at 5 dpi.

were obtained from T. Langer's laboratory and cultured in DMEM containing 10% heat-inactivated FBS (*47*).

Parasite culture and strains

T. gondii parasites of the type I RHΔ*ku80:mCherry*+ [previously described in (*48*)]; type I RHΔ*myr1* parasites and RHΔ*myr1::Myr1* were provided by M. Treeck, (Gulbenkian Institute) (*49*); type I RHΔcpsII:mCherry parasites were provided by D. Bzik (Dartmouth Geisel School of Medicine) (*33*). Type II Me49Δmyr1 *T. gondii* parasites were provided by J. Boothroyd (Stanford School of Medicine). Parasites were maintained by serial passage in HFF monolayers in complete DMEM (cDMEM). RHΔ*cpsII*: mCherry were maintained by serial passage in HFF monolayers in cDMEM supplemented with 0.2 mM uracil. DiCre parasites were provided by M. Meissner (*39*) Generation of DiCre type I parasites inducibly expressing DHFR-TS: To remove/insert needed restriction sites, KillerRed was amplified from the previously generated loxP-KillerRed-loxP-ATrX2 and reinserted between EcoRI and NsiI to remove the AvrII site and add an additional MfeI site (*50*). TGGT1_249180 was amplified from *Toxoplasma* cDNA and was cloned in between MfeI and AvrII sites replacing ATrX2. TUB8-loxP-KillerRed-loxP was amplified from the original loxP-KillerRed-loxP-ATrX2 vector and reinserted between ApaI and MfeI sites. RH DiCre parasites were transfected with 50 μg of the resulting plasmid. Positive transfectants were selected with mycophenolic acid (25 mg/ml) and xanthine (50 mg/ml) and cloned out. Clonal line was verified with immunofluorescence assay.

Plaque assay

One hundred of either type I RHΔ*ku80:mCherry*+ or RH DiCre: loxP-KillerRed-loxP-DHFR-TS were added to monolayers of confluent HFFs ± rapa (50 nM). At 7 dpi, monolayers were incubated with 100% MeOH for 1 min, followed by 20 min with crystal violet.

CRISPR-Cas9–mediated gene editing

Guide sequences used can be found in table S3. ATF4, MTHFD2, SHMT2 KO cells, and SLC19A1 knockdown (KD) cells were generated using CRISPR-Cas9–mediated gene editing through lentiviral transductions into the pLenti CRISPRv2 (Addgene no. 5296). HRI and GCN2 KO were generated using CRISPR-Cas9–mediated gene editing with the pLenti CRISPRv2 EIF2AK1/HRI (Addgene no. 218529) and the pLenti CRISPRv2 EIF2AK1/HRI (Addgene no. 218528), respectively. For production of lentiviral particles, 293T human embryonic kidney (HEK) cells were transduced using the X-tremeGENE 9 DNA Transfection Reagent (Roche) with 1 μg psPAX2 packaging vector (Addgene no. 12260), 0.3 μg pCMV-VSVG envelope vector (Addgene no. 8454) and 1 μg of the relevant plasmid of interest. The next day, the medium was exchanged, and 2 days posttransfection, the virus-containing supernatant was filtered with a 0.45 μM filter and supplemented with polybrene to a final concentration of 5 μg/ml. Virus-containing medium was added to the indicated cell lines for 24 hours and puromycin selection (3 μg/ml) was started after an additional 24 to 48 hours. Polyclonal cultures and individual clones were validated by immunoblotting or quantitative PCR (qPCR).

The eIF2α S51A substitution was engineered in AN3-12 cells using CRISPR-Cas9 technology, as described previously (*51*). DNA template sequences for small guide RNAs were designed online (http://crispor.org) and cloned into the Cas9-mCherry expressing plasmid (Addgene no. 21852). Corresponding guide and Cas9 expressing plasmids were cotransfected with a single-stranded DNA repair template (Integrated DNA Technologies), using Lipofectamine 2000 (Thermo Fisher Scientific) according to the manufacturer's instructions. mCherry-positive cells were singled in 96-well plates using FACSAria Fusion sorter and subjected to genotyping. DNA was extracted (DNA extraction solution, Epicentre Biotechnologies) and edited regions were specifically amplified by PCR. The PCR product was subjected to a restriction digest to identify positive clones. These clones have a gain of BglII restriction site due to a mutation in the repair template. Sanger sequencing was performed at Eurofins Genomics GmbH (Ebersberg, Germany). Positive clones were sorted before further experiments.

MTHFD2 and *ATF4* overexpression

Human *MTHFD2* cDNA amplified from ES-2 cells was cloned into pMSCV PIG (puro IRES GFP; Addgene no. 21654) at the XhoI and EcoRI sites. After production of viral particles and transduction, puromycin selected ES-2 cells were sorted for green fluorescent protein (GFP) expression using flow cytometry using BD FACSDiva software. The pTRIPZ-EGFP, pTRIPZ-ATF4, and pTRIPZ-ATF4DBD plasmids were a gift from B. D. Manning (Harvard T.H. Chan Public School of Health) (*25*). HEK-293T cells were cotransfected with the given pTRIPZ plasmid, the VSV-G envelope plasmid, and the ΔVPR lentiviral packaging plasmid using XTremeGene 9 Transfection Reagent (Roche). After viral production and transduction, cells were selected for puromycin. cDNA expression was induced with 1 μg/ml of doxycycline 24 hours before assays were conducted.

Flow cytometry analysis

To assess mitochondrial mass, monolayers of ES-2 cells expressing OMM-GFP were rinsed with phosphate-buffered saline (PBS), trypsinized, and fixed in 2% paraformaldehyde (PFA) in fluorescence-activated cell sorting (FACS) buffer (3% FBS in 1XPBS) for 10 min. After a brief spin, cells were resuspended in FACS buffer, and 10,000 events were analyzed on a BD LSRFortessa for GFP median fluorescence intensity (mFI) using BD FACSDiva software.

To assess parasite proliferation, monolayers of ES-2 cells infected with red fluorescent protein (RFP) expression parasites (RHΔku80:mCherry+) were rinsed with PBS, trypsinized, and fixed in 2% PFA in FACS buffer (3% FBS in PBS) for 10 min. After a brief spin, cells were resuspended in FACS buffer and 10,000 events analyzed on a LSRFortessa and the RFP mFI using BD FACSDiva software.

qPCR for mtDNA analysis

For mtDNA measurements, genomic DNA was isolated from cell pellets that were washed once with 1x PBS using the Blood and Tissue DNA extraction kit (Qiagen no. 69504). DNA was quantified by nanodrop. 50 ng of genomic DNA were amplified using PowerSYBR Green PCR Master Mix (Thermo Fisher Scientific no. A25742). Reactions were performed in 384 Hard-Shell microplates (BioRAD no. HSP3801) sealed with adhesive qPCR seal (Roche) in a and Bio-Rad Real-Time PCR system with the following cycler program: 95°C for 7 min followed by 35 cycles of 95°C for 10 s, 60°C for 30 s. Dissociation curves confirmed single PCR products, and signals were analyzed within the linear amplification range. Each sample was run in triplicate. Relative mtDNA copy number changes were calculated using the comparative ΔΔCt method (*52*) by determining Ct threshold values and using equations ΔΔCt = (Ct_mtDNA − Ct_control) at $t(n)$ − (Ct_mtDNA − Ct_control) at $t(0)$ and $2^{-\Delta\Delta Ct}$. The primers *DLOOP*, *mt-ND1*, *mt-CYTB*, *mt-ND6*, and *mt-COX1* as mitochondrial genes and *RUNX2* and *ACTB* as nuclear DNA controls can be found in table S3.

qPCR for mRNA analysis

For analysis of mRNA expression, RNA purification was performed using TriZol (Thermo Fischer Scientific; no. 15596018) according to the manufacturer's instructions. The reverse transcription (RT) reaction was done using 1 μg of RNA for each sample into cDNA using SuperScript VILO Master Mix (Thermo Fischer Scientific; no. 11755050). For each reaction, 2.5 ng of cDNA were amplified using PowerSYBR Green PCR Master Mix and Bio-Rad Real-Time PCR system. For each independent sample, RT-qPCR was performed in technical triplicates. The primer sequences used in this study can be found in table S3. Expression levels were calculated by the delta delta ct methods as described above, for which *ACTB* and *HPRT* was used as a control. Relative fold changes were calculated using the comparative ΔΔCt method (*52*) by determining Ct threshold values and using equations ΔΔCt = (Ct_targetgene − Ct_control) at $t(n)$ − (Ct_targetgene − Ct_control) at $t(0)$ and $2^{-\Delta\Delta Ct}$.

Immunoblotting and antibodies

Whole cells were harvested in chilled lysis buffer [50 mM Hepes-KOH pH 7.4, 40 mM NaCl, 2 mM EDTA, 1.5 mM NaVO4, 50 mM NaF, 10 mM NaPyrophosphate, 10 mM, NaBetaGlycerophosphate (disodium salt pentahydrate), 1% Triton X-100] and lysed for 30 min on ice. Lysates were subsequently centrifuged at 10 min at 14,000*g* at 4°C and the clarified supernatant was transferred into a fresh tube with 5X SDS for a final volume of 1X SDS. After SDS–polyacrylamide gel electrophoresis (SDS-PAGE) and gel transfer, membranes were blocked with tris-buffered saline (TBS)–0.05% Tween 20 (TBS-T) and 5% milk and the primary antibodies were incubated overnight. After incubation, blots were washed three times in TBS-T and then incubated with horseradish peroxidase (HRP)–conjugated anti-mouse immunoglobulin G (IgG) (CST no. 7076) or anti-rabbit IgG (CST no. 7074) at a 1:4000 dilution for 45 min and developed using a chemiluminescence system (Pierce ECL Western Blotting Substrate or Pierce SuperSignal West Atto Ultimate Sensitivity Substrate; Thermo Fisher Scientific). The following antibodies were used: ATF4 (CST no. 11815), VCL (CST no. 4650), pS6K (CST no. 97596), TUBA (Proteintech 66031-1-Ig), MTHFD2 (CST no. 41377), SHMT2 (CST no. 33443), MTHFD1L (Invitrogen no. PA5-100158), MTHFD1 (Sigma no. HPA015006), phospho-eIF2a (Ser51) (CST no. 9721), ACTB (CST no. 4970), OMA1 (Santa Cruz no. 515788), BIP (CST no. 3183), ATF6 (CST no. 65880), c-Myc (CST no. 18583), anti-DNA (EMD Millipore no. CBL186), GCN2 (CST no. 3302); GCN2 (abcam ab134053), TgGra45 (D. Soldati; University of Geneva), TgMAF1, and TgGRA7 (J. Boothroyd; Stanford University) antisera.

Live-cell imaging

Cells were plated on 6-well CELLview glass bottom cell culture dishes (Greiner Bio-One). The following morning, cells were infected with RH

mcherry expressing *Toxoplasma*. After 24 hours, cells were incubated with MitoTracker Deep Red (Thermo Fisher Scientific, 50 nM) and Picogreen 1ug/ml for 30 min and imaged using an Olympus IXplore SpinSR 50 mm spinning disk confocal microscope. Live cell imaging was performed in cDMEM with incubation at 37°C and 5% CO_2. All images were taken with a 100X/1.35 silicon oil objective and excitation with either 488, 561, or 640 laser lines, using ORCA-Flash4.0 cameras (Hamatsu), and cellSens Software.

EdU replication assay

EdU incorporation was detected using a Click-iT EdU AlexaFluor 488 labeling kit according to the manufacturer's instructions (C10637, Thermo Fisher Scientific) with minor deviations. For the EdU-labeling experiments, cells were processed for immunofluorescence analysis and stained with anti-DNA antibody.

Immunofluorescence assay

Cells were fixed using growth medium containing 3.7% PFA for 15 min at 37°C and permeabilized using 0.1% Triton X-100 in PBS for 20 min. After incubation with 3% bovine serum albumin (BSA) for 1 hour, cells were incubated with primary antibodies (ATF4, 1:250) overnight. The next day, cells were washed 3X with 1X PBS (5 min each) before incubation with secondary antibodies for 1 hour in the dark at room temperature. After secondary incubation, cells were washed 3X with 1X PBS. All images were taken with a 100X/1.35 silicon oil objective and excitation with either 405, 488, or 561 laser lines, using ORCA-Flash4.0 cameras (Hamatsu), and cellSens Software.

Proteomics sample preparation

As previously described (*53*), for preparing samples from immunoprecipitation, on-beads digestion was performed to elute the proteins off the beads. Before adding the elution buffer, the beads were washed with detergent-free buffer (50 mM Tris-HCl pH7.5) four times to remove any detergents used previously. Then 100 µl of the elution buffer [5 ng/µl trypsin, 50 mM Tris-HCl pH7.5, 1 mM Tris(2-carboxyethyl)phosphine, 5 mM chloroacetamide] was added to the beads and incubated at room temperature by vortexing from time to time, or rotating on a rotator. After 30 min, the supernatant was transferred to a 0.5 ml tube and incubated at 37°C overnight to ensure a complete tryptic digest. The digestion was stopped in the next morning by adding formic acid to the final concentration of 1%. The resulted peptides were cleaned with homemade StageTips. Alternatively, 4 µg of the eluted peptides were dried out and reconstituted in 9 µl of 0.1 M TEAB and labeled with tandem mass tags (TMT10plex, Thermo Fisher Scientific cat. no. 90110). Labeling was carried out according to manufacturer's instruction with the following changes: 0.5 mg of TMT10plex reagent was resuspended with 33 µl of anhydrous acetonitrile (ACN). Seven microliters of TMT10plex reagent in ACN was added to 9 µl of clean peptide in 0.1 M TEAB. The final ACN concentration was 43.75% and the ratio of peptides to TMT10plex reagent was 1:20. After 60 min of incubation the reaction was quenched with 2 µl of 5% hydroxylamine. Labeled peptides were pooled, dried, resuspended in 200 µl of 0.1% formic acid (FA), split into two equal parts, and desalted using homemade STAGE tips. One of the two parts was fractionated on a 1 mm × 150 mm ACQUITY column, packed with 130 Å, 1.7 µm C18 particles (Waters cat. no. SKU: 186006935), using an Ultimate 3000 UHPLC (Thermo Fisher Scientific). Peptides were separated at a flow of 30 µl/min with an 88 min segmented gradient from 1% to 50% buffer B for 85 min and from 50% to 95% buffer B for 3 min; buffer A was 5% ACN, 10 mM ammonium bicarbonate (ABC); buffer B was 80% ACN, 10 mM ABC. Fractions were collected every 3 min, pooled in two passes (1 + 17, 2 + 18 … etc.), and dried in a vacuum centrifuge (Eppendorf).

Liquid chromatography–tandem mass spectrometry analysis

For label-free quantification, peptides were separated on a 75 cm, 75 µm internal diameter Acclaim PepMap analytical column (Thermo Fisher Scientific, cat. no. 164939) using an EASY-nLC 1200 (Thermo Fisher Scientific). The column was maintained at 50°C. Buffers A and B were 0.1% FA in water and 0.1% FA in 80% ACN. Peptides derived from whole cells were separated on a segmented gradient from 6% to 31% buffer B for 230 min and from 31% to 50% buffer B for 10 min at 250 nl/min. Peptides derived from enriched mitochondria were separated on a segmented gradient from 6% to 31% buffer B for 110 min and from 31% to 50% buffer B for 10 min at 250 nl/min. Eluting peptides were analyzed on a QExactive HF mass spectrometer (Thermo Fisher Scientific). Peptide precursor m/z measurements were carried out at 60,000 resolution in the 300 to 1800 m/z range. The top 10 most intense precursors with charge state from 2 to 7 only were selected for higher-energy collisional dissociation (HCD) fragmentation using 25% normalized collision energy. The m/z values of the peptide fragments were measured at 30,000 resolution using a minimum automatic gain control (AGC) target of 10,000 and 55 ms maximum injection time. Upon fragmentation, precursors were put on a dynamic exclusion list for 45 s. TMT labeled peptides were separated on a 50 cm, 75 µm Acclaim PepMap column (Thermo Fisher Scientific, product no. 164942) and analyzed on a Orbitrap Lumos Tribrid mass spectrometer (Thermo Fisher Scientific) equipped with a high-field asymmetric waveform ion mobility spectrometry (FAIMS) device (Thermo Fisher Scientific). The FAIMS device was operated in two compensation voltages, −50 V and −70 V. Synchronous precursor selection based MS3 was used for the acquisition of the TMT10plex reporter ion signals. Peptide separations were performed on an EASY-nLC1200 using a 90 min linear gradient from 6% to 31% buffer; buffer A was 0.1% FA, buffer B was 0.1% FA, 80% ACN. The analytical column was operated at 50°C. Raw files were split based on the FAIMS compensation voltage using FreeStyle (Thermo Fisher Scientific).

Protein identification and quantification

Label-free quantification raw data were analyzed with MaxQuant version 1.6.0.13 (*54*) using the integrated Andromeda search engine (*55*). Peptide fragmentation spectra were searched against the canonical sequences of the human reference proteome, proteome ID UP000000589, and *Toxoplasma* reference proteome, proteome ID UP000005641, downloaded from UniProt. Methionine oxidation and protein N-terminal acetylation were set as variable modifications; cysteine carbamidomethylation was set as fixed modification. The digestion parameters were set to "specific" and "Trypsin/P," The minimum number of peptides and razor peptides for protein identification was 1; the minimum number of unique peptides was 0. Protein identification was performed at a peptide spectrum matches and protein false discovery rate (FDR) of 0.01. The "second peptide" option was on. Successful identifications were transferred between the different raw files using the "Match between runs" option. Exploratory data analysis and visualization was done using tidyverse in R (*56*, *57*). TMT data were analyzed using MaxQuant, version 1.6.17.0. The isotope purity correction factors, provided by the manufacturer, were included in the analysis. Differential expression analysis was performed using limma, in R (*58*). Volcano plots of WC and mitoIP proteins generated using Flaski (*59*). The mass spectrometry proteomics data have been deposited to the ProteomeXchange Consortium via the PRIDE (*60*) partner repository with the dataset identifier PXD064338.

Stable isotope labeling with L-glutamine-$^{15}N_2$

Two million ES-2 cells were seeded in a 10-cm dishes in DMEM containing 10% FBS and cultured for 16 hours. The next day, cells were washed once with 1x PBS, and the medium was replaced with glutamine-free DMEM containing 10% dFBS and 2 mM L-glutamine-$^{15}N_2$ (Cambridge Isotope Laboratories no. NLM-1328-0.25) for 24 hours. The following day, cells were either mock-infected or infected with *Toxoplasma* (RHΔ*ku80:mCherry*+) at a multiplicity of infection (MOI) of 4 in cDMEM

media in the absence of labeled L-glutamine-$^{15}N_2$ for 24 hpi. Parasites were isolated from infected monolayers and processed for metabolomics analysis.

Stable isotope labeling with L-serine-$^{13}C_3$

Five hundred thousand cells were seeded in a 6-well plate in DMEM containing 10% FBS. The following day, cells were either mock-infected or infected with *Toxoplasma* (RHΔ*ku80:mCherry*+) at an MOI of 4. After 12 hpi, the medium was replaced with serine-free DMEM containing 10% dFBS and 0.2 mM L-serine-$^{13}C_3$ (Cambridge Isotope Laboratories no. NLM-201595-68-8) for 10 hours. Mock infected and infected cells were then processed for metabolomics analysis.

Stable isotope labeling with 2,3,3-^{2}H-serine

WT and ATF4 KO ES-2 cells (500,000) were seeded in DMEM containing 10% FBS and cultured for 16 hours. The following day cells were washed once with PBS, and either mock-infected or infected with *Toxoplasma* strains RHΔ*ku80:mCherry* and RHΔ*cpsII:mCherry* at an MOI of 4 and 6, respectively, due to the lack of proliferation of RHΔ*cpsII:mCherry* parasites in minimal essential media (MEM) containing 10% dialyzed FBS, 2 mM L-glutamine and 0.2 mM [2,3,3-^{2}H] serine isotopolog (Cambridge Isotope Laboratories no. DLM-1073-1). At 24 hpi, cells were harvested for metabolomics analysis.

Toxoplasma isolation for metabolite extraction

Four million ES-2 cells were seeded in 10-cm dishes overnight and infected with *Toxoplasma* at an MOI of 4 the subsequent morning. At 24 hpi, infected cells were collected by scraping and washed with ice-cold Dulbecco's phosphate-buffered saline (DPBS) twice. All subsequent steps were performed at 4°C. Infected cells were resuspended in DPBS with phosphatase and proteases inhibitors and homogenized by passing 10 times through a 27½ G needle. The homogenates were spun down at 1500 rpm for 5 min to remove cell debris and filtered with a 5 μM filter. The final pellets containing parasite-enriched fractions were resuspended in cold metabolite extraction buffer. The purity of the *Toxoplasma*-enriched fractions was assessed by SDS-PAGE and immunoblot.

Extraction of polar metabolites

Cells were washed twice with 75 mM of ammonium carbonate pH = 7.4, and the plates were frozen in liquid nitrogen and stored at −80°C until metabolite extraction. For metabolite extraction, 1 ml of −20°C cold extraction buffer [HPLC-grade ultrapure 40% MeOH, 40% ACN, 20% water, containing 250 nM $^{13}C^{15}N$ Amino acids (Cambridge Isotope Laboratories MSK_A2-1.2), 100 ng/ml of $^{13}C_{10}$ ATP (Sigma 710695), 100 ng/ml $^{15}N_5$ adenosine 5′-diphosphate (ADP) (Sigma 741167), 100 ng/ml $^{13}C_{10}{}^{15}N_5$ AMP (Sigma 650676) and 20 ng/ml citric acid $^{2}H_4$ (Sigma 741167) as isotope-labeled internal standards] was added to each well of the frozen plate. The cells were then scraped, transferred to a new tube, and dissolved by sonication followed by an incubation for 30 min at 1500 rpm at 4°C. The metabolite-containing supernatant was cleared by centrifugation at 20,000*g* for 10 min and subsequently transferred to a speedvac concentrator to fully evaporate the extraction buffer and stored at −80°C until further analysis. The remaining protein pellet from the extraction was used to determine protein concentration of the sample.

Anion-exchange chromatography–mass spectrometry for the analysis of anionic metabolites

Extracted metabolites were resuspended in 150 μl of ultraperformance liquid chromatography–mass spectrometry (UPLC-MS)–grade water (Biosolve), of which 100 μl were transferred to polypropylene autosampler vials (Chromatography Accessories Trott, Germany) before anion-exchange chromatography–mass spectrometry (AEX-MS) analysis. The samples were analyzed using a Dionex ionchromatography system (Integrion Thermo Fisher Scientific), as described previously (*61*).

In brief, 5 μl of the resuspended polar metabolite extract were injected in push-partial mode, using an overfill factor of 1, onto a Dionex IonPac AS11-HC column (2 mm × 250 mm, 4 μm particle size, Thermo Fisher Scientific) equipped with a Dionex IonPac AG11-HC guard column (2 mm × 50 mm, 4 μm, Thermo Fisher Scientific). The column temperature was held at 30°C, and the auto sampler temperature was set to 6°C. A potassium hydroxide gradient was generated using a potassium hydroxide cartridge (Eluent Generator, Thermo Fisher Scientific), which was supplied with deionized water (Milli-Q IQ 7000, Millipore). The metabolite separation was carried at a flow rate of 380 μl/min, applying the following gradient conditions: 0 to 3 min, 10 mM KOH; 3 to 12 min, 10 to 50 mM KOH; 12 to 19 min, 50 to 100 mM KOH; 19 to 22 min, 100 mM KOH, 22 to 23 min, 100 to 10 mM KOH. The column was re-equilibrated at 10 mM for 3 min.

For the analysis of metabolic pool sizes, the eluting compounds were detected in negative ion mode using full scan measurements in the mass range m/z 77 to 770 on a Q-Exactive HF high resolution MS (Thermo Fisher Scientific). The heated electrospray ionization (ESI) source settings of the mass spectrometer were: spray voltage 3.2 kV, capillary temperature was set to 300°C, sheath gas flow 50 AU (arbitrary units), aux gas flow 20 AU at a temperature of 330°C, and a sweep gas flow of 2 AU. The S-lens was set to a value of 60. The LC-MS data analysis was performed using the TraceFinder software (version 5.1, Thermo Fisher Scientific). The identity of each compound was validated by authentic reference compounds, which were measured at the beginning and the end of the sequence. For data analysis, the area of the deprotonated $[M\text{-}H^+]^{-1}$ or doubly deprotonated $[M\text{-}^{2}H]^{-2}$ isotopolog mass peaks of every required compound were extracted and integrated using a mass accuracy <3 parts per million (ppm) and a retention time tolerance of <0.05 min as compared with the independently measured reference compounds. If no independent ^{12}C experiments were carried out, where the pool size is determined from the obtained peak area of the ^{12}C monoisotopolog, the pool size determination was carried out by summing up the peak areas of all detectable isotopologs per compound. These areas were then normalized, as performed for untraced ^{12}C experiments, to the internal standards, which were added to the extraction buffer, followed by a normalization to the protein content or the cell number of the analyzed samples. The relative isotope distribution of each isotopolog was calculated from the proportion of the peak area of each isotopolog toward the sum of all detectable isotopologs. Natural abundance of the measured isotopolog was corrected using the AccuCor package (*62*).

Sample preparation for folate detection

Cell extracts were prepared by homogenization of cell pellets by sonication in buffer containing 20 mM ammonia acetate, 0.1% ascorbic acid, 0.1% citric acid and 100 mM dithiothreitol at pH 7. Protein was removed by precipitation by addition of two volumes of ACN and centrifugation (12,000*g* at 4°C). Supernatants were transferred, lyophilized, stored at −80°C and resuspended in dH_2O before analysis. Folate analysis was carried out by ultraperformance liquid chromatography–tandem mass spectrometry (UPLC-MS/MS), as described previously (*63*, *64*). Lyophilized samples were resuspended in 25 μl water (milli-Q) and centrifuged for 5 min at 12,000*g* at 4°C. Metabolites were resolved by reversed-phase UPLC (Acquity UPLC BEH C18 column, Waters Corporation, UK). Solvents for UPLC were as follows: buffer A, 5% methanol, 95% Milli-Q water, and 5 mM dimethylhexylamine at pH 8.0; buffer B, 100% methanol and 5 mM dimethylhexylamine. The column was equilibrated with 95% buffer A:5% buffer B. The sample injection volume was 20 μl. The UPLC protocol consisted of 95% buffer A:5% buffer B for 1 min, followed by a gradient of 5 to 60% buffer B over 9 min and then 100% buffer B for 6 min before re-equilibration for 4 min. The metabolites were eluted at a flow rate of 500 μl/min and the wash step with 100% buffer B was at flow rate of 600 μl/min. The UPLC was coupled to a XEVO-TQS mass spectrometer (Waters Corporation) operating in negative-ion mode using the following settings: capillary

2.5 kV, source temperature 150°C, desolvation temperature 600°C, cone gas flow rate 150 liters/hour, and desolvation gas flow rate 1200 liters/hour. Folates were measured by multiple reaction monitoring with optimized cone voltage and collision energy for precursor and product ions (*63*, *65*). Peak areas were analyzed by TargetLynx software (Waters Corporation, UK).

Infection of mice with *Toxoplasma*

Six- to 8-week-old female C57BL/6 J mice were obtained from Charles River. All animal work was approved by local authorities (Landesamt für Natur, Umwelt und Verbraucherschutz Nordrhein-Westfalen, Germany LANUV 81-02.04.2020.A467), and animal procedures were carried out in accordance with European, national, and institutional guidelines and according to good practice of animal handling. Mice were maintained at the Max Planck Institute for Biology of Ageing with 12-hour light cycle and regular chow diet. When mice were 8 to 10 weeks old, after serial dilution in PBS, 50 RHΔ*ku80:mCherry* tachyzoites and 200 Me49:mScarlet tachyzoites were injected intraperitoneally. Tunicamycin (Sigma, no. 11089-65-9) was dissolved in 150 mM sucrose in PBS and injected intraperitoneally at 1 mg/kg, as previously described (*66*, *67*). ISRIB (Sigma, no. 1597403-47-8) was dissolved in dimethyl sulfoxide (DMSO) at 6.25 mg/ml and subsequently diluted in PBS at 0.25 mg/ml and delivered intraperitoneally to mice at a dose of 2.5 mg/kg per day every other day in the morning, as previously described (*68*). For vehicle, DMSO was diluted in PBS.

PEC isolation

Euthanized C57BL/6 J mice ($n = 5$ per treatment) were injected with 6 ml cold 1× PBS using a 26-gauge needle. Mice were palpated for 1 to 2 min, after which fluid contents were aspirated out of the peritoneum. Content was spun down at 1000 rpm for 5 min, washed, and resuspended in DMEM to a concentration of 2×10^6 per ml. Samples were then pellet and snap frozen in liquid nitrogen until further downstream analysis was performed accordingly.

Statistical analysis

All statistical analyses were performed using GraphPad Prism 9. A one-way analysis of variance (ANOVA) was used to compare means across multiple groups when testing an independent variable. A two-way ANOVA was used when testing the effects of two independent variables. Comparisons between two independent groups were performed using unpaired *t* tests, and multiple unpaired *t* tests were used when comparing several independent variables between two groups. To correct for multiple comparisons, the FDR was controlled using the two-stage step-up method of Benjamini, Krieger, and Yekutieli. The statistical test used for each analysis is specified in the figure legends.

Newly created materials

Newly created cell lines, parasite lines, and plasmids available upon request.

REFERENCES AND NOTES

1. J. W. Posakony, J. M. England, G. Attardi, Mitochondrial growth and division during the cell cycle in HeLa cells. *J. Cell Biol.* **74**, 468–491 (1977). doi: 10.1083/jcb.74.2.468; pmid: 885911
2. L. Pernas, L. Scorrano, Mito-Morphosis: Mitochondrial Fusion, Fission, and Cristae Remodeling as Key Mediators of Cellular Function. *Annu. Rev. Physiol.* **78**, 505–531 (2016). doi: 10.1146/annurev-physiol-021115-105011; pmid: 26667075
3. J. B. Spinelli, M. C. Haigis, The multifaceted contributions of mitochondria to cellular metabolism. *Nat. Cell Biol.* **20**, 745–754 (2018). doi: 10.1038/s41556-018-0124-1; pmid: 29950572
4. L. Pernas, C. Bean, J. C. Boothroyd, L. Scorrano, Mitochondria Restrict Growth of the Intracellular Parasite Toxoplasma gondii by Limiting Its Uptake of Fatty Acids. *Cell Metab.* **27**, 886–897.e4 (2018). doi: 10.1016/j.cmet.2018.02.018; pmid: 29617646
5. S. Kreimendahl, L. Pernas, Metabolic immunity against microbes. *Trends Cell Biol.* **34**, 496–508 (2024). doi: 10.1016/j.tcb.2023.10.013; pmid: 38030541
6. O. Rackham, A. Filipovska, Organization and expression of the mammalian mitochondrial genome. *Nat. Rev. Genet.* **23**, 606–623 (2022). doi: 10.1038/s41576-022-00480-x; pmid: 35459860
7. G. S. Ducker, J. D. Rabinowitz, One-Carbon Metabolism in Health and Disease. *Cell Metab.* **25**, 27–42 (2017). doi: 10.1016/j.cmet.2016.08.009; pmid: 27641100
8. J. Nikkanen *et al.*, Mitochondrial DNA Replication Defects Disturb Cellular dNTP Pools and Remodel One-Carbon Metabolism. *Cell Metab.* **23**, 635–648 (2016). doi: 10.1016/j.cmet.2016.01.019; pmid: 26924217
9. R. H. Hämäläinen *et al.*, Defects in mtDNA replication challenge nuclear genome stability through nucleotide depletion and provide a unifying mechanism for mouse progerias. *Nat. Metab.* **1**, 958–965 (2019). doi: 10.1038/s42255-019-0120-1; pmid: 32694840
10. S. T. Bond *et al.*, Mitochondrial damage in muscle specific PolG mutant mice activates the integrated stress response and disrupts the mitochondrial folate cycle. *Nat. Commun.* **16**, 2338 (2025). doi: 10.1038/s41467-025-57299-3; pmid: 40057508
11. H. Lahouassa *et al.*, SAMHD1 restricts the replication of human immunodeficiency virus type 1 by depleting the intracellular pool of deoxynucleoside triphosphates. *Nat. Immunol.* **13**, 223–228 (2012). doi: 10.1038/ni.2236; pmid: 22327569
12. M. H. Iltzsch, Pyrimidine salvage pathways in *Toxoplasma gondii*. *J. Eukaryot. Microbiol.* **40**, 24–28 (1993). doi: 10.1111/j.1550-7408.1993.tb04877.x; pmid: 8457800
13. C. J. Giuliano *et al.*, CRISPR-based functional profiling of the *Toxoplasma gondii* genome during acute murine infection. *Nat. Microbiol.* **9**, 2323–2343 (2024). doi: 10.1038/s41564-024-01754-2; pmid: 38977907
14. A. P. West *et al.*, Mitochondrial DNA stress primes the antiviral innate immune response. *Nature* **520**, 553–557 (2015). doi: 10.1038/nature14156; pmid: 25642965
15. H. G. Sprenger *et al.*, Cellular pyrimidine imbalance triggers mitochondrial DNA–dependent innate immunity. *Nat. Metab.* **3**, 636–650 (2021). doi: 10.1038/s42255-021-00385-9; pmid: 33903774
16. R. C. Scarpulla, Nuclear control of respiratory chain expression in mammalian cells. *J. Bioenerg. Biomembr.* **29**, 109–119 (1997). doi: 10.1023/A:1022681828846; pmid: 9239537
17. M. I. Ekstrand *et al.*, Mitochondrial transcription factor A regulates mtDNA copy number in mammals. *Hum. Mol. Genet.* **13**, 935–944 (2004). doi: 10.1093/hmg/ddh109; pmid: 15016765
18. M. Ikeda *et al.*, Overexpression of TFAM or twinkle increases mtDNA copy number and facilitates cardioprotection associated with limited mitochondrial oxidative stress. *PLOS ONE* **10**, e0119687 (2015). doi: 10.1371/journal.pone.0119687; pmid: 25822152
19. L. Augusto, P. H. Amin, R. C. Wek, W. J. Sullivan Jr., Regulation of arginine transport by GCN2 eIF2 kinase is important for replication of the intracellular parasite *Toxoplasma gondii*. *PLOS Pathog.* **15**, e1007746 (2019). doi: 10.1371/journal.ppat.1007746; pmid: 31194856
20. M. Franco, A. J. Shastri, J. C. Boothroyd, Infection by *Toxoplasma gondii* specifically induces host c-Myc and the genes this pivotal transcription factor regulates. *Eukaryot. Cell* **13**, 483–493 (2014). doi: 10.1128/EC.00316-13; pmid: 24532536
21. B. Ren *et al.*, *Toxoplasma* and *Eimeria* co-opt the host cFos expression for intracellular development in mammalian cells. *Comput. Struct. Biotechnol. J.* **19**, 719–731 (2021). doi: 10.1016/j.csbj.2020.12.045; pmid: 33510872
22. K. Pakos-Zebrucka *et al.*, The integrated stress response. *EMBO Rep.* **17**, 1374–1395 (2016). doi: 10.15252/embr.201642195; pmid: 27629041
23. P. M. Quirós *et al.*, Multi-omics analysis identifies ATF4 as a key regulator of the mitochondrial stress response in mammals. *J. Cell Biol.* **216**, 2027–2045 (2017). doi: 10.1083/jcb.201702058; pmid: 28566324
24. Y. Fu *et al.*, Mitochondrial DNA breaks activate an integrated stress response to reestablish homeostasis. *Mol. Cell* **83**, 3740–3753.e9 (2023). doi: 10.1016/j.molcel.2023.09.026; pmid: 37832546
25. M. E. Torrence *et al.*, The mTORC1-mediated activation of ATF4 promotes protein and glutathione synthesis downstream of growth signals. *eLife* **10**, e63326 (2021). doi: 10.7554/eLife.63326; pmid: 33646118
26. I. Ben-Sahra, G. Hoxhaj, S. J. H. Ricoult, J. M. Asara, B. D. Manning, mTORC1 induces purine synthesis through control of the mitochondrial tetrahydrofolate cycle. *Science* **351**, 728–733 (2016). doi: 10.1126/science.aad0489; pmid: 26912861
27. S. Kaspar *et al.*, Adaptation to mitochondrial stress requires CHOP-directed tuning of ISR. *Sci. Adv.* **7**, eabf0971 (2021). doi: 10.1126/sciadv.abf0971; pmid: 34039602
28. X. R. Bao *et al.*, Mitochondrial dysfunction remodels one-carbon metabolism in human cells. *eLife* **5**, e10575 (2016). doi: 10.7554/eLife.10575; pmid: 27307216
29. M. Franco *et al.*, A Novel Secreted Protein, MYR1, Is Central to *Toxoplasma*'s Manipulation of Host Cells. *mBio* **7**, e02231-15 (2016). doi: 10.1128/mBio.02231-15; pmid: 26838724
30. N. D. Marino *et al.*, Identification of a novel protein complex essential for effector translocation across the parasitophorous vacuole membrane of Toxoplasma gondii. *PLOS Pathog.* **14**, e1006828 (2018). doi: 10.1371/journal.ppat.1006828; pmid: 29357375
31. X. Guo *et al.*, Mitochondrial stress is relayed to the cytosol by an OMA1-DELE1-HRI pathway. *Nature* **579**, 427–432 (2020). doi: 10.1038/s41586-020-2078-2; pmid: 32132707
32. G. S. Ducker *et al.*, Reversal of Cytosolic One-Carbon Flux Compensates for Loss of the Mitochondrial Folate Pathway. *Cell Metab.* **23**, 1140–1153 (2016). doi: 10.1016/j.cmet.2016.09.011; pmid: 27732838
33. B. A. Fox, D. J. Bzik, *De novo* pyrimidine biosynthesis is required for virulence of *Toxoplasma gondii*. *Nature* **415**, 926–929 (2002). doi: 10.1038/415926a; pmid: 11859373

34. K. Barylyuk *et al.*, A Comprehensive Subcellular Atlas of the *Toxoplasma* Proteome via hyperLOPIT Provides Spatial Context for Protein Functions. *Cell Host Microbe* **28**, 752–766.e9 (2020). doi: 10.1016/j.chom.2020.09.011; pmid: 33053376
35. S. Greene, K. Watanabe, J. Braatz-Trulson, L. Lou, Inhibition of dihydroorotate dehydrogenase by the immunosuppressive agent leflunomide. *Biochem. Pharmacol.* **50**, 861–867 (1995). doi: 10.1016/0006-2952(95)00255-X; pmid: 7575649
36. E. F. Johnson, W. Hinz, C. E. Atreya, F. Maley, K. S. Anderson, Mechanistic characterization of *Toxoplasma gondii* thymidylate synthase (TS-DHFR)-dihydrofolate reductase: Evidence for a TS intermediate and TS half-sites reactivity. *J. Biol. Chem.* **277**, 43126–43136 (2002). doi: 10.1074/jbc.M206523200; pmid: 12192007
37. J. A. Kovacs *et al.*, Potent effect of trimetrexate, a lipid-soluble antifolate, on *Toxoplasma gondii*. *J. Infect. Dis.* **155**, 1027–1032 (1987). doi: 10.1093/infdis/155.5.1027; pmid: 2951446
38. W. D. Lee *et al.*, Tumor Reliance on Cytosolic versus Mitochondrial One-Carbon Flux Depends on Folate Availability. *Cell Metab.* **33**, 190–198.e6 (2021). doi: 10.1016/j.cmet.2020.12.002; pmid: 33326752
39. N. Andenmatten *et al.*, Conditional genome engineering in *Toxoplasma gondii* uncovers alternative invasion mechanisms. *Nat. Methods* **10**, 125–127 (2013). doi: 10.1038/nmeth.2301; pmid: 23263690
40. D. G. Mordue, F. Monroy, M. La Regina, C. A. Dinarello, L. D. Sibley, Acute toxoplasmosis leads to lethal overproduction of Th1 cytokines. *J. Immunol.* **167**, 4574–4584 (2001). doi: 10.4049/jimmunol.167.8.4574; pmid: 11591786
41. K. M. Massimine *et al.*, *Toxoplasma gondii* is capable of exogenous folate transport: A likely expansion of the BT1 family of transmembrane proteins. *Mol. Biochem. Parasitol.* **144**, 44–54 (2005). doi: 10.1016/j.molbiopara.2005.07.006; pmid: 16159678
42. A. Nzila, J. Okombo, J. Hyde, Malaria in the Era of Food Fortification With Folic Acid. *Food Nutr. Bull.* **37**, 153–163 (2016). doi: 10.1177/0379572116634511; pmid: 26944505
43. D. N. Meadows, R. H. Bahous, A. F. Best, R. Rozen, High Dietary Folate in Mice Alters Immune Response and Reduces Survival after Malarial Infection. *PLOS ONE* **10**, e0143738 (2015). doi: 10.1371/journal.pone.0143738; pmid: 26599510
44. F. Spragge *et al.*, Microbiome diversity protects against pathogens by nutrient blocking. *Science* **382**, eadj3502 (2023). doi: 10.1126/science.adj3502; pmid: 38096285
45. U. Elling *et al.*, A reversible haploid mouse embryonic stem cell biobank resource for functional genomics. *Nature* **550**, 114–118 (2017). doi: 10.1038/nature24027; pmid: 28953874
46. U. Elling *et al.*, Forward and reverse genetics through derivation of haploid mouse embryonic stem cells. *Cell Stem Cell* **9**, 563–574 (2011). doi: 10.1016/j.stem.2011.10.012; pmid: 22136931
47. M. J. Baker *et al.*, Stress-induced OMA1 activation and autocatalytic turnover regulate OPA1-dependent mitochondrial dynamics. *EMBO J.* **33**, 578–593 (2014). doi: 10.1002/embj.201386474; pmid: 24550258
48. L. Pernas *et al.*, Toxoplasma effector MAF1 mediates recruitment of host mitochondria and impacts the host response. *PLOS Biol.* **12**, e1001845 (2014). doi: 10.1371/journal.pbio.1001845; pmid: 24781109
49. M. Franco *et al.*, Erratum for Franco et al., "A Novel Secreted Protein, MYR1, Is Central to *Toxoplasma*'s Manipulation of Host Cells". *mBio* **9**, e01869-18 (2018). doi: 10.1128/mBio.01869-18; pmid: 30279290
50. M. Biddau *et al.*, Two essential Thioredoxins mediate apicoplast biogenesis, protein import, and gene expression in *Toxoplasma gondii*. *PLOS Pathog.* **14**, e1006836 (2018). doi: 10.1371/journal.ppat.1006836; pmid: 29470517
51. F. A. Ran *et al.*, Genome engineering using the CRISPR-Cas9 system. *Nat. Protoc.* **8**, 2281–2308 (2013). doi: 10.1038/nprot.2013.143; pmid: 24157548
52. K. J. Livak, T. D. Schmittgen, Analysis of relative gene expression data using real-time quantitative PCR and the $2^{-\Delta\Delta CT}$ Method. *Methods* **25**, 402–408 (2001). doi: 10.1006/meth.2001.1262; pmid: 11846609
53. X. Li *et al.*, Mitochondria shed their outer membrane in response to infection-induced stress. *Science* **375**, eabi4343 (2022). doi: 10.1126/science.abi4343; pmid: 35025629
54. J. Cox, M. Mann, MaxQuant enables high peptide identification rates, individualized p.p.b.-range mass accuracies and proteome-wide protein quantification. *Nat. Biotechnol.* **26**, 1367–1372 (2008). doi: 10.1038/nbt.1511; pmid: 19029910
55. J. Cox *et al.*, Andromeda: A peptide search engine integrated into the MaxQuant environment. *J. Proteome Res.* **10**, 1794–1805 (2011). doi: 10.1021/pr101065j; pmid: 21254760
56. H. Wickham *et al.*, Welcome to the Tidyverse. *J. Open Source Softw.* **4**, 1686 (2019). doi: 10.21105/joss.01686
57. R Core Team, R: A Language and Environment for Statistical Computing (R Foundation for Statistical Computing, 2017).
58. M. E. Ritchie *et al.*, limma powers differential expression analyses for RNA-sequencing and microarray studies. *Nucleic Acids Res.* **43**, e47 (2015). doi: 10.1093/nar/gkv007; pmid: 25605792
59. A. Iqbal, C. Duitama, F. Metge, D. Rosskopp, J. Boucas, Flaski, Zenodo (2021). doi: 10.5281/zenodo.4849515
60. Y. Perez-Riverol *et al.*, The PRIDE database at 20 years: 2025 update. *Nucleic Acids Res.* **53**, D543–D553 (2025). doi: 10.1093/nar/gkae1011; pmid: 39494541
61. M. Schwaiger *et al.*, Anion-Exchange Chromatography Coupled to High-Resolution Mass Spectrometry: A Powerful Tool for Merging Targeted and Non-targeted Metabolomics. *Anal. Chem.* **89**, 7667–7674 (2017). doi: 10.1021/acs.analchem.7b01624; pmid: 28581703
62. X. Su, W. Lu, J. D. Rabinowitz, Metabolite Spectral Accuracy on Orbitraps. *Anal. Chem.* **89**, 5940–5948 (2017). doi: 10.1021/acs.analchem.7b00396; pmid: 28471646
63. K. Y. Leung *et al.*, Partitioning of One-Carbon Units in Folate and Methionine Metabolism Is Essential for Neural Tube Closure. *Cell Rep.* **21**, 1795–1808 (2017). doi: 10.1016/j.celrep.2017.10.072; pmid: 29141214
64. T. A. Scott *et al.*, Host-Microbe Co-metabolism Dictates Cancer Drug Efficacy in *C. elegans*. *Cell* **169**, 442–456.e18 (2017). doi: 10.1016/j.cell.2017.03.040; pmid: 28431245
65. K. Y. Leung *et al.*, Folate metabolite profiling of different cell types and embryos suggests variation in folate one-carbon metabolism, including developmental changes in human embryonic brain. *Mol. Cell. Biochem.* **378**, 229–236 (2013). doi: 10.1007/s11010-013-1613-y; pmid: 23483428
66. B. Feng *et al.*, Endoplasmic Reticulum Stress Inducer Tunicamycin Alters Hepatic Energy Homeostasis in Mice. *Int. J. Mol. Sci.* **18**, 1710 (2017). doi: 10.3390/ijms18081710; pmid: 28777337
67. K. Yamamoto *et al.*, Induction of liver steatosis and lipid droplet formation in ATF6α-knockout mice burdened with pharmacological endoplasmic reticulum stress. *Mol. Biol. Cell* **21**, 2975–2986 (2010). doi: 10.1091/mbc.e09-02-0133; pmid: 20631254
68. S. Han *et al.*, Mitochondrial integrated stress response controls lung epithelial cell fate. *Nature* **620**, 890–897 (2023). doi: 10.1038/s41586-023-06423-8; pmid: 37558881

ACKNOWLEDGMENTS

We thank E. Cors, A. Bahat, S. Niftullayev, and T. Langer (MPI-AGE) for the generous sharing of reagents; the MPI-AGE Metabolomics Core, in particular F. Dethloff, C. Edlich-Muth, and Y. Hinze for advice on sample preparation and Shiny App support for metabolite analysis; the MPI-Proteomics facility; the MPI-AGE FACS and Imaging Core for flow cytometry and microscopy support; and the MPI-AGE Comparative Biology Core Facility, in particular S. Buhl and B. Bertalan. Print summary artwork is credited to G. Calabrese, Arts & Science. We thank the UCL GOSICH Biological Mass Spectrometry Facility and the NIHR Biomedical Research Centre at UCL and Great Ormond Street Hospital for support. We also thank J. Straub and A. Lamprakis for manuscript feedback and all members of the Pernas laboratory for helpful discussions. **Funding:** This work was supported by European Research Council ERC-StG-2019 852457 (L.P.); Deutsche Forschungsgemeinschaft SFB 1218, project ID 269925409 (L.P.); Packard Fellowships for Science and Engineering (L.P.); BWF-PATH (L.P.); Medical Research Council (W00500X) (N.D.E.G.); a Wellcome Investigator Award (217173_Z_19_Z) (L.S.); and the Howard Hughes Medical Institute (L.P.). **Author contributions:** Conceptualization: T.C.M., L.P.; Methodology: T.C.M., J.O., L.S., T.B., P.K., S.R., X.L., B.M.G., I.R., K.-Y.L., N.D.E.G., M.P., A.M., P.G., and L.P.; Investigation: All authors; Resources: K.A., M.D.H., M.S.D.; Nanostring analysis: T.C.M.; Proteomics analysis: L.P.; Funding acquisition: L.P.; Project administration: L.P.; Writing – original draft: T.C.M., L.P.; Writing – review & editing: All authors; Supervision: L.P. **Competing interests:** The authors declare that they have no competing interests. **Data and materials availability:** The mass spectrometry proteomics data have been deposited to the ProteomeXchange Consortium through the PRIDE (*60*) partner repository with the dataset identifier PXD064338. All other data are available in the main text or the supplementary materials. **License information:** Copyright © 2025 the authors, some rights reserved; exclusive licensee American Association for the Advancement of Science. No claim to original US government works. https://www.science.org/about/science-licenses-journal-article-reuse. This article is subject to HHMI's Open Access to Publications policy. HHMI lab heads have previously granted a nonexclusive CC BY 4.0 license to the public and a sublicensable license to HHMI in their research articles. This research was also funded in whole or in part by the Medical Research Council (W00500X) and Wellcome (217173_Z_19_Z), cOAlition S organizations, and by the European Research Council (ERC-StG-2019 852457); as required, the author will make the Author Accepted Manuscript (AAM) version available under a CC BY public copyright license.

SUPPLEMENTARY MATERIALS

science.org/doi/10.1126/science.adr6326
Figs. S1 to S16; Tables S1 to S3; MDAR Reproducibility Checklist

Submitted 10 July 2024; resubmitted 16 April 2025; accepted 19 June 2025
10.1126/science.adr6326

Check for

RESEARCH ARTICLE SUMMARY

OPTICAL MATERIALS

Hierarchical chiral supramolecular assemblies with strong and invertible chiroptical properties

Minju Kim†, Mingyue Zhang†, You-Liang Zhu, Yan Yan, Xin Pu, Woosung Choi, Sein Chung, Kilwon Cho, Jeongwon Kim, Vladimir Tsukruk, Zhenzhong Yang*, Nicholas A. Kotov*, Zhong-Yuan Lu*, Dong Ha Kim*, Zhiqun Lin*

Full article and list of author affiliations: https://doi.org/10.1126/science.adu0296

INTRODUCTION: Chirality is a fundamental characteristic of nature and living systems. Manifesting at multiple scales, both molecular and supramolecular chirality play essential roles across diverse disciplines, including physics, chemistry, biology, materials science, and nanotechnology. Polymer-based chiral supramolecular assemblies incorporating luminescent components have emerged as a promising class of circularly polarized luminescence (CPL)–active materials. These materials hold promise for applications in information encryption, imaging, display technologies, bioprobes, and spintronic and optoelectronic devices, while benefiting from the intrinsic advantages of polymers, including scalability, flexibility, and chemical diversity. However, conventional systems based on amphiphilic linear block copolymers (BCPs) struggle to achieve stable chiral structures with strong chiroptical activity, high quantum yield, and large luminescence dissymmetry factor (g_{lum}) because of the dynamic instability of linear polymer assemblies, inefficient chirality transfer, and inadequate emitter protection.

RATIONALE: Amphiphilic star–like BCPs differ fundamentally from their linear analogs by forming unimolecular micelles with superior structural integrity. We hypothesized that coassembling achiral star–like BCPs with small chiral molecules could overcome the limitations of linear polymeric systems. Their structural stability and amphiphilicity make them compatible with a broad range of luminescent emitters through multiple noncovalent interactions, potentially enabling a general and efficient route to CPL generation across the visible spectrum. To explore this, we synthesized 21-arm star-like poly(acrylic acid)-*block*-polystyrene (PAA-*b*-PS) and coassembled it with enantiomeric mandelic acid [(R/S)-MA] through hydrogen bonding between MA and the hydrophilic PAA block, inducing chiral supramolecular structures.

RESULTS: Chiral supramolecular structures were constructed by thermal annealing–driven chiral coassembly of star-like PAA-*b*-PS and (R/S)-MA in dimethylformamide. The resulting assemblies exhibited microscale helical fibrillar morphology, enhanced mechanical attributes, and strong, stable circular dichroism signals spanning 200 to 500 nm with a dissymmetry factor of 0.039, indicating efficient chirality transfer from MA to the supramolecular assemblies. Time-dependent morphological and chiroptical characterization, together with coarse-grained molecular dynamics simulations, revealed a hierarchical organization. Initially, molecular chirality of MA was transferred to the PAA chains, inducing conformational chirality. Upon prolonged annealing, the complexes packed into kinetically trapped, belt-like secondary nanostructures, which subsequently reorganized into thermodynamically favored tertiary fibrillar microstructures with defined handedness.

By leveraging the structural robustness and amphiphilicity of star-like BCPs, we demonstrated the versatility of coassemblies in generating CPL-active materials that emit strong CPL across the visible spectrum. We achieved high g_{lum} (up to 0.11 in the blue region) by incorporating diverse achiral emitters, including hydrophilic and hydrophobic dyes, aggregation-caused quenching and aggregation-induced emission luminogens, and PS-ligated perovskite nanocrystals synthesized using star-like BCPs as nanoreactors. Through noncovalent interactions including hydrogen bonding, π–π stacking, and hydrophobic interactions, efficient chirality transfer to the emitters was achieved. These coassemblies exhibited enhanced quantum yields and prolonged emission lifetimes, which were attributed to reduced thermal degradation and aggregation within the chiral supramolecular framework.

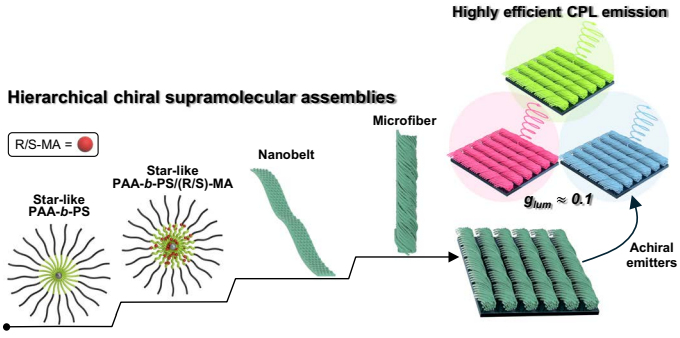

A universal strategy for creating full-color, highly efficient CPL-active materials through hierarchical chiral supramolecular assemblies. Starting from achiral star–like PAA-*b*-PS block copolymers, hierarchical organization is driven by complexation with chiral R/S-MA, forming nanobelts and subsequently helical microfibers through chiral supramolecular assemblies. Incorporation of diverse emitters ranging from hydrophilic and hydrophobic dyes to aggregation-caused quenching and aggregation-induced emission luminogens, as well as inorganic perovskite nanocrystals, into the chiral assemblies enables stable, full-color, tunable CPLs with high efficiency.

Furthermore, we demonstrated invertible chiroptical properties by modulating the assembly concentration and applying rapid solvent annealing using dimethylformamide-toluene mixtures. At high concentrations, densely packed rodlike structures were formed, exhibiting stronger chiroptical signals with opposite handedness. Coarse-grained molecular dynamics simulations and temperature-cycling experiments revealed that these inverted chiroptical states correspond to kinetically trapped, nonequilibrium structures.

CONCLUSION: We report the unique advantages of amphiphilic star-like BCPs in producing hierarchical chiral supramolecular assemblies that exhibit multiscale and tunable chirality, long-term stability, and enhanced mechanical properties. This strategy offers a universal and modular platform for developing full-color CPL-active materials with marked chiroptical performance. In particular, it enables strong red CPL, a longstanding challenge in many systems, highlighting its potential for emerging quantum technologies. □

*Corresponding author. Email: yangzhenzhong@tsinghua.edu.cn (Z.Y.); kotov@umich.edu (N.A.K.); luzhy@jlu.edu.cn (Z.-Y.L.); dhkim@ewha.ac.kr (D.H.K.); z.lin@nus.edu.sg (Z.L.)
†These authors contributed equally to this work. **Cite this article as M. Kim *et al.*, *Science* 389, eadu0296 (2025). DOI: 10.1126/science.adu0296**

OPTICAL MATERIALS

Hierarchical chiral supramolecular assemblies with strong and invertible chiroptical properties

Minju Kim[1,2]†, Mingyue Zhang[1]†, You-Liang Zhu[3], Yan Yan[4], Xin Pu[3], Woosung Choi[1,5], Sein Chung[6], Kilwon Cho[6], Jeongwon Kim[2], Vladimir Tsukruk[5], Zhenzhong Yang[7]*, Nicholas A. Kotov[8,9]*, Zhong-Yuan Lu[3]*, Dong Ha Kim[2,10,11,12,13]*, Zhiqun Lin[1]*

Supramolecular assemblies hold great promise for advanced chiral materials because of their structural diversity and dynamic features, but their low chiroptical activity limits practical applications. We report hierarchical supramolecular assemblies with giant chiroptical activity and mechanical attributes achieved through coassembly of achiral amphiphilic unimolecular micelles and chiral additives. Chiral fibrillar assemblies emerge from the nanostructured environment imposed by the micelles, driven by progressive chirality transfer through multiple hydrogen bonds between components. Integrating multifarious achiral luminescent molecules and nanocrystals into these assemblies leads to full-color circularly polarized luminescence–active materials with dissymmetry factors of ~10^{-1}. A concentration-dependent chirality inversion is accessed through tailoring the coassembly kinetics. This strategy enables efficient red CPL, crucial for quantum and optical technologies.

Chiral supramolecular assemblies, which are composed of molecules linked through one or more noncovalent interactions that facilitate chirality transfer, are nonsuperimposable on their mirror images and can modulate chiroptical activities (*1*–*3*). Tailoring the molecular structure of these constituents (*4*) and regulating noncovalent interactions (*5*–*7*) enables precise control over chiral supramolecular assembly (*8*). Various chiral supramolecular structures have been produced, including helical fibers (*4*), helical microtoroids (*6*), and spiral tubes (*7*). Incorporating luminescent components into chiral supramolecular assemblies can create materials with circularly polarized luminescence (CPL) for applications in light-emitting diodes (*9*), information encryption (*10*), and photoelectric (*11*) and spintronic devices (*12*).

Chiral assembly of achiral fluorescent molecules (*13*, *14*) or inorganic nanocrystals (*15*–*17*) within these structures promotes chirality transfer and enhances luminescence efficiency by mitigating aggregation-induced fluorescence quenching (*18*). However, developing polymer-based CPL-active materials with strong chiroptical properties, long-term stability, structural versatility, high quantum yield (QY), and a large luminescence dissymmetry factor (g_{lum} ≥10^{-1}) remains challenging given the difficulties in constructing assemblies with pronounced chirality and helical pitches comparable to visible wavelengths. Additionally, the instability of weakly bound and disordered fluorescent dopants contributes to relatively low chiroptical activity and thermal disorganization (*19*). A particular challenge lies in designing CPL-active composites that maintain high mechanical properties under extreme conditions (*20*).

Supramolecular assemblies of amphiphilic block copolymers (BCPs) are a promising platform for chiral photonics because of their structural versatility and well-established synthetic protocols. However, assemblies formed by combining achiral linear BCPs with chiral additives typically exhibit a low yield of helical structures with specific handedness and weak chiroptical properties localized in the ultraviolet (UV) region (*21*, *22*). These limitations arise because the dynamic micelles formed by linear BCPs tend to disassemble after varying concentration, solvent, temperature, and pH (*23*).

By contrast, amphiphilic star–like BCPs, featured by a three-dimensional (3D) architecture with linear arms radiating from a central core, form unimolecular micelles that offer superior structural stability compared with linear BCP micelles (*23*, *24*). Incorporating chirality through noncovalent interactions between achiral star–like BCPs and chiral additives offers a promising strategy to overcome the limitations of linear BCP-based assemblies. However, this approach remains underexplored because of the challenges in synthesizing amphiphilic star–like BCPs with a high density of arms, which are crucial for forming well-defined unimolecular micelles that can stably encapsulate chiral additives and foster strong interactions.

Herein, we present a general methodology for the assembly of achiral amphiphilic star–like BCPs and chiral molecules, yielding hierarchical chiral supramolecular structures to create efficient and invertible CPL-active materials. Specifically, 21-arm star-like poly(acrylic acid)-*block*-polystyrene (PAA-*b*-PS) was designed to form stable, nanoscopic unimolecular micelles with inner hydrophilic PAA blocks and outer hydrophobic PS blocks, facilitating hydrogen bonding between star-like PAA-*b*-PS and R- or S-mandelic acid [(R/S)-MA] and inducing supramolecular chirality with a maximum dissymmetry factor (g_{CD}) of ~10^{-1}. Time-dependent studies and molecular dynamics (MD) simulations revealed a thermodynamically favorable evolution from achiral star–like PAA-*b*-PS to chiral star–like PAA-*b*-PS/(R/S)-MA complexes, followed by the formation of nanobelts and ultimately microfibers. Incorporating achiral fluorescent dyes and perovskite nanocrystals (NCs) into these assemblies produced CPL-active materials with technologically promising g_{lum} values of ~10^{-1}, surpassing linear BCP-based approaches. The solvent evaporation rate and concentration of star-like BCPs played pivotal roles in forming kinetically trapped chiral structures during coassembly, imparting the chirality inversion. This work pioneers a versatile supramolecular coassembly strategy using star-like BCPs to construct intricate chiral structures and efficient and tailorable CPL-active materials, with potential applications in optoelectronics, anticounterfeiting, and spintronics.

Evolution of hierarchical chiral supramolecular fiber–like structures through coassembly

Amphiphilic, 21-arm star-like PAA-*b*-PS was synthesized following our reported approach (figs. S1 to S4 and supplementary text) (*25*). The integration of enantiopure MA into the inner hydrophilic PAA blocks was substantiated by the size expansion of the complexes compared with pristine star-like PAA-*b*-PS (fig. S5 and discussed in detail in the supplementary text). The noncovalent interactions between the PAA blocks and MA were identified by Fourier-transform infrared spectroscopy

[1]Department of Chemical and Biomolecular Engineering, National University of Singapore, Singapore, Singapore. [2]Department of Chemistry and Nanoscience, Division of Molecular and Life Sciences, College of Natural Sciences, Ewha Womans University, Seoul, Republic of Korea. [3]State Key Laboratory of Supramolecular Structure and Materials, College of Chemistry, Jilin University, Changchun, China. [4]School of Chemistry and Chemical Engineering, Anhui University of Technology, Ma'anshan, Anhui, China. [5]School of Materials Science and Engineering, Georgia Institute of Technology, Atlanta, GA, USA. [6]Department of Chemical Engineering, Pohang University of Science and Technology (POSTECH), Pohang, Republic of Korea. [7]Department of Chemical Engineering, Tsinghua University, Beijing, China. [8]Department of Chemical Engineering, University of Michigan, Ann Arbor, MI, USA. [9]National Science Foundation Center for Complex Particle Systems (COMPASS), University of Michigan, Ann Arbor, MI, USA. [10]College of Medicine, Ewha Womans University, Seoul, Republic of Korea. [11]Graduate Program in Innovative Biomaterials Convergence, Ewha Womans University, Seoul, Republic of Korea. [12]Basic Sciences Research Institute (Priority Research Institute), Ewha Womans University, Seoul, Republic of Korea. [13]Nanobio Energy Materials Center (National Research Facilities and Equipment Center), Ewha Womans University, Seoul, Republic of Korea. ***Corresponding author. Email: yangzhenzhong@tsinghua.edu.cn (Z.Y.); kotov@umich.edu (N.A.K.); luzhy@jlu.edu.cn (Z.-Y.L.); dhkim@ewha.ac.kr (D.H.K.); z.lin@nus.edu.sg (Z.L.)** †These authors contributed equally to this work.

(FTIR) (fig. S6). Density functional theory (DFT) calculations (fig. S7) further corroborated that one MA formed two [O–H···O] hydrogen bonds with a PAA repeating unit, with a negative formation energy of –17.24 kcal mol^{-1} for the PAA/S-MA complex, signifying an energetically stable bonding configuration. The strong hydrogen-bonding interactions efficiently transferred chirality from chiral additives to the originally achiral star–like BCPs (*26*).

Hierarchical chiral supramolecular assemblies (chiral microfibers) were created by drop-casting PAA-*b*-PS/(R/S)-MA solution, followed by a thermal annealing–driven coassembly process at 60°C (Fig. 1A, Materials and methods, and supplementary text). The prolonged annealing facilitated the chirality transfer from chiral MA to supramolecular coassembly, forming microscopic helical fiber-like structures. Scanning electron microscopy (SEM) images revealed the chiral additive–dependent handedness of these structures (Fig. 1, B and C): Star-like PAA-*b*-PS with R-MA formed right-handed structures, whereas those with S-MA produced left-handed ones, both with an average width of 4 ± 1 μm. High-magnification SEM and atomic force microscopy (AFM) images

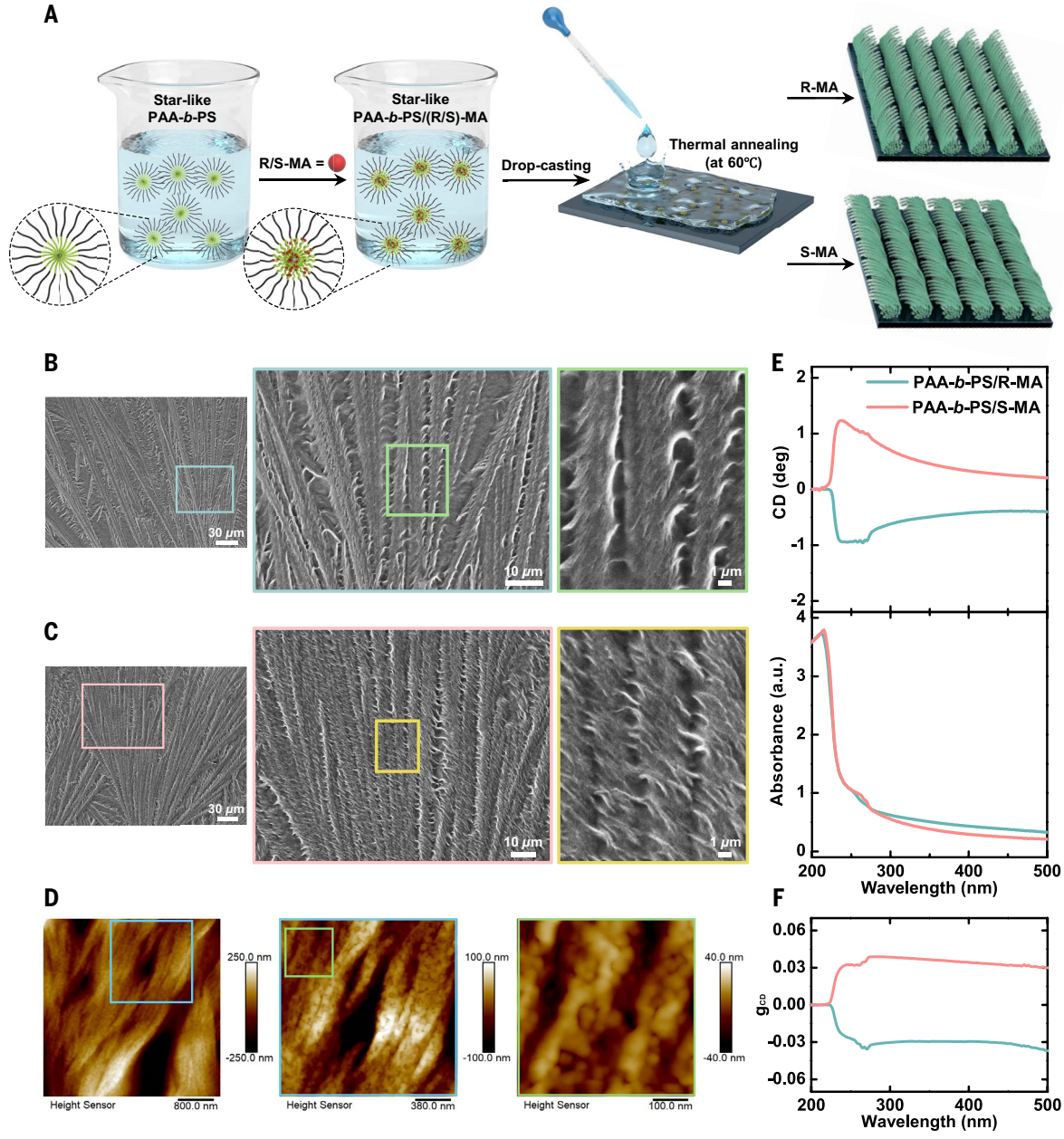

Fig. 1. Stepwise representation and characterization of hierarchical chiral supramolecular structures. (**A**) Schematic illustration depicting the route to hierarchical chiral structures through thermal annealing–driven coassembly of achiral star–like PAA-*b*-PS BCPs with chiral (R/S)-MA at 60°C for 24 hours. The molar ratio of a PAA repeating unit to MA was 1:2, and the concentration of star-like BCP solution in DMF was 2.5 mg ml^{-1}. (**B** and **C**) SEM images of chiral supramolecular fiber–like structures formed through the coassembly of achiral star–like PAA-*b*-PS with R-MA (B) and S-MA (C). The central images are magnifications of the regions marked by blue (B) and pink (C) boxes in the left images. The right images show further magnified views of the central images, corresponding to the areas marked by light green (B) and yellow (C) boxes, respectively. (**D**) AFM images of right-handed fiber-like structures (left image) resulting from coassembly of achiral star–like BCPs with R-MA, revealing nanobelt-like structures (center image; a close-up of the blue-boxed region in the left image) composed of densely packed dot-like aggregates (right image; a close-up of the green-boxed region in the center image). (**E**) CD and corresponding absorption spectra, along with (**F**) g_{CD} spectra of chiral supramolecular fiber–like structures formed through coassembly of achiral star–like BCPs with R-MA (cyan curve) and S-MA (pink curve).

showed that these fiber-like structures were composed of nanoscopic belt-like units (nanobelts; figs. S8 and S9). Further AFM imaging showed that the nanobelts consisted of densely packed dot-like structures (Fig. 1D). By contrast, pristine star-like PAA-*b*-PS under the same conditions yielded a mixed morphology of randomly populated lamellae and spheres without distinct chiral structures (fig. S10).

The circular dichroism (CD) spectra (Fig. 1E) reveal pronounced and broad bands between 200 and 500 nm, distinct from the UV-range molecular chirality of (R/S)-MA arising from the n-π* transition of the carboxylic acid group (fig. S11A) (*27*). Pure (R/S)-MA loses chirality upon thermal annealing because of its low thermal stability (fig. S11B), so the CD signals in Fig. 1E had to arise from the supramolecular chirality of the microfiber structures that resulted from chirality transfer from chiral (R/S)-MA to achiral star–like BCPs and ultimately to the assembled structures. The value of g_{CD} = CD[mdeg]/(32,980 × absorbance), reached 3.9×10^{-2} at 280 nm (Fig. 1F), outperforming those from the coassembly of achiral linear BCPs and chiral additives [e.g., g_{CD} = ~2.5×10^{-3} (*28*) and ~3.0×10^{-2} (*29*)] and from self-assembly of chiral BCPs [e.g., g_{CD} = ~3.0×10^{-2} (*30*) and ~10^{-3} (*31*)]. Although the large g_{CD} value included contributions from linear dichroism (LD) and linear birefringence (LB) effects, inherent to solid samples with macroscopic anisotropy, the intrinsic anisotropy factor remains substantially high with a maximum of 3.8×10^{-2} at 380 nm (figs. S12 and S13; see the supplementary text for details). These hierarchically coassembled supramolecular structures and their chiroptical properties heavily depend on many factors [e.g., thermal decomposition of MA (fig. S11B) and mobility of polymer chains (fig. S65, discussed below)]. Optimizing coassembly parameters, including MA/AA ratio (2:1 in Fig. 1 and 1:1 in fig. S14), PAA/PS ratio (table S1 and fig. S15), and concentration (2.5 mg ml^{-1} in Fig. 1 and 1 mg ml^{-1} and 5 mg ml^{-1} in fig. S16) enabled the development of chiral supramolecular structures with multiscale chirality and strong chiroptical properties.

We investigated the mechanical properties of chiral supramolecular structures with AFM nanoindentation using the Derjaguin-Muller-Toporov (DMT) model (*32*). The apparent DMT modulus images of the fiber-like structures revealed the anisotropy of the elastic modulus, matching the handedness of the structures (fig. S17, B and C), whereas a pristine star-like BCP film manifested a random modulus distribution (fig. S17A). Force-distance curve measurements (fig. S17, D to F, and supplementary text) revealed that the elastic modulus (E_s) of the chiral supramolecular fiber–like structures increased by 29% compared with that of pristine star-like BCP film. Furthermore, the chiral fiber-like structures exhibited a 79% enhancement in hardness (H) compared with the pristine BCP film. These results indicate that the tight helical packing induced by coassembling PAA-*b*-PS with chiral additives imparts enhanced mechanical properties to the supramolecular structures compared with the pristine counterpart.

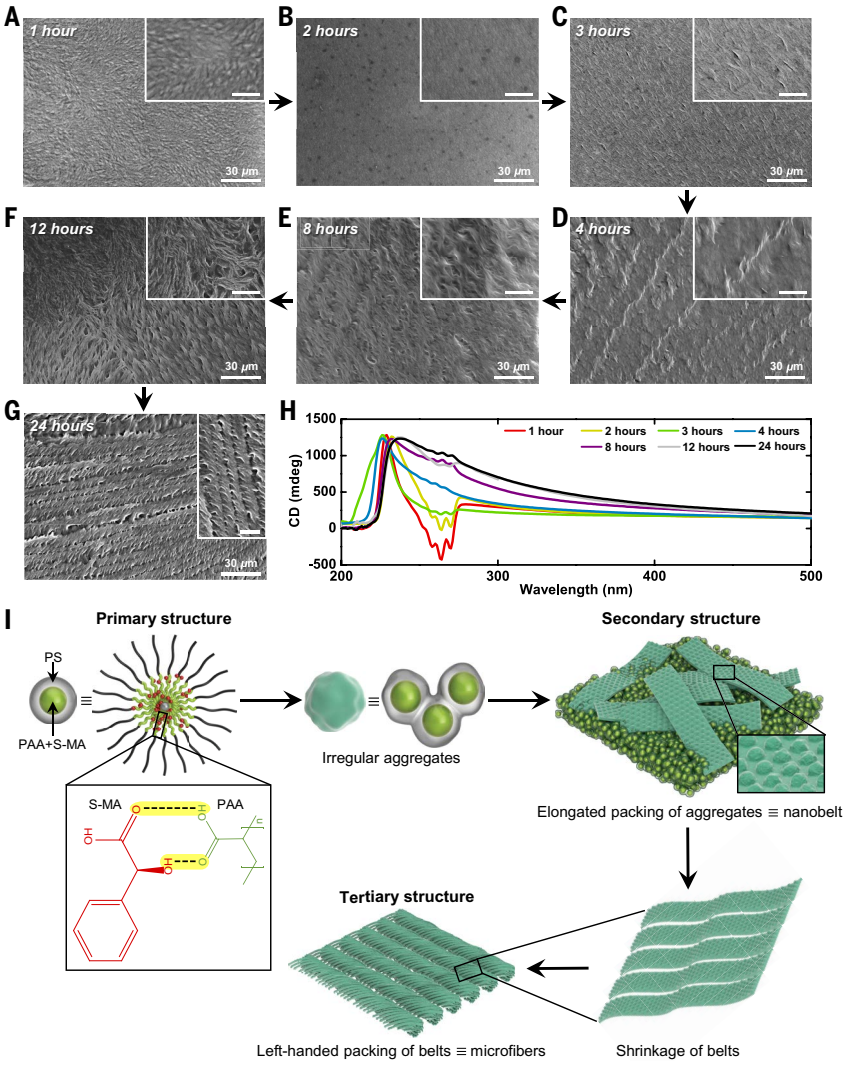

Fig. 2. Progressive morphological evolution and chirality transfer in hierarchical chiral supramolecular structures. (**A** to **G**) Sequential SEM images depicting morphological evolution of star-like PAA-*b*-PS/S-MA during the course of thermal annealing of the film (drop-casted from its DMF solution) at 60°C for 1 hour (A), 2 hours (B), 3 hours (C), 4 hours (D), 8 hours (E), 12 hours (F), and 24 hours (G). Scale bar in magnified images, 10 μm. (**H**) Time-dependent CD spectra of coassembly of star-like PAA-*b*-PS and S-MA indicating chirality transfer from MA molecules to hierarchical chiral supramolecular structures at 60°C, corresponding to the SEM images shown in (A) to (G). (**I**) Schematic representation of the proposed mechanism illustrating the formation of hierarchical chiral supramolecular structures underpinning the importance of slow solvent evaporation and prolonged thermal annealing in the coassembly process.

Mechanism of hierarchical chirality transfer into chiral supramolecular structures

To gain insight into the formation of fiber-like structures during coassembly under prolonged annealing at 60°C, a time-dependent CD study was performed (Fig. 2H). For the coassembly of star-like PAA-*b*-PS and S-MA, a bisignate exciton-type Cotton effect emerged at 250 nm after annealing for 1 hour. This CD behavior arose from the interaction between transition dipole moments of MA and the AA repeating units of PAA blocks (*33*). After 4-hour annealing, the Cotton effect diminished, merging into a single, positively signed peak indicative of supramolecular structural chirality. Upon further annealing until 24 hours, the CD band broadened and intensified over a wide wavelength range, signifying the complete emergence of supramolecular chirality. This finding highlights the necessity of extended annealing duration to attain optimized supramolecular chirality in coassembled structures.

Time-dependent morphological transformation into chiral microfibers was also explored. After 1 hour of annealing, solvent evaporation increased the density of the star-like PAA-*b*-PS/S-MA complex, causing swollen spherical micelles to adhere to one another and form irregular

yet evenly distributed dot-like aggregates to reduce interfacial energy (Fig. 2A and figs. S18A and S19A) (*34*). After 2-hour annealing, larger spherical aggregates comprising numerous dot-like aggregates with an average diameter of several hundred nanometers appeared (Fig. 2B and figs. S18B and S19B), and their dark edges indicated cracks caused by accelerated solvent evaporation from the top layer. After annealing for 3 hours, the spherical aggregates shrank with continuous solvent evaporation, and ordered, macroscopic patterns emerged as star-like PAA-*b*-PS/S-MA complexes packed more tightly (Fig. 2C and figs. S18C and S19C).

After 4 hours, the spherical aggregates disappeared completely (Fig. 2D and figs. S18D and S20A), indicating their nonequilibrium nature. Furthermore, their gradual disappearance at room temperature over a 7-day storage period suggested that these structures were metastable with low energy barriers (fig. S21A and supplementary text). Concurrently, distinct directional coassemblies formed, demonstrating that sufficient thermal annealing induced chirality in the assembly. After 8-hour annealing, elongated belt-like structures ~300 nm wide composed of closely packed dot-like aggregates formed (Fig. 2E and figs. S18E and S20B). These structures exhibited a preferred growth direction as they packed together, indicating structural evolution toward a thermodynamically favorable configuration.

After 12-hour annealing, the nanobelts contracted laterally as solvent evaporation continued (Fig. 2F and figs. S18F and S20C). They also entangled, forming tightly packed structures that function as nucleation sites for the fiber-like structures. Finally, after 24 hours, the nanobelts twisted together in a left-handed orientation, resulting in the formation of fiber-like structures (microfibers; Fig. 2G and figs. S18G and S20D) that underwent complete shrinkage as the solvent evaporated thoroughly during prolonged annealing. The morphological transition was also supported by grazing incidence small-angle x-ray scattering analysis, which revealed changes in scattering profiles, power-law exponents, and anisotropic scattering patterns (fig. S22 and see details in the supplementary text).

On the basis of time-dependent CD and corresponding morphology studies, the formation mechanism of hierarchical chiral supramolecular structures was rationalized as follows (Fig. 2I). Before drop-casting, chiral star–like BCPs were formed as primary structures through hybridization with MA, where the molecular chirality of MA was transferred to the conformational chirality of PAA chains by hydrogen bonding. During the initial annealing stage, as solvent evaporated, the star-like PAA-*b*-PS/S-MA complexes came into proximity to form small, irregular dot-like aggregates. We selected dimethylformamide (DMF) as the solvent because of its high boiling point (153°C) and slow evaporation rate (-4.2×10^{-4} kg s^{-1} m^{-2} at 60°C) (*35*), which are crucial to enable high polymer mobility throughout the annealing process, facilitating the transition of polymer chains with a helical phase into thermodynamically favorable chiral supramolecular structures.

As annealing progressed, the gradual solvent evaporation created a concentration gradient in the film, prompting the packing of irregular dot-like aggregates into nonequilibrium, kinetically trapped belt-like secondary structures (i.e., nanobelts, fig. S21B and supplementary text). Continuous evaporation of DMF led to contraction and tighter packing of nanobelts, while fresh nanobelts formed from the solution and propagated into the film. Finally, nanobelts adopted helical packing upon complete solvent evaporation, forming tertiary fiber-like structures (i.e., microfibers) with specific handedness.

This stepwise structural evolution is a direct consequence of the intricate interplay among the molecular chirality of MA, the conformational chirality of star-like PAA-*b*-PS, and supramolecular chirality induced by coassembly of star-like PAA-*b*-PS and MA. Chiral steric hindrance arising from the conformational chirality of the PAA/(R/S)-MA blocks in star-like PAA-*b*-PS disturbed van der Waals interactions between polymer chains and thus increased the enthalpic penalty of the star-like PAA-*b*-PS/(R/S)-MA complexes, and consequently the nanobelts. To counterbalance this enthalpic penalty and minimize the Gibbs free energy of the entire system, chiral packing and organization of the nanobelts were induced at higher structural levels, resulting in the helical packing of nanobelts to form microfibers (*36*). These thermodynamically favored fibrillar structures retained stable chiroptical properties and structural integrity even after long-term storage (100 days at room temperature) because of their inherent thermodynamic stability (fig. S23). Furthermore, their chiroptical properties and morphology remained unchanged over 10 heating-cooling cycles between 60° and 25°C (fig. S24), demonstrating their robustness and thermodynamic equilibrium.

To further elucidate the formation mechanism of hierarchical chiral supramolecular structures, we performed coarse-grained molecular dynamics (CG-MD) simulations under explicit solvent conditions using a constant chemical potential method. In the model (Fig. 3A, left panel, and fig. S25), 21 PAA-*b*-PS chains are connected to β-CD to construct 21-arm star-like PAA-*b*-PS. A similar approach was used to simulate star-like PAA-*b*-PS/(R/S)-MA (Fig. 3A, right two panels) by considering the interactions between MA and PAA blocks that facilitate chirality transfer and promote chiral configuration. MA molecules were not visually represented in the model to enhance simulation efficiency. Conformation-optimized PAA-*b*-PS/R-MA and PAA-*b*-PS/S-MA (60 polymer complexes in each system) were dissolved in DMF at a concentration of 2.5 mg ml^{-1} with the corresponding number of solvent molecules explicitly added and equilibrated in a cubic simulation box under 3D periodic boundary conditions.

CG-MD simulations were then performed in the canonical ensemble at T = 333 K to model the formation of chiral supramolecular structures. During the initial 150 μs of solvent evaporation (Fig. 3, B to D), where 99% of DMF molecules were removed, the freely dispersed PAA-*b*-PS/S-MA complexes spontaneously assembled into compact structures. Subsequent thermal annealing for 250 μs led to the formation of thermodynamically equilibrated, stacked multilayered structures with preferential helical arrangements (Fig. 3, E and F). The handedness of the assembly was evaluated by the rotational angles (θ) between adjacent layers consisting of PAA-*b*-PS/S-MA (Fig. 3G), where negative and positive rotational angles correspond to left-handedness and right-handedness, respectively. The energy profile per star-like PAA-*b*-PS/S-MA unit, plotted as a function of θ, displayed a minimum at –20°, indicating that left-handed chiral supramolecular structures are thermodynamically favored.

By contrast, the coassembly of PAA-*b*-PS/R-MA under the same evaporation and annealing conditions produced oppositely twisted structures (Fig. 3, H and I), with an energy minimum at +20° (Fig. 3J), demonstrating a thermodynamic preference for right-handed assemblies. These findings were further substantiated by statistical analysis of relative shifts between star-like PAA-*b*-PS/(R/S)-MA units in adjacent layers (Fig. 3, K and L), confirming a preference for right-handedness in PAA-*b*-PS/R-MA coassemblies and left-handedness in PAA-*b*-PS/S-MA coassemblies. Secondary energy minima at +20° for PAA-*b*-PS/S-MA (Fig. 3G) and at –20° for PAA-*b*-PS/R-MA (Fig. 3J), along with the presence of minor populations of oppositely handed configurations (Fig. 3, K and L), signified the presence of kinetically stable configurations with opposite handedness. These results implied that the intrinsic handedness of these coassemblies could be reversed by modulating external factors such as thermal annealing temperature, annealing time, or solvent.

CPL emission: organic and inorganic emitters integrated into the coassembly process

To create CPL-active supramolecular structures, we introduced various achiral fluorescent dyes, including blue-emitting 1-pyrenecarboxylic acid (PCA), green-emitting Oregon Green 488 (OG), and red-emitting rhodamine B (RhB), into the coassembly of star-like PAA-*b*-PS and (R/S)-MA. These dyes contain carboxyl, carbonyl, or hydroxyl groups, which are

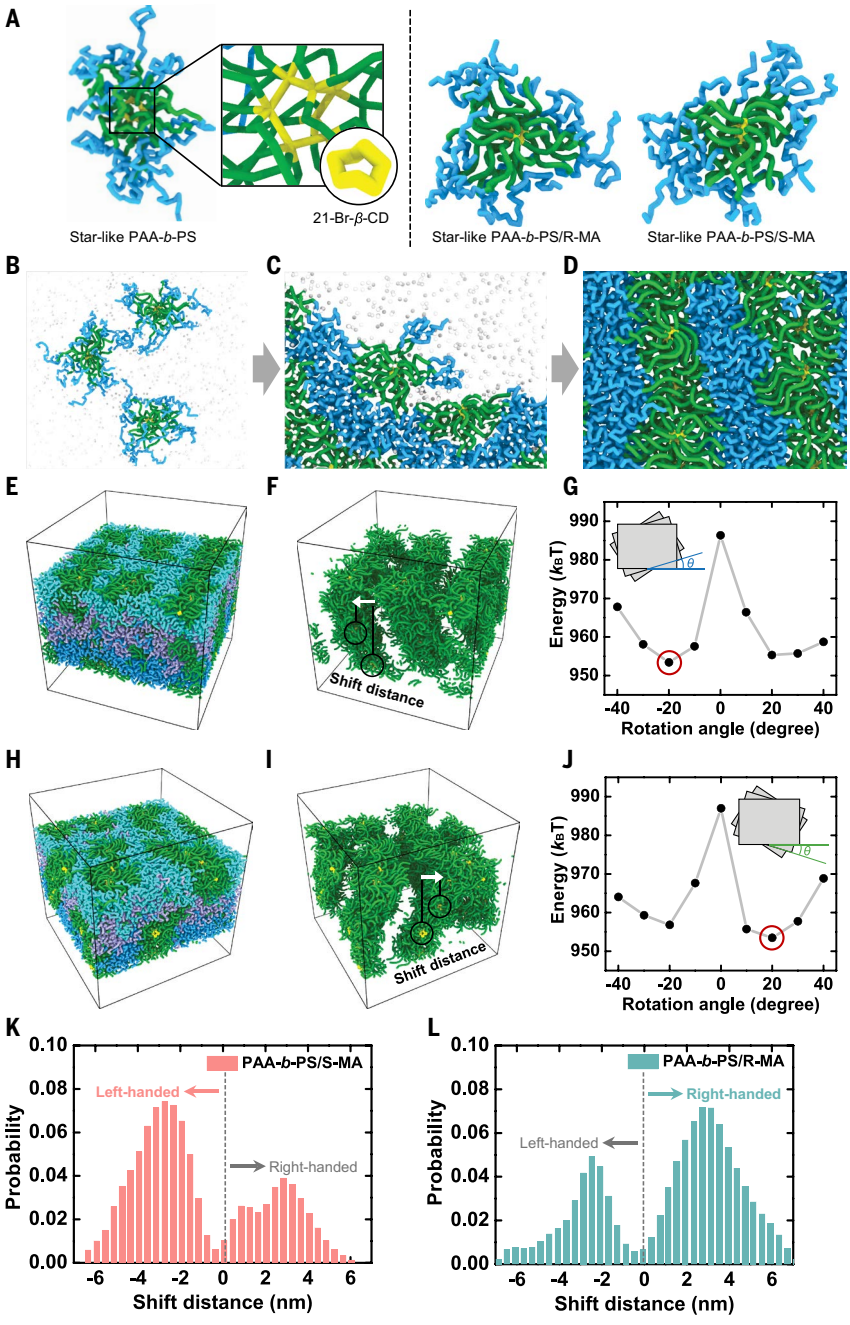

Fig. 3. CG-MD simulation of hierarchical chiral structures with preferred handedness yielded by coassembly of achiral star–like PAA-*b*-PS and chiral (R/S)-MA using DMF as the solvent. (**A**) Simulation model of star-like PAA-*b*-PS, star-like PAA-*b*-PS/R-MA, and star-like PAA-*b*-PS/S-MA, where the 21-Br-β-CD macroinitiator, PAA, and PS are color-coded in yellow, green, and blue, respectively. The PAA/R-MA blocks adopted a right-handed conformation, whereas the PAA/S-MA blocks exhibited a left-handed conformation, contrasting with the random conformation of PAA blocks in star-like PAA-*b*-PS. (**B** to **D**) Top-view snapshots of the coassembled structures of star-like PAA-*b*-PS/S-MA formed through gradual solvent evaporation at 333 K after 0 μs (B), 75 μs (C), and 150 μs (D). (**E**) 3D snapshot of the final coassembled structure of star-like PAA-*b*-PS/S-MA obtained after 250 μs of further thermal annealing, with multilayered structures distinguished by different colors (i.e., blue, purple, and cyan) in the PS blocks (green for PAA blocks). (**F**) Twisted configuration of the star-like PAA/S-MA cores within the assembled structure in (E). (**G**) Simulated profile of energy per star-like PAA-*b*-PS/S-MA unit as a function of rotational angle θ. (**H**) 3D snapshot of the final coassembled structure of star-like PAA-*b*-PS/R-MA formed after 250 μs of further thermal annealing. (**I**) Twisted configuration of the star-like PAA/R-MA cores within the assembled structure in (H) showing an opposite helicity to that in (F). (**J**) Simulated profile of energy per star-like PAA-*b*-PS/R-MA unit as a function of rotational angle θ. (**K** and **L**) Statistical analyses revealing the thermodynamically preferred handedness of chiral supramolecular structures by coassembly of star-like PAA-*b*-PS/S-MA (K) and star-like PAA-*b*-PS/R-MA (L). The unit of energy in (G) and (J) is k_BT, where k_B is the Boltzmann constant and T is the temperature.

crucial for coassembly through hydrogen bonding (Fig. 4, A to C, and fig. S26). In chiral supramolecular structures incorporating dye molecules, the absorption spectra revealed peak splitting corresponding to dye molecule aggregation through intermolecular interaction, including hydrogen bonding and π-π stacking (Fig. 4, D to F; fig. S27; and supplementary text) (*37*, *38*). The CD spectra showed mirror-symmetric responses aligned with their absorption bands (Fig. 4, G to I), with g_{CD}s of 2.0×10^{-2} (PCA, 420 nm), 8.0×10^{-3} (OG, 450 nm), and 1.0×10^{-2} (RhB, 525 nm) (fig. S28, A to C). In solution, no chirality transfer to the dyes was observed (fig. S29), emphasizing that thermal annealing–driven chiral coassembly was essential for the chiral arrangement of dye molecules and ruling out molecular interactions as the source of the observed chiroptical activity.

We then investigated the CPL emission of chiral supramolecular structures incorporating dyes. The PCA-incorporated structures emitted blue CPL at 450 nm, whereas those with OG and RhB emitted green and red CPL at 550 and 625 nm, respectively (Fig. 4, J to L). The handedness of CPL corresponded with the structure's geometric handedness. The g_{lum} values, calculated as $2(I_L - I_R)/(I_L + I_R)$ (where I_L and I_R represent the intensity of left-handed and right-handed CPL, respectively), were 0.11 for PCA (450 nm), 0.03 for OG (555 nm), and 0.09 for RhB (623 nm), corresponding to their respective emission bands (fig. S28, D to F), with QYs of 29.2%, 16%, and 12.4%, respectively. These QYs were higher than those of pure dye films (3%, 0%, and 0% for PCA, OG, and RhB, respectively), and the emission lifetimes were prolonged (Fig. 4, M to O, and table S2), attributed to reduced thermal degradation and suppression of aggregation-caused quenching (ACQ) through coassembly of dyes with star-like BCP and (R/S)-MA.

Compared with coassemblies of polymers and achiral dyes in other reports (table S3 and fig. S30), star-like BCP–derived supramolecular structures effectively created CPL-active materials with high CPL activities and QYs. Unlike most CPL systems limited to blue or green emission, our coassembly approach achieved high-performance red CPL, offering advantages for quantum technology because of its low optical loss. The absence of selective reflection effects, along with favorable hydrogen bonding among the PAA blocks, chiral additives, and dyes, as calculated by DFT simulations, confirmed that the CPL originates from coassembly driven by hydrogen-bonding interactions (figs. S31 to S33 and supplementary text). In our system, variations in hydrogen-bonding energy, aggregation behavior, and intrinsic emission stability of dye molecules led to differences in the chiroptical properties achieved through coassembly (figs. S32 to S34 and supplementary text).

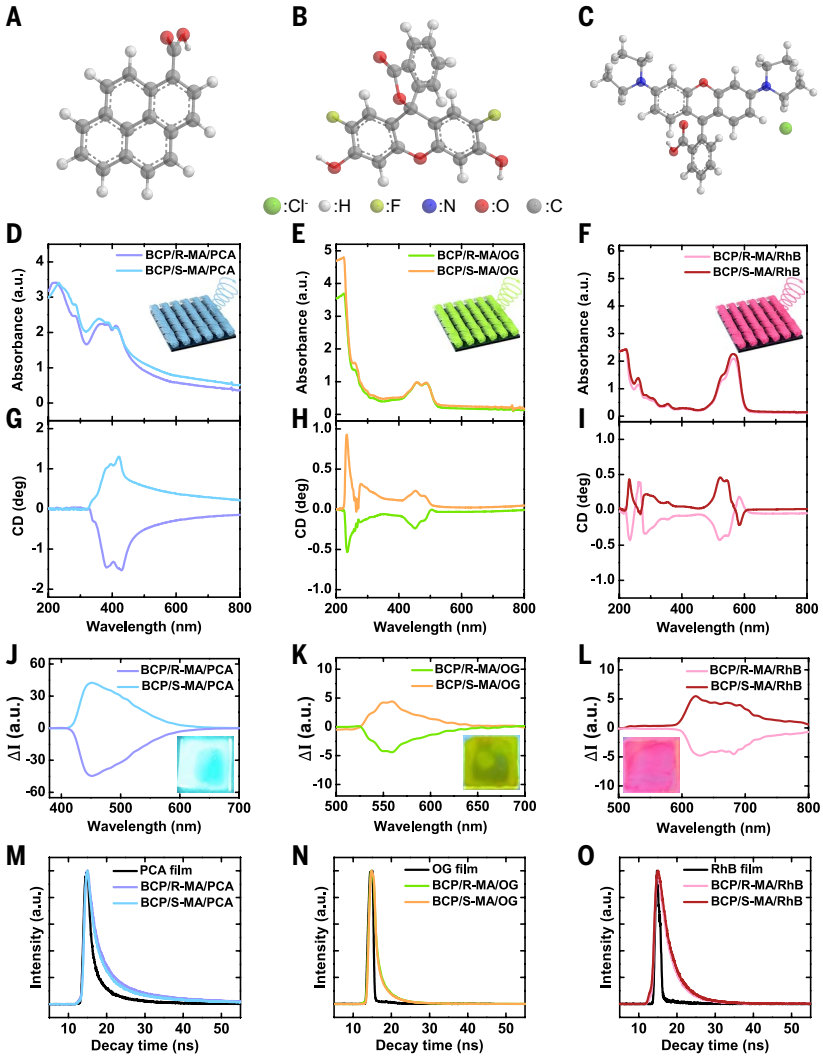

Fig. 4. Spectroscopic analysis of CPL-active chiral supramolecular structures. (**A** to **C**) Molecular structures of the three dye molecules: PCA (A), OG (B), and RhB (C). (**D** to **O**) Absorption [(D) to (F)] and corresponding CD spectra [(G) to (I)], CPL spectra [(J) to (L)], and normalized photoluminescence (PL) decay traces [(M) to (O)] of CPL-active chiral supramolecular structures incorporating PCA [(D), (G), (J), and (M)], OG [(E), (H), (K), and (N)], and RhB [(F), (I), (L), and (O)] molecules. CPL spectra for PCA- and RhB-incorporated structures were obtained using unpolarized 350-nm light excitation, and 488-nm excitation was used for OG-incorporated structures. All measurements were conducted at room temperature. PL decay traces in (M) and (O) were obtained with a pulsed excitation at 375 nm and that in (N) with a pulsed excitation at 450 nm. The pure OG film in (N) was prepared after 1-hour thermal annealing, because longer annealing led to emission quenching. ΔI represents the difference between I_L and I_R. Insets in (J) to (L) are photographs taken under 365-nm light irradiation.

SEM images revealed that incorporating PCA and OG yielded supramolecular fiber–like architectures with distinct handedness (figs. S35 and S36), consistent with the chiral structures created from coassembly of star-like BCP and (R/S)-MA without dyes. The morphology formed by introducing RhB resembled that of star-like BCP/S-MA achieved after 2 to 3 hours of thermal annealing (Fig. 2), suggesting that RhB, a bulky dye molecule, retarded the mobility of polymer chains and thus the evolution of chiral supramolecular structures (fig. S37). Prolonged thermal annealing of RhB-incorporated structures (48 hours; fig. S38) led to the formation of intertwined belt-like structures, resembling those observed after 8 to 12 hours, but failed to form thermodynamically equilibrated fiber-like structures because of limited mobility in the absence of solvent. Although CD and g_{CD} increased, the g_{lum} value decreased to 5.0×10^{-2} (at 602 nm) because of emission degradation, underscoring the need for optimized annealing conditions to facilitate effective chirality transfer while preventing self-aggregation and thermal degradation.

Beyond PCA, OG, and RhB, which exhibited ACQ, the chiral coassembly approach extends to hydrophobic aggregation-induced emission (AIE)–active dyes such as tetraphenylethylene (TPE) and hexaphenyl-1H-silole (HPS) (see the supplementary text). Structures incorporating TPE and HPS showed efficient chirality transfer, as evidenced by CD and CPL signals, with g_{lum} values of 0.11 and 0.05, respectively (figs. S39 and S40). The FTIR analysis revealed the π-π interaction between PS segments and TPE/HPS molecules (fig. S41), which we expected to mediate the chiral coassembly of dyes with star-like PAA-*b*-PS/(R/S)-MA. The SEM images showed the formation of belt-like structures rather than fiber-like assemblies (fig. S42), which was attributed to PS block expansion upon dye interaction (fig. S15), potentially leading to kinetically trapped assemblies.

Control experiments with ACQ dyes with different hydrogen-bonding capabilities, including pyrene (lacking carboxylic acids) and 9-fluorenone-2,7-dicarboxylic acid (with two carboxylic acids), demonstrate that multiple hydrogen bonds between the dyes and the PAA/MA blocks more effectively promoted chirality transfer than interactions between the dyes and the PS blocks (figs. S43 to S46 and supplementary text). Overall, this versatile coassembly approach leveraged the amphiphilic star–like block copolymer's ability to accommodate both hydrophobic and hydrophilic dyes regardless of their ACQ or AIE characteristics.

To further demonstrate the versatility and effectiveness of our approach in producing diverse CPL-active materials, achiral perovskite NCs were coassembled with star-like PAA-*b*-PS/(R/S)-MA. The in situ formation of $CsPbBr_3$ NCs within star-like PAA-*b*-PS/(R/S)-MA failed to impart chiroptical characteristics to the NCs (fig. S47) because oxygen atoms in the –COOH group of PAA blocks preferentially coordinated with Pb in $CsPbBr_3$ NCs, rather than forming hydrogen bonds with (R/S)-MA (*39*). Thus, to retain hydrogen bonding while introducing achiral perovskite NCs, PS-ligated $CsPbBr_3$ NCs, crafted with star-like PAA-*b*-PS nanoreactors (Fig. 5A, top two left panels) as described in our previous study (*40*–*42*), were exploited as achiral emitters (fig. S48). The surface of $CsPbBr_3$ NCs was intimately and permanently tethered with PS chains, ensuring their stability in the film state even during thermal annealing (*43*).

Figure 5A depicts the creation of PS-ligated $CsPbBr_3$ NC-incorporated chiral supramolecular structures through coassembly. Briefly, PS-ligated $CsPbBr_3$ NCs and star-like PAA-*b*-PS/(R/S)-MA were introduced into a solvent mixture of DMF and toluene at a 1:4 volume ratio (v/v). This ratio was chosen to ensure the dissolution of star-like PAA-*b*-PS/(R/S)-MA and the dispersion of PS-ligated $CsPbBr_3$ NCs while minimizing $CsPbBr_3$ NC decomposition by polar DMF. The resulting solution was then drop-cast onto a substrate and annealed at 50°C for 15 min. The faster evaporation of toluene accelerated the coassembly at this lower temperature (*44*). This strategy effectively mitigated $CsPbBr_3$ NC degradation during film deposition and thermal treatment. The resulting structures exhibited QYs of ~25.7%, higher than those of pure NC films (7.0%). Furthermore, their emission lifetimes were four times longer than those of pure NC films (fig. S49, table S4, and supplementary text), demonstrating the enhanced thermal stability provided by passivation with the star-like BCP and MA.

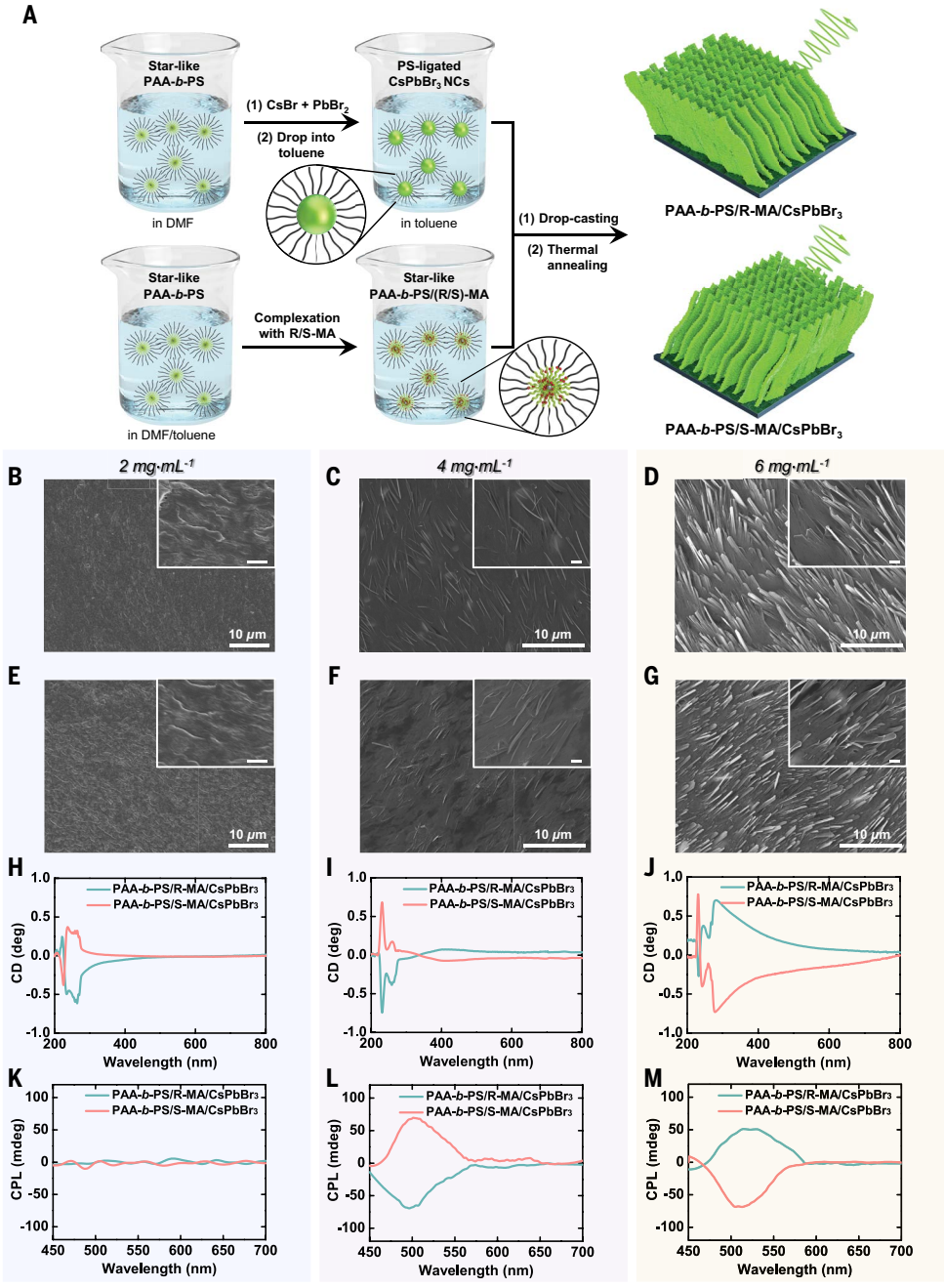

Fig. 5. Perovskite NC–incorporated chiral supramolecular structures and inversion of CPL emission. (**A**) Stepwise representation of creating CPL-active perovskite NC–incorporated chiral supramolecular structures achieved by coassembly of achiral star–like PAA-*b*-PS BCPs, enantiomerically pure (R/S)-MA, and PS-ligated $CsPbBr_3$ NCs. Specifically, thermal annealing was conducted at 50°C for 15 min right after drop-casting star-like PAA-*b*-PS/(R/S)-MA/$CsPbBr_3$ solution in the mixed solvents of DMF and toluene at a DMF:toluene ratio of 1:4 (v/v). The concentrations of the star-like BCP were 2, 4, and 6 mg ml^{-1}. Star-like PAA-*b*-PS used for complexing with MA through hydrogen bonding and for crafting PS-ligated $CsPbBr_3$ NCs were identical to $M_{n,\,PAA} = 100$ kg mol^{-1} and $M_{n,\,PS} = 190$ kg mol^{-1}. (**B** to **G**) SEM images of PS-ligated $CsPbBr_3$ NCs-incorporated chiral supramolecular structures formed at various star-like PAA-*b*-PS concentrations: 2 mg ml^{-1} [(B) and (E)], 4 mg ml^{-1} [(C) and (F)], and 6 mg ml^{-1} [(D) and (G)], with R-MA [(B) to (D)] and S-MA [(E) to (G)] molecules serving as chiral additives. Insets are magnified SEM images. Scale bar, 1 μm. (**H** to **M**) CD [(H) to (J)] and CPL [(K) to (M)] spectra of PS-ligated $CsPbBr_3$ NC-incorporated chiral supramolecular structures produced using star-like PAA-*b*-PS/(R/S)-MA solutions at different star-like PAA-*b*-PS concentrations: 2 mg ml^{-1} [(H) and (K)], 4 mg ml^{-1} [(I) and (L)], and 6 mg ml^{-1} [(J) and (M)]. CPL spectra were recorded under unpolarized 365-nm light excitation at room temperature.

Chiroptical properties of PS-ligated $CsPbBr_3$ NCs-incorporated structures depended on the concentration of star-like PAA-*b*-PS BCPs. At low concentration (2 mg ml^{-1}), irregular aggregates of randomly distributed star-like PAA-*b*-PS/(R/S)-MA and PS-ligated $CsPbBr_3$ NCs formed (Fig. 5, B and E, and fig. S50, A and D), displaying bisignate Cotton effects due to the conformational chirality of the PAA/MA chain (Fig. 5H and fig. S51, A and D). However, inefficient chiral coassembly with $CsPbBr_3$ NCs prevented CPL generation, resulting in only weak green emission from $CsPbBr_3$ NCs (Fig. 5K and fig. S52, A and D). At 4 mg ml^{-1}, these irregular aggregates transformed into supramolecular, rodlike structures with diameters of several hundred nanometers (Fig. 5, C and F, and fig. S50, B and E). The presence and spatial

distribution of PS-ligated $CsPbBr_3$ NCs within the structures were verified through x-ray diffraction and energy-dispersive spectroscopy elemental mapping (figs. S53 to S55). The rodlike structures exhibited intense CD signals (Fig. 5I and fig. S51, B and E) and strong CPL emission at 505 nm, with a g_{lum} of 2.2×10^{-2} (Fig. 5L and fig. S52, B and E).

The CPL signals, which correlated with the supramolecular handedness established during thermal annealing–driven coassembly (Fig. 1E), combined with the absence of selective reflection (fig. S56), suggested that the CPL emission originated from the chiral arrangement of achiral $CsPbBr_3$ NCs induced by chiral coassembly. As the concentration increased to 6 mg ml^{-1}, the rodlike structures aligned unidirectionally, forming densely packed arrays (Fig. 5, D and G, and fig. S50, C and F), and exhibited inverted CD responses, implying an opposite supramolecular handedness (Fig. 5J and fig. S51, C and F). This chirality inversion was further substantiated by the reversal of green CPL signals, with a g_{lum} of 1.2×10^{-2} at 510 nm (Fig. 5M and fig. S52, C and F). The bisignate CD responses at 335 nm shown in Fig. 5I originated from an ongoing concentration-dependent chirality inversion driven by kinetically trapped rodlike assemblies with strong chiroptical properties in the visible region (see details in the supplementary text). Consequently, these findings highlight that the strategic use of high concentrations, combined with a highly evaporative solvent (i.e., toluene), synergistically induced kinetically trapped coassemblies with opposite chirality (Fig. 5), preventing them from reaching thermodynamically favorable states (Figs. 1 to 4) (*45*).

To enhance the coassembly efficiency, PS-ligated $CsPbBr_3$ NCs with PS of half of the original molecular weight were coassembled with star-like PAA-*b*-PS/(R/S)-MA, forming well-ordered, long, rodlike structures (fig. S57). The structures manifested stronger CD signals with a g_{CD} of 4.8×10^{-2} at 480 nm (fig. S58, A and C), along with the amplified CPL emission with a g_{lum} of 0.12 at 470 nm (fig. S58, B and D). However, the shorter PS chains formed a sparser shell, reducing protection against heat, oxygen, moisture, and polar solvents (e.g., DMF), and led to a blue-shifted emission at 445 nm attributed to a thermally induced Br vacancy–related bandgap (*40*, *46*).

To improve the stability and coassembly efficiency, a star-like BCP with PS chains at two-thirds the original molecular weight was used, resulting in stronger CPL signals with a reduced blue shift at 500 nm and a g_{lum} of 6.7×10^{-2} (fig. S59). This value surpassed those recently reported in achiral perovskite NCs coassembled with chiral templates (table S5 and fig. S60), highlighting the critical role of PS-ligated $CsPbBr_3$ NCs within star-like PAA-*b*-PS nanoreactors for efficient chirality transfer and enhanced NC stability. This finding was further substantiated by the weak chiroptical properties and blue-shifted emission that we observed when using oleic acid/oleylamine–cocapped $CsPbBr_3$ NCs (fig. S61 and supplementary text).

Finally, for strongly CPL-emissive chiral structures incorporating organic dyes (PCA and TPE) and PS-ligated $CsPbBr_3$ NCs, artifact CPL signals caused by LD, LB effects, or residual birefringence of the spectrometer's photoelastic modulator were eliminated by averaging CPL and g_{lum} spectra from front and back sides at different rotational angles (figs. S62 to S64 and supplementary text). The calculated genuine g_{lum} values, excluding artifact contributions, were 9.5×10^{-2}, 9.0×10^{-2}, and 6.0×10^{-2}, respectively, which remained higher than those reported in similar studies using chiral coassembly approaches of polymers and achiral emitters (tables S3 and S5). These results corroborated the high intrinsic chiroptical properties of our chiral coassembled structures and demonstrated that although LD and LB effects contributed to the observed g_{lum} values, the high genuine g_{lum} values validated the effectiveness of our design.

Concentration-dependent inversion of supramolecular chirality

To elucidate the mechanism underlying the concentration-induced chirality inversion in $CsPbBr_3$ NC–incorporated structures (Fig. 5, I, J, L, and M), star-like PAA-*b*-PS/(R/S)-MA complexes in a DMF-toluene solvent mixture (v/v = 1:4) were drop-cast at different BCP concentrations and then annealed at 50°C for 15 min (without PS-ligated $CsPbBr_3$ NCs; fig. S65A). The incompatibility of toluene with PAA, combined with the relatively low annealing temperature and rapid solvent evaporation, restricted the mobility of the BCPs during coassembly. At low concentration (1 mg ml^{-1}), assemblies exhibited bisignate Cotton effects (fig. S66), likely because of exciton coupling from hydrogen-bonding interactions.

At 2 mg ml^{-1}, the PAA-*b*-PS/R-MA and PAA-*b*-PS/S-MA assemblies showed negative and positive CD signals, respectively (fig. S65H), reflecting the conformational handedness of the PAA/(R/S)-MA chains (*47*) and suggesting the formation of right-handed and left-handed chains, respectively, but not distinct chiral supramolecular structures (figs. S65, B and E, and S67, A and D). Instead, macroporous structures with randomly distributed star-like PAA-*b*-PS nanoparticles formed, likely through solvent evaporation-induced vesicle-to-pore morphological transition, which would reduce interfacial tension between hydrophilic PAA and toluene (*48*, *49*).

At 4 mg ml^{-1}, irregularly oriented microscopic rodlike structures began to emerge alongside smaller macroporous structures (figs. S65, C and F, and S67, B and E). At 6 mg ml^{-1}, the number of rodlike structures increased, exhibiting uniform orientation and dense packing (figs. S65, D and G, and S67, C and F). As the concentration increased, CD signals decreased and eventually inverted (fig. S65, H to J), suggesting that rodlike structure formation and orientation may lead to opposite supramolecular chirality. The maximum g_{CD} value of the rodlike structures formed at 6 mg ml^{-1} reached 0.1 at 380 nm, highlighting their strong chiroptical activity (fig. S68). The minimal LD and LB contributions (1.4%) to the observed CD signals (figs. S69 and S70 and supplementary text) further confirmed their strong intrinsic chiroptical properties.

CG-MD simulations were performed to investigate the favorable handedness of coassembled structures formed during rapid annealing at a high concentration of star-like BCP (6 mg ml^{-1}). PAA-*b*-PS/S-MA complexes were dissolved in DMF-toluene and equilibrated in a simulation box under periodic boundary conditions. The system was simulated under canonical ensemble conditions at T = 323 K, with 99% of the solvent removed through simulated evaporation over 150 μs. Subsequent thermal annealing for 50 μs led to the formation of directionally aligned PAA-*b*-PS/S-MA structures without obvious twisting (fig. S71A), consistent with SEM observations (fig. S65G). The energy profile plotted against θ showed a minimum at +10° (fig. S71B), indicating a preference for right-handed structures. However, this minimum was higher than that observed under slow annealing (Fig. 3G), suggesting that the handedness is kinetically driven by the rapid coassembly process. This finding was consistent with the inverted chirality observed in the CD spectrum (fig. S65J). Together, these results highlight the critical role of highly evaporative toluene in restricting polymer mobility, leading to kinetically trapped structures with reversed chirality, contrasting with the thermodynamically preferred structures formed in pure DMF (Figs. 1 to 4).

The rodlike structures exhibited enhanced chiroptical properties (g_{CD} value from 0.1 to 0.16) after 100 days at room temperature, likely because of further supramolecular structural evolution during long-term storage, with improved alignment extending to the bottom layers (fig. S72). Upon heating at 60°C for 6 hours, their initially inverted chiroptical properties reverted, accompanied by a transformation into nanoscale belt-like structures (fig. S73, A to D) resembling those formed by thermal annealing using DMF (Fig. 2, E and F).

Their stability at room temperature suggests that the rodlike structures are kinetically trapped, nonequilibrium structures with high energy barriers. However, heating-induced chiroptical inversion signifies that external energy input can overcome these barriers, although full transition to fiber-like structures remains hindered by limited molecular mobility at high concentration. Further heating-cooling

cycles caused a gradual yet minor decline in chiroptical properties, likely because of continued structural evolution into belt-like structures with lower chirality (fig. S73, E and F). Nevertheless, this decrease remained minimal, and the belt-like structures showed no detectable deformation or degradation (fig. S73, G and H), demonstrating good thermal stability.

This concentration-dependent chirality inversion could be transferred to achiral dye molecules (e.g., PCA, OG, and RhB) through coassembly (figs. S74 to S82). At 2 mg ml^{-1}, dye molecule-incorporated chiral structures exhibited weak CD signals and CPL emission because insufficient building blocks were present for effective chirality transfer, with the SEM images showing random aggregation and no distinct chiral structures. At 4 mg ml^{-1}, strong CD signals and CPL emission (g_{lum}: 2.6×10^{-2} for PCA at 510 nm, 8.0×10^{-2} for OG at 515 nm, and 3.7×10^{-2} for RhB at 615 nm) were observed, along with sparsely distributed rigid rodlike structures. At 6 mg ml^{-1}, chiroptical properties reversed (structures with R-MA: positive CD and CPL; structures with S-MA: negative CD and CPL), with the SEM images showing densely packed, aligned rodlike structures. The bisignate CPL signals in PCA-incorporated structures arose from CPL reabsorption because of substantial CD-CPL overlap at the higher-energy emission band, which disappeared at a higher BCP concentration of 8 mg ml^{-1} (figs. S83 and S84; see details in the supplementary text) (*50*). These results demonstrated that concentration-dependent chiroptical inversion driven by highly evaporative solvents could be applied to a variety of emitters to achieve robust, full-color, and tunable CPL performance.

Discussion

We have demonstrated here that hierarchical fibrillar supramolecular assemblies with pronounced multiscale chirality, long-term stability, and enhanced mechanical strength can be achieved by leveraging the stable unimolecular micellar architecture of achiral amphiphilic star–like PAA-*b*-PS BCPs and multiple hydrogen bonding between PAA blocks and the chiral additive (R/S)-MA. Time-dependent CD measurements, morphological studies, and CG-MD simulations revealed a stepwise evolution toward thermodynamically favorable chiral structures during coassembly. This strategy provides a universal platform for generating full-color CPL-active materials with high g_{lum} values (~10^{-1}) by incorporating diverse achiral fluorescent dyes and perovskite NCs. These findings highlight an efficient hierarchical chirality transfer in which molecular chirality directs supramolecular assembly, subsequently propagating chirality to luminescent components within the structure.

Moreover, a concentration-dependent inversion of supramolecular chirality underscores the role of solvent interactions and removal in forming kinetically trapped structures with inverted chirality. This coassembly approach offers strong, full-color, and tunable CPL activity, showcasing the potential of star-like BCPs for high-performance CPL-active materials in chiral optoelectronic and spintronic devices. Of particular importance is the ability to achieve strong red CPL emission, which remains rare and is especially valuable for advanced quantum technologies because of its low optical loss and high information-encoding capacity. Finally, given the diversity of nonlinear BCPs with unimolecular micellar architectures (e.g., bottlebrush-like, hyperbranched, and Janus structures) and various characteristics (e.g., semiconducting, stimuli responsive, etc.), this method provides a pathway to create diverse hierarchical chiral supramolecular assemblies and CPL-active materials and devices with tailored functionalities.

Materials and methods

Materials

Toluene (≥99.5%), dichloromethane (DCM, ≥99.5%), α-bromoisobutyryl bromide (BiBB, 98%), anisole (99%), 2-butanone (methyl ethyl ketone, MEK, ≥99.0%), DMF (anhydrous, 99.8%), 1-methyl-2-pyrrolidinone (NMP, anhydrous, 99.5%), *N*,*N*,*N*′,*N*″,*N*″-pentamethyldiethylenetriamine (PMDETA, 99%), diethyl ether (anhydrous, ≥99.0%), ethanol (anhydrous, ≥99.5%), calcium hydride (CaH_2, powder, 0-2 mm, reagent grade, ≥90%), sodium bicarbonate ($NaHCO_3$, ≥99.7%), aluminum oxide powder (activated, neutral, Brockmann I), tetrahydrofuran (THF, ≥99.0%), acetone (≥99.5%), deuterated chloroform ($CDCl_3$, 99.96 atom % D), acetic acid (≥99.7%), RhB (≥95%), cesium bromide (99.999% trace metals basis), lead(II) bromide (≥98%), oleylamine (technical grade, 70%), oleic acid (technical grade, 90%), (R)-(−)-mandelic acid (R-MA, ≥99%), and (S)-(+)-mandelic acid (S-MA, ≥99%) were purchased from Sigma-Aldrich and used without further purification. TPE (≥98%), HPS (≥95%), pyrene (Py, ≥ 97%), and 9-fluorenone-2,7-dicarboxylic acid (FDCA, ≥95%) were purchased from Aladdin Scientific Corp and used without further purification. Trifluoroacetic acid (TFA, ≥99.5%) and 2′,7′-difluorofluorescein (Oregon Green 488, OG) were obtained from Thermo Fisher Scientific and used without further purification. β-cyclodextrin (β-CD, ≥97%, Sigma-Aldrich) was subjected to vacuum drying for 48 hours at 60°C and then distilled under azeotropic conditions in toluene for 2 hours at 120°C before the esterification reaction. Copper(I) bromide (CuBr, 98%, Sigma-Aldrich) was stirred for 2 hours in acetic acid, then filtered, washed with ethanol and diethyl ether, and finally dried under vacuum at room temperature overnight. Styrene (St, ≥99%, Sigma-Aldrich) and tert-butyl acrylate (tBA, 98%, Sigma-Aldrich) were distilled over CaH_2 under reduced pressure before use. 1-Pyrenecarboxylic acid (PCA, 97%, Sigma-Aldrich) was purified through crystallization using ethanol as a solvent.

Synthesis of star-like PAA-b-PS

Figure S1 illustrates the stepwise synthesis of amphiphilic star–like unimolecular poly(acrylic acid)-block-polystyrene (PAA-*b*-PS) (*51*).

Synthesis of brominated β-CD initiator (denoted 21-Br-β-CD)

21 hydroxyl end groups of each β-CD molecule were transformed into 2-bromo-2-methylpropionate (BMP) groups through esterification, resulting in the formation of a macroinitiator denoted 21-Br-β-CD. Specifically, β-CD (2.5 mmol) was dissolved in anhydrous NMP (40 ml), and the solution was cooled to 0°C in an ice bath. BiBB (105 mmol) was then gradually added over an hour with continuous vigorous stirring. After the complete addition of BiBB, stirring was sustained for an additional hour at 0°C. Subsequently, the mixture was allowed to gradually return to room temperature, followed by stirring for another 23 hours. The crude solution was then diluted with DCM and subjected to multiple washes with saturated $NaHCO_3$ aqueous solution and deionized water. The final product was collected by removing the DCM under reduced pressure using a rotary evaporator and drying the residue in a vacuum oven overnight at room temperature.

Synthesis of star-like poly(tert-butyl acrylate) (PtBA)

The first step entailed mixing 21-Br-β-CD (macroinitiator), CuBr (catalyst), PMDETA (ligand), tBA (monomer), and MEK (solvent) in an ampoule, keeping the molar ratio of bromine in 21-Br-β-CD, CuBr, PMDETA, MEK, and tBA at 1:1:2:2000:1000. The mixture was purged with N_2 for an hour to remove any oxygen. After this, the sealed ampoule was placed in a preheated oil bath at 60°C. To stop the polymerization at predetermined times, the ampoule was removed from the bath, quickly cooled in an ice bath, and exposed to air. The crude solution was then diluted with acetone, passed through a neutral alumina column to remove the catalyst, and precipitated in a water/methanol mixture (v/v = 1:1). After filtration, the final product was dried in a vacuum oven at room temperature.

Synthesis of star-like poly(tert-butyl acrylate)-block-polystyrene (PtBA-b-PS)

The as-prepared star-like P*t*BA polymer, CuBr, PMDETA, styrene, and anisole were mixed in an ampoule and purged with nitrogen gas for 1 hour to eliminate oxygen. The molar ratio for bromine in star-like P*t*BA, CuBr, PMDETA, anisole, and St was maintained at 1:1:2:2000:1000. The ampoule was then sealed and submerged in an oil bath set at 90°C.

To stop the polymerization at specific intervals, the ampoule was removed from the bath, rapidly cooled in an ice bath, and then exposed to air. The resulting crude solution was diluted with THF, passed through a neutral alumina column to remove the catalyst, and precipitated in a water/methanol mixture (v/v = 1:1). After filtration, the final product was dried in a vacuum oven at room temperature.

Synthesis of star-like poly(acrylic acid)-block-polystyrene (PAA-b-PS)

The initial step involved dissolving the star-like P*t*BA-*b*-PS in anhydrous DCM. TFA was then gradually added under vigorous stirring at room temperature to initiate hydrolysis. After 24 hours, the DCM was removed through a rotary evaporator. The resulting product, amphiphilic PAA-*b*-PS, underwent a dissolution-precipitation process using DCM and methanol for purification. Finally, the purified product was dried in a vacuum oven at room temperature.

Crafting of chiral fiber-like supramolecular structures

Chiral fiber-like supramolecular structures were fabricated through coassembly of star-like BCP and R/S-MA. Initially, star-like PAA-*b*-PS (2.5 mg) and a certain amount of R/S-MA were dissolved in 1 ml of DMF and stirred for a minimum of 2 days at room temperature to ensure sufficient hydrogen-bonding interactions between PAA blocks of star-like PAA-*b*-PS and R/S-MA. The molar ratio of the PAA repeating unit to MA was maintained at 1:2. The solution was then purified by passing through a 200 nm PTFE filter, followed by evenly drop-casting onto a substrate (e.g., silica, glass, or quartz, depending on the characterization method; silica for SEM imaging, glass, and quartz for chiroptical characterizations). Subsequently, the film was annealed at 60°C for 24 hours, during which time the solvent slowly evaporated, allowing the progressive formation of fiber-like structures (i.e., microfibers).

Creation of CPL-active, dye molecules-incorporated supramolecular structures

Star-like PAA-*b*-PS (2.5 mg) and R/S-MA were initially mixed in 1 ml of DMF. The mixture was then stirred at room temperature for at least 48 hours, maintaining a molar ratio of the PAA repeating unit to MA at 1:2. For dye incorporation, specific amounts of achiral fluorescent dye molecules were dissolved in small volumes of DMF (<100 μl). The dyes included blue-emitting PCA, green-emitting OG, red-emitting RhB, as well as TPE, HPS, pyrene (Py), and 9-fluorenone-2,7-dicarboxylic acid (FDCA). The molar ratios of the PAA repeating unit to PCA, OG, RhB, TPE, HPS, Py, and FDCA were set at 4:1, 10:1, 10:1, 5:1, 10:1, 10:1, and 10:1, respectively. The dyes were then added to the above solution containing PAA-*b*-PS and R/S-MA. The resulting solution was stirred continuously for an additional 24 hours in an ice bath at temperatures between 5° and 10°C, in a dark environment, to prevent light- or heat-induced degradation of the dyes. Subsequently, the solution was filtered through a 200 nm PTFE syringe filter and evenly drop-cast onto various substrates, including silica, glass, and quartz. The resulting film was thermally annealed at 60°C for 24 hours, allowing the solvent to gradually evaporate, yielding chiral supramolecular structures.

Creation of aligned rodlike supramolecular structures with inversible chirality

Aligned rodlike supramolecular structures were prepared by coassembly of star-like BCP and R/S-MA. The process began with dissolving star-like PAA-*b*-PS and R/S-MA in 0.2 ml of DMF. The mixture was then stirred continuously at room temperature for a minimum of 48 hours. Subsequently, 0.8 ml of toluene was added, and the stirring was extended for an additional 24 hours. The volume ratio of toluene to DMF was maintained at 4:1, and the molar ratio of the PAA repeating unit to MA was kept consistent at 1:2. The concentration of the star-like PAA-*b*-PS solution was adjusted to 2 mg ml^{-1}, 4 mg ml^{-1}, and 6 mg ml^{-1}. The solution was purified by passing through a 200 nm PTFE filter and evenly drop-cast onto various substrates, such as silica, glass, and quartz. The resulting film was annealed at 50°C for 15 min, during which the solvent rapidly evaporated, progressively forming and aligning rodlike supramolecular structures.

Synthesis of PS-ligated $CsPbBr_3$ NCs

To synthesize PS-ligated $CsPbBr_3$ NCs, 3 mg of star-like PAA-*b*-PS was first dissolved in 1 ml of DMF at room temperature. Subsequently, CsBr and $PbBr_2$ were sequentially added to the solution. The molar ratio of the PAA repeating unit to CsBr and $PbBr_2$ was meticulously maintained at 1:1:1. This mixture was then stirred continuously at room temperature for a minimum of three days, allowing sufficient time for the precursors to thoroughly diffuse into the inner PAA core. Afterwards, the precursor solution was rapidly injected into toluene, immediately forming PS-ligated $CsPbBr_3$ NCs in the solution. The PS-ligated $CsPbBr_3$ NCs solution was then purified using toluene as a solvent and hexane as a precipitant, maintaining a volume ratio of toluene to hexane at 1:2. Finally, the precipitated PS-ligated $CsPbBr_3$ NCs was redispersed in toluene.

Creation of PS-ligated $CsPbBr_3$ NCs-incorporated chiral supramolecular structures

Star-like PAA-*b*-PS and R/S-MA were dissolved in 0.2 ml of DMF, maintaining a 1:2 molar ratio of PAA to MA. The mixture was stirred at room temperature for 48 hours, followed by the addition of 0.3 ml of toluene, with stirring continued for another 24 hours. Then, 0.5 ml of PS-ligated $CsPbBr_3$ NCs solution was added, maintaining a 28:1 concentration ratio of star-like PAA-*b*-PS in the PAA-*b*-PS/(R/S)-MA solution to star-like PAA-*b*-PS used as the nanoreactor for $CsPbBr_3$ NCs. The total concentration of the star-like PAA-*b*-PS solution was adjusted to 2 mg ml^{-1}, 4 mg ml^{-1}, and 6 mg ml^{-1}. The solution was drop-cast onto substrates (i.e., silica, glass, and quartz) and annealed at 50°C for 15 min, forming CPL-active, perovskite NCs-incorporated chiral supramolecular structures.

DFT simulations

All DFT calculations were performed with the Gaussian 09 program package (*52*). The geometries were optimized at B3LYP (*53*) in combination with the 6-311G(d) atomic basis set for all nonmetal atoms. All optimized structures were confirmed to be local minima by normal-mode analysis with all positive frequencies. All geometry optimizations were performed without symmetry constraints. The evaluated fundamental frequencies have been optimized with the help of visualization program GaussView (*54*). The formation energy (E_f) was calculated according to the following equation:

$$E_f = E_{total} - E_{PAA} - E_{MA}$$

where E_{total}, E_{PAA} and E_{MA} are the energies of PAA/MA, PAA and MA, respectively.

CG-MD simulations

To assess large temporal and spatial scales, we performed MD simulations with CG models, which took a group of atoms as a bead (fig. S25). Specifically, a bead-spring model was used with the three types of beads (type A, B, and C) and the bead size of 1 nm. In CG-MD simulations, the reduced units of length, energy, mass, and time were σ_0 = 1.0 nm, $\epsilon_0 = 2.77$ kJ mol^{-1}, $m_0 = 1000.0$ amu, and $\tau_0 = 1.0$ ns, respectively. Specifically, the time scale mapping of τ_0 is obtained by fitting the diffusion constant of solvent DMF to its experimental value (*55*). The nonbonded interactions between CG beads were described by Lennard-Jones potential:

$$V_{LJ}(r) = 4\epsilon_{ij}\left[\left(\frac{\sigma_{ij}}{r_{ij}}\right)^{12} - \left(\frac{\sigma_{ij}}{r_{ij}}\right)^{6}\right]$$

where r_{ij} is the distance between bead i and j, and the interaction parameters ϵ_{ij} and σ_{ij} are listed in table S6. We note this potential was truncated at $r_{cut} = 2.5\ \sigma_0$.

The harmonic potential was used to describe bond stretching interactions in the bead-spring model:

$$V_{bond}(r) = \frac{1}{2}K_{bond}(r - r_0)^2$$

where $r_0 = 1.0\ \sigma_0$ and $K_{bond} = 1000.0\ \epsilon_0\ \sigma_0^{-2}$. The angle bending interactions for polymer chains were described by a harmonic potential:

$$V_{angle}(\theta) = \frac{1}{2}K_{angle}(\theta - \theta_0)^2$$

where $K_{angle} = 100.0\ \epsilon_0$, $\theta_0 = 128.57°$ for ∠C-C-C, $\theta_0 = 150.0°$ for ∠A-A-A, $\theta_0 = 120.0°$ for ∠A-C-A, and $\theta_0 = 150.0°$ for ∠C-C-A. The dihedral torsion interactions for polymer chains were described by a harmonic potential:

$$V_{dihedral}(\psi) = \frac{1}{2}K_{dihedral}(\psi - \psi_0)^2$$

where $K_{dihedral} = 20.0\ \epsilon_0$, $\Psi_0 = 20.0°$ for ∠A-A-A-A in star-like PAA-*b*-PS/S-MA, and $\Psi_0 = -20.0°$ for ∠A-A-A-A in star-like PAA-*b*-PS/R-MA.

The system used for evaporation simulation consisted of 60 star-like polymers. The CG-MD simulations were performed at a time interval of 0.5 ps per integration step, under canonical ensemble conditions at T = 333 K. The final structures were obtained from CG-MD simulations conducted under explicit solvent conditions. To simulate the evaporation process, we used a constant chemical potential method (*56*), using a delete zone with a thickness of $10\sigma_0$ at the top of simulation box. When solvent particles entered this zone from the gas phase of the solution, each particle had a probability of $P = 1.0 \times 10^{-4}$ of turning into a ghost particle. Once converted, ghost particles no longer interacted with their surroundings. The evaporation process was simulated for 3.0×10^8 time steps (150 μs) with $dt = 0.0005\tau_0$. The simulation was performed in a cubic box, starting from a dilute polymer solution and continuing until a thin polymer film was formed. During this process, the number density of star-like polymers increased from 1.0×10^{-4} nm^{-3} to 1.0×10^{-3} nm^{-3}. An annealing process was then simulated by increasing the temperature from 333 K to 450 K, and subsequently cooling it back to 333 K over 1.0×10^8 time steps (50 μs). A bulk system composed of three layers of the polymer film was constructed, and an additional annealing simulation was performed for 4.0×10^8 time steps (200 μs) to yield equilibrium structures. To facilitate the statistical analysis of energy and structural distribution, simulations were performed with a set of biased rotational angles. The resulting equilibrium structures were analyzed to detect chiral transfer from a single layer to multiple layers. All simulations were performed using the in-house developed software on a GPU (*57*, *58*).

Characterization

The molecular weight and polydispersity of star-like P*t*BA and P*t*BA-*b*-PS were determined using gel permeation chromatography (GPC; Shimadzu). The GPC was equipped with a G1362A refractive detector, a G1314A variable wavelength detector, and two columns: a 5 μm LP gel mixed bed column (molecular weight range: 200 to 3×10^6 g mol^{-1}) and a 5 μm LP gel column (500 Å, molecular weight range: 500 to $2\ 10^4$ g mol^{-1}). The GPC was calibrated using monodisperse linear PS as the standard, with THF as the mobile phase at a flow rate of 1.0 ml min^{-1} at 35°C. Proton nuclear magnetic resonance spectroscopy (^{1}H NMR, Bruker Avance III 400) was used to verify the bromination efficiency of 21-Br-β-CD using $CDCl_3$ as the solvent. The successful transformation of star-like P*t*BA-*b*-PS into star-like PAA-*b*-PS through hydrolysis was confirmed by FTIR (Nicolet 6700). The hydrodynamic sizes of star-like diblock copolymers were measured using dynamic light scattering (DLS, Wyatt DynaPro), using DMF as the solvent, at 25°C. Atomic force microscopy (AFM, Bruker Dimension Icon 3100) was used for morphological study in soft tapping mode and for nanoindentation tests in contact mode. Photoluminescence of the samples was investigated using Shimadzu UV-2450 and JASCO FP-8500 spectrophotometers. The noncovalent interactions among the coassembly building blocks were investigated using an INVENIO FTIR spectrometer (Bruker) equipped with an attenuated total reflectance (ATR) accessory, with a wavenumber interval of 1 cm^{-1} and 64 scans. The photoluminescence (PL) spectra and PL decay curves were measured using an Edinburgh FLS1000 fluorescence spectrophotometer equipped with pulsed diode lasers at excitation wavelengths of 375 nm and 450 nm. The circularly polarized luminescence (CPL) emission was analyzed using two methods: (1) by placing left- and right-handed circular polarizers in front of the detector of a Shimadzu UV-2450 spectrometer, and (2) by using a JASCO CPL-300 spectrophotometer. The wavelength-dependent DC (direct current, in volts) trace obtained with the JASCO CPL-300 spectrophotometer corresponds to fluorescence intensity. CD and LD spectra were recorded using JASCO J-815 and J-1500 CD spectrometers. The CD dissymmetry factors, g_{CD} = CD[mdeg]/(32, 980 × absorbance), and the luminescence dissymmetry factors, $g_{lum} = 2(I_L - I_R)/(I_L + I_R)$ = [(CPL[mdeg] × ln10)/(32,980 × DC(V)], were calculated at the absorption and emission bands of the chiral structures. I_L and I_R represent the intensities of left- and right-handed CPL, respectively, and DC denotes the direct current voltage output, corresponding to the total luminescence intensity. Both CD and CPL measurements were conducted at room temperature in the transmission mode.

Polarized light microscopy (PLM) was performed with Olympus BX53F fluorescence microscope equipment with a polarizer (U-AN360P) and a compensator (U-TP137). The absolute photoluminescence quantum yield (PLQY) of the samples was characterized using a Hamamatsu Quantaurus-QY Plus spectrometer and Edinburgh FLS1000 fluorescence spectrophotometer equipped with an integrating sphere. The excitation wavelengths were set at 350 nm for PCA-incorporated samples, 488 nm for OG-incorporated samples, and 350 nm for RhB-incorporated samples. SEM measurements were performed using Hitachi S3400 and Hitachi SU8230 systems, under accelerating voltages of 5 kV and 10 kV respectively, and a JSM-7610F (JEOL) system, under an accelerating voltage of 15 kV. Elemental distribution within the samples was characterized using an energy dispersive x-ray spectrometer on a JSM-7610F (JEOL) system. To enhance the conductivity for SEM measurement, chiral supramolecular structures were coated with a thin layer of gold and platinum using a Hummer 6 sputter coater. Transmission electron microscopy measurements were performed using a JEM-2100Plus (JEOL). The x-ray diffraction pattern was collected using a SPIN-1200D x-ray diffractometer (EPLEX) under Ni-filtered Cu−Kα radiation (λ = 1.5418 Å). Grazing incidence small-angle x-ray scattering measurements were performed using the 3C SAXS-I beamline at the Pohang Accelerator Laboratory (PLS-II, South Korea) with an x-ray energy of 11.3 keV, a sample-to-detector distance of 5007.65 mm, and a fixed incident angle of 0.08°.

REFERENCES AND NOTES

1. M. Liu, L. Zhang, T. Wang, Supramolecular chirality in self-assembled systems. *Chem. Rev.* **115**, 7304–7397 (2015). doi: 10.1021/cr500671p; pmid: 26189453
2. M. Zhang *et al.*, Chiral macromolecules and supramolecular assemblies: Synthesis, properties and applications. *Prog. Polym. Sci.* **151**, 101800 (2024). doi: 10.1016/j.progpolymsci.2024.101800
3. Y. Kim *et al.*, Reconfigurable chiroptical nanocomposites with chirality transfer from the macro- to the nanoscale. *Nat. Mater.* **15**, 461–468 (2016). doi: 10.1038/nmat4525; pmid: 26726996
4. G. F. Liu, L. Y. Zhu, W. Ji, C. L. Feng, Z. X. Wei, Inversion of the supramolecular chirality of nanofibrous structures through co-assembly with achiral molecules. *Angew. Chem. Int. Ed.* **55**, 2411–2415 (2016). doi: 10.1002/anie.201510140; pmid: 26663528
5. X. Zha *et al.*, Handedness inversion of chiral 3-aminophenol formaldehyde resin nanotubes mediated by metal coordination. *Angew. Chem. Int. Ed.* **60**, 7759–7769 (2021). doi: 10.1002/anie.202013790; pmid: 33368984

6. C. Du, Z. Li, X. Zhu, G. Ouyang, M. Liu, Hierarchically self-assembled homochiral helical microtoroids. *Nat. Nanotechnol.* **17**, 1294–1302 (2022). doi: 10.1038/s41565-022-01234-w; pmid: 36329269
7. X. Zhang, J. Zou, K. Tamhane, F. F. Kobzeff, J. Fang, Self-assembly of pH-switchable spiral tubes: Supramolecular chemical springs. *Small* **6**, 217–220 (2010). doi: 10.1002/smll.200901067; pmid: 19859941
8. M. L. Ślęczkowski, M. F. J. Mabesoone, P. Ślęczkowski, A. R. A. Palmans, E. W. Meijer, Competition between chiral solvents and chiral monomers in the helical bias of supramolecular polymers. *Nat. Chem.* **13**, 200–207 (2021). doi: 10.1038/s41557-020-00583-0; pmid: 33257888
9. Z. Geng, Y. Zhang, Y. Zhang, Y. Quan, Y. Cheng, Amplified circularly polarized electroluminescence behavior triggered by helical nanofibers from chiral co-assembly polymers. *Angew. Chem. Int. Ed.* **61**, e202202718 (2022). doi: 10.1002/anie.202202718; pmid: 35318788
10. Y. Shi *et al.*, Recyclable soft photonic crystal film with overall improved circularly polarized luminescence. *Nat. Commun.* **14**, 6123 (2023). doi: 10.1038/s41467-023-41884-5; pmid: 37777553
11. J. Wang *et al.*, Aqueous synthesis of low-dimensional lead halide perovskites for room-temperature circularly polarized light emission and detection. *ACS Nano* **13**, 9473–9481 (2019). doi: 10.1021/acsnano.9b04437; pmid: 31373789
12. R. Rodríguez *et al.*, Mutual monomer orientation to bias the supramolecular polymerization of [6]helicenes and the resulting circularly polarized light and spin filtering properties. *J. Am. Chem. Soc.* **144**, 7709–7719 (2022). doi: 10.1021/jacs.2c00556; pmid: 35404592
13. C. Wang, L. Liu, J. Wang, Y. Yan, Electrochemically switchable circularly polarized photoluminescence within self-assembled conducting polymer helical microfibers. *J. Am. Chem. Soc.* **144**, 19714–19718 (2022). doi: 10.1021/jacs.2c10023; pmid: 36260365
14. B. Yue *et al.*, In situ regulation of microphase separation-recognized circularly polarized luminescence via photoexcitation-induced molecular aggregation. *ACS Nano* **16**, 16201–16210 (2022). doi: 10.1021/acsnano.2c05056; pmid: 36130082
15. Y. Shi, P. Duan, S. Huo, Y. Li, M. Liu, Endowing perovskite nanocrystals with circularly polarized luminescence. *Adv. Mater.* **30**, e1705011 (2018). doi: 10.1002/adma.201705011; pmid: 29363205
16. J. Yan *et al.*, Self-assembly of chiral nanoparticles into semiconductor helices with tunable near-infrared optical activity. *Chem. Mater.* **32**, 476–488 (2019). doi: 10.1021/acs.chemmater.9b04143
17. S. Jiang, N. A. Kotov, Circular polarized light emission in chiral inorganic nanomaterials. *Adv. Mater.* **35**, e2108431 (2023). doi: 10.1002/adma.202108431; pmid: 35023219
18. Y. Huang *et al.*, Reducing aggregation caused quenching effect through co-assembly of PAH chromophores and molecular barriers. *Nat. Commun.* **10**, 169 (2019). doi: 10.1038/s41467-018-08092-y; pmid: 30635576
19. Y. He, S. Lin, J. Guo, Q. Li, Circularly polarized luminescent self-organized helical superstructures: From materials and stimulus-responsiveness to applications. *Aggregate (Hoboken)* **2**, e141 (2021). doi: 10.1002/agt2.141
20. J. Lu *et al.*, Nano-achiral complex composites for extreme polarization optics. *Nature* **630**, 860–865 (2024). doi: 10.1038/s41586-024-07455-4; pmid: 38811736
21. C.-C. Yang, P. Puneet, I.-M. Lin, Y.-W. Chiang, R.-M. Ho, Self-assembled helical superstructures of polystyrene-b-poly (2-vinyl pyridine) with inversed helicity from induced chirality. *Giant (Oxf.)* **7**, 100059 (2021). doi: 10.1016/j.giant.2021.100059
22. X. Lu *et al.*, Double-helical nanostructures with controllable handedness in bulk diblock copolymers. *Angew. Chem. Int. Ed.* **57**, 15148–15152 (2018). doi: 10.1002/anie.201809676; pmid: 30225925
23. X. Li *et al.*, From precision synthesis of block copolymers to properties and applications of nanoparticles. *Angew. Chem. Int. Ed.* **57**, 2046–2070 (2018). doi: 10.1002/anie.201705019; pmid: 28786158
24. Y. Liu, J. Wang, M. Zhang, H. Li, Z. Lin, Polymer-ligated nanocrystals enabled by nonlinear block copolymer nanoreactors: Synthesis, properties, and applications. *ACS Nano* **14**, 12491–12521 (2020). doi: 10.1021/acsnano.0c06936; pmid: 32975934
25. X. Pang, L. Zhao, W. Han, X. Xin, Z. Lin, A general and robust strategy for the synthesis of nearly monodisperse colloidal nanocrystals. *Nat. Nanotechnol.* **8**, 426–431 (2013). doi: 10.1038/nnano.2013.85; pmid: 23728076
26. M. Kim *et al.*, Block copolymer enabled synthesis and assembly of chiral metal oxide nanoparticle. *ACS Nano* **17**, 7611–7623 (2023). doi: 10.1021/acsnano.3c00047; pmid: 37011403
27. A. C. Evans *et al.*, Chiroptical characterization tools for asymmetric small molecules - experimental and computational approaches for electronic circular dichroism (ECD) and anisotropy spectroscopy. *RSC Adv.* **11**, 1635–1643 (2021). doi: 10.1039/D0RA06832B; pmid: 35424126
28. J. Yuan, X. Lu, Q. Li, Z. Lü, Q. Lu, Reversible micrometer-scale spiral self-assembly in liquid crystalline block copolymer film with controllable chiral response. *Angew. Chem. Int. Ed.* **60**, 12308–12312 (2021). doi: 10.1002/anie.202101102; pmid: 33749105
29. J. Yuan *et al.*, Molecular chirality and morphological structural chirality of exogenous chirality-induced liquid crystalline block copolymers. *Macromolecules* **55**, 1566–1575 (2022). doi: 10.1021/acs.macromol.1c02445
30. R. A. Scanga *et al.*, Asymmetric polymerization-induced crystallization-driven self-assembly of helical, rod-coil poly(aryl isocyanide) block copolymers. *J. Am. Chem. Soc.* **145**, 6319–6329 (2023). doi: 10.1021/jacs.2c13354; pmid: 36913666
31. X. Cheng *et al.*, Controlling the multiple chiroptical inversion in biphasic liquid-crystalline polymers. *Angew. Chem. Int. Ed.* **60**, 24430–24436 (2021). doi: 10.1002/anie.202109084; pmid: 34505335
32. M. Griepentrog, G. Krämer, B. Cappella, Comparison of nanoindentation and AFM methods for the determination of mechanical properties of polymers. *Polym. Test.* **32**, 455–460 (2013). doi: 10.1016/j.polymertesting.2013.01.011
33. G. Pescitelli, ECD exciton chirality method today: A modern tool for determining absolute configurations. *Chirality* **34**, 333–363 (2022). doi: 10.1002/chir.23393; pmid: 34791704
34. J. Wei *et al.*, Solvent evaporation induced aggregating assembly approach to three-dimensional ordered mesoporous silica with ultralarge accessible mesopores. *J. Am. Chem. Soc.* **133**, 20369–20377 (2011). doi: 10.1021/ja207525e; pmid: 22047467
35. D. L. Chinaglia *et al.*, Influence of the solvent evaporation rate on the crystalline phases of solution-cast poly (vinylidene fluoride) films. *J. Appl. Polym. Sci.* **116**, 785–791 (2010). doi: 10.1002/app.31488
36. R.-M. Ho *et al.*, Transfer of chirality from molecule to phase in self-assembled chiral block copolymers. *J. Am. Chem. Soc.* **134**, 10974–10986 (2012). doi: 10.1021/ja303513f; pmid: 22621336
37. O. Valdes-Aguilera, D. Neckers, Aggregation phenomena in xanthene dyes. *Acc. Chem. Res.* **22**, 171–177 (1989). doi: 10.1021/ar00161a002
38. V. Czikklely, H. Forsterling, H. Kuhn, Extended dipole model for aggregates of dye molecules. *Chem. Phys. Lett.* **6**, 207–210 (1970). doi: 10.1016/0009-2614(70)80220-2
39. Y. He *et al.*, Dual-protected metal halide perovskite nanosheets with an enhanced set of stabilities. *Angew. Chem. Int. Ed.* **60**, 7259–7266 (2021). doi: 10.1002/anie.202014983; pmid: 33393190
40. Y. J. Yoon *et al.*, Enabling tailorable optical properties and markedly enhanced stability of perovskite quantum dots by permanently ligating with polymer hairs. *Adv. Mater.* **31**, e1901602 (2019). doi: 10.1002/adma.201901602; pmid: 31192498
41. Y. Liu *et al.*, Polar organic solvent-tolerant perovskite nanocrystals permanently ligated with polymer hairs via star-like molecular bottlebrush trilobe nanoreactors. *Nano Lett.* **19**, 9019–9028 (2019). doi: 10.1021/acs.nanolett.9b04047; pmid: 31692361
42. S. Liang *et al.*, Metal halide perovskite nanorods with tailored dimensions, compositions and stabilities. *Nat. Synth.* **2**, 719–728 (2023). doi: 10.1038/s44160-023-00307-5
43. Y. He *et al.*, Unconventional route to dual-shelled organolead halide perovskite nanocrystals with controlled dimensions, surface chemistry, and stabilities. *Sci. Adv.* **5**, eaax4424 (2019). doi: 10.1126/sciadv.aax4424; pmid: 31819900
44. S. S. Barjoee, M. R. Elmi, V. T. Varaoon, S. S. Keykhosravi, F. Karimi, Hazards of toluene storage tanks in a petrochemical plant: Modeling effects, consequence analysis, and comparison of two modeling programs. *Environ. Sci. Pollut. Res. Int.* **29**, 4587–4615 (2022). doi: 10.1007/s11356-021-15864-5; pmid: 34414542
45. J. Li *et al.*, Programmable supramolecular chirality in non-equilibrium systems affording a multistate chiroptical switch. *Nat. Commun.* **14**, 5030 (2023). doi: 10.1038/s41467-023-40698-9; pmid: 37596287
46. Y. Lu *et al.*, Negative thermal quenching $CsPbBr_3$ glass-ceramic based on intrinsic radiation and vacancy defect co-induced dual-emission. *J. Eur. Ceram. Soc.* **41**, 3635–3642 (2021). doi: 10.1016/j.jeurceramsoc.2021.01.039
47. T. Wen *et al.*, Controlled handedness of twisted lamellae in banded spherulites of isotactic poly(2-vinylpyridine) as induced by chiral dopants. *Angew. Chem. Int. Ed.* **54**, 14313–14316 (2015). doi: 10.1002/anie.201506186; pmid: 26447740
48. S. Suárez-Suárez, G. A. Carriedo, A. Presa Soto, Porous films by the self-assembly of inorganic rod-*b*-coil block copolymers: Mechanistic insights into the vesicle-to-pore morphological evolution. *Soft Matter* **12**, 3084–3092 (2016). doi: 10.1039/C5SM02861B; pmid: 26898560
49. P. Alonso-Cristobal, M. Laurenti, F. Sanchez-Muniz, E. López-Cabarcos, J. Rubio-Retama, Polymeric nanoparticles with tunable architecture formed by biocompatible star shaped block copolymer. *Polymer* **53**, 4569–4578 (2012). doi: 10.1016/j.polymer.2012.08.016
50. W. R. Kitzmann, J. Freudenthal, A. M. Reponen, Z. A. VanOrman, S. Feldmann, Fundamentals, advances, and artifacts in circularly polarized luminescence (CPL) spectroscopy. *Adv. Mater.* **35**, e2302279 (2023). doi: 10.1002/adma.202302279; pmid: 37658497
51. X. Pang, L. Zhao, M. Akinc, J. K. Kim, Z. Lin, Novel amphiphilic multi-arm, star-like block copolymers as unimolecular micelles. *Macromolecules* **44**, 3746–3752 (2011). doi: 10.1021/ma200594j
52. M. Staffilani *et al.*, Anion binding within the cavity of π-metalated calixarenes. *J. Am. Chem. Soc.* **119**, 6324–6335 (1997). doi: 10.1021/ja9702172
53. S. Grimme, J. Antony, S. Ehrlich, H. Krieg, A consistent and accurate ab initio parametrization of density functional dispersion correction (DFT-D) for the 94 elements H-Pu. *J. Chem. Phys.* **132**, 154104 (2010). doi: 10.1063/1.3382344; pmid: 20423165
54. R. Dennington, T. Keith, J. Millam. "GaussView, version 5.0" (Gaussian, 2007); www.gaussian.com.

55. I. R. Cooke, M. Deserno, Solvent-free model for self-assembling fluid bilayer membranes: Stabilization of the fluid phase based on broad attractive tail potentials. *J. Chem. Phys.* **123**, 224710 (2005). doi: 10.1063/1.2135785; pmid: 16375498
56. C. Perego, M. Salvalaglio, M. Parrinello, Molecular dynamics simulations of solutions at constant chemical potential. *J. Chem. Phys.* **142**, 144113 (2015). doi: 10.1063/1.4917200; pmid: 25877568
57. Y. L. Zhu *et al.*, GALAMOST: GPU-accelerated large-scale molecular simulation toolkit. *J. Comput. Chem.* **34**, 2197–2211 (2013). doi: 10.1002/jcc.23365; pmid: 24137668
58. Y.-L. Zhu *et al.*, Employing multi-GPU power for molecular dynamics simulation: An extension of GALAMOST. *Mol. Phys.* **116**, 1065–1077 (2018). doi: 10.1080/00268976.2018.1434904

ACKNOWLEDGMENTS

We thank D. Bukharina, M. Kim, M. Buxton, N. Yan, Y. S. Ang, and L. Yung for technical assistance. **Funding:** This work was primarily supported by the Ministry of Education (MOE), Singapore, under its Academic Research Fund Tier 2 program (grants T2EP50123-0032 and T2EP10223-0006) and the Agency for Science, Technology and Research (A*STAR) under its RIE2025 MTC IRG program (grant M23M6c0106). D.H.K. acknowledges support from the Basic Science Research Program (Priority Research Institute) funded by the Ministry of Education (grant 2021R1A6A1A10039823). Z.-Y.L. acknowledges support from the National Natural Science Foundation of China (grant 22133002). N.A.K. acknowledges support from the National Science Foundation (grant 2243104), Center for Complex Particle Systems (COMPASS) (grant 2317423), and CBET-EPSRC (grant 2418861). Z.Y. acknowledges support from the National Natural Science Foundation of China (grant 52293472). V.T. acknowledges support from Air Force Office of Scientific Research Award (grant FA9550-23-1-0641) and the National Science Foundation (grant DMR 2404081). GI-SAXS measurements were performed at the 3C SAXS-I, 9A U-SAXS beamlines of the Pohang Accelerator Laboratory (PLS-II), Republic of Korea. **Author contributions:** Z.L., D.H.K., Z.-Y.L., N.A.K., and Z.Y. conceived the idea and supervised the research. M.K. and M.Z. designed and conducted the experiments. Y.-L.Z., X.P., and Z.-Y.L. performed the MD simulations. Y.Y. performed the DFT computations. S.C. and K.C. conducted GI-SAXS measurements and analyzed the results. M.K., M.Z., W.C., J.K., V.T., D.H.K., and Z.L. analyzed the data and discussed the results. M.K., M.Z., V.T., N.A.K., Z.-Y.L., D.H.K., and Z.L. wrote the original draft. **Competing interests:** M.K., D.H.K., and Z.L. have filed a patent application related to this work. The remaining authors declare no competing interests. **Data and materials availability:** All data are available in the main text or the supplementary materials. **License information:** Copyright © 2025 the authors, some rights reserved; exclusive licensee American Association for the Advancement of Science. No claim to original US government works. https://www.science.org/about/science-licenses-journal-article-reuse

SUPPLEMENTARY MATERIALS

science.org/doi/10.1126/science.adu0296
Supplementary Text; Figs. S1 to S84; Tables S1 to S6; References (*59*–*118*)

Submitted 21 October 2024; resubmitted 19 April 2025; accepted 6 June 2025
10.1126/science.adu0296

Check for

RESEARCH ARTICLE SUMMARY

PLANT COMMUNICATION

Linalool-triggered plant-soil feedback drives defense adaptation in dense maize plantings

Dongsheng Guo†, Zilin Liu†, Jos M. Raaijmakers†, Yachun Xu, Jinghui Yang, Matthias Erb, Jiabao Zhang, Yong-Guan Zhu, Jianming Xu*, Lingfei Hu*

Full article and list of author affiliations: https://doi.org/10.1126/science.adv6675

INTRODUCTION: Planting crops more densely increases overall yields, but it also raises the risk of pest and pathogen outbreaks. Although plants can modify their architecture to adapt to crowded conditions, how they adjust their immune responses remains largely unknown. Understanding how plants manage these trade-offs is critical for sustainable agriculture, especially in the context of increasing global food demands.

RATIONALE: Plants release chemical cues, such as volatiles, that inform neighbors of environmental conditions. One such compound, linalool, is a constitutively emitted leaf volatile in maize and other grasses. We hypothesized that linalool could act as a signal in densely planted fields, triggering plant-soil feedback that prepares neighboring plants for potential biotic stress. We explored how linalool shapes root signaling, soil microbiota, and ultimately plant defense and growth.

RESULTS: Field surveys revealed that maize plants in the inner rows of densely planted fields suffered less herbivore damage than those at the edges but that they also had reduced growth. Laboratory soil–transplantation experiments confirmed that soils conditioned by high-density plantings decreased plant biomass while enhancing resistance to insects, nematodes, and pathogens. These effects extended across genotypes and species.

Volatile profiling identified linalool as a key compound increasing with planting density. Exposure of maize to synthetic linalool reproduced the feedback effects, which required the presence of a living plant. Mechanistically, linalool activated jasmonate signaling in roots and up-regulated genes that drive the biosynthesis and exudation of the specialized metabolite HDMBOA-Glc. This exudate reshaped the rhizosphere microbiome, selectively enriching bacteria that suppressed plant growth but increased resistance in subsequently grown plants. Soil sterilization and microbial inoculation confirmed that these microbes were essential for the feedback loop.

In plants grown in linalool-conditioned soil, defense-related signaling, particularly salicylic acid signaling, was up-regulated, whereas growth-promoting metabolic pathways were down-regulated. Plants lacking salicylic acid signaling did not show growth-defense trade-offs, confirming salicylic acid's role in expressing the feedback-triggered defense.

CONCLUSION: This study uncovers a volatile-triggered feedback mechanism through which maize adapts its defense in crowded environments. The constitutive emission of linalool primes neighboring plants by activating root jasmonate signaling, promoting HDMBOA-Glc exudation, and altering the rhizosphere microbiome. This, in turn, leads to elevated defense and suppressed growth in subsequent plants through salicylic acid signaling. These findings shed light on how plants integrate aboveground cues and belowground processes to optimize defense in high-density settings. Harnessing this natural defense pathway through breeding, microbial inoculants, or synthetic biology could enable the development of crops that are more resilient and require fewer chemical inputs. □

*Corresponding author. Email: jmxu@zju.edu.cn (J.X.); lingfeihu@zju.edu.cn (L.H.)
†These authors contributed equally to this work. **Cite this article as D. Guo *et al.*, *Science* 389, eadv6675 (2025). DOI: 10.1126/science.adv6675**

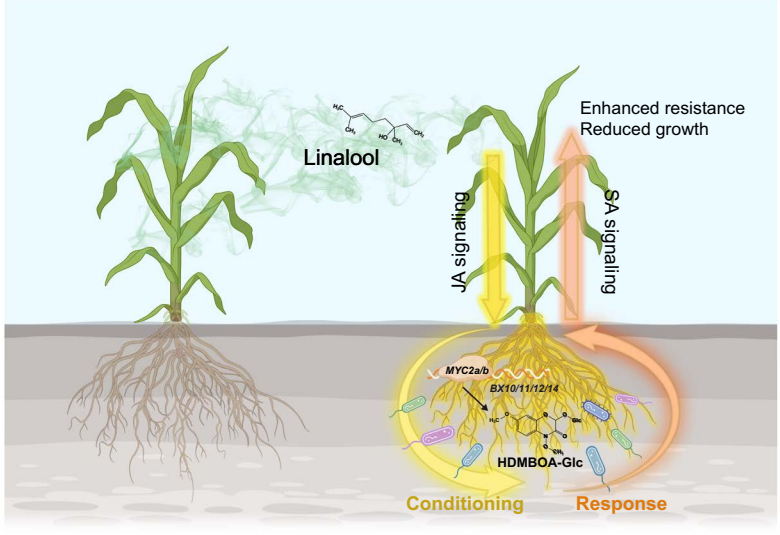

Model illustrating how dense planting triggers plant-soil feedback to enhance maize resistance. High-density planting increases canopy linalool, which activates systemic jasmonic acid (JA) signaling and HDMBOA-Glc exudation from roots. These exudates selectively enrich rhizosphere bacteria that induce salicylic acid (SA) signaling, thereby enhancing maize resistance. This defense-promoting feedback comes at a cost to maize growth. Some components of this figure were created by BioRender.com.

PLANT COMMUNICATION

Linalool-triggered plant-soil feedback drives defense adaptation in dense maize plantings

Dongsheng Guo[1,2]†, Zilin Liu[1,2]†, Jos M. Raaijmakers[3,4]†, Yachun Xu[1], Jinghui Yang[1], Matthias Erb[5], Jiabao Zhang[6], Yong-Guan Zhu[7], Jianming Xu[1]*, Lingfei Hu[1,2]*

High planting density boosts crop yields but also heightens pest and pathogen risks. How plants adapt their defenses under these conditions remains unclear. In this study, we reveal that maize enhances its defense in high-density conditions through a plant-soil feedback mechanism triggered by the leaf volatile linalool. Linalool activates jasmonate signaling in neighboring plants and promotes root exudation of benzoxazinoids, especially 2-(2-hydroxy-4,7-dimethoxy-1,4-benzoxazin-3-one)-β-d-glucopyranose (HDMBOA-Glc). These exudates in turn reshape the rhizosphere microbiome composition to favor growth of specific bacterial taxa that trigger broad-spectrum resistance, albeit at the cost of maize growth. This microbiome-driven feedback loop is governed by salicylic acid signaling. Our findings uncover intricate chemical signaling in high-density cropping, which is instrumental for improving soil health and designing sustainable strategies that balance the trade-off between plant growth and defense.

Enhancing crop yields is crucial to ensuring global food security and achieving United Nations Sustainable Development Goal 2: Zero Hunger by 2030 (*1*). Increasing planting density was and still is a key agronomic strategy for maximizing crop productivity (*2*). Over the past few decades, this strategy has substantially contributed to yield improvements across regions including the United States, China, Brazil, and France (*3*). Research on dense planting has primarily focused on how plants adapt their phenotypic plasticity to thrive under high-density conditions. In maize (*Zea mays*), for example, high-density planting induces changes in both shoot and root architecture, including steeper leaf angles and more compact root systems to minimize competition for light and nutrients (*4*–*6*). These traits have been harnessed in breeding programs to develop high-density–tolerant cultivars aimed at further increasing yield potential (*7*, *8*).

Although dense planting enhances overall yield, it also heightens the risk of disease outbreaks and herbivore infestations, a factor that is often overlooked. Denser plantings can modify the microclimate, reducing air circulation and increasing moisture retention on plant surfaces, which fosters conditions favorable to pathogen proliferation (*9*, *10*). Moreover, closely spaced plants allow for the rapid spread of herbivores and pathogens (*11*, *12*). However, how plants adjust their defense mechanisms to mitigate increased vulnerability to pathogens and herbivores in dense planting conditions remains poorly understood. This knowledge gap limits the potential for fully optimizing dense planting practices for sustainable agriculture.

[1]State Key Laboratory of Soil Pollution Control and Safety, College of Environmental and Resource Sciences, Zhejiang Provincial Key Laboratory of Agricultural Resources and Environment, Zhejiang University, Hangzhou, China. [2]Hainan Institute, Zhejiang University, Yazhou District, Sanya, China. [3]Netherlands Institute of Ecology, Department of Microbial Ecology, Wageningen, Netherlands. [4]Institute of Biology, Leiden University, Leiden, Netherlands. [5]Institute of Plant Sciences, University of Bern, Bern, Switzerland. [6]State Key Laboratory of Soil and Sustainable Agriculture, Institute of Soil Science, Chinese Academy of Sciences, Nanjing, China. [7]Research Center for Eco-environmental Sciences, Chinese Academy of Sciences, Beijing, China. ***Corresponding author. Email: jmxu@zju.edu.cn (J.X.); lingfeihu@zju.edu.cn (L.H.)** †These authors contributed equally to this work.

Plant-plant interactions are crucial for shaping community composition and dynamics, particularly in high-density environments (*13*, *14*). Various environmental cues, such as light quality and quantity (*15*), root exudates (*16*), and leaf volatiles (*17*–*19*), provide essential information about the proximity and physiological status of neighbors, as well as potential threats. Clearly, the presence, intensity, and reliability of these cues are highly dependent on proximity: At high planting densities, neighbors are closer, making chemical signals stronger, whereas at low densities these cues may be too weak to trigger effective responses. In this context, could plants in high-density environments use these cues to mitigate the risks of disease and herbivory, ultimately benefiting the performance and fitness of the entire plant community?

We addressed this question by investigating the defense plasticity of maize plants in a dense planting environment. Our findings uncover an intricate mechanism by which plants adjust their growth and defenses through leaf volatile–mediated plant-plant interactions and plant-soil feedback, enabling adaptation to high-density planting conditions.

Results

Planting density affects plant growth and defense in the field through plant-plant interactions

To investigate whether planting density affects plant defense through plant-plant interactions, we conducted a herbivory survey across four independent maize fields. On the basis of the optimal maize planting density in China (*3*), Fields I and II were planted at a relatively low density (~60,000 plants ha^{-1}), whereas Fields III and IV were planted at a high density (~120,000 plants ha^{-1}). Each field was divided into inner sections and outer edges to assess spatial variation in plant growth and herbivory (Fig. 1A). Under high-density conditions, plant-plant interactions such as shading and reduced air circulation are typically more intense in the inner sections of crop stands than at the outer edges. In high-density fields (Fields III and IV), herbivore damage was significantly lower in the inner sections compared with the outer edges (Fig. 1B). Conversely, plant height, shoot biomass, grain yield per ear, and 1000-grain weight were greater at the edges than in the interior of these high-density fields (fig. S1). However, these patterns were absent in the low-density fields (Fields I and II) (Fig. 1B and fig. S1). These results suggest that plant-plant interactions play a critical role in modulating growth and defense in dense planting environments.

Planting density affects plant growth and defense through plant-soil feedback

To assess whether planting density influences plant growth and defense through plant-soil feedback, while excluding the direct effects of root-root interactions, we first cultivated individual maize plants in separate pots filled with field bulk soil until four-leaf stage in the greenhouse. These plants were then arranged at varying planting densities—50, 100, 150, and 200 plants m^{-2} (Fig. 1C). With increasing density, both photosynthetically active radiation and the red-to-far-red light ratio beneath the canopy declined (fig. S2), confirming that a high-density light environment was successfully established (*20*). After 3 days of density treatment, we removed the plants but retained the conditioned soils. New maize plants were then planted into these conditioned soils and spaced to prevent direct density effects on their growth and defense (Fig. 1C). This experimental design ensured that any observed differences in the growth or defense of new plants were attributed to plant-soil feedback rather than direct root-root interactions or immediate density effects.

We observed that as planting density during the conditioning phase increased, the shoot biomass of new maize plants during the response phase progressively decreased, with the highest biomass found in soils previously conditioned at 50 plants m^{-2} and the lowest at 200 plants m^{-2} (Fig. 1, D and E). Plants grown in soils conditioned at 200 plants m^{-2} also exhibited smaller root systems, shorter plant height, and lower

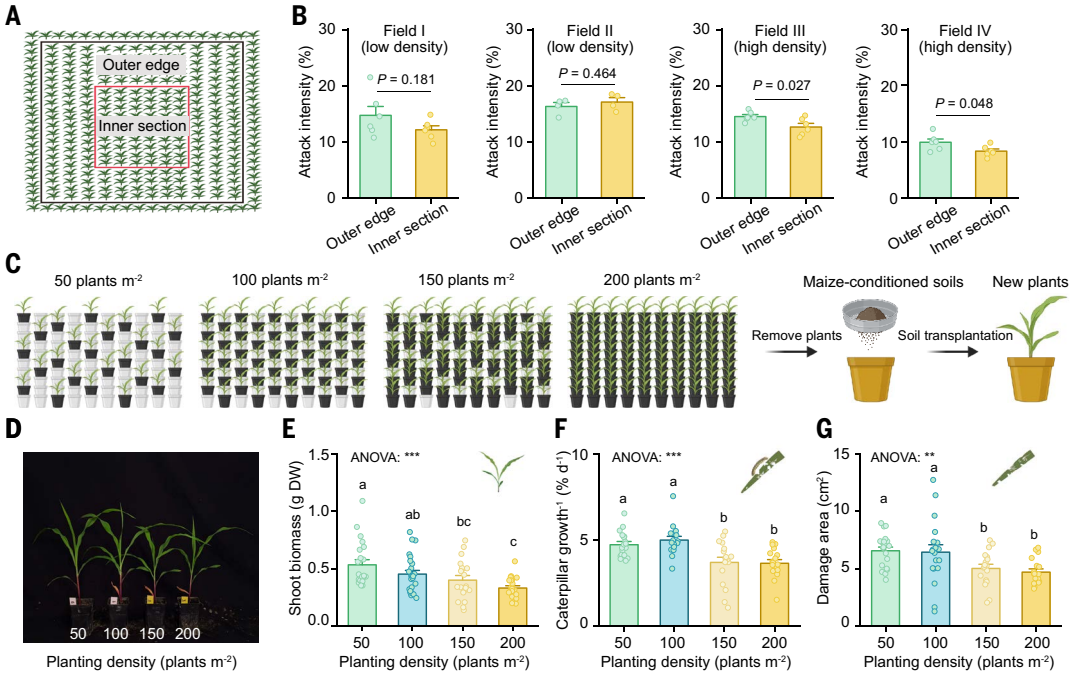

Fig. 1. Planting density enhances defense and reduces growth through plant-soil feedback. (**A**) Diagram of the herbivory survey conducted in maize fields. The field was divided into inner sections and outer edges as shown. (**B**) Herbivory attack intensities in the inner sections and outer edges of four independent maize fields [+ standard error (SE), $n = 4$ or 6 biological replicates; one biological replicate includes 100 to 256 individual plants]. Field I (660 m^2) and Field II (600 m^2) were planted with the maize cultivar Taiyanghua6 at a low planting density (~60,000 plants ha^{-1}). Field III (2100 m^2) and Field IV (2200 m^2) were planted at a higher density (~120,000 plants ha^{-1}). Data points represent individual replicate samples. The exact *P* values for each comparison are indicated in the figure (two-sided Student's *t* test). (**C**) Experimental design for soil transplantation trials. Individual maize plants were grown in separate pots until four-leaf stage. These plants were then arranged at varying planting densities for 3 days. White pots indicate bulk soil without a plant. After 3 days of density treatment, we removed the plants but retained the conditioned soils. The soils from each density treatment were homogenized and sieved. New maize plants were then planted into these conditioned soils and spaced to prevent direct density effects on their growth and defense. This figure was generated by the BioRender software. (**D**) Growth phenotype of new maize plants grown in soils previously conditioned by plants at varying densities. (**E** to **G**) Shoot biomass in grams, dry weight (g DW) (E), caterpillar weight gain in percent per day (% d^{-1}) (F), and leaf damage (G) of new maize plants grown in soils previously conditioned by plants at varying densities (+ SE, $n = 16$ to 24). Data points represent individual replicate samples. Different letters (a, b, and c) denote significant differences between treatments [analysis of variance (ANOVA) followed by multiple comparisons of false discovery rate (FDR)–corrected least squares means (LS means); $P < 0.05$]. Asterisks indicate overall ANOVA significance (***$P < 0.001$, **$P < 0.01$). Raw data, exact biological replicates, and *P* values for all comparisons in this figure are provided in Figshare (*62*).

chlorophyll content throughout their growth (fig. S3). By contrast, insect resistance of new maize plants showed an opposite trend, being lowest in soils conditioned at 50 plants m^{-2} and highest at 200 plants m^{-2} (Fig. 1, F and G, and fig. S4). Larvae of the leaf chewing herbivore fall armyworm (*Spodoptera frugiperda*) grew less and caused less damage to maize plants grown in soils conditioned at 150 and 200 plants m^{-2} (Fig. 1, F and G). Likewise, the root-knot nematode *Meloidogyne incognita* formed fewer galls on roots of plants grown in soils conditioned at 200 plants m^{-2} (fig. S4, A and B). Northern corn leaf blight disease caused by the fungus *Exserohilum turcicum* was also less prevalent in plants grown in soils previously conditioned at 200 plants m^{-2} (fig. S4, C and D). Similarly, replication and virulence of rice black-streaked dwarf virus, which causes maize rough dwarf disease, were significantly reduced in plants grown in soils conditioned at 200 plants m^{-2} (fig. S4, E and F). Taken together, these findings indicate that planting density triggers plant-soil feedback, resulting in decreased plant growth but enhanced defenses against above- and below-ground herbivores as well as fungal and viral pathogens.

Next, we asked whether the observed planting density–induced plant-soil feedback effects depend on the maize genotype. We planted three additional maize cultivars (B104, W22, and KN5585) in bulk soil at planting densities of 50 and 200 plants m^{-2} and subsequently grew each in its respective conditioned soil. High planting densities consistently decreased growth and enhanced resistance across all tested maize cultivars (fig. S5). To test whether the observed plant-soil feedback occurs across plant species, we cultivated maize plants alongside ryegrass (*Lolium perenne*) or barley (*Hordeum vulgare*) and assessed the feedback effects in maize-conditioned soils (fig. S6A). High-density planting with ryegrass or barley also decreased the growth and enhanced herbivore resistance of the subsequently grown maize plants (fig. S6, B to D). To test whether the observed feedback effects are specific to maize, we grew ryegrass or barley in soils previously conditioned by maize at densities of 50 or 200 plants m^{-2} (fig. S7A). Both ryegrass and barley exhibited enhanced herbivore resistance and reduced growth when grown in high-density, maize-conditioned soils (fig. S7, B and C). Lastly, we conditioned soils using ryegrass or barley themselves at low and high planting densities and found that these species also displayed increased resistance under high-density soil conditions (fig. S8). Together, these results demonstrate that planting density alters plant-soil feedback in a manner that suppresses plant growth while enhancing defense. These effects are consistent across maize genotypes and are functionally transferable between different plant species.

Leaf volatile linalool drives planting density–mediated plant-soil feedback

Dense planting may cause leaf volatile accumulation and canopy shade, both of which can influence the physiological status of neighboring plants (*15*, *21*). We hypothesized that these factors might drive plant-plant interactions and thereby affect new plants through plant-soil feedback. To this end, we profiled the leaf volatiles released by maize

plants grown at various densities in an open-air environment using solid-phase microextraction (fig. S9A). Linalool was the most pronounced plant volatile, and its concentration varied according to planting density (Fig. 2A and fig. S9, B and D). Linalool is constitutively released by maize leaves (*22*), and we further detected its emission in both ryegrass and barley (fig. S10), which suggests its broader occurrence across plant species. To evaluate the contribution of linalool to the observed plant-soil feedback effects on growth and defense, we constructed a dispenser releasing synthetic linalool. By adjusting the exposure distance, we simulated the physiological concentrations observed at different planting densities (fig. S9, C and D). We found that exposure to linalool at a distance of ~5 cm (Lin5) significantly enhanced herbivore resistance and reduced growth in newly planted maize (Fig. 2, B to D, and fig. S9, D and E). On the basis of these results, we adopted this exposure setup (referred to as the "Lin" treatment hereafter) for subsequent experiments.

Next, we used *tps2* mutant plants, which are deficient in linalool biosynthesis but still experience leaf shading under high-density conditions (Fig. 2E and fig. S11). New maize plants grown in the soils of high-density *tps2* mutants did not exhibit enhanced herbivore resistance or reduced growth (Fig. 2, F to H). However, when we supplemented the *tps2* mutants with physiological doses of linalool using dispensers, the feedback effects on growth and defense of new maize plants reappeared (Fig. 2, F to H). Taken together, these results indicate that the leaf volatile linalool, rather than leaf shading, is sufficient to trigger the plant-soil feedback mediated by dense planting.

Linalool triggers plant-soil feedback by inducing root JA signaling

We exposed soil to linalool in the absence of plants and subsequently assessed the soil's impact on the maize plants (fig. S12A). The results showed no changes in growth nor in herbivore resistance of the new plants (fig. S12, B to D), indicating that the presence of a receiver plant is essential for linalool-mediated plant-soil feedback. Considering that plant volatiles are known to influence phytohormone signaling (*23*), with putative effects on root physiology and thereby on plant-soil feedback, we measured phytohormone levels in maize roots after linalool exposure. We found that linalool exposure of receiver plants significantly increased jasmonic acid (JA) and JA-isoleucine (JA-Ile) levels in the roots, whereas levels of abscisic acid (ABA), salicylic acid (SA), and indole-3-acetic acid (IAA) remained unchanged (Fig. 3A). To further investigate the role of jasmonate signaling in plant-soil feedback, we used jasmonate-deficient *lox8* mutant plants as linalool-receiving plants. Compared with wild-type plants, *lox8* mutants displayed markedly reduced jasmonate levels in their roots, both with and without linalool exposure (fig. S13). Linalool exposure failed to induce plant-soil feedback effects on growth and herbivore resistance when *lox8* plants were used as conditioners (Fig. 3, B to D).

Because jasmonates can be exuded from roots into the rhizosphere (*24*), we also explored whether linalool triggers jasmonate exudation. However, quantification of jasmonate levels in the rhizosphere soil after linalool exposure revealed no significant changes (Fig. 3A). Taken together, these findings suggest that linalool-induced JA signaling in maize roots is critical for initiating plant-soil feedback but that it does not act through the direct exudation of jasmonates into the soil.

Linalool triggers plant-soil feedback through benzoxazinoid exudation

Benzoxazinoids (BXs) are exuded by plant roots into the soil, influencing plant growth and herbivore resistance (*25*). We hypothesized that linalool may regulate plant-soil feedback by regulating BX biosynthesis. To test this, we quantified BX levels in both the roots and rhizosphere

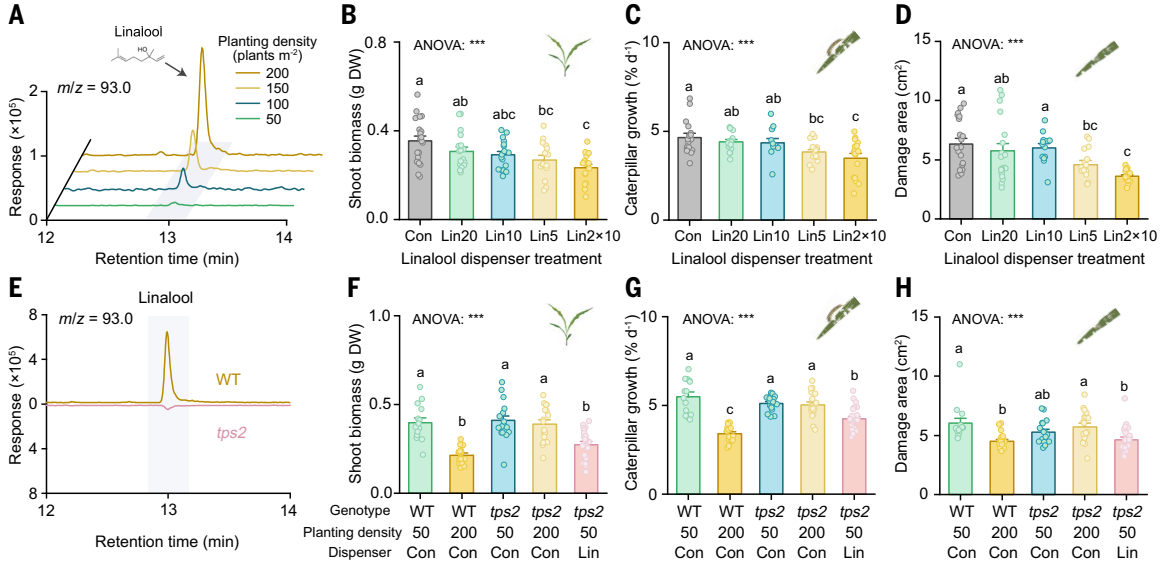

Fig. 2. Linalool drives planting density–mediated plant-soil feedback. (**A**) Selected gas chromotagraphy–mass spectrometry (GC/MS) ion chromatograms of volatiles from maize plants grown at various densities in an open-air environment using solid-phase microextraction (for detailed information of volatile profiles and linalool concentration, see fig. S9, B and D). *m/z*, mass/charge ratio. (**B** to **D**) Shoot biomass (B), caterpillar weight gain (C), and leaf damage (D) of new maize plants grown in soils previously conditioned by plants exposed to control (Con) or synthetic linalool (Lin) released by a dispenser (+ SE, $n = 12$ to 20) (for the schematic setup of maize plants exposed to dispensers, refer to fig. S9, C and E). Data points represent individual replicate samples. Different letters indicate significant differences between treatments (ANOVA followed by multiple comparisons of FDR-corrected LS means; $P < 0.05$). Asterisks indicate overall ANOVA significance (***$P < 0.001$). (**E**) GC/MS selected ion chromatograms of volatiles from wild-type (WT) and linalool-deficient mutant *tps2* (the detailed linalool amount in WT and *tps2* plants are presented in fig. S11). (**F** to **H**) Shoot biomass (F), caterpillar weight gain (G), and leaf damage (H) of new maize plants grown in soils previously conditioned by WT or *tps2* plants at planting densities of 50 or 200 plants m^{-2} or by *tps2* plants at 50 plants m^{-2} complemented with synthetic linalool via a dispenser (+ SE, $n = 14$ to 24). Data points represent individual replicate samples. Different letters (a, b, and c) indicate significant differences between treatments (ANOVA followed by multiple comparisons of FDR-corrected LS means; $P < 0.05$). Asterisks indicate overall ANOVA significance (***$P < 0.001$). Raw data, exact biological replicates, and *P* values for all comparisons in this figure are provided in Figshare (*62*).

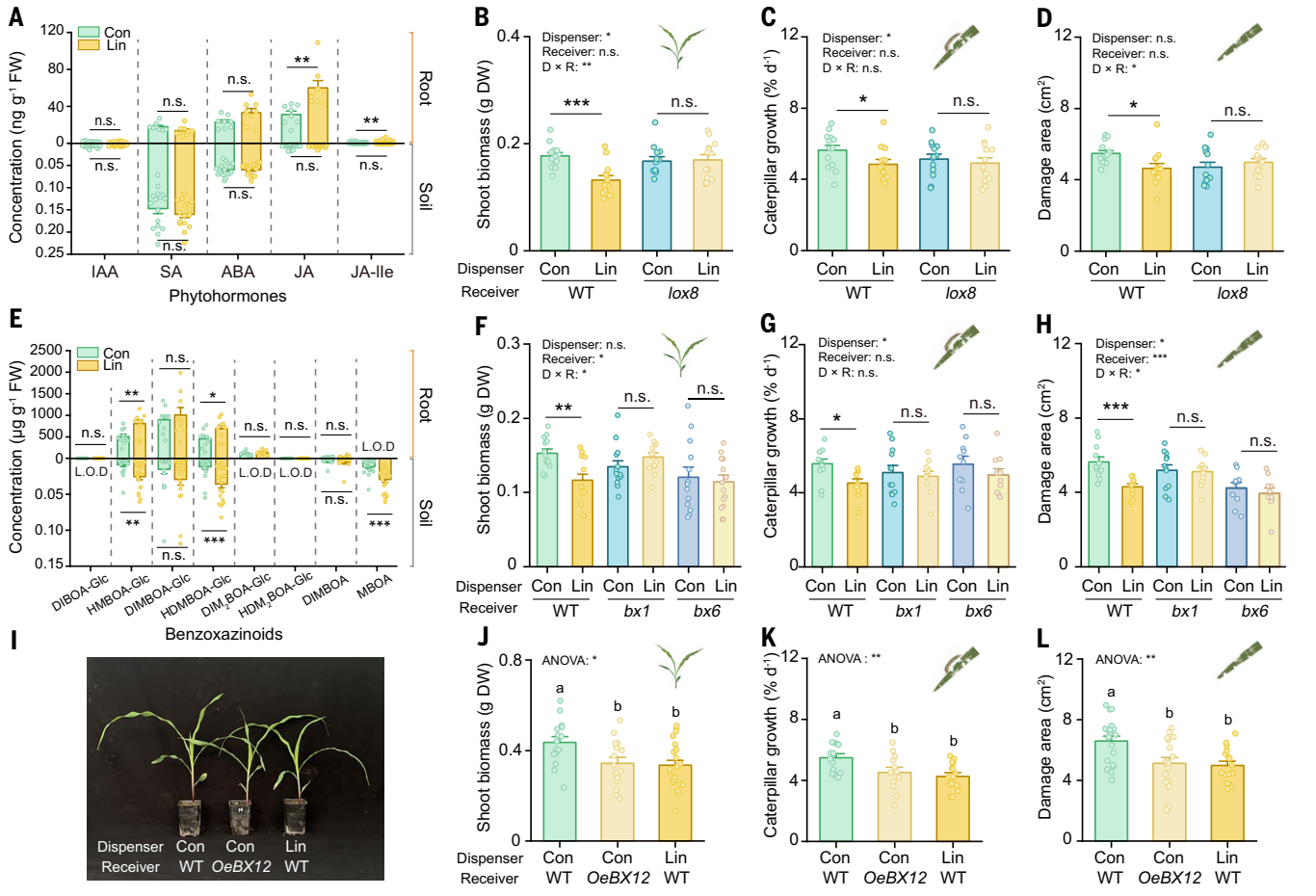

Fig. 3. Linalool triggers plant-soil feedback through JA signaling and BX exudation. (**A**) Concentrations of IAA, SA, ABA, JA, and JA-Ile in the roots or rhizosphere soil of control (Con)– and linalool (Lin)–exposed maize plants (+ SE, $n = 8$ to 16). n.s., not significant. Data points represent individual replicate samples. Asterisks indicate significant differences between treatments (two-sided Student's t test; $^{**}P < 0.01$). ng g^{-1} FW, nanograms per gram fresh weight. (**B** to **D**) Shoot biomass (B), caterpillar weight gain (C), and leaf damage (D) of new maize plants grown in soils previously conditioned by WT and *lox8* plants after Con or Lin exposure (+ SE, $n = 13$). Data points represent individual replicate samples. Asterisks indicate significant differences between treatments (ANOVA followed by pairwise comparisons of FDR-corrected LS means; $^{*}P < 0.05$; $^{**}P < 0.01$; $^{***}P < 0.001$). (**E**) Concentrations of BXs in the roots or rhizosphere soil of Con- and Lin-exposed maize plants (+ SE, $n = 9$ to 20). DIBOA-Glc, 2-(2,4-dihydroxy-1,4-benzoxazin-3-one)-β-d-glucopyranose; HMBOA-Glc, 2-(2-hydroxy-7-methoxy-1,4-benzoxazin-3-one)-β-d-glucopyranose; DIMBOA-Glc, 2-(2,4-dihydroxy-7-methoxy-1,4-benzoxazin-3-one)-β-d-glucopyranose; HDMBOA-Glc, 2-(2-hydroxy-4,7-dimethoxy-1,4-benzoxazin-3-one)-β-d-glucopyranose; DIM_2BOA-Glc, 2-(2,4-dihydroxy-6,7-dimethoxy-l,4-benzoxazin-3-one)-β-d-glucopyranose; HDM_2BOA-Glc, 2-(2-hydroxy-4,7,8-trimethoxy-1,4-benzoxazin-3-one)-β-d-glucopyranose; DIMBOA, 2,4-dihydroxy-7-methoxy-1,4-benzoxazin-3-one; MBOA, 6-methoxy-benzoxazolin-2-one. Data points represent individual replicate samples. Asterisks indicate significant differences between treatments (two-sided Student's t test; $^{*}P < 0.05$; **, $P < 0.01$; $^{***}P < 0.001$). μg g^{-1} FW, micrograms per gram fresh weight. L.O.D, limit of detection. (**F** to **H**) Shoot biomass (F), caterpillar weight gain (G), and leaf damage (H) of new maize plants grown in soils previously conditioned by WT, *bx1*, and *bx6* plants after Con or Lin exposure (+ SE, $n = 10$ to 13). Data points represent individual replicate samples. Asterisks indicate significant differences between treatments (ANOVA followed by pairwise comparisons of FDR-corrected LS means; $^{*}P < 0.05$; $^{**}P < 0.01$; $^{***}P < 0.001$). (**I**) Growth phenotype of new maize plants grown in soils previously conditioned by WT or *OeBX12* plants after Con or Lin exposure. (**J** to **L**) Shoot biomass (J), caterpillar weight gain (K), and leaf damage (L) of new maize plants growing in soils previously conditioned by WT or *OeBX12* plants after Con or Lin exposure (+ SE, $n = 12$ to 21). Data points represent individual replicate samples. Different letters (a and b) indicate significant differences between treatments (ANOVA followed by multiple comparisons of FDR-corrected LS means; $P < 0.05$). Asterisks indicate overall ANOVA significance ($^{*}P < 0.05$; $^{**}P < 0.01$). Raw data, exact biological replicates, and P values for all comparisons in this figure are provided in Figshare (62).

soil of maize plants after linalool exposure. We observed significant increases in HMBOA-Glc and HDMBOA-Glc in both roots and rhizosphere soil, along with their degradation product, 6-methoxy-benzoxazolin-2-one (MBOA), in the rhizosphere (Fig. 3E). We then used two BX-deficient mutants, *bx1* and *bx6*, as linalool-receiving plants. The *bx1* mutant produces only trace amounts of all BX types, whereas the *bx6* mutant is deficient in HMBOA-Glc, HDMBOA-Glc, and other BX derivatives, but is highly enriched in DIBOA-Glc (26, 27). Both mutants failed to exhibit linalool-induced soil feedback effects on plant growth and resistance (Fig. 3, F to H), highlighting the putative contributions of HMBOA-Glc and HDMBOA-Glc in the observed linalool-mediated feedback.

Because the biosynthetic pathway of HMBOA-Glc is not yet fully elucidated and because MBOA is a breakdown product of BXs and has well-documented effects on plant-soil feedback (25), we focused our attention on HDMBOA-Glc. We overexpressed the HDMBOA-Glc biosynthesis gene *ZmBX12* in B73-329 maize (hereafter *OeBX12*), leading to consistently elevated HDMBOA-Glc levels (27). When *OeBX12* plants were used as receivers, the enhanced herbivore resistance and reduced growth were observed in subsequently grown maize plants, even in the absence of linalool exposure (Fig. 3, I to L). These findings demonstrated that linalool-induced BX exudation, particularly HDMBOA-Glc, is both necessary and sufficient to initiate plant-soil feedback.

Linalool-induced HDMBOA-Glc exudation is regulated by JA signaling

We analyzed the expression of genes involved in the JA and BX pathways in the roots of maize plants after linalool exposure. Linalool treatment significantly up-regulated the expression of key JA biosynthesis genes, including *ZmLOX8*, *ZmAOS*, and *ZmOPR2*, as well as JA signaling genes *ZmMYC2a* and *ZmMYC2b* (*28*–*30*) (Fig. 4A). Concurrently, linalool altered the expression of BX biosynthesis genes, increasing the levels of *ZmBX10/11*, *ZmBX12*, and *ZmBX14*, while decreasing *ZmBX2* and *ZmBX13* expression (Fig. 4A and fig. S14). The expression of JA biosynthesis and signaling genes (*ZmLOX8*, *ZmAOS*, *ZmMYC2a*, and *ZmMYC2b*) was positively correlated with the expression of HDMBOA-Glc biosynthesis genes (*ZmBX10/11*, *ZmBX12*, and *ZmBX14*) (Fig. 4B), suggesting a link between linalool-induced JA signaling and HDMBOA-Glc biosynthesis.

Because *ZmMYC2a* and *ZmMYC2b* have been reported to regulate BX biosynthesis (*28*), we further investigated the connections between JA signaling and HDMBOA-Glc production using *lox8*, *bx1*, and *bx6* mutants. Disruption of JA biosynthesis in *lox8* led to significantly reduced levels of HDMBOA-Glc and other BX derivatives (Fig. 4C). However, knockout or impairment of BX biosynthesis (*bx1* and *bx6*) did not affect linalool-induced JA and JA-Ile levels (Fig. 4, D and E). These results suggest that linalool induces HDMBOA-Glc biosynthesis and exudation primarily through the JA signaling pathway.

Linalool triggers plant-soil feedback through soil microbiota

Rhizosphere-associated microbes respond to hormonal changes in plant roots (*31*) and play an important role in mediating plant-soil feedback (*32*, *33*). We therefore hypothesized that linalool might trigger the feedback by altering the composition and activities of soil microbiota. To test this hypothesis, we grew linalool-exposed maize plants in sterilized bulk soil, and we also reintroduced microbial communities into the sterilized soils by adding suspensions from natural soils conditioned by either control- or linalool-exposed plants. In sterilized soils, the feedback effects on plant growth and resistance were absent. However, these effects were fully restored when microbial suspensions from linalool-treated soils were added (Fig. 5, A to C). These results suggest that soil microbiota are essential for linalool-triggered plant-soil feedback.

Identification of rhizosphere-associated bacteria involved in dense planting–induced soil feedback

Next, we compared the bacterial operational taxonomic unit (OTUs) between control and linalool treatments and found that 111 OTUs were enriched and 129 depleted by linalool exposure (Fig. 5I and data S1). To identify specific bacterial taxa associated with these OTUs, we cultured bacteria from the rhizosphere of both control- and linalool-treated plants, focusing on those sharing 97% 16*S* ribosomal RNA (rRNA) gene similarity

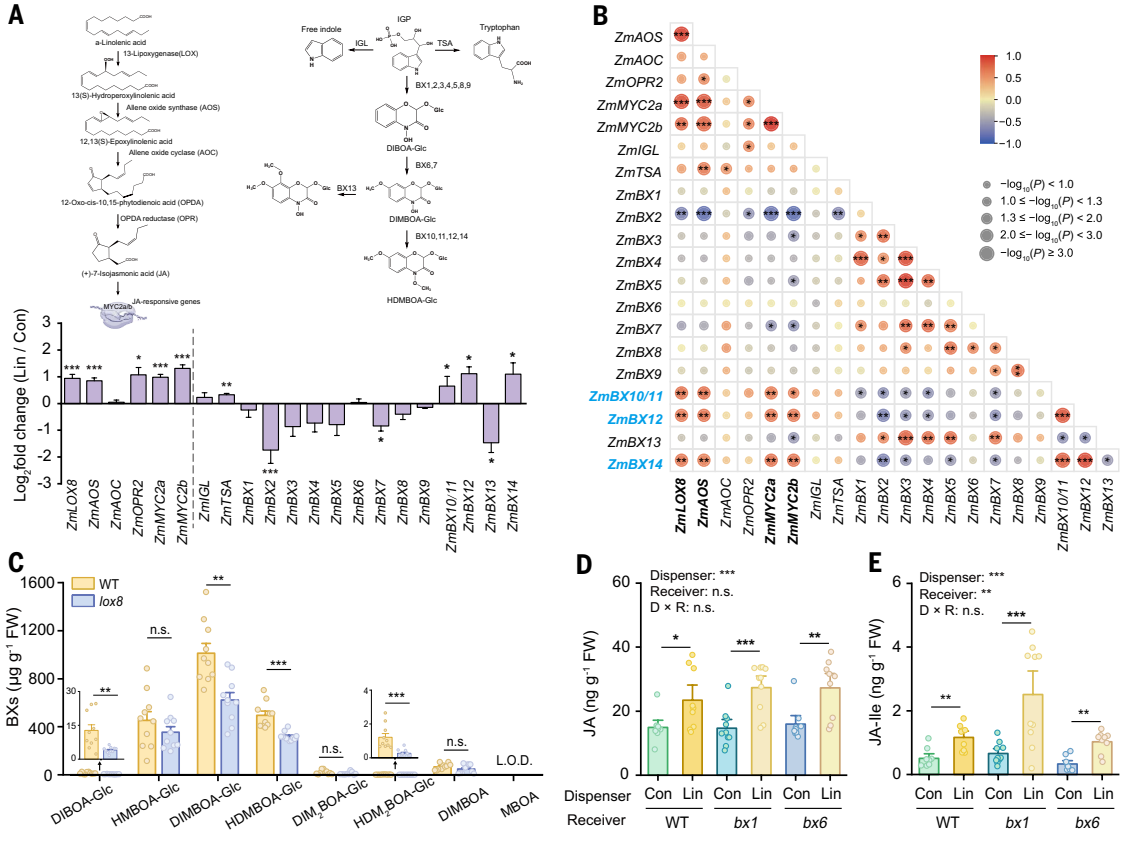

Fig. 4. Linalool-induced HDMBOA-Glc exudation is regulated by JA signaling. (**A**) Log_2 fold changes in the expression of JA and BX biosynthesis genes in maize roots after control (Con) or linalool (Lin) exposure (+ SE, $n = 6$ to 8). Asterisks indicate significant differences between treatments (two-sided Student's *t* test; $*P < 0.05$; $**P < 0.01$; $***P < 0.001$). Full datasets are available in fig. S14. Certain components of this figure were generated using BioRender software. (**B**) Pearson correlations between the expression of JA biosynthesis genes and BX biosynthesis genes. Asterisks indicate statistically significant correlations ($*P < 0.05$; $**P < 0.01$; $***P < 0.001$). Genes involved in HDMBOA-Glc biosynthesis are highlighted in bold blue. Genes involved in JA signaling are highlighted in bold black. (**C**) BX content in the roots of WT plants and *lox8* mutants (+ SE, $n = 10$). Data points represent individual replicate samples. Asterisks indicate significant differences between plant genotypes (two-sided Student's *t* test; $**P < 0.01$; $***P < 0.001$). (**D** and **E**) JA and JA-Ile concentrations in the roots of WT plants and *bx1* and *bx6* mutants after Con or Lin exposure (+ SE, $n = 9$ to 10). Data points represent individual replicate samples. Asterisks indicate significant differences between treatments (ANOVA followed by pairwise comparisons of FDR-corrected LS means; $*P < 0.05$; $**P < 0.01$; $***P < 0.001$). Raw data, exact biological replicates, and *P* values for all comparisons in this figure are provided in Figshare (*62*).

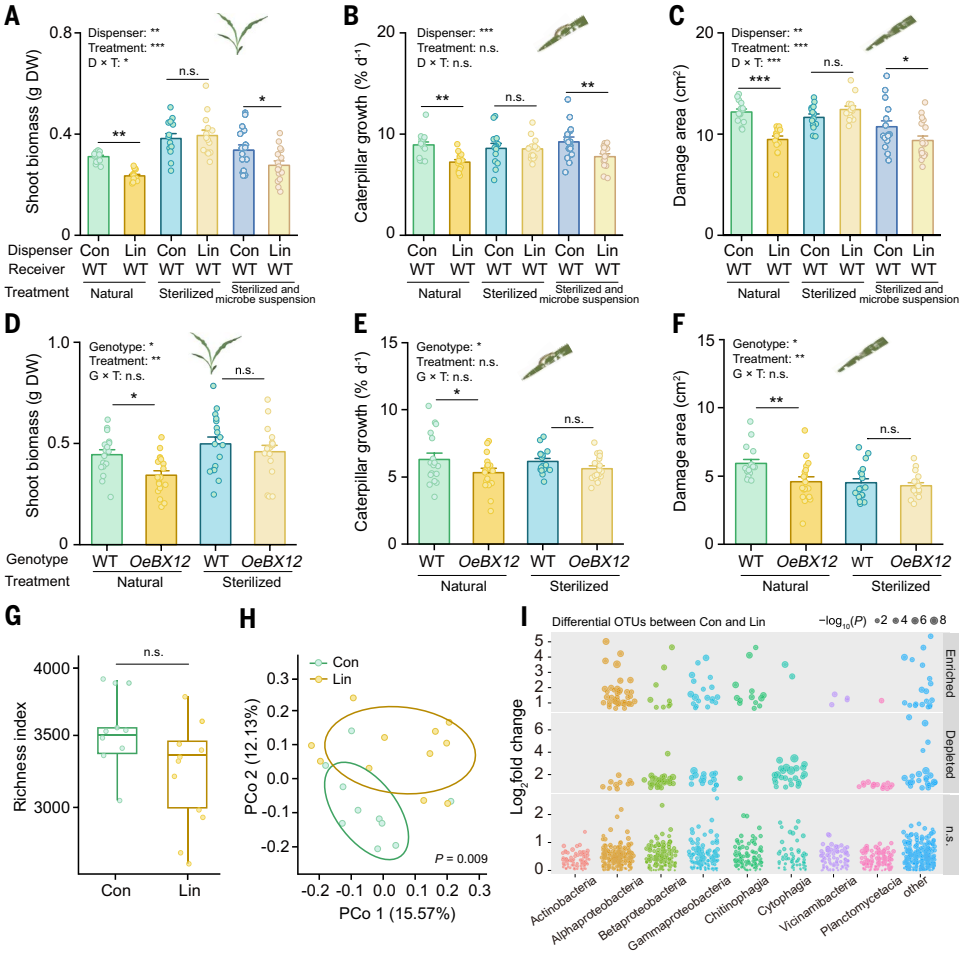

Fig. 5. Soil bacteria mediate linalool-triggered plant-soil feedback. (**A** to **C**) Shoot biomass (A), caterpillar weight gain (B), and leaf damage (C) of maize plants growing in soils previously conditioned by control (Con)– or linalool (Lin)–exposed WT plants (+ SE, $n = 14$ to 18). Soils were either left untreated (natural), x-ray sterilized, or x-ray sterilized and complemented with microbe suspensions from the respective natural soils. Data points represent individual replicate samples. Asterisks indicate significant differences between treatments (ANOVA followed by pairwise comparisons of FDR-corrected LS means; $*P < 0.05$; $**P < 0.01$; $***P < 0.001$). (**D** to **F**) Shoot biomass (D), caterpillar weight gain (E), and leaf damage (F) of maize plants grown in soils previously conditioned by WT or *OeBX12* plants (+ SE, $n = 17$ to 18). Soils were either left untreated (natural) or x-ray sterilized. Data points represent individual replicate samples. Asterisks indicate significant differences between treatments (ANOVA followed by pairwise comparisons of FDR-corrected LS means; $*P < 0.05$; $**P < 0.01$; $***P < 0.001$). (**G**) Richness index of bacterial communities in the rhizosphere of Con- and Lin-exposed maize plants ($n = 10$ to 11). The horizontal bars within boxes represent medians. The tops and bottoms of boxes represent the 75th and 25th percentiles, respectively. Data points represent individual replicate samples. (**H**) Principle coordinates analysis (PCoA) of the rhizosphere bacterial communities of Con- or Lin-exposed maize plants (PERMANOVA by Adonis). Data points represent individual replicate samples. (**I**) Differential bacteria OTUs between Con- or Lin-exposed maize plants. Each dot represents a single OTU. OTUs enriched or depleted in the soil of Lin-exposed plants were shown (edgeR; FDR-adjusted $P < 0.1$). Raw data, exact biological replicates, and *P* values for all comparisons in this figure are provided in Figshare (*62*).

with detected OTUs. In total, we isolated 94 strains that were significantly enriched in the rhizosphere of linalool-exposed plants (Fig. 6A and data S2).

We then assessed the growth of these 94 strains in minimal media supplemented with microbe-free soil extracts derived from control- or linalool-exposed plants, which retained soluble compounds. Growth assays revealed that 13 strains showed significantly enhanced growth, whereas one strain exhibited suppressed growth in response to linalool-treated soil extracts (Fig. 6A and data S3). To test whether these effects were mediated by HDMBOA-Glc, we measured HDMBOA-Glc levels in the same soil extracts and analyzed their correlation with bacterial growth (data S3). Among the 14 responsive strains, 13 showed a positive correlation between their growth and HDMBOA-Glc concentration, and one strain (L74) did not (Fig. 6A, pie charts; and data S3). We then tested the direct effects of synthetic HDMBOA-Glc on these 14 strains and one negative control strain (L2), previously unaffected by linalool. HDMBOA-Glc stimulated the growth of 12 out of 13 enriched strains but inhibited L9 and L74 (Fig. 6B and fig. S15). The negative control L2 remained unaffected. These results establish a functional link between the root exudate HDMBOA-Glc and growth modulation of specific bacterial taxa enriched in the rhizosphere of linalool-exposed plants.

Next, we complemented soils previously conditioned at 50 plants m^{-2} with these individual bacterial strains and assessed their effects on newly planted maize. Inoculation with HDMBOA-Glc-enriched strains, except for L57 and L91, significantly reduced plant growth, mimicking the phenotypic responses observed in soils conditioned at 200 plants m^{-2} (Fig. 6C). Similarly, inoculation with the enriched strains, except for L57, L78, and L91, significantly enhanced plant resistance (Fig. 6, D and E). By contrast, inoculation with L9, which was depleted by HDMBOA-Glc treatment, promoted plant growth but suppressed resistance in plants grown in soils conditioned at 50 plants m^{-2}. Inoculation with L74 (also depleted strain) or L2 (unaffected strain) had no significant impact on plant growth or defense (Fig. 6, C and E). These findings demonstrate that HDMBOA-Glc–responsive bacterial taxa play an essential role in conferring plant-soil feedback triggered by high planting density and linalool signaling.

Linalool-triggered plant-soil feedback depends on SA signaling

We analyzed the phytohormones, metabolites, and gene expression in new maize plants grown in soils previously conditioned by either control- or linalool-exposed plants. Soils from linalool-exposed plants did not affect levels of defensive metabolites such as BXs or flavonoids but did lead to a reduction in primary metabolites (Fig. 7A and fig. S16). In terms of phytohormones, soils from linalool-exposed plants significantly enhanced SA levels in both the leaves and roots, accompanied by the up-regulation of SA-related signaling genes, such as *ZmWRKY28* and *ZmTGA1* (Fig. 7A and figs. S16 to S18). Additional signaling genes, including *ZmMDL*, *ZmPAL*, *ZmNPR1*, and *ZmNPR3*, were up-regulated in either roots or leaves (Fig. 7A and fig. S17). Conversely, the JA precursor 12-oxo-phytodienoic acid (OPDA) and the JA biosynthesis gene *ZmAOS* were down-regulated in the leaves and roots. IAA and its biosynthesis gene *ZmYucca2* were also specifically down-regulated in the leaves of plants grown in soils from linalool-exposed plants. Defense marker genes were up-regulated in either roots or leaves (Fig. 7A and fig. S17). These findings demonstrate that soils conditioned by linalool-exposed plants induce substantial metabolic and defense reprogramming in new maize plants.

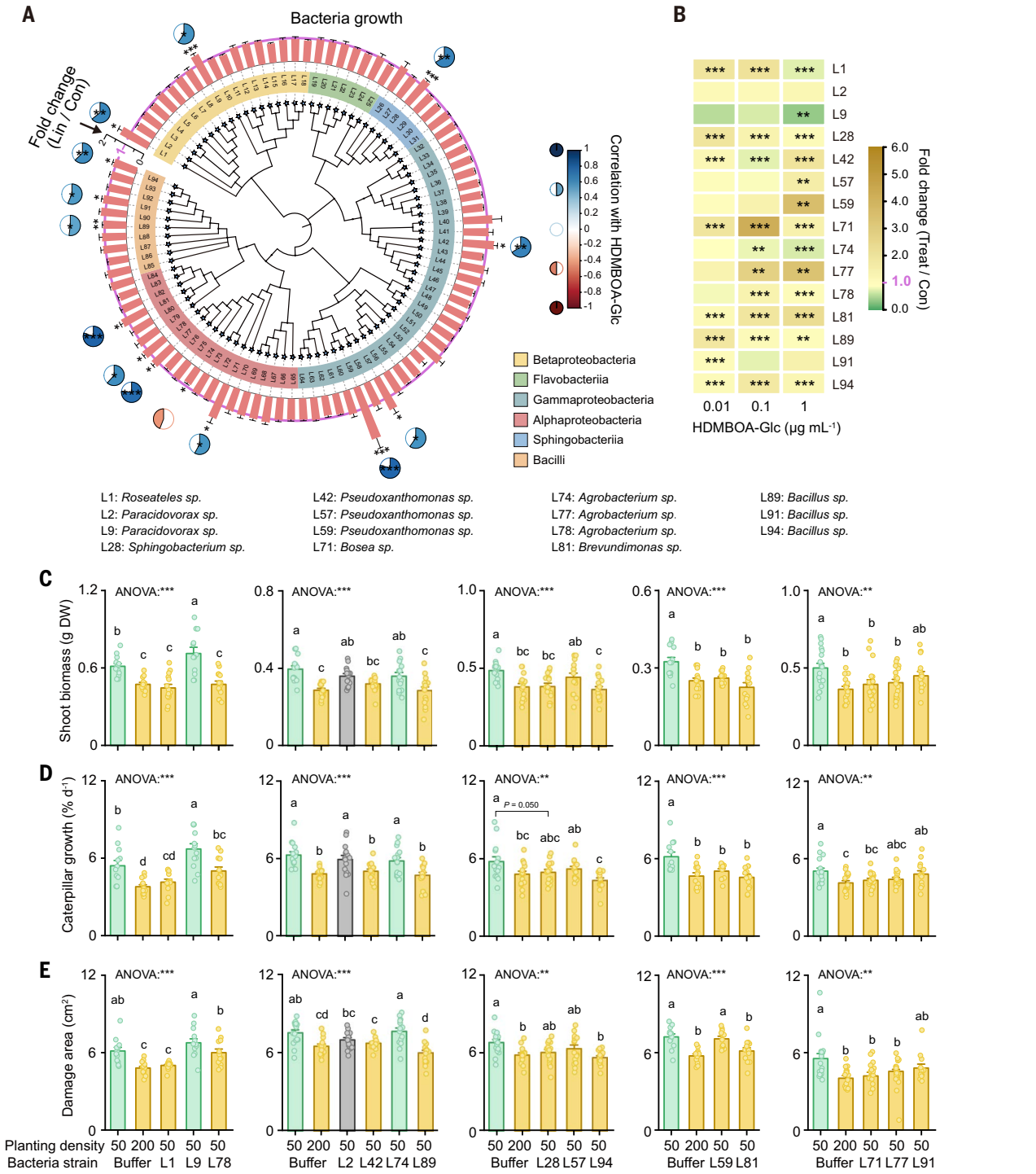

Fig. 6. HDMBOA-Glc–activated bacterial taxa contribute to linalool-triggered plant-soil feedback. (**A**) Phylogenetic trees and growth of 94 bacterial strains isolated from the rhizosphere of maize plants after linalool exposure ($n = 8$). The innermost circle shows the phylogenetic tree of the 94 bacterial strains, with different colors representing various classes. The second circle (pink bars) shows the fold change in growth of the 94 strains when cultivated in soil extracts from control (Con)– or linalool (Lin)–treated plants. The outermost circle (pie charts) indicates the Pearson correlation between bacterial growth and HDMBOA-Glc concentrations in soil extracts from control- or linalool-treated plants. Fold-change values <1.0 indicate reduced growth, while values >1.0 indicate enhanced growth. Asterisks indicate significant correlations (*$P < 0.05$; **$P < 0.01$; ***$P < 0.001$). For full datasets, we refer to Data S3. (**B**) Heatmaps showing the growth of 15 HDMBOA-Glc–enriched, –depleted, or unaffected bacterial strains after synthetic HDMBOA-Glc treatment. Color intensity indicates the fold changes in bacterial growth upon synthetic HDMBOA-Glc treatment relative to control treatment ($n = 6$ to 8). Fold-change values <1.0 indicate reduced growth, while values >1.0 indicate enhanced growth (full datasets are available in fig. S15). (**C** to **E**) Shoot biomass (C), caterpillar weight gain (D), and leaf damage (E) of wild-type maize plants grown in soils conditioned at 50 plants m^{-2}. These soils were inoculated with HDMBOA-Glc–responsive bacterial strains (+ SE, $n = 12$ to 18). Data points represent individual replicate samples. Different letters indicate significant differences between treatments (ANOVA followed by multiple comparisons of FDR-corrected LS means, $P < 0.05$). Asterisks indicate overall ANOVA significance (**$P < 0.01$; ***$P < 0.001$). Raw data, exact biological replicates, and P values for all comparisons in this figure are provided in Figshare (*62*).

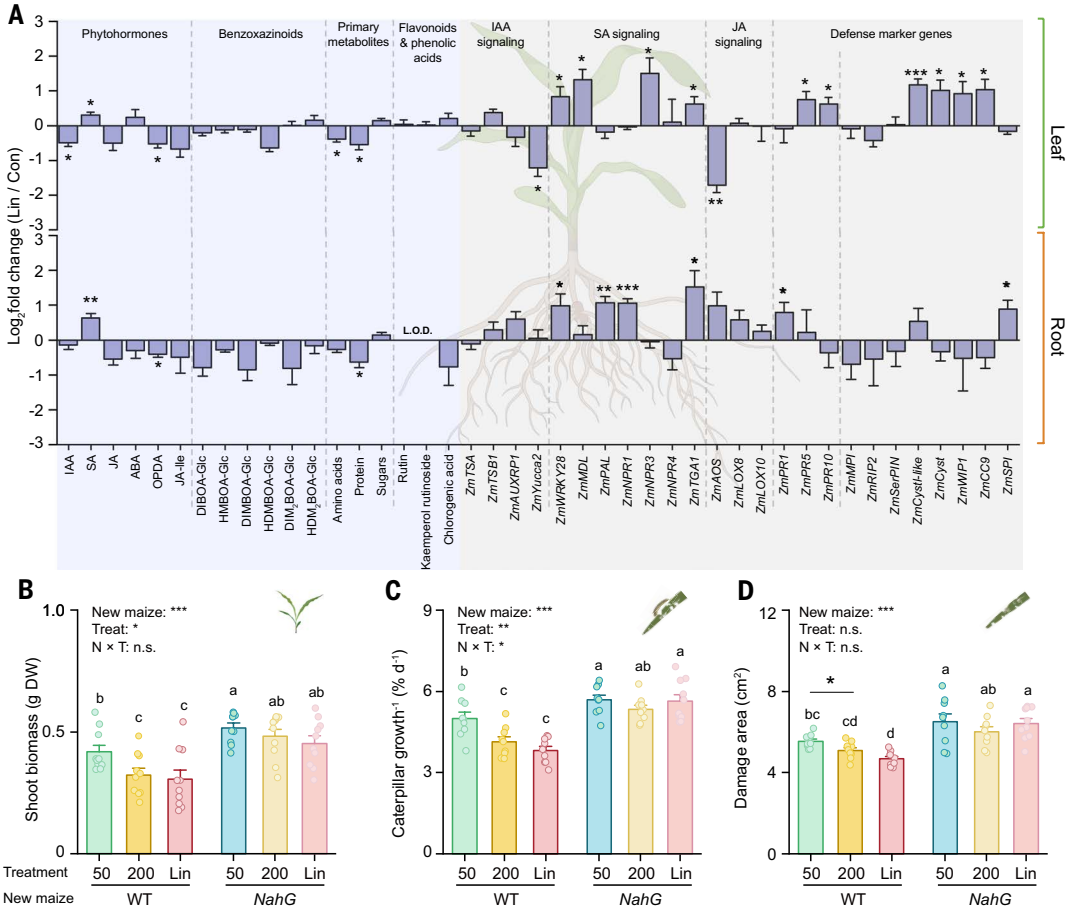

Fig. 7. SA signaling in new maize plants is essential for linalool-triggered plant-soil feedback. (**A**) Log_2 fold changes in phytohormones, metabolites, and gene expression in the leaf and roots of maize plants grown in soils previously conditioned by control (Con)– or linalool (Lin)–exposed receiver plants ($n = 6$ to 10) (full datasets are available in figs. S16 and S17). Certain components of this figure were generated using BioRender software. (**B** to **D**) Shoot biomass (B), caterpillar weight gain (C), and leaf damage (D) of WT and *NahG* overexpression plants grown in soils previously conditioned at 50 or 200 plants m^{-2} or in soils previously conditioned by Lin-exposed plants (+ SE, $n = 9$ to 10). Data points represent individual replicate samples. Different letters indicate significant differences between treatments (ANOVA followed by multiple comparisons of FDR-corrected LS means; $P < 0.05$). Asterisks indicate overall ANOVA significance (*$P < 0.05$; **$P < 0.01$; ***$P < 0.001$). Pairwise comparisons between selected groups were performed using two-sided Student's *t* test (*$P < 0.05$). Raw data, exact biological replicates, and *P* values for all comparisons in this figure are provided in Figshare (*62*).

Because the increase in SA levels and signaling was the most pronounced in new maize plants and because SA is known to play a key role in the growth and defense trade-off (*34*, *35*), we hypothesized that these altered SA levels might drive the observed shifts in growth and defense in new maize plants grown in soils conditioned by high-density plants. We thus grew the SA-deficient *NahG* lines in soils previously conditioned at 50 or 200 plants m^{-2} (*36*), as well as in soils conditioned by linalool-exposed plants. Our results showed that the feedback effects triggered by planting density on plant growth and herbivore resistance were abolished in the *NahG* lines (Fig. 7, B to D), confirming that SA signaling is required for the dense planting–mediated plant-soil feedback effects on growth and defense.

Discussion

Unlike most maize volatiles, which are specifically induced by biotic or abiotic stress (*37*), linalool is constitutively released, making it a logical candidate for signaling under high-density conditions. Herbivory-induced green leaf volatiles can trigger plant-soil feedback, affecting plant growth and resistance (*38*); our study, however, found that green leaf volatiles were not detectable under high–planting density conditions. Moreover, they induced distinct growth and resistance patterns compared with those observed for linalool (*38*), suggesting that these volatiles are unlikely to play a major role in dense planting–induced plant-soil feedback. However, we cannot completely rule out the potential contribution of other undetected volatiles in our experimental system.

Although linalool stimulates JA biosynthesis in roots, it does not increase JA levels in the rhizosphere, suggesting that JA exudation is an active process not directly regulated by linalool. Disruption of JA biosynthesis resulted in significantly reduced levels of HDMBOA-Glc and other BXs, whereas BX biosynthesis mutants did not affect JA levels. This directional dependency indicates that linalool-induced JA signaling acts upstream of BX biosynthesis and exudation. Supporting this, we observed a positive correlation between the expression of JA biosynthesis and signaling genes and HDMBOA-Glc biosynthesis genes. Furthermore, the JA signaling genes *ZmMYC2a* and *ZmMYC2b* have been shown to directly bind to the promoters of BX biosynthesis genes, transactivating their expression and promoting the production of HDMBOA-Glc and other BX derivatives (*28*). These findings support a model in which JA signaling, mediated by MYC2 transcription factors, orchestrates linalool-triggered BX biosynthesis and root exudation, thereby modulating interactions with the rhizosphere microbiome (fig. S18).

Although linalool has been reported to possess antibacterial properties (*39*), our findings suggest that linalool does not act directly on soil microbes but rather influences them indirectly through physiological

changes in the roots of neighboring plants. Only 3 days of high-density treatment were sufficient to trigger plant-soil feedback, implying that rhizosphere microbial communities belowground can respond rapidly to volatile cues aboveground. These microbial compositional shifts appear to persist long enough to alter the growth and defense phenotypes of subsequently grown plants, highlighting the speed and stability of volatile-mediated plant-microbe interactions in dense cropping systems.

Microbial communities are highly responsive to environmental context, and changes in the presence or abundance of specific taxa can reflect localized conditions such as plant density (*40*). Although microbial populations are dynamic, their functional roles can remain sufficiently consistent to serve as indicators of environmental change. In this context, microbiome members may serve not only as mediators of plant-soil feedback but also as conveyors of ecological information (*41*). Our findings support the hypothesis that plants may use microbial signals as indicators of local plant population density, allowing them to fine-tune their growth and defense responses accordingly (*42*).

To begin to understand the importance of the rhizosphere microbial taxa, we used 97% identity of the 16*S* amplicon sequences to link isolated bacterial strains to OTUs. This identity threshold has its limitations to fully capture species- or function-level variation because it may group together taxa with genetic and functional divergence, including members of different genera (*43*). A more comprehensive approach would involve whole-genome sequencing of both the microbiome and the cultured isolates to capture their full functional potential at the species or even strain level. In addition, future studies should explore the role of rhizosphere-associated fungi and more-complex synthetic microbial consortia, including both bacterial and fungal members (*44*).

We observed similar growth and resistance phenotypes in *bx6* and *OeBX12* lines under control conditions, despite their markedly different HDMBOA-Glc levels (*27*). This suggests that additional BX intermediates or regulatory factors may contribute to the observed phenotypes. HDMBOA-Glc and its degradation product, MBOA, are known to have antimicrobial or growth-promoting properties (*45*, *46*), which may explain their ability to enrich and deplete specific soil bacteria. MBOA accumulated in rhizosphere soils after linalool exposure, which is consistent with findings that MBOA triggers similar feedback effects, enhancing herbivore resistance and reducing growth (*25*). Thus, linalool-driven root HDMBOA-Glc exudation modulates the composition of the rhizosphere microbiota, driving the observed plant-soil feedback (fig. S18).

Although JA is classically associated with antiherbivore defenses (*47*), our data showed reduced JA signaling in the plants subsequently planted, suggesting that JA may not directly mediate the observed resistance at this stage. By contrast, SA signaling proved essential for the expression of enhanced resistance, aligning with previous findings in maize (*36*, *48*, *49*). The concurrent up-regulation of other defense-related genes implies that additional signaling pathways may also contribute.

Linalool-induced JA signaling occurs during the conditioning phase, where it promotes the exudation of BXs and shapes the rhizosphere microbiome. In the response phase, the subsequently grown plants rely primarily on SA signaling to express enhanced defense phenotypes (fig. S18). This suggests a temporal decoupling between signal perception (JA-driven) and defense expression (SA-driven), with each hormone acting at distinct stages of the feedback loop (*50*, *51*). In a densely planted field, such hormonal dynamics may operate within a single generation through continuous cycles of linalool perception and response. Plants might sense volatiles from neighbors, adjust their exudate profiles, and modulate their associated microbiota accordingly. This could enable real-time reinforcement of systemic resistance through microbiome-mediated signaling. Coordinated JA and SA signaling, both spatially and temporally, may thus be a key feature of plant adaptation to dense cropping systems. Disentangling intergenerational versus intragenerational roles of these pathways represents an exciting avenue for future research. In particular, elucidating how maize leaves perceive and transduce linalool signals will be essential for resolving this regulatory complexity.

The physiological changes of maize plants in the response phase offer insights into the trade-offs involved in volatile-mediated plant-soil feedback. First, increased herbivore resistance in subsequently grown maize plants correlates with elevated expression of defense-related genes (*52*), whereas reduced plant growth was associated with lower levels of free amino acids and soluble proteins. Second, we observed a classic JA/SA signaling trade-off (*53*), with decreased JA biosynthesis and increased SA biosynthesis. This reprogramming of primary metabolism toward enhanced defense suggests that maize plants prioritize defense over growth under high-density conditions, likely as an adaptive response to biotic pressures from neighboring plants (*54*, *55*). Although this trade-off limits biomass accumulation, the enhanced resistance to herbivores and pathogens may outweigh the costs, particularly in environments with high biotic stress. Furthermore, the reduction in growth and increase in defense could be beneficial in agricultural systems, potentially lowering pesticide inputs and reducing the risk of lodging to some extent. Although individual plant yield is reduced in dense planting systems, overall crop yield is often higher compared with that observed for low-density planting (*2*, *8*, *56*). This highlights the importance of balancing growth and defense in optimizing plant performance under dense planting conditions.

Informed by these findings, we propose to use linalool as a breeding target for regionally adapted maize varieties. In regions with high pathogen or pest pressure, breeding or engineering crop varieties with enhanced linalool emission or increased BX biosynthesis could optimize plant defenses in dense planting systems. Conversely, in areas with lower biotic stress, reducing linalool biosynthesis or improving planting designs to enhance air circulation could prevent linalool accumulation, thereby increasing maize productivity in dense cultivation. Substantial field research will be necessary to translate these strategies into practice. It is important to note that the field experiments presented in this study were not intended to directly test the linalool-mediated feedback mechanism but were designed to examine whether planting density influences plant growth and resistance under natural conditions. Rigorous field validation, such as the application of synthetic linalool under controlled field conditions and the assessment of downstream responses, will be essential and represents a promising direction for future research. Our study provides new insights into plant plasticity in response to environmental cues (fig. S18), highlighting the importance of volatile-mediated plant-soil feedback as a promising strategy for sustainable agricultural intensification and global food security.

Materials and methods

Plants

In this study, we used maize (*Zea mays*), barley (*Hordeum vulgare*, cultivar Eunova), and ryegrass (*Lolium perenne*, cultivar Pr521). The maize genotypes included the linalool-deficient mutant *tps2* and its wild-type (WT) B73; two BX-deficient mutants, *bx1* and *bx6*, and their WT W22; the HDMBOA-Glc overexpression line *OeBX12* and its WT B73-329; the JA-deficient mutant *lox8* and its WT W22; and the SA-deficient line *NahG* and its WT KN5585. The genotypes *bx1*, *bx2*, and *NahG* have been previously described and characterized (*27*, *36*).

The *OeBX12* line was specifically created for this study. Briefly, the open reading frame of the *ZmBX12* gene was cloned from CML322 inbred line and inserted into a *pCombia3300-ZmUbi*-derived binary vector. The constructed vectors were transformed into the recipient line B73-329 via *Agrobacterium tumefaciens*-mediated transformation. Transformed lines exhibiting the strongest HDMBOA-Glc accumulation phenotypes were selected for propagation. Homozygous lines were used for experiments alongside the WT line B73-329. Overexpression of *ZmBX12* was confirmed by quantitative real-time polymerase chain reaction (QRT-PCR) as described in the "Gene expression analysis" section, and HDMBOA-Glc over-accumulation in the roots was determined as described in the "Secondary metabolite analysis" section.

The *lox8* mutant was acquired from the Maize Genetics Cooperation Stock Center at the University of Illinois at Urbana-Champaign (Maize COOP; http://maizecoop.cropsci.uiuc.edu) as a mixture of WT, heterozygous, and homozygous seeds. Homozygous individuals were genotyped using gene-specific primers and further selfed for experiments. The effects of the *lox8* mutation on jasmonate biosynthesis were confirmed by quantifying the levels of JA, and JA-Ile using the protocol described in the "Phytohormone analysis" section.

The *tps2* mutant was obtained from the Maize EMS Database (maizeEMSDB; http://maizeems.qlnu.edu.cn). The *tps2* mutant harbors a single C-to-T mutation in the first exon, resulting in a premature termination codon of the *tps2* gene (fig. S11A). The effects of the *tps2* mutation on linalool biosynthesis were confirmed by profiling volatile compounds using the protocol described in the "Volatile profiling" section (fig. S11B).

Field survey

To explore whether planting density affects plant growth and defense through plant-plant interactions, a herbivory survey was conducted across four independent maize fields in Ledong, Hainan Province, China, during the winter of 2024. The fields surveyed were as follows: Field I (18°33′50″N, 108°55′13″E; area: 660 m^2), Field II (18°33′54″N, 108°55′09″E; area: 600 m^2), Field III (18°34′1″N, 108°54′57″E; area: 2100 m^2), and Field IV (18°34′10″N, 108°54′56″E; area: 2200 m^2). In China, the optimal planting density for maize is estimated to range between approximately 71,000 to 86,000 plants ha^{-1} (*3*). Accordingly, Fields I and II were planted with the maize cultivar Taiyanghua6 at a planting density of ~60,000 plants ha^{-1}, which falls below the standard agronomic recommendation. In contrast, Fields III and IV were planted at a high density of around 120,000 plants ha^{-1}, exceeding current best practices and reflecting emerging strategies for ultra-dense planting aimed at maximizing yield. To evaluate plant-plant interactions, each field was divided into inner sections and outer edges, and variations in growth and herbivory were assessed across these regions (Fig. 1A). For each area, four to six blocks were randomly selected, providing four to six biological replicates per treatment. At the tasseling stage, 100 to 256 plants (depending on field size) were randomly selected from each block to quantify herbivory damage. Herbivore damage was visually evaluated using a standardized leaf damage rating scale and quantified using a weighted attack intensity, following the FAO-recommended method described by Kalqutny *et al.* (*57*). Additionally, the plant height, shoot biomass, 1000-grain weight and grain yield per ear were measured in these four fields.

Soil conditioning by different planting densities

To investigate how planting density influences plant growth and defense through plant-soil feedback, we collected natural soil from a field in Hangzhou, China (30.3076 N, 120.0749 E). This bulk soil was sieved through a 4.75-mm mesh and air-dried for 48 hours. The soil was then placed into 400 ml or 12-liter sterile pots. Uniformly pre-germinated maize B73 seeds were sown in these pots. The maize plants were grown in a greenhouse maintained at 28°C ± 2°C with 55% relative humidity, a 14:10 hour light/dark cycle, and a light intensity of 350 μmol m^{-2} s^{-1}. The environment was complemented by continuous vertical airflow at 0.5 ms^{-1}. Plants were watered as needed. At the four-leaf stage, approximately 12 days post-planting, maize plants were repositioned at varying planting densities—50, 100, 150 and 200 plants m^{-2}—for a period of 3 days. (Fig. 1C). These were arranged within a well-ventilated transparent plastic sheet with an open-air top for 8 hours per day (9:00 a.m. to 5:00 p.m.). Three days after this density treatment, the plants were removed, and the soil was collected and sieved to be used for growing new plants. New maize plants were then planted into these conditioned soils and spaced to prevent direct density effects on their growth and defense. This experimental design ensured that any observed differences in the growth or defense of new plants were attributed to plant-soil feedback rather than direct root-root interactions or immediate density effects. The planting density were characterized by the levels of photosynthetically active radiation (PAR) and the red-to-far-red (R/FR) light ratio beneath the plant canopy. PAR, quantum efficiency (Eq), red light ratio (Rratio), and photosynthetic photon flux density (PPFD) were detected using spectrometer PLA-20 (EVERFINE Corporation, China). R/FR = [Eq×Rratio-PPFD (FR)]/ PPFD (FR).

Feedback experiment

Uniformly pre-germinated B73 seeds were sown individually in soils previously conditioned by maize plants grown at different planting densities. The new maize plants were spaced and cared for as described above. Shoot root biomass and plant resistance were assessed for these new plants. Specifically, shoot biomass was recorded 14 days after planting in 400-ml pots. Shoots and roots were harvested, oven-dried at 60°C for 2 days, and weighed to determine biomass. Details on plant resistance evaluation are provided in the "Plant resistance evaluation" section.

To determine whether plant density-triggered feedback effects are genotype-specific, three additional maize cultivars, B104, W22, and KN5585, were planted in soils previously conditioned by their respective cultivar at 50 or 200 plants m^{-2}. Plant growth and resistance for B104, W22, and KN5585 were assessed as described above.

To investigate whether plant density-triggered feedback occurs between different plant species, maize plants were cultivated alongside 10-day-old ryegrass (15 to 20 plants per pot) or barley (15 to 20 plants per pot), and the feedback effects in maize-conditioned soils were assessed as described above (fig. S6A).

To determine whether the observed feedback effects are specific to maize, we also grew ryegrass or barley in soils previously conditioned by maize at planting densities of 50 or 200 plants m^{-2} (fig. S7A). Additionally, ryegrass and barley were used to condition soils at low and high planting densities, and their subsequent growth and herbivore resistance were evaluated in their own conditioned soils (fig. S8A).

Plant resistance evaluation

Growth and damage of leaf herbivores: To assess the impact of planting density-triggered plant-soil feedback on maize resistance to leaf herbivores, we evaluated the growth and damage caused by fall armyworm (*Spodoptera frugiperda*) larvae. The larvae were reared on an artificial diet as previously described (*26*). A single starved, pre-weighed second instar larva was placed individually in a cylindrical mesh cage (1-cm height, 2.4-cm diameter). These cages were clipped onto the leaves of individual plants grown in soils conditioned at either 50 or 200 plants m^{-2}. The cage position was adjusted daily to provide sufficient food for the larvae. Larval mass was measured 3 to 5 days after the experiment began. Leaf damage was quantified by scanning the leaves and determining the area removed using Digimizer software.

Infection ability of root herbivores: To evaluate the effect of planting density-triggered plant-soil feedback on maize resistance to root herbivores, we assessed the infectivity of the root-knot nematode (*Meloidogyne incognita*). Nematode eggs were collected from infected tomato roots using a syringe needle and incubated at 28°C for 2 to 4 days to hatch J2 juveniles. Fourteen-day-old maize seedlings, grown in soils conditioned at either 50 or 200 plants m^{-2}, were inoculated with approximately 400 J2s. Fourteen days after infection, the number of galls and root biomass were recorded as previously described (*58*).

Infectivity of fungal pathogens: To determine the impact of planting density-triggered plant-soil feedback on maize resistance to plant pathogens, we evaluated the infectivity of *Exserohilum turcicum*, the causative agent of northern corn leaf blight (NCLB), which is a devastating prevalent disease in maize field. *E. turcicum* was incubated at 24°C for 2 days in Potato Dextrose Broth (PDB) with shaking (180 rpm). The fungus was harvested by centrifugation (5000 g, 10 min), resuspended

in distilled water, and filtered through cotton percale to remove mycelium, collecting the spores. Spores were then suspended to a concentration of 1×10^4 ml^{-1} using a hemocytometer. Maize plants were initially grown in 1-liter pots to condition soil at either 50 or 200 plants m^{-2}, as described above. The conditioned soils were then pooled into 12-liter pots, and new maize plants were individually transplanted in these larger pots. Forty-five days after planting, spore suspensions were evenly sprayed on the new plants. Twenty days after inoculation, lesion areas were excised from the leaves, adhered to A4 paper, scanned, and the lesion area was quantified using Digimizer software.

Virulence of rice black-streaked dwarf virus: To investigate the effect of planting density-triggered plant-soil feedback on maize resistance to phytovirus, we assessed the virulence of rice black-streaked dwarf virus (RBSDV), an arbovirus transmitted by planthoppers (*Laodelphax striatellus*) that causes maize rough dwarf (MRD) disease. New maize plants grown in soils conditioned at 50 or 200 plants m^{-2} were randomly arranged in a 0.5 m^3 insect-proof tent. At the two-leaf stage, these plants were artificially inoculated with RBSDV by allowing viruliferous planthoppers to feed on them for 3 days. The tent was then removed, and the infected plants were rearranged in the greenhouse. MRD symptoms were evaluated 80 days after inoculation. Disease severity index (DSI) calculation and scoring criteria were conducted as previously described (*59*). Virus concentration was also determined by QRT-PCR using primers RB-CP-216-F (CTTCATGATAGACTGCAAACCGTA) and RB-CP-359-R (ACAAATTCTTCACTTAGGTCGTT).

Volatile profiling

To assess maize volatile dynamics at different planting densities in situ, we employed the solid phase microextraction (SPME) method to profile leaf volatiles. A SPME fiber was positioned above the canopies of 14-day-old maize plants grown at 50, 100, 150 or 200 plants m^{-2}. The fiber absorbed volatiles for 60 min. The incubated fibers were then immediately analyzed using GC-MS (Agilent 7820A GC) according to previously established settings and protocols (*18*).

To investigate linalool emission from maize, ryegrass, barley, and *tps2* mutant plants, volatiles were collected using a dynamic headspace sampling system and Super-Q traps. Detailed information on the volatile sampling system and analysis methods has been previously published (*18*).

Construction and optimization of linalool dispensers

To confirm the effects of linalool in triggering plant-soil feedback, we constructed a dispenser designed to release synthetic linalool, as previously detailed (*18*). To ensure that maize plants were exposed to a physiological dose of synthetic linalool, corresponding to the amounts emitted by maize plants at different planting densities, we placed SPME fibers at varying distances (5 cm, 10 cm, 20 cm) from the dispenser. Additionally, fibers were placed midway between two dispensers positioned 20 cm apart in 0.07 m^2 open-air plastic cylinders (30 cm in diameter, 1 m in height, open at the top) to capture the gradient of emitted linalool (fig. S9C). The volatile compounds adsorbed by the SPME fibers were analyzed as described in the "Volatile profiling" section. We found that at a distance of 5 cm from a single linalool dispenser, the linalool concentration simulated the levels measured under a planting density of 150 plants m^{-2} (fig. S9D).

Soil conditioning via linalool exposure

To simulate the physiological linalool concentrations associated with different maize planting densities, we adjusted the exposure setup (fig. S9D). Maize plants were exposed to a linalool dispenser placed at varying distances: ~5 cm, 10 cm, 20 cm, or between two dispensers spaced 20 cm apart, to replicate the concentrations observed in different planting density conditions (fig. S9E). After 3 days of exposure (6 hours per day), soils from both the control- and linalool-exposed plants were collected and used to grow new maize plants. The growth and defense responses of these plants were then assessed as detailed in the "Feedback experiment" section to evaluate the feedback effects. Our findings indicated that exposure to linalool at a 5-cm distance, which mimics concentrations found under a planting density of 150 plants m^{-2}, effectively triggered plant-soil feedback effects (Fig. 2, B to D, and fig. S9E). Therefore, for all subsequent experiments, maize plants were exposed to a linalool dispenser at a 5-cm distance (hereafter referred to as "Lin").

Soil BX analysis

To determine the BX concentrations in soil, rhizosphere soil surrounding maize roots was carefully collected. Three maize seedlings, along with their adhering rhizosphere soil, were placed into a sealable bag. The bag was gently shaken to avoid damaging the roots while ensuring sufficient rhizosphere soil was collected. The collected soil was then sieved through a 250-μm mesh to remove root residues. The BXs in the sieved soil were extracted and analyzed following the procedure described (*26*).

Phytohormone analysis

For phytohormone analysis in maize leaves and roots, OPDA, JA, JA-Ile, SA, IAA, and ABA were extracted using ethyl acetate with isotopically labeled standards (1 ng for d_6-JA, d_6-JA-Ile, d_4-SA, d_5-IAA and d_6-ABA) and quantified via ultra-performance liquid chromatography–tandem mass spectrometry (UPLC-MS/MS), following the methods in our previous work (*18*).

For phytohormone analysis in conditioned soil, soil samples were collected and processed as described in the above "Soil BX analysis" section. A 10-g soil sample was thoroughly homogenized in 10 ml of acetone. The mixture was subjected to vigorous vortexing for 5 min, followed by centrifugation at 4000 g for 10 min. The supernatant was collected and further centrifuged at 15,000 g for 10 min. The final supernatant was evaporated to dryness, and the residue was dissolved in ethyl acetate, supplemented with isotopically labeled standards. The supernatant was then evaporated to dryness, redissolved in methanol and analyzed using UPLC-MS/MS (*60*).

Gene expression analysis

QRT-PCR was used to measure gene expression levels in maize leaves and roots. Total RNA was isolated using the Tiangen Plant RNA Purification Kit (TIANGEN, China) according to the manufacturer's instructions. Eight hundred nanograms of each RNA sample was reverse transcribed using the PrimerScript RT Master Mix (Takara, China). The QRT-PCR assays were performed on a LightCycler 96 Instrument (Roche, Switzerland) using the KAPA SYBR FAST qPCR Master Mix (Kapa Biosystems, USA). The maize actin gene (*ZmActin*) was used as an internal reference to normalize cDNA concentrations. Relative gene expression levels were calculated using the $2^{-\Delta\Delta Ct}$ method. The primers used for QRT-PCR of all tested genes are listed in data S4.

Microbial sterilization and complementation

To investigate the role of soil microbiota in linalool-mediated feedback, bulk field soil was either sterilized by x-ray irradiation [50 kilograys (kGy)] at Shanghai Co-Elit Agricultural Sci Tech Company, China, or left untreated (Natural). The sterilized soil was also complemented with microbe suspensions obtained from soils of control- and linalool-exposed plants. The microbe suspensions were prepared by mixing 400 ml of soil with 400 ml of autoclaved Milli-Q water. The mixture was allowed to stand for 2 hours to let larger soil particles settle. The supernatant was then passed through a 250-μm sieve, followed by two successive 10-μm sieves to retain nematodes and spores of most species of arbuscular mycorrhiza, while allowing the suspended microorganisms to pass through. A volume of 100 ml of these microbial suspensions was used to complement the sterilized soil. This process resulted in six soil treatments: natural control soil, natural linalool-exposed soil, sterilized control soil, sterilized linalool-exposed soil, and sterilized

control and linalool soils complemented with microbial suspensions. Maize plants were planted in these soils and exposed to either control or linalool dispensers as previously described. After exposure, new maize plants were planted into the conditioned soils, and their growth and herbivore resistance were assessed according to the feedback experiment protocol.

Soil bacteria profiling

Rhizosphere soil samples were collected as described previously (*38*). Approximately 200 mg of fine rhizosphere soil was used for DNA extraction with the FastDNA SPIN Kit for Soil (MP Biomedicals, USA), following the manufacturer's instructions. The V4-V5 region of the bacterial 16*S* rRNA gene was amplified using the primers 515F (5′-GTGCCAGCMGCCGCGGTAA-3′) and 907R (5′-CCGTCAATTCCTTTGAGTTT-3′). PCR products were verified for size and purity by gel electrophoresis, followed by gel purification with the E.Z.N.A. Gel Extraction Kit (Omega, USA) and subsequent DNA quantification. Sequencing libraries were prepared using the NEBNext Ultra II DNA Library Prep Kit for Illumina (New England Biolabs, USA) according to the manufacturer's protocols, incorporating index codes for sample identification. Library quality was assessed with a Qubit 2.0 Fluorometer (Thermo Fisher Scientific, USA), and sequencing was performed on an Illumina HiSeq PE250 platform (Illumina Nova 6000, USA) by Novogene (Novogene, China). The 16*S* rRNA gene sequences were analyzed using EasyAmplicon, following the approach outlined by Liu *et al.* (*61*). Operational taxonomic units (OTUs) were generated with a similarity threshold of 97% (-otutab, -id 0.97), and taxonomic annotation was performed using USEARCH with the RDP database (-sintax_cutoff 0.6). Bray-Curtis diversity metrics were calculated using EasyAmplicon, with pairwise Anosim tests and permutational multivariate analysis of variance (PERMANOVA) conducted with 999 permutations. The results were visualized through principal coordinates analysis (PCoA) plots. Differential OTU abundance was analyzed for OTUs with a mean relative abundance >0.01% using edgeR, and *P* values were adjusted using the false discovery rate (FDR) with a threshold of 0.1.

Isolation and identification of rhizosphere-associated bacteria

To isolate linalool-responsive bacteria strains, soils from control- and linalool-exposed plants were vortexed in 0.1 M phosphate-buffered saline for 5 min. The resulting suspensions were serially diluted, plated on 9-cm Petri dishes, and cultivated on various media including Nutrient Broth agar (NA), tryptic soy agar (TSA), 1:10 (v/v) TSA, Reasoner's 2A agar (R2A), Luria Bertani (LB) agar, and 1:10 (v/v) LB agar. After 2 to 5 days of incubation, single colonies were isolated by streak plating. Genomic DNA was extracted from the purified bacterial colonies, and the 16*S* rRNA gene was amplified. The PCR products were validated by Sanger sequencing using the 27F (5′-GAGTTTGATCATGGCTCAG-3′) and 1492R (5′-GGTTACCTTGTTACGACTT-3′) primers. Bacteria that shared >97% 16*S* rRNA gene sequence similarity with OTUs enriched in the rhizosphere of linalool-treated plants were selected as candidates for subsequent experiments (data S2). We focused on strains enriched under linalool exposure conditions, as these could be experimentally reintroduced into low-density soils to test their functional roles (see "Bacterial complementation experiment" section). In contrast, selectively removing depleted strains from high-density soils to assess their specific contributions remains technically challenging with current methodologies.

Bacterial growth analysis

To evaluate the effect of linalool exposure on the growth of rhizosphere-associated bacteria, soil extracts were collected from both control- and linalool-exposed maize plants. The extracts were prepared by suspending 10 g of conditioned soil in 10 ml of water. Subsequently, the mixture was vortexed at 2000 g for 10 min, followed by centrifugation at 6000 g for another 10 min. Finally, the supernatant was filtered through a 0.22-μm Nalgene filter unit. These filtered extracts were then mixed with culture medium in a 9:1 ratio (v/v). For the bacterial growth, 1 μl of a 0.1 OD pre-cultured bacterial suspension was inoculated into 200 μl of the fresh soil extract mixture in 96-well microtiter plates.

Bacterial growth was determined by measuring absorbance at 600 nm using a Microplate Reader (Biotek, Synergy H1, USA) after 24 hours of incubation (180 rpm, 30°C). To examine the correlation between HDMBOA-Glc concentrations in soil and bacterial growth, we quantified the concentration of HDMBOA-Glc and performed a Pearson correlation analysis to assess the relationship between HDMBOA-Glc levels and bacterial growth.

Direct influence of HDMBOA-Glc on bacterial growth

To assess the direct impact of synthetic HDMBOA-Glc on the growth of rhizosphere-associated bacteria, we quantified bacterial proliferation in soil extracts treated with varying concentrations of HDMBOA-Glc. Soil extracts were collected from field bulk soil with no detectable HDMBOA-Glc. The extracts were prepared as described in the "Bacterial growth analysis" section above. Synthetic HDMBOA-Glc was added to 200 μl of the soil extracts to achieve final concentrations of 0, 0.01, 0.1, and 1 μg ml^{-1}. Subsequently, 1 μl of each precultivated bacteria strains with an OD of 0.1 was inoculated into the 200-μl soil extracts in 96-well microtiter plates. After 24 hours of incubation, 50 μl of the planktonic bacterial suspension was collected, serially diluted, and plated on 9-cm Petri dishes. The plates were incubated for 1 to 3 days, depending on the growth kinetics of the bacterial strains. Phenotypic observations were documented through photographic records of the bacterial colonies. Colony-forming units (CFU) were counted using a Dot Counting Camera (developed by Beijing Pengtuzhumeng Technology Co., Ltd.), and the counts were adjusted according to the dilution factor.

Bacterial complementation experiment

To test whether HDMBOA-Glc-responsive microbes are sufficient to induce growth and defense effects in maize plants, we selected 13 HDMBOA-Glc-enriched strains, 1 depleted strain, and 1 unaffected strain to complement the soils previously conditioned at 50 plants m^{-2}. Each bacterial strain was cultivated in its respective liquid medium for 1 to 2 days in a shaker (180 rpm, 30°C) and harvested by centrifugation (5000 to 12,000 g, 10 min). The harvested bacteria were washed three times with ddH_2O and resuspended in ddH_2O to a final concentration of 1×10^7 CFU ml^{-1}. For the inoculation, 10 ml of each bacterial suspension was added to the conditioned soils. Uniformly pregerminated WT maize seeds were individually sown in these bacteria-complemented soils. Shoot biomass, herbivore resistance, and leaf damage area were quantified as described above.

Primary metabolite analysis

To assess the impact of linalool-triggered plant-soil feedback on primary metabolites, we quantified free amino acids, total sugars, and soluble protein levels in the maize grown in soils conditioned by linalool-exposed plants. Free amino acids were analyzed using the UPLC-MS/MS method (*26*). Total soluble proteins were determined using the Bradford assay, and total sugars were measured with the 3,5-dinitrosalicylic acid (DNS) method. For sugar analysis, 0.5 g of fresh leaf tissue was homogenized in 1 ml of deionized water and 500 μl of 6 M HCl, then sealed and incubated at 90°C for 30 min. After cooling to room temperature, the mixture was neutralized with 500 μl of 6 M NaOH, and the final volume was adjusted to 2 ml with thorough mixing. Following centrifugation at 12,000 rpm for 10 min, 200 μl of the supernatant was collected. This supernatant was then heated to 95°C, after which an equal volume of DNS reagent (Macklin) was added until a red coloration developed. Absorbance was measured at 540 nm using a Microplate Reader (Biotek, Synergy H1, USA).

Secondary metabolite analysis

To assess the impact of linalool-triggered plant-soil feedback on secondary metabolites, we quantified the levels of BXs, flavonoids, and

phenolic acids in maize grown in soils conditioned by linalool-exposed plants following a standardized procedure. Briefly, 50 mg of flash-frozen maize leaf or root samples were extracted with 1 ml of an acidified H_2O/MeOH solution (50:50 v/v, containing 0.1% formic acid). The extracts were analyzed using an Acquity UPLC-MS/MS system equipped with an electrospray ionization source, using the parameters established in our previous work (*26*). Absolute concentrations of BXs, flavonoids and phenolic acids were determined using standard curves generated from pure synthetic compounds.

Feedback experiment with SA-deficient lines

The uniform and pre-germinated *NahG* overexpression lines as well as its WT KN5585 plants were individually sown in soils which were previously conditioned by control- or linalool-exposed B73 plants. These plants were taken care of as described above. The shoot biomass, herbivore resistance and leaf damage of *NahG* overexpression and KN5585 plants were determined as described in above sections.

Statistical analysis

Data were analyzed using linear models followed by analysis of variance (ANOVA). Continuous data such as plant biomass, herbivore growth, metabolites, volatile compounds, and gene expression levels were analyzed using linear models followed by ANOVA. For discrete data, such as gall numbers, virus copies, and bacterial counts, generalized linear mixed models (GLMMs) with a Poisson distribution followed by ANOVA were used. When necessary, pairwise or multiple comparisons of least squares means (LS means) were corrected using the FDR method. PCoA of Bray-Curtis distances was employed to compare bacterial profiles between control and linalool treatments, with significant differences determined by Monte Carlo tests with 999 permutations. Pearson correlation was used to assess the associations between the expression of BX and JA biosynthesis genes, as well as the correlations between HDMBOA-Glc concentration and bacterial growth. All statistical analyses were performed using R version 4.2.0, utilizing packages including "car", "emmeans", "vegan", "RVAideMemoire", "pheatmap", "dplyr", "phyloseq", "edgeR", "multcomp", "corrplot", "lme4", "reshape2", "magrittr", and "tidyr".

REFERENCES AND NOTES

1. United Nations Department of Economic and Social Affairs, "Transforming our world: The 2030 Agenda for Sustainable Development" (UN.org, 2015); https://sdgs.un.org/2030agenda.
2. J. Deng *et al.*, Models and tests of optimal density and maximal yield for crop plants. *Proc. Natl. Acad. Sci. U.S.A.* **109**, 15823–15828 (2012). doi: 10.1073/pnas.1210955109; pmid: 22891337
3. N. Luo *et al.*, China can be self-sufficient in maize production by 2030 with optimal crop management. *Nat. Commun.* **14**, 2637 (2023). doi: 10.1038/s41467-023-38355-2; pmid: 37149677
4. M. B. Mantilla-Perez, M. G. Salas Fernandez, Differential manipulation of leaf angle throughout the canopy: Current status and prospects. *J. Exp. Bot.* **68**, 5699–5717 (2017). doi: 10.1093/jxb/erx378; pmid: 29126242
5. W. Ren *et al.*, Genome-wide dissection of changes in maize root system architecture during modern breeding. *Nat. Plants* **8**, 1408–1422 (2022). doi: 10.1038/s41477-022-01274-z; pmid: 36396706
6. K. Thorup-Kristensen *et al.*, Digging deeper for agricultural resources, the value of deep rooting. *Trends Plant Sci.* **25**, 406–417 (2020). doi: 10.1016/j.tplants.2019.12.007; pmid: 31964602
7. J. Tian *et al.*, Maize smart-canopy architecture enhances yield at high densities. *Nature* **632**, 576–584 (2024). doi: 10.1038/s41586-024-07669-6; pmid: 38866052
8. J. Tian *et al.*, Teosinte ligule allele narrows plant architecture and enhances high-density maize yields. *Science* **365**, 658–664 (2019). doi: 10.1126/science.aax5482; pmid: 31416957
9. F. Romero *et al.*, Humidity and high temperature are important for predicting fungal disease outbreaks worldwide. *New Phytol.* **234**, 1553–1556 (2022). doi: 10.1111/nph.17340; pmid: 33713447
10. M. Blandino, A. Reyneri, F. Vanara, Effect of plant density on toxigenic fungal infection and mycotoxin contamination of maize kernels. *Field Crops Res.* **106**, 234–241 (2008). doi: 10.1016/j.fcr.2007.12.004
11. A. G. Power, Plant community diversity, herbivore movement, and an insect-transmitted disease of maize. *Ecology* **68**, 1658–1669 (1987). doi: 10.2307/1939858; pmid: 29357176
12. J. Moral, J. Jurado-Bello, M. I. Sánchez, R. de Oliveira, A. Trapero, Effect of temperature, wetness duration, and planting density on olive anthracnose caused by *Colletotrichum* spp. *Phytopathology* **102**, 974–981 (2012). doi: 10.1094/PHYTO-12-11-0343; pmid: 22957821
13. R. Zhang, K. Tielbörger, Density-dependence tips the change of plant-plant interactions under environmental stress. *Nat. Commun.* **11**, 2532 (2020). doi: 10.1038/s41467-020-16286-6; pmid: 32439842
14. International PLANTCOM network; The ecologically relevant genetics of plant-plant interactions. *Trends Plant Sci.* **28**, 31–42 (2023). doi: 10.1016/j.tplants.2022.08.014; pmid: 36114125
15. M. Huber, N. M. Nieuwendijk, C. K. Pantazopoulou, R. Pierik, Light signalling shapes plant-plant interactions in dense canopies. *Plant Cell Environ.* **44**, 1014–1029 (2021). doi: 10.1111/pce.13912; pmid: 33047350
16. C. H. Kong *et al.*, Plant neighbor detection and allelochemical response are driven by root-secreted signaling chemicals. *Nat. Commun.* **9**, 3867 (2018). doi: 10.1038/s41467-018-06429-1; pmid: 30250243
17. L. Hu, Integration of multiple volatile cues into plant defense responses. *New Phytol.* **233**, 618–623 (2022). doi: 10.1111/nph.17724; pmid: 34506634
18. M. Ye, G. Glauser, Y. Lou, M. Erb, L. Hu, Molecular dissection of early defense signaling underlying volatile-mediated defense regulation and herbivore resistance in rice. *Plant Cell* **31**, 687–698 (2019). doi: 10.1105/tpc.18.00569; pmid: 30760558
19. M. Ye *et al.*, Indole primes defence signalling and increases herbivore resistance in tea plants. *Plant Cell Environ.* **44**, 1165–1177 (2021). doi: 10.1111/pce.13897; pmid: 32996129
20. C. L. Ballaré, R. Pierik, The shade-avoidance syndrome: Multiple signals and ecological consequences. *Plant Cell Environ.* **40**, 2530–2543 (2017). doi: 10.1111/pce.12914; pmid: 28102548
21. V. Ninkovic, D. Markovic, M. Rensing, Plant volatiles as cues and signals in plant communication. *Plant Cell Environ.* **44**, 1030–1043 (2021). doi: 10.1111/pce.13910; pmid: 33047347
22. T. C. J. Turlings, U. B. Lengwiler, M. L. Bernasconi, D. Wechsler, Timing of induced volatile emissions in maize seedlings. *Planta* **207**, 146–152 (1998). doi: 10.1007/s004250050466
23. L. Hu, K. Zhang, Z. Wu, J. Xu, M. Erb, Plant volatiles as regulators of plant defense and herbivore immunity: Molecular mechanisms and unanswered questions. *Curr. Opin. Insect Sci.* **44**, 82–88 (2021). doi: 10.1016/j.cois.2021.03.010; pmid: 33894408
24. L. D. Lopes, P. Wang, S. L. Futrell, D. P. Schachtman, Sugars and jasmonic acid concentration in root exudates affect maize rhizosphere bacterial communities. *Appl. Environ. Microbiol.* **88**, e00971-22 (2022). doi: 10.1128/aem.00971-22; pmid: 36073926
25. L. Hu *et al.*, Root exudate metabolites drive plant-soil feedbacks on growth and defense by shaping the rhizosphere microbiota. *Nat. Commun.* **9**, 2738 (2018). doi: 10.1038/s41467-018-05122-7; pmid: 30013066
26. L. Hu *et al.*, Soil chemistry determines whether defensive plant secondary metabolites promote or suppress herbivore growth. *Proc. Natl. Acad. Sci. U.S.A.* **118**, e2109602118 (2021). doi: 10.1073/pnas.2109602118; pmid: 34675080
27. L. Hu *et al.*, Plant iron acquisition strategy exploited by an insect herbivore. *Science* **361**, 694–697 (2018). doi: 10.1126/science.aat4082; pmid: 30115808
28. C. Ma *et al.*, ZmMYC2s play important roles in maize responses to simulated herbivory and jasmonate. *J. Integr. Plant Biol.* **65**, 1041–1058 (2023). doi: 10.1111/jipb.13404; pmid: 36349965
29. I. F. Acosta *et al.*, tasselseed1 is a lipoxygenase affecting jasmonic acid signaling in sex determination of maize. *Science* **323**, 262–265 (2009). doi: 10.1126/science.1164645; pmid: 19131630
30. S. A. Christensen *et al.*, Maize death acids, 9-lipoxygenase-derived cyclopente(a)nones, display activity as cytotoxic phytoalexins and transcriptional mediators. *Proc. Natl. Acad. Sci. U.S.A.* **112**, 11407–11412 (2015). doi: 10.1073/pnas.1511131112; pmid: 26305953
31. S. L. Lebeis *et al.*, Salicylic acid modulates colonization of the root microbiome by specific bacterial taxa. *Science* **349**, 860–864 (2015). doi: 10.1126/science.aaa8764; pmid: 26184915
32. J. M. Raaijmakers, E. T. Kiers, Rewilding plant microbiomes. *Science* **378**, 599–600 (2022). doi: 10.1126/science.abn6350; pmid: 36356130
33. V. J. Carrión *et al.*, Pathogen-induced activation of disease-suppressive functions in the endophytic root microbiome. *Science* **366**, 606–612 (2019). doi: 10.1126/science.aaw9285; pmid: 31672892
34. Y. Peng, J. Yang, X. Li, Y. Zhang, Salicylic acid: Biosynthesis and signaling. *Annu. Rev. Plant Biol.* **72**, 761–791 (2021). doi: 10.1146/annurev-arplant-081320-092855; pmid: 33756096
35. T. van Butselaar, G. Van den Ackerveken, Salicylic acid steers the growth-immunity tradeoff. *Trends Plant Sci.* **25**, 566–576 (2020). doi: 10.1016/j.tplants.2020.02.002; pmid: 32407696
36. Y. B. Setotaw *et al.*, Salicylic acid positively regulates maize defenses against lepidopteran insects. *Plant Divers.* **46**, 519–529 (2024). doi: 10.1016/j.pld.2024.03.004; pmid: 39280976
37. T. C. J. Turlings, M. Erb, Tritrophic interactions mediated by herbivore-induced plant volatiles: Mechanisms, ecological relevance, and application potential. *Annu. Rev. Entomol.* **63**, 433–452 (2018). doi: 10.1146/annurev-ento-020117-043507; pmid: 29324043

38. L. Hu *et al.*, Herbivory-induced green leaf volatiles increase plant performance through jasmonate-dependent plant-soil feedbacks. *Nat. Plants* **11**, 1001–1017 (2025). doi: 10.1038/s41477-025-01987-x; pmid: 40312547
39. W. Mączka, A. Duda-Madej, M. Grabarczyk, K. Wińska, Natural compounds in the battle against microorganisms-linalool. *Molecules* **27**, 6928 (2022). doi: 10.3390/molecules27206928; pmid: 36296521
40. J. Nguyen, J. Lara-Gutiérrez, R. Stocker, Environmental fluctuations and their effects on microbial communities, populations and individuals. *FEMS Microbiol. Rev.* **45**, fuaa068 (2021). doi: 10.1093/femsre/fuaa068; pmid: 33338228
41. H. Liu, C. A. Macdonald, J. Cook, I. C. Anderson, B. K. Singh, An ecological loop: Host microbiomes across multitrophic interactions. *Trends Ecol. Evol.* **34**, 1118–1130 (2019). doi: 10.1016/j.tree.2019.07.011; pmid: 31422890
42. C. J. E. Metcalf, L. P. Henry, M. Rebolleda-Gómez, B. Koskella, Why evolve reliance on the microbiome for timing of ontogeny? *mBio* **10**, e01496-19 (2019). doi: 10.1128/mBio.01496-19; pmid: 31594812
43. J. S. Johnson *et al.*, Evaluation of 16S rRNA gene sequencing for species and strain-level microbiome analysis. *Nat. Commun.* **10**, 5029 (2019). doi: 10.1038/s41467-019-13036-1; pmid: 31695033
44. E. C. Mehlferber *et al.*, A cross-systems primer for synthetic microbial communities. *Nat. Microbiol.* **9**, 2765–2773 (2024). doi: 10.1038/s41564-024-01827-2; pmid: 39478083
45. J. Maresh, J. Zhang, D. G. Lynn, The innate immunity of maize and the dynamic chemical strategies regulating two-component signal transduction in *Agrobacterium tumefaciens*. *ACS Chem. Biol.* **1**, 165–175 (2006). doi: 10.1021/cb600051w; pmid: 17163664
46. L. Thoenen *et al.*, The lactonase BxdA mediates metabolic specialisation of maize root bacteria to benzoxazinoids. *Nat. Commun.* **15**, 6535 (2024). doi: 10.1038/s41467-024-49643-w; pmid: 39095376
47. M. Erb, P. Reymond, Molecular interactions between plants and insect herbivores. *Annu. Rev. Plant Biol.* **70**, 527–557 (2019). doi: 10.1146/annurev-arplant-050718-095910; pmid: 30786233
48. S. Ziemann *et al.*, An apoplastic peptide activates salicylic acid signalling in maize. *Nat. Plants* **4**, 172–180 (2018). doi: 10.1038/s41477-018-0116-y; pmid: 29483684
49. W. Yuan *et al.*, Maize phenylalanine ammonia-lyases contribute to resistance to *Sugarcane mosaic virus* infection, most likely through positive regulation of salicylic acid accumulation. *Mol. Plant Pathol.* **20**, 1365–1378 (2019). doi: 10.1111/mpp.12817; pmid: 31487111
50. L. Zhang, X. Wu, C. Tian, R. Schneiter, Seasonal changes in salicylic and jasmonic acid levels in poplar with differing stress responses. *Forests* **15**, 1896 (2024). doi: 10.3390/f15111896
51. S. Betsuyaku *et al.*, Salicylic acid and jasmonic acid pathways are activated in spatially different domains around the infection site during effector-triggered immunity in *Arabidopsis thaliana*. *Plant Cell Physiol.* **59**, 8–16 (2018). doi: 10.1093/pcp/pcx181; pmid: 29177423
52. L. Hu, M. Ye, M. Erb, Integration of two herbivore-induced plant volatiles results in synergistic effects on plant defence and resistance. *Plant Cell Environ.* **42**, 959–971 (2019). doi: 10.1111/pce.13443; pmid: 30195252
53. C. M. J. Pieterse, D. Van der Does, C. Zamioudis, A. Leon-Reyes, S. C. M. Van Wees, Hormonal modulation of plant immunity. *Annu. Rev. Cell Dev. Biol.* **28**, 489–521 (2012). doi: 10.1146/annurev-cellbio-092910-154055; pmid: 22559264
54. S. C. Turner, J. A. Schweitzer, Plant neighbors differentially alter a focal species' biotic interactions through changes to resource allocation. *Ecology* **105**, e4395 (2024). doi: 10.1002/ecy.4395; pmid: 39299794
55. J.-K. Weng, J. H. Lynch, J. O. Matos, N. Dudareva, Adaptive mechanisms of plant specialized metabolism connecting chemistry to function. *Nat. Chem. Biol.* **17**, 1037–1045 (2021). doi: 10.1038/s41589-021-00822-6; pmid: 34552220
56. L. Tang *et al.*, Density resistance evaluation of maize varieties through new "*Density-Yield Model*" and quantification of varietal response to gradual planting density pressure. *Sci. Rep.* **8**, 17281 (2018). doi: 10.1038/s41598-018-35275-w; pmid: 30470761
57. S. H. Kalqutny, N. Nonci, A. Muis, The incidence of fall armyworm *Spodoptera frugiperda* JE Smith (FAW)(Lepidoptera: Pyralidae), a newly invasive corn pest in Indonesia. *IOP Conf. Ser. Earth Environ. Sci.* **911**, 012056 (2021). doi: 10.1088/1755-1315/911/1/012056
58. H. Zhang *et al.*, Cover crop rotation suppresses root-knot nematode infection by shaping soil microbiota. *New Phytol.* **245**, 363–377 (2025). doi: 10.1111/nph.20220; pmid: 39468918
59. Q. Liu *et al.*, A *helitron*-induced RabGDIα variant causes quantitative recessive resistance to maize rough dwarf disease. *Nat. Commun.* **11**, 495 (2020). doi: 10.1038/s41467-020-14372-3; pmid: 31980630
60. Q. Jiang *et al.*, Two leucine-rich repeat receptor-like kinases initiate herbivory defense responses in tea plants. *Hortic. Res.* **12**, uhae281 (2024). doi: 10.1093/hr/uhae281; pmid: 39850371
61. Y. X. Liu *et al.*, EasyAmplicon: An easy-to-use, open-source, reproducible, and community-based pipeline for amplicon data analysis in microbiome research. *iMeta* **2**, e83 (2023). doi: 10.1002/imt2.83; pmid: 38868346
62. L. Hu, Linalool-triggered plant-soil feedback drives defense adaptation in dense maize plantings, Figshare (2025); https://doi.org/10.6084/m9.figshare.29231894.v1.
63. Y. X. Liu, EasyAmplicon v1.12, GitHub (2021); https://github.com/YongxinLiu/EasyAmplicon/releases/tag/v1.12.

ACKNOWLEDGMENTS

We thank Hefei Fengle Seed Co. for assistance with the field trials; J. Wu at Kunming Institute of Botany, Chinese Academy of Sciences, for sharing the SA-deficient *NahG* maize lines; and J. Wu at Zhejiang University for sharing the rice black-streaked dwarf virus. **Funding:** This work was supported by the National Key Research and Development Project of China (2021YFD1900200), the Zhejiang Provincial Natural Science Foundation of China (LR25D010001), the National Natural Science Foundation of China (42377285), the Science and Technology special fund of Hainan Province (ZDYF2024XDNY161), and the 111 Project (B17039). **Author contributions:** Study design: J.X., L.H.; Experimental design and supervision: D.G., J.M.R., M.E., J. Z., Y.-G.Z., J.X., L.H.; Data collection and analysis: D.G., Z.L., Y.X., J.Y., L.H.; Initial draft: J.M.R., J.X., L.H.; Final version: All authors. **Competing interests:** The authors declare that they have no competing interests. **Data and materials availability:** All data needed to evaluate the conclusions in the paper are present in the main text or the supplementary materials. The raw sequencing data of soil bacteria have been deposited in the Genome Sequence Archive in the National Genomics Data Center, China National Center for Bioinformation/Beijing Institute of Genomics, Chinese Academy of Sciences (CRA026253), and are publicly accessible at https://ngdc.cncb.ac.cn/gsa. All data generated and/or analyzed during this study are available via Figshare (*62*). The source code of the soil microbiota analysis is available on GitHub (*63*). Additional materials related to this paper may be requested from the corresponding authors. **License information:** Copyright © 2025 the authors, some rights reserved; exclusive licensee American Association for the Advancement of Science. No claim to original US government works. https://www.science.org/about/science-licenses-journal-article-reuse

SUPPLEMENTARY MATERIALS

science.org/doi/10.1126/science.adv6675
Figs. S1 to S18; Data S1 to S4; MDAR Reproducibility Checklist

Submitted 28 January 2025; accepted 10 June 2025

10.1126/science.adv6675

Check for

RESEARCH ARTICLE SUMMARY

PROTEIN SIMULATIONS

Scalable emulation of protein equilibrium ensembles with generative deep learning

Sarah Lewis†, Tim Hempel†, José Jiménez-Luna†, Michael Gastegger†, Yu Xie†, Andrew Y. K. Foong†, Victor García Satorras†, Osama Abdin†, Bastiaan S. Veeling†, *et al.*

Full article and list of author affiliations: https://doi.org/10.1126/science.adv9817

INTRODUCTION: Proteins constitute the functional building blocks of life and are central to drug discovery and biotechnology. We now have technologies to determine protein sequence and predict protein structure at the genomic scale, but this is not the case for protein function. Protein function relies on dynamical mechanisms, particularly the transitions between long-lived protein structures (conformational states) and the association with and dissociation from other proteins and ligands (compositional states). The coupling between conformational and compositional state changes, and the probability of these states under a given set of conditions (temperature, solvation, concentration), determine "how proteins work" on a molecular scale. Although biophysical experiments and molecular dynamics (MD) simulations can reveal such structure-dynamics relationships with high accuracy, these methods suffer from low throughput.

RATIONALE: As a step toward solving this throughput challenge, we developed a biomolecular emulator (BioEmu) that samples the approximate equilibrium distribution of structures of single protein chains. BioEmu is a generative deep-learning system that can generate thousands of statistically independent structure samples per hour on a single graphics processing unit (GPU). BioEmu leverages AlphaFold to encode the protein sequence into a rich sequence-structure representation, which inputs into a diffusion model that efficiently samples three-dimensional structures. BioEmu was trained in three stages: It was pretrained on a processed version of the AlphaFold database (AFDB) in such a way as to incentivize the model to associate each protein sequence with a diverse set of structures. Training was continued on a vast dataset of MD simulations of thousands of proteins and more than 200 ms of aggregate simulation time. And finally, BioEmu was fine-tuned on more than 500,000 experimental protein stabilities using a technology developed here, property-prediction fine-tuning (PPFT).

RESULTS: We tested BioEmu on a variety of protein systems that are dissimilar from training proteins and benchmarked its performance on three tasks: (i) Predicting known conformational changes including large domain motions, local unfolding transitions, and the formation of cryptic binding pockets while achieving success rates of sampling the known references of between 55 and 90%. (ii) Emulating equilibrium distributions of both protein folding and native-state conformational transitions that can be generated by high-throughput MD simulation, demonstrating errors in free-energy differences below 1 kcal/mol and speedups of four to five orders of magnitude. (iii) Predicting experimentally measured stabilities of folded states of small proteins by directly generating equilibrium ensembles and explaining structure-stability relationships of mutants, achieving errors below 1 kcal/mol and correlation coefficients greater than 0.6 for both absolute folding free energies and folding free-energy changes of mutants.

CONCLUSION: BioEmu has various practical use cases, including complementing present MD simulation workflows, interpreting protein experiments in terms of structural mechanisms, identifying binding pockets and allosteric mechanisms in drug discovery, and generating ensembles for dynamical protein design. Our demonstration that the large upfront costs of MD simulation and experimental data generation can be amortized and that the prediction error decreases with an increasing amount of diverse training data indicates a path forward for predicting biomolecular function at the genomic scale. □

Corresponding author. Frank Noé (franknoe@microsoft.com) †These authors contributed equally to this work. **Cite this article as S. Lewis *et al.*, *Science* 389, eadv9817 (2025). DOI: 10.1126/science.adv9817**

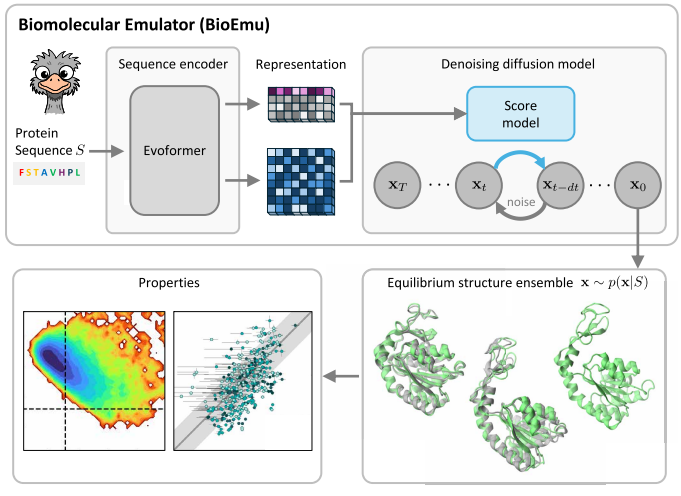

Illustration of the BioEmu model and workflow. BioEmu generates equilibrium protein structure ensembles by combining AlphaFold's sequence representation with a diffusion model trained on vast simulation and experimental data. These ensembles enable rapid computation of properties such as protein stability, achieving speeds that are orders of magnitude faster than MD simulation. [Emu illustration by F.N.]

PROTEIN SIMULATIONS

Scalable emulation of protein equilibrium ensembles with generative deep learning

Sarah Lewis[1]†, Tim Hempel[1]†, José Jiménez-Luna[1]†, Michael Gastegger[1]†, Yu Xie[1]†, Andrew Y. K. Foong[1]†, Victor García Satorras[1]†, Osama Abdin[1]†, Bastiaan S. Veeling[1]†, Iryna Zaporozhets[1,2], Yaoyi Chen[1,2], Soojung Yang[1], Adam E. Foster[1], Arne Schneuing[1], Jigyasa Nigam[1], Federico Barbero[1], Vincent Stimper[1], Andrew Campbell[1], Jason Yim[1], Marten Lienen[1], Yu Shi[1], Shuxin Zheng[1], Hannes Schulz[1], Usman Munir[1], Roberto Sordillo[1], Ryota Tomioka[1], Cecilia Clementi[1,2,3], Frank Noé[1,2,3]*

Following the sequence and structure revolutions, predicting functionally relevant protein structure changes at scale remains an outstanding challenge. We introduce BioEmu, a deep learning system that emulates protein equilibrium ensembles by generating thousands of statistically independent structures per hour on a single graphics processing unit (GPU). BioEmu integrates more than 200 milliseconds of molecular dynamics (MD) simulations, static structures, and experimental protein stabilities using new training algorithms. It captures diverse functional motions—including cryptic pocket formation, local unfolding, and domain rearrangements—and predicts relative free energies with 1 kilocalorie per mole accuracy compared with millisecond-scale MD and experimental data. BioEmu provides mechanistic insights by jointly modeling structural ensembles and thermodynamic properties. This approach amortizes the cost of MD and experimental data generation, demonstrating a scalable path toward understanding and designing protein function.

Proteins and protein complexes are the functional building blocks of life and play a central role in drug development and biotechnology. Although next-generation sequencing and deep learning–based structure prediction tools (*1*–*4*) have revolutionized access to sequence and structure, scalable methods for exploring protein function remain elusive. A key driver of protein function is the ability to transition between distinct conformational states (i.e., sets of different structures), often coupled to the binding of ligands or other proteins. For example, actin's ability to form muscle fibers arises from its conformational dynamics, which is regulated by adenosine triphosphate (ATP) and adenosine diphosphate (ADP) (Fig. 1A).

Technologies in use now that quantitatively probe such conformational transitions and their coupling with binding states are not scalable. Single-molecule experiments can provide the full equilibrium distributions of observables such as intramolecular distances (*5*) but require bespoke molecular constructs and time-consuming data collection. Cryo–electron microscopy (cryo-EM) can resolve multiple conformational states of biomolecular complexes and their probabilities (*6*), but these experiments are time-consuming and costly. Molecular dynamics (MD) simulation is, in principle, a universal tool that allows both the structure and dynamics of biomolecules to be explored at all-atom resolution. However, biomolecular force fields are far from perfect, and the sampling problem makes studying protein folding or association with MD a feat of epic computational costs—even with special-purpose supercomputers or enhanced sampling methods (*7*, *8*). Machine-learned (ML) coarse-grained MD models have an opportunity to achieve similar accuracy as all-atom MD at two to three orders of magnitude lower computational cost (*9*, *10*) but are still under development.

The grand challenge to complete our understanding of protein function thus motivates the development of a technology that can elucidate protein conformational states and binding states, as well as their associated probabilities. This technology should ideally achieve an accuracy comparable to that of a converged MD simulation, or a cryo-EM experiment with multiconformation analysis, but it should only require a few hours of wall-clock time and cost no more than a few dollars per experiment. Boltzmann generators (*11*) have demonstrated that physics-based generative ML models can sample equilibrium distributions of arbitrary molecular energy functions; however, scaling such approaches to large macromolecules while maintaining high sample efficiency is challenging. Concurrently, data-based generative ML models, such as diffusion models, are now widely used in protein-structure prediction and design (*2*, *4*). Such models (*12*–*14*), as well as perturbation-based derivatives of AlphaFold (*15*, *16*), have also been shown to be capable of generating distinct protein structures and can be combined with MD simulation to alleviate the sampling problem (*17*). As of yet, generative ML systems have mainly demonstrated an ability to qualitatively sample distinct protein conformational states. A demonstration that generative ML can quantitatively match equilibrium ensembles and predict experimental observables is critical going forward (*18*).

Model

We developed a biomolecular emulator called BioEmu—a generative deep-learning system designed to approximately sample from the equilibrium distribution of protein conformations. BioEmu uses a similar model architecture as Distributional Graphormer (DiG) (*12*) but employs a distinct training approach. Starting from the input protein sequence, single and pair representations of the sequence are computed using the AlphaFold2 evoformer (*1*). This sequence representation serves as input to a denoising diffusion model that generates protein structures (Fig. 1, B and C, and materials and methods). Sequence encoding is performed only once per protein, and an efficient integration scheme enables structure generation in as few as 30 to 50 denoising steps (fig. S11 and materials and methods). As a result, 10,000 independent protein structures from the learned equilibrium distribution can be sampled within minutes to a few hours on a single graphics processing unit (GPU), depending on their size.

A major challenge in training BioEmu is the absence of a single high-quality data source for protein equilibrium distributions, owing to the aforementioned challenges with experimental methods and MD (*19*). We therefore integrated training data from different, complementary sources. BioEmu was pretrained on a clustered version of the AlphaFold database (AFDB) using a data augmentation strategy that encourages it to sample diverse conformations (Fig. 1, D and E, and materials and methods). In a second stage, we continued training the model on more than 200 ms of all-atom MD data of thousands of small to medium-sized proteins (Fig. 1D, table S1, and materials and methods). To mitigate the sampling problem, MD data were reweighed toward equilibrium using either Markov state models (*20*) or weights from experimental data, when possible (materials and methods). Finally, we fine-tuned the model on 500,000 sequences of the MEGAscale dataset (*21*), a large-scale, homogeneous collection of in vitro protein stability measurements (Fig. 1D). As the MEGAscale dataset does not contain structures, we developed a new algorithm called property-prediction fine-tuning (PPFT) that can efficiently incorporate experimental measurements into diffusion model training (see section "Predicting protein stabilities" and materials and methods). To ensure

[1]AI for Science, Microsoft Research. [2]Freie Universität Berlin, Berlin, Germany. [3]Department of Chemistry, Rice University, Houston, TX, USA. ***Corresponding author. Email: franknoe@microsoft.com** †These authors contributed equally to this work.

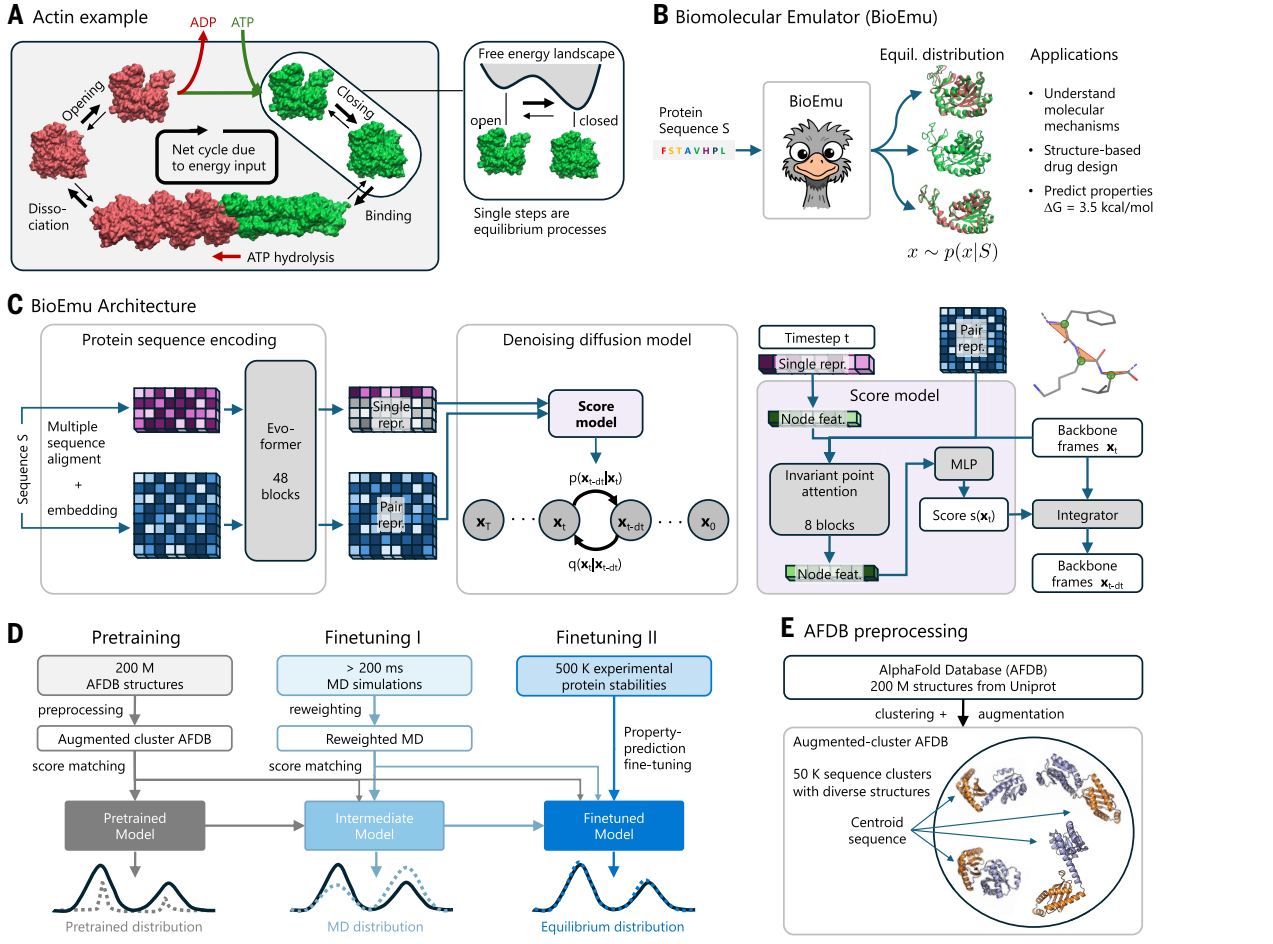

Fig. 1. Overview of model and architecture. (**A**) Actin as a representative example of protein function driven by conformational changes. Actin filament formation depends on an open-close transition of monomers, which is controlled by ADP and ATP binding. (**B**) Given a protein sequence, BioEmu samples protein structures from an approximate equilibrium distribution, from which properties such as free-energy differences can be computed. [Emu illustration by F.N.] (**C**) ML model architecture consisting of protein sequence encoder, denoising diffusion model, and score model. The protein structure is represented using coarse-grained backbone frames. (**D**) Data integration and model training pipeline. (**E**) Data processing pipeline for pretraining. MLP, multilayer perceptron; repr., representation; feat., features.

generalization, we filtered our training set such that no protein had more than 40% sequence similarity to a predefined holdout set, including all reported test proteins of at least 20 residues or longer. The term "BioEmu" refers to the fine-tuned model, trained on AFDB, MD simulations, and experimental protein-stability measurements. Subsequent results used this model unless otherwise indicated.

Sampling conformational changes related to protein function

We consider the ability to qualitatively sample distinct, biologically relevant conformations as a foundation for building a quantitative equilibrium sampler. Therefore, we first tested whether BioEmu could predict known conformational changes and compared this capability with AFCluster (*15*), AlphaFlow (*13*), DiG (*12*), and uniform multiple-sequence alignment (MSA) subsampling (*22*) as representative baseline methods (materials and methods). To benchmark BioEmu's ability to capture functionally relevant structural variability, we curated four benchmark sets comprising around 100 proteins with experimentally validated transitions (figs. S1 to S4). The first set, OOD60, assesses sequence generalization. The remaining three sets target specific types of conformational change: domain motions, local unfolding transitions, and cryptic pocket formations.

OOD60 is designed to test strong generalization: Its proteins were deposited in the Protein Data Bank (PDB) after the AlphaFold2 cutoff date and share no more than 60 and 40% sequence similarity with the AlphaFold2 monomer model and BioEmu training sets, respectively. OOD60 includes various challenging cases such as large-scale conformational changes induced by binding with other biomolecules (fig. S1). BioEmu significantly outperformed all baselines on this benchmark (fig. S7). For the other benchmarks, BioEmu matched or exceeded baseline performance, except in predicting apo states of cryptic pockets, where AFCluster performed best. The performance gap was especially pronounced for proteins outside the AlphaFold2 training set (fig. S7).

The domain motion benchmark consists of proteins that undergo large-scale motions as part of their functional cycle (Fig. 2A). In the open-close transition of adenylate kinase, the closed state brings the substrates together to catalyze the ATP + AMP ⇌ 2ADP reaction. Single-molecule experiments have confirmed that opening and closing occurs reversibly on timescales of tens of microseconds when the substrates are bound (*23*). BioEmu predicts a range of open and closed states, including close matches with crystallographic structures. A second example is the open-close transition of LAO-binding protein, which is required to bind and release lysine, arginine, and ornithine for transport across membranes as part of the ATP-binding cassette protein family. Another interesting example of domain motions is that of the receptor module that regulates the concentration of cyclic

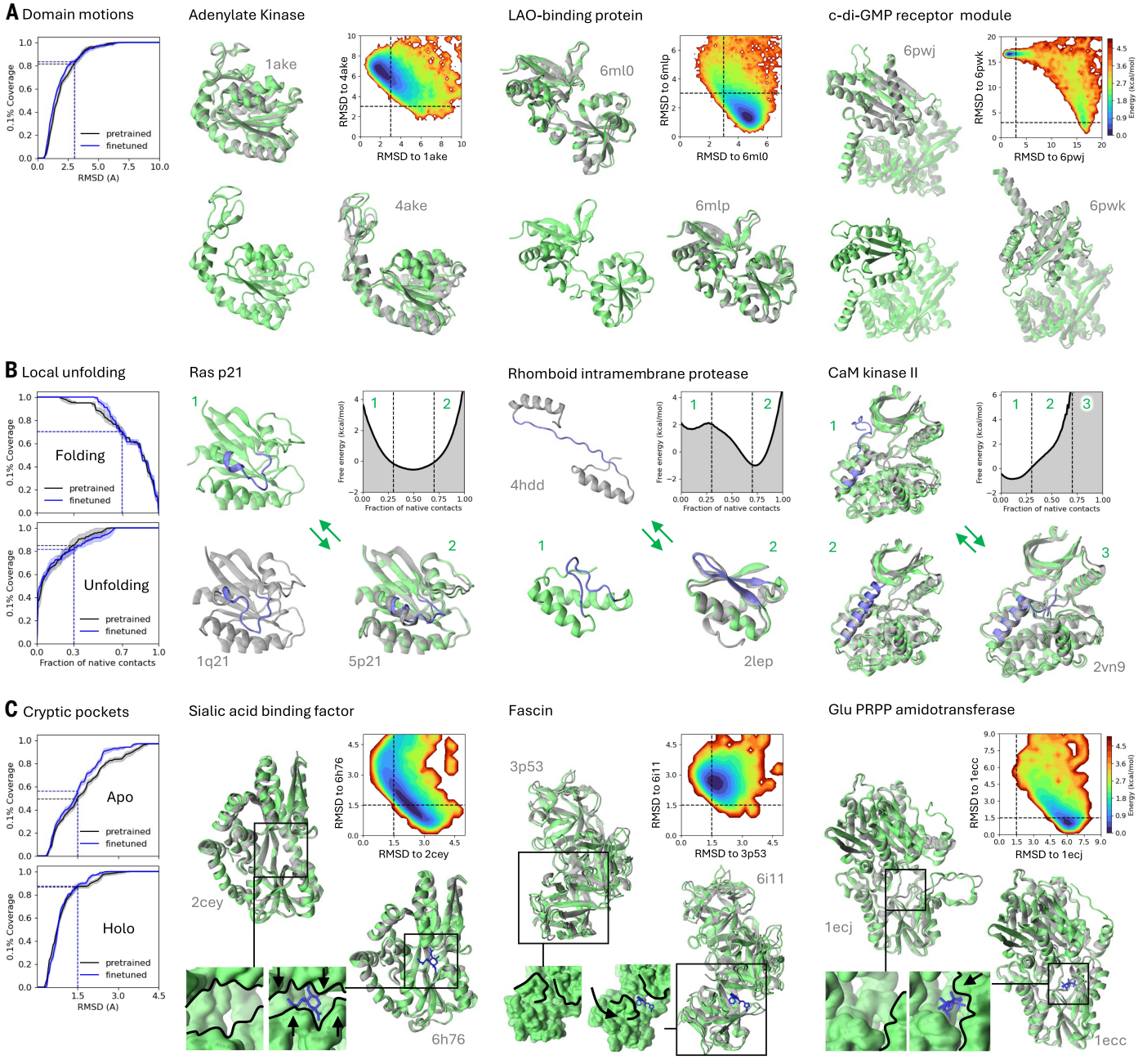

Fig. 2. BioEmu samples functionally distinct protein conformations. (**A**) Large-scale domain motions. (**B**) Local unfolding or unbinding of parts of the protein. (**C**) Formation of cryptic binding pockets that are not present in the apo ground state. The left column shows the coverage of pretrained and fine-tuned BioEmu models, defined as the percentage of reference structures that are sampled by at least 0.1% of samples within a given distance. Global and local RMSD are used for domain motions and cryptic pocket formation benchmarks, respectively, and the fraction of native contacts for local unfolding. Successful coverage of reference states is defined by probability density left of and below the dashed lines in the energy landscape plots of (A) and (C) and outside the dashed lines in (B). BioEmu sampled structures are shown in green, PDB structures in gray, and key secondary structure elements in blue. CaM, calcium-calmodulin dependent; LAO, lysine arginine ornithine. See table S4 for 12-letter PDB codes and original citations.

di–guanosine monophosphate (cyclic-di-GMP) in bacteria. In this case, one domain undergoes a large-scale rotation and repacks to the other domain with a completely different contact pattern. See fig. S2 for 19 further examples. Overall, BioEmu predicted 83% of the reference experimental structures with ≤3-Å root mean square deviation (RMSD) (Fig. 2A), indicating the model's ability to predict which protein regions are rigid and which are flexible, as well as which resulting motions can occur.

Next, we considered local unfolding transitions, in which part of a protein chain unfolds or detaches from its main structure as part of a signaling pathway (Fig. 2B). Predicting local unfolding challenges the model to correctly rank the relative stabilities of a protein's fold. A famous example of local unfolding is Ras p21, a protein whose mutants are often linked to cancer development; the local unfolding of Ras p21 is a conformational switch that signals cell growth (*24*). In its active state, stabilized by binding guanosine triphosphate (GTP), the switch II region forms a short α helix, which partially unfolds in the inactive guanosine diphosphate (GDP)–bound state. Rhomboid intramembrane protease is a more complex case that involves domain swapping. Its monomeric form features a globular conformation, whereas in its

dimeric form, the central β sheet unfolds and the helices of the two monomers bind to each other. Finally, CaM kinase II presents an autoinhibition mechanism, wherein the N terminus binds into the active site. BioEmu correctly predicted the local unfolding of these structure elements and sampled 70% of the folded and 81% of the locally unfolded states across 20 protein examples (Fig. 2B and fig. S3).

As a final class of conformational changes, we considered the formation of pockets that are absent in the apo PDB structure but can form to bind a small molecule (Fig. 2C). Such "cryptic" binding pockets can be discovered with high-performance MD simulation (*25*, *26*), but the millisecond timescales often involved in the spontaneous opening of such pockets make MD on commercial hardware rarely viable for in silico drug-discovery pipelines. We curated 34 cases of experimentally validated formation of cryptic binding pockets from the literature (fig. S4). The sialic acid binding factor presents a case where a large opening in the apo state can partially close and form a binding site for the ligand. Fascin is a four-domain protein where two domains can rotate with respect to each other to reveal a binding site. In Glu PRPP amidotransferase, part of the chain is unfolded in the apo state and can fold into a structure that completes the binding site for the ligand. To ensure capturing subtle changes, we defined success by a very strict 1.5-Å RMSD threshold to the apo and holo reference structures. Surprisingly, the model had a strong preference for holo states, successfully predicting the cryptic pocket in 86% of cases, whereas it only succeeded in predicting 56% of the apo structures, indicating further room for improvement (Fig. 2C). We hypothesize that the model may be picking up a bias implicit in the embeddings—proteins may have only one or a few apo structures deposited in the PDB, but it is common to find multiple structures of the same protein with different small molecules bound.

To conclude, we conducted several tests to confirm that BioEmu's multiconformation prediction is a hallmark of generalization rather than memorization of sequence-structure pairs. BioEmu's ability to predict multiple conformations depends only weakly on the sequence similarity between the query molecule and the training set, with the clearest trend seen for domain motions where the final performance is reached at 30% sequence similarity (fig. S5 and materials and methods). As our test proteins contain examples that overlap with the AlphaFold2 training set, we ablated whether multiconformation prediction performance stems from trivial extraction of the information already present in the AlphaFold2 evoformer embeddings. To this end, we trained an end-to-end version of the model that uses MSA information directly, instead of pretrained embeddings, on a training set that is at most 40% similar in sequence to any protein belonging to the multiconformation benchmarks. The resulting model showed similar performance in the previously mentioned multiconformation benchmarks to that of the fine-tuned BioEmu (fig. S6 and materials and methods).

Emulating MD equilibrium distributions

A major motivation for developing BioEmu was to overcome the well-known sampling problem in MD: Simulating the full range of protein conformations and estimating their equilibrium probabilities often requires extensive MD simulations, on the order of 100 μs to 10 ms (*7*, *8*, *27*). These timescales are necessary to capture rare but functionally important transitions, yet achieving them is computationally demanding, if not prohibitive, even with specialized supercomputers (*28*) or large-scale distributed simulations integrated using statistical models (*8*, *29*). Here, we assessed BioEmu's ability to emulate the equilibrium distribution that would be sampled with extensive MD simulations. To this end, we amassed all-atom simulations of proteins with a total aggregated simulation time of more than 200 ms (table S1), which were used for fine-tuning BioEmu (Fig. 1D).

Before analyzing the model trained on the full dataset, we first tested whether our machine-learning architecture and training protocol permit learning to emulate long-timescale MD equilibrium distributions. To this end, we used D. E. Shaw Research (DESRES) simulations of 12 fast-folding proteins generated on the Anton supercomputer (*7*). For each protein, we fine-tuned a separate model on the other 11 proteins and evaluated it on the held-out 12th, an approach known as leave-one-out cross-validation (see materials and methods). This setup ensures that each test case is evaluated independently of its training data and avoids bias from arbitrary train-test splits in this small dataset. As expected, the AFDB-pretrained model predicted the native state but performed poorly in sampling the full free-energy surface (fig. S9). Surprisingly, however, the "DESRES–fine-tuned models," each trained on only 11 fast folders, predicted free-energy surfaces on the held-out proteins that closely matched the MD ground truth (Fig. 3A and fig. S9). For all proteins, the model predicted both the native as well as the unfolded states with similar shapes on the free-energy landscape. In many cases, several or all folding intermediates visible on the two-dimensional (2D) free-energy surface were predicted (Fig. 3A and fig. S9): For beta-beta-alpha protein (BBA), both MD and the DESRES–fine-tuned models predicted the existence of an intermediate with the α helix formed and the β sheet broken. For protein G, both MD and the DESRES–fine-tuned model sampled intermediates with half of the β sheet still formed, whereas the other half and most of the helix were broken. For homeodomain, MD and the model agreed in the prediction of an intermediate with only one helix turn unwound, whereas the unfolded states still featured some degree of helical propensity. There was excellent agreement of the predicted secondary structure propensities with the MD data (Fig. 3A). Quantitatively, the mean absolute error between the MD and model 2D free-energy landscapes was only 0.74 kcal/mol, ranging from 0.30 kcal/mol for BBA to 1.63 kcal/mol for λ-repressor, which is on the order of differences expected from two different classical MD force fields (*30*, *31*).

We compared the computational costs of MD data generation and BioEmu in GPU-hours (on a NVIDIA Titan V; Fig. 3A, top right). For all BioEmu results shown here, we drew 10,000 samples, which incurred computational costs of less than 1 GPU-minute for Chignolin to around 1 GPU-hour for λ-repressor. For MD, we considered the cost for generating the DESRES simulations, whose lengths were chosen to include roughly 10 folding-unfolding transitions. The MD costs then ranged from 2000 GPU-hours for Chignolin to more than 100,000 GPU-hours for NTL9, resulting in a speedup of BioEmu over MD of four to five orders of magnitude. We also note that for most proteins shown here, performing sufficiently long MD simulations to directly observe folding and unfolding in single trajectories is still not possible on consumer-grade hardware but instead requires a much more complex methodological framework (*29*, *32*).

The main BioEmu model was fine-tuned on more than 200 ms of MD simulations with Amber force fields at or near a temperature of 300 K (table S1). We chose to combine data from slightly different simulation conditions because each of these MD models is inherently imperfect, and we regarded experimental data as being more reliable for weighing between conformations (Fig. 1D). Differences in the simulation conditions of our own generated data were intentional; for example, AMBER ff99sb-disp (*33*) was chosen to avoid spuriously misfolded states produced by other force fields in the context of protein folding (materials and methods). A large fraction of training data, 46 ms, is dedicated to 1100 CATH domains, common building blocks of protein structure (*34*) (materials and methods). We designated 17 CATH systems with a simulation time of more than 100 μs as a test set and report statistics comparing MD and model distributions (Fig. 3B, fig. S10, and materials and methods). Similar to DESRES simulations, BioEmu predicts the native state with local fluctuations and typically several other substates and structures sampled by MD. Most secondary structure propensities matched well (Fig. 3B). We observed a free-energy mean absolute error over the converged test set of 0.9 kcal/mol, which was again comparable to the differences expected between different MD force fields.

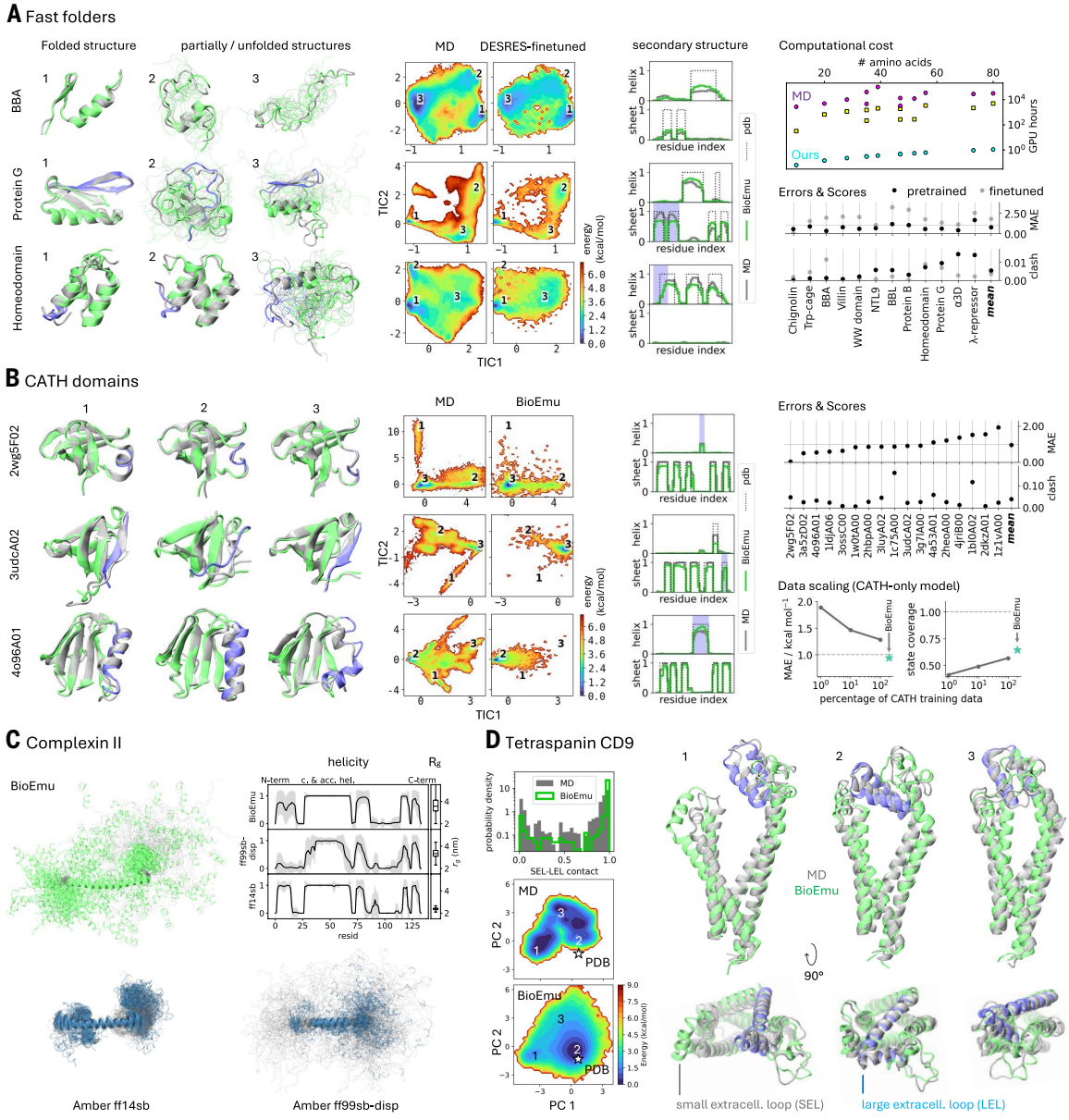

Fig. 3. BioEmu achieves fast emulation of all-atom MD equilibrium distributions. (**A**) DESRES fast-folding proteins. From left to right are representative structures (green, model; gray, MD; blue, regions of interest), free-energy surfaces over slowest time-lagged independent components (TIC) (*54*), secondary structure propensities, computational cost for MD (magenta, full DESRES data; yellow, single folding-unfolding roundtrip) versus model (cyan, 10,000 samples), and mean absolute error (MAE) of free-energy differences and fraction of unphysical model samples. (**B**) CATH domains. Structures, free-energy surfaces, and errors are as in (A). Shown at the bottom right is data scaling for the specialized CATH-only model with free-energy MAE and state coverage as a function of training data. The cyan star indicates BioEmu. (**C**) Complexin II: Structures, helix content, and radius of gyration (R_g) as predicted by BioEmu versus two all-atom force fields. (**D**) Tetraspanin CD9 results from BioEmu and MD (*37*). Shown is the open-closed transition, represented as a histogram in logarithmic scale of small and large extracellular loop (SEL-LEL) contacts, as defined in (*37*). Two-dimensional principal components (PC) analysis of $\exp(-d_{ij})$ of Ca-Ca distances d_{ij} between SEL and LEL. The open star marks the experimental structure (6k4j).

To understand whether our model's ability to sample accurate equilibrium distributions is limited by training data or model expressivity, we trained three models with the same architecture as BioEmu from scratch, using only 1, 10, and 100% of the CATH systems in the training dataset. We observed decreased free-energy errors and an increased coverage of the conformations sampled by MD as the amount of training proteins increased (Fig. 3B, bottom right), suggesting that the model can be further improved by adding more training data. Notably, the fine-tuned model's error on the same test set was further reduced to 0.9 kcal/mol, demonstrating the potential benefit of pretraining and integrating multiple datasets even if they do not use identical simulation conditions.

Finally, we evaluated BioEmu for two case studies that involve larger proteins: complexin II (134 amino acids) and tetraspanin CD9 (225 amino acids). Complexin II is an intrinsically disordered protein (IDP) from the neurotransmitter release apparatus (*35*). IDPs tend to be difficult to sample with MD; however, BioEmu can efficiently emulate a flexible ensemble of complexin II structures (Fig. 3C) while reproducing known secondary structure elements such as the central and accessory helices (*35*, *36*). Achieving convergence of IDPs of this size with all-atom MD is unpractical. At an order of magnitude higher computational cost than with BioEmu, we conducted ~5 μs of MD simulations with all-atom MD, which are most likely not converged but already

display qualitatively different behavior: The AMBER ff14sb force field produced a very rigid compact structure with a small radius of gyration and little to no variation in secondary structure content, whereas AMBER ff99sb-disp tended to destabilize known secondary structure elements (Fig. 3C).

Tetraspanin CD9, the second case study, plays a role in cell adhesion and fusion (Fig. 3D). The large extracellular loop of CD9 is part of our OOD60 test set (fig. S1) in which our pretrained model samples both crystallographic reference structures (PDB entries 6rlo and 6rlr), whereas the BioEmu model fine-tuned on MD data samples 6rlo but discards 6rlr. This is consistent with the observation that both structures exist in crystal environments; however, 6rlr cannot be realized in a folded monomeric protein and is therefore correctly discarded when fine-tuning BioEmu (fig. S12, A to C). We also sampled the full-length CD9 structure, which has less than 40% sequence similarity to both the BioEmu and AlphaFold training sets (Fig. 3D). In agreement with MD simulations of previous work (*37*), BioEmu predicted the widely open state 1 and closed state 2 and similar contact distributions between the small and large extracellular loops as reported in (*37*). A principal components analysis revealed that BioEmu and MD sample similar sets of conformations (Fig. 3D). MD predicts an experimentally unknown metastable closed state 3, which is unstable in BioEmu. BioEmu samples closed structures (state 2) that are very similar to the experimental structure 6k4j (1.9-Å RMSD), whereas the closest MD sample has an RMSD of 4.6 Å to the crystal structure (fig. S12D).

Predicting protein stabilities

Understanding protein stability is crucial for various applications in molecular biology, drug design, and biotechnology. From a modeling point of view, predicting a protein's stability is a specific case of predicting the equilibrium probabilities of its different conformational states, and these all arise from the same underlying biophysics. We therefore wanted to train BioEmu so that the proportion of samples in folded and unfolded states matches the experimentally measured protein stability. We classify protein structures as folded or unfolded based on their fraction of native contacts and define the folding free-energy as $\Delta G = G_{\text{folded}} - G_{\text{unfolded}}$ (materials and methods). To facilitate protein stability prediction, BioEmu was trained on 502,442 mutant sequences generated from 361 wild types, a subset of the more than 674,000 experimental measurements in the MEGAscale dataset (materials and methods) (*21*). We evaluated BioEmu on a test set of randomly chosen mutants from 95 wild types. For a subset of 271 wild-type proteins and 21,458 mutants, we additionally conducted a total of 25 ms of all-atom MD simulations of the folded and unfolded states (materials and methods). To address MD sampling and force-field issues, we weighed the folded and unfolded samples based on the experimentally measured protein stabilities (materials and methods). To accelerate training convergence and leverage the large number of MEGAscale measurements, we developed the PPFT algorithm (Fig. 4A and materials and methods), which integrates experimental expectation values, such as protein stabilities, into diffusion model training without requiring protein structures. PPFT uses fast approximate sampling with only eight denoising steps, which we observed to be sufficient to confidently predict whether each sampled structure will be classified as folded or unfolded. By comparing the mean foldedness of sampled structures with experimental measurements and backpropagating the error, our model could be efficiently trained to match experimental protein stabilities.

BioEmu achieved a mean absolute error of less than 0.9 kcal/mol and a Spearman correlation coefficient of approximately 0.6 for the MEGAscale test proteins (Fig. 4B). The BioEmu ensembles also correlated well with stability changes of point mutants, as measured by the change of folding free energy $\Delta\Delta G$, achieving mean absolute errors of less than 0.8 kcal/mol and a Spearman correlation coefficient above 0.6 (Fig. 4C). Errors of approximately 1 kcal/mol were achieved for test proteins that had 40% sequence similarity with the training set, but the best performance was obtained for test sets that included sequences with 50% or greater similarity (Fig. 4, B and C). As there are only 361 distinct wild-type sequences in the MEGAscale training data, it is likely that generalization performance can be further improved with a training dataset that is more diverse in protein sequence space.

To check whether BioEmu makes physically reasonable predictions outside the MEGAscale set of proteins, we tested it on proteins that are known to be very stable or unstable. We first selected stable proteins from ProThermDB (*38*) with a $\Delta G < -8$ kcal/mol (materials and methods). Our model consistently sampled these proteins in their folded states with a fraction of native contacts that always exceeded 0.65 (Fig. 4D). To test whether our model systematically predicts IDPs as unfolded, we used the CALVADOS test set (*39*). Most proteins sampled displayed a radius of gyration (R_g) similar to that of random coil structures and mostly larger than that of typical folded proteins (Fig. 4E). Unlike other models (*40*, *41*), ours has not been directly trained on IDPs; nonetheless, it provides zero-shot predictions of R_g that correlate well with experimental measurements (Fig. 4E).

In comparison to black-box methods that predict protein stability directly from sequences (*42*–*45*), BioEmu has competitive or superior prediction accuracy. However, in contrast to a black-box prediction of ΔG, we can analyze the structure ensemble generated by our model to reveal insights on mutation-caused stability changes. To illustrate this point, in Fig. 4F, we show mutants of the design protein HHH_rd1_0335 and PDB entry 2JWS. In HHH_rd1_0335, the mutation I7P ($Ile^7 \rightarrow Pro$) leads to a destabilization of the first helix, as indicated by the model's prediction of a $\Delta\Delta G$ of 1.8 kcal/mol compared with the experimental 2.1 kcal/mol. The analysis shows a decrease in average helicity that particularly affects the helix where the mutation is located. For 2jws, the mutation I24D ($Ile^{24} \rightarrow Asp$) in the middle helix results in partial unfolding, with the model predicting a $\Delta\Delta G$ of 2.1 kcal/mol, which closely matches the experimental value of 2.9 kcal/mol. This mutation replaces a hydrophobic residue with a negatively charged aspartate, disrupting core stability and leading to a localized structural change. These analyses highlight BioEmu's ability to correlate predictions of thermodynamics with structural causes, which is not possible with black-box prediction models.

Discussion

In this work, we introduce BioEmu, a generative machine-learning system that can approximately sample the equilibrium distributions of proteins and through that explore two key aspects of molecular function: protein conformations and their equilibrium probabilities. We have shown that the system can sample experimentally known structures of proteins undergoing a variety of conformational changes, approximate the equilibrium distributions of extensive MD simulations, and predict experimentally measured protein stabilities within errors of 1 kcal/mol. The cost of running inference is on the order of 1 GPU-hour per computational experiment, which is many orders of magnitude less than running MD simulations, even if enhanced sampling methods are invoked, and orders of magnitude cheaper than experiments that can provide detailed structure-function relationships. Nonetheless, there are further opportunities to reduce BioEmu's inference cost. Conditional flow-matching (*46*) can be used to generate protein structures using even fewer integration steps (*47*). The computational cost of evaluating the transformer network in the score model (Fig. 1C) can potentially be reduced by leveraging sparse or low-rank attention mechanisms.

BioEmu and MD simulation are complementary: Our system was trained on large amounts of MD simulation data for soluble proteins, and within this scope, it has shown that it can approximate MD distributions at a tiny fraction of the MD simulation costs. However, BioEmu is not designed to generalize beyond this scope; for example, membrane environments and small-molecule ligands are not represented in either the model or the training data, and reliable predictions cannot be

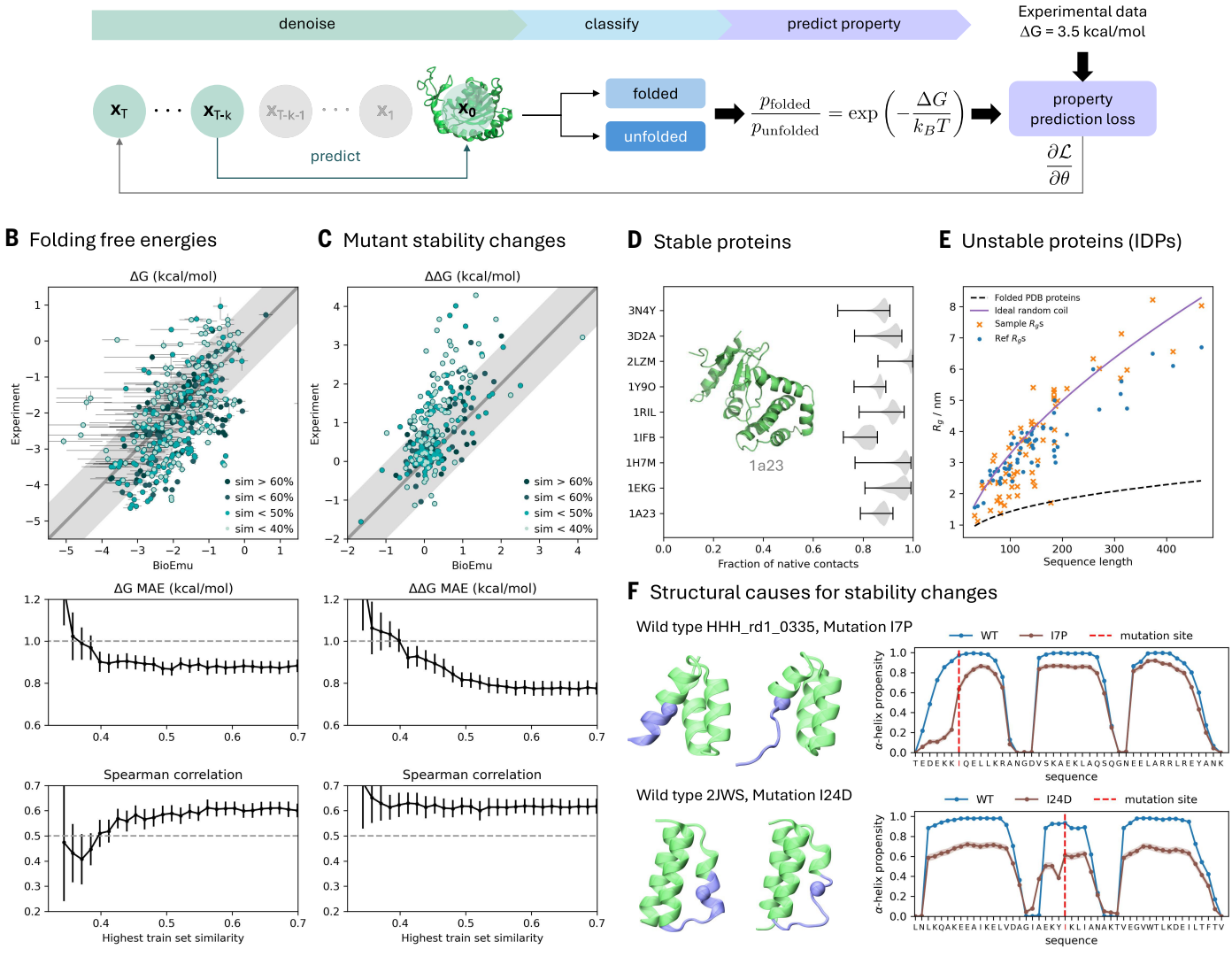

Fig. 4. Prediction of experimentally measured protein stabilities. (**A**) PPFT algorithm for fine-tuning a pretrained diffusion model to match experimentally measurable properties such as the protein's stability. (**B**) Comparison of experimental measurements of folding free energies (*21*) with model predictions, generated by direct sampling and counting of folded and unfolded states for test proteins, the mean absolute error (MAE), and the Spearman correlation coefficient as a function of the sequence similarity between test and training proteins. The gray shaded region represents an error range of ±1 kcal/mol. (**C**) Same as (B) for the change in folding stability upon point mutation. (**D**) Validation that very stable proteins that are not included in the MEGAscale experimental dataset are consistently predicted as folded. Bars and shading indicate the minimum, maximum, and distribution of sampled values, respectively. (**E**) Validation that IDPs reported in (*39*) and (*41*) are predicted as unfolded. Comparison of the radius of gyration (R_g) for model (orange crosses), experimental measurement (blue dots), and Flory scaling (*55*). (**F**) Analysis of the effect of two destabilizing mutants on the folded structures as predicted by the model: HHH_rd1_0335 with mutation I7P and 2JWS with mutation I24D. See table S4 for 12-letter PDB codes and original citations. WT, wild type.

assumed when such factors play a key role in the process. By contrast, MD can be readily generalized to such conditions, though it remains constrained by the sampling problem. Our system can be used to generate an approximation to the equilibrium distribution, and MD trajectories can be launched from a BioEmu ensemble to obtain chemically accurate all-atom structures, refine the distribution, and even compute dynamical properties. We therefore do not expect emulators such as BioEmu to make MD simulation obsolete; rather, we anticipate that MD will increasingly serve as a data generation and validation tool. A similar shift of roles is already in progress for other simulator-emulator pairs such as quantum chemistry methods and machine-learned force fields.

An important limitation of BioEmu is that it generates distributions entirely empirically, whereas MD simulation uses potential energy functions, which are connected to equilibrium distributions and expectation values by statistical mechanics. If direct access to a reduced potential energy function $u(x)$ was available that is consistent with the generated distribution by $p(x) \propto e^{-u(x)}$, it could be used for reweighting and making rigorous enhanced sampling simulations available through the emulator. BioEmu can potentially also be improved by going beyond score matching and using energy or forces information from MD force fields at training time, as considered in Boltzmann generators (*11*) and variational force matching (*9*, *48*).

Although BioEmu samples approximate equilibrium distribution, it does not model protein dynamics, which is done by MD and other methods (*49*), nor does its training incorporate dynamical information as it does for Markov state models (*20*). A pragmatic approach to generate a dynamic ensemble is to predict starting points with BioEmu and launch MD simulations from them. A starting point for a more

principled methodology that can both model dynamics and exploit dynamical information in the training data is the implicit transfer operator approach (*50*).

We have demonstrated that by using the PPFT method developed here, BioEmu can be efficiently fine-tuned on experimental data. In this work, we have chosen to do that for protein stabilities using the MEGAscale dataset because it presents a very favorable trade-off of large data scale and quantitative reliability. However, in principle, PPFT can be used to fine-tune BioEmu and other diffusion models to match any set of experimental observables, including nuclear magnetic resonance data, small-angle x-ray scattering, fluorescence measurements, and so on. Being able to fine-tune the generated ensemble to arbitrary experimental data is an important advantage compared with MD force fields: These can also be tuned to fit experimental data (*51*), but the processes that give rise to the experimental observables must be sampled during the training process, a task that is tedious or even unfeasible for observables that involve complex rare events, such as folding free energies.

A widely used feature of AlphaFold is its ability to predict confidence in an output structure, and a similar confidence module for BioEmu would be highly desirable. Training a confidence module is relatively straightforward in AlphaFold, which serves a single prediction task (structure) and relies on a single ground truth dataset (the PDB), whereas equilibrium structure ensembles serve multiple downstream tasks and observables and no universal ground truth dataset is available. Confidence prediction or uncertainty quantification of arbitrary observables thus remains an important future research direction and may leverage ongoing research in the deep-learning community (*52*). Even a rough notion of model confidence in observables, such as free-energy differences, could be exploited to improve training data efficiency: In the MD community, Markov state models and other kinetic models have been used to guide MD data production in an active learning loop (*8*, *53*), and a similar approach could be implemented to have BioEmu request new MD or experimental data that are most likely to increase model confidence.

Another limitation of the present system is that it emulates single protein chains under a fixed thermodynamic condition of 300 K. A proper emulator for proteins requires conditioning on experimentally and biologically relevant parameters such as temperature and pH and needs to be able to model multiple interacting molecules, as proteins rarely have a function on their own. We envision two ways of achieving this: (i) training on additional MD simulation data at relevant thermodynamic ranges and (ii) incorporating relevant additional experimental data (e.g., melting curves for temperature) into fine-tuning strategies.

An important future direction is to extend BioEmu's modalities by incorporating multiple protein chains and ligands, which are already included in recent biomolecular structure prediction systems (*2*, *4*). Presently, oligomer and ligand binding state are implicit, which may cause biases in the training data to show up in the sampled distribution. A hallmark of this may be BioEmu's preference to predict holo over apo structures in the cryptic pocket benchmark (Fig. 2C). Such biases in the sampling distribution can be avoided by explicitly conditioning the prediction of the structure ensemble to ligands, which is, however, hampered by the lack of training data. Although we have shown that the ability to accurately emulate the equilibrium distributions of small proteins increases with more training data, the sampling problem limits MD as a data-generation engine. The development of highly scalable experimental techniques is key for training machine-learning models that can predict conformational and binding states of large biomolecular complexes, as well as the subtle differences of binding affinities that underlie biomolecular function.

Our results demonstrate that the large upfront costs of MD simulation and experimental data generation can be amortized by a deep-learning emulator whose prediction error decreases with an increasing amount of high-quality training data. This indicates a path forward for predicting biomolecular function at the genomic scale.

Materials and methods are available in the supplementary materials.

REFERENCES AND NOTES

1. J. Jumper *et al.*, Highly accurate protein structure prediction with AlphaFold. *Nature* **596**, 583–589 (2021). doi: 10.1038/s41586-021-03819-2; pmid: 34265844
2. J. Abramson *et al.*, Accurate structure prediction of biomolecular interactions with AlphaFold 3. *Nature* **630**, 493–500 (2024). doi: 10.1038/s41586-024-07487-w; pmid: 38718835
3. M. Baek *et al.*, Accurate prediction of protein structures and interactions using a three-track neural network. *Science* **373**, 871–876 (2021). doi: 10.1126/science.abj8754; pmid: 34282049
4. R. Krishna *et al.*, Generalized biomolecular modeling and design with RoseTTAFold All-Atom. *Science* **384**, eadl2528 (2024). doi: 10.1126/science.adl2528; pmid: 38452047
5. F. Ritort, Single-molecule experiments in biological physics: Methods and applications. *J. Phys. Condens. Matter* **18**, R531–R583 (2006). doi: 10.1088/0953-8984/18/32/R01; pmid: 21690856
6. X.-C. Bai, G. McMullan, S. H. Scheres, How cryo-EM is revolutionizing structural biology. *Trends Biochem. Sci.* **40**, 49–57 (2015). doi: 10.1016/j.tibs.2014.10.005; pmid: 25544475
7. K. Lindorff-Larsen, S. Piana, R. O. Dror, D. E. Shaw, How fast-folding proteins fold. *Science* **334**, 517–520 (2011). doi: 10.1126/science.1208351; pmid: 22034434
8. N. Plattner, S. Doerr, G. De Fabritiis, F. Noé, Complete protein-protein association kinetics in atomic detail revealed by molecular dynamics simulations and Markov modelling. *Nat. Chem.* **9**, 1005–1011 (2017). doi: 10.1038/nchem.2785; pmid: 28937668
9. J. Wang *et al.*, Machine learning of coarse-grained molecular dynamics force fields. *ACS Cent. Sci.* **5**, 755–767 (2019). doi: 10.1021/acscentsci.8b00913; pmid: 31139712
10. N. E. Charron *et al.*, Navigating protein landscapes with a machine-learned transferable coarse-grained model. *Nat. Chem.* **17**, 1284–1292 (2025). doi: 10.1038/s41557-025-01874-0; pmid: 40681718
11. F. Noé, S. Olsson, J. Köhler, H. Wu, Boltzmann generators: Sampling equilibrium states of many-body systems with deep learning. *Science* **365**, eaaw1147 (2019). doi: 10.1126/science.aaw1147; pmid: 31488660
12. S. Zheng *et al.*, Predicting equilibrium distributions for molecular systems with deep learning. *Nat. Mach. Intell.* **6**, 558–567 (2024). doi: 10.1038/s42256-024-00837-3
13. J. Jing, B. Berger, T. Jaakkola, "AlphaFold meets flow matching for generating protein ensembles" in *Proceedings of the 41st International Conference on Machine Learning* (JMLR, 2024), pp. 22277–22303.
14. Z. Qiao, W. Nie, A. Vahdat, T. F. Miller III, A. Anandkumar, State-specific protein–ligand complex structure prediction with a multiscale deep generative model. *Nat. Mach. Intell.* **6**, 195–208 (2024). doi: 10.1038/s42256-024-00792-z
15. H. K. Wayment-Steele *et al.*, Predicting multiple conformations via sequence clustering and AlphaFold2. *Nature* **625**, 832–839 (2024). doi: 10.1038/s41586-023-06832-9; pmid: 37956700
16. P. Bryant, F. Noé, Structure prediction of alternative protein conformations. *Nat. Commun.* **15**, 7328 (2024). doi: 10.1038/s41467-024-51507-2; pmid: 39187507
17. B. P. Vani, A. Aranganathan, D. Wang, P. Tiwary, AlphaFold2-RAVE: From sequence to Boltzmann ranking. *J. Chem. Theory Comput.* **19**, 4351–4354 (2023). doi: 10.1021/acs.jctc.3c00290; pmid: 37171364
18. A. Aranganathan, X. Gu, D. Wang, B. Vani, P. Tiwary, Modeling Boltzmann-eighted structural ensembles of proteins using artificial intelligence–based methods. *Curr. Opin. Struct. Biol.* **91**, 103000 (2025). doi: 10.1016/j.sbi.2025.103000; pmid: 39923288
19. R. E. Amaro *et al.*, The need to implement FAIR principles in biomolecular simulations. *Nat. Methods* **22**, 641–645 (2025). doi: 10.1038/s41592-025-02635-0; pmid: 40175561
20. J.-H. Prinz *et al.*, Markov models of molecular kinetics: Generation and validation. *J. Chem. Phys.* **134**, 174105 (2011). doi: 10.1063/1.3565032; pmid: 21548671
21. K. Tsuboyama *et al.*, Mega-scale experimental analysis of protein folding stability in biology and design. *Nature* **620**, 434–444 (2023). doi: 10.1038/s41586-023-06328-6; pmid: 37468638
22. D. del Alamo, D. Sala, H. S. Mchaourab, J. Meiler, Sampling alternative conformational states of transporters and receptors with AlphaFold2. *eLife* **11**, e75751 (2022). doi: 10.7554/eLife.75751; pmid: 35238773
23. H. Y. Aviram *et al.*, Direct observation of ultrafast large-scale dynamics of an enzyme under turnover conditions. *Proc. Natl. Acad. Sci. U.S.A.* **115**, 3243–3248 (2018). doi: 10.1073/pnas.1720448115; pmid: 29531052
24. F. B. Fromowitz *et al.*, ras p21 expression in the progression of breast cancer. *Hum. Pathol.* **18**, 1268–1275 (1987). doi: 10.1016/S0046-8177(87)80412-4; pmid: 3315956
25. J. B. Greisman *et al.*, Discovery and validation of the binding poses of allosteric fragment hits to protein tyrosine phosphatase 1b: From molecular dynamics simulations to x-ray crystallography. *J. Chem. Inf. Model.* **63**, 2644–2650 (2023). doi: 10.1021/acs.jcim.3c00236; pmid: 37086179
26. M. I. Zimmerman *et al.*, SARS-CoV-2 simulations go exascale to predict dramatic spike opening and cryptic pockets across the proteome. *Nat. Chem.* **13**, 651–659 (2021). doi: 10.1038/s41557-021-00707-0; pmid: 34031561

27. T. J. Lane, D. Shukla, K. A. Beauchamp, V. S. Pande, To milliseconds and beyond: Challenges in the simulation of protein folding. *Curr. Opin. Struct. Biol.* **23**, 58–65 (2013). doi: 10.1016/j.sbi.2012.11.002; pmid: 23237705
28. D. E. Shaw *et al.*, Atomic-level characterization of the structural dynamics of proteins. *Science* **330**, 341–346 (2010). doi: 10.1126/science.1187409; pmid: 20947758
29. J. D. Chodera, F. Noé, Markov state models of biomolecular conformational dynamics. *Curr. Opin. Struct. Biol.* **25**, 135–144 (2014). doi: 10.1016/j.sbi.2014.04.002; pmid: 24836551
30. R. B. Best, J. Mittal, Free-energy landscape of the GB1 hairpin in all-atom explicit solvent simulations with different force fields: Similarities and differences. *Proteins* **79**, 1318–1328 (2011). doi: 10.1002/prot.22972; pmid: 21322056
31. D. F. Hahn, V. Gapsys, B. L. de Groot, D. L. Mobley, G. Tresadern, Current state of open source force fields in protein-ligand binding affinity predictions. *J. Chem. Inf. Model.* **64**, 5063–5076 (2024). doi: 10.1021/acs.jcim.4c00417; pmid: 38895959
32. A. Laio, M. Parrinello, Escaping free-energy minima. *Proc. Natl. Acad. Sci. U.S.A.* **99**, 12562–12566 (2002). doi: 10.1073/pnas.202427399; pmid: 12271136
33. P. Robustelli, S. Piana, D. E. Shaw, Developing a molecular dynamics force field for both folded and disordered protein states. *Proc. Natl. Acad. Sci. U.S.A.* **115**, E4758–E4766 (2018). doi: 10.1073/pnas.1800690115; pmid: 29735687
34. I. Sillitoe *et al.*, CATH: Increased structural coverage of functional space. *Nucleic Acids Res.* **49**, D266–D273 (2021). doi: 10.1093/nar/gkaa1079; pmid: 33237325
35. J. Malsam *et al.*, Complexin suppresses spontaneous exocytosis by capturing the membrane-proximal regions of VAMP2 and SNAP25. *Cell Rep.* **32**, 107926 (2020). doi: 10.1016/j.celrep.2020.107926; pmid: 32698012
36. Q. Zhou *et al.*, The primed SNARE-complexin-synaptotagmin complex for neuronal exocytosis. *Nature* **548**, 420–425 (2017). doi: 10.1038/nature23484; pmid: 28813412
37. R. Umeda *et al.*, Structural insights into tetraspanin CD9 function. *Nat. Commun.* **11**, 1606 (2020). doi: 10.1038/s41467-020-15459-7; pmid: 32231207
38. R. Nikam, A. Kulandaisamy, K. Harini, D. Sharma, M. M. Gromiha, ProThermDB: Thermodynamic database for proteins and mutants revisited after 15 years. *Nucleic Acids Res.* **49**, D420–D424 (2021). doi: 10.1093/nar/gkaa1035; pmid: 33196841
39. G. Tesei *et al.*, Conformational ensembles of the human intrinsically disordered proteome. *Nature* **626**, 897–904 (2024). doi: 10.1038/s41586-023-07004-5; pmid: 38297118
40. G. Tesei, K. Lindorff-Larsen, Improved predictions of phase behaviour of intrinsically disordered proteins by tuning the interaction range. *Open Res. Eur.* **2**, 94 (2023). doi: 10.12688/openreseurope.14967.2; pmid: 37645312
41. J. Zhu *et al.*, Precise generation of conformational ensembles for intrinsically disordered proteins via fine-tuned diffusion models. bioRxiv 2024.05.05.592611 [Preprint] (2024); https://doi.org/10.1101/2024.05.05.592611.
42. J. Ouyang-Zhang, D. Diaz, A. Klivans, P. Krähenbühl, Predicting a protein's stability under a million mutations. *Adv. Neural Inf. Process. Syst.* **36**, 76229–76247 (2023).
43. M. Cagiada, S. Ovchinnikov, K. Lindorff-Larsen, Predicting absolute protein folding stability using generative models. *Protein Sci.* **34**, e5233 (2025). doi: 10.1002/pro.5233; pmid: 39673466
44. P. Notin *et al.*, ProteinGym: Large-scale benchmarks for protein fitness prediction and design. *Adv. Neural Inf. Process. Syst.* **36**, 64331–64379 (2023).
45. T. Widatalla, R. Rafailov, B. Hie, Aligning protein generative models with experimental fitness via Direct Preference Optimization. bioRxiv 2024.05.20.595026 [Preprint] (2024); https://doi.org/10.1101/2024.05.20.595026.
46. Y. Lipman, R. T. Q. Chen, H. Ben-Hamu, M. Nickel, M. Le, Flow matching for generative modeling. arXiv:2210.02747 [cs.LG] (2022).
47. J. Yim *et al.*, Fast protein backbone generation with SE(3) flow matching. arXiv:2310.05297 [q-bio.QM] (2023).
48. W. G. Noid *et al.*, The multiscale coarse-graining method. I. A rigorous bridge between atomistic and coarse-grained models. *J. Chem. Phys.* **128**, 244114 (2008). doi: 10.1063/1.2938860; pmid: 18601324
49. L. Klein *et al.*, Timewarp: Transferable acceleration of molecular dynamics by learning time-coarsened dynamics. *Adv. Neural Inf. Process. Syst.* **36**, 52863–52883 (2023).
50. M. Schreiner, O. Winther, S. Olsson, Implicit transfer operator learning: Multiple time-resolution models for molecular dynamics. *Adv. Neural Inf. Process. Syst.* **36**, 36449–36462 (2023).
51. T. Fröhlking, M. Bernetti, N. Calonaci, G. Bussi, Toward empirical force fields that match experimental observables. *J. Chem. Phys.* **152**, 230902 (2020). doi: 10.1063/5.0011346; pmid: 32571067
52. J. Gawlikowski *et al.*, A survey of uncertainty in deep neural networks. *Artif. Intell. Rev.* **56**, 1513–1589 (2023). doi: 10.1007/s10462-023-10562-9
53. H. Sidky, W. Chen, A. L. Ferguson, Machine learning for collective variable discovery and enhanced sampling in biomolecular simulation. *Mol. Phys.* **118**, e1737742 (2020). doi: 10.1080/00268976.2020.1737742
54. G. Pérez-Hernández, F. Paul, T. Giorgino, G. De Fabritiis, F. Noé, Identification of slow molecular order parameters for Markov model construction. *J. Chem. Phys.* **139**, 015102 (2013). doi: 10.1063/1.4811489; pmid: 23822324
55. H. Hofmann *et al.*, Polymer scaling laws of unfolded and intrinsically disordered proteins quantified with single-molecule spectroscopy. *Proc. Natl. Acad. Sci. U.S.A.* **109**, 16155–16160 (2012). doi: 10.1073/pnas.1207719109; pmid: 22984159
56. S. Lewis *et al.*, Molecular dynamics dataset for "scalable emulation of protein equilibrium ensembles with generative deep learning": Octapeptides. Zenodo (2025); https://doi.org/10.5281/zenodo.15641199.
57. S. Lewis *et al.*, Molecular dynamics dataset for "scalable emulation of protein equilibrium ensembles with generative deep learning": CATH domains. Zenodo (2025); https://doi.org/10.5281/zenodo.15629740.
58. S. Lewis *et al.*, Molecular dynamics dataset for "scalable emulation of protein equilibrium ensembles with generative deep learning": MegaSim. Zenodo (2025); https://doi.org/10.5281/zenodo.15641184.
59. G. M. Visani, W. Galvin, M. Pun, A. Nourmohammad, "H-Packer: Holographic rotationally equivariant convolutional neural network for protein side-chain packing" in *Proceedings of the 18th Machine Learning in Computational Biology Meeting*, vol. 240 of *Proc. Mach. Learn. Res.*, D. A. Knowles, S. Mostafavi, Eds. (PMLR, 2024), pp. 230–249.
60. P. Eastman *et al.*, OpenMM 7: Rapid development of high performance algorithms for molecular dynamics. *PLOS Comput. Biol.* **13**, e1005659 (2017). doi: 10.1371/journal.pcbi.1005659; pmid: 28746339
61. BioEmu benchmarks, Github (2025); https://github.com/microsoft/bioemu-benchmarks.
62. S. Lewis *et al.*, Supplementary data for "scalable emulation of protein equilibrium ensembles with generative deep learning". Zenodo (2025); https://doi.org/10.5281/zenodo.15672282.

ACKNOWLEDGMENTS

We thank the entire Microsoft Research AI for Science team and thank, in particular, the following individuals for valuable support and discussions: C. Liu, P. Jin, T.-Y. Liu, C. M. Bishop, B. Kruft, J. Köhler, T. Vogels, M. Segler, R. van den Berg, M. Federici, S. Markou, M. Riechert, and L. Sun. We thank M. Steinegger (Seoul National University) for his invaluable help in publishing the BioEmu inference code on ColabFold and T. Nishizawa (University of Tokyo) for sharing the CD9 simulation data. Furthermore, we thank colleagues from FU Berlin for valuable discussions and advice, particularly N. E. Charron, K. Elez, and A. S. Pasos Trejo. Additionally, we thank G. R. Bowman and A. M. Trent (University of Pennsylvania) as well as S. Singh (MSKCC) for their help with Folding@Home data. We also thank N. Plattner (University of Basel) for her support. **Funding:** All work was funded by Microsoft. **Author contributions:** Data curation, generation, and benchmarks: S.L., T.H., J.J.-L., I.Z., Y.C., C.C., F.N.; Software: S.L., T.H., J.J.-L., M.G., Y.X., A.Y.K.F., V.G.S., O.A., B.S.V., Y.C., S.Y., A.S., J.N., F.B., V.S., A.C., J.Y., M.L., H.S., R.T.; Methodology: S.L., T.H., J.J.-L., M.G., Y.X., A.Y.K.F., V.G.S., O.A., B.S.V., I.Z., Y.C., S.Y., A.E.F., A.S., J.N., F.B., V.S., A.C., J.Y., M.L., Y.S., S.Z., R.T., F.N.; Results generation, analysis, validation, and visualization: S.L., T.H., J.J.-L., M.G., Y.X., A.Y.K.F., V.G.S., O.A., B.S.V., I.Z., Y.C., A.E.F., R.T., C.C., F.N.; Writing: S.L., T.H., J.J.-L., M.G., Y.X., A.Y.K.F., V.G.S., O.A., I.Z., Y.C., R.T., C.C., F.N.; Project administration: R.S., U.M.; Software lead: S.L., B.S.V.; Simulation data lead: T.H.; Project lead and conceptualization: F.N. **Competing interests:** A US patent application for the algorithms and training methods described in this paper has been filed under the title "Prediction of protein structure ensembles." The following authors are listed as inventors in the patent application: S.L., T.H., J.J.-L., M.G., Y.X., A.Y.K.F., V.G.S., O.A., B.S.V., S.Y., A.S., and F.N. **Data and materials availability:** As presently no standard database for MD data exists [see (*19*) for a discussion], MD data were either downloaded from various sources or generated for this work. See table S1 and materials and methods for a description of all datasets with download links. The MD training data produced as part of this study are available at Zenodo under the permissive Community Data License Agreement CDLA 2.0; see (*56*–*58*). The DESRES data for fast-folding proteins cannot be redistributed according to the DESRES data license. Researchers are requested to contact DESRES directly for obtaining this dataset and a license. The BioEmu model and inference code are available under MIT license at https://github.com/microsoft/bioemu and can be installed using "pip install bioemu" for scalable execution on Linux desktops or clusters. Internal training code is not published because it is specialized to a Microsoft-internal Azure cloud environment. To facilitate the development of a community training code for BioEmu, the pretraining AFDB cluster definition and a sample implementation of PPFT are available in the same GitHub repository. A simple way to test the model is available through https://github.com/sokrypton/ColabFold. Side-chain reconstruction and relaxation of generated structures for downstream analyses are also provided through the hpacker (*59*) and OpenMM (*60*) packages, respectively. Code for benchmarking BioEmu or other models for their ability to sample multiple protein conformations, free-energy surfaces, and folding free energies (Figs. 2, 3B, and 4A and figs. S1 to S4) is provided under MIT license at https://github.com/microsoft/bioemu-benchmarks (*61*). The version of the BioEmu code and model used in this paper, as well as the BioEmu model samples used for generating the figures, has been archived at Zenodo (*62*). **License information:** Copyright © 2025 the authors, some rights reserved; exclusive licensee American Association for the Advancement of Science. No claim to original US government works. https://www.science.org/about/science-licenses-journal-article-reuse

SUPPLEMENTARY MATERIALS

science.org/doi/10.1126/science.adv9817
Materials and Methods; Figs. S1 to S12; Tables S1 to S4; Algorithms 1 and 2; References (*63*–*126*); MDAR Reproducibility Checklist

Submitted 17 January 2025; accepted 27 June 2025; published online 10 July 2025
10.1126/science.adv9817

Check for

RESEARCH ARTICLES

ANCIENT PROTEINS

The proteome of the late Middle Pleistocene Harbin individual

Qiaomei Fu[1,2]*, Fan Bai[1], Huiyun Rao[1]*, Shaokun Chen[3], Yannan Ji[4], Aoran Liu[3], E. Andrew Bennett[1], Feng Liu[1], Qiang Ji[3]*

Denisovans are a hominin group primarily known through genomes or proteins, but their precise morphological features remain elusive because of the fragmentary nature of the discovered fossils. Here, we report 95 endogenous proteins retrieved from a nearly complete cranium from Harbin, China, dating to at least 146,000 years ago and previously assigned to a new species, *Homo longi*. This individual has three Denisovan-derived amino acid variants and clusters with Denisova 3, suggesting that the Harbin individual belongs to a Denisovan population. This study fills the gap between morphological and molecular evidence, enhancing our understanding of Denisovans' spatiotemporal dispersal and evolutionary history.

Denisovans represent an ancient hominin group distributed in Asia, and two genetically distinct populations have been identified using ancient DNA from Denisovans in Siberia and introgressed regions in modern humans (*1*–*4*). The currently known physical remains of Denisovans encompass a sparse assemblage of teeth, bone fragments, a phalanx, and a partial cranial fragment from a Denisovan cave in Siberia (*1*–*6*) that have limited diagnostic features for identifying different hominin groups. Thus, Denisovans to date have primarily been identified by DNA evidence. Recent advances in mass spectrometry technology have enabled the recovery of ancient hominin proteins from Early Pleistocene contexts (*7*–*11*) (Fig. 1A), expanding studies of Denisovans from solely genomic to proteomic as well. One benefit of proteomic analysis is that proteins are better preserved than DNA, thus expanding molecular studies into time periods thought to be out of reach for ancient DNA survival. Proteomic analysis has allowed the identification of more Denisovan-related specimens outside of Siberia, including a partial mandible and a rib from Baishiya Cave in China (*9*, *10*) and a Denisovan mandible from the Penghu Channel in Taiwan (*12*), as well as the collection of proteomic data from a possible Denisovan molar from the Tam Ngu Hao 2 (Cobra Cave) limestone cave in Laos (*11*). Identifying Denisovan-like specimens in China dating as far back as 160,000 years has broadened our knowledge of the geological range and time span of this extinct population. However, all fossil hominin specimens from which Denisovan-like genomic or proteomic material has been retrieved are fragmentary. Thus, despite Denisovans having been identified as a distinct archaic human lineage relative to Neanderthals and modern humans in 2010, we still do not know what they looked like.

Previous studies have inferred that Denisovans may have been widely distributed in East Asia (*13*, *14*), where substantial Middle Pleistocene hominin specimens have been unearthed. Some of these fossils [e.g., Xujiayao (*15*) and Harbin (*16*, *17*)], with nearly complete crania and informative morphological characteristics, have been suggested as possible Denisovans given their age, geography, and archaic features. However, whether a connection exists between these hominin fossils and Denisovans remains unclear. Retrieving ancient DNA or proteins from any of these fossils would help to identify whether they were Denisovans and, if so, to finally associate informative morphological characteristics with Denisovan genomic and proteomic material. Clarifying Denisovan morphology would greatly expand the identification of Denisovans across Asia and assist in calibrating Asia's Middle Pleistocene hominin systematics, further improving our understanding of the spatiotemporal dispersal of hominin populations in Asia and the relationship of Denisovans to recent Asian populations.

The Harbin fossil is an undistorted and nearly complete cranium discovered in the Harbin area of Heilongjiang Province, China (*16*, *18*) (Fig. 1A). Direct uranium-series dating of the cranium yielded a minimum age of ~146 thousand years ago (ka), whereas regional stratigraphic correlations suggest a possible origin from the upper part of the Upper Huangshan Formation (138 to 309 ka) (*19*). In one paper, it was made the type specimen of a new hominin species, *Homo longi* ("Dragon Man") (*16*). Since the first report of this cranium in 2021, intense debate has arisen regarding its taxonomic affiliation. Using morphology and phylogenetic analyses, it was grouped with Xiahe1 from Baishiya Karst Cave on the Tibetan Plateau (*18*), which was previously identified as a Denisovan-related population through proteomic analysis (*9*). Furthermore, a range of other Middle Pleistocene Chinese fossils, such as Dali, Hualongdong, and Jinniushan, were grouped with Harbin in these morphological analyses (*18*). The work on Harbin has since been extended to include the early Pleistocene Yunxian 2 cranium (often classified as *H. erectus*), the Penghu mandible, Xujiayao, and fossils from Denisova Cave, which in this work were grouped within the same clade as Harbin and were determined to be more closely related to *H. sapiens* than to Neanderthals (*20*). However, other recent morphological studies (*15*, *20*, *21*) have suggested that Harbin and Xiahe are not closely related. These studies have argued for three distinct groups: (i) the Julurens/Denisovans group (e.g., Xujiayao, Xiahe, and Penghu) characterized by larger cranial capacity and some shared Neanderthal features; (ii) the "Dragon Man" group (Harbin, Dali, and Jinniushan); and (iii) a third group consisting of Narmada, Maba, and Hualongdong.

Across these studies, the lack of genomic or proteomic material from a Middle Pleistocene specimen with informative morphology has impeded definitive phylogenetic assignments, particularly for Denisovans. Given the nearly complete morphology of the Harbin cranium, any ancient DNA or protein recovered from this individual would provide crucial evidence to connect molecular material to morphology, thereby improving our understanding of human evolutionary genealogy during the Middle Pleistocene in Asia.

Results

To understand the phylogenetic placement of the Harbin cranium, we first attempted to retrieve ancient DNA from six samples from the petrous bone and teeth (4.8 to 9.5 mg each) of the Harbin individual. No sample showed evidence of ancient human DNA (see the materials and methods and table S1). Subsequently, to assess the preservation of ancient proteins, we extracted proteins from two petrous samples (64.3 and 35.1 mg). Different fractions were collected to maximize amino acid sequence coverage, including an ammonium bicarbonate fraction, three acid-soluble fractions (>10, 3 to 10, and >3 kD), and two acid-insoluble fractions (see the materials and methods and data S2).

Recovery of the endogenous proteome

To gain more comprehensive information about the Harbin individual, a proteome was recovered by searching against a database composed of the modern human proteome and translated common bone and dentine protein sequences from archaic hominin genomes (see the supplementary text, section S2). A total of 308,458 peptide-spectrum matches (PSMs) and 20,455 peptides were identified by PEAKS Online (*22*). The peptides matching multiple genes were considered as nonunique and were excluded from subsequent analysis. We then assessed whether ancient hominin proteins were present in the Harbin individual by

[1]Key Laboratory of Vertebrate Evolution and Human Origins, Institute of Vertebrate Paleontology and Paleoanthropology, Chinese Academy of Sciences, Beijing, China. [2]College of Earth and Planetary Sciences, University of Chinese Academy of Sciences, Beijing, China. [3]Hebei International Joint Research Center for Paleoanthropology, Hebei GEO University, Shijiazhuang, China. [4]Chinese Academy of Geological Sciences, Beijing, China. ***Corresponding author. Email: jiqiang@hgu.edu.cn (Q.J.); fuqiaomei@ivpp.ac.cn (Q.F.) raohuiyun@ivpp.ac.cn (H.R.)**

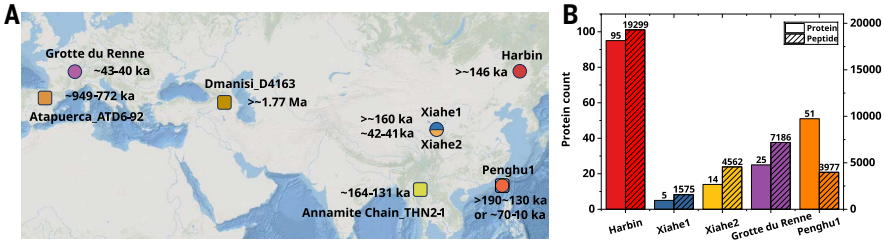

Fig. 1. Geographic locations and proteomic profiles for the Pleistocene hominin individuals with palaeoproteomic data. (**A**) Map of the geographic locations and hominin specimens studied by palaeoproteomic analysis. Circles with different colors indicate different bone or dentine specimens; squares with different colors indicate different enamel specimens. Because Xiahe1 and Xiahe2 were discovered at the same site, each specimen is represented by half of the same circle. Because both bone and enamel of Penghu1 have been analyzed, this is indicated as a circle within a square. Detailed information is provided in data S1. (**B**) Protein and peptide counts identified from five specimens. The data from Penghu1 were obtained from a related study (*12*). Because no accurate, nonredundant peptide counts were reported for the remaining three specimens, their data were obtained by processing corresponding raw proteomic data files using the same strategy as that used for Harbin.

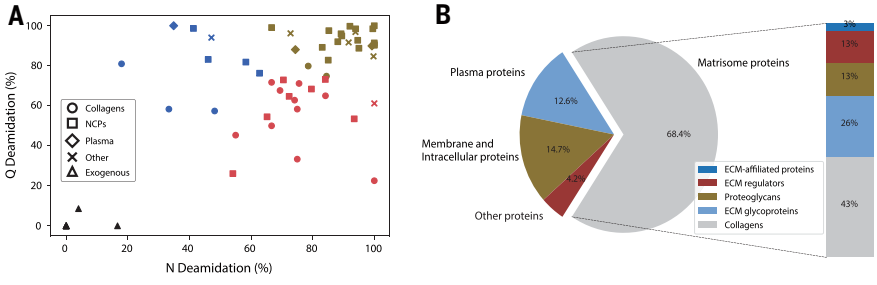

Fig. 2. Proteomic profile of the Harbin cranium. (**A**) Deamidation values of the identified proteins used in cluster analysis: 0% indicates no deamidation and 100% indicates complete deamidation. There is a clear separation between contaminating proteins (group 1: black) and endogenous proteins (group 2: red, group 3: blue, and group 4: brown) based on K-means cluster analysis. Cluster details are described in the supplementary text, section S2. Different shapes represent different types of proteins. "NCPs" refers to noncollagen matrisome proteins. (**B**) Composition across the 95 proteins retrieved for the Harbin individual. "Plasma proteins" here refers to nonmatrisome plasma proteins.

By retrieving 95 proteins with as many as 19,299 peptides from the Harbin cranium (>146 ka) (Fig. 1B), we not only increased the limited pool of proteomes retrieved from hominins dating to >100 ka, we also sequenced a much larger portion of the human proteome than from all other ancient individuals (protein count: 5 to 51; peptide count: 1575 to 7186). Comparing with previously published proteomic data, there was a significant 11.25-fold increase in peptide count over the dentine proteome of the contemporaneous Xiahe1 mandible (>160 ka) (*9*). There was also a higher peptide quantity relative to the younger Xiahe2 rib (*10*) and the Grotte du Renne bone fragments (*8*) (Fig. 1B). These results demonstrate the recovery of a highly informative ancient hominin proteome from the Harbin petrous bone.

Species confirmation

To determine the population assignment of the Harbin individual at a proteomic scale, we calculated peptide counts covering amino acid substitutions unique to modern humans, Neanderthals, Denisovans, chimpanzees, gorillas, and orangutans within all 95 endogenous proteins obtained. A minimum of two peptides was required for each position. In total, 122 single–amino acid polymorphisms (SAPs) were recovered from this endogenous proteome, showing a clear connection between the Harbin cranium and the Denisovans (Fig. 3 and data S4). First, positions derived in the gorillas, chimpanzees, and orangutans were all ancestral in the Harbin individual, with a match frequency of 100% (2025/2025 peptides, 102 positions). The Harbin cranium also showed 15 derived amino acid variants assigned to the *Homo* genus with a match frequency of 100% (74/74 peptides). These SAPs confidently assigned this individual to the *Homo* genus, which is consistent with the preliminary species confirmation based on matrix-assisted laser desorption/ionization (MALDI) spectra and a collagen database search (see the supplementary text, section S1).

calculating the deamination values of glutamine (Q) and asparagine (N) in the detected proteins based on peptide intensity, which required at least two Q/N-containing peptides. Higher deamination values of Q or N suggest a more extensive degradation of related proteins and thus can be used to authenticate the retrieved ancient proteome (*7*–*9*). There are 59 proteins with both reliable Q and N deamidation values, and 48 proteins with either reliable Q or reliable N deamidation values. Proteins with both reliable Q and N deamidation values were included for cluster analysis to discriminate endogenous from contaminating proteins (Fig. 2A). Eight proteins (including keratins and trypsin) with low deamination values of Q and N (Q deamidation average: 1.07 ± 3.04%; N deamidation average: 2.58 ± 5.86%) were excluded as contaminants (group 1 in Fig. 2A), which is consistent with previously published common contaminants (*8*, *23*). The remaining 51 proteins showed elevated deamidation values (Q deamidation range: 22.56 to 100%; N deamidation range: 17.97 to 100%) (groups 2, 3, and 4 in Fig. 2A) and were considered authentic ancient proteins. In addition, 44 of 48 proteins showed reliable elevated Q or N deamidation values (Q deamidation range: 30 to 100%; N deamidation range: 44.77 to 100%). In total, 95 proteins with elevated deamidation values were detected and were considered to belong to the Harbin individual's endogenous proteome (data S3). The main composition of these 95 proteins included 68.4% matrisome proteins (54 core matrisome proteins and 11 matrisome-associated proteins) and 12.6% nonmatrisome plasma proteins (Fig. 2B), which is comparable to those described from well-preserved bone specimens (*24*) (see the supplementary text, section S3).

Population assignment and possible physiological insight

We then evaluated all of the SAPs within the *Homo* genus and only retained positions with enough peptides and reliable PSMs (see the materials and methods and data S5). No reliable SAPs derived in Neanderthals were detected, whereas one SAP derived in modern humans showed the ancestral amino acid variant for the Harbin individual with a match frequency of 100% (2/2 peptides, 1 position). Finally, we identified four positions unique to Denisovans, of which three showed derived Denisovan amino acid variants with a match frequency of 86.57% (4/4, 109/126, and 3/4 peptides; data S4), and the remaining position retained the ancestral amino acid variant covered by two peptides and 13 PSMs.

We further investigated what amino acids these four Denisovan-derived positions showed in the Harbin individual, two Xiahe individuals (*9*, *10*), Penghu1, and Denisova 3 (*3*) (Table 1 and table S2). One Denisovan-derived allele (COL1A2 R996K) in the Harbin individual was already identified in the two Xiahe individuals and Penghu1, as well as in the Denisova 3 genome, which showed a homozygous derived allele at the corresponding genomic position. Even though COL1A2 996R was observed in Harbin at a low percentage of PSMs (4.5%) and related intensity (0.6%), the possibility of heterozygosity at this position cannot be excluded. For the three remaining positions not covered in the Xiahe individuals and Penghu1, Denisova 3 was

heterozygous at all corresponding genomic positions, whereas the Harbin cranium was homozygous derived for one position (COL18A1 G1033R), heterozygous for a second (COL26A1 R196G), and homozygous ancestral for a third (COL4A3 R368H). However, these amino acid alleles are not of high quality (Table 1). Because current proteomic search engines may not work so well on the accurate identification of PTM locations (table S2), particularly those in collagen, and because none of these three positions was detected in pFind, future studies could potentially uncover additional insights from the data by using complementary approaches for validation reliability [e.g., Orthrus (*25*)]. However, the identification of one highly confident and two potential Denisovan-derived amino acid variants supports the conclusion that the Harbin individual was from a Denisovan population.

Pathogenicity predictions for related protein variants were sourced from the AlphaMissense dataset (*26*). Of all the SAPs, only a heterozygous COL2A1 G1170S variant in the Harbin cranium is predicted to be pathogenic, being previously reported to possibly cause skeletal abnormalities such as avascular necrosis of the femoral head, Legg-Calvé-Perthes disease, premature hip osteoarthritis, and Stickler syndrome type 1 (*27*–*30*). The specific impact of the heterozygous state on the morphology and health of this individual is uncertain and requires further analysis using ancient phenotypic data and mutation expressivity studies.

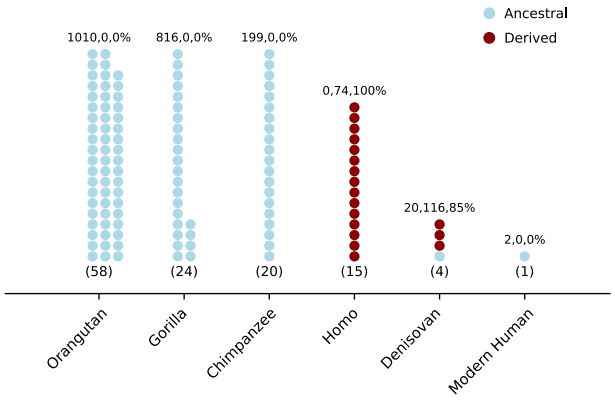

Fig. 3. SAP assignments for the Harbin cranium. Filled circles represent the observed genotype for each amino acid in the Harbin individual (blue: ancestral amino acids; red: derived amino acids). The number of ancestral and derived peptide counts, respectively, followed by the frequency of derived peptides, are shown at the top of the bar separated by commas. The number of SAPs is shown at the bottom of the bar in parentheses.

Phylogenetic reconstruction

To determine a more specific taxonomic attribution for the Harbin cranium, we reconstructed the consensus sequences of its endogenous proteins for phylogenetic analysis. For each endogenous protein of the Harbin cranium, reliable alleles were retained if they met the following requirements: PSM count ≥2, PSM ratio ≥10%, and intensity ratio ≥10% (*31*). Three confident heterozygous positions in which multiple amino acid alleles were retained with reliable spectra were identified in the Harbin cranium (Table 1). Consensus protein sequences were generated, with one variant randomly selected for heterozygous positions, and positions with single peptide coverage or indistinguishable, unreliable, or less-reliable SAPs were marked as "X." Less-confident sites (COL18A 1033, COL26A1 196, and COL4A3 368) related to Denisovans were also assigned to "X." We obtained 9422 amino acid positions from 88 proteins for the Harbin cranium, which is 11.37% of the total concatenated protein sequence alignment. The reference dataset for phylogenetic analysis was built using translated protein sequences from previously published high-coverage genomes, including Denisova 3 (*3*), two Neanderthals (Altai Neanderthal and Vindija19) (*32*, *33*), one early modern human (Ust'-Ishim) (*34*), present-day human individuals (*35*), and a chimpanzee (*36*, *37*). Two different sets of modern human individuals were used, one with 58 global present-day humans and the other with 64 pan-African individuals.

The phylogenetic trees for these two datasets are highly congruent with a commonly accepted primary topology also found for nuclear genomes, i.e., *H. sapiens* is a sister group to a clade containing Neanderthals and Denisovans (Fig. 4 and fig. S4). This contrasts with morphology-based phylogenetic analyses (*18*, *20*) suggesting that Harbin was in the sister group to the *H. sapiens* clade rather than to Neanderthals. The Harbin cranium and Denisovan 3 form a monophyletic group with high support (posterior probability 100% in the pan-African dataset and 98%

Table 1. Details of SAPs within *Homo* sp. identified in the Harbin cranium*

SAP assignment	Protein	Position	Accession no.	No. of peptides	No. of PSMs	Harbin	Xiahe1	Xiahe2	Penghu1	Denisova3	Altai Neanderthal	Vindija19	Ust'-Ishim	HGDP frequency	Great apes
Denisovan	**COL1A2**	**996**	**P08123**	**109/17**	**2277/107**	**K/R†**	**K**	**K**	**K**	**K**	**R**	**R**	**R**	**Fixed R**	**R**
Denisovan	COL18A1	1033	P39060	4	4	R‡	X	X	X	R,G	G	G	G	Fixed G	G
Denisovan	COL26A1	196	Q96A83	3/1	3/1	G/R‡	X	X	X	G,R	R	R	R	Fixed R	R
Denisovan	**COL4A3**	368	**Q01955**	2	13	R‡	**X**	**X**	X	**H,R**	**R**	**R**	**R**	**Fixed R**	R
Xiahe1	**COL2A1**	583	**P02458**	10/7	15/10	E/G†	**G**	**E**	E	**E**	**E**	**E**	**E**	**Fixed E**	E
Harbin	COL2A1	1022	P02458	17/1	28/1	M/V†	V	V	X	V	V	V	V	Fixed V	V
Harbin	SCARA3	490	Q6AZY7	2	2	A‡	X	X	X	G	G	G	G	Fixed G	G
Harbin heterozygous	COL1A2	549	P08123	234/50	1647/189	A/P	X	A	A	A	A	A	A	P (23.7%), A (76.3%)	A
Harbin heterozygous	COL2A1	601	P02458	12/13	68/21	IL/V	X	V	V	V	V	V	V	Fixed V	V
Harbin heterozygous	COL2A1	1170	P02458	38/33	207/158	G/S	G	G	G	G	G	G	G	Fixed G	G
Modern human	KNG1	178	P01042	2	5	T	X	X	X	T	T	T	M	M (47.8%), T (52.2%)	T

*Positions are based on the Uniprot accession number for the related human proteins. The listed amino acid calls for Xiahe1 (*9*), Xiahe2 (*39*), and Penghu1 (*12*) were obtained from the published protein sequences. The amino acid calls for Denisova3 (*3*), Altai Neanderthal (*32*), Vindija19 (*33*), and Ust'-Ishim (*34*) were translated from genomic data. The frequency was calculated from 929 high-coverage genomes of the Human Genome Diversity Project (*35*). †Considered less-reliable identifications because these amino acid alleles do not fulfill the requirements of PSM count ≥2, PSM ratio ≥10%, and intensity ratio ≥10% (*31*), and therefore the possibility of heterozygosity is low for these sites. Some derived alleles, such as COL1A2 996K and COL2A1 1022 M, appear to be better supported than the ancestral ones. ‡Considered less-reliable identifications because of limited spectra support (COL26A1 196R and SCARA3 490A), relatively low-quality spectra (COL18A1 1033R and COL26A1 196G), or possible contaminant origins (COL4A3 368R). For COL18A1 1033R, none of the supported spectra show a predominance of y ions. For COL26A1 196G, all supported PSMs have this SAP at the N terminus without surrounding y and b ions, which is consistent with the fragmentation patterns for HCD, where b1 and y_{N-1} ions are usually missing in the MS/MS spectrum (*40*). For COL4A3 368R, the supported peptides may also match possible contaminants such as mouse or bacteria.

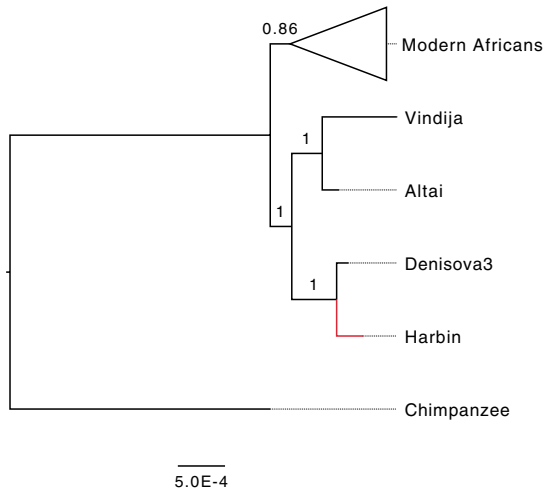

Fig. 4. Phylogenetic position of the Harbin cranium through Bayesian analysis using the dataset with 64 pan-Africans. Chimpanzee (*Pan troglodytes*) was used as an outgroup.

in the global dataset). This result is consistent with the population assignment using SAPs described above, in which we assigned the Harbin individual to a Denisovan population.

Discussion and conclusions

Recent studies have demonstrated the high potential of paleoproteomic analysis in tracking human evolutionary history, extending insights into geographical areas and time periods where substantial genetic information is absent (*7*, *9*, *38*). In this study, despite the lack of preserved ancient human DNA in the petrous bone and teeth of the Harbin cranium, abundant proteins were found, resulting in a high-quality archaic hominin proteome. Through proteomic analysis, we were able to definitively identify this individual as Denisovan.

By using proteomic analysis to connect the Harbin individual's nearly complete cranium with Denisovans, we now have the first comprehensive morphological blueprint for Denisovan populations, helping to address an unresolved question that has persisted over the past decade about what Denisovans looked like. In addition, the findings from our ancient proteomic analysis provide solid evidence that Denisovans were widely distributed across East Asia, as has been inferred in previous studies (*12*–*14*, *18*, *20*). The Harbin cranium, along with Xiahe1, Xiahe2, and Penghu1, have all been grouped through proteomic analysis with Denisovans, with a geographical range extending from Northeast China to the Tibetan Plateau to Taiwan and a chronological range spanning from the late Middle Pleistocene to the late Pleistocene. This study finally connects more complete Denisovan morphology to the genomic and proteomic data previously studied, further improving our understanding of Denisovan spatiotemporal dispersal and evolutionary history.

Additionally, proteomic identification of the Harbin cranium prompts a reconsideration of Asia's Middle Pleistocene hominin systematics. Denisovan populations in East Asia inhabited a variety of environments, including low-lying plains, high plateaus, and subtropical woodlands. Furthermore, many hominin fossils across East Asia, such as Yunxian 2, Dali, Jinniushan, and Hualongdong, show morphological features similar to those found in the Harbin cranium (*18*, *20*). Our findings strongly suggest that despite studies suggesting that this group may be distinguished from fossils more similar morphologically to the Denisovan-linked Xiahe individuals (e.g., Xujiayao and Penghu), these hominins potentially also belong to Denisovan populations. Additional molecular sampling of Middle and Late Pleistocene hominin fossils in East Asia, especially any with ancient DNA, will be necessary for determining the differentiation and dispersal patterns of Denisovan populations in East Asia and how these East Asian archaic hominins interacted with other archaic human populations and affected more recent Asian populations.

REFERENCES AND NOTES

1. J. Krause *et al.*, *Nature* **464**, 894–897 (2010).
2. D. Reich *et al.*, *Nature* **468**, 1053–1060 (2010).
3. M. Meyer *et al.*, *Science* **338**, 222–226 (2012).
4. V. Slon *et al.*, *Sci. Adv.* **3**, e1700186 (2017).
5. B. T. Viola, P. Gunz, S. Neubauer, "A parietal fragment from Denisova cave," paper presented at the 88th Annual Meeting of the American Association of Physical Anthropologists, Cleveland, OH, 27 to 30 March 2019.
6. S. Brown *et al.*, *Nat. Ecol. Evol.* **6**, 28–35 (2022).
7. F. Welker *et al.*, *Nature* **580**, 235–238 (2020).
8. F. Welker *et al.*, *Proc. Natl. Acad. Sci. U.S.A.* **113**, 11162–11167 (2016).
9. F. Chen *et al.*, *Nature* **569**, 409–412 (2019).
10. H. Xia *et al.*, *Nature* **632**, 108–113 (2024).
11. F. Demeter *et al.*, *Nat. Commun.* **13**, 2557 (2022).
12. T. Tsutaya *et al.*, *Science* **388**, 176–180 (2025).
13. J. Ruan *et al.*, *Science* **381**, 699–704 (2023).
14. D. Reich *et al.*, *Am. J. Hum. Genet.* **89**, 516–528 (2011).
15. X. Wu, C. J. Bae, *Paleoanthropology* (2024).
16. Q. Ji, W. Wu, Y. Ji, Q. Li, X. Ni, *Innovation (Camb.)* **2**, 100132 (2021).
17. É. Harney, N. Patterson, D. Reich, J. Wakeley, *Genetics* **217**, iyaa045 (2021).
18. X. Ni *et al.*, *Innovation (Camb.)* **2**, 100130 (2021).
19. Q. Shao *et al.*, *Innovation (Camb.)* **2**, 100131 (2021).
20. X. Feng *et al.*, The phylogenetic position of the Yunxian cranium elucidates the origin of Dragon Man and the Denisovans. bioRxiv 594603 [Preprint] (2024); https://doi.org/10.1101/2024.05.16.594603.
21. C. J. Bae, W. Liu, X. Wu, Y. Zhang, X. Ni, *Innovation (Camb.)* **4**, 100527 (2023).
22. L. Xin *et al.*, *Nat. Commun.* **13**, 3108 (2022).
23. H. Rao *et al.*, *Sci. Rep.* **10**, 16674 (2020).
24. E. Cappellini *et al.*, *J. Proteome Res.* **11**, 917–926 (2012).
25. Y. Chiang, M. J. Collins, Orthrus: an AI-powered, cloud-ready, and open-source hybrid approach for metaproteomics. bioRxiv 623814 [Preprint] (2024); https://doi.org/10.1101/2024.11.15.623814.
26. J. Cheng *et al.*, *Science* **381**, eadg7492 (2023).
27. Y. F. Liu *et al.*, *N. Engl. J. Med.* **352**, 2294–2301 (2005).
28. Y. Miyamoto *et al.*, *Hum. Genet.* **121**, 625–629 (2007).
29. P. Su *et al.*, *Arthritis Rheum.* **58**, 1701–1706 (2008).
30. S. Savasta *et al.*, *Eur. J. Pediatr.* **174**, 697–701 (2015).
31. P. P. Madupe *et al.*, *Science* **388**, 969–973 (2025).
32. K. Prüfer *et al.*, *Nature* **505**, 43–49 (2014).
33. K. Prüfer *et al.*, *Science* **358**, 655–658 (2017).
34. Q. Fu *et al.*, *Nature* **514**, 445–449 (2014).
35. A. Bergström *et al.*, *Science* **367**, eaay5012 (2020).
36. Z. N. Kronenberg *et al.*, *Science* **360**, eaar6343 (2018).
37. Y. Mao *et al.*, *Cell* **187**, 1547–1562.e13 (2024).
38. F. Welker *et al.*, *Nature* **576**, 262–265 (2019).
39. H. Xia, Y. Li, D. Zhang, F. Chen, *Kexue Tongbao* **69**, 5155–5160 (2024).
40. C. Shao, Y. Zhang, W. Sun, *J. Proteomics* **109**, 26–37 (2014).
41. Y. Perez-Riverol *et al.*, *Nucleic Acids Res.* **53**, D543–D553 (2025).

ACKNOWLEDGMENTS

We thank R. Yang, S. Yang and M. Shi for help in the laboratory; F. Yang and J. Wang for conducting some of the LC MS/MS runs; S. Tang for visualizing the figure; Z. Wu and Z. Zhou for initial investigations; M. A. Yang, W. Ping, and S. Pääbo for helpful comments; and the BSI team for making special improvements for our PEAKS Online software. **Funding:** This work was supported by the Chinese Academy of Sciences (CAS) (grant YSBR-019) and the National Natural Science Foundation of China (grant 41842039). **Author contributions:** Q.F. designed and supervised the research project. Q.J. prepared the archaeological samples and materials. Q.F., H.R., and F.B. analyzed data. E.A.B. and F.B. prepared the database. H.R, Q.F., and F.L. performed or supervised the wet laboratory work. Q.F. wrote the manuscript. Q.F., H.R., E.A.B., and Q.J. revised the manuscript. Q.F., H.R., E.A.B., and F.B. wrote and prepared the supplementary information. All authors discussed, critically revised, and approved the final version of the manuscript. **Competing interests:** The authors declare no competing interests. **Data and materials availability:** All proteomic mass spectrometry data have been deposited to the ProteomeXchange Consortium through the PRIDE (*41*) partner repository with dataset identifier PXD058447. Protein consensus sequences for the Harbin cranium used for phylogenetic analysis are available in data S6. **License information:** Copyright © 2025 the authors, some rights reserved; exclusive licensee American Association for the Advancement of Science. No claim to original US government works. https://www.science.org/about/science-licenses-journal-article-reuse

SUPPLEMENTARY MATERIALS

science.org/doi/10.1126/science.adu9677
Materials and Methods; Supplementary Text; Figs. S1 to S4; Tables S1 and S2; References (*42*–*101*); MDAR Reproducibility Checklist; Data S1 to S7

Submitted 29 November 2024; accepted 9 June 2025; published online 18 June 2025
10.1126/science.adu9677

CARBON ALLOTROPES

Solution-phase stabilization of a cyclocarbon by catenane formation

Yueze Gao[1]*, Prakhar Gupta[1], Igor Rončević[2], Coral Mycroft[1], Paul J. Gates[3], Anthony W. Parker[4], Harry L. Anderson[1]*

Cyclo[*N*]carbons, molecular rings consisting solely of *N* carbon atoms, have previously been studied in the gas phase and on surfaces at cryogenic temperatures, but they are generally considered too reactive to be studied under ambient laboratory conditions. In this study, we report the synthesis of a cyclo[48]carbon catenane, in which the C_{48} ring is protected by being threaded through three other macrocycles. This cyclo[48]carbon [4]catenane is stable enough for spectroscopic characterization in solution at room temperature. Its mass spectrum displays the expected molecular ions; its ^{13}C nuclear magnetic resonance spectrum gives a single resonance for all 48 sp^1 carbon atoms at 72.9 parts per million; and its Raman spectrum shows an intense peak at 1890 inverse centimeters, similar to linear polyynes.

Diverse carbon clusters, including cyclo[*N*]carbons up to $N = 36$, have been characterized in the gas phase (*1–3*), but the only molecular carbon allotropes yet to have been studied under ambient conditions are the fullerenes. Recently, several cyclo[*N*]carbons ($N = 6$, 10, 12, 13, 14, 16, 18, 20, and 26) have been synthesized on surfaces by atom manipulation and investigated by using scanning probe microscopy at temperatures of 4 to 10 K (*4–10*). However, all reported attempts at synthesizing cyclocarbons in solution have been unsuccessful (*11–16*), and it is generally assumed that they are too reactive to survive in solution or in the solid state above liquid helium temperatures. Their high reactivity stems from the fact that the conversion of sp^1 carbon into cross-linked amorphous sp^2 or sp^3 carbon is thermodynamically favorable, and many materials with a high mass fraction of sp^1 acetylenic carbon are explosive for the same reason (*17*). In this work, we show that cyclo[48]carbon can be stabilized by supramolecular encapsulation by formation of a [4]catenane, in which the ring of carbon atoms is threaded through three covalent macrocycles ($\mathbf{M_3}$). The cyclo[48]carbon [4]catenane $\mathbf{C_{48}{\cdot}M_3}$ is stable enough for spectroscopic characterization in solution under ambient conditions. This work was inspired by the pioneering studies of Cram (*18*) and Warmuth (*19*), who demonstrated that the highly reactive species cyclobutadiene and *ortho*-benzyne, respectively, can be stabilized by supramolecular encapsulation. Although catenane formation does not completely encapsulate the cyclocarbon, we reasoned that the presence of the threaded macrocycles would hinder cyclocarbon molecules from reacting together to form a cross-linked material and increase the lifetime in solution.

Synthesis

The cyclocarbon catenane $\mathbf{C_{48}{\cdot}M_3}$ was prepared from a masked precursor, $\boldsymbol{m}$-$\mathbf{C_{48}{\cdot}M_3}$ (Fig. 1), which was synthesized by oxidative palladium-catalyzed Glaser coupling cyclo-oligomerization of a [2]rotaxane, prepared by active metal template–directed synthesis (*16, 20-26*), as detailed in the supplementary materials. The cobalt carbonyl phosphine masking groups stabilize $\boldsymbol{m}$-$\mathbf{C_{48}{\cdot}M_3}$ and act as temporary stoppers during its synthesis. The macrocycle **M** includes two nitrogen sites for binding copper during the active metal template–directed synthesis. We chose a macrocycle based on 2,2'-bipyridine rather than phenanthroline to make it less susceptible to oxidation (*27*) and aggregation. The macrocycle features *ortho*-methyl substituents to generate a more cylindrical cavity. The masked cyclo[48]carbon [4]catenane $\boldsymbol{m}$-$\mathbf{C_{48}{\cdot}M_3}$ was treated with *meta*–chloroperbenzoic acid (mCPBA) (*20*), followed by purification by gel-permeation chromatography, to give unmasked $\mathbf{C_{48}{\cdot}M_3}$ as an orange-red solution. A range of conditions was screened to optimize this unmasking reaction and purification protocol (table S1), and the best results were obtained using mCPBA in combination with 2,2'-bipyridine (2,2'-bipy) at 0°C with a short reaction time (3 min), followed by quenching excess mCPBA with phenanthroline (*27*). Phenanthroline and 2,2'-bipy were added because they react with mCPBA faster than the macrocycle **M**, thus protecting it from *N*-oxide formation. $\mathbf{C_{48}{\cdot}M_3}$ is not stable in the solid state, and evaporation of the solvent must be avoided during its synthesis. Solutions of $\mathbf{C_{48}{\cdot}M_3}$ in deuterated solvents for analysis by nuclear magnetic resonance (NMR) spectroscopy were prepared by unmasking $\boldsymbol{m}$-$\mathbf{C_{48}{\cdot}M_3}$ in CD_2Cl_2, followed by gel-permeation chromatography, eluting with $CDCl_3$.

Spectroscopic characterization

The first clear evidence for the formation of $\mathbf{C_{48}{\cdot}M_3}$ was provided by mass spectrometry. The mass spectrum of $\mathbf{C_{48}{\cdot}M_3}$ (Fig. 2) shows peaks for $[\mathbf{C_{48}{\cdot}M_3} + 3H]^{3+}$ at mass/charge ratio (m/z) = 783.596 (base peak), $[\mathbf{C_{48}{\cdot}M_3} + 2H]^{2+}$ at m/z = 1174.896, and $[\mathbf{C_{48}{\cdot}M_2} + 2H]^{2+}$ at m/z = 879.763, all of which fit extremely well to the predicted isotope distributions (Fig. 2). The peak attributed to the [3]catenane appears to arise from a trace by-product generated by cleavage of the macrocycle during unmasking. This interpretation is supported by ^1H NMR analysis and model reactions on a [2]rotaxane, which show traces of macrocycle cleavage accompanying unmasking (see supplementary materials section 3.2).

The ^1H and ^{13}C NMR spectra of $\mathbf{C_{48}{\cdot}M_3}$ (recorded in $CDCl_3$ at –35°C) are compared with those of a reference [2]rotaxane $\mathbf{Si_2C_{16}{\cdot}M}$ in Fig. 3. This reference rotaxane contains the same macrocycle **M** as the catenane, and the ^1H NMR spectra of both compounds are very similar [except for signals from the tri-*iso*-propylsilyl group at 1.05 parts per million (ppm), not shown in Fig. 3]. The ^{13}C NMR spectra of the two compounds are also similar, except that $\mathbf{Si_2C_{16}{\cdot}M}$ has eight well-resolved signals owing to sp^1 carbon atoms at 89.8, 86.4, and 63.0 to 61.9 ppm, whereas $\mathbf{C_{48}{\cdot}M_3}$ gives a single intense peak at 72.9 ppm for all 48 sp^1 carbons. The simple ^1H and ^{13}C NMR spectra of $\mathbf{C_{48}{\cdot}M_3}$ demonstrate that it has a symmetrical structure and that the threaded macrocycles move rapidly around the cyclocarbon ring, making all 48 sp^1 carbon environments equivalent on the NMR timescale. This type of dynamic behavior often arises in catenanes when there is no strong interaction between the macrocycles (*20*, *28*). The ^{13}C chemical shift of the cyclic C_{48} unit in the [4]catenane (72.9 ppm) is higher than that for the carbons at the center of a linear C_{48} polyyne [4]rotaxane (63.7 ppm) by 9.2 ppm (*20*, *29*). This increase in chemical shift is consistent with previous experimental and computational studies that report a downfield shift in the ^{13}C NMR spectra of strained polyynes (*30–32*).

Dilute solutions of $\mathbf{C_{48}{\cdot}M_3}$ in organic solvents decompose slowly at room temperature. In dichloromethane, $\mathbf{C_{48}{\cdot}M_3}$ has a half-life of

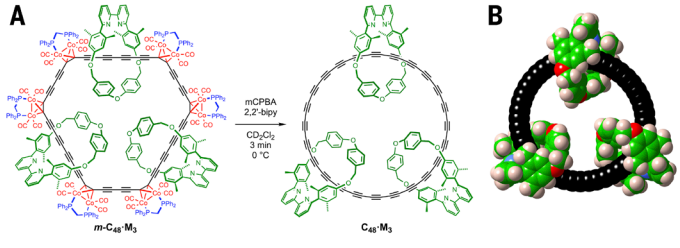

Fig. 1. Unmasking of $\mathbf{C_{48}{\cdot}M_3}$. (**A**) Synthesis of $\mathbf{C_{48}{\cdot}M_3}$ and (**B**) a projection of its calculated geometry to show the van der Waals surface. The optimized geometry of $\mathbf{C_{48}{\cdot}M_3}$ was calculated by the PM6 method; see supplementary materials.

[1]Department of Chemistry, Chemistry Research Laboratory, Oxford University, Oxford, UK. [2]Department of Chemistry, The University of Manchester, Oxford Road, Manchester, UK. [3]School of Chemistry, University of Bristol, Cantock's Close, Clifton, Bristol, UK. [4]Central Laser Facility, Research Complex at Harwell, STFC, Rutherford Appleton Laboratory, Harwell Campus, Didcot, UK. ***Corresponding author. Email: yueze.gao@chem.ox.ac.uk (Y.G.); harry.anderson@chem.ox.ac.uk (H.L.A.)**

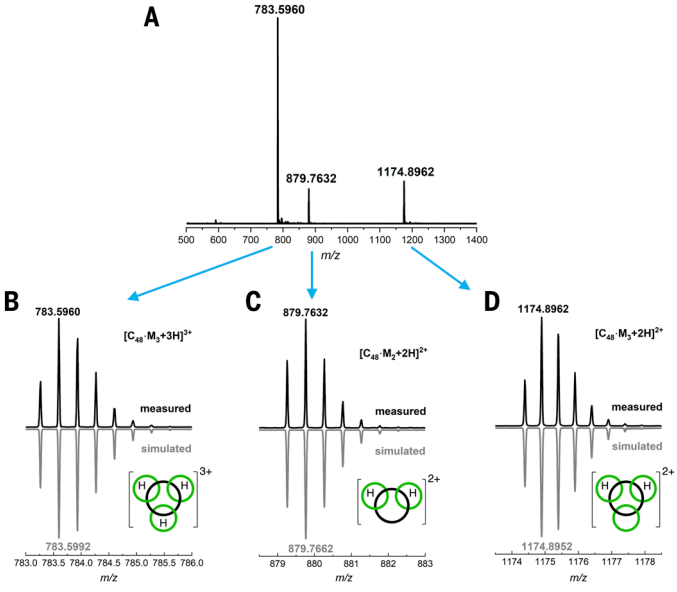

Fig. 2. Mass spectrum of C_{48}·M_3. (**A**) The whole high-resolution nanoelectrospray quadrupole orthogonal acceleration–time-of-flight mass spectrum, run in 3:1 toluene:formic acid, and expansions of the signals from (**B**) [**C_{48}·M_3** + 3H]$^{3+}$ at m/z = 783.596, (**C**) [**C_{48}·M_2** + 2H]$^{2+}$ at m/z = 879.763, and (**D**) [**C_{48}·M_3** + 2H]$^{2+}$ at m/z = 1174.896.

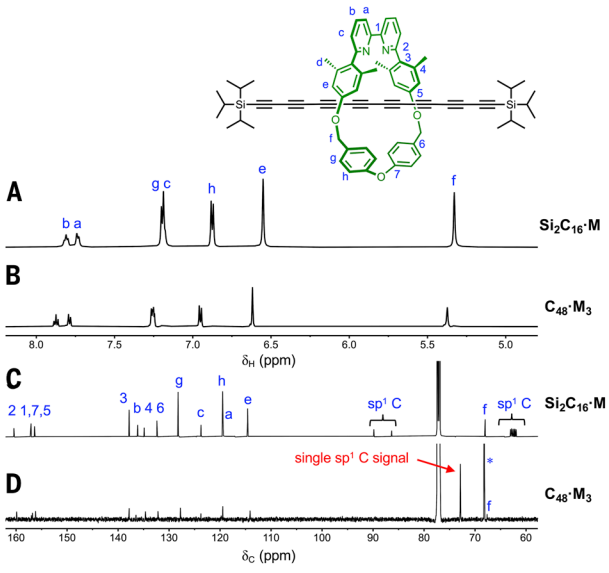

Fig. 3. ^{1}H and ^{13}C NMR spectra. (**A** and **B**) ^{1}H NMR spectra (600 MHz, $CDCl_3$, diffusion edited, −35°C) and (**C** and **D**) ^{13}C NMR spectra (150 MHz, −35°C) of the reference [2]rotaxane [(A) and (C)] and the [4]catenane **C_{48}·M_3** [(B) and (D)]. The asterisk indicates a signal arising from a trace of tetrahydrofuran. δ, chemical shift (in ppm).

92 hours (3 μM concentration, 20°C), as shown by the decay of the ultraviolet-visible (UV-vis) absorption bands in Fig. 4A. The rate of decomposition of **C_{48}·M_3** is not strongly dependent on concentration: When monitored by ^{1}H NMR spectroscopy at 300 μM concentration (20°C, $CDCl_3$), the rate of decomposition is similar to that when monitored by UV-vis at 3 μM concentration (fig. S10). The catenane is much less stable in the solid state, and removal of the solvent by evaporation results in immediate decomposition to give insoluble material. We also tested unmasking of the corresponding cyclo[48]carbon cobaltcarbonyl phosphine complex with no threaded macrocycles, ***m*-C48** (for synthesis, see scheme S5). Treatment of a dilute (1 μM) solution of ***m*-C48** in dichloromethane with mCPBA gives a lemon yellow solution with a similar UV-vis absorption spectrum to that of **C_{48}·M_3**, indicating the formation of unmasked cyclo[48]carbon. This naked cyclocarbon decomposed with a half-life of about 1 hour at 20°C at 0.9 μM concentration (fig. S12A) and much more rapidly at higher concentrations (fig. S12E), preventing purification or characterization by mass spectrometry or NMR spectroscopy. The identification of this noncatenane cyclo[48]carbon must be regarded as tentative because, so far, we have only characterized it by UV-vis spectroscopy, yet the match with the absorption spectra of **C_{48}·M_3** strongly suggests that this species is **C_{48}** (fig. S14). The absorption bands of this putative cyclo[48]carbon are shifted to shorter wavelengths than those of **C_{48}·M_3**, by about 7 nm, as generally observed when comparing polyyne polyrotaxanes with the naked polyyne dumbbells (*20*, *24*) (see also fig. S15 for comparison of the UV-vis spectra of **Si_2C_{16}** and **Si_2C_{16}·M**). We have not yet purified **C_{48}**, and the presence of by-products from the unmasking reaction probably affect its stability, but it appears that decomposition of **C_{48}** is much more concentration-dependent than that of **C_{48}·M_3**. Solutions of **C_{48}** in dichloromethane decompose with a half-life of less than a minute at a precursor concentration of 15 μM (fig. S12E).

The UV-vis absorption spectrum of the **C_{48}·M_3** [4]catenane is compared with that of a linear end-capped C_{48} polyyne [4]rotaxane **Tr*C_{48}·M'$_3$** (*20*) in Fig. 4B. The linear polyyne exhibits a progression of intense absorption bands in the visible region (400 to 500 nm), with the 0-0 transition at 480 nm, whereas the spectrum of the cyclocarbon catenane is most intense in the UV (350 to 400 nm), with a dominant 0-0 transition at 386 nm. The suppression of long-wavelength absorption bands is a general feature of cyclic π systems, when compared with their linear analogs, owing to the difference in selection rules (*33*–*35*). Time-dependent density function theory (TD-DFT) calculations on cyclo[48]carbon and the linear polyyne $C_{48}H_2$ (in a vacuum) closely resemble the observed spectra of **C_{48}·M_3** and **Tr*C_{48}·M'**$_3$ (see vertical bars in Fig. 4B and fig. S16).

The resonance Raman spectrum of **C_{48}·M_3** exhibits an intense peak at 1890 cm^{-1} (recorded in $CDCl_3$ with excitation at 514 nm; Fig. 4C), similar to the transitions observed in the Raman spectra of linear polyynes (*36*–*39*). **C_{48}·M_3** also exhibits a weaker peak at 2012 cm^{-1}. Both peaks were reproduced by computational simulations, supporting assignment of the 1890 and 2012 cm^{-1} to the symmetric (A_{1g}) C–C stretching vibration and the doubly degenerate asymmetric (E_{2g}) C–C stretch, respectively (blue bars, Fig. 4C; see supplementary materials section 8 for details). The experimental Raman spectrum of **C_{48}·M_3** is also similar to the predicted Raman spectra of cyclocarbons such as C_{30} (*40*).

Conclusions and outlook

We have synthesized a cyclocarbon that is sufficiently stable in solution under ambient conditions to permit characterization using standard spectroscopic techniques, whereas previously cyclocarbons have only been characterized in the gas phase or on surfaces at temperatures of 4 to 10 K. The factors that enabled us to achieve this objective are (i) the use of threaded macrocycles to provide supramolecular encapsulation, conferring enhanced stability by hindering access to the cyclocarbon; (ii) the selection of a large cyclocarbon, C_{48}, with a low level of strain (*41*); and (iii) the development of mild reaction conditions for unmasking the masked cyclocarbon intermediate. The **C_{48}·M_3** is moderately stable in solution at 20°C, with a half-life of 92 hours. It is much more stable than the naked cyclo[48]carbon, with a half-life of about 1 hour at 20°C and 0.9 μM concentration, which decomposes rapidly at higher concentrations. Even unprotected cyclo[48]carbon is much more stable than reactive intermediates, such as *ortho*-benzyne, which only persists for a few nanoseconds under typical solution-phase conditions (*42*, *43*). The stabilization of C_{48} by catenane formation is analogous to the stabilization of *ortho*-benzyne by encapsulation in a hemicarcerand (*19*); however a view of the van der Waals surface of **C_{48}·M_3** (Fig. 1B) shows that only part of the cyclocarbon is encapsulated by the threaded macrocycles. These results may inspire the

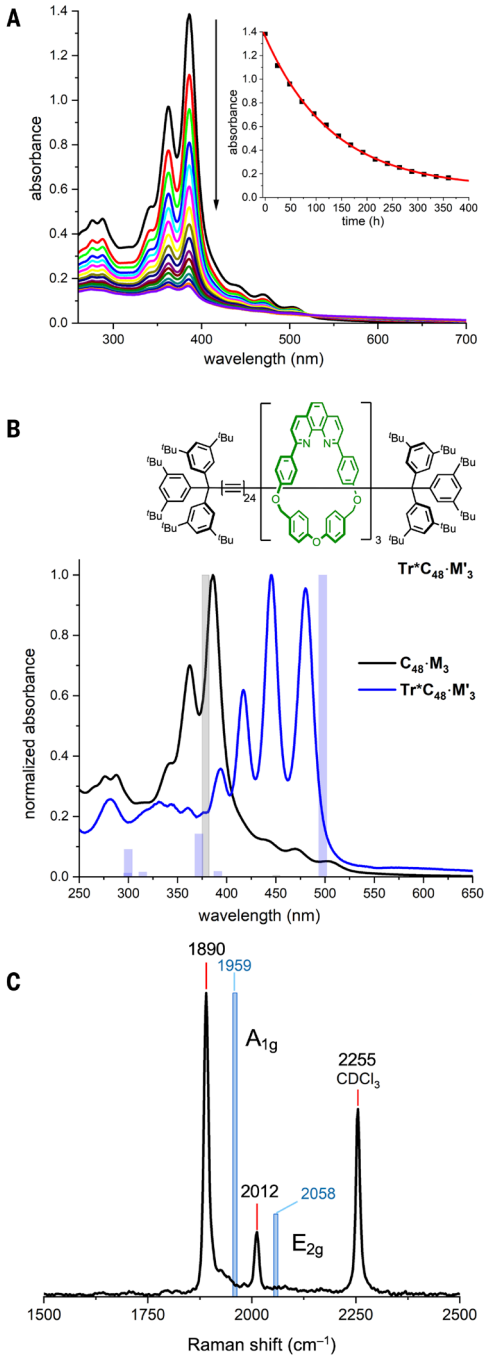

Fig. 4. Optical spectra of C_{48}·M_3. (**A**) UV-vis spectra in CH_2Cl_2 recorded over 360 hours, showing the rate of decomposition at 20°C in the dark (1-cm path length; 3 μM). The insert shows a fit of the absorbance at 386 nm to a first-order decay with a half-life of 92 hours. (**B**) Comparison of UV-vis spectra of **C_{48}·M_3** (black) and linear C_{48} polyyne [4]rotaxane (**Tr*C_{48}·M'$_3$**, blue); vertical bars show vertical transitions from TD-DFT calculations. (**C**) Raman spectrum obtained by using an excitation wavelength of 514 nm; vertical blue bars denote calculated peaks.

design of other host molecules that are even more effective in stabilizing cyclocarbons through supramolecular encapsulation.

REFERENCES AND NOTES

1. A. Van Orden, R. J. Saykally, *Chem. Rev.* **98**, 2313–2357 (1998).
2. H. L. Anderson, C. W. Patrick, L. M. Scriven, S. L. Woltering, *Bull. Chem. Soc. Jpn.* **94**, 798–811 (2021).
3. S. J. P. Marlton *et al.*, *J. Phys. Chem. A* **127**, 1168–1178 (2023).
4. K. Kaiser *et al.*, *Science* **365**, 1299–1301 (2019).
5. L. M. Scriven *et al.*, *J. Am. Chem. Soc.* **142**, 12921–12924 (2020).
6. L. Sun *et al.*, *Nature* **623**, 972–976 (2023).
7. Y. Gao *et al.*, *Nature* **623**, 977–981 (2023).
8. L. Sun *et al.*, *Nat. Commun.* **15**, 7649 (2024).
9. F. Albrecht *et al.*, *Science* **384**, 677–682 (2024).
10. L. Sun, Y. Guo, W. Xiang, W. Xu, *Nat. Synth.* (2025).
11. B. K. Collins, J. A. Gladysz, *Chemistry* **30**, e202402833 (2024).
12. Y. Tobe *et al.*, *J. Am. Chem. Soc.* **122**, 1762–1775 (2000).
13. F. Diederich, Y. Rubin, O. L. Chapman, N. S. Goroff, *Helv. Chim. Acta* **77**, 1441–1457 (1994).
14. F. Diederich, Y. Rubin, *Angew. Chem. Int. Ed.* **31**, 1101–1123 (1992).
15. F. Diederich *et al.*, *Science* **245**, 1088–1090 (1989).
16. P. Gawel, S. L. Woltering, Y. Xiong, K. E. Christensen, H. L. Anderson, *Angew. Chem. Int. Ed.* **60**, 5941–5947 (2021).
17. C. L. Cook, E. R. H. Jones, M. C. Whiting, *J. Chem. Soc.* 2883–2891 (1952).
18. D. J. Cram, M. E. Tanner, R. Thomas, *Angew. Chem. Int. Ed.* **30**, 1024–1027 (1991).
19. R. Warmuth, *Angew. Chem. Int. Ed.* **36**, 1347–1350 (1997).
20. C. W. Patrick *et al.*, *Nat. Chem.* **16**, 193–200 (2024).
21. C. W. Patrick *et al.*, *Angew. Chem. Int. Ed.* **61**, e202116897 (2022).
22. S. L. Woltering, P. Gawel, K. E. Christensen, A. L. Thompson, H. L. Anderson, *J. Am. Chem. Soc.* **142**, 13523–13532 (2020).
23. D. R. Kohn, P. Gawel, Y. Xiong, K. E. Christensen, H. L. Anderson, *J. Org. Chem.* **83**, 2077–2086 (2018).
24. L. D. Movsisyan *et al.*, *J. Am. Chem. Soc.* **138**, 1366–1376 (2016).
25. L. D. Movsisyan *et al.*, *Org. Lett.* **14**, 3424–3426 (2012).
26. N. Weisbach, Z. Baranová, S. Gauthier, J. H. Reibenspies, J. A. Gladysz, *Chem. Commun.* **48**, 7562–7564 (2012).
27. R. Antkowiak, W. Z. Antkowiak, *Heterocycles* **47**, 893–909 (1998).
28. Y. Segawa *et al.*, *Science* **365**, 272–276 (2019).
29. W. A. Chalifoux, R. R. Tykwinski, *Nat. Chem.* **2**, 967–971 (2010).
30. A. Spantulescu, T. Luu, Y. Zhao, R. McDonald, R. R. Tykwinski, *Org. Lett.* **10**, 609–612 (2008).
31. M. Kreuzahler, A. Adam, G. Haberhauer, *Chemistry* **25**, 12689–12693 (2019).
32. H. Siera, S. Mehrparvar, J. Fax, M. Kreuzahler, G. Haberhauer, *Angew. Chem. Int. Ed.* **62**, e202301465 (2023).
33. M. Bednarz, P. Reineker, E. Mena-Osteritz, P. Bäuerle, *J. Lumin.* **110**, 225–231 (2004).
34. M. Hoffmann *et al.*, *Angew. Chem. Int. Ed.* **47**, 4993–4996 (2008).
35. B. M. Wong, *J. Phys. Chem. C Nanomater. Interfaces* **113**, 21921–21927 (2009).
36. H. Tabata, M. Fujii, S. Hayashi, T. Doi, T. Wakabayashi, *Carbon* **44**, 3168–3176 (2006).
37. Y. Gao, R. R. Tykwinski, *Acc. Chem. Res.* **55**, 3616–3630 (2022).
38. Y. Gao *et al.*, *Nat. Chem.* **12**, 1143–1149 (2020).
39. N. R. Agarwal *et al.*, *J. Raman Spectrosc.* **44**, 1398–1410 (2013).
40. Z. Liu, T. Lu, Q. Chen, *Chem. Asian J.* **16**, 56–63 (2021).
41. T. Lu, Z. Liu, Q. Chen, *Chin. Phys. B* **31**, 126101 (2022).
42. G. Porter, J. I. Steinfeld, *J. Chem. Soc. A* **877–878**, 877 (1968).
43. G. Dauvergne *et al.*, *J. Org. Chem.* **87**, 11141–11147 (2022).
44. I. Rončević, DFT output files for stabilization of a cyclocarbon by catenane formation, Zenodo (2025); https://doi.org/10.5281/zenodo.15241185.
45. Y. Gao, P. Gupta, H. L. Anderson, Experimental NMR spectroscopy data of the paper "Solution-phase stabilization of a cyclocarbon by catenane formation", Zenodo (2025); https://doi.org/10.5281/zenodo.15615121.

ACKNOWLEDGMENTS

We thank V. Mikhailov for mass measurements and A. Rubio and M. Vitek for discussions. **Funding:** European Research Council grant 885606, ARO-MAT (H.L.A., Y.G.); European Commission Horizon 2020 grant project 101019310 CycloCarbonCatenane (Y.G., H.L.A.); UKRI Horizon Europe Guarantee MSCA Postdoctoral Fellowship EIDelPath, EP/X030075/1 (I.R., H.L.A.). Computational resources were provided by Cirrus UK National Tier-2 HPC Service at EPCC (http://www.cirrus.ac.uk), funded by the University of Edinburgh and EPSRC (EP/P020267/1); Ministry of Education, Youth, and Sports of the Czech Republic through the e-INFRA CZ (ID 90140). **Author contributions:** Conceptualization: H.L.A., Y.G., P.G.; Experimental work: Y.G., P.G.; Theoretical analysis and computational simulations: I.R.; Mass spectrometry: P.J.G.; Raman spectroscopy: A.W.P., Y.G.; NMR spectroscopy: C.M., Y.G.; Writing: All authors. **Competing interests:** The authors declare that they have no competing interests. **Data and materials availability:** All experimental data are reported in the main text and supplementary materials (*44*, *45*).

License information: Copyright © 2025 the authors, some rights reserved; exclusive licensee American Association for the Advancement of Science. No claim to original US government works. https://www.science.org/about/science-licenses-journal-article-reuse.

This research was funded in whole or in part by European Commission Horizon 2020 (grant project 101019310 CycloCarbonCatenane) and UKRI Horizon Europe (MSCA Postdoctoral Fellowship EIDelPath, EP/X030075/1), cOAlition S organizations, and by the European Research Council (grant 885606). The author will make the Author Accepted Manuscript (AAM) version available under a CC BY public copyright license.

SUPPLEMENTARY MATERIALS

science.org/doi/10.1126/science.ady6054
Materials and Methods; Supplementary Text; Figs. S1 to S66; References (*46*–*51*)

Submitted 28 April 2025; accepted 18 June 2025

10.1126/science.ady6054

METHANOGENESIS

Modulation of methyl-coenzyme M reductase expression alters the isotopic composition of microbial methane

Jonathan Gropp[1,2], Markus Bill[3], Max K. Lloyd[4], Rebekah A. Stein[1]†, Dipti D. Nayak[2,5]*‡, Daniel A. Stolper[1]‡

The stable isotopic composition of microbial methane varies substantially, and the underlying causes are debated. In this work, we experimentally controlled the abundance of the central enzyme in methanogenesis, methyl–coenzyme M reductase (MCR), in *Methanosarcina acetivorans* and tested whether its cellular concentration alters methane isotopic compositions. We found that during growth on methanol and acetate, lowering the expression of *mcr* increases the degree of hydrogen isotope exchange between methane and water. Using an isotope-enabled model of methanogenesis, we found that these changes result from an increase in reversibility of enzymes involved in the oxidation of the substrate methyl group. This result indicates that methane produced from organic compounds can deviate from commonly assumed pathway-specific isotope effects, with implications for the interpretation of environmentally relevant methane sources.

Methane is a potent greenhouse gas and energy resource that is generated mostly through low-temperature microbial methanogenesis and high-temperature catagenesis of organic matter. The stable carbon ($^{13}C/^{12}C$) and hydrogen (D/H) isotopic compositions of methane sources vary substantially and, as such, are commonly used to fingerprint gas origins [e.g., (*1*–*5*)] (Fig. 1A). We focus here on the variability in the isotopic composition of microbial methane, which for the past half century was generally assumed to be set by the specific metabolic pathway of methanogenesis (e.g., from H_2 and CO_2, acetate, or methylated compounds) due to irreversible, pathway-specific kinetic isotope effects (*1*) (Fig. 1B). We term this the "substrate hypothesis."

Substrate concentrations are also known to correlate with methane isotopic compositions (*6*, *7*). Specifically, microbial methane derived from environments with low substrate availability (e.g., deep-sea sediments) often has carbon and hydrogen isotopic compositions consistent with formation in isotopic equilibrium with both CO_2 and H_2O, and in equilibrium among the methane isotopologues (*8*–*10*). By contrast, environments with higher substrate availability (e.g., wetlands and laboratory cultures) yield methane in isotopic disequilibrium both with substrates and among the methane isotopologues [e.g., (*4*, *6*, *11*, *12*)]. The observed relationship between substrate concentration and methane isotopic composition is hypothesized to be governed by the degree of reversibility of the methanogenic pathway, that is, the relative ratio of the reverse and forward flux of enzymes (*6*, *7*, *13*–*16*). Per this "reversibility hypothesis," as substrate concentrations decrease, the free-energy gradient available in the environment for methanogenesis (ΔG) approaches low absolute values, promoting equilibrium conditions and leading to high enzymatic reversibility. This reversibility is expressed by increased isotopic exchange between methane and water-derived hydrogen (Fig. 1, C and D) and CO_2-derived carbon. As substrate concentrations increase, the ΔG gradient increases, and the system approaches fully irreversible conditions expressed by isotopic disequilibrium in methane (Fig. 1B).

Until recently, experimental evidence for the reversibility hypothesis was limited (*6*, *7*, *17*, *18*), which led some researchers to propose that the near-equilibrium isotopic signatures of microbial methane in substrate-limited environments might instead arise from anaerobic methanotrophs (*19*–*22*). Recently, Mayumi *et al.* (*16*) grew hydrogenotrophic methanogens (i.e., methanogens that grow on H_2 and CO_2) in coculture with acetate-oxidizing bacteria in the laboratory at high hydrostatic pressures and observed that they produce methane that is close to isotopic equilibrium with CO_2 (for carbon) and H_2O (for hydrogen). They interpreted these results in the context of the reversibility hypothesis and proposed that by increasing methane solubility through the high hydrostatic pressures, the ΔG gradient available for methanogenesis was reduced sufficiently to induce enzymatic reversibility. They further proposed that isotopic disequilibrium in shallow surface environments, such as terrestrial environments (Fig. 1A), stems from growth at lower hydrostatic pressures. Most prior work on the reversibility hypothesis has focused on comparing hydrogenotrophic methanogens at high substrate concentrations in a laboratory with those in substrate-limited deep-sea sediments and coalbed systems [e.g., (*10*, *14*, *15*)]. By contrast, most of the biogenic methane emitted to the atmosphere is generated by methanogens found in terrestrial ecosystems that use organic compounds such as acetate or methanol (*23*, *24*). The processes that control enzymatic reversibility in this key group of methanogens are not nearly as well constrained theoretically or experimentally as those for hydrogenotrophic methanogens.

To rectify this gap, we explicitly explored the reversibility hypothesis in a methanogen that grows on acetate and methanol. We evaluated this hypothesis by controlling the expression of the key and final enzyme of methanogenesis—methyl–coenzyme M reductase (MCR) (*25*)—and by studying its effect on the isotopic composition of the methane produced. This approach differs from prior work where the ΔG of methanogenesis was set by modulating substrate or product concentrations (*6*, *7*, *16*–*18*). We took this enzyme-centered experimental approach because it is well known that changes in growth conditions (e.g., substrate or product concentration, temperature, or pressure) often induce physiological responses that modulate enzyme activity and metabolite pools, which, in turn, modify enzymatic reversibility (*26*).

Isotopic approach for determining enzymatic reversibility of methanogenesis

We controlled the expression of the chromosomal MCR operon (*mcr*) in a mutant *Methanosarcina acetivorans* strain using the tetracycline-inducible expression platform (*27*, *28*). Controlled changes in *mcr* expression levels induce a global transcriptomic response and, at sufficiently low tetracycline concentrations, limit methanogenic growth (*28*). We tested for changes in the reversibility of methanogenesis as a function of *mcr* expression by measuring the hydrogen isotopic composition of methane, $\delta D\text{-}CH_4$ {$\delta D = 1000 \times ([D]/[H]_{sample}/[D]/[H]_{reference} - 1)$ in per mil (‰)}, during growth on the environmentally relevant substrates methanol and acetate. This method provides a straightforward measure of isotope exchange and thus enzymatic reversibility: Under fully irreversible conditions, three hydrogens of methane are derived from the substrate methyl group and one comes from water (*29*, *30*) (Fig. 1B). Conversely, higher pathway reversibility increases the amount of water-derived hydrogen in methane, resulting in a change in $\delta D\text{-}CH_4$ (Fig. 1, C and D). We constrained the relative

[1]Department of Earth and Planetary Science, University of California, Berkeley, Berkeley, CA, USA. [2]Department of Molecular and Cell Biology, University of California, Berkeley, Berkeley, CA, USA. [3]Energy Geosciences Division, Lawrence Berkeley National Laboratory, Berkeley, CA, USA. [4]Department of Geosciences, Pennsylvania State University, University Park, PA, USA. [5]Department of Plant and Microbial Biology, University of California, Berkeley, Berkeley, CA, USA. ***Corresponding author. Email: dnayak@berkeley.edu** †Present address: Travertine Technologies, Boulder, CO, USA. ‡These authors contributed equally to this work.

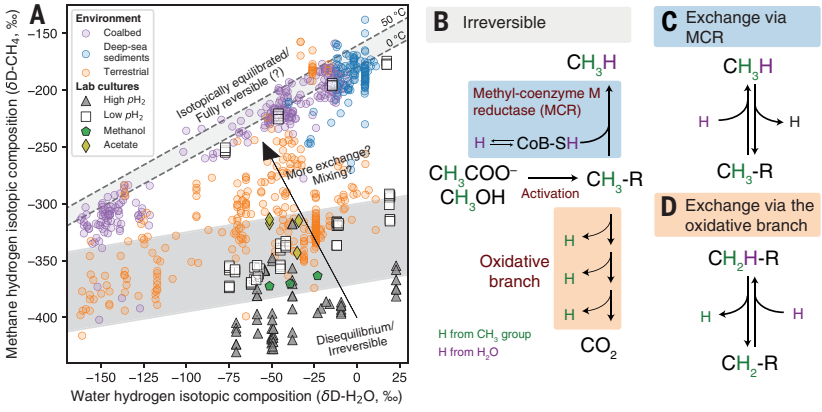

Fig. 1. Hydrogen isotopic exchange during methanogenesis. (**A**) Hydrogen isotopic compositions of biogenic methane and water. The light gray shaded area represents the CH_4-H_2O hydrogen isotopic equilibrium between 0° and 50°C (*10*). The dark gray shaded area represents the end members for methanogenic growth on organic substrates such as acetate or methanol, where the methane is derived from the methyl group [based on (*1*)]. The arrow presents processes by which points between these end members could form through either mixing of the end members or variations in degrees of isotopic exchange between methane and water (*10*,*15*,*16*). Data are taken from previous compilations (*10*). We include data from prior experiments for acetoclastic and methylotrophic growth but note that the δD-CH_4 from such experiments (unlike hydrogenotrophic cultures) depends not only on δD-H_2O but also on the δD of the methyl source. (**B**) A schematic representation of irreversible methylotrophic methanogenesis (on methanol) and acetoclastic methanogenesis (on acetate). The hydrogen atoms are colored by their source (methyl-derived hydrogen is green, and water-derived hydrogen is purple). (**C** and **D**) Potential hydrogen exchange reactions with water during CH_3-R reduction to methane by MCR (C) or during CH_3-R oxidation through the oxidative branch (D). Reversible reactions replace methyl-derived hydrogen (green) in methane with water-derived hydrogen (purple). CoB, Coenzyme B (7-mercaptoheptanoylthreonine phosphate).

change in reversibility for growth at different tetracycline concentrations by varying the hydrogen isotope contrast between the methyl group in the substrate and the water in the growth-medium. The larger the initial contrast, the greater the change in the hydrogen isotopic composition of methane for a given amount of enzymatic reversibility.

Lowering *mcr* expression decreases growth rates and increases enzymatic reversibility

We observed that for growth on both methanol and acetate, lowering expression of *mcr* relative to wild-type (WT) levels systematically changed δD-CH_4. Specifically, in a plot of δD-CH_4 versus δD-H_2O (Fig. 2, A and B), as the expression of *mcr* decreased, the slope increased and the *y* intercept decreased. We also observed a decrease in growth rates at low tetracycline concentrations (<10 μg/ml), consistent with prior work (*28*) (Fig. 2C, figs. S2 and S3, and table S1). As such, growth rate also correlated with changes in δD-CH_4. Also consistent with prior work, growth transitioned from exponential to linear at the end of experiments for growth on 0 μg/ml tetracycline on methanol and 1 μg/ml tetracycline on acetate. This was due to the extreme limitation of *mcr* in these treatments. Calculated growth rates for these specific experiments only included the exponential portions of the growth curves [see supplementary materials (SM)]. Although absolute specific growth rates were up to 10 times lower on acetate than on methanol (Fig. 2C), the relationship between relative growth rates (i.e., the ratio of the growth rate of the mutant strain at a given tetracycline concentration to the growth rate of the WT strain, on a given substrate) and slopes of δD-CH_4 versus δD-H_2O (which we used as a measure of the isotopic response) were similar (Fig. 2D). We return to these relationships in the next sections.

The observed changes in δD-CH_4 can be explained either by changes in enzymatic reversibility, which alter the extent of hydrogen isotope exchange between methyl groups and water, or by changes in the expressed (unidirectional) kinetic isotope effects of the enzymes that happen to correlate with *mcr* expression levels. We ruled out the latter because the specific enzymes used for methanogenesis do not change with changes in *mcr* expression (*28*), and, as such, their intrinsic isotope effects should be conserved. Therefore, we propose and proceeded with the interpretation that lowering the expression of *mcr* changes the reversibility of the core methanogenic pathway.

The oxidative branch exchanges hydrogen isotopes between water and the methylated precursor of methane

To interpret our results quantitatively, we developed isotope-enabled models of methanogenesis on methanol and acetate (see SM for details). The models include the following key steps of methanogenesis (Fig. 3, A and B): (i) substrate activation to a methylated precursor (CH_3-R), (ii) CH_3-R reduction to methane by MCR, (iii) CH_3-R oxidation (through the oxidative branch of methanogenesis) to generate electrons for methane production on methanol or metabolites and electrons for anabolic reactions on acetate (*31*), and (iv) conversion of CH_3-R to biomass. The relative fluxes of CH_3-R to the reductive and oxidative branches and to biomass are shown in Fig. 3, A and B. As detailed in the SM, we first calibrated the enzymatic kinetic isotope effects based on the WT experiments. Next, we fit the δD-CH_4 versus δD-H_2O data for each *mcr* expression treatment by assuming that the enzymatic kinetic isotope effects are constant across substrates and treatments and that the only variable parameter is the reversibility of a given enzymatically catalyzed step.

We present the model fits using normalized δD-CH_4 data by subtracting the corresponding δD-CH_4 of a treatment versus the WT condition and denote it as Δδ D-CH_4 (experiment minus WT at a given δD-H_2O) (Fig. 3, C and D). The model fits for a given *mcr* expression level yielded two related parameters: (i) the amount of water-derived hydrogen in the methane from the oxidative branch and MCR above the 25% minimum from the final hydrogen addition by MCR to CH_3-R (Figs. 1B and 3, E and F) and (ii) the reversibility of MCR and the oxidative branch (Fig. 3, G and H). We note that our parameterization of the oxidative branch assumes that the reversibility (r) of the three distinct hydrogen isotope-exchange reactions are the same and combines them into one net reversibility term (r_{net}) (Fig. 3, A and B). Following (*32*), r_{net} is calculated as the average reversibility across all three steps: $r_{net} = 1/3(r^3 + r^2 + r)$.

For growth on methanol, we found that lowering *mcr* expression increased the percentage of water-derived hydrogens from the oxidative branch from 1 to 11%, whereas MCR always contributed ≤1% (Fig. 3E; see figures for uncertainties). Accordingly, the reversibility of the oxidative branch increased from 0.05 for WT expression levels to up to 0.39 at the lowest *mcr* expression level (Fig. 3G). By contrast, MCR reversibility remained low throughout (maximum reversibility of 0.02; Fig. 3G). These results are also visually apparent in the δD-CH_4 versus δD-H_2O trends. Specifically, based on the methanol and water isotopic compositions used, increasing MCR reversibility rotates and pivots the δD-CH_4 versus δD-H_2O slope toward CH_4-H_2O isotopic equilibrium (fig. S4A), whereas changes in oxidative branch reversibility rotate the slope and decrease the intercept (fig. S4B) but do not allow for complete isotopic equilibration. The latter rotation and intercept decrease occurred in our data (Figs. 2, A and B, and 3, C and D), demonstrating visually that changes in the reversibility of the oxidative branch underlie the observed isotopic changes.

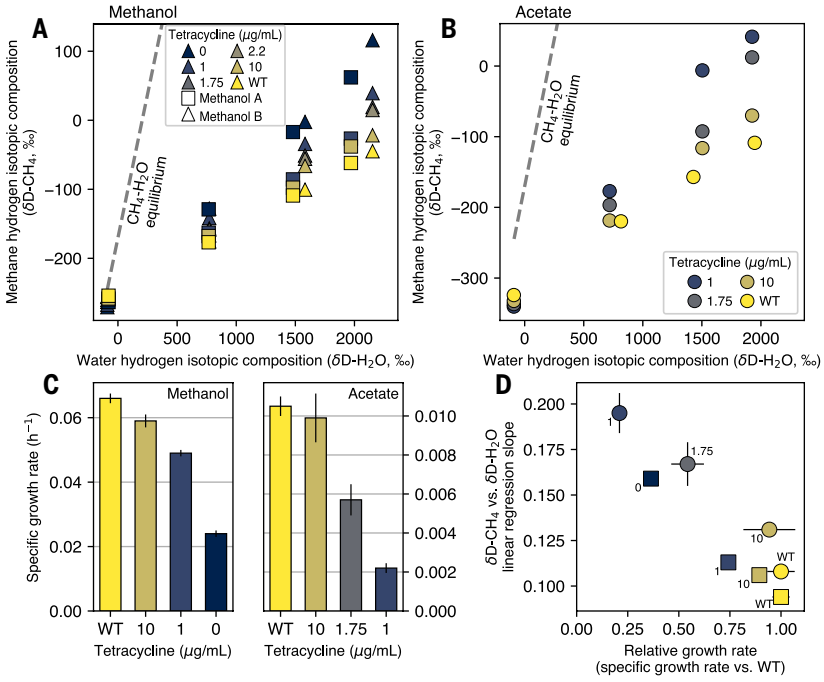

Fig. 2. The hydrogen isotopic composition of methane and growth rate depend on *mcr* expression. (**A** and **B**) The relationship between δD of methane and source water during growth on different tetracycline concentrations that correspond to different concentrations of MCR in vivo during growth on methanol (A) and acetate (B). Note that two different sets of methanol growth experiments were conducted (denoted by Methanol A and Methanol B, with initial methanol concentrations of 60 and 125 mM, respectively). The gray dashed line denotes CH_4-H_2O hydrogen isotopic equilibrium at a growth temperature of 37°C (*39*). (**C**) The specific growth rates of the WT strain and the mutant strain with tetracycline-inducible *mcr* expression at different tetracycline concentrations as indicated (error bars represent mean ± SE of four biological replicates). Specific growth rates on methanol were measured only for the methanol A experiments. Some cultures (0 μg/ml tetracycline on methanol and 1 μg/ml tetracycline on acetate) exhibited linear growth after a few doublings (figs. S2 and S3). Specific growth rates were calculated during exponential growth for these cultures. (**D**) The slopes of the linear regression of δD of methane versus H_2O for methanol [from (A); in squares] and acetate [from (B); in circles] plotted against the relative growth rates, which represent the specific growth rate at a given tetracycline concentration relative to that of the WT strain on that substrate. Error bars of the linear regression slopes and the growth rates represent 1 standard error.

The model makes an explicit and testable prediction for the carbon isotopic composition of methane ($\delta^{13}C$-CH_4) during growth on methanol. As described in the SM, we predicted that under our experimental conditions, increased reversibility in MCR would cause $\delta^{13}C$-CH_4 to increase, whereas increased reversibility for the oxidative branch would cause $\delta^{13}C$-CH_4 to decrease. The differences stem from the contributions of equilibrium and kinetic isotope effects to $\delta^{13}C$-CH_4 in the two branches. We observed that $\delta^{13}C$-CH_4 decreased by up to 5.5‰ as *mcr* transcript levels decreased (fig. S5). These data thus provide independent evidence that decreasing *mcr* expression increases the reversibility of the oxidative branch but not MCR.

We now turn to the experiments for growth on acetate. Although graphical depictions of acetoclastic methanogenesis commonly omit the oxidative branch, it is essential during growth on acetate, especially in minimal growth medium (as used here), because it generates redox equivalents and intermediates for anabolic reactions (*31*, *33*). Its inclusion in our model is critical because it, along with MCR, can catalyze hydrogen isotope exchange reactions (*34*). We assumed that between 1 and 5% of acetate methyl groups enter the oxidative branch. We used a range for this flux because it is not presently well constrained (see SM for more details) but must be less than the maximum measured flux of acetate methyl groups to biomass [~7%; (*35*)] (Fig. 3B). As we explain later in this paragraph, the magnitude of this flux in the model does not set the amount of water-derived hydrogen but does influence the estimated degree of reversibility in the pathway. Based on these assumptions, we found that lowering *mcr* expression caused the percentage of water-derived hydrogens in methane from the oxidative branch to increase from 2 to 13%, whereas MCR always contributed <1% (recall that this is in addition to the minimum 25% from the final hydrogen addition by MCR to CH_3-R). We show in Fig. 3H that these results are independent of the chosen flux of methyl groups through the oxidative branch (also see fig. S6). As formally shown in the SM, this independence is expected because the measured changes in δD-CH_4 versus δD-H_2O are directly controlled by the amount of water-derived hydrogen incorporated into methane. By contrast, the reversibility of the oxidative branch does depend on this flux because lower fluxes require higher reversibility to incorporate a given amount of water-derived hydrogen into methane and vice versa. Importantly, for a given specified flux through the oxidative branch, we found that oxidative branch reversibility increased with decreasing *mcr* expression, whereas MCR reversibility stayed low. Specifically, oxidative branch reversibility increased from 0.35 to 0.79 with decreasing *mcr* expression at a 5% flux and from 0.73 to 0.95 at a 1% flux (Fig. 3H). MCR reversibility remained <0.01 for all cases.

Finally, during growth on acetate, $\delta^{13}C$-CH_4 stayed effectively constant (<1.5‰ difference) across all levels of *mcr* expression (fig. S5). These data are consistent with our model if exchange occurs mostly in the more reduced intermediates of the oxidative branch, preventing expression of carbon isotope exchange (see SM).

Bioenergetic basis for changes in the isotopic composition of methane

The key finding of this study is that by lowering *mcr* expression, we controllably and systematically increased the degree of hydrogen isotope exchange between methane and water during growth on both acetate and methanol. Based on the results of our metabolic model, this is accomplished through increased reversibility of the enzymes involved in the oxidative branch of methanogenesis and not MCR. From a thermodynamic perspective, changes in enzymatic reversibility ultimately result from changes in ΔG gradients across the various enzymatically controlled reactions (*13*). When we lowered the expression of *mcr*, the cellular levels of MCR changed relative to other enzymes of the methanogenic pathway, including many of the enzymes involved in the oxidative branch [(*28*); fig. S7]. Such changes independently support our finding of changes in oxidative branch reversibility based on the isotopic measurements. Regardless, changes in relative enzyme concentrations would alter the pool size of metabolic intermediates in the methanogenic pathway. These changed metabolite concentrations are expected to alter ΔG gradients across enzymatically catalyzed steps (*26*), thereby changing the enzymatic reversibility of methanogenesis.

A fundamental question that arises from our work is why did lowering the expression of *mcr* lead to changes in the reversibility of the oxidative branch but not MCR? We hypothesize that this is due to differences in the bioenergetics of the reactions. Specifically, the oxidative branch has a smaller standard ΔG ($\Delta G'^0$) than MCR ($\Delta G'^0$ of −6 versus −25 kJ/mol, respectively) (table S6). Given these $\Delta G'^0$ values, relatively small changes in metabolite concentrations in the oxidative branch allow for large changes in enzymatic reversibility. Conversely, larger changes in metabolite concentrations are required to change enzymatic reversibility in MCR, which likely did not occur in our

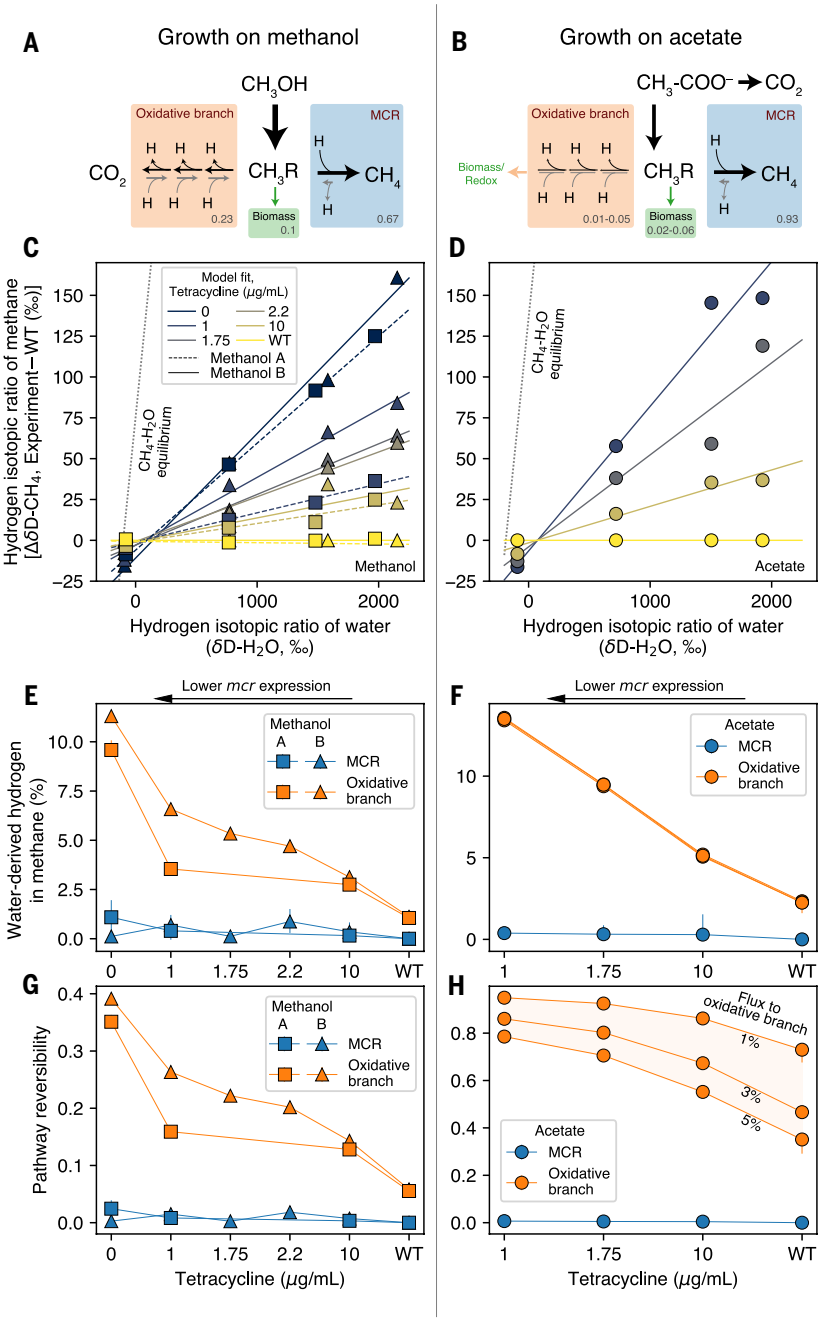

Fig. 3. Estimated degree of hydrogen isotope exchange depends on *mcr* expression. Hydrogen isotopic exchange pathways for methanogenic growth on (**A**) methanol or (**B**) acetate. Numbers at the bottom right corners of the colored boxes correspond to the relative amount of methyl groups going through MCR, through the oxidative branch, or to biomass. (**C** and **D**) Model results for different levels of *mcr* expression (Methanol A and B are the same as in Fig. 2A; symbols are the same as in Fig. 2, A and B). (**E** and **F**) The water-derived hydrogen atom content in methane from the oxidative branch (orange symbols) and MCR (blue symbols) for different levels of *mcr* expression. The values are for hydrogens in addition to the 25% contributed during irreversible methanogenesis through MCR. (**G** and **H**). The calculated reversibility for MCR (blue symbols) and the oxidative branch (orange symbols) for different levels of *mcr* expression. The orange lines in (F) and (H) represent a flux of methyl groups through the oxidative branch of 1, 3, and 5% during growth on acetate. These lines collapse on each other in (F) for growth on acetate but do not in (H). The modeled ratio of methyl groups in the oxidative branch to methyl groups in the reductive branch during growth on methanol is always kept at 0.25:0.75. The error bars represent the 95% range of the model results.

experiments (fig. S8). Thus, although we did not change the overall ΔG gradient available to cells through changes in substrate concentration, by modifying *mcr* expression, we likely induced changes in the distribution of that ΔG between the methyl reduction and methyl oxidation steps due to intrinsic thermodynamic constraints (Fig. 1, B to D). These observations demonstrate how the bioenergetics of individual enzymes in methanogenesis, as constrained by the environmental ΔG available, control the isotopic composition of methane.

Finally, in addition to enzymatic reversibility, the ΔG available to methanogens is expected to also control cell-specific growth and methane production rates (*14*, *15*), with higher ΔG inducing faster rates for both. As such, it is reasonable to expect that growth rate, enzymatic reversibility, and methane isotopic compositions will be correlated in our experiments. Indeed, we observed this: As we lowered *mcr* expression, growth rates decreased, whereas isotope exchange rates with water increased. When changes in relative growth rates are compared with oxidative branch reversibility, experiments on methanol and acetate exhibit similar relationships (Fig. 2D and fig. S9), despite up to a 10 times difference in absolute growth rates. Based on these shared responses in relative growth rate, enzyme reversibility, and methane isotopic compositions, we proceed with the hypothesis that our results can be extended, at least qualitatively, to the environment.

Connection to the biogeochemistry of environmental methanogenesis

This work is important for the interpretation of the isotopic composition of environmental methane emitted to the atmosphere, especially from terrestrial systems (e.g., lakes, wetlands, rumens, rice paddies, etc.), which represent ≈70% the of the total methane flux emitted to the atmosphere (*24*). Consequently, a fundamental understanding of the mechanisms that set the isotopic composition of terrestrial methane emissions is critical for quantifying and predicting future trends of the global methane budget (*24*). As discussed earlier, the isotopic composition of terrestrial methane is commonly assumed to be set by the relative contributions of hydrogenotrophic and acetoclastic methanogens, with the assumption that the individual pathways exhibit different (fully irreversible) kinetic isotope effects [e.g., (*36*, *37*)]. By contrast, our experimental work shows that enzymatic reversibility also plays a role in setting the isotopic composition during growth on acetate and methanol.

Beyond our experiments, and from a thermodynamic perspective, we consider enzymatic reversibility to be potentially important in setting the isotopic composition of methane in terrestrial environments. These environments have smaller ΔG gradients available for methanogenesis relative to lab settings, where enzymes are assumed to be largely irreversible, but have higher ΔG gradients than deep subsurface environments, which are assumed to be largely reversible [e.g., (*38*); Figs. 1A and 4). Under such conditions, we propose that the ΔG gradient causes MCR to be wholly or partially irreversible (creating the disequilibrium isotopic signal in Fig. 1A), but ΔG gradients are sufficiently small that the enzymes of the oxidative branch are partially or completely reversible (Fig. 4). The patterns of isotopic exchange would

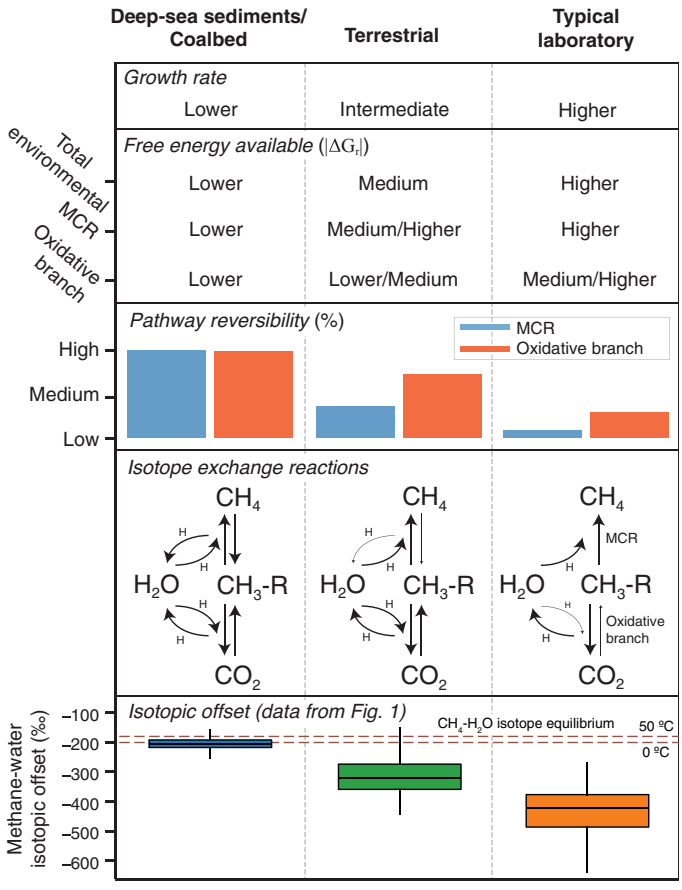

Fig. 4. Degree of free-energy availability influences pathway-specific reversibility, growth rate, and methane isotopic composition. A conceptual illustration of factors that control how ΔG changes the reversibility of enzymatically catalyzed isotope-exchange reactions and growth rate. The total environmental ΔG available to methanogenesis is distributed among the reactions in the methanogenic pathway. Based on the standard ΔG of the reactions, the oxidative branch is expected to have a lower fraction of ΔG available relative to MCR. The isotopic offset (bottom panel) for data points in Fig. 1A is shown as $1000*\ln{}^{D}\alpha$, where ${}^{D}\alpha = (1000 + \delta D\text{-}CH_4)/(1000 + \delta D\text{-}H_2O)$. The box-and-whisker plots of compiled data (*10*) are given along with the values expected for equilibrium at 50° and 0°C, where the center line represents the median, box limits are upper and lower quartiles, and whiskers are minimum and maximum values. In the isotopic exchange reactions, lighter-weight arrows indicate more limited exchange relative to heavier-weight arrows.

vary depending on the ΔG available, which could explain the large range of values observed in the hydrogen isotopic composition of terrestrial methane at a given water isotopic composition seen in the environment. More isotopic exchange would move samples toward the isotopic equilibrium line, and less exchange would move samples farther from it (see arrow in Fig. 1A). We thus propose that enzymatic reversibility (governed by the ΔG available) along with substrate-specific effects should be considered together in the study of methane from terrestrial systems and similar environments that display methane in isotopic disequilibrium.

Finally, our work provides a framework to integrate environmental factors with the physiology of methanogens to better understand the processes that set the isotopic composition of biogenic methane. Specifically, we propose that environmental properties such as temperature, pressure, substrate availability, and isotopic signatures are linked through the partitioning of the available ΔG gradient in the environment across different enzymatic steps in methanogenesis (Fig. 4). Thus, it is the cellular response of a methanogen to environmental constraints that, in a coupled fashion, determines the enzymatic reversibility, growth rate, and isotopic composition of the methane.

REFERENCES AND NOTES

1. M. J. Whiticar, *Chem. Geol.* **161**, 291–314 (1999).
2. Y. Ueno, K. Yamada, N. Yoshida, S. Maruyama, Y. Isozaki, *Nature* **440**, 516–519 (2006).
3. C. R. Webster, P. R. Mahaffy, *Planet. Space Sci.* **59**, 271–283 (2011).
4. P. M. J. Douglas, E. Stratigopoulos, S. Park, D. Phan, *Biogeosciences* **18**, 3505–3527 (2021).
5. M. Menoud *et al.*, *Earth Syst. Sci. Data* **14**, 4365–4386 (2022).
6. D. L. Valentine, A. Chidthaisong, A. Rice, W. S. Reeburgh, S. C. Tyler, *Geochim. Cosmochim. Acta* **68**, 1571–1590 (2004).
7. H. Penning, C. M. Plugge, P. E. Galand, R. Conrad, *Glob. Change Biol.* **11**, 2103–2113 (2005).
8. D. A. Stolper *et al.*, *Science* **344**, 1500–1503 (2014).
9. J. J. Jautzy, P. M. J. Douglas, H. Xie, J. M. Eiler, I. D. Clark, *Earth Planet. Sci. Lett.* **562**, 116841 (2021).
10. A. C. Turner *et al.*, *Geochim. Cosmochim. Acta* **314**, 223–269 (2021).
11. D. T. Wang *et al.*, *Science* **348**, 428–431 (2015).
12. D. A. Stolper *et al.*, *Geochim. Cosmochim. Acta* **161**, 219–247 (2015).
13. D. A. Beard, H. Qian, *PLOS ONE* **2**, e144 (2007).
14. S. Ono, J. H. Rhim, E. C. Ryberg, *Geochim. Cosmochim. Acta* **325**, 296–315 (2022).
15. J. Gropp, Q. Jin, I. Halevy, *Sci. Adv.* **8**, eabm5713 (2022).
16. D. Mayumi *et al.*, *Science* **386**, 1372–1376 (2024).
17. T. Okumura *et al.*, *Prog. Earth Planet. Sci.* **3**, 14 (2016).
18. J. H. Rhim, S. Ono, *Geochim. Cosmochim. Acta* **335**, 383–399 (2022).
19. S. Scheller, M. Goenrich, R. K. Thauer, B. Jaun, *J. Am. Chem. Soc.* **135**, 14975–14984 (2013).
20. J. J. Marlow *et al.*, *MSphere* **2**, e00309-17 (2017).
21. G. Wegener, J. Gropp, H. Taubner, I. Halevy, M. Elvert, *Sci. Adv.* **7**, eabe4939 (2021).
22. J. Liu *et al.*, *Geochim. Cosmochim. Acta* **348**, 165–186 (2023).
23. R. Conrad, *Pedosphere* **30**, 25–39 (2020).
24. M. Saunois *et al.*, *ESSD* **17**, 1873–1958 (2025).
25. R. K. Thauer, A.-K. Kaster, H. Seedorf, W. Buckel, R. Hedderich, *Nat. Rev. Microbiol.* **6**, 579–591 (2008).
26. B. A. Wing, I. Halevy, *Proc. Natl. Acad. Sci. U.S.A.* **111**, 18116–18125 (2014).
27. A. M. Guss, M. Rother, J. K. Zhang, G. Kulkarni, W. W. Metcalf, *Archaea* **2**, 193–203 (2008).
28. G. L. Chadwick, G. A. Dury, D. D. Nayak, *Appl. Environ. Microbiol.* **90**, e0222023 (2024).
29. M. J. Pine, H. A. Barker, *J. Bacteriol.* **71**, 644–648 (1956).
30. M. J. Pine, W. Vishniac, *J. Bacteriol.* **73**, 736–742 (1957).
31. P. E. Jablonski, A. A. DiMarco, T. A. Bobik, M. C. Cabell, J. G. Ferry, *J. Bacteriol.* **172**, 1271–1275 (1990).
32. W. Wiechert, *Biophys. J.* **93**, 2255–2264 (2007).
33. A. M. Guss, B. Mukhopadhyay, J. K. Zhang, W. W. Metcalf, *Mol. Microbiol.* **55**, 1671–1680 (2005).
34. D. S. Gruen *et al.*, *Geochim. Cosmochim. Acta* **237**, 339–356 (2018).
35. K. L. Londry, K. G. Dawson, H. D. Grover, R. E. Summons, A. S. Bradley, *Org. Geochem.* **39**, 608–621 (2008).
36. J. P. Chanton, D. Fields, M. E. Hines, *J. Geophys. Res. Biogeosci.* **111**, G04004 (2006).
37. C. K. McCalley *et al.*, *Nature* **514**, 478–481 (2014).
38. J. Beer, C. Blodau, *Geochim. Cosmochim. Acta* **71**, 2989–3002 (2007).
39. J. Gropp, M. A. Iron, I. Halevy, *Geochim. Cosmochim. Acta* **295**, 237–264 (2021).

ACKNOWLEDGMENTS

Work at Lawrence Berkeley National Laboratory was funded by the US Department of Energy, Office of Science, Office of Basic Energy Sciences, Chemical Sciences, Geosciences, and Biosciences Division, under award no. DE-AC02-05CH11231. **Funding:** This work was funded by an EMBO postdoctoral fellowship (J.G.), the Institute for Environmental Sustainability (IES) (J.G.), an Alfred P. Sloan Research Fellowship sponsored by the Sloan Foundation (D.A.S., D.D.N.), the Searle Scholars Program sponsored by the Kinship Foundation (D.D.N.), a Beckman Young Investigator Award sponsored by the Arnold and Mabel Beckman Foundation (D.D.N.), a Simons Early Career Investigator in Marine Microbial Ecology and Evolution Award sponsored by the Simons Foundation (D.D.N.), a Packard Fellowship in Science and Engineering sponsored by the David and Lucile Packard Foundation (D.D.N.), and the Chan-Zuckerberg Biohub – San Francisco Investigator Program (D.D.N.). **Author contributions:** Conceptualization: J.G., D.D.N., D.A.S.; Funding acquisition: J.G., D.D.N., D.A.S.; Investigation: J.G., M.B., M.K.L., R.A.S.; Supervision: D.D.N., D.A.S.; Writing – original draft: J.G., D.D.N., D.A.S.; Writing – review & editing: J.G., M.B., M.K.L., R.A.S., D.D.N., D.A.S. **Competing interests:** The authors declare that they have no competing interests. **Data and materials availability:** All data are available in the manuscript or the supplementary materials.

License information: Copyright © 2025 the authors, some rights reserved; exclusive licensee American Association for the Advancement of Science. No claim to original US government works. https://www.science.org/about/science-licenses-journal-article-reuse

SUPPLEMENTARY MATERIALS

science.org/doi/10.1126/science.adu2098
Materials and Methods; Supplementary Text; Figs. S1 to S10; Tables S1 to S7; References (*40*–*59*); MDAR Reproducibility Checklist

Submitted 28 October 2024; accepted 16 May 2025

10.1126/science.adu2098

MANY-BODY DYNAMICS

Observation of many-body dynamical localization

Yanliang Guo[1]†, Sudipta Dhar[1]†, Ang Yang[2]†, Zekai Chen[1], Hepeng Yao[3], Milena Horvath[1], Lei Ying[2]*, Manuele Landini[1], Hanns-Christoph Nägerl[1]*

The quantum kicked rotor is a paradigmatic model system in quantum physics. As a driven quantum system, it features dynamical localization, specifically Anderson localization in momentum space. However, the interacting many-body kicked rotor is believed to break localization. Here, we present evidence for many-body dynamical localization for the Lieb-Liniger version of the many-body quantum kicked rotor. After some initial evolution, the momentum distribution of interacting quantum-degenerate bosonic atoms in one-dimensional geometry, kicked hundreds of times by means of a pulsed sinusoidal potential, stops spreading. Our results shed light on the boundary between the classical, chaotic world and the realm of quantum physics.

Chaos is a phenomenon that is found almost everywhere in our daily life, and it plays a central role in many of the sciences. Nonlinear complex systems, which appear abundantly in mathematics, physics, biology, ecology, meteorology, economics, and other fields, are generally subject to chaotic dynamics (*1*). The long-time evolution sensitively depends on the initial conditions and is inherently unpredictable. Chaos, although it has a negative connotation, is often very useful. It is intimately connected to ergodicity, and dense sampling of the available phase space drives many important processes (*2*), from thermodynamics to biology. Although the emergence of chaos in classical systems is well understood (*2*), its appearance in quantum physics and its relation to relaxation and thermalization in quantum many-body systems have been a topic of ongoing debate since the very beginnings of quantum physics (*3*, *4*). Most quantum systems do relax, though more and more systems have been identified by theory and in experiment for which ergodicity is evidently broken. Examples include many-body localized cold atoms in lattices (*5*), many-body scar states of interacting Rydberg atom arrays (*6*), and prethermalized samples of bosons in low dimensions (*7*, *8*). Central questions for quantum many-body physics are hence: What ingredients are needed to restore ergodicity? When does a drive, i.e., the pumping of energy into the system, lead to chaos and subsequently to heating? Do driven interacting many-body systems necessarily have to thermalize?

A minimal physical system to study chaotic behavior in a driven system is a rotating object periodically kicked by an external force (*9*). A transition from integrable to chaotic diffusive motion is found as the kick strength crosses a critical value. Its quantum version, known as the quantum kicked rotor (QKR) (*9*, *10*), is a paradigmatic example in which quantum coherence can prevent the system from absorbing energy even in the strong-driving regime, in stark contrast to the classical counterpart. This quantum interference–induced phenomenon can be understood as Anderson localization in momentum space (*11*–*13*). It is termed dynamical localization (DL) and has been demonstrated experimentally in dilute ultracold atomic gases (*14*–*16*).

The QKR is a highly idealized single-particle model system. Realistic systems consist of many particles that interact with each other. Interactions almost always lead to a randomization of the many-body dynamics (*17*, *18*). Driving an interacting quantum many-body system further increases the complexity. For the case of the many-body QKR, a breakdown of DL has been proposed using mean-field approaches (*19*–*21*), and indeed, recent cold-atom experiments with either weakly interacting one-dimensional (1D) (*22*) or strongly interacting 3D gases (*23*) align with these proposals. However, recent theoretical work (*24*–*28*) suggests that DL may persist in an interacting, even strongly interacting, many-body quantum system. Specifically, interacting 1D bosonic gas as an ideal Lieb-Lininger QKR is proposed to support many-body dynamical localization (MBDL). Driving a strongly correlated interacting system surprisingly may not have to result in chaotic dynamics or in a thermalized state.

Here we report the observation of MBDL in interaction-tunable 1D Bose gases. Using quantum-degenerate samples of Cs atoms, we realize the Lieb-Liniger QKR, a paradigmatic model for the simulation of driven interacting quantum many-body systems. We tune the interaction strength from the noninteracting regime to the Tonks-Girardeau (TG) regime (*29*–*32*) and find signatures of MBDL in the freezing of the momentum distribution and in the saturation of the energy and the entropy as the 1D Bose gases are kicked hundreds of times. The first-order correlation function exhibits a markedly different decay in the two limiting cases of zero and strong interactions. Our results are in agreement with recent proposals (*24*–*26*) and are captured qualitatively by our modeling.

Experimental setup and model

The experiment starts by loading a Bose-Einstein condensate (BEC) of Cs atoms (*33*) into an array of narrow 1D tubes created by a 2D optical lattice as illustrated in Fig. 1A. The laser beams forming the lattice propagate in the horizontal x-y plane at right angle to each other, and their power is adiabatically ramped up to give a lattice depth of $30E_r$, where $E_r = \pi^2\hbar^2/(2ma^2)$ is the recoil energy. Here, $a = \lambda/2 = \pi/k_L = 532.25$ nm is the lattice spacing with the wave number k_L that is set by the wavelength λ of the lattice light, and m is the atomic mass. At this depth, tunneling between the tubes is fully suppressed, and the tubes can be considered as independent 1D systems (*34*, *35*). A magnetic field B along the vertical z-direction controls the interatomic interaction (*36*) as quantified by γ, the dimensionless 1D Lieb-Liniger interaction parameter (*37*). By choosing values between $\gamma = 0$ and $\gamma = 11$, we cover the range from the noninteracting, single-particle regime well into the strongly interacting TG regime in which the bosons have fermionized. The atoms are levitated against gravity by means of a gradient of B. The finite transversal extent of the lattice beams results in weak harmonic trapping with trap frequency $\nu_z = 14.7(3)$ Hz along the tubes' direction. We partially compensate this trap by means of a horizontally propagating blue-detuned antitrap laser beam. This forms a flat-bottom potential, as illustrated in Fig. 1B. Typically, we fill about 10^4 tubes, with a weighted average of 18 atoms per tube. At this stage, the 1D systems are in equilibrium with a temperature of ~2 nK, which is estimated by the thermometry method demonstrated in (*38*, *39*). Calculated 1D density distributions $n_{1D}(z)$ for various values of γ are included in Fig. 1B.

We next implement the QKR procedure. A longitudinal standing wave with lattice spacing a and depth V_z is periodically pulsed on with period T and square-pulse duration T_p for a number of N_p pulses as illustrated in Fig. 1C. We choose $T = 60$ μs and 80 μs, $T_p = 10$ μs, and $V_z = 20E_r$, resulting in a dimensionless kick strength $K = 3.3$ and $K = 4.4$ respectively; see below and (*40*) for the definition of K. For values of N_p between 1 and 1101, the entire pulse sequence takes up to 66 and 88 ms, respectively. Figure 1D illustrates the density distribution for the many-body case during the kicking procedure. We obtain the longitudinal momentum distribution $n(k)$ using a 20-ms time-of-flight (TOF) absorption-imaging technique. A typical absorption image is shown in Fig. 1E, and $n(k)$ is obtained as a probability distribution by integration along the transversal direction and normalizing by the atom number. For a faithful

[1]Institut für Experimentalphysik und Zentrum für Quantenphysik, Universität Innsbruck, Innsbruck, Austria. [2]School of Physics and Zhejiang Key Laboratory of Micro-nano Quantum Chips and Quantum Control, Zhejiang University, Hangzhou, China. [3]DQMP, University of Geneva, Geneva, Switzerland. ***Corresponding author. Email: leiying@zju.edu.cn (L.Y.); christoph.naegerl@uibk.ac.at (H.-C.N.)** †These authors contributed equally to this work.

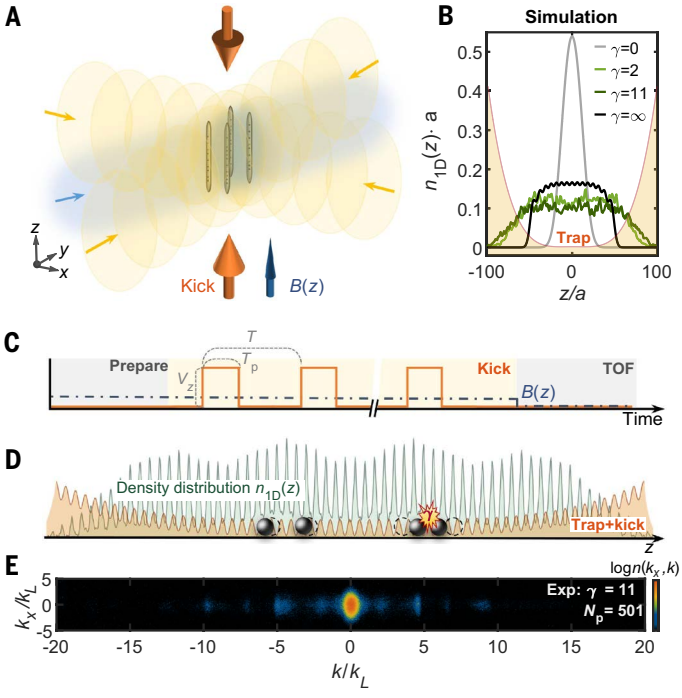

Fig. 1. Experimental implementation of MBDL. (**A**) Sketch of the 3D BEC loaded into an array of 1D tubes generated by the 2D optical lattice (yellow) and partially compensated by a blue-detuned optical anti-trap (blue). The QKR lattice propagates along the vertical *z* direction. (**B**) Calculated ground-state many-body 1D spatial density $n_{1D}(z)$ for the flat-bottom trap in units of a^{-1} for various values of the interaction parameter γ. The data for $\gamma = 2$ and $\gamma = 11$ were obtained from a quantum Monte Carlo calculation at a temperature of 2 nK, and the data for $\gamma = 0$ and $\gamma = \infty$ are the zero-temperature results from a one-cycle Floquet map and fermionization method (*32*,*40*,*42*). (**C**) Schematic of the experimental QKR sequence with N_p pulses sandwiched between the preparation and TOF-imaging procedures. (**D**) Illustration of $n_{1D}(z)$ (green) for four interacting atoms in a cosine standing-wave potential in the flat-bottom trap (orange) for $\gamma = \infty$. The anti-nodes of $n_{1D}(z)$ register with the nodes of the kick potential. The envelope of $n_{1D}(z)$ with the four bumps reflects the presence of four atoms. (**E**) Typical absorption image for $\gamma = 11$ after $N_p = 501$ kicks showing the spatial density after TOF in color coding (the detailed amplitude can be seen in the momentum distribution of Fig. 2) and integrated along the line-of-sight.

measurement of $n(k)$, the particle interaction is switched off via a Feshbach resonance's zero crossing (*36*) during TOF. From $n(k)$, we subsequently compute the kinetic energy E, the information entropy S, and the one-body correlation function $G^{(1)}$.

We model the system by the explicitly time-dependent Lieb-Liniger QKR Hamiltonian. For N interacting bosons with mass m moving in a 1D tube at zero temperature, it reads (*24*, *26*)

$$H(t)=\sum_{i=1}^{N}\left[\frac{P_i^2}{2m}+\hbar\kappa\cos\left(2k_L z_i\right)\sum_{N_p}\delta_{T_p}\left(t-N_pT\right)+V_{ext}\left(z_i\right)\right]+g_{1D}\sum_{i<j}^{N}\delta\left(z_i-z_j\right) \quad (1)$$

Here, $\hbar\kappa = V_z T_p/2$ sets the kick strength $K = 8TE_r\kappa/\hbar$. The first three terms represent the QKR for a single particle at position z_i moving in the trap potential V_{ext}. The last summand models the δ-type pairwise contact interaction whose strength g_{1D} is related to γ via $\gamma = mg_{1D}/n_{1D}\hbar^2$. Details of our modeling are given in (*40*).

Freezing of the momentum distribution

We first turn to the evolution of the momentum distribution as N_p is increased. Figure 2 presents the experimental results of $n(k)$ for two limiting values of the interaction strength, namely for vanishing ($\gamma = 0$) and for very strong interactions ($\gamma = 11$). In the former case, the system is in the single-particle regime; in the latter, it is deeply in the TG regime. Starting with the first kick, higher-momentum states are populated, primarily the ones with $\pm 2\hbar k_L$. For the noninteracting case, some of the population is subsequently transferred to higher-momentum states, but eventually further transfer is halted and the distribution becomes stationary, as can be seen from comparing the data sets with $N_p = 301$ and $N_p = 1001$. The system is dynamically localized (*15*, *16*, *23*). In the interacting case, the change in the momentum distribution from $N_p = 1$ to about $N_p = 301$ is much more pronounced. However, the subsequent evolution, in particular from $N_p = 501$ to $N_p = 1101$, appears to have stopped. Examples of $n(k)$ after the first kick and in the localized state after $N_p = 801$ for the noninteracting and the strongly interacting cases are shown in Fig. 2, C and D, respectively. As we will argue below, the interacting system, after some initial evolution toward a broadened distribution, has entered the regime of MBDL.

We use the Jensen-Shannon divergence J to quantitatively study the evolution of $n(k)$. It is a measure of the overlap of two probability distributions (*41*) with values between $J = 0$ (full overlap) and $J = 1$ (no overlap) (*40*). Figure 3A presents the time evolution of J between the momentum distribution at N_p and $N_p + 100$ for both the noninteracting and the strongly interacting cases, as N_p is stepped in units of 50. Initially, as the distributions still change, the value for J is large compared to the noise floor. But quite quickly, J drops toward the noise level. For the noninteracting case, the noise level is reached already after the first step, and overlap cannot be distinguished from noise beyond $N_p = 300$. The system has undergone dynamical localization. For the interacting case, this takes about $N_p = 450$ kicks. Afterwards, the change in the distributions is minimal and can no longer be distinguished from the noise. The system has undergone MBDL. This can also be seen from a direct comparison of two typical measured distributions taken at $N_p = 701$ and $N_p = 1001$ for the strongly interacting case $\gamma = 11$, as shown in the inset of Fig. 3A. Within the error bars, the two structured distributions are the same; even the slight shifts away from the multiples of $2\hbar k_L$ are well aligned. This is notable, as the interacting system has been kicked 300 times more for the later measurement. Evidently, the interplay of quantum coherence and strong interactions prevents the breaking of localization.

Saturation of the energy and entropy

We further quantify the behavior observed above by analyzing the longitudinal kinetic energy $\langle E_z\rangle \propto \langle k^2\rangle$ and the information entropy $S = -\sum_k n(k)\log[n(k)]$ for various values of γ. The former is measure of the absorbed energy, and the latter relates to the degree of thermalization in the system. The data are taken for two values of the kick strength, $K = 3.3$ ($T = 60$ μs) and $K = 4.4$ ($T = 80$ μs), and, in addition to the previous choice of $\gamma = 0$ and $\gamma = 11$, for intermediate values of γ. The experimental results are shown in Fig. 3, B and D. For all values of γ, both observables, after an initial rise, settle to constant values after a few hundred kicks. Evidently, the evolution has stopped. The limiting values depend on γ: The larger γ, the larger the localization energy and the localization entropy for a given K. The limiting values also depend on K. One can see a clear difference for the data taken for $\gamma = 11$, with a smaller kick strength but a higher kick frequency giving larger localization values. However, all this behavior is in stark contrast to what happens when the system is subject to random kicks. In that case, as shown in Fig. 3B, the energy increases diffusively without bounds. For both the strongly and the noninteracting scenarios, $n(k)$ ultimately ends up as a uniform distribution in our measured momentum window [see details in (*40*)]. Therefore, quantum coherence is crucial to the emergence of the DL and MBDL phases. We note that for a time evolution up to $N_p = 1001$, atom loss is small and transversal

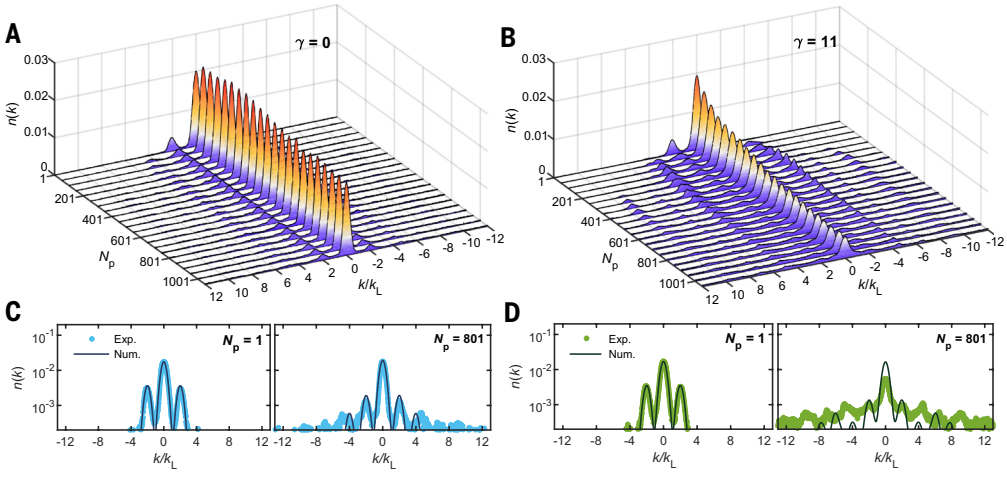

Fig. 2. Evolution of the 1D momentum distribution. Measured $n(k)$ for the noninteracting (**A**) and strongly interacting case (**B**) for a kick strength $K = 3.3$. In (A) and (B), the number of kicks N_p is increased from 1 to 1051 in steps of 50. Example distributions are shown in (**C**) and (**D**) for $N_p = 1$ and 801 for $\gamma = 0$ and $\gamma = 11$, respectively. The data are compared to numerically calculated distributions for $\gamma = 0$ and $\gamma = \infty$ (*40*). Because of the finite TOF duration, these are convoluted by Gaussians whose waist is half of the flat-bottom length. Note also that the higher-order momentum peaks are shifted to higher momentum values by up to $1\hbar k_L$. This also results from the fact that the TOF is finite as the atoms effectively experience some TOF during the evolution before they are released (*23*). All experimental distributions are the average of three realizations.

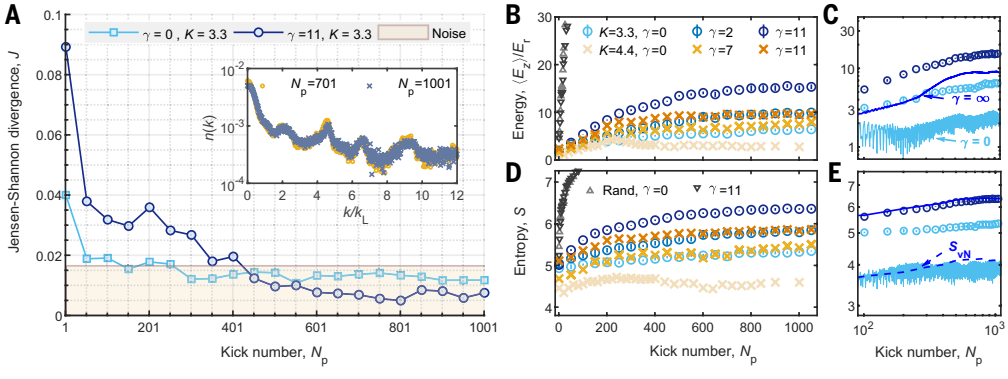

Fig. 3. Evidence for MBDL. (**A**) Jensen-Shannon divergence J between the momentum distributions at N_p and $N_p + 100$ as N_p is stepped in units of 50, for the noninteracting ($\gamma = 0$, light blue squares) and the strongly interacting ($\gamma = 11$, dark blue circles) cases. The orange shaded area indicates the typical shot-to-shot noise determined by comparing three repeats at $N_p = 501$. Inset: Comparison of measured $n(k)$ at $N_p = 701$ and at $N_p = 1001$ for the strongly interacting case $\gamma = 11$. (**B** and **D**) Time evolution of the kinetic energy $\langle E_z \rangle$ (B) and of the information entropy S (D) for various values of the 1D interaction strength γ as indicated and for two values of the kick strength $K = 3.3$ ($T = 60$ μs, circles) and $K = 4.4$ ($T = 80$ μs, crosses). For comparison, the measured time evolution of noninteracting ($\gamma = 0$, gray up-triangles) and strongly interacting ($\gamma = 11$, black down-triangles) gases is shown for random kicks. (**C** and **E**) Comparing the energy (C) and entropy (E) calculated for the noninteracting (light blue solid line) and infinitely interacting cases (dark blue solid line) (*40*) to the data with $\gamma = 0$ (light blue circles) and $\gamma = 11$ (dark blue circles) for the case of $K = 3.3$ on a log-log scale. Fast oscillations for the theory data for $\gamma = 0$ are not resolved. Additionally, the calculated von-Neumann entropy S_{vN} for infinite interactions is shown (dashed line). The statistical error in (B) through (E) is smaller than the symbol size.

excitations are negligible. Stronger interactions lead to slightly higher atom loss, but losses remain below 25%. We also note that we can increase γ to values that are much larger than the ones used here, e.g., to $\gamma = 86$. For this choice, we find increased atom loss and pronounced transversal excitations. These become evident already after about 100 kicks. Details on loss and transversal excitations are discussed in (*40*).

In Fig. 3, C and E, we compare the results for vanishing and very strong interactions to our theory data, obtained in the two limiting cases $\gamma = 0$ and $\gamma \to \infty$, for which calculations can be carried out. Although the experimental data lie above the theory predictions, the growth trend for the energy and the entropy for experiment and theory agree reasonably well. In particular, theory confirms the onset of localization after around 500 kicks. The theory allows us to also calculate the von-Neumann entropy $S_{vN} = -\mathrm{Tr}[\rho \log \rho]$, where ρ is the one-particle density matrix (*40*, *42*, *43*). It is a measure of the entanglement generated in the system. It also settles to a constant value, and its growth trend is almost the same as for the information entropy.

One-body correlation function

We now turn to the quantum coherence of our kicked many-body system. It is contained in the one-particle density matrix $\rho(z, z') = \langle \hat{\Psi}^\dagger(z') \hat{\Psi}(z) \rangle$, where $\hat{\Psi}$ is the many-body field operator. It governs the functional form of the one-body correlation function via $G^{(1)}(z) \propto \int \rho(z, z') dz'$. In practice, one gets $G^{(1)}(z)$ from the Fourier transform of $n(k)$ (*29*, *39*). The experimental results for $G^{(1)}(z)$ of the QKR are presented in Fig. 4 for the TG regime and the noninteracting regime for two kick strengths and for three values of N_p in the localized regime. As a consequence of the frozen momentum distribution, $G^{(1)}(z)$ does not depend on N_p after MBDL has occurred (the data for different values of N_p are offset for visibility). The decay for the strongly interacting case is well fit by an exponential for intermediate distances. A frozen correlation length is considered to be a property of the effectively thermalized TG gas in MBDL phase, as predicted for trapping-free systems (*26*, *27*). The exponential fit is not expected to cover $G^{(1)}$ for very short distances, which via Fourier transform correspond to the region of large momenta. This is compatible with a predicted algebraic-like decay for large momenta in the MBDL phase (*25*–*27*). Our data are in fact consistent with a $n(k) = C_{th} k^{-4}$ behavior. Here, the weight C_{th} is Tan's contact of the effectively thermalized TG gas (*26*, *44*, *45*) [see details in (*40*)]. Contrary to the TG case, for the noninteracting system, $G^{(1)}(z)$ exhibits a Lorentzian decay behavior. This implies an exponential decay in momentum space, signaling Anderson-like localization (*11*). Although the one-body correlation function for the MBDL phase requires more theoretical studies, especially for finite interactions and for trapped systems, the change in the behavior of the correlation function from one regime to the other highlights the many-body effect in the MBDL dynamics.

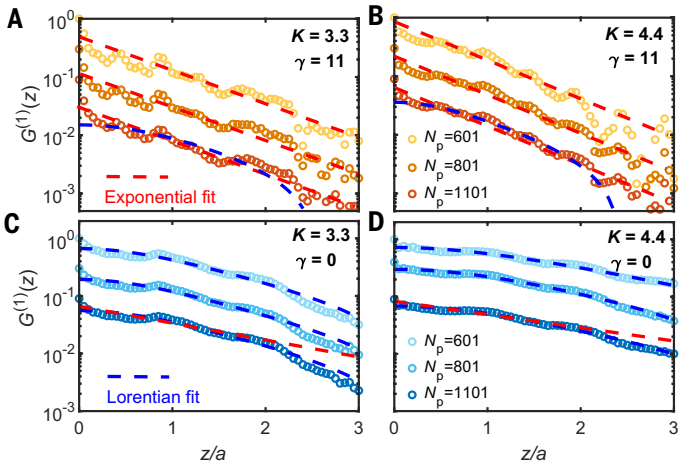

Fig. 4. Decay of the one-body correlation function for DL and MBDL. (**A** and **B**) One-body correlation function $G^{(1)}(z)$ for strong interactions ($\gamma = 11$) and two kick strengths and for $N_p = 601, 801$, and 1101, as indicated. The different datasets have been offset for better visibility. Exponential fits to the data for the range $z/a = 0.25$ to 2.5 are indicated by the red dashed lines. (**C** and **D**) Same as (A) and (B), but for the noninteracting case ($\gamma = 0$). Lorentzian decays have been fit to the experimental data over the full range (blue dashed lines). For comparison, Lorentzian and exponential fits are included in the plots shown in [(A) and (B)] and [(C) and (D)], respectively.

Discussion and outlook

In this study, we have observed and analyzed a many-body phase termed MBDL by periodically kicking a TG gas confined in a flat-bottom trap. Our observations reveal that the momentum distribution of a strongly correlated system freezes despite the periodic kicks and preserves its characteristic interference structure. The kinetic energy and the information entropy show suppressed growth and saturation. We conclude that the quantum many-body system does not fall into the regime of thermalization and chaos. The differences for the momentum distributions and the correlation functions between the noninteracting scenario and the strongly interacting one highlight the impact of the many-body effects under the periodic driving. Our findings raise a series of questions to experiment and theory: As the absence of thermalization does not exclude the presence of chaos (*46*), then what is the role of chaos in the MBDL phase, and how can it be quantified experimentally and by theory? What other mechanisms apart from random kicking could break MBDL in our Lieb-Liniger setting, and how do chaos and thermalization emerge from these? What happens for intermediate interactions in the presence of inhomogeneous trapping for which integrability is expected to be broken? As interactions for our system are short-ranged in real space and hence necessarily long-ranged in momentum space, is there a mapping to real-space localized states for the case of long-range real-space interactions (*47*, *48*)? How is the relation to other many-body localized states that are, e.g., found in a lattice setting (*49*) for which localization happens in real space? The observation of MBDL, in view of recent theoretical research (*24*–*27*), opens the door to a further exploration of the emergence of chaos in a many-body setting.

REFERENCES AND NOTES

1. S. H. Strogatz, *Nonlinear Dynamics and Chaos with Student Solutions Manual: With applications to Physics, Biology, Chemistry, and Engineering* (CRC press, 2018).
2. G. L. Baker, J. P. Gollub, *Chaotic Dynamics: An Introduction* (Cambridge Univ. Press, 1996).
3. M. Berry, *Phys. Scr.* **40**, 335–336 (1989).
4. L. D'Alessio, Y. Kafri, A. Polkovnikov, M. Rigol, *Adv. Phys.* **65**, 239–362 (2016).
5. P. Bordia, H. Lüschen, U. Schneider, M. Knap,I. Bloch, *Nat. Phys.* **13**, 460–464 (2017).
6. H. Bernien *et al.*, *Nature* **551**, 579–584 (2017).
7. Y. Le, Y. Zhang, S. Gopalakrishnan, M. Rigol, D. S. Weiss, *Nature* **618**, 494–499 (2023).
8. D. Abanin, W. De Roeck, W. W. Ho, F. Huveneers, *Commun. Math. Phys.* **354**, 809–827 (2017).
9. F. Haake, *Quantum Signatures of Chaos* (Springer, 1991).
10. M. Santhanam, S. Paul, J. B. Kannan, *Phys. Rep.* **956**, 1–87 (2022).
11. P. W. Anderson, *Phys. Rev.* **109**, 1492–1505 (1958).
12. S. Fishman, D. R. Grempel, R. E. Prange, *Phys. Rev. Lett.* **49**, 509–512 (1982).
13. D. R. Grempel, R. E. Prange, S. Fishman, *Phys. Rev. A Gen. Phys.* **29**, 1639–1647 (1984).
14. F. L. Moore, J. C. Robinson, C. F. Bharucha, B. Sundaram, M. G. Raizen, *Phys. Rev. Lett.* **75**, 4598–4601 (1995).
15. I. Manai *et al.*, *Phys. Rev. Lett.* **115**, 240603 (2015).
16. G. Lemarié *et al.*, *Phys. Rev. A* **80**, 043626 (2009).
17. M. Srednicki, *Phys. Rev. E Stat. Phys. Plasmas Fluids Relat. Interdiscip. Topics* **50**, 888–901 (1994).
18. M. Rigol, V. Dunjko, M. Olshanii, *Nature* **452**, 854–858 (2008).
19. S. Lellouch, A. Rançon, S. De Bièvre, D. Delande, J. C. Garreau, *Phys. Rev. A* **101**, 043624 (2020).
20. D. L. Shepelyansky, *Phys. Rev. Lett.* **70**, 1787–1790 (1993).
21. G. Gligorić, J. D. Bodyfelt, S. Flach, *Europhys. Lett.* **96**, 30004 (2011).
22. J. H. See Toh *et al.*, *Nat. Phys.* **18**, 1297–1301 (2022).
23. A. Cao *et al.*, *Nat. Phys.* **18**, 1302–1306 (2022).
24. C. Rylands, E. B. Rozenbaum, V. Galitski, R. Konik, *Phys. Rev. Lett.* **124**, 155302 (2020).
25. R. Chicireanu, A. Rançon, *Phys. Rev. A* **103**, 043314 (2021).
26. V. Vuatelet, A. Rançon, *Phys. Rev. A* **104**, 043302 (2021).
27. V. Vuatelet, A. Rançon, *Quantum* **7**, 917 (2023).
28. M. Fava, R. Fazio, A. Russomanno, *Phys. Rev. B* **101**, 064302 (2020).
29. B. Paredes *et al.*, *Nature* **429**, 277–281 (2004).
30. T. Kinoshita, T. Wenger, D. S. Weiss, *Science* **305**, 1125–1128 (2004).
31. E. Haller *et al.*, *Science* **325**, 1224–1227 (2009).
32. J. M. Wilson *et al.*, *Science* **367**, 1461–1464 (2020).
33. T. Kraemer *et al.*, *Appl. Phys. B* **79**, 1013–1019 (2004).
34. M. Olshanii, *Phys. Rev. Lett.* **81**, 938–941 (1998).
35. I. Bloch, J. Dalibard, W. Zwerger, *Rev. Mod. Phys.* **80**, 885–964 (2008).
36. T. Weber, J. Herbig, M. Mark, H.-C. Nägerl, R. Grimm, *Science* **299**, 232–235 (2003).
37. M. A. Cazalilla, R. Citro, T. Giamarchi, E. Orignac, M. Rigol, *Rev. Mod. Phys.* **83**, 1405–1466 (2011).
38. Y. Guo *et al.*, *Sci. Adv.* **10**, eadk6870 (2024).
39. Y. Guo *et al.*, *Nat. Phys.* **20**, 934–938 (2024).
40. See supplementary materials.
41. J. Lin, *IEEE Trans. Inf. Theory* **37**, 145–151 (1991).
42. M. Rigol, A. Muramatsu, *Phys. Rev. A* **72**, 013604 (2005).
43. M. Thamm, H. Radhakrishnan, H. Barghathi, B. Rosenow, A. Del Maestro, *Phys. Rev. B* **106**, 165116 (2022).
44. S. Tan, *Ann. Phys.* **323**, 2987–2990 (2008).
45. H. Yao, D. Clément, A. Minguzzi, P. Vignolo, L. Sanchez-Palencia, *Phys. Rev. Lett.* **121**, 220402 (2018).
46. C. Lim, K. Matirko, A. Polkovnikov, M. O. Flynn, arXiv:2401.01927 [cond-mat.stat-mech] (2024).
47. R. M. Nandkishore, S. L. Sondhi, *Phys. Rev. X* **7**, 041021 (2017).
48. N. Defenu *et al.*, *Rev. Mod. Phys.* **95**, 035002 (2023).
49. D. A. Abanin, E. Altman, I. Bloch, M. Serbyn, *Rev. Mod. Phys.* **91**, 021001 (2019).
50. M. Troyer, B. Ammon, E. Heeb, *Lect. Notes Comput. Sci.* **1505**, 191–198 (1998).
51. A. F. Albuquerque *et al.*, *J. Magn. Magn. Mater.* **310**, 1187–1193 (2007).
52. B. Bauer *et al.*, *J. Stat. Mech.* **2011**, P05001 (2011).
53. Y. Guo *et al.*, Observation of many-body dynamical localization [Data set], Zenodo (2024); https://doi.org/10.5281/zenodo.11229166.

ACKNOWLEDGMENTS

Funding: The Innsbruck team acknowledges funding by a Wittgenstein prize grant under Austrian Science Fund (FWF) project no. Z336-N36, by the European Research Council (ERC) under project no. 789017, by an FFG infrastructure grant with project no. FO999896041, and by the FWF's COE 1 and quantA. M.H. thanks the doctoral school ALM for hospitality, with funding from the FWF under project no. W1259-N27. The team at Zhejiang University is supported by the National Key R&D Program of China (grant no. 2022YFA1404203) and the National Natural Science Foundation of China (grant no. 12375021). H.Y. is also supported by the Swiss National Science Foundation under grant no. 200020-188687. **Author contributions:** The work was conceived by H.-C.N., Y.G., M.L., L.Y., S.D., and Z.C. Experiments were performed by Y.G. and S.D. Data were analyzed by Y.G., A.Y., and Z.C. Theoretical models and simulation were done by L.Y., A.Y., H.Y., and Z.C. Preparation of experiments was done by Y.G, S.D., and M.H. Manuscript preparation was mainly contributed by H.-C.N., Y.G., L.Y., Z.C., A.Y., and M.L. **Competing interests:** The authors declare no competing interests. **Data and materials availability:** The quantum Monte Carlo calculations make use of the ALPS scheduler library and statistical analysis tools (*50*–*52*). The data shown in the main text and supplementary materials are available at Zenodo (*53*).

License information: Copyright © 2025 the authors, some rights reserved; exclusive licensee American Association for the Advancement of Science. No claim to original US government works. https://www.science.org/about/science-licenses-journal-article-reuse

SUPPLEMENTARY MATERIALS

science.org/doi/10.1126/science.adn8625
Materials and Methods; Supplementary Text; Figs. S1 to S9; References (*54*–*59*)

Submitted 4 January 2024; accepted 17 June 2025

10.1126/science.adn8625

FUNGAL GENETICS

Early germline sequestration in a basidiomycete fungus

Markus Hiltunen Thorén[1,2], Boel Olsson[1], Peter Jan Vonk[1], Mattias Siljestam[1], Johan Reimegård[3], Martin Ryberg[4], Hanna Johannesson[1,2]*

In sexual organisms, inheritance of new mutations is highly dependent on the timing of germline definition. Here, we used the fairy ring–forming fungus *Marasmius oreades* to challenge the general assumption of a late germline separation in the Fungi. We collected mushrooms from different parts of rings over a 7-year period and identified new mutations in different tissues by whole-genome sequencing. We found evidence that fertile and sterile tissues had accumulated different mutations, suggesting that the germ line, destined for spore production, is already defined in the mycelium in this species. Moreover, the germ line carried fewer mutations than sterile tissues, indicating a lower mutation rate. Our findings suggest that early germline sequestration is more widespread than previously considered across multicellular life.

In the late 1800s, August Weismann laid the foundation for our current understanding of mechanisms of inheritance by proposing that only germ cells carry heritable information from one generation to the next. Since then, it has been widely accepted that unitary organisms—those for which the program of development is predictable and determinate—define their germ line early during development. In these organisms, only variants that arise in the germ line can have evolutionary importance, as somatic variants become extinct as the body of the organism perishes. In fungi, plants, and non-bilaterian metazoans, by contrast, the prevailing assumption is that the germ line is defined at a late stage of development, close in time to the production of gametes. Consequently, variants that arise during growth may enter the germ line (*1*–*4*). Many of these latter organisms are modular; i.e., they show indeterminate body plans composed of iterated units or modules. In modular organisms, the development of sexual tissue necessarily takes place later in the life cycle, as there must be a totipotent stem cell in each module that produces the somatic cells and eventually the germ line (*5*). However, fungi are notably diverse in terms of reproductive traits, and we present evidence that the current model is overly simplified for this group of organisms.

Theory predicts that an early sequestration of the germ line is beneficial in multicellular organisms for at least two reasons. First, defining cell fate at an early developmental stage reduces the risk of competition between cells and, hence, stabilizes multicellular cooperation (*1*, *6*). Second, the protected environment ensures that the integrity of the genetic material in the germ line is maintained over generations. As most mutations with an effect on fitness are deleterious, a reduced germline mutation rate is expected to have a selective advantage (*7*). Indeed, empirical evidence from animals of a lower mutation rate in the germ line than the soma has emerged in recent years (*8*–*10*). It has been suggested that early germline sequestration is a derived trait in bilaterian animals that has evolved from an ancestor for which the germ cell lineage was defined during later stages of ontogeny (*1*, *11*). In nonbilaterian animals, as well as in plants and fungi, the ancestral developmental mode is thought to be retained (*1*). In light of recent results, however, the assumption of a late sequestration has been challenged in both cnidaria and plants (*12*–*17*) but, to our knowledge, so far not in fungi.

In this study, we show that segregation of germ line from the soma occurs in a mushroom-forming fungus and that the germ line destined for production of the sexual basidiospores is predetermined. By taking advantage of the circularly expanding mycelial growth of a fairy ring–forming fungus, we traced the accumulation of de novo mutations within two fungal individuals over time, as well as their transmission to the next generation through the basidiospores formed by the fruiting bodies (mushrooms) at the edge of the rings (Fig. 1). By collecting fruiting bodies from different parts of the rings over a 7-year period and dissecting and sequencing the genomes of their fertile and sterile tissues, we generated a dataset that allowed detection of previously unrecognized mutations that could be used as markers for different tissue types. We found that spores and the spore-producing lamellae have shared mutations, and these were clearly distinct from the mutations found in the sterile tissues of the fruiting body. Furthermore, mutations in the respective tissue types were shared between fruiting bodies collected in close physical vicinity, as well as from the same sector of the fairy ring over different years. These results reveal that the germ line is stable over time and, hence, must have been defined at an early stage in the fungal mycelium. Because multicellularity in animals and fungi have separate origins (*18*), our findings suggest that germline sequestration has arisen multiple times over multicellular evolution and that the notion of this phenomenon being a strictly metazoan invention should be reconsidered.

Different lineages form sterile and fertile tissues in mushrooms of *Marasmius oreades*

To investigate the transgenerational mutation transmission in a basidiomycete, we used *M. oreades*, which is well known for forming fairy

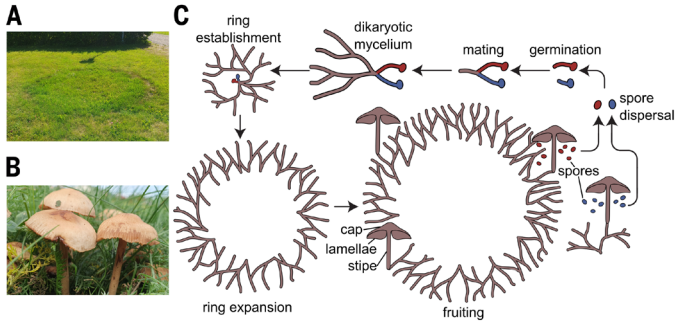

Fig. 1. Fairy rings of *Marasmius oreades* can be used to study the rise and fate of mutations. (**A**) Fairy rings of *M. oreades* are common in lawns across the Northern Hemisphere. Each ring is formed by a discrete individual of the fungus (*19*). The fungal mycelium grows underground, giving rise to dense and vigorous vegetation during humid weather. (**B**) Fruiting bodies (up to ~8 cm in height) emerge seasonally from the underground mycelium along the edge of the ring. (**C**) During the life cycle of *M. oreades*, two monokaryotic mycelia (bearing nuclei of single genotypes, indicated by red and blue color) must mate (fuse) to form a dikaryotic mycelium (with two genetically distinct nuclei; brown). After formation, the dikaryotic individual expands radially over time while the mycelium in the center dies off, giving rise to the characteristic fairy ring phenotype. The mushrooms formed along the ring periphery are composed of the stipe and the cap, which bears the spore-forming lamellae. In the lamellae, the nuclei fuse (karyogamy) and immediately enter meiosis. After meiosis, haploid mononucleate spores (basidiospores) are formed and dispersed to find compatible mates and form new fairy rings. Different parts of the ring will independently accumulate mutations over growth that can be traced in both the mushrooms and basidiospores. Hence, the ring can be used as a natural, long-term evolution experiment, in which we are able to trace the rise and fate of mutations over the life cycle. [Photos by M. Hiltunen Thorén]

[1]Department of Ecology, Environment and Plant Sciences, Stockholm University, Stockholm, Sweden. [2]The Royal Swedish Academy of Sciences, Stockholm, Sweden. [3]Department of Cell and Molecular Biology, National Bioinformatics Infrastructure Sweden, Science for Life Laboratory, Uppsala University, Uppsala, Sweden. [4]Department of Organismal Biology, Evolutionary Biology Centre, Uppsala University, Uppsala, Sweden. ***Corresponding author. Email: hanna.johannesson@su.se**

rings in meadows and lawns (Fig. 1, A and B). Fairy rings of *M. oreades* initiate mycelial growth with a mating event between two compatible hyphae emerging from basidiospores (Fig. 1C). From this point of origin, the mycelium expands radially outwards, accumulating mutations as it grows (*19*). The study of mutation accumulation is facilitated by a well-curated reference genome of the species (*20*), allowing whole-genome resequencing analysis of fruiting body tissues. By comparison of fruiting bodies from different sectors of the ring, and with all shared variants assumed to be ancestral to the individual, any differences between fruiting bodies can be inferred to have been caused by new mutations (*19*). We collected fruiting bodies during the mushroom seasons between 2016 and 2023, primarily from one fairy ring in Uppsala, Sweden (ring 43). In 2023, we also sampled another fairy ring (ring 06). We collected basidiospores and separated different fruiting body tissues: lamellae (fertile), stipe and remaining cap (both sterile), and extracted DNA from pooled spores and each tissue separately. Our final dataset consisted of 142 spore and tissue isolations, collected from 59 fruiting bodies over a 7-year period (fig. S1 and data S1).

After sequencing, variant calling, and a stringent variant-filtering procedure (*21*), a total of 230 new mutations were identified (data S2). When analyzing the spatial distribution of mutations within fruiting bodies, we found that spores and lamellae shared mutations (Fig. 2). This result was not surprising, because spores are produced on specialized cells called basidia that are formed on the lamellae. However, the remainder of the fruiting body—the sterile tissues—showed a clearly distinct pattern of mutations. In a subset of fruiting bodies, we made further divisions of the tissues, and the pattern was consistently different between fertile and sterile parts (fig. S2). Mushrooms originate from aggregations of hyphae called knots, which soon develop into primordia and finally into the mature fruiting bodies (*22*). Studies in the basidiomycete genus *Coprinopsis* showed that already in the developing primordia, differentiating tissues can be distinguished (*23*). In light of our results, cells or nuclei destined for different tissues are likely separated from the earliest stages of mushroom development, suggesting a mechanism of predetermination. In our data, although the overarching distinction between fertile and sterile tissues remained consistent, some mutations occurring at a high frequency in one of the tissues were also found at low frequency in the opposite tissue type. The explanation for this pattern can be technical, such as incomplete separation of tissues during dissection or resulting from spores attaching to the exterior of the stipe. Data collection for our study was performed in two rounds, and in the second round (*21*) (data S1), extra caution was taken during tissue isolation to minimize cross contamination. The second-round data showed an overall lower frequency of the opposite genotype than data from our first round, indicating that cross contamination by small amounts of tissue was driving this signal. It is also possible that a low proportion of the lineage-forming lamellae is integrated into the stipe, and vice versa in lamellae. At present, we cannot rule out any of these explanations. However, even if the low-frequency mutations have a biological explanation, the large-scale difference between tissues is apparent, and mutations can be completely and consistently assigned as present or absent in either tissue type by drawing an allelic fraction cutoff value at 0.20 (i.e., if <20% of the reads at a certain site carry the mutation in a tissue sample, we consider it as absent in that tissue).

The germ line is defined during early dikaryotic development and is preserved over years of growth

The timing of germline sequestration is of fundamental importance for organismal development and evolution. The distribution of the variants between mushrooms allowed us to indirectly infer how long the two lineages had been separated. We found that the distinction between fertile and sterile tissues was consistent between fruiting bodies, so that lamellae of different fruiting bodies shared mutations, whereas the stipes shared other sets of mutations (Fig. 3 and fig. S3). This pattern was consistent in space, as fruiting bodies collected in close vicinity were more similar than distant fruiting bodies, and in time, as mushrooms collected in 2016 shared some of their mutations with mushrooms collected in concurrent years (Fig. 3). Notably, in ring 06, one mutation was shared between all stipe samples but absent in all lamella samples. As these fruiting bodies were collected from opposite sides of the fairy ring, the genotypes must have been separated very early during mycelial growth. An explanation for this pattern could be that a nonnative genetic element, such as a plasmid, accessory chromosome, or foreign organism, is acting selfishly to guide certain hyphae to form spores. We could not find any such DNA (*21*). Hence, we propose that *M. oreades* has evolved an intrinsic system that sequesters the germ line from the soma, starting at the establishment of the dikaryotic mycelium or soon thereafter. Consequently, the mutations that we identified in the fertile tissues can be considered germline mutations, and the ones in sterile tissues, somatic mutations.

To investigate how the germline and somatic lineages are physically organized in the mycelium of *M. oreades*, we analyzed the distribution of new mutations in the fairy rings (*21*). We found that phylogenetic trees constructed from germline and somatic mutations, with each having several unresolved nodes because of low numbers of mutations, did not show any incongruent splits (fig. S4; see supplementary text for details). Although the organization of germ line and soma needs further detailed study, this result supports a model in which they are closely associated during mycelial growth, possibly as coexisting nuclei within the same hyphae, or as separate hyphae growing in close proximity in the soil.

The germ line is homogeneous, whereas somatic tissues consist of mosaic genotypes

Like most mushroom-forming fungi, the life cycle of *M. oreades* is dominated by a dikaryotic stage, during which two genetically distinct nuclei coexist in each hyphal compartment (Fig. 1) (*19*, *24*). This nuclear configuration, analogous to diploidy, implies that polymorphisms between the nuclei would appear close to a 0.5 fraction in mapped sequencing reads. For variants ubiquitous to all samples in each fairy ring and assumed to have been present in the two parents, this pattern was apparent (Fig. 4A). Mutations transmitted to the basidiospores also followed this pattern (Fig. 4A). Whereas individual spores are haploid and mononucleate, in our spore pools both nuclear genotypes could be found in equal frequencies. In lamellae, the pattern was similar, but a tail toward lower frequencies was found, consistent with the presence of a low proportion of other genotypes. However, many mutations found in stipes showed a frequency below 0.5 (Fig. 4A and fig. S5). To control for inaccuracies in determining the frequency of new mutations from whole-genome sequencing (WGS) reads,

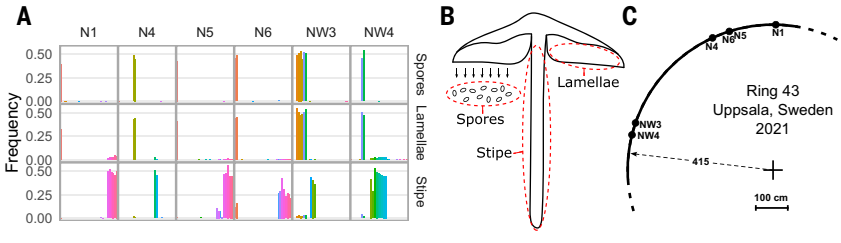

Fig. 2. Fertile and sterile tissues of *Marasmius oreades* show distinct patterns of de novo mutations. Fertile tissues (i.e., spores and lamellae) and sterile tissue (i.e., the stipe) differ in the set of mutations they carry. (**A**) Frequency (allelic fraction) of mutations in the reads covering the mutated site, shown in a subset of the data for fruiting bodies where spores were collected. In the faceting, columns indicate fruiting bodies, and rows indicate tissues. Different mutations are coded by color and position along the *x* axis. (**B**) Schematic illustration of the three dissected tissues from *M. oreades* fruiting bodies. (**C**) Sampling map of where fruiting bodies in (A) were collected. Radius distance is in centimeters.

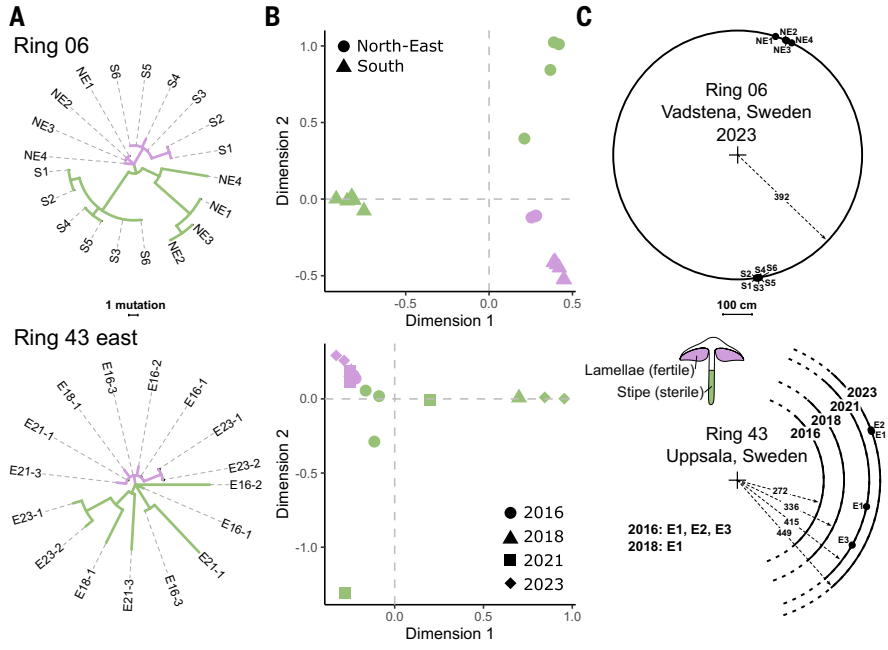

Fig. 3. Consistent separation of germ line and soma over time and space. (**A**) Phylograms (maximum parsimony; branch length shows the number of mutations as indicated by the scale bar) of genotypes of lamellae (purple) and stipes (green) from fruiting bodies collected from ring 06 (top) and the eastern side of ring 43 (bottom; subset of the data from ring 43). All branches are fully supported. All fruiting bodies from ring 06 were collected in 2023. For ring 43, fruiting bodies were collected in 2016, 2018, 2021, and 2023, and for this ring, the year of sampling is included in sample name. See fig. S4 for a tree of all data from stipes and lamellae from ring 43. (**B**) Multidimensional scaling of the mutations in the samples represented in (A) (top, ring 06; bottom, eastern side of ring 43. For ring 06, symbols indicate directions, and for ring 43, year of sampling). Coloring according to tissue type as in (A). (**C**) Maps of fairy rings 06 (top) and 43 (bottom) where samples depicted in (A) and (B) were collected. Note that for ring 43, the precise sampling positions for mushrooms collected in 2016 (n = 3) and 2018 (n = 1) were not recorded.

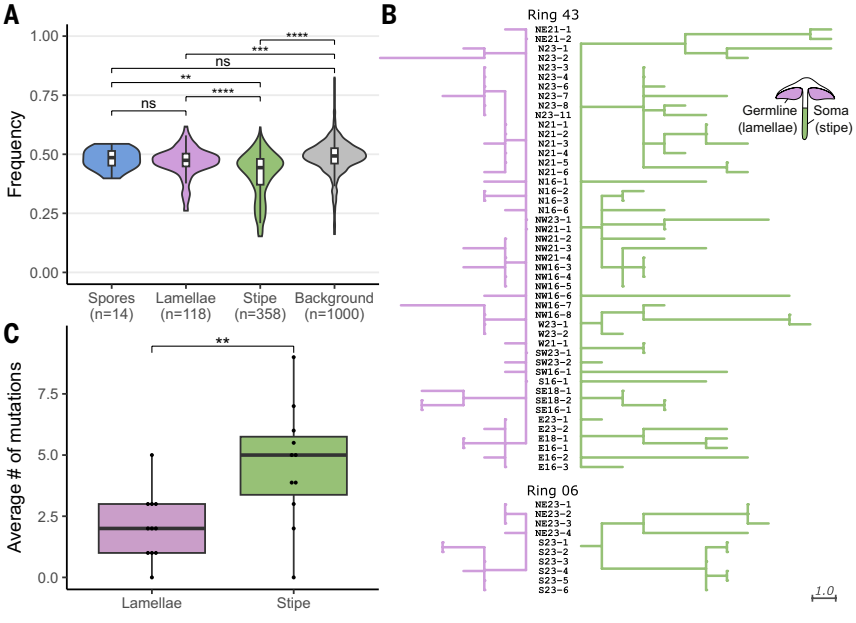

Fig. 4. Germ line and soma accumulate mutations at different rates. (**A**) Frequency of reads carrying mutations (allelic fractions) in spores (germ line; blue), lamellae (germ line; purple), stipes (soma; green), and a genome-wide random sample of a thousand single-nucleotide polymorphisms [i.e., heterozygous positions in the ancestral genotype (gray)]. Significantly different distributions are indicated. $^{**}P < 0.01$; $^{***}P < 0.001$; $^{****}P < 0.0001$; ns, not significant; Wilcoxon rank sum test. (**B**) Maximum parsimony trees from germline (left; purple) and somatic (right; green) mutations. The scale bar indicates the number of mutations. (**C**) Average number of mutations in lamellae (germ line; purple) and stipes (soma; green), counting only mutations with an allelic fraction >0.4. Stipes have accumulated significantly more mutations. Fold change: 2.2-fold; $^{**}P = 0.005$; Welch two-sample t test.

The germ line accumulates fewer mutations than the soma

Consistent with the prediction of a maintenance of genome integrity in the germ line, we found fewer germline than somatic mutations (55 and 175, respectively), indicating a lower mutation rate. To make a relative comparison of the number of mutations that had accumulated over a given time, we selected only samples from 2023, and only variants with a frequency above 0.4 were retained. Trees were calculated from the remaining variants (fig. S7 and table S1), and the average number of mutations per fruiting body was determined to be 4.6 in somatic tissue and 2.1 in germline tissue (Fig. 4C; 2.2-fold difference, $P < 0.01$; Welch two-sample t test). As there may be purifying selection in either of the lineages, we also investigated the mutation rate in only noncoding regions, which revealed a consistent pattern (2.2 versus 1.2 somatic and germline mutations; 1.8-fold difference; $P < 0.05$). From consecutive measurements of ring diameter over years, we estimated ring 43 to have been established in 2006 and ring 06 in 2010 (table S2). From this information, we calculated the mutation accumulation rates to 0.27 (soma) and 0.17 (germline) mutations per fruiting body and year in ring 43, and 0.37 (soma) and 0.13 (germline) in ring 06.

If the germ line is sequestered in *M. oreades* to counteract the deleterious effects of mutation accumulation during growth, the difference in mutation accumulation rate between germ line and soma has to be robust to mutations that occur during meiosis. That is, if meiosis introduces a high number of mutations, the relative difference between the two lineages would be less pronounced and thus less likely to be the driver of germline sequestration. Our previously generated sequencing data from single-spore cultures (*20*) allowed us to estimate the meiotic mutation rate to, at maximum, 0.26 mutations per spore per meiosis (*21*). Hence, in the hypothetical scenario that the somatic lineage would also enter meiosis, the adjusted average numbers of mutations are 4.9

we quantified the frequencies of two mutations by digital polymerase chain reaction. This assay confirmed the frequencies observed from WGS within a 5% margin (fig. S6). The patterns revealed by these analyses can be explained by a single germline genotype forming the fertile tissues in each mushroom, whereas nuclei of multiple genotypes converge to form the sterile parts.

versus 2.4 (a 2.0-fold difference). The signal of a lower mutation rate in the germ line than in the soma is thus in the same range when meiotic mutations are included in the analysis.

We characterized the germline and somatic mutations in terms of their distribution across the genome, base spectrum of substitution, and trinucleotide context (figs. S8 and S9), as well as potential fitness effects. Overall, the differences were minor, which may indicate that similar factors cause mutations in both soma and germ line (see supplementary text for details). However, the low number of germline mutations offers limited power to detect any differences between the lineages.

Discussion

Here, we show evidence that early germline sequestration has evolved in a mushroom-forming fungus. In animals, the germ line is defined either through maternally inherited determinants (preformation) or by expression of factors that induce germline formation (epigenesis) (*25*, *26*). *M. oreades*, like many other fungi, is isogamous, and the germ line is thus unlikely to be defined by preformation. Although we can only speculate on the mechanistic basis for germline definition in *M. oreades*, it is more likely to involve a process similar to epigenesis, in which an interplay between epigenetic reprogramming and expression of certain factors induces the distinction. Further studies, including microscopy and comparative analyses of the epigenomes and transcriptomes of tissues across the life cycle, are needed to reveal both the spatial distribution of the germ line and soma in *M. oreades* and the mechanisms of their differentiation.

A proposed evolutionary advantage of germline sequestration is protection from the environment and a reduced mutation rate. Consistent with this hypothesis, we found fewer mutations in the germ line than in the soma, and this pattern held when accounting for the effect of genetic mosaicism in somatic tissue, as well as meiotic mutations. Previously, we observed a low rate of somatic mutation accumulation in *M. oreades* (*19*), and the rate appears to be even lower in the germ line. In this study, we inferred the mutation rate on the basis of the number of mutations that had accumulated over time, and there could be multiple explanations for the observed differences. In animals, a combination of a lower nuclear division rate, protection from external mutagens, differential transcriptional patterns, and/or an increased activity of the DNA repair machinery determines differences in somatic and germline mutation rates (*27*–*30*). Similar factors likely play a role in *M. oreades*. The difference in mutation numbers could also be explained by selection purging some of the mutations that arise. In our data, we see no signal of selection, but the numbers may be too low for any patterns to emerge. The difference in relative mutation rate between germ line and soma is robust to the exclusion of coding mutations, supporting that our data show a lower mutation rate in the germ line. When comparing the magnitude of the observed rate difference in this study (~2-fold) with that of, e.g., humans and mice, which is reported to be ~10-fold (*8*), it is questionable whether it is large enough to provide a benefit to the fungus on its own or whether other benefits, such as enforcing cooperation, have driven the evolution of germline sequestration.

The assumed benefits of early germline sequestration should lead to an evolutionary pressure for this phenomenon to evolve in different multicellular lineages. The reason it has so far not been found in fungi could be the result of lack of tractable study systems or that it is not a ubiquitous phenomenon across the fungal kingdom. Among fungi, we find very large individuals, such as *Armillaria bulbosa*—of which an individual mycelium may reach an age of 1500 years and cover >15 ha (*31*)—but also many species that complete the life cycle in a couple of weeks. We propose that the evolutionary pressure to minimize mutations would be strongest in the former group. Furthermore, as discussed by Buss (*1*), it can be hypothesized that certain life-cycle and developmental characteristics are necessary for germline sequestration to evolve. Many fungi are modular, which puts constraints on the evolution of germline sequestration, as a totipotent cell has to be present in each module. On the basis of these two assumptions, we expect a sequestered germ line to have evolved primarily in fungi with a long life span and in which spores are produced sexually, such as *M. oreades*. In many ways, the life cycle of *M. oreades* is reminiscent of that of bilaterian animals: Both have a dominant, often long-lived phase with two copies of the genome per cell; reproduce by haploid propagules produced after meiosis; and have limited to no clonal reproduction. This life cycle is common across mushroom-forming fungi, and it would not be surprising if germline sequestration is widespread in this group of organisms.

REFERENCES AND NOTES

1. L. W. Buss, *The Evolution of Individuality*, vol. 796 (Princeton Univ. Press, 1988).
2. M. E. Orive, *Theor. Popul. Biol.* **59**, 235–249 (2001).
3. T. Fagerström, A. G. B. Poore, *Selection* **1**, 123–134 (2001).
4. S. Schmitt *et al.*, *Proc. Natl. Acad. Sci. U.S.A.* **121**, e2313312121 (2024).
5. T. Fagerström, D. A. Briscoe, P. Sunnucks, *Trends Ecol. Evol.* **13**, 117–120 (1998).
6. R. E. Michod, D. Roze, *Heredity* **86**, 1–7 (2001).
7. M. Lynch, *Trends Genet.* **26**, 345–352 (2010).
8. B. Milholland *et al.*, *Nat. Commun.* **8**, 15183 (2017).
9. A. Cagan *et al.*, *Nature* **604**, 517–524 (2022).
10. L. Moore *et al.*, *Nature* **597**, 381–386 (2021).
11. C. Juliano, G. Wessel, *Science* **329**, 640–641 (2010).
12. S. Barfield, G. V. Aglyamova, M. V. Matz, *Proc. Biol. Sci.* **283**, 20152128 (2016).
13. R. Lanfear, *PLOS Biol.* **16**, e2005439 (2018).
14. L. Wang *et al.*, *PLOS Biol.* **17**, e3000191 (2019).
15. A. Burian, *Front. Plant Sci.* **12**, 707740 (2021).
16. A. Burian, P. Barbier de Reuille, C. Kuhlemeier, *Curr. Biol.* **26**, 1385–1394 (2016).
17. J. M. Watson *et al.*, *Proc. Natl. Acad. Sci. U.S.A.* **113**, 12226–12231 (2016).
18. L. G. Nagy, G. M. Kovács, K. Krizsán, *Biol. Rev. Camb. Philos. Soc.* **93**, 1778–1794 (2018).
19. M. Hiltunen, M. Grudzinska-Sterno, O. Wallerman, M. Ryberg, H. Johannesson, *Curr. Biol.* **29**, 2758–2765.e6 (2019).
20. M. Hiltunen, S. L. Ament-Velásquez, H. Johannesson, *Genome Biol. Evol.* **13**, evab126 (2021).
21. Materials and methods are available as supplementary materials.
22. U. Kües, *Microbiol. Mol. Biol. Rev.* **64**, 316–353 (2000).
23. T. R. Matthews, D. J. Niederpruem, *Arch. Mikrobiol.* **88**, 169–180 (1973).
24. K. I. Mallett, L. M. Harrison, *Can. J. Bot.* **66**, 1111–1116 (1988).
25. C. G. Extavour, M. Akam, *Development* **130**, 5869–5884 (2003).
26. S. Strome, D. Updike, *Nat. Rev. Mol. Cell Biol.* **16**, 406–416 (2015).
27. C. Tomasetti, B. Vogelstein, *Science* **347**, 78–81 (2015).
28. C. Chen, H. Qi, Y. Shen, J. Pickrell, M. Przeworski, *Genetics* **207**, 255–267 (2017).
29. J. Vermezovic, L. Stergiou, M. O. Hengartner, F. d'Adda di Fagagna, *Cell Death Differ.* **19**, 1847–1855 (2012).
30. A. Bujarrabal-Dueso *et al.*, *Nat. Struct. Mol. Biol.* **30**, 475–488 (2023).
31. M. L. Smith, J. N. Bruhn, J. B. Anderson, *Nature* **356**, 428–431 (1992).
32. M. Hiltunen Thorén *et al.*, Germline evolution in *Marasmius oreades*: Mutation verification by Sanger sequencing, FigShare (2024); https://doi.org/10.6084/m9.figshare.27280212.

ACKNOWLEDGMENTS

The authors acknowledge assistance during laboratory procedures from A. Khodabandeh and A. Jensen for insightful discussions. Genome sequencing was performed by the SNP&SEQ Technology Platform in Uppsala. The facility is part of the National Genomics Infrastructure (NGI) Sweden and Science for Life Laboratory. The SNP&SEQ Platform is also supported by the Swedish Research Council and the Knut and Alice Wallenberg Foundation. **Funding:** The Bergianus Foundation (to H.J.) and Olle Engkvist Foundation (to H.J.). **Author contributions:** Conceptualization: M.H.T., H.J., and M.R. Methodology: M.H.T., B.O., P.J.V., M.S., and J.R. Investigation: M.H.T., B.O., P.J.V., M.S., and J.R. Visualization: M.H.T., B.O., P.J.V., M.S., and J.R. Funding acquisition: H.J. Supervision: M.R. and H.J. Writing – original draft: M.H.T. and H.J. Writing – review & editing: M.H.T., B.O., P.J.V., J.R., M.S., M.R., and H.J. **Competing interests:** The authors declare that they have no competing interests. **Data and materials availability:** Raw sequencing data are available in the NCBI Sequence Read Archive repository under the BioProject accession number PRJNA1083412. Raw Sanger sequences for mutation verification are available in the FigShare repository (*32*). **License information:** Copyright © 2025 the authors, some rights reserved; exclusive licensee American Association for the Advancement of Science. No claim to original US government works. https://www.science.org/about/science-licenses-journal-article-reuse

SUPPLEMENTARY MATERIALS

science.org/doi/10.1126/science.adu8580
Materials and Methods; Supplementary Text; Figs. S1 to S11; Tables S1 to S4; References (*33*–*55*); MDAR Reproducibility Checklist; Data S1 to S4

Submitted 2 December 2024; accepted 6 June 2025

10.1126/science.adu8580

STRUCTURAL METHODS

Diffraction of helium and hydrogen atoms through single-layer graphene

Carina Kanitz[1], Jakob Bühler[1], Vladimír Zobač[2], Joseph J. Robinson[1], Toma Susi[2]*, Maxime Debiossac[1], Christian Brand[1]*

Diffraction of atoms from surfaces provides detailed insights into structures, interactions, and dynamical processes. However, the method is currently limited to measurements in reflection—diffraction through materials has only been demonstrated for subatomic particles and is an outstanding challenge for atoms. In this work, we diffract helium and hydrogen atoms at kilo–electron volt energies through single-layer graphene at normal incidence. Despite the atoms' high kinetic energy as well as coupling to the electronic system of graphene, we observe coherent scattering. This preservation of coherence was the result of the limited momentum transfer between the projectile and the lattice, resulting from interaction times on the femtosecond scale.

A mere 7 years after de Broglie published his seminal work on the wave nature of massive particles in 1923 (*1*), diffraction had been demonstrated for electrons (*2*, *3*), atoms, and diatomic molecules (*4*). Key to this success were crystalline materials that act as gratings for matter waves. They were used in reflection for electrons by Davisson and Germer (*2*) and for atoms and molecules by Estermann and Stern (*4*). Crystal lattices also played a critical role in demonstrating diffraction of electrons in transmission by Thomson (*5*).

Whereas electron diffraction revolutionized microscopy (*6*), diffraction and interferometry of atoms became an indispensable tool for modern physics (*7*–*14*). Atom interferometers are used to measure atomic properties (*15*, *16*), define fundamental constants (*17*–*20*), and search for physics beyond the standard model (*21*, *22*). Atom diffraction from surfaces provides information on materials, such as electronic structure, binding interactions, and dynamical processes (*11*, *12*). The latter includes the movement of adsorbents on the surface, ranging from the diffusion of atoms (*11*, *23*) and molecules (*24*, *25*) to layer deposition in molecular beam epitaxy (*26*). Atom diffraction is complemented by incoherent scattering, which is characterized by an exchange of energy between the atoms and the surface (*27*). This provides additional insights into mechanical properties and dynamics of the surfaces (*28*–*32*), their internal states (*33*–*36*), and even the existence of transient bonds (*37*). Thus, atom-based experiments combine a neutral probe with a high sensitivity to a wide variety of physical phenomena.

Given the broad success of electron diffraction in transmission, it is highly attractive to also establish atom diffraction through materials. This corresponds to the atomic counterpart of the transmission experiment done with electrons by Thomson (*5*). However, atom diffraction at surfaces has been restricted to reflection because there are several requirements that must be met to obtain usable diffraction data. The coherence of the matter wave must be preserved during transmission to render diffraction possible and requires that the interaction between atom and crystal is sufficiently weak to conceal the exact path of the projectile through the grating. During the passage, the distance between the matter wave and the grating atoms is on the order of 1 Å, which leads to a substantial overlap of the atomic orbitals of the projectile with those of the grating. Transmitting an atom through a material while preserving coherence thus seems a formidable task.

We demonstrate diffraction of helium and atomic hydrogen through free-standing single-layer graphene. We use atoms with a kinetic energy component E_0 normal to the lattice of up to 1.6 keV, three orders of magnitude larger than in any previous atomic diffraction experiment (*11*, *38*). Diffraction in this regime is even more surprising because it was previously shown that decoherence prevails as soon as the kinetic energy normal to the surface exceeds only a few electron volts (*12*). Furthermore, such atoms have sufficient energy to damage the crystalline grating (*39*).

Atom-crystal interactions

We chose single-layer graphene as a grating for atoms in transmission given its electronic and mechanical properties. Its high conductivity effectively dissipates electronic excitations, which makes it robust against irradiation damage. At the same time, the strong, atomically thin membrane limits coupling with the projectiles, increasing the chances for coherent transmission compared with a thin graphite sample, for instance. Graphene can be routinely prepared as free-standing material on suitable support structures.

Regarding the matter wave, helium was chosen because it is inert and the smallest neutral atom. Although atomic hydrogen is lighter than helium, its unpaired electron leads to stronger couplings to graphene (*37*, *40*), which might destroy the coherence of the matter wave.

To find suitable experimental conditions for diffraction, we modeled the interaction of the atoms with the crystal using time-dependent density functional theory molecular dynamics simulations (*41*) (Fig. 1 and materials and methods). The most critical parameters are the energy loss to the grating and the exchanged transverse momentum Δp (*42*). As long as Δp is below Heisenberg's momentum uncertainty p_{uncert} of the carbon atoms in graphene, coherence should be preserved. The in-plane momentum uncertainty can be estimated as $m_C\sqrt{\langle v^2\rangle} = 2.1\times10^{-23}\,\mathrm{kg\cdot m/s}$, with $\langle v^2\rangle$ the mean square in-plane velocity and m_C the mass of the carbon atom (*42*). For helium transmitted through the center of a hexagon, the simulations predict that Δp is smaller than p_{uncert} for a beam energy E_0 above 100 eV (Fig. 1B).

This result by itself may appear counterintuitive because helium does not penetrate graphene at ambient conditions (*43*). Thus, we must increase the atom's energy to push it through the lattice. However, this greater energy does not lead to an increased momentum transfer because the interaction time is decreasing (Fig. 1A). By making the atoms travel faster, we can also mitigate the increase of Δp when the projectile passes the crystal closer to a grating atom (*42*).

A high beam energy, however, enhances the energy loss to the electronic structure of graphene (Fig. 1C). The energy loss has a minimum around $E_0 = 250$ eV, increases with beam energy, and reaches several electron volts at $E_0 = 1500$ eV. A good compromise between the energy loss and the momentum transfer is expected for beam energies between 400 and 600 eV. For hydrogen, the momentum transfer to the crystalline lattice is smaller by about an order of magnitude compared with that of helium (Fig. 1B). At the same time, the energy loss to graphene is much more pronounced, reaching 16 eV at a beam energy of 1500 eV.

Coherent diffraction in transmission

A schematic of the experimental setup is depicted in Fig. 2A and described in more detail in the materials and methods. We prepared a beam of helium ions or protons in the energy range between 250 and 1600 eV with an ion gun and then neutralized it using a gas-filled charge-exchange cell (*38*, *44*). At these energies, we expect virtually all atoms that impinge on clean single-layer graphene to be transmitted (supplementary text). The de Broglie wavelength $\lambda_{\mathrm{dB}} = h/\sqrt{2mE_0}$ of the atoms is defined by the beam kinetic energy E_0, the atomic mass m, and Planck's constant h. In the considered energy range, λ_{dB} lies between 400 and 1800 fm. At the position of the grating, the transverse coherence amounted to a least five

[1]German Aerospace Center (DLR), Institute of Quantum Technologies, Ulm, Germany. [2]Faculty of Physics, University of Vienna, Vienna, Austria. *Corresponding author. Email: toma.susi@univie.ac.at (T.S.); christian.brand@dlr.de (C.B.)

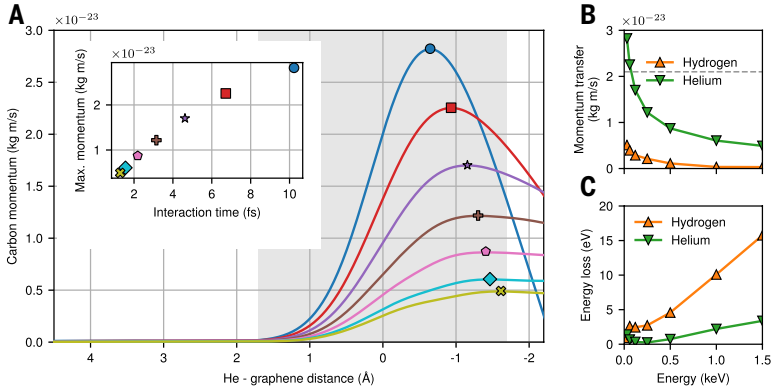

Fig. 1. Coupling of fast atoms to graphene. (**A**) Transverse momentum of a carbon atom in graphene during the hexagon-center transmission of helium at different kinetic energies: 30 eV (circle), 60 eV (square), 120 eV (star), 250 eV (plus), 500 eV (pentagon), 1000 eV (diamond), and 1500 eV (cross). The gray area depicts the van der Waals interaction region of ±1.7 Å. The inset shows the corresponding interaction time (duration for the projectile passing through the interaction region). (**B**) Transverse momentum transfer to a carbon atom while helium or hydrogen transmit the lattice depending on the projectile kinetic energy. The broken line corresponds to the in-plane momentum uncertainty of carbon in graphene. (**C**) Energy loss to the electronic system while helium or hydrogen passes the material depending on the projectile kinetic energy. In (B) and (C), the symbols are calculations, and the lines are to guide the eye.

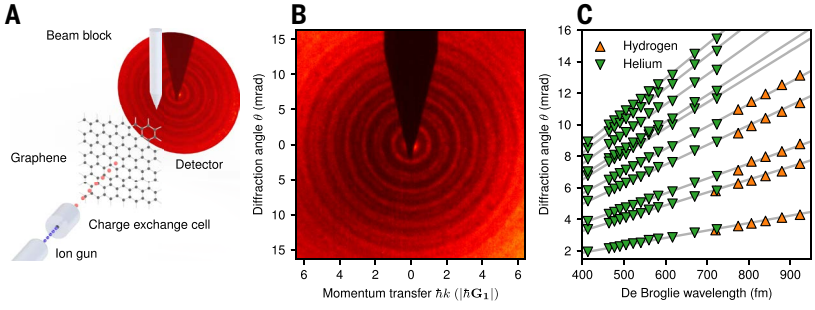

Fig. 2. Atomic diffraction through polycrystalline free-standing single-layer graphene. (**A**) A beam of H^+ or He^+ (blue spheres) is prepared using an ion gun and then neutralized in a charge-exchange cell. After collimation to better than 1 mrad (full width at half maximum), the neutral beam (red spheres) impinges onto the graphene sample at normal incidence. The transmitted signal is visualized using a position-sensitive detector (microchannel plate) stacked onto a phosphorus screen and is recorded with a camera. (**B**) Diffraction of helium at 706 eV through polycrystalline graphene results in Debye-Scherrer rings exhibiting diffraction angles of more than 15 mrad. (**C**) Experimental verification of the diffraction equation. The diffraction angle θ of hydrogen (orange) and helium (green) is plotted versus the de Broglie wavelength (corresponding to kinetic energies between 390 and 1600 eV). The lines represent expected diffraction angles $\sin(\theta) = |\mathbf{G}| / k_0$.

times the lattice constant a of graphene, and the minimum longitudinal coherence is about $50 \times \lambda_{dB}$, which was sufficient for multislit diffraction.

The matter wave impinges with a momentum $\hbar k_0 = h / \lambda_{dB}$ at the honeycomb lattice of graphene, with reduced Planck constant $\hbar$. During diffraction, the grating imparts transverse momentum to the matter wave in integer multiples of the reciprocal basis vectors $\hbar\mathbf{G}_1$ and $\hbar\mathbf{G}_2$. Those are proportional to the inverse of the lattice constant a. The diffraction angle θ is then given by the ratio of imparted momentum to forward momentum $\sin(\theta) = |\mathbf{G}| / k_0$, where $\mathbf{G} = n_1\mathbf{G}_1 + n_2\mathbf{G}_2$ and both n_1 and n_2 are integer numbers. The small lattice constant led to diffraction angles on the order of several milliradians that can be well resolved with a position-sensitive detector (Fig. 2).

In our experiment, the atomic beam had a diameter of ~300 μm when it reached the suspended polycrystalline graphene. Instead of individual diffraction peaks arising from a single lattice orientation, we thus expect Debye-Scherrer rings (*45*), reflecting the random orientations of the different crystal domains in the sample. We resolved patterns exhibiting more than 10 distinct rings at angles reaching up to 15 mrad (Fig. 2B).

To verify that the peaks are caused by beam diffraction, we plotted the angular positions of the Debye-Scherrer rings against the de Broglie wavelength (Fig. 2C). We observed an excellent agreement between the experimental data and the theoretical diffraction angles both for hydrogen and helium. We therefore conclude that the patterns result from the coherent interaction with the lattice and are the result of diffraction.

Coupling to the crystal lattice

Whereas the beam energy determines the peak positions, simulations predicted that it also influenced the couplings to the lattice. To explore this, we compare the azimuthally averaged intensity traces for helium at various beam energies (Fig. 3A and fig. S2). At the lowest energy, we distinguished more than 20 diffraction rings. They corresponded to about eight reciprocal vectors exchanged with the surface, as $\mathbf{G}_1$ and $\mathbf{G}_2$ span a two-dimensional (2D) lattice (fig. S1 and supplementary text). With increasing energy, the higher diffraction orders vanished and were replaced by a broad unstructured background. This background dominated at large diffraction angles, that is, when $k > 8 \cdot |\mathbf{G}_1|$ at $E_0 = 1208$ eV. That trend persisted even when increasing the angular resolution of the experiment (fig. S4 and supplementary text). For hydrogen, the damping of higher diffraction orders was even more pronounced, and the patterns consisted only of a few diffraction orders (Fig. 3, B and C, and fig. S3). Nevertheless, we observed diffraction for hydrogen in the energy range from 250 to 1600 eV. These observations are fascinating because they suggest that the atoms have lost several electron volts of energy to the grating yet still preserved their coherence. We attributed the more pronounced energy loss of hydrogen compared with that of helium to the unpaired electron and thus a higher reactivity, as previously observed for hydrogen at lower energies (*36*, *37*).

Discussion and outlook

Atomic diffraction through nanomachined gratings has been a successful field for decades (*7*, *46*–*49*). We go beyond that by demonstrating diffraction of atomic matter waves through a crystal. Though we expect substantial couplings to the lattice, we resolved diffraction patterns corresponding to momentum transfers of up to $\pm 8\hbar|\mathbf{G}_1|$. To reach a comparable momentum splitting for rubidium atoms using a light grating at 780 nm, it would be necessary to scatter more than 58,000 photons (supplementary text). Our platform thus realizes the beamsplitter with the largest known momentum transfer for atoms in transmission. To achieve this, we illuminated graphene at normal incidence with atomic beams in the kilo–electron volt energy range. Unexpectedly, this high energy did not lead to the grating's disintegration. Although some samples were irradiated for more than 100 hours, we did not observe any degradation of the grating's performance. Because diffraction is sensitive to the phase accumulated by the interfering particles, the method provides a detailed picture about couplings of atoms with matter. At the same time, the de Broglie wavelength in the femtometer range offers an excellent resolution in momentum space.

With this study, we open the door to use complex particles for transmission experiments. In contrast to electrons, atoms exhibit internal degrees of freedom. Thus, matter waves can be easily prepared in specific internal states, thus widely expanding current possibilities in transmission experiments. Such studies might have far-reaching implications for

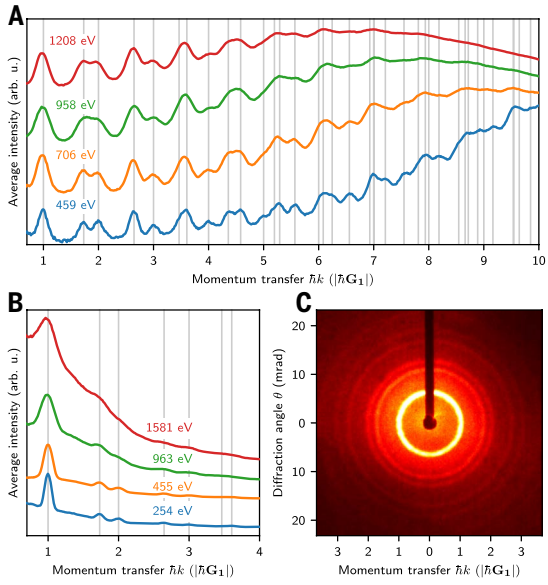

Fig. 3. Energy-dependent atomic diffraction through single-layer graphene. (**A** and **B**) The experimental azimuthally averaged intensity at various kinetic energies is plotted versus momentum transfer in units of the graphene reciprocal lattice vector $\mathbf{G}_1$ for helium (A) and hydrogen (B). Vertical lines indicate the calculated diffraction angles. arb. u., arbitrary units. (**C**) Diffraction pattern of hydrogen atoms at 455 eV.

a variety of research areas. Neutral atoms in the energy regime of our experiment are omnipresent in interstellar space and the magnetosphere (*50*–*52*). Interference measurements might thus provide insights into interactions with surfaces or small constituents, such as polycyclic aromatic hydrocarbons. From the standpoint of materials research, it would be fascinating to extend the experiments to other crystals and their heterostructures (supplementary text and figs. S5 to S7).

The use of single crystals is interesting because it would allow for separating coherent and incoherent contributions of the diffraction patterns. The method might even open new avenues to study organic and biological materials whose sensitivity to ionizing radiation remains a substantial limitation (*53*). There is also a possibility for applications in structural biology, where established cryogenic transmission electron microscopy–based techniques are limited by radiolysis damage resulting from the use of ionizing radiation as probe (*53*). Neutral atom beams, on the contrary, can be expected to couple less strongly to the electronic system of the target materials. This makes them a promising alternative to electrons for damage-free characterization of biological assemblies.

Finally, combining crystalline transmission gratings into interferometers might give rise to new quantum-based sensors. Fast atoms have advantages for detecting gravitational waves (*54*) compared with cold-atom experiments (*55*) and might give rise to new multidimensional interferometers (*56*).

REFERENCES AND NOTES

1. L. de Broglie, *Nature* **112**, 540 (1923).
2. C. Davisson, L. H. Germer, *Nature* **119**, 558–560 (1927).
3. G. P. Thomson, A. Reid, *Nature* **119**, 890 (1927).
4. I. Estermann, O. Stern, *Z. Phys.* **61**, 95–125 (1930).
5. G. P. Thomson, *Nature* **120**, 802 (1927).
6. E. Ruska, *Rev. Mod. Phys.* **59**, 627–638 (1987).
7. A. D. Cronin, J. Schmiedmayer, D. E. Pritchard, *Rev. Mod. Phys.* **81**, 1051–1129 (2009).
8. G. Rosi, F. Sorrentino, L. Cacciapuoti, M. Prevedelli, G. M. Tino, *Nature* **510**, 518–521 (2014).
9. P. Asenbaum, C. Overstreet, M. Kim, J. Curti, M. A. Kasevich, *Phys. Rev. Lett.* **125**, 191101 (2020).
10. D. Becker *et al.*, *Nature* **562**, 391–395 (2018).
11. D. Farias, K.-H. Rieder, *Rep. Prog. Phys.* **61**, 1575–1664 (1998).
12. H. Winter, A. Schüller, *Prog. Surf. Sci.* **86**, 169–221 (2011).
13. B. Holst *et al.*, *Phys. Chem. Chem. Phys.* **23**, 7653–7672 (2021).
14. G. Bracco, B. Holst, Eds., *Surface Science Techniques*, *Springer Series in Surface Science* (Springer, 2013).
15. W. F. Holmgren, M. C. Revelle, V. P. A. Lonij, A. D. Cronin, *Phys. Rev. A* **81**, 053607 (2010).
16. Y. Y. Fein *et al.*, *Phys. Rev. X* **10**, 011014 (2020).
17. R. H. Parker, C. Yu, W. Zhong, B. Estey, H. Müller, *Science* **360**, 191–195 (2018).
18. C. D. Panda *et al.*, *Nat. Phys.* **20**, 1234–1239 (2024).
19. J. B. Fixler, G. T. Foster, J. M. McGuirk, M. A. Kasevich, *Science* **315**, 74–77 (2007).
20. L. Morel, Z. Yao, P. Cladé, S. Guellati-Khélifa, *Nature* **588**, 61–65 (2020).
21. P. Hamilton *et al.*, *Science* **349**, 849–851 (2015).
22. M. S. Safronova *et al.*, *Rev. Mod. Phys.* **90**, 025008 (2018).
23. J. Kelsall, P. S. M. Townsend, J. Ellis, A. P. Jardine, N. Avidor, *Phys. Rev. Lett.* **126**, 155901 (2021).
24. A. Tamtögl *et al.*, *Nat. Commun.* **12**, 3120 (2021).
25. H. Hedgeland *et al.*, *Nat. Phys.* **5**, 561–564 (2009).
26. P. Atkinson *et al.*, *Appl. Phys. Lett.* **105**, 021602 (2014).
27. G. Benedek, J. P. Toennies, *Surf. Sci.* **299-300**, 587–611 (1994).
28. A. Al Taleb, H. K. Yu, G. Anemone, D. Farías, A. M. Wodtke, *Carbon* **95**, 731–737 (2015).
29. C. Büchner *et al.*, *Phys. Rev. Lett.* **120**, 226101 (2018).
30. S. D. Eder *et al.*, *Phys. Rev. Lett.* **127**, 266102 (2021).
31. J. S. Becker, R. D. Brown, D. R. Killelea, H. Yuan, S. J. Sibener, *Proc. Natl. Acad. Sci. U.S.A.* **108**, 977–982 (2010).
32. M. Tømterud *et al.*, *Carbon* **238**, 120150 (2025).
33. M. Tømterud *et al.*, *Nat. Phys.* **19**, 1910–1915 (2023).
34. B. Liu *et al.*, *Phys. Rev. Lett.* **132**, 176202 (2024).
35. A. Al Taleb, D. Farías, *J. Phys. Condens. Matter* **28**, 103005 (2016).
36. O. Bünermann *et al.*, *Science* **350**, 1346–1349 (2015).
37. H. Jiang *et al.*, *Science* **364**, 379–382 (2019).
38. P. Rousseau, H. Khemliche, A. G. Borisov, P. Roncin, *Phys. Rev. Lett.* **98**, 016104 (2007).
39. O. Lehtinen *et al.*, *Phys. Rev. B* **81**, 153401 (2010).
40. J. Lienemann *et al.*, *Phys. Rev. Lett.* **106**, 067602 (2011).
41. V. Zobač, M. Kuisma, A. H. Larsen, T. Rossi, T. Susi, *J. Chem. Phys.* **162**, 124117 (2025).
42. C. Brand *et al.*, *New J. Phys.* **21**, 033004 (2019).
43. J. S. Bunch *et al.*, *Nano Lett.* **8**, 2458–2462 (2008).
44. A. Schüller, S. Wethekam, H. Winter, *Phys. Rev. Lett.* **98**, 016103 (2007).
45. V. K. Pecharsky, P. Y. Zavalij, *Fundamentals of Powder Diffraction and Structural Characterization of Materials* (Springer, 2009).
46. D. W. Keith, M. L. Schattenburg, H. I. Smith, D. E. Pritchard, *Phys. Rev. Lett.* **61**, 1580–1583 (1988).
47. O. Carnal, M. Sigel, T. Sleator, H. Takuma, J. Mlynek, *Phys. Rev. Lett.* **67**, 3231–3234 (1991).
48. J. Fujita *et al.*, *Nature* **380**, 691–694 (1996).
49. T. Nesse *et al.*, *Phys. Rev. A* **95**, 063618 (2017).
50. S. A. Fuselier *et al.*, *Science* **326**, 962–964 (2009).
51. M. Mendillo, J. Baumgardner, B. Flynn, W. J. Hughes, *Nature* **348**, 312–314 (1990).
52. J. L. Burch *et al.*, *Science* **291**, 619–624 (2001).
53. L. A. Baker, J. L. Rubinstein, in *Cryo-EM Part A Sample Preparation and Data Collection*, G. J. Jensen, Ed., vol. 481 of *Methods in Enzymology* (Academic Press, 2010), pp. 371–388.
54. R. Y. Chiao, A. D. Speliotopoulos, *J. Mod. Opt.* **51**, 861–899 (2004).
55. A. Roura, D. R. Brill, B. L. Hu, C. W. Misner, W. D. Phillips, *Phys. Rev. D* **73**, 084018 (2006).
56. B. Barrett, P. Cheiney, B. Battelier, F. Napolitano, P. Bouyer, *Phys. Rev. Lett.* **122**, 043604 (2019).
57. C. Kanitz, J. Bühler, J. J. Robinson, M. Debiossac, C. Brand, Diffraction data of helium and hydrogen atoms through polycrystalline graphene, data set, Zenodo (2025). https://doi.org/10.5281/zenodo.15430453.
58. T. Susi, Ehrenfest molecular dynamics trajectories of neutral hydrogen and helium transmission through the single-layer graphene, data set, Zenodo (2025). https://doi.org/10.5281/zenodo.15526534.

ACKNOWLEDGMENTS

We thank P. Roncin and M. Arndt for their long-standing support of the project, including advice and many fruitful discussions over the years. We further thank M. Efremov, A. Wodtke, B. Stickler, and J. Kotakoski for useful discussions. **Funding:** This study was supported by Austrian Science Fund grant P 36264-N (V.Z. and T.S.). **Author contributions:** Conceptualization: C.B.; Data curation: C.K., J.B., V.Z.; Formal analysis: J.B., V.Z., M.D.; Funding acquisition: T.S., C.B.; Investigation: C.K., J.J.R.; Methodology: C.B., M.D., C.K., J.B., T.S.; Project administration: C.B.; Resources: T.S., C.B.; Software: C.K., J.B., V.Z.; Supervision: C.B., T.S., M.D.; Validation: C.K., T.S.; Visualization: J.B., V.Z.; Writing – original draft: C.B. and M.D. with input from all authors; Writing – review & editing: C.B., M.D., T.S., C.K., J.B., V.Z., J.J.R. **Competing interests:** The authors declare that they have no competing interests. **Data and materials availability:** Data and simulation code used in the analysis have been deposited in Zenodo (*57*,*58*). Additional materials will be made available to any researcher for the purposes of reproducing or extending the analysis. **License information:** Copyright © 2025 the authors, some rights reserved; exclusive licensee American Association for the Advancement of Science. No claim to original US government works. https://www.science.org/about/science-licenses-journal-article-reuse

SUPPLEMENTARY MATERIALS

science.org/doi/10.1126/science.adx5679
Materials and Methods; Supplementary Text; Figs. S1 to S7; References (*59*–*71*); Reproducibility Checklist

Submitted 20 March 2025; accepted 12 June 2025

10.1126/science.adx5679

NUCLEAR FUSION

Predicting fusion ignition at the National Ignition Facility with physics-informed deep learning

Brian K. Spears[1], Scott Brandon[1], Dan T. Casey[1], John E. Field[1]†, Jim A. Gaffney[1,2], Kelli D. Humbird[1]*, Andrea L. Kritcher, Michael K. G. Kruse[1], Eugene Kur[1], Bogdan Kustowski[1], S. Langer[1], Dave Munro[1]†, Ryan Nora[1], J. Luc Peterson[1], Dave J. Schlossberg[1], Paul Springer[1], Alex Zylstra[1,3]‡

An inertial confinement fusion experiment, carried out at the National Ignition Facility, has achieved ignition by generating fusion energy exceeding the laser energy that drove the experiment. Prior to the experiment, a generative machine learning model that combines radiation hydrodynamics simulations, deep learning, experimental data, and Bayesian statistics was used to predict, with a probability greater than 70%, that ignition was the most likely outcome for this shot.

Here we describe both the prediction and the model, which is a jointly informed deep learning model that merges simulations with experiments, and accounts for several sources of uncertainty. Our model can adapt to modified designs, serve as a tool to make decisions about future experiments, and provide a robustness metric in design optimization studies.

The inertial confinement fusion (ICF) program of the US Department of Energy (DOE) (*1*, *2*) aims to use the world's most energetic laser system, the National Ignition Facility (NIF) (*3*, *4*, *5*, *6*), to compress and heat a millimeter-sized capsule containing the hydrogen isotopes deuterium and tritium (DT). Upon compression, nuclear reactions within the DT fuel produce fusion energy. On 5 December 2022, NIF researchers fielded an ICF experiment that was driven by 2.05 MJ of ultraviolet (UV) laser energy and produced 3.15 MJ of neutron fusion yield (*7*), thereby exceeding, for the first time, the ignition requirements as laid out by the National Academies of Science (NAS) in 1997 (*8*).

Computer simulations of ICF performance play an essential role in the design of NIF experiments. About a dozen ignition experiments are performed each year at the NIF, and researchers must rely heavily on simulations to optimize experimental designs. The success of these efforts requires the development of predictive models that can accurately estimate observable quantities of interest before an experiment is executed. However, any practical simulation must make simplifying assumptions to reduce computational cost, such as introducing axes of symmetry or leveraging reduced order models; these simplifications often result in discrepancies between simulation predictions and experimental observations.

To reduce the discrepancies between simulations and experiments, simulations have been historically "tuned" by adjusting uncertain parameters in the model in a "post-shot" to match experimental measurements (*9*, *10*). These tuned models are then used to make small extrapolations in a "pre-shot" for future experiments. This tuning method—along with empirical models (*11*) and analytical theory—has substantially advanced understanding and performance of ICF implosions in recent years, culminating in a series of improvements ultimately leading to fusion ignition (*7*, *12*–*15*).

[1]Lawrence Livermore National Laboratory, Livermore, CA, USA. [2]Focused Energy Inc., Redwood City, CA, USA. [3]Pacific Fusion, Fremont, CA, USA. ***Corresponding author. Email: humbird1@llnl.gov** †Retired.

Although the manual post-shot tuning approach has proved useful for small extrapolations in design space, truly predictive computer models are needed to inform decisions regarding laser upgrades or designs of future high-yield facilities that will operate in considerably different regimes. Thus, when considering new designs in untested regions of parameter space, it is vital to understand and quantify the uncertainties in post-shot models to account for many possible scenarios. Quantifying these uncertainties is particularly challenging as a result of sparse experimental data, vast design space, and computationally expensive simulations. Here, we describe how a statistical analysis of a series of recent NIF experiments (*16*–*20*) enabled us to accurately estimate the expected performance of a previously untested ICF experiment design with credible and quantified uncertainty. This work combines several improved techniques for data-driven predictive modeling of ICF experiments, including large databases of simulations generated with advanced high-performance computing (HPC) workflows (*21*, *22*), Bayesian post-shot analysis (*23*), and the machine learning technique of transfer learning (*24*–*27*) (Fig. 1). Data-driven modeling of ICF experiments has gained popularity in recent years (*28*, *29*). However, these approaches lack rigorous, data-driven uncertainty quantifications, which is proving to be of great importance given the variability observed in recent NIF ICF experiments (*28*, *29*).

We have developed a predictive model as an extension to the previously published Bayesian post-shot analysis (*23*); our model quantifies the variability in the series of the near-repeat experiments that were carried out from 2021 to 2022. This "variability model" provides distributions of expected variations in fielding conditions for NIF Hybrid-E experiments, which are forward-propagated through machine learning models of designs undergoing testing to make predictions of performance variability of upcoming experiments.

In September 2022, NIF executed its first ICF experiment driven with a newly achievable laser energy of 2.05 MJ (an upgrade from the previous maximum of 1.9 MJ). This design achieved >1 MJ of yield with a clear path forward for further improvements. In anticipation of the second experiment to be driven at 2.05 MJ of laser energy, we applied our approach a week prior to the successful ignition shot in December 2022 and predicted that the design had a 74% chance of exceeding break-even yield, significantly higher than any previous design. Our predicted 50% confidence interval (CI) neutron yield of [2, 7.2] MJ is consistent with the experimental result of 3.15 MJ, and other experimental observables are also in agreement with expectations. Furthermore, subsequent repeat experiments of the December 2022 design are also consistent with our predicted variability distribution. This outcome demonstrates a promising approach to predictive modeling of ICF experiments and provides a framework for developing data-driven models for other complex systems.

Inertial confinement fusion

To achieve fusion ignition using the ICF approach, DT fuel must be compressed to a very high density and temperature while remaining spatially confined for a sufficient amount of time (*30*–*34*). Most experiments at the NIF use an "indirect" approach in which a DT-filled capsule is placed inside a cylindrical gold or uranium cavity, or "hohlraum" (fig. S1). The capsule consists of multiple concentric spherical shells of an ablator material such as high-density carbon (diamond) and a small percentage of high-Z dopant (*35*, *36*). The capsule is suspended inside the hohlraum by a thin membrane known as the support tent. Once inside the NIF target chamber, the capsule is filled with DT fusion fuel through a small (2- to 10-μm) fill tube and cooled to cryogenic temperatures near the triple point of hydrogen to create a smooth ice layer on the target's inner surface and DT gas in the center. Intense UV (351-nm) laser light from the NIF impinges on the interior surface of the hohlraum and is converted to a Planckian x-ray spectrum with a high-energy component coming from atomic M-shell transitions of electrons in the hohlraum wall. The x-rays rapidly heat and ablate the outer capsule material, resulting in an inward "drive" and imploding the capsule. The drive pressure

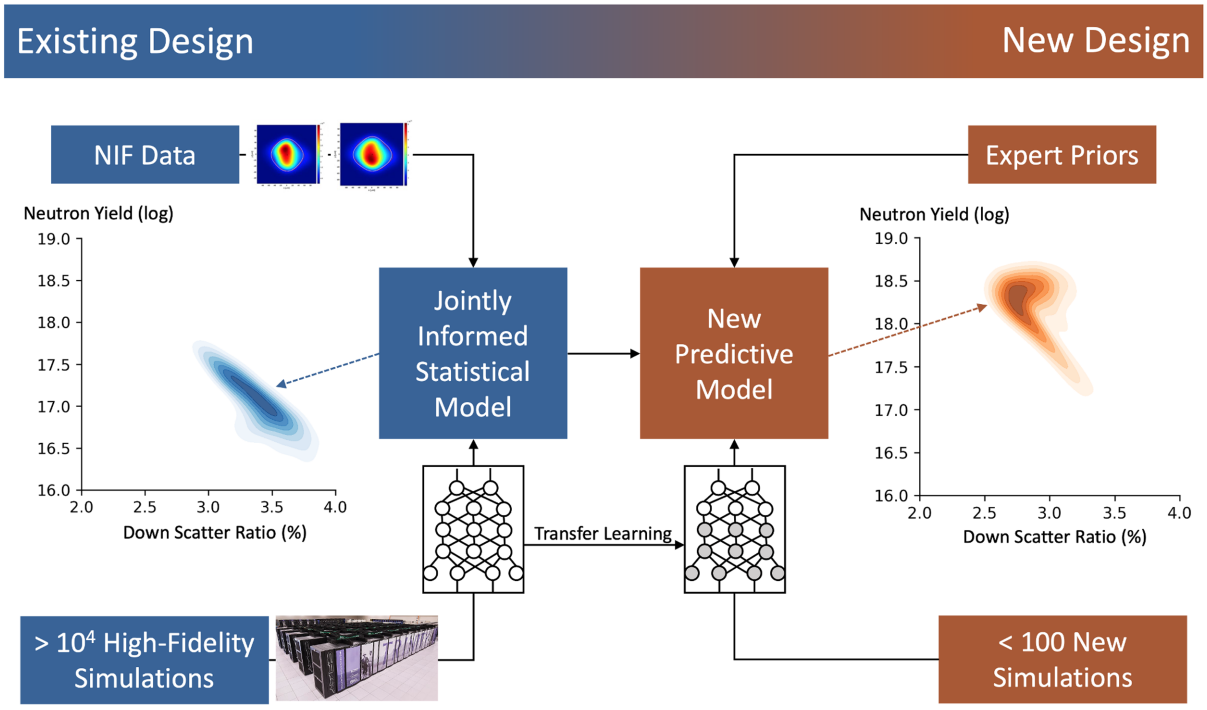

Fig. 1. Workflow for predicting variability of a proposed experiment. Our predictive model for complex experiments combines large databases of simulations, Bayesian analysis, and the machine learning technique of transfer learning to build a statistical model that is jointly informed by experimental and simulation datasets. The model is first built on previously fielded NIF experiments using a statistical model jointly informed by simulation and experiments. This model provides input conditions that capture model uncertainty and shot-to-shot variability observed in a series of NIF experiments. The input conditions are then applied to a proposed design for a future experiment, producing a distribution of expected outcomes based on prior experiments.

features a carefully executed time history designed to launch a series of converging shocks intended to achieve high compression of the fuel. At peak compression, the capsule volume is reduced by 10,000 times, producing central hotspot pressures of hundreds of gigabars, and ion temperatures of several kilo–electron volts (keV). These extreme conditions cause the DT fuel in the hotspot to fuse, producing high-energy neutrons and alpha particles. The alpha particles deposit their energy in the surrounding cold DT fuel shell, generating a propagating fusion burn wave that consumes the fuel until the implosion reaches minimum volume and then starts to expand, ultimately losing confinement. When the energy produced through fusion reactions exceeds the driver energy used to initiate the implosion, the experiment meets the NAS definition of "ignition."

Predicting ignition

Our goal is to provide quantitative predictions, ahead of time and with uncertainties, of the fusion yield and other key diagnostic signatures (*37*) while incorporating previously collected NIF data, high-fidelity physics simulations, and subject matter expert knowledge.

We begin by analyzing previous experiments to determine the input conditions that are consistent with measured data. By performing Bayesian inference on each individual shot and then combining the resultant distributions, we construct a generative model that quantifies all shot-to-shot variations across the series of experiments. This generative model can then create predictions for yet-to-be-performed experiments.

Because multiphysics ICF simulations are expensive (requiring several compute node-hours each), directly including the simulator in the Bayesian analysis would be prohibitive. Instead, we rely on deep neural network (DNN) surrogates trained on a large simulation database that spans the conditions for all shots. This simulation-based (but data-driven) approach allows for expedient and physically meaningful Bayesian analysis of sparse data.

In the following sections, we detail the process of generating the simulation database, performing Bayesian post-shot analyses, and building the global variability model. We take this variability model, which is a distribution of input conditions consistent with past experimental data and apply it as a "prior" to make predictions for a new ICF experiment.

ICF simulations to understand shot-to-shot variability

ICF implosions are simulated in a multistage approach using the radiation hydrodynamics code HYDRA (*38*), which employs a detailed set of physics processes such as laser transport (*10*, *39*, *40*), radiation transfer, hydrodynamics, thermodynamics, and nuclear processes. First, an integrated calculation that models the lasers, hohlraum, and capsule is run using the pulse and capsule parameters for a proposed design. Integrated simulations are necessary to describe the radiation drive on the capsule; however, highly resolved hohlraum and capsule simulations are too computationally expensive to run routinely. To produce diagnostic quantities, a second round of capsule-only simulations is necessary. The capsule-only implosion is driven with a frequency-dependent radiation source generated by the integrated simulation, which is typically tuned to match a prior experiment similar to the proposed design (*10*). These detailed simulations enable modeling of effects such as mixing between the fuel–ablator interface (*41*), perturbations from the fill tube (*42*–*44*) and capsule support tent (*45*, *46*), and asymmetries in the radiation drive (*47*–*49*).

Often, the exact impact of engineering features and capsule quality cannot be anticipated ahead of the experiment and must instead be inferred afterwards by determining which degradation mechanisms (and their values) must be applied to a simulation to match experimental observations. Similarly, the drive symmetry history of the implosion cannot be measured precisely but must be inferred by matching simulations to data that describes the shape of the imploding hotspot and shell. In this work, we take a statistical approach to inferring the simulation input conditions that produce outputs consistent with experimental data.

We simulate a series of experiments beginning with the first demonstration of yield >1 MJ in August 2021 (NIF shot N210808) (*50*) before demonstrating energy gain >1 with the NIF shot N221204. Between these two landmark experiments, the ICF program executed experiments attempting to repeat N210808. The experiments did not achieve the same performance but did provide data critical to understanding shot-to-shot repeatability of ignition-class designs (*28*, *29*).

To understand the range of input conditions consistent with experimental observables and to quantify the variability of N210808 and its repeat experiments, a database (*51*) of two-dimensional (2D) axisymmetric simulations centered around the nominal N210808 design is generated. The simulations span an 8D parameter space (table S1). These inputs are included in the study because they are known to be uncertain or variable in experiments and can meaningfully affect observable quantities of interest. The simulation input values are generated through a combination of Latin hypercube sampling (*52*) and an adaptive technique to increase the number of samples in proximity of the experimental data (*53*). The database of simulations is executed on the Trinity supercomputer at Los Alamos National Laboratory and is driven by the UQ Pipeline High Performance Computing workflow manager (*54*). The database comprises >150,000 simulations, with each simulation taking approximately 900 central processing unit (CPU) hours to complete (*55*).

The simulation database is used to build an accurate deep neural network emulator of HYDRA in the 8D design space that matches several simulation outputs (table S2). The neural network enables rapid Bayesian post-shot analysis (*23*) of the N210808 experiment and its repeats and provides the foundation of our predictive model.

Modeling shot-to-shot variability

Our predictive model is trained on seven observed quantities collected from each previous experimental shot (N210808 and repeats) and describes the expected performance of future shots through a probabilistic model for variations of simulation input parameters (table S1). After training, the probabilistic model approximates the distribution of shot-to-shot variations consistent with past experiments; predictions for new designs can be made by propagating the variability model through models of the proposed design, introducing prior transformations based on known design changes if necessary.

Posing the variability model in terms of simulation inputs (as opposed to outputs) is a key concept in the development of our approach and offers several advantages that far outweigh the increased model complexity. First, the simulation inputs are readily interpretable and thus conducive to understanding our results. Second, modeling variability in the input space and propagating to outputs using the emulator of HYDRA allows us to train our model by matching multiple outputs to experimental data exhibiting physics-based, simulation-derived correlations. This approach considerably increases the information available to the model because correlations between different outputs across shots [for example, neutron yield and down-scatter ratio (DSR), the ratio of energetically down-scattered neutrons at 10 to 12 MeV to the primary neutrons at 13 to 15 MeV energy] are highly informative about the nature of the shot-to-shot variations. Modeling variability in the output space would require these correlations be learned from limited data, substantially reducing the information available to constrain variability. Put another way, constructing our model around input variability allows us to include a second source of information—the simulations—and is crucial to its success in learning variations from the very sparse data available.

The generative model used in this work consists of a multivariate normal distribution with unknown mean vector μ and covariance matrix Σ, which are to be learned from the N210808 and its repeat shots. The mean and covariance are explored using Markov chain Monte Carlo (MCMC), which generates samples from a nonparametric posterior distribution with potentially complex high-dimensional structure. Using MCMC allows our model to describe highly correlated shot-to-shot variations over the HYDRA inputs, which are not meaningfully limited by the multivariate normal assumption. However, for practical purposes, we introduce a weak prior on μ to ensure that the variations remain physical, as well as a prior on Σ to ensure required symmetry and positive definiteness. A complete description of the model and priors is given in (*56*).

There are a total of 44 parameters in the generative model: eight components of μ, eight diagonal, and 28 off-diagonal elements of Σ. Our model is trained by drawing samples from the posterior distribution of model inputs for each shot in the training data. This sampling introduces a further eight parameters per training shot which are propagated through a DNN surrogate (*57*) of the HYDRA simulations to make predictions of experimental observables and form the likelihood function for the MCMC. We therefore need to explore a joint space of ~100 parameters during inference—a potentially expensive computational task. We found that this expense is considerably reduced by exploiting the differentiability of the model that is afforded by the following strategies: using DNNs, enforcing independence between the inferred per-shot simulation inputs, and initializing the inference with per-shot inputs taken from a previous inference. These improvements allow the generative model to be trained in a few CPU hours, and the MCMC chains perform well in convergence and autocorrelation metrics.

Predicting the variability of the N221204 design

With the trained generative model in hand, we can generate samples of the inputs for future shots that are of the same design as the training shots. To make predictions for a different design, the generated samples can be modified to reflect expected changes in input conditions. We achieve such modifications through analytical transformations of the generative model informed by the shot designer. In the case of N221204, our transformations reflect a known change in capsule quality as well as anticipated problems controlling the Legendre mode-2 drive asymmetry, which determines how prolate or oblate the implosion is throughout the drive. With the designer input, we confirmed that the existing generative model gave variations consistent with expectations, meaning that no explicit transformation was needed for this experiment.

The next stage entails efficiently propagating the transformed input distributions into simulation outputs. The expected variations in performance for a new design are generated by propagating samples from the input distribution through a model of the new design to obtain a distribution of expected outputs. Rather than creating a new large database of HYDRA simulations to propagate the input distribution, which would be computationally expensive and take several weeks to execute, we use a sparse sampling technique to create a small set of new simulation points from a nonanalytic input distribution. We leverage a technique called "transfer learning" to create a N221204 surrogate model that is sufficiently accurate in the relevant regions of parameter space. Transfer learning (TL) (*58*) ultimately adapts a neural network trained for one task to a different, related task using a relatively small amount of training data.

Sparse samples from the input distribution are generated through stochastic collocation (SC) (*59*, *60*), a multivariate cubature integration technique that is suitable for exactly integrating low-order polynomials over a domain weighted by a correlated probability distribution. The solution of a SC problem provides a set of nodes with corresponding weights such as the well-known univariate Gaussian-quadrature integration rules. The nodes and weights are determined by solving a system of polynomial equations in multiple dimensions. We solve this system approximately with a few different initializations, resulting in 57 SC points (nodes) to use for TL.

These specially selected points are passed as input parameters to a HYDRA model of the N221204 design. This model uses a radiation drive and capsule geometry that differ from N210808 in two major ways: (i) the N221204 design uses an outer ablator that is 6 μm thicker and (ii) increases the laser energy to 2.05 MJ (compared with the 1.9-MJ pulse of N210808). The set of 57 HYDRA simulations are postprocessed to

produce output quantities of interest including the neutron yield, DSR, ion temperature, burn duration, bang time, and more.

Building upon the prior success of TL in ICF to adapt between many simulations and a small number of experiments, we pursue the simpler task of adapting one set of HYDRA simulations to another. We begin by setting aside ~20% of the 57 simulations to serve as a validation set; the remainder serve as training data. We take the previous N210808 surrogate and continue training the first and last layers on the new data while freezing the middle layers. Which layers to freeze is determined by the new surrogate's performance on the validation set, and we found that our choice resulted in a transfer-learned model that accurately models the N221204 design.

TL allows us to balance a rapid turnaround time—necessary for making predictions of new experiments—against surrogate performance. The TL surrogate is less accurate upon cross-validation for the new design (N221204, average $R^2 = 0.88$) than the original surrogate is on the original design (N210808, average $R^2 = 0.96$). This level of surrogate error is insignificant compared with the uncertainties in the input conditions, and additional interrogation of the surrogate since making the predictions indicates that including additional N221204 simulation data does not meaningfully change our assessment. Overall, this approach allows us to make reliable predictions of design variability with as few as 57 simulations of the new design.

With the N221204 neural network surrogate, we can now make predictions for the upcoming experiment by forward propagating the prior distribution to produce the distribution of expected experimental observables. As the neural network is an accurate HYDRA emulator, the resulting distributions respect correlations between outputs and are thus physically consistent. We therefore use our probabilistic model to calculate quantitative measures of predicted performance for comparison with previous shots.

Figure 2 illustrates the predicted distribution of outcomes of the N221204 experiment in the form of 1D and 2D kernel density estimates (KDEs) of the neutron yield (in $\log_{10}$ units) versus the DSR (in percent), along with near-repeat experiments executed in the following months. It is important to stress that the predicted distribution is only trained on the 1.9-MJ data and so does not change as new 2.05-MJ data are collected; as a result, the 2.05-MJ data allow us to independently validate the prediction. The largest outlier, indicated in orange, has an anomalously high mode-1 asymmetry compared with the other experiments and thus is less consistent with our assumed input distribution than the other experiments. However, all of the 2.05-MJ repeat experiments are consistent with the 95% CI produced by our model. Also included in the plot is the corresponding distribution for the N210808 design, with the data from that experiment and subsequent repeats indicated. The experimental data plotted here are listed in table S5. Figure S5 includes additional outputs illustrated as a pair plot, including the ion temperature (keV), the burn duration [picoseconds (ps)], and the Legendre mode P2 of the neutron image (micrometers), which is positive for a prolate implosion, negative for an oblate implosion, and zero for a symmetrical implosion.

Our results predict that N221204 could reach physics regimes that are inaccessible to the previous N210808 design. With an approximately round or slightly prolate hotspot shape (when P2/P0 is near zero or slightly positive), the new design has a higher probability to reach the NAS definition of ignition, whereby target energy gain exceeds 1. Quantitatively, the chance of achieving ignition increased from 0.5% for the N210808 experiment to 74% for the N221204 design; this is a considerable increase in the probability of achieving ignition compared with the previous best-performing design fielded on NIF.

The experiment N221204 fell on the 4th decile of both predicted yield and DSR. The other experiments fell on the 2nd decile of yield and 8th decile of DSR (N220919), the 3rd decile of yield and 10th decile of DSR (N230618), the 4th decile of yield and 8th decile of DSR (N230729), and the 3rd decile of yield and 9th decile of DSR (N230904). Independently this might suggest a slight overprediction of yield and underprediction of DSR, but taken together we have the expected distribution of experiments relative to confidence contours (one out of five experiments outside the 80% contour, two out of five outside 60%, etc.).

Figure 2 illustrates the importance of matching multiple outputs by our model. Considering yield variations alone implies a wide range of possible outcomes of the future experiment, roughly between 0.1 and 15 MJ. Comparing yield against the DSR or other outputs, however, shows that the probable outcomes are restricted to a much narrower corridor because the model is informed of physics correlations learned from the simulations.

Near-repeat experiments of the N221204 design continue to sample the predicted yield-DSR distributions from this modeling method without updating the underlying variability model, providing essential data for validating our approach. A more complete discussion of these validation studies, and a quantification of the uncertainties in our predicted distribution, is given in (*56*).

This capability of quantifying the probability of a certain yield outcome enables better-informed decision-making when considering experiment design. For example, at NIF the high-yield shots can be used as a source of neutrons to study material properties, and fielding these "ride-along" experiments can be expensive and time-consuming. With our analysis, the probability that an upcoming DT experiment will achieve yield necessary to provide useful data can be quantified, and if the probability is low (i.e., <50% probability of achieving minimum required yield), it might not be worth fielding a complex ride-along.

We are also using this model to compare and inform routine design decisions, such as which capsule from the available targets for a given experiment is expected to perform best and which simple modifications to the baseline N221204 design might decrease the yield variability (fig. S6). This modeling method (*61*) is now routinely included in shot

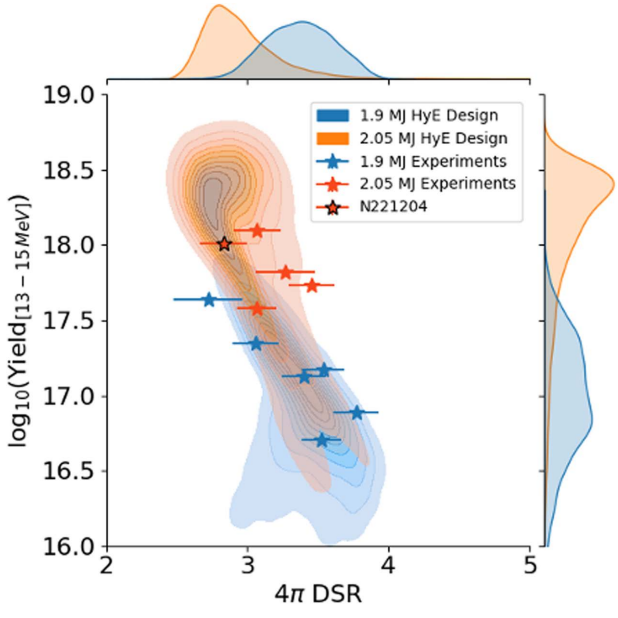

Fig. 2. Primary yield (measure of performance) versus DSR (percent) (measure of confinement). The variability model for the 1.9-MJ Hybrid-E (N210808) design (blue) was derived from the 1.9-MJ Hybrid-E series of experiments (blue stars). The 2.05-MJ Hybrid-E prediction (orange) of the first shot with the target gain >1 (N221204, black outline), was made before the series of the 2.05-MJ experiments (red stars); these subsequent shots validate the prediction. The KDEs plot contours every 10% between 10 and 80%; the single-variable KDEs are projected onto the upper *x*- and *y*-axes. Corresponding experimental measurements for the shots are indicated by stars with a 1-sigma experimental error bar. Experiments outside the 80% contour are still consistent at the 95% level (within error bars).

planning for high-performance experiments to corroborate predictions of traditional methods that are often used for determining detector settings to ensure good data return.

Furthermore, our modeling method will be used not only to predict experiments with modified designs, but it may also help understand whether—and at what cost—future upgrades of the laser facility (for instance, increasing laser energy or peak power) may overcome potential limits of the performance in this region of design space. In addition to using our model for making predictions, it may also be used to compute the robustness metric (fig. S6) in the process of automatic optimization of future designs, and there is a plan to execute this work on an exascale HPC machine in the coming year (*62*). Finally, our methodology is not specific to ICF and could be applied to other areas of research requiring science-informed extrapolation to determine new configurations of complex engineering systems. Additional information on the methodology behind the predictive model and potential applications is provided in the supplemental materials, including information on the simulations, machine learning modeling, and design optimization examples along with references (*57*–*66*).

Discussion and outlook

We have performed a quantitative and physically meaningful prediction of a controlled fusion experiment that achieved a target gain >1. The prediction was made ahead of time using a combination of HPC simulations, previous experimental data, Bayesian statistics, and deep learning. The predictive model combines data and complex physics simulations to make ICF performance predictions when extrapolated to experimentally untested regimes. Our model accounts for inevitable variability in fielding conditions, including fluctuations in laser delivery and capsule quality, uncertainties in input conditions caused by experimental measurement uncertainty, and intentional design changes for the upcoming experiment. By combining Bayesian analysis of previous experiments with transfer learning to efficiently train surrogate models for new designs, we can predict the distribution of expected outcomes for upcoming experiments within days. This method presents opportunities to optimize design decisions under credible, data-informed uncertainties for future NIF experiments. Broadly, this work introduces an approach to predictive modeling in the sparse data regime that extends beyond fusion ignition.

REFERENCES AND NOTES

1. S. W. Haan *et al.*, *Nucl. Fusion* **44**, S171–S176 (2004).
2. J. D. Lindl *et al.*, *Phys. Plasmas* **11**, 339–491 (2004).
3. G. Miller, E. Moses, C. Wuest, *Nucl. Fusion* **44**, S228–S238 (2004).
4. E. M. Campbell, W. J. Hogan, *Plasma Phys. Contr. Fusion* **41**, B39–B56 (1999).
5. E. I. Moses, R. N. Boyd, B. A. Remington, C. J. Keane, R. Al-Ayat, *Phys. Plasmas* **16**, 041006 (2009).
6. M. L. Spaeth *et al.*, *Fus. Sci. Technol.* **69**, 25–145 (2016).
7. H. Abu-Shawareb *et al.*, *Phys. Rev. Lett.* **132**, 065102 (2024).
8. National Research Council, *Review of the Department of Energy's Inertial Confinement Fusion Program: The National Ignition Facility* (The National Academies Press, 1997).
9. O. L. Landen *et al.*, *Phys. Plasmas* **18**, 051002 (2011).
10. O. S. Jones *et al.*, *Phys. Plasmas* **19**, 056315 (2012).
11. S. H. Glenzer *et al.*, *Science* **327**, 1228–1231 (2010).
12. A. L. Kritcher *et al.*, *Phys. Rev. E* **109**, 025204 (2024).
13. O. A. Hurricane *et al.*, *Phys. Rev. Lett.* **132**, 065103 (2024).
14. A. Pak *et al.*, *Phys. Rev. E* **109**, 025203 (2024).
15. M. S. Rubery *et al.*, *Phys. Rev. Lett.* **132**, 065104 (2024).
16. A. Kritcher *et al.*, *Bull. Am. Phys. Soc.* **27**, 112704 (2020).
17. A. B. Zylstra *et al.*, *Phys. Rev. Lett.* **126**, 025001 (2021).
18. A. B. Zylstra *et al.*, *Nature* **601**, 542–548 (2022).
19. A. L. Kritcher *et al.*, *Nat. Phys.* **18**, 251–258 (2022).
20. H. Abu-Shawareb *et al.*, *Phys. Rev. Lett.* **129**, 075001 (2022).
21. R. Nora, J. L. Peterson, B. K. Spears, J. E. Field, S. Brandon, *Stat. Anal. Data Min.* **10**, 230–237 (2017).
22. S. H. Langer *et al.*, in *2016 Second Workshop on In Situ Infrastructures for Enabling Extreme-Scale Analysis and Visualization* (ISAV, 2016); pp. 1–6.
23. J. A. Gaffney *et al.*, *Phys. Plasmas* **26**, 082704 (2019).
24. K. D. Humbird, J. L. Peterson, J. Salmonson, B. K. Spears, *Phys. Plasmas* **28**, 042709 (2021).
25. K. D. Humbird, J. L. Peterson, B. K. Spears, R. G. McClarren, *IEEE Trans. Plasma Sci.* **48**, 61–70 (2019).
26. B. Kustowski *et al.*, *IEEE Trans. Plasma Sci.* **48**, 46–53 (2019).
27. B. Kustowski *et al.*, *Mach. Learn. Sci. Technol.* **3**, 015035 (2022).
28. D. Casey *et al.*, *Phys. Rev. E* **108**, L053203 (2023).
29. A. Pak *et al.*, *Phys. Rev. Lett.* **131**, 065101 (2023).
30. J. D. Lawson, *Proc. Phys. Soc. B* **70**, 6–10 (1957).
31. S. Atzeni, J. Meyer-ter-Vehn, *The Physics of Inertial Fusion: Beam Plasma Interaction, Hydrodynamics, Hot Dense Matter*, vol. 125 (OUP Oxford, 2004).
32. J. Lindl, *Phys. Plasmas* **2**, 3933–4024 (1995).
33. O. A. Hurricane *et al.*, *Rev. Mod. Phys.* **95**, 025005 (2023).
34. J. Nuckolls, L. Wood, A. Thiessen, G. Zimmerman, *Nature* **239**, 139–142 (1972).
35. J. Biener *et al.*, *Nucl. Fusion* **49**, 112001 (2009).
36. T. Braun *et al.*, *Nucl. Fusion* **63**, 016022 (2022).
37. J. D. Kilkenny *et al.*, *Fus. Sci. Technol.* **69**, 420–451 (2016).
38. M. M. Marinak *et al.*, *Phys. Plasmas* **8**, 2275–2280 (2001).
39. O. S. Jones *et al.*, *Phys. Plasmas* **24**, 056312 (2017).
40. D. J. Strozzi *et al.*, *Phys. Rev. Lett.* **118**, 025002 (2017).
41. A. B. Zylstra *et al.*, *Phys. Plasmas* **27**, 092709 (2020).
42. A. Pak *et al.*, *Phys. Rev. Lett.* **124**, 145001 (2020).
43. C. R. Weber *et al.*, *Phys. Plasmas* **27**, 032703 (2020).
44. B. Bachmann *et al.*, *Phys. Rev. E* **101**, 033205 (2020).
45. V. A. Smalyuk *et al.*, *Phys. Plasmas* **25**, 072705 (2018).
46. S. H. Baxamusa *et al.*, *Langmuir* **30**, 5126–5132 (2014).
47. D. Turnbull *et al.*, *Phys. Plasmas* **23**, 052710 (2016).
48. L. Divol *et al.*, *Phys. Plasmas* **24**, 056309 (2017).
49. M. Hohenberger *et al.*, *Phys. Plasmas* **26**, 112707 (2019).
50. A. L. Kritcher *et al.*, *Phys. Rev. E* **106**, 025201 (2022).
51. R. C. Nora *et al.*, *Phys. Plasmas* **30**, 092705 (2023).
52. M. D. McKay, R. J. Beckman, W. J. Conover, *Technometrics* **21**, 239–245 (1979).
53. J. A. Gaffney *et al.*, *Contrib. Plasma Phys.* **63**, e202200190 (2023).
54. S. Brandon *et al.*, "Ensemble calculation via the llnl uq pipeline: A user's guide" (*Tech. Rep. LLNL-SM-480999*, 2011).
55. D. Morton, in *55th AIAA Aerospace Sciences Meeting 2017* (AIAA, 2017); pp. 12578.
56. J. A. Gaffney *et al.*, *Phys. Plasmas* **31**, 092702 (2024).
57. K. D. Humbird, J. L. Peterson, R. G. Mcclarren, *IEEE Trans. Neural Netw. Learn. Syst.* **30**, 1286–1295 (2019).
58. S. J. Pan, Q. Yang, *IEEE Trans. Knowl. Data Eng.* **22**, 1345–1359 (2010).
59. M. Navarro, J. Witteveen, J. Blom, Polynomial chaos expansion for general multivariate distributions with correlated variables. arXiv.1406.5483 [math.NA] (2014).
60. M. Navarro, J. Witteveen, J. Blom, in *Proceedings of the 1st International Conference on Uncertainty Quantification in Computational Sciences and Engineering*. (UNCECOMP, 2015), pp. 218–236.
61. B. Kustowski *et al.*, paper presented at the 65th Annual Meeting of the APS Division of Plasma Physics (APS, 2023); pp. BO07.00005.
62. J. L. Peterson *et al.*, *Phys. Plasmas* **31**, 062711 (2024).
63. D. Lewandowski, D. Kurowicka, H. Joe, *J. Multivariate Anal.* **100**, 1989–2001 (2009).
64. D. Sivia, J. Skilling, *Data Analysis: A Bayesian Tutorial* (OUP Oxford, 2006).
65. A. O. Abril-Pla *et al.*, *PeerJ Comput. Sci.* **9**, e1516 (2023).
66. M. D. Hoffman, A. Gelman, The No-U-Turn Sampler: Adaptively Setting Path Lengths in Hamiltonian Monte Carlo. arXiv.1111.4246 [stat-CO] (2021).

ACKNOWLEDGMENTS

The authors thank the international Inertial Confinement Fusion collaboration and the LLNL ICF program. **Funding:** This work was performed under the auspices of the US Department of Energy by Lawrence Livermore National Laboratory under contract DE-AC52-07NA27344. LLNL-JRNL-855927. **Author contributions:** Methodology: B.K.S., J.E.F., J.A.G., K.D.H., M.K.G.K., E.K., B.K., R.N., and J.L.P. Investigation: B.K.S., J.A.G., K.D.H., M.K.G.K., E.K., B.K., R.N., and J.L.P. Writing: B.K.S., J.A.G., K.D.H., M.K.G.K., E.K., B.K., R.N., J.L.P. Resources: S.B., D.T.C., S.L., A.L.K., D.M., D.J.S., P.S., and A.Z. **Competing interests:** The authors declare no competing interests. **Data and materials availability:** Relevant NIF experimental data is included in the SM of this manuscript. Distribution of the Hydra software and output for simulations falls under legal restrictions of the US government's Export Administration Regulation (EAR), license 6D001. Access to the code may require an export license from the Department of Commerce, Bureau of Industry and Security. Subject to that provision, readers may inquire about the software by contacting Lawrence Livermore National Laboratory. **License information:** Copyright © 2025 the authors, some rights reserved; exclusive licensee American Association for the Advancement of Science. No claim to original US government works. https://www.science.org/content/page/science-licenses-journal-article-reuse

SUPPLEMENTARY MATERIALS

science.org/doi/10.1126/science.adm8201
Supplementary Text; Figs. S1 to S7; Tables S1 to S6

Submitted 15 November 2023; accepted 16 June 2025

10.1126/science.adm8201

BIOCATALYSIS

Artificial farnesol epoxidase enables a concise synthesis of meroterpenoids

Jinxin Wang[1,2]†, Yunpeng Yin[1]†, Quan Zhang[1], Wei-Dong Zhang[2,3]*, Jian Li[1]*

Efficient asymmetric epoxidation reactions have been developed for both the head end and tail end double bonds of farnesol, greatly facilitating the synthesis of terpenoid natural products. However, the lack of methods for direct asymmetric epoxidation of the relatively inert internal alkene of farnesol has posed major challenges in the synthesis of many terpenoids. In this study, we describe the engineering of an epoxidase capable of selectively epoxidizing the internal alkene of farnesol with high regioselectivity and enantioselectivity. The resulting epoxidized intermediate has been successfully applied to simplify the synthesis of a variety of meroterpenoids, reducing the total number of synthetic steps by more than half in most cases.

Farnesol, a linear terpene composed of three isoprene units, is one of the most commonly used starting materials for the total synthesis of terpenoids. In the total synthesis of natural products using farnesol, many synthetic chemists have independently focused on the choice of asymmetric epoxidation as the initial step for functionalization and the introduction of the first asymmetric center (Fig. 1A). This preference arises from the bifunctional reactivity of epoxides (*1*), which, upon ring opening, can form carbon–carbon or carbon–heteroatom bonds. Moreover, the direction of ring-opening can be finely controlled through acids, bases, or radicals. In addition to the inherent reactivity of epoxides, based on the pioneering work of Sharpless and others (*2*, *3*), synthetic chemists can achieve highly selective epoxidations of both the "head" (C2 to C3) and "tail" (C10 to C11) regions of farnesol. For example, epoxidation of the tail region of farnesol, directed by the coordination of the primary alcohol at the terminal position, can be achieved with >90% regioselectivity and 82% enantioselectivity (ee) through Sharpless epoxidation (*4*) (Fig. 1A). These tail region epoxides have been successfully employed in the efficient synthesis of sesquiterpenes with a 5,7-fused ring system and polyether natural products (*4*–*7*). By contrast, epoxidation of the head region of farnesol provides a textbook precursor for polyene cyclization (*8*–*12*). The synthesis of these head-region epoxides typically involves Corey–Zhang modified Sharpless dihydroxylation of the head alkene (*13*), followed by cyclization. The regioselectivity is derived from steric hindrance around the terminal alkene, which is relatively lower than that around other alkenes, resulting in >90% regioselectivity and 94% ee in most cases (Fig. 1A). Overall, with these asymmetric epoxidation methods, farnesol has been used as an efficient substrate to simplify the synthesis of a variety of terpenoid compounds. Unfortunately, achieving high regio- and ee for epoxidation of the internal double bond (C6 to C7) of farnesol remains an unmet challenge. The Miller research group (*14*) made a breakthrough by discovering the first selective chemical catalyst for the epoxidation of the internal double bond of farnesol. However, the regioselectivity of 43% and an ee of 10% are still insufficient for synthetic purposes. This unmet problem clearly limits the further application of farnesol in terpenoid synthesis.

The difficulty in achieving selective epoxidation of this internal double bond of farnesol lies in the substantial steric hindrance and the distance from the coordinating functional groups, which makes the use of small-molecule catalysts challenging. By contrast, enzyme-catalyzed systems rely on molecular recognition on the conformation of the molecule rather than a single factor such as functional groups or steric factors, giving enzymes a natural advantage in selectively oxidizing such nonfunctionalized double bonds. In recent years, advances in directed evolution have enabled the modification of enzyme catalysts to perform nonnatural reactions (*15*, *16*). When combined with efficient chemical reactions, this strategy expands the chemical space accessible to chemists (*17*, *18*). These advances have also begun to greatly influence the development of the total synthesis of natural products (*19*–*22*).

We have employed enzyme library screening and directed evolution to fill the gap in the selective epoxidation of farnesol's internal double bond (Fig. 1B). The resulting epoxide with high optical purity has enabled us to simplify the synthetic routes to key intermediates for polyethers and polycyclic terpenes. By employing a trimethylsilyl (TMS)-boosted cascade cyclization, we successfully synthesized 11 terpene natural products from the epoxidation product. Our approach has reduced the longest linear sequence up to 74% compared with previous synthetic routes.

Development of epoxidase and simplification of epoxide synthesis

We first focused on the development of a regio- and enantioselective epoxidase for the epoxidation of the internal olefin of farnesol, the key step in our synthesis (Fig. 2A). A previous study (*23*) described the use of $P450_{BM3}$-CYP4C7 chimeras to catalyze the hydroxylation and epoxidation of long-chain substrates, and this report inspired us to explore the potential of using $P450_{BM3}$ to achieve mid-chain epoxidation of farnesol. Among the reported chimeras, we selected the one with the highest selectivity for the internal olefin of farnesol. However, this approach only yielded a regioselectivity of 34% and an ee of 20%. Consequently, we screened an existing enzyme library in our lab (*24*) and discovered that the F87A mutant of $P450_{BM3}$ exhibited moderate regio- and ee for compound **4**. The selectivity of the F87A mutant was not sufficient to meet the requirements for synthesis. Using the crystal structure of $P450_{BM3}$ (Protein Data Bank 1JPZ) (*25*), we chose several amino acid residues that are likely critical for the reaction outcome to perform mutagenesis (see fig. S1). We initially performed site-saturation mutagenesis on several bulky and hydrophobic residues located near the substrate-binding site, including L75, V78, M177, L181, I263, and L437. Mutations at L75, V78, L181, I263, and L437 resulted in reduced reactivity and selectivity compared with the parental enzyme. However, the M177C mutation led to a variant EPO2 (Fig. 2A) with improved selectivity for epoxidation at the internal double bond and enhanced ee. Subsequently, we conducted iterative rounds of site-saturation mutagenesis on small residues within the catalytic pocket, namely, A74, A82, and A330. Each generation of variants showed varying degrees of improvement in selectivity, yielding a more selective mutant, EPO5. Given the considerable structural changes in the catalytic pocket of EPO5 compared with the original enzyme, we revisited the mutagenesis of residues L75, V78, L181, I263, and L437 based on the EPO5 scaffold.

[1]Frontiers Science Center for Transformative Molecules, School of Chemistry and Chemical Engineering, State Key Laboratory of Synergistic Chem-Bio Synthesis, Shanghai Key Laboratory for Molecular Engineering of Chiral Drugs and Zhangjiang Institute for Advanced Study, Shanghai Jiao Tong University, Shanghai, China. [2]Department of Phytochemistry, School of Pharmacy, Second Military Medical University (Naval Medical University), Shanghai, China. [3]Institute of Medicinal Plant Development, Chinese Academy of Medical Sciences & Peking Union Medical College, Beijing, P.R. China. ***Corresponding author. Email: wdzhangy@hotmail.com (W.-D.Z.); jianlizcz@sjtu.edu.cn (J.L.)** †These authors contributed equally to this work.

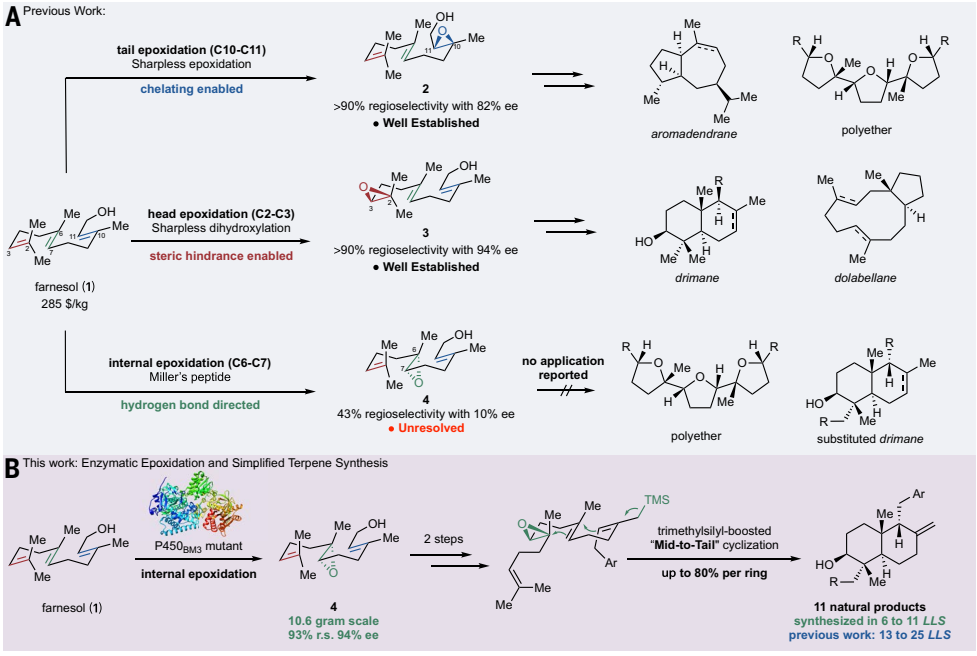

Fig. 1. (**A**) Conventional farnesol epoxidation methods and synthetic applications. (**B**) Our enzymatic internal epoxidation of farnesol rand simplified terpene synthesis. ee, enantiomeric excess; r.s., regioselectivity; TMS, trimethylsilyl; LLS, longest linear sequence.

Mutations at V78 now had a beneficial effect on the reaction outcome, leading to the final optimized farnesol epoxidase, EPO6 (Fig. 2A). The final mutant, the epoxidase EPO6, displayed both satisfactory regioselectivity and ee. Notably, this selectivity was maintained when the reaction was scaled to a 10-g scale.

Once we obtained farnesol internal epoxide with high optical purity, we leveraged its innate reactivity to perform functionalization at either the head or tail region of the molecule (Fig. 2B). We selected several challenging epoxide intermediates reported in the literature and applied our epoxidation product to simplify their synthesis. For example, in Jamison's synthesis (*26*) of the polyether natural product intermediate **5**, challenges with alkene selectivity necessitated oxidation of the terminal olefin to an electron-deficient alkene prior to epoxidizing the internal olefin, resulting in a 10-step process starting from farnesol. By contrast, our approach requires only one steps: epoxidation of the internal

Fig. 2. Development of epoxidase and simplification of epoxide synthesis. (**A**) Directed evolution of $P450_{BM3}$ for the 6,7-epoxidation of farnesol. (**B**) Simplified synthesis of key intermediates through 6,7-epoxy-farnesol. ee, enantiomeric excess; Sharpless AE, Sharpless asymmetric epoxidation; TIPS, triisopropylsilyl; Shi AE, Shi asymmetric epoxidation; NBS, *N*-bromosuccinimide; Sharpless AD, Sharpless asymmetric dihydroxylation; DIBAL-H, diisobutylaluminum hydride; TFA, trifluoroacetic acid; TBDPS, tert-butyldiphenylsilyl; TBAF, tetrabutylammonium fluoride.

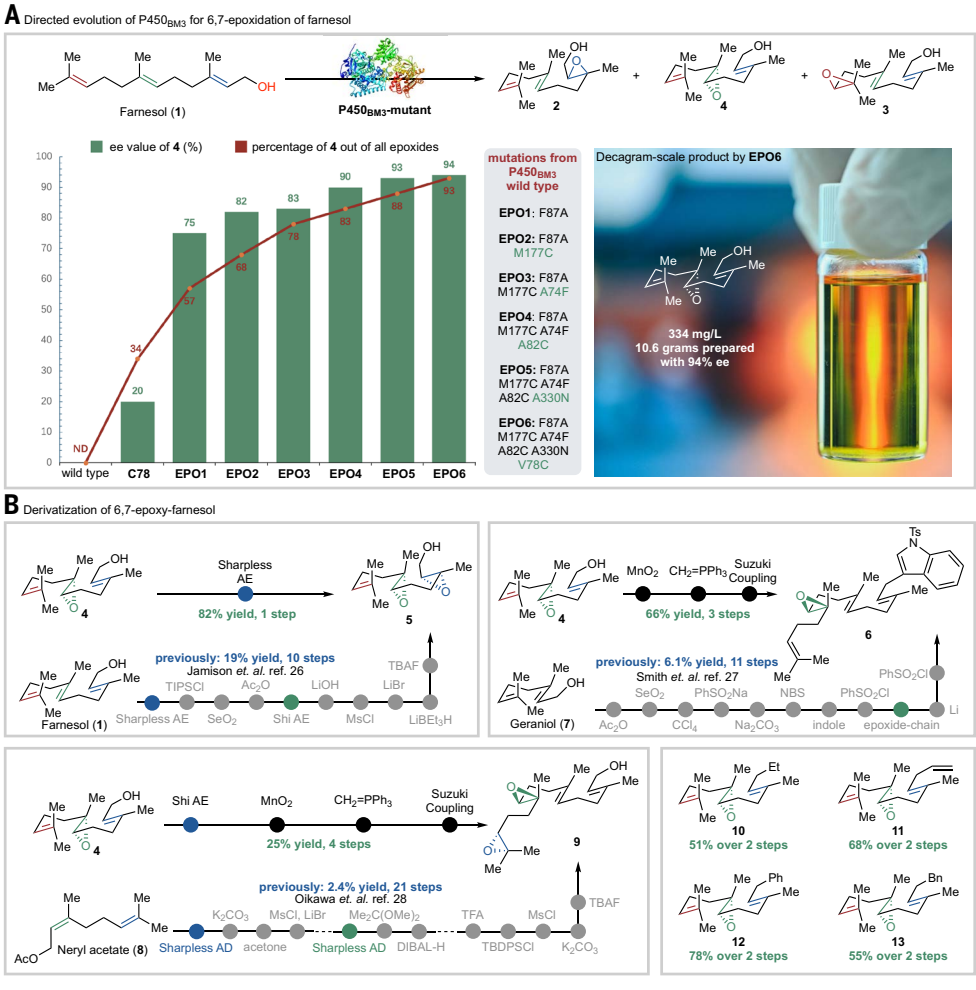

olefin using EPO6, followed by Sharpless epoxidation directed by the terminal hydroxyl group. Similarly, in Smith's synthesis (*27*) of the polyene cascade cyclization precursor **6**, a small-fragment coupling strategy was employed to overcome selectivity issues, resulting in an 11-step total synthesis. By using our epoxidase combined with a homologation and the Suzuki coupling strategy, we were able to complete the synthesis of compound **6** in just three steps. Likewise, Oikawa's synthesis (*28*) of the long-chain double epoxide compound **9** involved fragments coupling over a 21-step process to circumvent selectivity challenges. By applying the same homologation and Suzuki coupling strategy, we reduced the synthesis to four steps. Moreover, the allylic alcohol in our epoxidation product can undergo allylation reactions (*29*). We tested various allylation reactions, all of which give high yields.

Exploration of the polycyclization and simplification of meroterpenoid synthesis

The initiation of mid-to-tail cascade cyclization from polyene intermediates has long been a challenging problem. As a result of the high barriers presented by preassembly, the efficiency of mid-to-tail cyclization is far lower than that of the classical head-to-tail cascade cyclization, with the latter typically achieving 70% efficiency per ring for head-to-tail type cascades (*30*). Under many classic cyclization conditions, mid-to-tail reactions often give <15% yield or even fail to yield any cyclized products (*27*, *31*). Upon obtaining compound **6**, we immediately attempted a Lewis acid–initiated cascade cyclization (Fig. 3). Under $BF_3{\cdot}OEt_2$ catalysis, the reaction proceeded with the same low efficiency as that reported by Smith (*27*), yielding only 10% of the cyclized product **17**-9β that terminated with a mixture of exocyclic and endocyclic double bond. We then explored a titanium (III)–initiated cascade cyclization. Catalytic amounts (*32*) of titanium (III) failed to yield any cyclized product, whereas stoichiometric amounts (*33*) produced a yield of 15%. Clearly, such low efficiency is insufficient for synthetic purposes. More importantly, both cyclization approaches yielded exclusively the β-oriented product at the C9 position, whereas our synthesis requires both α- and β-oriented C9 products. To address this issue, we adopted a strategy used in the literature (*30*, *34*) for modifying the termination mode of head-to-tail cascade cyclizations. We synthesized a substrate **16** with an allyl-TMS group at the tail. Under classical $BF_3{\cdot}OEt_2$ conditions, this substrate has a higher cyclization efficiency. After screening various Lewis acids, we identified $EtAlCl_2$ as the optimal catalyst, achieving a cyclization efficiency of 65% (81% per ring) on a 50 mg scale, and 52% (72% per ring) on a gram scale. Our experiments revealed that this TMS-boosted termination strategy is particularly effective for mid-to-tail cyclizations, providing greater improvement than those in the head-to-tail systems. Although only a 1:1 mixture of diastereomers was obtained, the cyclization efficiency of β-isomer doubled compared with that without the TMS group, and the overall cyclization efficiency increased fourfold. Moreover, the reaction produced both stereoisomers at C9, corresponding to different natural product configurations. After obtaining the cyclized product **17**, we separated the two isomers and removed the protecting groups to complete the total synthesis of the emindole SA in six steps, cutting the number of steps by more than half compared with previous synthesis (*27*). This cyclization mode enabled the first total synthesis of emindole DA, featuring an α-oriented side chain at C9.

Subglutinol-type molecules (*35*), which feature a pyrone structure, represent a diverse family of natural products. The synthesis of compounds with an α-oriented side chain at the C9 position through

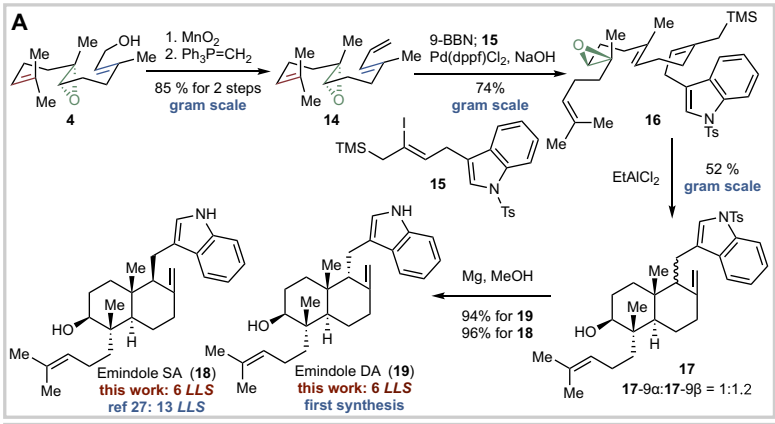

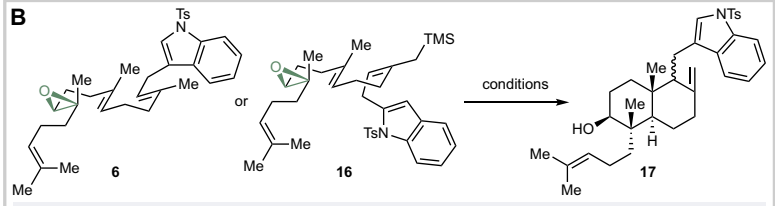

Entry	Substrates	Conditions	Yields	17-9α:17-9β
1	**6**	$BF_3{\cdot}Et_2O$, CH_2Cl_2, –40 °C (ref. 27)	ca. 10%	**17**-9β only
2	**6**	$TiCp_2Cl_2$, Mn, TMSCl, *i*-Pr_2NEt, THF	N.D.	–
3	**6**	$TiCp_2Cl_2$, Zn, THF	15%	**17**-9β only
4	**16**	$EtAlCl_2$, CH_2Cl_2, –78 °C	65%	1:1.2
5	**16**	other Lewis acids (see SM for detail)	17 to 60%	1:1.1 to 1:1.6

Fig. 3. Exploration of the polycyclization and simplification of indole terpenoid synthesis. (**A**) Synthesis of emindole SA and emindole DA. (**B**) Conditions screening of polycyclization. 9-BBN, 9-borabicyclo[3.3.1]nonane; dppf, 1,1'-*bis*(diphenylphosphino)ferrocene; LLS, longest linear sequence; TMS, trimethylsilyl.

classical polycyclization has been particularly challenging. Prior synthetic approaches commonly involved stepwise installation of the isoprenyl and pyrone side chains onto the labdane scaffold. By employing our homologation and Suzuki coupling strategy, we efficiently obtained the cyclization precursor **21** (Fig. 4). Under the catalysis of $EtAlCl_2$, compound **21** underwent cyclization with a slightly higher yield than its indole analog, providing the cyclized product **22** in 62% yield with a diastereomeric ratio of 1:1.2. After acetylation at the C3 secondary alcohol in 88% yield, nalanthalide **26** could be obtained in six steps. To achieve the chemical transformation between the nalanthalide to subglutinols, we applied the regioselective oxyselenenylation-deselenenylation reaction developed by Sharpless (*36*) to obtain trans allylic alcohol **23**. Subsequent hydrolysis of the acetyl group and γ-pyrone under basic conditions, and SN2' type cyclization of the crude allylic diol with a catalytic amount of $PdCl_2(MeCN)_2$ afforded the natural product subglutinol B in a single stereoisomeric manner. With the aid of the epoxidase EPO6, the entire synthetic route was completed in just nine steps, which is considerably fewer than the 14 to 25 steps reported in previous work (*37*–*40*). Using a similar strategy, we successfully synthesized eight related natural products, all with shorter synthetic routes than those reported in the literature (*38*–*42*); for a detailed synthetic route, see the supplementary materials. In the biosynthesis of natural products such as emindoles and subglutinols (*43*, *44*), different microorganisms have evolved distinct sets of epoxidases, terpene cyclases, and post-modification oxidases for each natural product. Compared with biosynthesis, the epoxidase we developed performs the epoxidation reaction at an earlier stage and the resulting epoxide

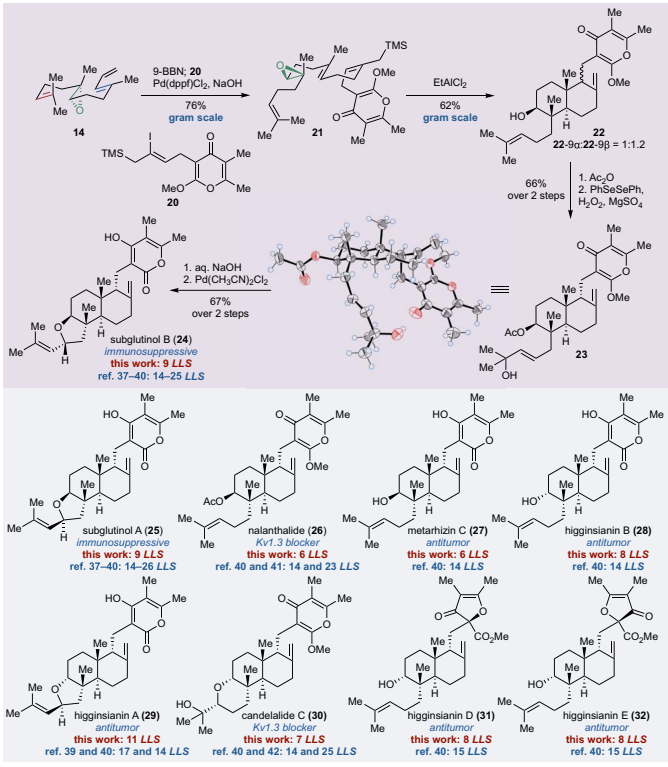

Fig. 4. Simplified synthesis of meroterpenoids. Simplified synthesis of subglutinol B (pink). Other related meroterpenoids synthesized in this work (gray), see detailed synthetic routes in the SM. 9-BBN, 9-borabicyclo[3.3.1]nonane; dppf, 1,1'-*bis*(diphenylphosphino)ferrocene; TMS, trimethylsilyl; *LLS*, longest linear sequence.

can serve as a divergence point, enabling the synthesis of different classes of natural products in a divergent and collaborative manner.

Conclusions

We successfully addressed the challenge of the selective epoxidation of farnesol's internal double bond through the directed evolution of $P450_{BM3}$ into a regio- and enantioselective epoxidase, EPO6. This enzyme enables highly selective production of farnesol internal epoxide with excellent optical purity and decagram scale, which facilitates the simplified synthesis of key intermediates for polyether and polycyclic terpenoid natural products. Moreover, we demonstrated that combining enzymatic catalysis with a TMS-boosted polycyclization strategy allowed for substantial reductions in the number of synthetic steps, streamlining the total synthesis of meroterpenoids such as emindoles and subglutinols. Our work underscores the potential of integrating directed evolution, enzyme catalysis, and innovative chemical strategies to address complex challenges in organic synthesis, providing new opportunities for the efficient production of bioactive natural products.

REFERENCES AND NOTES

1. J. G. Smith, *Synthesis* **1984**, 629–656 (1984).
2. K. B. Sharpless, *Angew. Chem. Int. Ed.* **41**, 2024–2032 (2002).
3. Q.-H. Xia, H.-Q. Ge, C.-P. Ye, Z.-M. Liu, K.-X. Su, *Chem. Rev.* **105**, 1603–1662 (2005).
4. E. J. Corey, D.-C. Ha, *Tetrahedron Lett.* **29**, 3171–3174 (1988).
5. K. Foo *et al.*, *Angew. Chem. Int. Ed.* **51**, 11491–11495 (2012).
6. J. Carreras, M. Livendahl, P. R. McGonigal, A. M. Echavarren, *Angew. Chem. Int. Ed.* **53**, 4896–4899 (2014).
7. I. Vilotijevic, T. F. Jamison, *Angew. Chem. Int. Ed.* **48**, 5250–5281 (2009).
8. E. J. Corey, X.-M. Cheng, *The Logic of Chemical Synthesis* (Wiley, 1995) pp. 234–236.
9. A. G. M. Barrett, T.-K. Ma, T. Mies, *Synthesis* **51**, 67–82 (2019).
10. J. Justicia *et al.*, *Chemistry - A European Journal* **10**, 1778–1788 (2004).
11. S. A. Snyder, E. J. Corey, *J. Am. Chem. Soc.* **128**, 740–742 (2006).
12. K. Surendra, E. J. Corey, *J. Am. Chem. Soc.* **131**, 13928–13929 (2009).
13. E. J. Corey, J. Zhang, *Org. Lett.* **3**, 3211–3214 (2001).
14. P. A. Lichtor, S. J. Miller, *Nat. Chem.* **4**, 990–995 (2012).
15. E. N. Kissman *et al.*, *Nature* **631**, 37–48 (2024).
16. H. Renata, Z. J. Wang, F. H. Arnold, *Angew. Chem. Int. Ed.* **54**, 3351–3367 (2015).
17. D. C. Miller, S. V. Athavale, F. H. Arnold, *Nat. Synth.* **1**, 18–23 (2022).
18. N. J. Turner, E. O'Reilly, *Nat. Chem. Biol.* **9**, 285–288 (2013).
19. C. N. Stout, H. Renata, *Acc. Chem. Res.* **54**, 1143–1156 (2021).
20. C. R. Zwick III, H. Renata, *Nat. Prod. Rep.* **37**, 1065–1079 (2020).
21. J. Li, A. Amatuni, H. Renata, *Curr. Opin. Chem. Biol.* **55**, 111–118 (2020).
22. B. Hong, T. Luo, X. Lei, *ACS Cent. Sci.* **6**, 622–635 (2020).
23. C.-K. J. Chen, T. Kh. Shokhireva, R. E. Berry, H. Zhang, F. A. Walker, *J. Biol. Inorg. Chem.* **13**, 813–824 (2008).
24. X. Liu, Y. Xu, L. Li, J. Li, *J. Am. Chem. Soc.* **146**, 26243–26250 (2024).
25. D. C. Haines, D. R. Tomchick, M. Machius, J. A. Peterson, *Biochemistry* **40**, 13456–13465 (2001).
26. J. Tanuwidjaja, S.-S. Ng, T. F. Jamison, *J. Am. Chem. Soc.* **131**, 12084–12085 (2009).
27. J. D. Rainier, A. B. Smith III, *Tetrahedron Lett.* **41**, 9419–9423 (2000).
28. K. Tagami *et al.*, *J. Am. Chem. Soc.* **135**, 1260–1263 (2013).
29. A. Gansäuer, J. Justicia, A. Rosales, B. Rinker, *Synlett* **2005**, 1954–1956 (2005).
30. R. A. Shenvi, E. J. Corey, *Org. Lett.* **12**, 3548–3551 (2010).
31. J. F. Arteaga, H. R. Diéguez, J. A. González-Delgado, J. F. Quílez del Moral, A. F. Barrero, *Eur. J. Org. Chem.* **2011**, 5002–5011 (2011).
32. A. Gansäuer, M. Pierobon, H. Bluhm, *Angew. Chem. Int. Ed.* **37**, 101–103 (1998).
33. W. A. Nugent, T. V. RajanBabu, *J. Am. Chem. Soc.* **110**, 8561–8562 (1988).
34. N. K. N. Yee, R. M. Coates, *J. Org. Chem.* **57**, 4598–4608 (1992).
35. A. A. Q. Al-Khdhairawi *et al.*, *Org. Biomol. Chem.* **17**, 8943–8957 (2019).
36. T. Hori, K. B. Sharpless, *J. Org. Chem.* **43**, 1689–1697 (1978).
37. H. Kim *et al.*, *J. Am. Chem. Soc.* **131**, 3192–3194 (2009).
38. T. Kikuchi, M. Mineta, J. Ohtaka, N. Matsumoto, T. Katoh, *Eur. J. Org. Chem.* **2011**, 5020–5030 (2011).
39. R. R. Merchant *et al.*, *J. Am. Chem. Soc.* **140**, 7462–7465 (2018).
40. Y. Ji *et al.*, *J. Am. Chem. Soc.* **146**, 9395–9403 (2024).
41. T. Abe *et al.*, *Tetrahedron Lett.* **47**, 3251–3255 (2006).
42. T. Oguchi, K. Watanabe, K. Ohkubo, H. Abe, T. Katoh, *Chemistry* **15**, 2826–2845 (2009).
43. L. Barra, I. Abe, *Nat. Prod. Rep.* **38**, 566–585 (2021).
44. H. Wang, Y. Yang, I. Abe, *Angew. Chem. Int. Ed.* **63**, e202415279 (2024).

ACKNOWLEDGMENTS

We thank H. Renata and A. Li for valuable suggestions and helpful discussions. We thank L. Li from the Instrumental Analysis Center of Shanghai Jiao Tong University for technical help with single-crystal analysis. **Funding:** This work was supported by the Shanghai Municipal Science and Technology Major Project (to J.L. and W.-D.Z.), National Key R&D Program of China [grant 2022YFC3502000 (to W.-D.Z.) and grant 2023YFA1506700 (to J.L.)], Fundamental Research Funds for the Central Universities [grant 23X010301599, 24X010301678 (to J.L.)], National Natural Science Foundation of China [grant 82430119, 82141203 (to W.-D.Z.)], The Ability Establishment of Sustainable Use for Valuable Chinese Medicine Resources [grant 2060302 (to W.-D.Z.)] and Chinese Academy of Medical Sciences (CAMS) Innovation Fund for Medical Sciences [grant 2023-I2M-3-009 (to W.-D.Z.)]. **Author contributions:** J.W., W.-D.Z., and J.L. developed the conceptual framework of the manuscript. J.W., Y.Y., Q.Z., W.-D.Z., and J.L. designed all the experiments described in the manuscript. J.L. wrote the manuscript. J.W., Y.Y., Q.Z., and W.-D.Z. assisted in writing and editing the manuscript. **Competing interests:** The authors declare no competing interests. **Data and materials availability:** Crystallographic data are available free of charge from the Cambridge Crystallographic Database Centre (CCDC) under CCDC 2392688 (for product **19**), CCDC 2392572 (for product **23**), CCDC 2393066 (for product **24**) and CCDC 2392709 (for product **40**). The characterization data and detailed experimental procedures are available in the supplementary materials. **License information:** Copyright © 2025 the authors, some rights reserved; exclusive licensee American Association for the Advancement of Science. No claim to original US government works. https://www.science.org/content/page/science-licenses-journal-article-reuse

SUPPLEMENTARY MATERIALS

science.org/doi/10.1126/science.adt2096
Materials and Methods; Spectroscopic and Chromatographic Data; Figs. S1 to S5; Tables S1 to S23; References (*45*–*55*); MDAR Reproducibility Checklist; HPLC Spectra; NMR Spectra

Submitted 23 October 2024; accepted 5 June 2025

10.1126/science.adt2096

2D MATERIALS

Strong interactions and isospin symmetry breaking in a supermoiré lattice

Yonglong Xie[1,2,3]*†, Andrew T. Pierce[1]*†‡, Jeong Min Park[2]†, Daniel E. Parker[1], Jie Wang[1,4], Patrick Ledwith[1], Zhuozhen Cai[1], Kenji Watanabe[5], Takashi Taniguchi[6], Eslam Khalaf[1], Ashvin Vishwanath[1], Pablo Jarillo-Herrero[2]*, Amir Yacoby[1]*

In multilayer moiré heterostructures, the interference of multiple twist angles ubiquitously leads to tunable ultralong-wavelength patterns known as supermoiré lattices. However, their impact on the system's many-body electronic phase diagram remains largely unexplored. We present local compressibility measurements revealing numerous incompressible states resulting from supermoiré lattice–scale isospin symmetry breaking driven by strong interactions. By using the supermoiré lattice occupancy as a probe of isospin symmetry, we observed an unexpected doubling of the miniband filling near $\nu = -2$, possibly indicating a hidden phase transition or normal-state pairing proximal to the superconducting phase. Our work establishes supermoiré lattices as a tunable parameter for designing quantum phases and as an effective tool for unraveling correlated phenomena in moiré materials.

The interplay between different length scales in low-dimensional electronic systems can radically alter their properties (*1*). This principle has been demonstrated by experiments on two-dimensional moiré superlattices in a magnetic field, including graphene aligned with hexagonal boron nitride (hBN) and magic-angle twisted bilayer graphene (*2*–*14*). In systems with three or more layers, this design concept does not require an external magnetic field and instead utilizes the interference between multiple moiré patterns. Such interference can lead to the emergence of a new superlattice distinct from the original moirés. A recent example that realizes this concept is twisted trilayer graphene (TTG), a system consisting of three consecutively stacked layers of graphene (*15*–*17*) (Fig. 1A) with small twist angles θ_{ij}. Each rotation θ_{ij} is expected to produce a moiré pattern with wavelength $\lambda_{ij} \sim a/\theta_{ij}$, where $a = 0.246$ nm is the graphene lattice constant. Notably, when $\theta_{12} \approx -\theta_{23}$ and thus $\theta_{13} \ll \theta_{12}, \theta_{23}$, the structure of TTG is well approximated by a complex double-periodic pattern characterized by two competing length scales (Fig. 1B). Indeed, scanning tunneling microscopy (STM) (*18*) and scanning transmission electron microscopy (*19*) experiments on TTG have revealed a long-wavelength periodic potential at the "moiré of moiré" wavelength $\lambda_{SM} \sim a/\theta_{13}$—referred to below as a supermoiré lattice—that universally coexists with the parent moiré lattice with wavelength $\lambda_M \sim a/\theta_{12}$. The supermoiré length scale is considerably larger than that of the underlying moiré scale, which prompts several key questions: Are interactions important on this length scale? Are the reported correlated phases in TTG, in particular superconductivity, related to the presence of a supermoiré lattice? Does the supermoiré lattice offer new possibilities for realizing exotic quantum phases?

The supermoiré lattice can modify the electronic properties of TTG in several ways. At the single-particle level, the supermoiré potential folds each of the parent moiré bands into a set of minibands that possess reduced bandwidth and rearranged quantum geometry as compared with the parent moiré bands (*20*–*24*) (Fig. 1C). The resulting minibands likely vary in the degree to which their spectral weights follow the parent moiré versus the supermoiré lattice. Some electrons may localize on the supermoiré lattice, and the addition of the supermoiré potential may play an important role in the system's many-body phenomena. An immediate question that follows is whether the isospin symmetry, which is broken on the moiré scale, is also broken on the supermoiré scale despite the smallness of $U_{SM} \sim e^2/l_{SM}$ compared with $U_M \sim e^2/l_M$. Furthermore, TTG supports correlated states that break the translation symmetry of the parent moiré superlattice resulting from strong electron-electron interactions (*25*, *26*). However, the incommensurability of the supermoiré lattice explicitly disrupts the parent moiré translation symmetry, calling into question whether such states remain favorable. These unresolved questions underscore the wealth of unexplored physics brought forth by the supermoiré lattice, which, to date, remains largely untapped.

In this study, we observed strongly correlated phases enabled by the presence of a supermoiré lattice in a magic-angle twisted trilayer graphene (MATTG) device. Our local thermodynamic measurements with a scanning single-electron transistor microscope revealed that the supermoiré lattice strongly modifies the topological moiré bands and gives rise to numerous incompressible states resulting from electron localization and supermoiré lattice–scale isospin symmetry breaking. Our MATTG device was fabricated through the "cut-and-stack" technique (*10*) and placed on a metal back gate [see (*27*) and fig. S1]. Transport measurements on the device revealed the typical well-established phenomenology of MATTG (*16*, *17*, *25*, *28*), namely, pronounced superconductivity on the hole-doped side near $\nu = -2$ and a sequence of resistive states most prominent under electron doping. We also observed an additional weak resistance peak near and on the hole-doped side of the charge neutrality, which is suggestive of the supermoiré lattice. Overall, the phenomenology as revealed by transport is consistent with the known properties of MATTG.

Signature of supermoiré lattice and incompressibility

Our local magnetic field–dependent inverse compressibility data (Fig. 1D) measured at a fixed location (see fig. S1A) reveals a considerably richer phase diagram than suggested by transport. We observed numerous incompressible peaks, corresponding to ground states with a thermodynamic gap. Conventionally, these states can be classified according to the Streda formula, $\nu = C\frac{\phi}{\phi_0} + s$, where ν is the electron density per unit cell, ϕ is the magnetic flux per unit cell, ϕ_0 is the magnetic flux quantum, and C and s are quantum numbers that characterize the Chern number and the number of filled bands per unit cell relative to charge neutrality. In the presence of two superlattices, electrons can be attached to either lattice, and the value of s—the intercept of the incompressible state along the ν axis—can be further separated into ν_m and ν_{sm}, which correspond to the number of electrons added to the moiré and supermoiré unit cells, respectively. Because of the spin and valley degrees of freedom, ν_m and ν_{sm} are expected to span from −4 to 4. In Fig. 1E, we identify all thermodynamic gaps in the phase diagram and classify them into one of four groups according to the ordered triple (C, ν_m, ν_{sm}); for a complete table of the observed states, see tables S1 and S2. First, the incompressible states corresponding to integer ν_m with $\nu_{sm} = 0$ (gray lines in Fig. 1E) are simple Chern insulators (ChI) or integer quantum Hall

[1]Department of Physics, Harvard University, Cambridge, MA, USA. [2]Department of Physics, Massachusetts Institute of Technology, Cambridge, MA, USA. [3]Department of Physics and Astronomy, Smalley-Curl Institute and Rice Advanced Materials Institute, Rice University, Houston, TX, USA. [4]Center of Mathematical Sciences and Applications, Harvard University, Cambridge, MA, USA. [5]Research Center for Electronic and Optical Materials, National Institute for Material Science, Tsukuba, Japan. [6]Research Center for Materials Nanoarchitectonics, National Institute for Material Science, Tsukuba, Japan. ***Corresponding author. Email: yx71@rice.edu (Y.X.); atp66@cornell.edu (A.T.P.); pjarillo@mit.edu (P.J.-H.); yacoby@g.harvard.edu (A.Y.)** †These authors contributed equally to this work. ‡Present address: Kavli Institute at Cornell for Nanoscale Science, Ithaca, NY, USA.

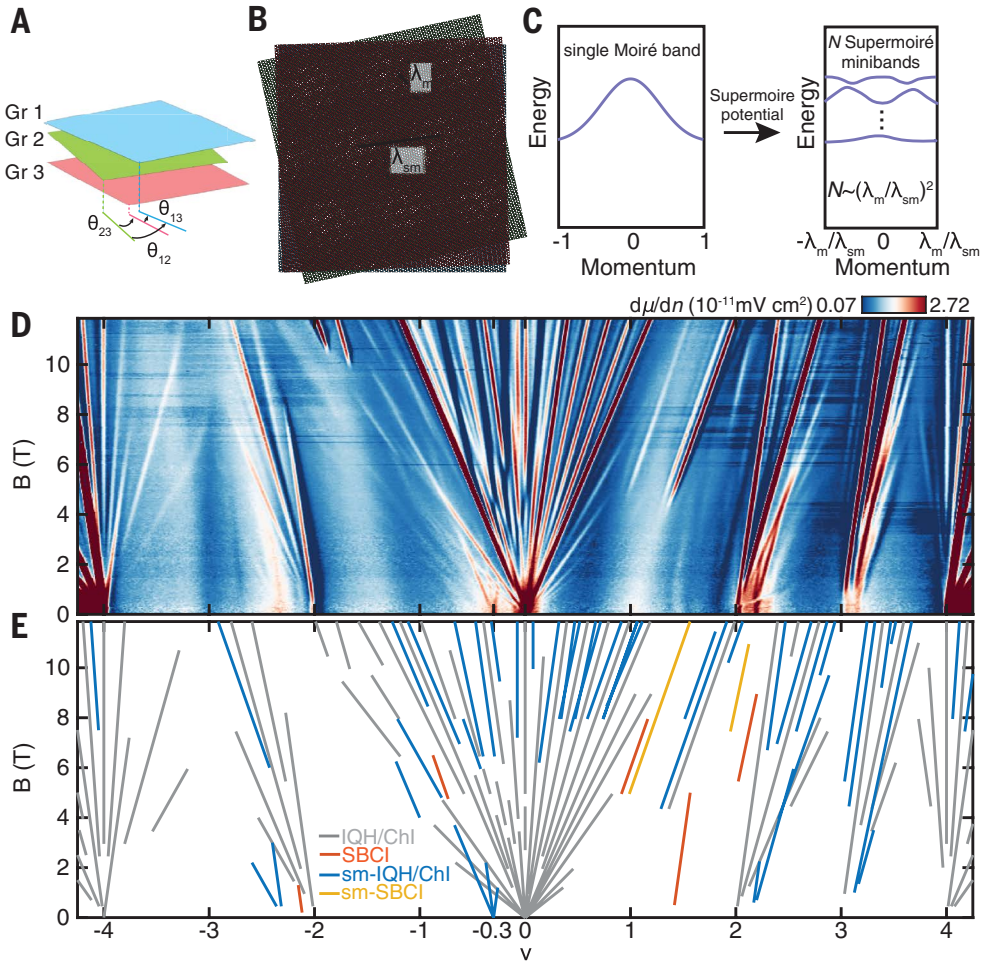

Fig. 1. Incompressible states at commensurate and incommensurate fillings of the moiré unit cell. (**A**) TTG formed by consecutively stacking three layers of graphene (labeled "Gr 1" to "Gr 3") small twist relative angles θ_{ij}. (**B**) Sketch of TTG lattice exhibiting a principal moiré wavelength λ_m and a larger supermoiré wavelength λ_{sm}. (**C**) Sketch of a single parent moiré flat band in momentum space (left panel) and the sequence of minibands that results from Brillouin zone folding (right panel). (**D**) Local inverse compressibility $d\mu/dn$ plotted as a function of electron density, in units of electrons per moiré unit cell ν, and magnetic field B. The data was taken at T = 550 mK. (**E**) Wannier diagram identifying the incompressible states present in (A). Gray (orange) lines correspond to IQH states or ChIs (SBCIs) emanating from integer (commensurate) fraction of the moiré unit cell of twisted trilayer graphene. Blue (yellow) lines correspond to IQH/ChIs (SBCIs) with a nonzero supermoiré band filling (sm-IQH/ChI, blue; sm-SBCI, yellow).

(IQH) states and are hallmarks of TTG readily observed in transport measurements (*16*, *17*, *25*). Second, features with finite C, fractional ν_m, and $\nu_{sm} = 0$ (orange lines in Fig. 1E) are classified as symmetry-broken Chern insulators (SBCIs), likely arising from the spontaneous breaking of the moiré unit cell translation symmetry, and therefore represent topological charge density waves. Lastly, we observed two previously unexplored classes of gapped states with $\nu_{sm} \neq 0$ that we term sm-IQH/ChI (integer ν_m, blue lines) and sm-SBCI (fractional ν_m, yellow lines)—which demonstrate that the presence of the supermoiré lattice strongly alters the electronic properties of the system—and that are the focus of this work. We also observed an intricate pattern of negative compressibility near charge neutrality (*26*).

The most immediate signature of the supermoiré lattice is the weak satellite incompressible peak at $\nu = -0.3$, which develops into a Landau fan with a principal Chern number sequence of $C = -6$, -2, and $+2$ (Fig. 2, A and D). The observed fourfold sequence confirms that $\nu = -0.3$ marks the full filling of the supermoiré unit cell with four electrons corresponding to spin and valley degeneracy, and we therefore identify these incompressible states as having $\nu_{sm} = -4$. The size of the supermoiré unit cell exceeds that of the principal moiré by a factor of $(0.3/4)^{-1} \sim 13$ and yields a corresponding wavelength of 32.6 nm. These values are comparable to those from direct imaging experiments of supermoiré lattices (*18*, *19*) and correspond to an angle misalignment between the top and bottom graphene sheets of 0.43°. To further corroborate our identification of this feature as coming from the supermoiré lattice, we imaged a region of the device in which one of the graphene flakes terminates, leaving only a region of twisted bilayer graphene that allowed us to independently determine the angle of the three graphene sheets (fig. S5). Thus, the appearance of a satellite Landau fan near the charge neutrality shows that the supermoiré lattice gives rise to a distinct set of bands at the single-particle level.

As the magnetic field was increased near the charge neutrality, besides a typical sequence of isospin symmetry–broken quantum Hall ferromagnetic states (QHFMs), we detected a series of satellite incompressible peaks that are offset along the ν axis by $\delta\nu = \pm 0.075$ (see fig. S2). This density offset precisely translates to $\delta\nu_{sm} = \pm 1$, suggesting that this sequence of sm-IQH states comes about by filling one isospin symmetry–broken supermoiré miniband atop the parent QHFM to maintain the same isospin polarization. We observed similar phenomenology at high magnetic field near $\nu = \pm 4$, where additional families of incompressible states offset by $\delta\nu = \pm 0.075$ appear (Fig. 1E). These observations suggest a general tendency for the isospin symmetry of the sm-IQH/ChI states to follow that of the neighboring moiré ChIs near $\nu = 0$ and ± 4.

Supermoiré isospin symmetry breaking at zero field

Near $\nu = +2$ and $+3$, we observed supermoiré-enabled incompressible states down to zero magnetic field, suggesting that the supermoiré electrons undergo a cascade of isospin phase transitions mirroring that of the parent moiré insulators. Specifically, at $\nu = +2$, we detected a sharp incompressible peak at zero field and a Landau level (LL) sequence of +2, +4, and +6. These observations are consistent with the expectation that strong interactions select two out of the four moiré bands to fill and form a correlated insulator. Notably, at $\nu = +2.15$, we observed an additional incompressible peak comparable in size to that at $\nu = 2$, along with a "duplicated" twofold sequence of LLs. From the identical LL sequences, we conclude that the sm-ChI at $\nu = 2.15$ shares the same isospin polarization as the parent moiré $\nu = 2$ insulator. Moreover, the density offset precisely matches that expected for two electrons per supermoiré unit cell and further demonstrates the supermoiré lattice–scale isospin symmetry breaking, which likely results from minimizing the exchange energy between electrons in moiré and supermoiré lattices. At $\nu = +3$, we observed a weaker zero-field incompressible peak together with a nondegenerate LL sequence of +2, +3, +4, corresponding to fully broken isospin symmetry. Similar to the behavior at $\nu = 2$, a satellite incompressible sm-ChI peak with comparable magnitude is present at the nearby filling $\nu = \pm 3.075$, with the offset $\delta\nu = \pm 0.075$ reflecting the single-remaining supermoiré band. Thus, the isospin symmetry of the sm-ChIs about $\nu = 3$ follows that of the parent ChIs in a manner resembling $\nu = 2$.

The salient features of our data at low magnetic field are surprisingly well captured by a phenomenological mean-field model with strong interactions between all electrons, both moiré and supermoiré. Given the strong separation of moiré and supermoiré length scales, we anticipate the formation of large regions of alternating-twist mirror-symmetric trilayer separated by mirror symmetry–breaking domain walls, as shown in recent direct imaging experiments (*18*, *19*). TTG stands in stark contrast to twisted bilayers, in which a large layer misalignment necessarily violates the magic-angle condition (supplementary text S2). Therefore, we assume that the electrons in the system can be separated into two species according to whether they inhabit the moiré or supermoiré lattice, and we consider a phenomenological density of states for each species, with a smaller bandwidth for supermoiré electrons owing to their larger length scale. We include strong contact interactions $U_{\text{m-m}}$, $U_{\text{m-sm}}$, and $U_{\text{sm-sm}}$, that are independent of spin and valley. The model may then be solved [see (*27*) for full details] at a mean-field level under standard approximations (*10*, *12*, *29*), yielding the occupations of each species and the compressibility as a function of filling shown in Fig. 2, J to O. Near charge neutrality, where the effects of interaction-induced dispersion are expected to be weakest, thanks to the vanishing Hartree potential, our model reproduces the satellite peak observed at $\nu = -0.3$, validating the choice of the single-particle parameters in our model. Near $\nu = +2$ and $\nu = +3$, where Hartree effects are substantial, the computed compressibility curves qualitatively resemble those observed experimentally: In both cases, only one satellite peak appears at higher density than the parent moiré ChI. This occurs because

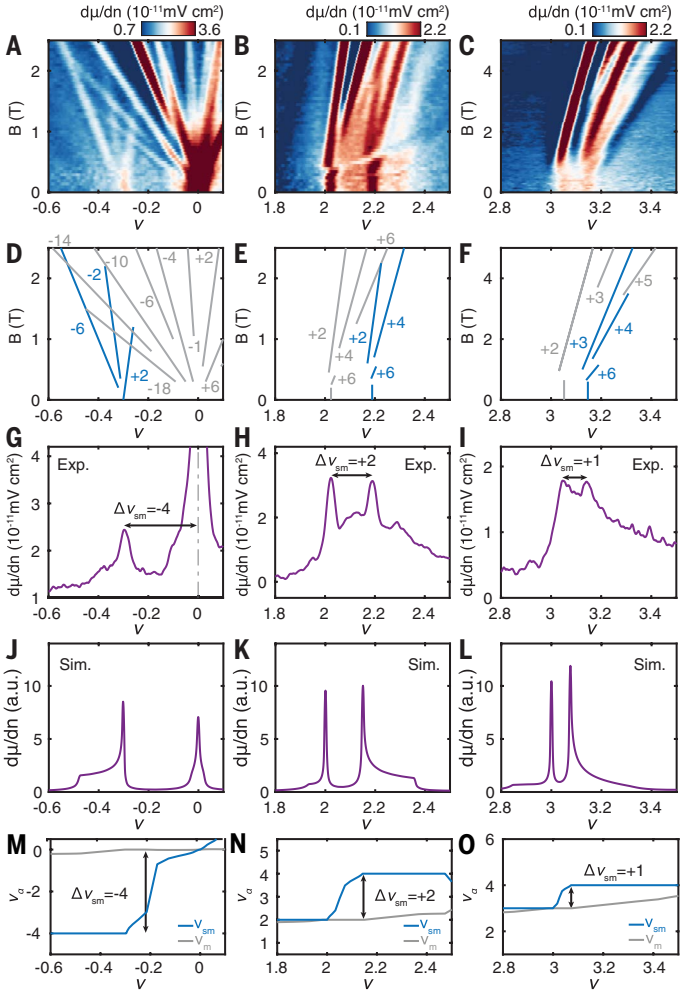

Fig. 2. Supermoiré isospin symmetry breaking down to zero magnetic field. (**A** to **C**) Zoomed-in view of local inverse compressibility near $\nu = 0$ (A), $\nu = +2$ (B), and $\nu = +3$ (C). (**D** to **F**) Wannier diagrams highlighting the incompressible states observed in (A) to (C) colored according to the classification of Fig. 1B. Gray lines denote states emanating from integer fillings of the moiré unit cell, and blue lines correspond to states where an integer number of additional supermoiré minibands are filled or emptied. (**G** to **I**) Experimental $d\mu/dn$ ($\times 10^{-11}$ mV cm^{-2}) line traces near $\nu = 0$ (G), $\nu = +2$ (H), and $\nu = +3$ (I) and averaged over 0 to 200 mT. The density offsets between the incompressible peaks approximately correspond to −4, +2, and +1 electron(s) per supermoiré unit cell, respectively. (**J** to **L**) Simulated $d\mu/dn$ traces near $\nu = 0$ (J), $\nu = +2$ (K), and $\nu = +3$ (L) calculated according to the mean-field model (supplementary text S6) exhibit density offsets matching those in (G) to (I). a.u., arbitrary units. (**M** to **O**) Simulation results for the total supermoiré filling near $\nu = 0$ (M), $\nu = +2$ (N), and $\nu = +3$ (O). All data were taken at T = 550 mK.

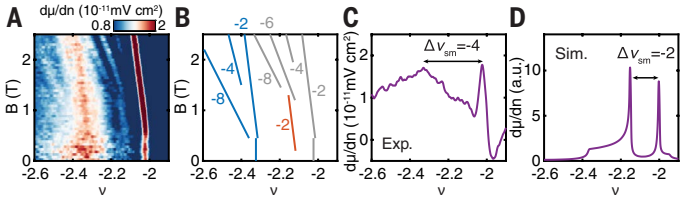

Fig. 3. Isospin symmetry anomaly near $\nu = -2$ probed by the supermoiré lattice. (**A**) Zoomed-in view of local inverse compressibility $d\mu/dn$ ($\times 10^{-11}$ mV cm^{-2}) near $\nu = -2$. (**B**) Wannier diagram highlighting the incompressible states observed in (A) colored according to the classification of Fig. 1B. (**C**) Experimental $d\mu/dn$ line trace near $\nu = -2$ averaged over 0 to 200 mT. The density offset between the broad incompressible peak and the moiré-correlated insulator corresponds to a filling of four additional holes per supermoiré unit cell, in agreement with the extrapolated intercepts of the LL sequences observed to emerge starting around 1 T. (**D**) Mean-field simulation (supplementary text S6) results near $\nu = -2$ predict the appearance of an incompressible state at a filling of two holes per supermoiré unit cell in disagreement with the experiment, suggesting the presence of beyond–mean field electronic correlations. All data were taken at T = 550 mK.

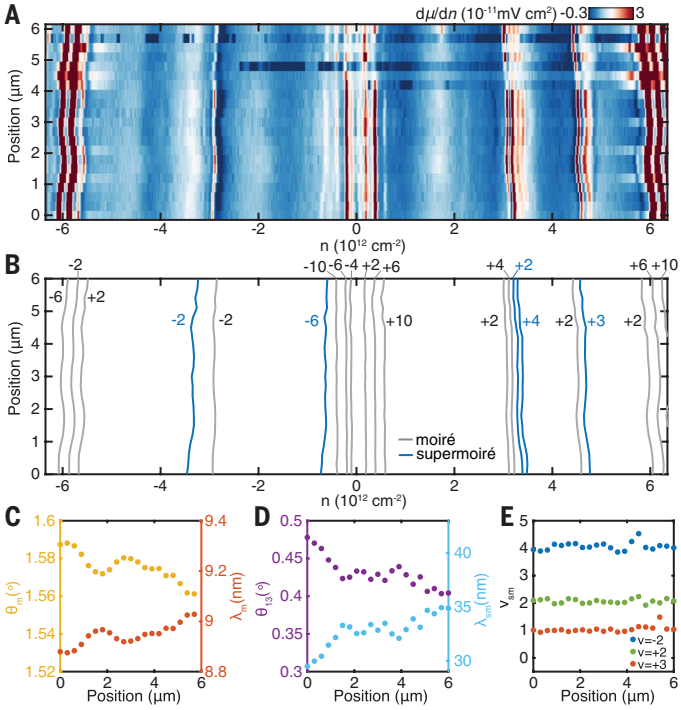

Fig. 4. Ubiquitous supermoiré isospin order. (**A**) Spatial dependence of local inverse compressibility dμ/dn as a function of electron density measured at $B = 2$ T. (**B**) Trajectories of the incompressible states observed in (A). The numbers denote the Chern number of each incompressible state. (**C** and **D**) Local twist angle and moiré wavelength (C) and supermoiré angle and wavelength (D) estimated with the data in (A) (supplementary text S3). (**E**) Isospin flavor degeneracy near moiré filling of −2, +2, and +3 as a function of distance. All data were taken at T = 550 mK.

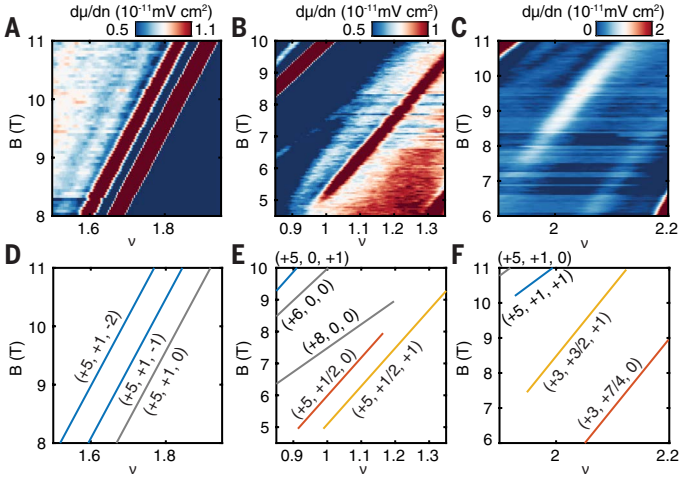

Fig. 5. Additional supermoiré states. (**A** to **C**) Measurements of dμ/dn ($\times 10^{-11}$ mV cm^{-2}) in various density ranges between 6 and 12 T showing additional supermoiré states. (**D** to **F**) Wannier diagrams corresponding to the states observed in (A) to (C), colored according to the classification used in Fig. 1B. Gray, orange, blue, and yellow lines denote the ChIs, SBCIs, sm-ChIs, and sm-SBCIs, respectively. All data were taken at T = 550 mK.

Stoner ferromagnetism ensures that an equal number of moiré and supermoiré isospin species are populated together at integer fillings. Additional doping then populates the supermoiré electrons, thanks to their lower kinetic energy, until they are fully filled, leading to a satellite incompressible state. These results are robust, depending only weakly on the density of states profile, as long as the kinetic energy of supermoiré electrons is substantially smaller than that of moiré electrons (fig. S6). Overall, the agreement between our data and model calculations indicates that the Coulomb interactions involving the supermoiré electrons are also strong, making them key to understanding the correlated phases in the system.

Isospin symmetry anomaly near $\nu = -2$

The behavior of the isospin degree of freedom on the hole-doped side stands in marked contrast to that on the electron-doped side and cannot be explained with the phenomenological model described above. At $\nu = -2$, we observed a sharp incompressible peak at zero magnetic field and a LL sequence of −2, −4, −6, ..., which is consistent with twofold degeneracy (Fig. 3, A and B). Whereas our model predicts a supermoiré isospin transition near $\nu = -2.15$ (Fig. 3D), we instead detected a broad peak near $\nu = -2.3$ (Fig. 3C). This unexpected doubling of the supermoiré filling is confirmed by the presence of LLs emanating from $\nu = -2.3$: We found a LL sequence of −2, −4, −8, which, after accounting for the $C = -2$ offset from the $N = 0$ LL of the Dirac bands, translates to 0, −2, −6, identical to that observed at $\nu = -0.3$. Incidentally, the recovery of fourfold supermoiré filling coincides with the density range at which superconductivity is observed in transport measurements. By contrast, superconductivity is absent on the electron-doped side, where isospin symmetry is broken.

A natural interpretation of the apparent doubling of supermoiré filling is a hidden phase transition between $\nu = -2$ and $\nu = -2.3$ from an isospin symmetry–broken phase to a fourfold isospin-symmetric state. Such a phase transition may generally be present in TTG but may only be detectable by examining its interplay with the supermoiré potential, using local imaging techniques such as our high-resolution local compressibility measurements.

Alternatively, the doubling of supermoiré filling can result from the formation of paired charge $2e$ objects rather than individual electrons, which will produce the feature at $\nu = -2.3$ while maintaining the broken twofold isospin degeneracy. This scenario is consistent with the pseudogap-like behavior observed in STM studies between $\nu = -2$ and -3 at energy scales considerably greater than T_c, which can be interpreted as a signature for preformed pairs. The supermoiré potential is likely to favor the formation of commensurate charge density wave orders of these charge $2e$ objects, leading to an incompressible feature at $\nu = -2.3$. Further studies are required to identify the microscopic origin of the observed doubling of supermoiré filling and its relation to the superconductivity in MATTG.

Spatially resolved measurements

To firmly correlate the isospin symmetry characteristics inferred from the local compressibility measurements with the presence of the supermoiré lattice, we performed spatially resolved compressibility measurements over a 6-μm span. We first presented measurements taken at $B = 2$ T (Fig. 4, A and B), where the absence of the Dirac bands other than their $N = 0$ LLs enabled us to estimate the isospin degeneracy at various fillings most accurately. Features associated with supermoiré potential (Fig. 4B, blue) were visible over the entire range, despite the variations in the exact density at which they emerged. At each location, we quantified the local twist angle and top-bottom angle mismatch (Fig. 4, C and D) by comparing the position of the full filling IQH/ChI (±2, ±4) and the separation between the (−6, 0, −4) and (−6, 0, 0), respectively. Over 6 μm, the local twist angle θ_m varied by 0.03°, and θ_{13} varied by 0.08°,

corresponding to a supermoiré wavelength from 30 to 35 nm. The variations in local twist angle are not correlated with those in the mismatch. Using the same dataset, we characterized the local filling-dependent isospin degeneracy by extracting the supermoiré density offset in units of electrons per supermoiré unit cell [see (*27*) for full details]. We found that, at all positions investigated, the system retained an isospin degeneracy of four at $\nu = -2$, whereas at filling $\nu = +2$, the degeneracy was reduced to two, and at filling $\nu = +3$, the degeneracy was reduced to one. Notably, at zero magnetic field, all the principal moiré and supermoiré incompressible peaks analyzed above were observed to be robust over the full 6-μm range (fig. S3), suggesting that the pattern of symmetry breaking identified in Figs. 2 and 3 holds globally to zero magnetic field. Lastly, spatially resolved measurements over a 12-μm span at 11 T showed a consistent pattern of supermoiré–isospin symmetry breaking despite marked changes in local twist and supermoiré angle (fig. S4).

Strong interactions and topology

Our data also shows that the supermoiré potential generates quantum phases with distinct isospin order and energy gaps. First, whereas the parent Chern insulator with (+5, +1, 0) is spin-valley polarized, removing two holes to form (+5, +1, −2) entails a different isospin structure (Fig. 5, A and D). Second, the (+5, +1/2, +1) sm-SBCI has a larger gap and persists over a wider field range than its proximate (+5, +1/2, 0) moiré SBCI (Fig. 5, B and E). This observation and the lack of any nearby moiré insulator for the sm-SBCI (+3, +3/2, +1) (Fig. 5, C and F) imply that the supermoiré states may emerge from mechanisms independent of parent moiré states.

We now highlight the rich interplay between the supermoiré potential and the topological moiré bands. Near $\nu = 0, \pm 4$ (fig. S7) and $\nu = +2$ (Fig. 2, B and E), sm-IQH and sm-ChI states duplicate the sequence of the principal IQH/ChI states, indicating that the fully filled supermoiré minibands contribute a zero net Chern number. By contrast, near $\nu = +3$ (Fig. 3, C and F), the supermoiré sequence shifts by 1. The (+2, +3, 0) state, likely a translation symmetry–breaking trivial insulator, gives way to a valley-polarized (+3, +3, +1) sm-ChI, which either restores translation symmetry through a phase transition or arises from a $C = +1$ supermoiré miniband. Regardless of the origin, these observations hold over the full 6-μm range that we investigated (Fig. 4, A and B), indicating that the apparent reconstruction of the ground state topology at $\nu = +3$ occurs generally.

Discussion and outlook

The abundance of incompressible states that we observed suggests that the supermoiré potential may be used as a tuning knob for designing correlated quantum phases in twisted multilayers. The observation of isospin symmetry breaking on the supermoiré lattice highlights its usefulness as a probe of isospin symmetry in moiré systems. The contrasting isospin symmetry patterns on the electron-doped side versus those on the hole-doped side provide an important constraint for understanding the superconductivity in TTG and may be indispensable in describing superconducting quadri- and pentalayer graphene (*30*–*32*), because the effect of the supermoiré potential is expected to become more important as the number of graphene layers is increased.

REFERENCES AND NOTES

1. M. Yankowitz *et al.*, *Nat. Phys.* **8**, 382–386 (2012).
2. Y. Cao *et al.*, *Phys. Rev. Lett.* **117**, 116804 (2016).
3. Y. Cao *et al.*, *Nature* **556**, 80–84 (2018).
4. Y. Cao *et al.*, *Nature* **556**, 43–50 (2018).
5. S. L. Tomarken *et al.*, *Phys. Rev. Lett.* **123**, 046601 (2019).
6. S. Wu, Z. Zhang, K. Watanabe, T. Taniguchi, E. Y. Andrei, *Nat. Mater.* **20**, 488–494 (2021).
7. K. P. Nuckolls *et al.*, *Nature* **588**, 610–615 (2020).
8. Y. Saito *et al.*, *Nat. Phys.* **17**, 478–481 (2021).
9. I. Das *et al.*, *Nat. Phys.* **17**, 710–714 (2021).
10. J. M. Park, Y. Cao, K. Watanabe, T. Taniguchi, P. Jarillo-Herrero, *Nature* **592**, 43–48 (2021).
11. Y. Choi *et al.*, *Nature* **589**, 536–541 (2021).
12. A. T. Pierce *et al.*, *Nat. Phys.* **17**, 1210–1215 (2021).
13. J. Yu *et al.*, *Nat. Phys.* **18**, 825–831 (2022).
14. Y. Xie *et al.*, *Nature* **600**, 439–443 (2021).
15. E. Khalaf, A. J. Kruchkov, G. Tarnopolsky, A. Vishwanath, *Phys. Rev. B* **100**, 085109 (2019).
16. J. M. Park, Y. Cao, K. Watanabe, T. Taniguchi, P. Jarillo-Herrero, *Nature* **590**, 249–255 (2021).
17. Z. Hao *et al.*, *Science* **371**, 1133–1138 (2021).
18. S. Turkel *et al.*, *Science* **376**, 193–199 (2022).
19. I. M. Craig *et al.*, *Nat. Mater.* **23**, 323–330 (2024).
20. J. Shi, J. Zhu, A. H. MacDonald, *Phys. Rev. B* **103**, 075122 (2021).
21. M. Anđelković, S. P. Milovanović, L. Covaci, F. M. Peeters, *Nano Lett.* **20**, 979–988 (2020).
22. N. Leconte, J. Jung, *2D Mater.* **7**, 031005 (2020).
23. Z. Zhu, P. Cazeaux, M. Luskin, E. Kaxiras, *Phys. Rev. B* **101**, 224107 (2020).
24. Z. Zhu, S. Carr, D. Massatt, M. Luskin, E. Kaxiras, *Phys. Rev. Lett.* **125**, 116404 (2020).
25. C. Shen *et al.*, *Nat. Mater.* **22**, 316–321 (2023).
26. A. T. Pierce *et al.*, *Nat. Phys.* **2025** (2025).
27. See supplementary materials.
28. X. Liu, N. J. Zhang, K. Watanabe, T. Taniguchi, J. I. A. Li, *Nat. Phys.* **18**, 522–527 (2022).
29. U. Zondiner *et al.*, *Nature* **582**, 203–208 (2020).
30. J. M. Park *et al.*, *Nat. Mater.* **21**, 877–883 (2022).
31. G. W. Burg *et al.*, *Nat. Mater.* **21**, 884–889 (2022).
32. Y. Zhang *et al.*, *Science* **377**, 1538–1543 (2022).
33. Y. Xie, Strong interactions and isospin symmetry breaking in a supermoiré lattice, version 1, Harvard Dataverse (2024); https://doi.org/10.7910/DVN/SOQBZN.
34. D. E. Parker, DanielEricParker/HF0d: Published Version, Zenodo (2025); https://doi.org/10.5281/zenodo.15635374.

ACKNOWLEDGMENTS

We acknowledge discussions with A. Stern and A. Uri. **Funding:** This work was sponsored by the Army Research Office under award W911NF-21-2-0147 and by the Gordon and Betty Moore Foundation EPiQS initiative through grant GBMF 9468. Help with transport measurements and data analysis were supported by the NSF (grant DMR-1809802) and the STC Center for Integrated Quantum Materials (NSF grant DMR-1231319). P.J-H. also acknowledges support from the Gordon and Betty Moore Foundation's EPiQS Initiative through grant GBMF 9463, the CIFAR Quantum Materials Program, and the Fundación Ramón Areces. A.T.P. and P.L. acknowledge support from the Department of Defense through the National Defense Science and Engineering Graduate Fellowship (NDSEG) Program. Y.X. acknowledges partial support from the Harvard Quantum Initiative in Science and Engineering. During the revision of this work, Y.X. was supported by NSF CAREER grant DMR-2339623 and Robert A. Welch Foundation grant C-2219, and A.Y. was partly supported by the Gordon and Betty Moore Foundation through grant GBMF 12762. Y.X., A.T.P., and A.Y. acknowledge support from the Harvard Quantum Initiative Seed Fund. A.V. was supported by a Simons Investigator award and by the Simons Collaboration on Ultra-Quantum Matter, which is a grant from the Simons Foundation (651440, A.V.). E.K. was supported by a Simons Investigator Fellowship, by NSF-DMR 1411343, and by the German National Academy of Sciences Leopoldina through grant LPDS 2018-02, a Leopoldina fellowship. This research is funded in part by the Gordon and Betty Moore Foundation's EPiQS Initiative, grant GBMF8683, to D.E.P. K.W. and T.T. acknowledge support from the JSPS KAKENHI (grants 21H05233 and 23H02052) and World Premier International Research Center Initiative (WPI), MEXT, Japan. This work was performed in part at the Center for Nanoscale Systems (CNS), a member of the National Nanotechnology Infrastructure Network, which is supported by the NSF under award ECS-0335765. CNS is part of Harvard University. **Author contributions:** Y.X., A.T.P., J.M.P., P.J.-H., and A.Y. conceived and designed the experiment; A.T.P., Y.X., and Z.C. performed the scanning SET experiment and analyzed the data with input from A.Y.; J.M.P. and P.J.-H. designed and provided the samples and contributed to the analysis of the results; D.E.P., J.W., P.L., E.K., and A.V. performed the theoretical analysis.; K.W. and T.T. provided hBN crystals. All authors participated in discussions and in the writing of the manuscript. **Competing interests:** The authors declare that they have no competing interests. **Data and materials availability:** The data and materials that support the findings of this study are available on Harvard Dataverse (*33*). The code for simulating the compressibility is available on the GitHub repository (https://github.com/DanielEricParker/HF0d) and archived at Zenodo (*34*). **License information:** Copyright © 2025 the authors, some rights reserved; exclusive licensee American Association for the Advancement of Science. No claim to original US government works. https://www.science.org/about/science-licenses-journal-article-reuse

SUPPLEMENTARY MATERIALS

science.org/doi/10.1126/science.adl2544
Materials and Methods; Supplementary Text; Figs. S1 to S7; Tables S1 and S2; References (*35*–*36*)

Submitted 20 November 2023; accepted 17 June 2025; published online 3 July 2025
10.1126/science.adl2544

BIOCATALYSIS

Enantioconvergent benzylic C(sp^3)–N coupling with a copper-substituted nonheme enzyme

Xuzhong Shen[1], Xiahe Chen[2], Yihang Xiao[1], Jesse B. Brown[3], James G. Zhang[1], Xinyuan Ji[1], Jinyan Rui[1], Marc Garcia-Borràs[4,5], Yi Rao[3]*, Yunfang Yang[2]*, Xiongyi Huang[1]*

Copper-catalyzed radical C(sp^3)–N coupling has become a major focus in synthetic catalysis over the past decade. However, achieving this reaction manifold by using enzymes has remained elusive. In this study, we introduce a photobiocatalytic approach for radical benzylic C(sp^3)–N coupling using a copper-substituted nonheme enzyme. Using rhodamine B as a photoredox catalyst, we identified a copper-substituted phenylalanine hydroxylase that facilitates enantioconvergent decarboxylative amination between *N*-hydroxyphthalimide esters and anilines. Directed evolution remodeled the active site, resulting in high enantioselectivities for most substrates. On the basis of molecular modeling and mechanistic studies, we propose that the enzyme accommodates a copper-anilide complex that reacts with a benzylic radical. This study expands the scope of non-natural biocatalytic transition metal catalysis to copper-catalyzed radical coupling.

The construction of C(sp^3)–N bonds represents an indispensable process in organic synthesis because of the prevalence of nitrogen-containing molecules in bioactive compounds, pharmaceuticals, and functional materials (*1*, *2*). Among the various strategies for C(sp^3)–N bond formation, copper-catalyzed radical C(sp^3)–N coupling has emerged as a leading approach over the past decade. In this reaction manifold, a C(sp^3) radical is intercepted by a Cu(II)-amido complex, resulting in the formation of the C(sp^3)–N bond alongside the generation of the Cu(I) species (Fig. 1A) (*3*, *4*). By integrating this copper-catalyzed coupling process with diverse radical generation strategies, a wide range of transformations has been developed, leading to a paradigm shift in both synthetic amination methodologies and the field of copper catalysis (*4*–*7*).

In parallel with these advances in synthetic chemistry, biocatalytic methods for constructing C(sp^3)–N bonds have represented another rapidly growing research area in the past 20 years (Fig. 1B) (*8*). The engineering of natural biocatalytic amination systems, such as transaminases and imine reductases, has enabled efficient and scalable processes for pharmaceutical synthesis (*9*, *10*). More recently, the integration of non-natural reaction mechanisms into enzymes has facilitated the development of a few challenging C–N bond–forming reactions, such as asymmetric lactam synthesis (*11*), stereoselective primary amination of C(sp^3)–H bonds (*12*–*16*), hydroamination of alkenes (*17*, *18*), and enantioselective radical C–N_3 bond formation (*19*–*24*). In this context, incorporating copper-catalyzed radical C(sp^3)–N coupling into biocatalysis is appealing because it would merge the genetic tunability and selectivity of enzymes with the broad reaction scope of copper radical catalysis. This integration could provide expanded opportunities for addressing synthetic challenges in catalytic amination reactions that are difficult to achieve with conventional methods.

In this context, decarboxylative amination represents a highly desirable addition to the biocatalytic toolbox for constructing C(sp^3)–N bonds because it provides an efficient route to convert abundant and readily available carboxylic acids (or their derivatives) into amines (*25*). In the past decade, radical catalytic strategies have enabled a variety of decarboxylative reactions for C(sp^3)–N bond formation (*26*). Pioneering works by the Fu, Peters, Hu, and MacMillan groups have demonstrated the versatility of copper-based catalytic systems in facilitating these transformations (*27*–*29*). Despite these advances, a general catalytic strategy for enantioconvergent decarboxylative C(sp^3)–N coupling has yet to be established and remains a challenge (*26*, *30*). We envision that developing a copper-based enzymatic system capable of generating a copper-amido complex in its active site could provide a powerful platform to address this challenge. By leveraging the chiral environment of enzymes as well as the power of directed evolution to tailor this environment, such a system could enable C(sp^3)–N coupling with high enantiocontrol.

Conceptualization of a metalloenzymatic system for radical C(sp^3)–N coupling

As a model reaction to identify initial enzyme activity, we drew inspiration from the copper photocatalytic system developed by the Hu group for the decarboxylative amination of *N*-hydroxyphthalimide (NHPI) esters (Fig. 1C) (*28*, *31*, *32*). This system is especially appealing because the activation of NHPI esters for radical transformations has been well established in enzymes containing organic cofactors, such as flavoenzymes and thiamine diphosphate (ThDP)–dependent enzymes (*33*, *34*). More recently, our group demonstrated that this process can be integrated with nonheme iron enzymes for enantioconvergent decarboxylative azidation, in which radical species are intercepted by an Fe(III)–N_3 intermediate (*22*). We therefore focused on copper-substituted nonheme iron enzymes that could potentially accommodate a copper-amido complex for radical interception. Compared with natural copper proteins, nonheme iron enzymes offer greater structural diversity and versatility in mediating abiotic radical transformations (*21*–*24*, *35*–*42*). Moreover, the metal-coordinating sites of nonheme iron enzymes are known to bind alternative metals, including nickel, cobalt, and copper (*43*, *44*). Previous studies have also demonstrated the applicability of copper-substituted nonheme enzymes in catalyzing non-natural reactions, including Diels–Alder reactions and Michael additions (*45*, *46*). Taken together, we anticipate that this copper-substitution strategy will leverage the chemical reactivity of copper to enable radical C–N bond formation while retaining the ability of nonheme enzyme scaffolds to accommodate non-natural substrates, such as NHPI esters, for radical transformations.

Initial enzyme discovery for decarboxylative C–N coupling

On the basis of the rationale outlined above, we first assembled a nonheme enzyme library for initial activity screening. To establish this enzyme library, we used initial docking studies to assess the potential of various nonheme enzymes to accommodate both aniline and the model NHPI ester substrate **1a** in their active sites (figs. S6 to S11). From this in silico screening, we identified eight nonheme enzymes with suitable active-site environments. The enzymes were subsequently tested in clarified lysate form with excess Cu(II) for decarboxylative amination, using NHPI ester **1a** as the substrate, aniline **2b** as the amine coupling partner, and rhodamine B as the photocatalyst (table S1). Through this screening, only phenylalanine hydroxylase (PAH) from *Chromobacterium violaceum* (*Cv*PAH) exhibited promising initial activity and produced the desired amination product in 1.1% yield and 10% enantiomeric excess (ee). Evaluation of various amine coupling partners with wild-type *Cv*PAH showed that *N*-methylaniline **2a** was more active than aniline **2b**,

[1]Department of Chemistry, Johns Hopkins University, Baltimore, MD, USA. [2]College of Chemical Engineering, Zhejiang University of Technology, Hangzhou, Zhejiang, China. [3]Department of Chemistry and Biochemistry, Utah State University, Logan, UT, USA. [4]Institut de Química Computacional i Catàlisi (IQCC), Universitat de Girona, Catalonia, Spain. [5]Departament de Química, Universitat de Girona, Catalonia, Spain. *Corresponding author. Email: xiongyi@jhu.edu (X.H.); yangyf@zjut.edu.cn (Y.Y.); yi.rao@usu.edu (Y.R.)

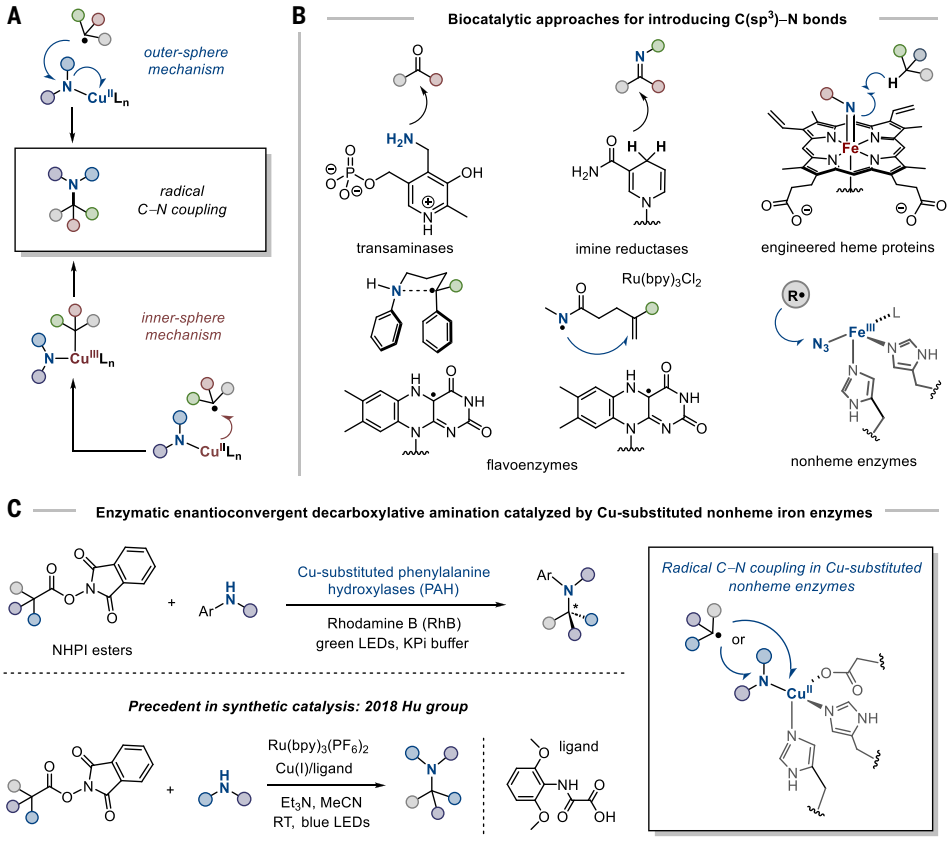

Fig. 1. Design of an enzymatic platform for asymmetric radical C(sp^3)–N coupling. (**A**) Synthetic catalytic systems for radical C(sp^3)–N coupling can proceed through either an outer-sphere mechanism involving homolytic substitution or an inner-sphere mechanism through reductive elimination from a Cu(III) intermediate. (**B**) Representative biocatalytic systems for introducing C(sp^3)–N bonds. (**C**) Design of a biocatalytic system that uses copper-substituted nonheme iron enzymes for asymmetric radical C(sp^3)–N coupling, enabled by radical generation through photoredox decarboxylation of NHPI esters.

providing the amination product **3a** in 1.5% yield and 16% ee. Alkyl amines, amides, and sulfonamides were found to be ineffective for this transformation (table S2). We next conducted a few control experiments (table S3). When the enzyme catalyst was removed from the reaction or replaced *Cv*PAH with bovine serum albumin (BSA), only racemic product was formed. The catalytic performance of iron, cobalt, and nickel were also evaluated, all of which produced only trace amounts of the amination product, highlighting the necessity of using copper for this transformation.

Optimization of *Cv*PAH for decarboxylative amination

With this initial activity in hand, we next sought to enhance the catalytic performance of *Cv*PAH through directed evolution. *Cv*PAH belongs to the family of pterin-dependent aromatic amino acid hydroxylases (AAAHs) (*47*). The enzyme active site features a binding site for the tetrahydrobiopterin (BH_4) cofactor to facilitate O_2 activation and a flexible loop and adjacent residues that bind the aromatic amino acid substrate (Fig. 2A) (*48*). We hypothesized that residues in the native BH_4 and phenylalanine binding sites might be potential mutational hotspots for enhancing the catalytic performance of *Cv*PAH in decarboxylative amination. Guided by this hypothesis and preliminary molecular dynamics (MD) simulation studies of wild-type *Cv*PAH containing copper-*N*-methylanilide complex (fig. S12), we selected 20 active-site residues for site-saturation mutagenesis (SSM) and subsequent screening (Fig. 2A and table S4).

For each library, the top 15 variants identified with gas chromatography–mass spectrometry (GC-MS) on the basis of their activity were further evaluated for enantioselectivity by using chiral high-performance liquid chromatography (HPLC). This combined approach enabled us to evaluate mutants that might enhance enantioselectivity, even if they resulted in a slight decrease in activity. Before initiating the evolution campaign, we first screened a collection of *Cv*PAH variants previously developed in our laboratory to identify a better starting variant than the wild-type *Cv*PAH (table S4). This initial screening led to the identification of the F107L/Y130P double mutant, which exhibited improved enantioselectivity (66% ee) for the target transformation (Fig. 2B and table S4). Using this double mutant as the parent, we performed a series of SSM and screening and ultimately obtained a quintuple mutant, *Cv*PAH F107L/Y130S/W180A/P134L/Y179W (hereinafter referred to as *Cv*PAH-aminase), which produced product **3a** in 19% yield and 94% ee (Fig. 2B). MD simulations and cavity analysis of the copper-*N*-methylanilide–bound enzyme revealed that the introduced mutations generated a single, enlarged cavity in the active site of *Cv*PAH-aminase that was about 1.4 times larger than the total volume of the separate cavities in wild-type *Cv*PAH (Fig. 2C and figs. S12D and S13E). Docking studies suggested that the expanded pocket of *Cv*PAH-aminase facilitates the accommodation of NHPI ester **1a** in the active site compared with that of the wild-type enzyme (figs. S12E and S13F).

Substrate scope evaluation

With the final variant in hand, we optimized various reaction parameters to improve the reaction yield. Considering the mass balance, the majority of NHPI ester **1a** was consumed, with only ~9% remaining after the reaction (table S5). Approximately 4% of the consumed **1a** underwent unidentified hydrolytic processes, as indicated by the formation of NHPI. Around 80% was consumed through redox activation, based on the amount of *N*-phthalimide produced. Of this redox-activated portion, only 16% was converted into the desired amination product. The fate of the remaining 64% remains unclear because only trace amounts of side products associated with radical pathways, such as desaturation and dimerization, were detected. To improve the conversion of either NHPI substrate **1a** or *N*-methylaniline **2a** into the desired product, we systematically optimized the photocatalyst and the concentrations and ratios of all reaction components (tables S6 to S15). We found that other xanthene-type photocatalysts, such as eosin B and eosin Y, resulted in lower reaction yields (<7.0%) relative to rhodamine B, whereas ruthenium- and iridium-based photocatalysts produced even lower yields (< 2.5%). For all these cases, high enantioselectivity (94% ee) was consistently maintained (table S6). We also observed a decline in reaction performance at higher copper concentrations, likely owing to decreased protein stability as the copper concentration increased (figs. S3 to S5).

After extensive optimization, the ideal reaction conditions were established by using final concentrations of 1.25 mM copper(II) sulfate, 5.0 mM ascorbic acid, 10 mM *N*-methylaniline, 45 mM NHPI ester **1a**, and 100 μM rhodamine B as the photocatalyst. Under these conditions, the final amination product **3a** was obtained with a 92% yield and 94% ee by using clarified cell lysate derived from an OD_{600} = 50 whole-cell suspension expressing *Cv*PAH-aminase (where OD_{600} is the optical density of a sample measured at a wavelength of 600 nm). We performed a few

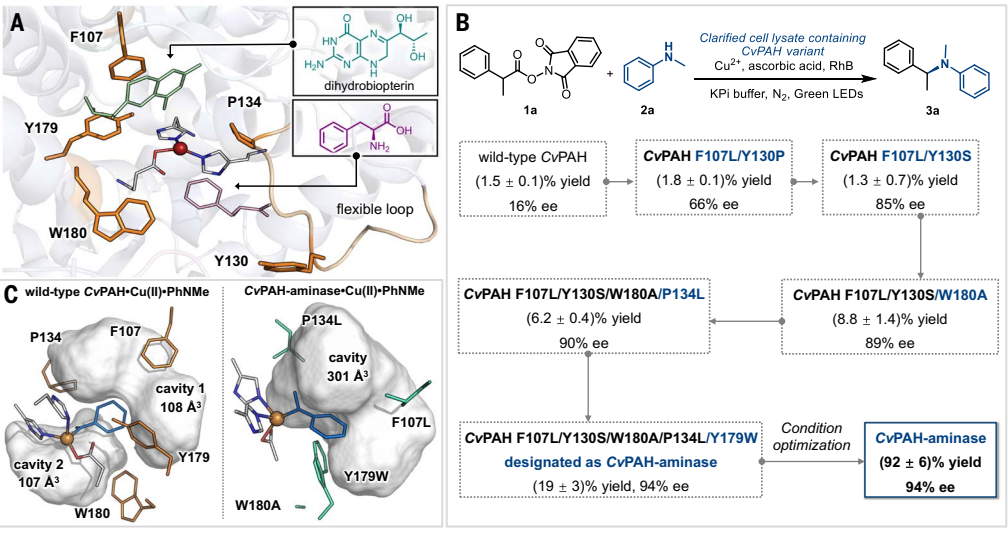

Fig. 2. Optimization of *Cv*PAH for photodecarboxylative C–N coupling through directed evolution. (**A**) The active site of wild-type *Cv*PAH contains a binding pocket for the biopterin cofactor (deep green thick sticks) and a binding region for the phenylalanine substrate (deep pink thick sticks). Residues with beneficial mutations identified are F107, Y130, P134, Y179, and W180 (orange sticks). The phenylalanine substrate is docked into the wild-type *Cv*PAH by using the crystal structure bound with the oxidized cofactor dihydrobiopterin [PDB: 1LTV (*48*)]. Single-letter abbreviations for the amino acid residues are as follows: A, Ala; F, Phe; L, Leu; P, Pro; W, Trp; and Y, Tyr. In the mutants, other amino acids were substituted at certain locations; for example, F107L indicates that phenylalanine at position 107 was replaced by leucine. (**B**) Key mutants identified during the directed evolution campaign and their catalytic performances. Detailed information on the evolution campaign and reaction optimization is provided in tables S4 to S14. (**C**) MD simulations and cavity analysis of wild-type *Cv*PAH and *Cv*PAH-aminase with bound copper-*N*-methylanilide complex (figs. S12D and S13E).

additional control experiments based on this optimized condition. When using lysates from cells harboring expression vectors that lack the *Cv*PAH gene, only 2.0% of the amination product **3a** was observed, indicating minimal contribution from nonenzymatic processes (table S13). Both the reaction yield and enantioselectivity were much higher when using clarified lysate compared with purified proteins (table S14). This difference is primarily attributed to the reduced stability of *Cv*PAH in its purified form under the reaction conditions, particularly its low tolerance to Cu(II) (figs. S3 to S5). Consistent with this analysis, further reducing the copper concentration from 1.25 mM largely restored the high reaction yield and enantioselectivity in purified protein reactions (table S15). The improved yield was mainly due to a higher proportion of redox-activated **1a** being converted into the final amination product **3a** (table S16).

With the optimized condition in hand, we proceeded to investigate the substrate scope of *Cv*PAH-aminase (Fig. 3). The reaction accommodated various aromatic substituents on the NHPI ester, yielding corresponding amination products with yields between 6.3 and 92% and enantioselectivities from 36 to 97% ee. Additionally, the reaction can be scaled up to produce 36 mg of product **3a** with 94% ee and an 85% isolated yield. This scale can be further increased to obtain 68 mg of **3a** with an 81% isolated yield and 94% ee by simply changing the reaction vessel (fig. S15). The inclusion of a bulky *para*-isobutyl group on the NHPI ester reduced both yield and enantioselectivity (**3f**), likely because of steric constraints imparted by the enzyme active site. Changes at the benzylic position also markedly affected the reaction efficiency (**3g**, **3h**, and **3i**). NHPI esters from primary benzylic acids resulted in low yields (**3j** and **3k**), and substrates from nonbenzylic carboxylic acids were ineffective in the reaction (**1b**). Furthermore, the use of NHPI ester **1c**, derived from a tertiary benzylic acid, completely abolished reactivity. In both cases, the majority of NHPI substrates **1b** and **1c** remained unreacted with minimal redox activation, as indicated by the low levels of *N*-phthalimide formation (table S16).

We next explored the scope of the amine coupling partner using NHPI ester **1a** as the model substrate. The reaction was less sensitive to aromatic substituents on the aniline compared with those on the NHPI esters. For all tested amines, yields generally exceeded 40%, and enantioselectivity was over 90% ee. The use of benzylamine completely inhibited the decarboxylative amination reaction, instead producing an amidation product (compound **5**). Time-dependent analysis showed that within 30 min, the amidation product formed in 62% yield relative to benzylamine, whereas only 0.5% of the amidation product was observed when aniline was used as the coupling partner (table S17). Control experiments that use lysates from cells lacking the *Cv*PAH gene in the expression vector, as well as lysates from cells expressing a double-alanine mutant, further confirmed that the amidation is likely a nonenzymatic process (table S17). Despite the incompatibility with alkyl amines, high yields and enantioselectivity were maintained with variations on the *N*-substituents of aniline (**3r**, **3s**, and **3t**)

The reaction is not limited to NHPI esters as radical precursors. The tetrachloro-*N*-hydroxyphthalimide ester **9** is also effective in this transformation, yielding the amination product with 60% yield and 90% ee. By contrast, the combination of a free carboxylic acid with a hypervalent iodine(III) reagent exhibited no activity (table S20). Oxime ester **6** can be used in this biocatalytic amination platform, producing the ring-opening amination product **7** with 5.1% yield and 42% ee (Fig. 3 and table S18). Katritzky salts were also found to be viable radical precursors for this transformation, albeit with a relatively higher background reaction as compared with that of oxime ester **6** (table S19), likely because of the increased reactivity of the reagent. When using Katritzky salts as the radical precursor, we observed low-level but noticeable product formation in the C–N coupling with benzylamine, suggesting the potential of this system for coupling with alkyl amines. Furthermore, this result indicates that the low activity of alkyl amines may be partly due to the greater challenge in forming a copper-amido complex compared with anilines, as previously studied by Warren and co-workers (*49*, *50*). Despite this current limitation, these findings highlight the versatility of the *Cv*PAH-based platform in interfacing with diverse radical generation strategies for C–N coupling.

Mechanistic studies

We conducted a series of experiments to gain a deeper mechanistic understanding of this photobiocatalytic decarboxylative amination. First, we studied the enantioconvergence by monitoring the change in the enantiomeric ratio of the racemic NHPI substrate **1a** and the amination product **3a** as the reaction progressed (Fig. 4A and table S21). Throughout the reaction, the enantiomeric excess of product **3a** consistently remained at 94% ee, whereas the NHPI substrate remained racemic. Additionally, we conducted the same time-dependent experiment using the chiral NHPI substrate (***R***)-**1a**, starting with 64% ee. Similar to the studies with racemic **1a**, no changes in the enantioselectivity of either the substrate or the product were observed (table S21). These results suggest that the enzyme can effectively convert both (*R*)- and (*S*)-NHPI substrates into achiral substrate radicals for C–N bond formation. The addition of 1 equivalent of either TEMPO

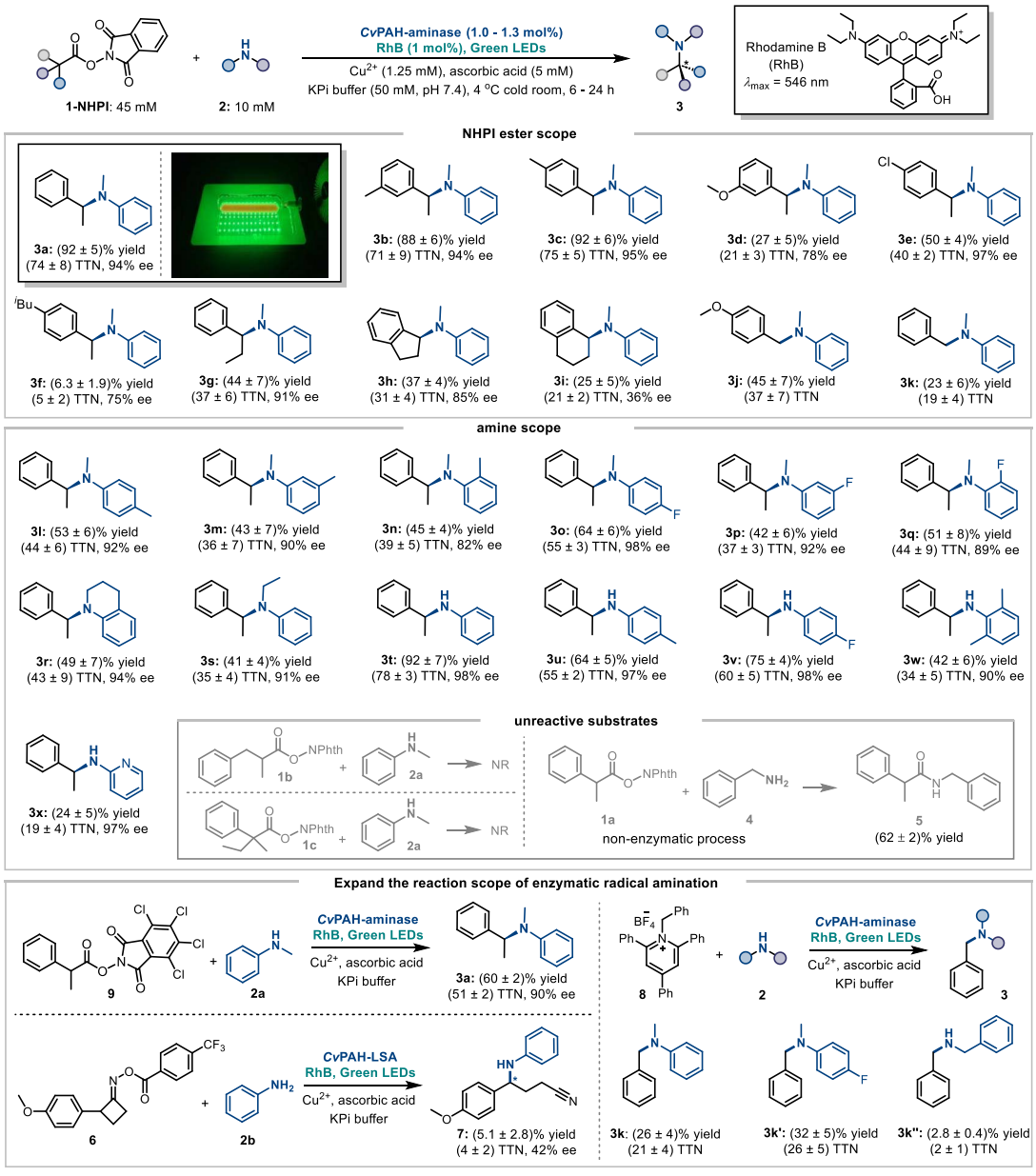

Fig. 3. Evaluation of substrate and reaction scope of radical C–N coupling catalyzed by *Cv*PAH-aminase. The procedure is detailed in the general procedure (G) in section II of the supplementary materials, with the final concentrations of each reactant as follows: NHPI substrate **1** (45 mM), amine coupling partner **2** (10 mM), rhodamine B photocatalyst (100 μM, 1 mol %), $CuSO_4$ (1.25 mM), and ascorbic acid (5 mM), with enzyme loading ranging from 1.0 to 1.3 mol % relative to the amine. The reaction is carried out in 400 μl of clarified lysates obtained from an OD_{600} = 50 whole-cell suspension (50 mM KPi buffer, pH 7.4) for 6 to 24 hours. The protein concentrations of the *Cv*PAH-aminase in cell lysates ranged between 102 and 133 μM. The protein concetration is determined through general procedure (F) of the supplementary materials. The procedure for preparative scale synthesis is detailed in the supplementary materials, section VII. The procedures for ring-opening amination and deaminative C–N coupling are outlined in the supplementary materials, section VIII. The yield was calculated on the basis of the amine coupling partner. The data presented are mean values of two technical duplicates from biological triplicates (six replicate runs in total) by using cell lysate, with error bars indicating the standard deviation from the mean.

[(2,2,6,6-tetramethylpiperidin-1-yl)oxyl] or DMPO (5,5-dimethylpyrroline-*N*-oxide) radical trap dramatically decreased the reaction yield to below 3.0% (Fig. 4B and tables S22 and S23). An allylic probe substrate **1d** yielded a 1.7:1 ratio of the terminal amination product ***3y*** to the internal amination product ***3y'***. Additionally, the use of a cyclopropyl radical clock substrate **1e** led to the exclusive formation of the rearranged homoallylic amination product ***3z***. These findings support the involvement of a carbon-centered radical species in this enzymatic C–N coupling reaction. However, it remains unclear whether radical generation occurs within the active site or in close proximity to the enzyme before seemingly migrating into the active site for the bond-forming process (*33*, *51*, *52*). The use of substrates such as oxime ester **6** and Katritzky salt **8** seems to suggest that radical formation might occur outside the active site owing to their large sizes. However, initial docking studies suggest that the active site of *Cv*PAH-aminase is sufficiently large to accommodate these two substrates (fig. S14). Further studies are needed to fully explore this mechanistic question.

We then investigated the interactions between the photocatalyst and various reaction components using fluorescence spectroscopy (figs. S16 to S19). Fluorescence polarization studies revealed a dissociation

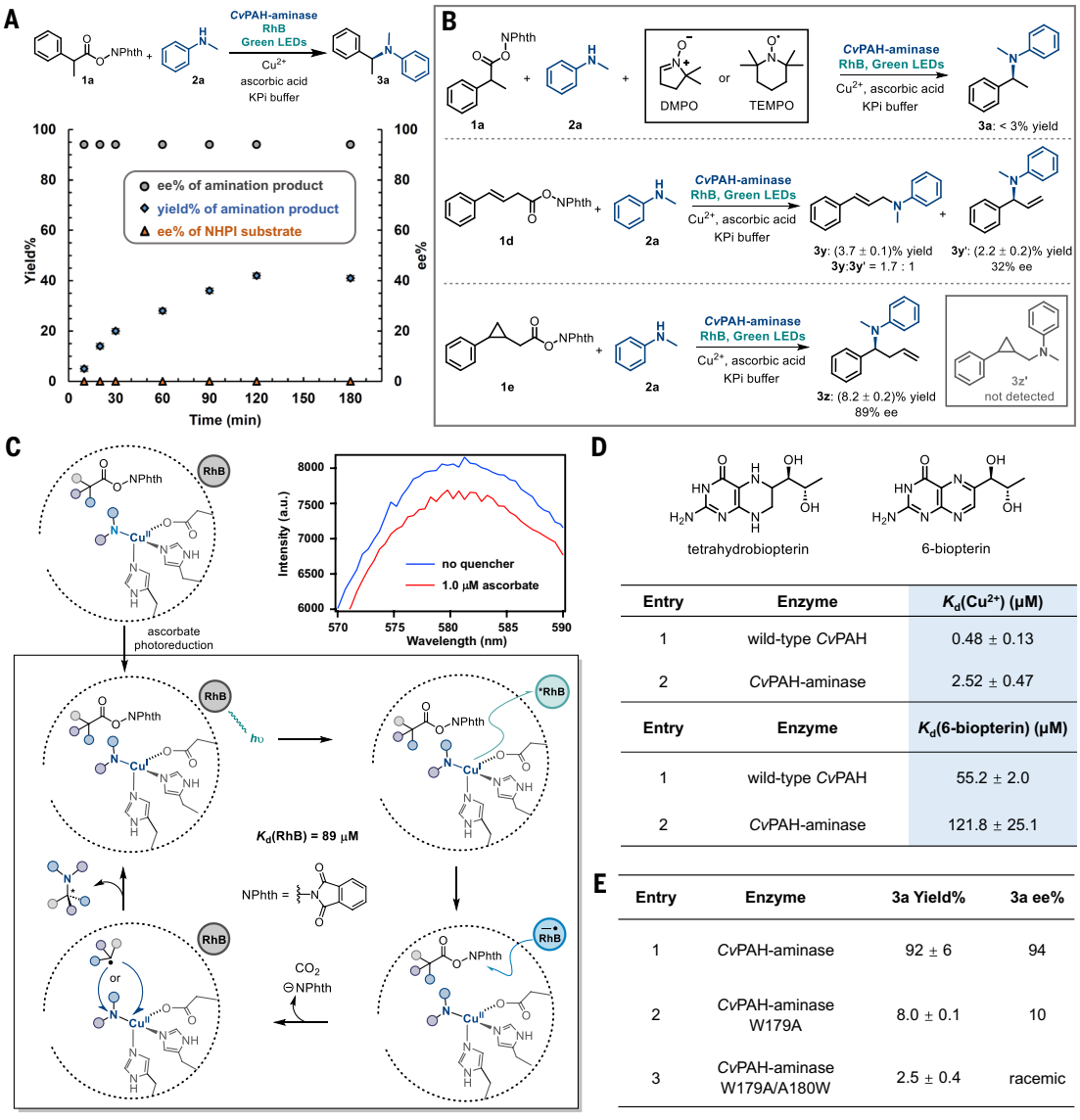

Entry	Enzyme	$K_d(Cu^{2+})$ (μM)
1	wild-type *Cv*PAH	0.48 ± 0.13
2	*Cv*PAH-aminase	2.52 ± 0.47

Entry	Enzyme	K_d(6-biopterin) (μM)
1	wild-type *Cv*PAH	55.2 ± 2.0
2	*Cv*PAH-aminase	121.8 ± 25.1

Entry	Enzyme	3a Yield%	3a ee%
1	*Cv*PAH-aminase	92 ± 6	94
2	*Cv*PAH-aminase W179A	8.0 ± 0.1	10
3	*Cv*PAH-aminase W179A/A180W	2.5 ± 0.4	racemic

Fig. 4. Mechanistic studies. (**A**) Change of substrate and product enantiomeric excess over the course of the reaction (table S21). (**B**) Radical trapping and radical clock studies (supplementary materials, section VIII). (**C**) Plausible reaction mechanism and fluorescence quenching of rhodamine B (5.0 μM final concentration) by AH^- in the presence of *Cv*PAH-aminase (1.0 μM final concentration) (supplementary materials, section XI). (**D**) Analysis of copper and biopterin binding to *Cv*PAH and its variants through tryptophan fluorescence quenching (supplementary materials, section XII). (**E**) Site-directed mutagenesis analysis of key mutations introduced in *Cv*PAH-aminase (table S26).

constant (K_d) of 89 μM between rhodamine B (RhB) and *Cv*PAH-aminase, which falls within the typical range of RhB binding to proteins (K_d = 10 to 100 μM) (*53*, *54*). Fluorescence quenching experiments showed that *N*-methylaniline is not an effective quencher of RhB compared with ascorbate (AH^-). This observation is consistent with the stronger reducing power of AH^- relative to anilines [$E_m(A^{\bullet-}/AH^-)$ = 0.33 V versus standard hydrogen electrode (SHE) in water (*55*); $E_{p/2}$(*N*-methylaniline$^{+\bullet}$/*N*-methylaniline) = 0.9 V versus SHE in water (*56*); E(RhB*/RhB$^{\bullet-}$) = 1.21 V versus saturated calomel electrode (SCE) in water (*57*)]. Additionally, NHPI ester **1a** also did not quench the fluorescence of RhB, which is consistent with the relatively weak oxidizing power of NHPI esters [$E_{p/2}$(NHPI-ester/NHPI-ester$^{\bullet-}$) = –1.5 to –1.8 V versus SCE in MeCN (*58*)] and the modest reducing power of RhB* [E(RhB$^{+\bullet}$/RhB*) = –0.55 V versus SCE in water (*57*)]. These findings suggest that the initial single-electron transfer (SET) most likely occurs between photoexcited RhB* and AH^-, generating reduced rhodamine B (RhB$^{\bullet-}$). We further propose that before the catalytic cycle, RhB$^{\bullet-}$ first reduces the Cu(II) center of *Cv*PAH to Cu(I) because AH^- is known to be insufficiently reducing to achieve this reduction [$E(Cu^{2+}/Cu^{+}) > 0.36$ V versus SHE in water for wild-type *Cv*PAH] (*59*), whereas RhB$^{\bullet-}$ is a much stronger reductant [E(RhB/RhB$^{\bullet-}$) = –0.96 V versus SCE in water (*57*)]. After this initial reduction, the Cu(I) center enters the catalytic cycle depicted in Fig. 4C, which proceeds through initial oxidation of Cu(I) to Cu(II) by RhB*, followed by activation of the NHPI ester substrate by the reduced RhB$^{\bullet-}$. Because of the difficulty in generating discrete Cu(I)-bound *Cv*PAH, our current quenching data could not explore factors such as the coordination of Cu(I) with NHPI esters, which has been shown to enhance the ability of NHPI esters to quench RhB* (discussions are provided in fig. S20 and tables S24 and S25) (*28*). Further mechanistic investigations such as transient absorption spectroscopy will be required to distinguish between these possibilities.

Tryptophan fluorescence quenching (Fig. 4D) (*60*) revealed relatively tight binding of Cu^{2+} to *Cv*PAH-aminase with $K_d(Cu^{2+}) = 2.52 \pm 0.47$ μM.

This affinity is weaker than that of wild-type *Cv*PAH [$K_d(Cu^{2+}) = 0.48 \pm 0.13$ μM], likely because of the introduction of the F107L and Y130S mutations (detailed discussion is provided in the supplemetary materials, section XII). We also compared the biopterin-binding affinities of wild-type *Cv*PAH and *Cv*PAH-aminase. Because of commercial availability constraints, we conducted these studies using 6-biopterin. The wild-type *Cv*PAH bound 6-biopterin with a K_d of 55.2 ± 2.0 μM, which is consistent with previously reported affinities of various pterins for PAH (*61*). *Cv*PAH-aminase showed a weaker binding affinity of 6-biopterin, with a K_d of 121.8 ± 25.1 μM. This reduced affinity is likely due to the F107L mutation because F107 is a key residue involved in pterin binding through π–π stacking interactions (discussions are provided in figs. S27 and S28). Despite differences in biopterin binding, the influence of endogenous pterins from *E. coli* on the reaction should be low, given their very low intracellular concentration (~0.3 μg/g wet cells), which corresponds to ~0.03 μM in our lysates prepared from OD_{600} = 50 whole-cell suspensions (discussions are provided in figs. S27 and S28) (*61*, *62*). We also studied the reaction impact of key mutations Y179W, W180A, and F107L in the final *Cv*PAH-aminase variant (Fig. 4E and table S26). Introducing a W179A mutation to *Cv*PAH-aminase reduced product yield from 92 to 8.0% and enantioselectivity from 94 to 10% ee (Fig. 4E, entry 2). We then introduced an A180W mutation to the *Cv*PAH-aminase W179A variant, resulting in an A179/W180 double mutant for comparison with the W179/A180 configuration in *Cv*PAH-aminase. As shown in Fig. 4E, entry 3, the A179/W180 mutant nearly abolished enzyme activity, producing only racemic product at 2.5% yield. These results indicate the cooperative role of the 179 and 180 sites in influencing this reaction.

This study introduces a biocatalytic strategy for decarboxylative C–N bond formation. This work also establishes PAHs as a powerful platform for enantioselective radical C–N bond formation. We envision that interfacing various radical generation mechanisms with this metalloenzymatic platform will enable diverse biocatalytic amination reactions unprecedented in biology.

REFERENCES AND NOTES

1. E. Vitaku, D. T. Smith, J. T. Njardarson, *J. Med. Chem.* **57**, 10257–10274 (2014).
2. G. Mlostoń, *Chem. Heterocycl. Compd.* **53**, 1 (2017).
3. C. Huang, Z. Wan, A. Zhu, C. Chen, *Chin. J. Chem.* **42**, 1161–1174 (2024).
4. G. C. Fu, *ACS Cent. Sci.* **3**, 692–700 (2017).
5. A. Hossain, A. Bhattacharyya, O. Reiser, *Science* **364**, eaav9713 (2019).
6. Q.-S. Gu, Z.-L. Li, X.-Y. Liu, *Acc. Chem. Res.* **53**, 170–181 (2020).
7. Z.-L. Li, G.-C. Fang, Q.-S. Gu, X.-Y. Liu, *Chem. Soc. Rev.* **49**, 32–48 (2020).
8. H.-N. Yin, P.-C. Wang, Z. Liu, *Bioorg. Chem.* **144**, 107108 (2024).
9. A. K. Gilio, T. W. Thorpe, N. Turner, G. Grogan, *Chem. Sci.* **13**, 4697–4713 (2022).
10. S. A. Kelly *et al.*, *Chem. Rev.* **118**, 349–367 (2018).
11. S. Roy *et al.*, *Nat. Catal.* **7**, 65–76 (2024).
12. S. V. Athavale *et al.*, *J. Am. Chem. Soc.* **144**, 19097–19105 (2022).
13. Z.-J. Jia, S. Gao, F. H. Arnold, *J. Am. Chem. Soc.* **142**, 10279–10283 (2020).
14. Z. Liu *et al.*, *J. Am. Chem. Soc.* **144**, 80–85 (2022).
15. R. Mao *et al.*, *Nat. Catal.* **7**, 585–592 (2024).
16. A. Das *et al.*, *J. Am. Chem. Soc.* **146**, 20556–20562 (2024).
17. F. C. Raps, A. Rivas-Souchet, C. M. Jones, T. K. Hyster, *Nature* **637**, 362–368 (2025).
18. Y. Ye *et al.*, *Nat. Chem.* **15**, 206–212 (2023).
19. M. L. Matthews *et al.*, *Nat. Chem. Biol.* **10**, 209–215 (2014).
20. C. A. Gomez, D. Mondal, Q. Du, N. Chan, J. C. Lewis, *Angew. Chem. Int. Ed.* **62**, e202301370 (2023).
21. J. Rui *et al.*, *Science* **376**, 869–874 (2022).
22. J. Rui *et al.*, *Nat. Catal.* **7**, 1394–1403 (2024).
23. J. G. Zhang, A. J. Huls, P. M. Palacios, Y. Guo, X. Huang, *J. Am. Chem. Soc.* **146**, 34878–34886 (2024).
24. L.-P. Zhao *et al.*, *Angew. Chem. Int. Ed.* **64**, e202506361 (2025).
25. H. Chen, Y. A. Liu, X. Liao, *Synthesis (Stuttg.)* **53**, 1–29 (2021).
26. X. Li, X. Yuan, J. Hu, Y. Li, H. Bao, *Molecules* **28**, 4249 (2023).
27. W. Zhao, R. P. Wurz, J. C. Peters, G. C. Fu, *J. Am. Chem. Soc.* **139**, 12153–12156 (2017).
28. R. Mao, A. Frey, J. Balon, X. Hu, *Nat. Catal.* **1**, 120–126 (2018).
29. Y. Liang, X. Zhang, D. W. C. MacMillan, *Nature* **559**, 83–88 (2018).
30. J. Kweon, B. Park, D. Kim, S. Chang, *Nat. Commun.* **15**, 3788 (2024).
31. G. Barzanò, R. Mao, M. Garreau, J. Waser, X. Hu, *Org. Lett.* **22**, 5412–5416 (2020).
32. R. Mao, J. Balon, X. Hu, *Angew. Chem. Int. Ed.* **57**, 9501–9504 (2018).
33. Y. Xu *et al.*, *Nature* **625**, 74–78 (2024).
34. P. D. Clayman, T. K. Hyster, *J. Am. Chem. Soc.* **142**, 15673–15677 (2020).
35. Q. Zhao *et al.*, *Nat. Synth.* **3**, 958–966 (2024).
36. B. Wang *et al.*, *Angew. Chem. Int. Ed.* **62**, e202311099 (2023).
37. L.-P. Zhao *et al.*, *Nat. Synth.* **3**, 967–975 (2024).
38. N. W. Goldberg, A. M. Knight, R. K. Zhang, F. H. Arnold, *J. Am. Chem. Soc.* **141**, 19585–19588 (2019).
39. M. A. Vila, V. Steck, S. Rodriguez Giordano, I. Carrera, R. Fasan, *ChemBioChem* **21**, 1981–1987 (2020).
40. M. Davidson, M. McNamee, R. Fan, Y. Guo, W.-C. Chang, *J. Am. Chem. Soc.* **141**, 3419–3423 (2019).
41. H. He *et al.*, *Angew. Chem. Int. Ed.* **64**, e202423507 (2025).
42. Z. Wan *et al.*, *Nat. Synth.* 10.1038/s44160-025-00788-6 (2025).
43. H. Eom, W. J. Song, *J. Biol. Inorg. Chem.* **24**, 517–531 (2019).
44. A. Pordea, *Curr. Opin. Chem. Biol.* **25**, 124–132 (2015).
45. J. Podtetenieff, A. Taglieber, E. Bill, E. J. Reijerse, M. T. Reetz, *Angew. Chem. Int. Ed.* **49**, 5151–5155 (2010).
46. R. Matsumoto *et al.*, *Chem. Sci.* **14**, 3932–3937 (2023).
47. P. F. Fitzpatrick, *Arch. Biochem. Biophys.* **735**, 109518 (2023).
48. H. Erlandsen *et al.*, *J. Mol. Biol.* **320**, 645–661 (2002).
49. E. S. Jang *et al.*, *J. Am. Chem. Soc.* **136**, 10930–10940 (2014).
50. S. Wiese *et al.*, *Angew. Chem. Int. Ed.* **49**, 8850–8855 (2010).
51. L. Cheng *et al.*, *Science* **381**, 444–451 (2023).
52. Y. Ouyang, C. G. Page, C. Bilodeau, T. K. Hyster, *J. Am. Chem. Soc.* **146**, 13754–13759 (2024).
53. S. Millan, L. Satish, S. Kesh, Y. S. Chaudhary, H. Sahoo, *J. Photochem. Photobiol. B* **162**, 248–257 (2016).
54. Y. Feng, W. Liu, R. Mercadé-Prieto, X. D. Chen, *J. Photochem. Photobiol. A* **408**, 113092 (2021).
55. J. J. Warren, J. M. Mayer, *J. Photochem. Photobiol. A* **132**, 7784–7793 (2010).
56. P. R. Erickson *et al.*, *J. Phys. Chem. A* **119**, 3233–3243 (2015).
57. S. Gary, M. Landry, S. Bloom, *Synlett* **34**, 1911–1914 (2023).
58. C. R. Azpilcueta-Nicolas, J.-P. Lumb, *Beilstein J. Org. Chem.* **20**, 346–378 (2024).
59. S. O. Pember, J. J. Villafranca, S. J. Benkovic, *Biochemistry* **25**, 6611–6619 (1986).
60. R. T. Carr, S. J. Benkovic, *Biochemistry* **32**, 14132–14138 (1993).
61. A. L. Pey *et al.*, *FASEB J.* **20**, 2130–2132 (2006).
62. K. Ikemoto *et al.*, *Biol. Chem.* **383**, 325–330 (2002).

ACKNOWLEDGMENTS

We thank P. Mortimer and the JHU Mass Spectrometry Facility for analytical support. We are also grateful to M. Greenberg and T. Warren for their insightful discussions during the preparation of this manuscript. **Funding:** Financial support was provided by the Johns Hopkins University and the National Institute for General Medical Sciences (R35GM147639) (to X.H.). This work was also supported by the National Natural Science Foundation of China (22371256 and 21978272) (to Y.Y.) and the Fundamental Research Funds for the Provincial Universities of Zhejiang (RF-C2022006) (to Y.Y.). This work was also supported by the Generalitat de Catalunya AGAUR 2021SGR00623 project (to M.G.-B.), the Spanish MICINN (Ministerio de Ciencia e Innovación) PID2022-141676NB-I00 and TED2021-130173B-C42 projects, and RYC 2020-028628-I grant (to M.G.-B). This work was also supported by the National Science Foundation under grant 2427209 (to Y.R.). **Author contributions:** X.H. conceived the project. X.H. and X.S. designed the experiments. X.S., X.J., and J.R. performed initial screening. X.S. performed directed evolution experiments and results analysis. X.S. and Y.X. performed substrate scope study. J.G.Z. performed tryptophan fluorescence quenching experiments and data analysis. J.B.B. performed the fluorescence quenching experiments of rhodamine B, under the guidance of Y.R.; Y.Y. directed the computational studies. X.C. performed MD simulation studies and docking analysis, under the guidance of Y.Y. Results analyses of all computational data were performed by M.G.-B., Y.Y., X.H., and X.C.; X.H. wrote the manuscript, with input from all other authors. Y.Y. wrote the computational section of the manuscript and the supplementary materials. J.B.B. and Y.R. wrote the fluorescence quenching section of the main text and the supplementary materials. **Competing interests:** A provisional patent application has been under preparation through Johns Hopkins University based on the results presented herein with X.S., X.H., J.R., J.G.Z. as inventors (JHU reference no. C18645). The other authors declare no competing interests. **Data and materials availability:** All data are available in the main text or the supplementary materials. All data needed to evaluate the conclusions in this study are present in the main text or the supplementary materials. **License information:** Copyright © 2025 the authors, some rights reserved; exclusive licensee American Association for the Advancement of Science. No claim to original US government works. https://www.science.org/about/science-licenses-journal-article-reuse

SUPPLEMENTARY MATERIALS

science.org/doi/10.1126/science.adt5986
Materials and Methods; Supplementary Text; Figs. S1 to S28; Tables S1 to S26; References (*63*–*118*); MDAR Reproducibility Checklist

Submitted 3 October 2024; accepted 4 June 2025

10.1126/science.adt5986

EVOLUTIONARY BIOLOGY

Cross-species implementation of an innate courtship behavior by manipulation of the sex-determinant gene

Ryoya Tanaka[1,2*†], Yusuke Hara[2†], Kosei Sato[2], Soh Kohatsu[2], Hinata Murakami[3], Tomohiro Higuchi[3], Takeshi Awasaki[4], Shu Kondo[5], Atsushi Toyoda[6], Azusa Kamikouchi[1,3], Daisuke Yamamoto[2*]

In accepting a courting male, *Drosophila subobscura* females require nuptial gift giving in which a male gives regurgitated crop contents to her mouth to mouth. No similar behavior is found in *D. melanogaster*. By clonal activation of neurons expressing the male-determinant FruM, we identified insulin-like peptide–producing cells (IPCs) and their putative postsynaptic targets, proboscis-innervating motoneurons, as those critical for gift giving. We demonstrate that loss of FruM from *D. subobscura* IPCs abrogates neurite extension and gift giving, whereas FruM overexpression in their *D. melanogaster* counterparts induces overgrowth of neurites that harbor functional synapses, culminating in increased regurgitation. We suggest that the acquisition of FruM expression by IPCs was a key event occurring in an ancestral *D. subobscura* that conferred a latent capability to perform nuptial gift giving.

What is the neural mechanism that determines the presence or absence of a specific action in an otherwise conserved innate behavior? As a first step in addressing this question, we focused on nuptial gift giving (NGG) in the courtship ritual of *Drosophila subobscura*, a species separated from the *D. melanogaster* lineage ~30 to 35 million years ago (*1*–*3*). The male fly presents a droplet of regurgitated crop contents on his mouth tip in front of a female fly, who may extend her proboscis and suck up the droplet (Fig. 1, A and B). No *Drosophila* species other than *D. subobscura* exhibits any similar behavior (Fig. 1, C to I, and movies S1 and S2) (*4*), with the single exception of *D. persimilis*, the males of which occasionally show similar NGG, although this behavior is dispensable for female acceptance (*5*). By thermogenetically stimulating a few neurons that express sex-specific products of the *fruitless* (*fru*) gene FruM (*6*, *7*) by means of stochastic mosaicism, we have identified a few subsets of *fru* neurons that are capable of eliciting courtship-associated regurgitation in *D. subobscura*.

Clonal stimulation of *fru* neurons induces regurgitation

To conduct mosaic analysis of NGG, we genome edited *D. subobscura* so that the flies carried three constructs, *fru*^{so}*-GAL4*, *UAS>STOP>dTrpA1::Myc*, and *hs-flp*, a minimal triad required for generating simple flip-out clones of a small number of *fru* neurons (fig. S1, A and B). Because *dTrpA1* encodes a cation channel that opens at temperatures around 30°C, the ambient temperature was increased from 18° to 29°C to determine whether the test flies exhibited regurgitation in response to this temperature change. We obtained two fly groups: a regurgitation-positive and a regurgitation-negative group. Their brains were then dissected and subjected to anti-Myc antibody staining to visualize neurons expressing *dTrpA1::Myc*, which had been thermogenetically activated in behavioral assays. The neurons thus visualized were scarce, although heterogeneous neuron populations were present, allowing us to identify

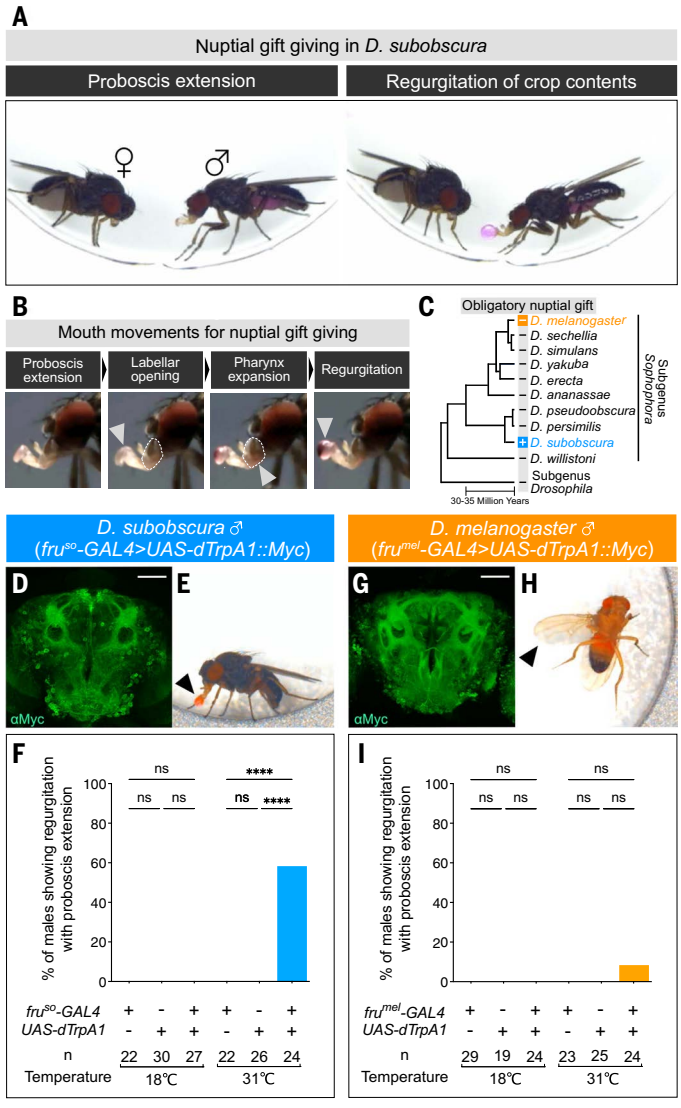

Fig. 1. NGG in *D. subobscura*. (**A**) Male proboscis extension (left) and regurgitation (right) in preparation for the gift of a droplet. (**B**) Mouth movements for NGG: proboscis extension, labellar opening (arrowhead: widened labellum), pharynx expansion (arrowhead: enlarged pharynx; compare the contours of the constricted and dilated pharynx shown with broken lines in the middle left and middle right panels) and regurgitation (the arrowhead: a droplet). (**C**) Phylogenetic tree (branches not to scale) highlighting the presence (+) or absence (−) of reported evidence for obligatory NGG. (**D** to **I**) The *fru* circuit [(D) and (G)] that induces courtship actions [(E), (F), (H), and (I)] in *D. subobscura* [(D) to (F)] and *D. melanogaster* [(G) to (I)] males. (D and G) Anterior view of the *fru* circuit visualized with *fru-GAL4*. Scale bar, 50 μm. (E and H) Courtship actions (arrowheads) induced by *dTrpA1* activation (regurgitation in *D. subobscura*; wing extension in *D. melanogaster*). (F and I) Quantification of regurgitation induced by activation of the *fru* circuit in *D. subobscura* (F) and *D. melanogaster* (I) males. ****$P <$ 0.0001; ns, not significant by the Fisher's exact test for count data and the Hochberg method for *P* value adjustment (table S6).

[1]Division of Biological Science, Graduate School of Science, Nagoya University, Nagoya, Aichi, Japan. [2]Advanced ICT Research Institute, National Institute of Information and Communications Technology, Kobe, Hyogo, Japan. [3]Graduate School of Life Sciences, Tohoku University, Sendai, Miyagi, Japan. [4]Department of Biology, School of Medicine, Kyorin University, Mitaka, Tokyo, Japan. [5]Department of Biological Science and Technology, Faculty of Advanced Engineering, Tokyo University of Science, Katsushika, Tokyo, Japan. [6]Advanced Genomics Center, National Institute of Genetics, Mishima, Shizuoka, Japan. ***Corresponding author. Email: tanaka.ryoya.z3@f.mail.nagoya-u.ac.jp (R.T.); daichan@nict.go.jp (D.Y.)**
†These authors contributed equally to this work.

major groups of *fru* neurons (Fig. 2, A and B, and tables S1 and S2) in *D. subobscura* males based on anatomical similarities to putative homologous neurons in *D. melanogaster* (*8*–*10*). For the *fru* neurons in the subesophageal ganglion (SG), we tentatively divided them into four large heterogeneous groups: lateral (L), medial (M), anterior (a), and posterior (p) neurons (Fig. 2B). We then calculated the proportion of mosaic flies in which each neural group was activated during the thermogenetic behavioral assays (the active-upon-warming score or A-score; Fig. 2C and tables S1 and S2). We reasoned that the neural groups in which the A-score was higher for the regurgitating than the nonregurgitating fly group would be promising candidates for neurons contributing to regurgitation. We should note, however, that regurgitation is known to occur after the ingestion of a large amount of liquid food in various flies (fig. S2, A and B) (*11*, *12*), and this assay alone does not distinguish NGG-associated regurgitation from postfeeding regurgitation.

Insulin neurons promote NGG

Two neuronal groups attracted our attention, pars intercerebralis (PI) neurons and L-pSG neurons, because they were labeled more often in the regurgitating than in the nonregurgitating fly group (Fig. 2C and tables S1 and S2). Note, however, that a substantial proportion (38.5%) of nonregurgitating flies carried anti-Myc–labeled PI neurons. This is presumably because dTrpA1 was also expressed in other neurons that suppress regurgitation (tables S1 and S2). The PI neurons labeled in regurgitating mosaic flies resembled insulin-like peptide–producing cells (IPCs) in *D. melanogaster* (Fig. 2A) (*13*). To test whether IPCs are involved in NGG, these neurons were thermogenetically activated through the *dilp2*^{sopA}*-GAL4* driver (Fig. 3, A and B, and fig. S3, A to H). We found that IPC activation substantially increased the incidence of NGG (Fig. 3C), and the probability of observing regurgitation in response to elevated temperature increased as the number of *dTrpA1*-expressing IPCs increased (fig. S1C). Conversely, the males carrying inactivated IPCs engaged less frequently in NGG than did control males (Fig. 3D). Furthermore, the *dilp2* mutant males showed a reduction in the number of NGGs compared with control males (Fig. 3E). However, general courtship activities as measured by the courtship index were not affected by IPC activation, IPC inactivation, or the *dilp2* mutation (fig. S4, A to C). Additionally, in solitary males, thermogenetic activation of IPCs similarly promoted regurgitation (fig. S4D). These observations indicate that IPCs accelerate NGG.

We then investigated whether activities in IPCs affect male fitness. Single females were given a choice between two males, one carrying IPCs activated through dTrpA1 and the other carrying IPCs with no dTrpA1, to determine which males were more successful in mating. Our results showed that IPC-activated males copulated at a higher rate than unmanipulated males under such competitive conditions (Fig. 3F). We conclude that IPCs are positive modulators of NGG, and IPC activities may confer higher fitness on males.

Insulin neurons are recruited to the courtship circuit

To clarify whether IPCs express FruM in these two *Drosophila* species, IPCs were doubly stained with anti-FruM and anti-Dilp2 antibodies (Fig. 3G and fig. S5, A and B). Sixteen to 18 IPCs were marked with the anti-sDilp2, and most (16 or 17) of these were also labeled with anti-FruM in *D. subobscura* (Fig. 3G, left, and table S3). By contrast, none of 16 *D. melanogaster* IPCs were labeled by anti-FruM (Fig. 3G, right, and table S3), suggesting that IPCs express FruM in *D. subobscura* but not in *D. melanogaster*.

Courtship initiator P1 neurons modulate IPC activities

In *D. melanogaster*, male-specific P1 neurons (20/hemisphere) in the *fru* circuit play a role in triggering courtship (*9*). We found that compared with those of their *D. melanogaster* counterparts, apical dendrites of *D. subobscura* IPCs were substantially longer and extended laterally (Fig. 3, H and J). To generate a P1-specific GAL4, we introduced a *D. melanogaster*–derived enhancer sequence (*R71G01-GAL4*) or its homologous *D. subobscura* sequence into the *D. subobscura* genome. However, neither transgene yielded GAL4 expression in P1 neurons in *D. subobscura*. As an alternative approach, *Venus* inserted into the *fru* second exon, which was fused with *Chrimson* (*fru*$^{Chrimson::Venus}$), was used to label the entire *fru* circuit (*3*). This visualized a neurite extruding from the lateral junction of the *fru* circuit, which appeared to contact the dendrites of *D. subobscura* IPCs (fig. S6). We next examined the effect of *fru* knockdown targeted to IPCs (fig. S7A) on neurite structures and on NGG performance in *D. subobscura* males. *fru* knockdown led to not only a loss of elongated dorsolateral arbors but also to a reduction in the incidence of NGG (Fig. 3, I, K, and L). By contrast, *fru* knockdown had no effect on the number of IPCs (fig. S7B). Next, we optogenetically stimulated the entire *fru* circuit while recording membrane electrical responses from an IPC. LED illumination induced excitatory responses in the IPC, which were diminished by Ca^{2+} deprivation that blocks synaptic activities, leaving the nonsynaptic component intact. Subtracting the nonsynaptic component from the total response recorded from

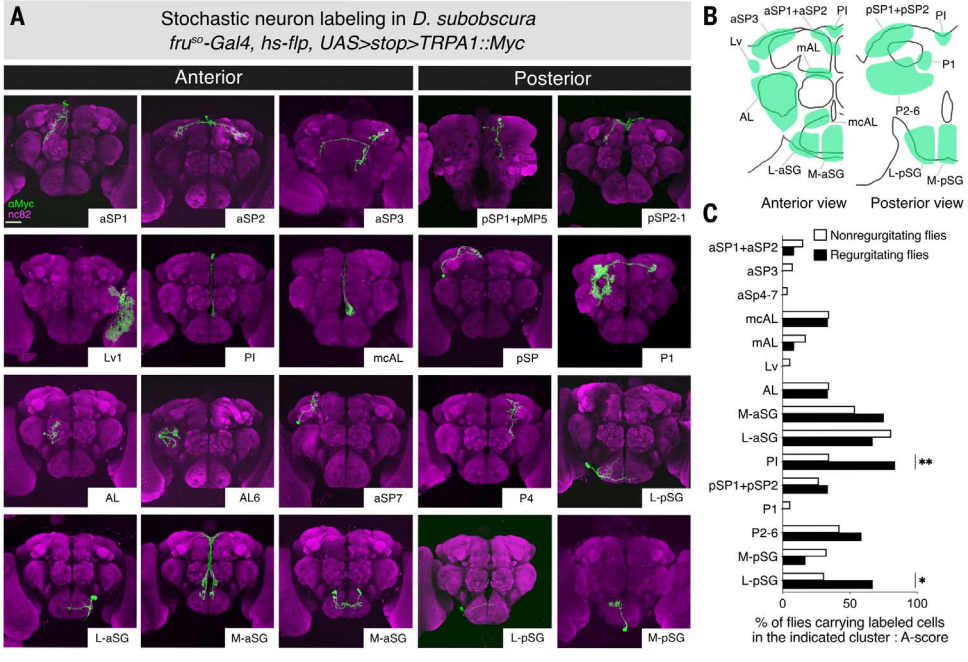

Fig. 2. Flip-out mosaicism identifies *fru*-positive neuronal groups that induce regurgitation upon activation in *D. subobscura* males. (**A**) Examples of clones of different neuronal groups obtained by partial stacks of original images. The names of the neuronal groups are indicated below each image. Scale bar, 50 μm. (**B**) Schematic drawing of the locations of neuronal clusters defined in this study. Anterior (left) and posterior (right) views are shown. (**C**) Behavioral assay results with mosaic flies. Proportions (abscissa: A-score, %) of flies carrying *dTrpA1*-expressing clones in the indicated neural cluster for regurgitating (solid bars) and nonregurgitating (open bars) groups are shown. Fisher's exact test was used for statistical analysis of count data (table S6). $^{**}P < 0.01$; $^{*}P < 0.05$.

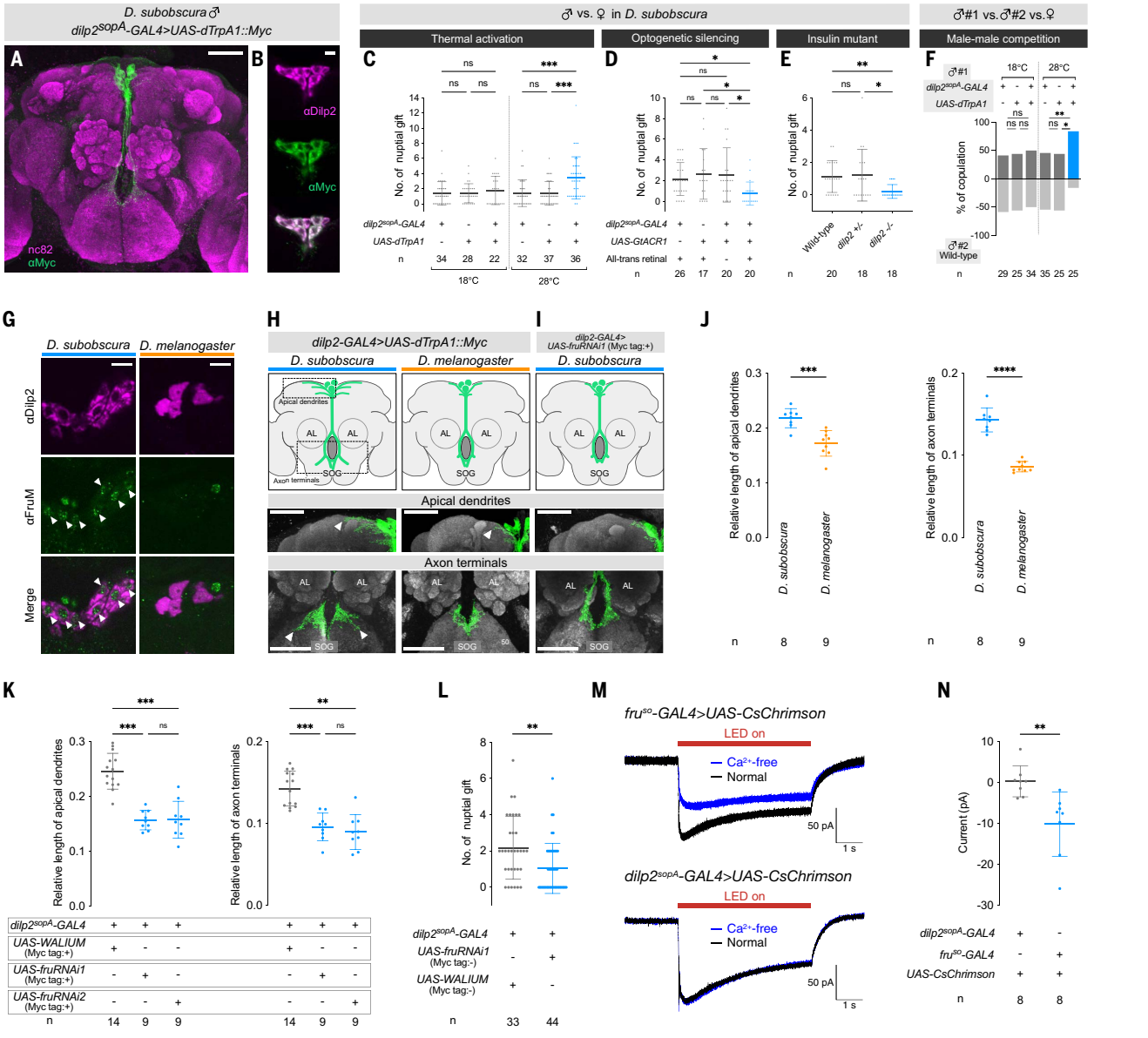

Fig. 3. Importance of FruM expression for NGG. (**A**) IPCs of *D. subobscura* males. (**B**) Double staining with anti-sDilp2 (top) and anti-Myc (middle) and the merged images (bottom). (**C** to **E**) Effects of IPC activation (C), inactivation (D), or *dilp2* mutants (E) on NGG. (**F**) Effect of IPC activation on competitive mating. (**G**) Double staining with anti-Dilp2 (top) and anti-FruM (middle) in *D. subobscura* (left) and *D. melanogaster* (right) and the merged images (bottom). Arrowheads: anti-FruM–positive nuclei. (**H** and **I**) Examples (bottom) and schematics (top) of IPC neurites in *D. subobscura* [(H), left], *D. melanogaster* [(H), right] and *D. subobscura* with *fru* knockdown (I). (**J**) Size comparisons of neurites between *D. subobscura* and *D. melanogaster*. (**K**) Effects of *fru* knockdown on neurite sizes. (**L**) Effects of *fru* knockdown on NGG. (**M**) Responses of IPCs in normal (black) or Ca^{2+}-free (blue) saline upon photoactivation of the *fru* circuit or IPCs. (**N**) Comparisons of synaptic components between the two stimulation conditions. Error bars in (C) to (E), (J) to (L), and (N) represent the mean ± SD. Statistics are reported in table S6. ****$P < 0.0001$; ***$P < 0.001$; **$P < 0.01$; *$P < 0.05$; ns, not significant. Scale bars, 50 μm in (A), (H), and (I) and 10 μm in (B) and (G).

the IPC in normal saline, we succeeded in isolating synaptic inputs from the *fru* circuit to the IPC (Fig. 3, M and N). We also ran another experiment to selectively activate IPCs with *dilp2-GAL4* in the presence and absence of Ca^{2+}. In this case, no synaptic component in light-induced depolarization was detected, as expected. We conclude that functional connections exist between the *fru* circuit and IPCs in *D. subobscura*.

Overexpression of FruBM, but not FruAM or FruEM, in *D. melanogaster* IPCs induced dendrite outgrowth, phenocopying *D. subobscura* IPCs (Fig. 4, A and B, and fig. S8). To test whether extended dendrites have anatomical contact with P1 neurons, we performed double staining of the brain with two markers, IPC-specific *Dilp2-GAL4* and *R71G01-lexA*, the latter of which drives expression in the P1a subpopulation of P1 neurons (*14*, *15*). In FruBM-overexpressing IPCs, potential connections with P1 neurons were found in the superior lateral protocerebrum but not in IPCs lacking FruBM overexpression (Fig. 4C). To assess the functional relevance of the FruM-dependent dendritic remodeling, we optogenetically stimulated P1 neurons while monitoring electrical activities from a *D. melanogaster* IPC. In control IPCs without FruBM overexpression, we detected small (~4 mV) excitatory postsynaptic potentials (EPSPs) time-locked to light stimuli applied to P1 neurons (Fig. 4, D to F, and fig. S9A). We found that these EPSPs were mediated by the nicotinic acetylcholine receptor, as shown by the fact that they were blocked by d-tubocurarine (50 μM; fig. S9A).

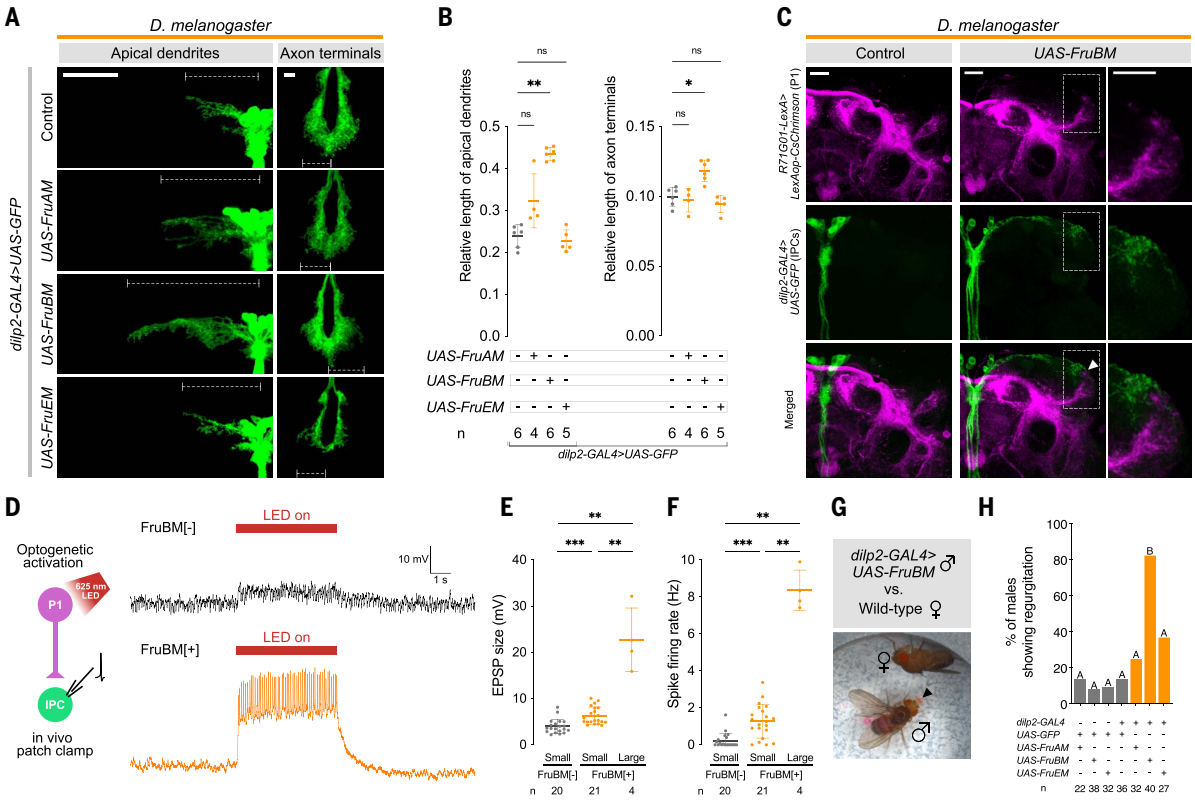

Fig. 4. Effects of FruM overexpression in IPCs on anatomy, physiology, and behavior in *D. melanogaster* males. (**A**) Dendrites (left) and terminals (right) of control or FruM-overexpressing IPCs. Scale bars, 50 μm (left) and 10 μm (right). (**B**) Effects of FruM overexpression on neurite sizes. (**C**) Stacked images of P1 neurons (top) and IPCs (middle) with (right) and without (left) FruBM and the merged images (bottom). An arrowhead indicates a possible connection site for P1 neurons and IPCs. Scale bar, 20 μm. (**D**) Voltage records from a control (FruBM[−]) and FruBM-overexpressing (FruBM[+]) IPC (right) and the experimental design (left). Horizontal bars indicate P1 stimulation (right). (**E**) EPSPs from FruBM[−] ($n = 20$) and FruBM[+] IPCs ($n = 25$). (**F**) Spike rates during P1 activation in FruBM[−] and FruBM[+] IPCs. (**G**) FruBM[+] male regurgitating during courtship. An arrowhead indicates the droplet. (**H**) Effects of FruM on regurgitation frequencies. *UAS-GFP* was used to equalize, across the genotypes tested, the copy number of *mini-w*$^+$, which has effects on fly behaviors (*28*). Bars labeled with the same letter are not significantly different ($P < 0.05$). Error bars in (B), (E), and (F) represent the mean ± SD. Statistics are reported in table S6. ***$P < 0.001$; **$P < 0.01$; *$P < 0.05$; ns, not significant.

The cholinergic input could impinge onto IPCs at the contact point with P1 neurons previously detected by GRASP (*16*). Alternatively, some unidentified cholinergic neurons might intervene between P1 neurons and IPCs to produce small EPSPs in the latter. Upon FruBM overexpression, a subset of IPCs (four of 25 cells) produced very large EPSPs of 20 mV or even larger, which initiated a train of spikes (Fig. 4, D to F, and fig. S9, A and B), whereas most IPCs with FruBM overexpression provoked only small EPSPs (Fig. 4, D and E). We did not observe similar EPSPs in IPCs without FruBM overexpression (neither the 20 IPCs in this series of experiments nor the 20 IPCs in the other experiments without FruBM overexpression). The FruBM-dependent large EPSPs were unaffected by d-tubocurarine, indicating that they represent synaptic inputs distinctly different from the cholinergic small EPSPs (fig. S9A). It remains to be determined which neurotransmitter is involved in the generation of FruBM-dependent large EPSPs. We postulate that it is the extended dendrites induced by FruBM overexpression that mediated these noncholinergic large EPSPs. Cholinergic small EPSPs were larger in IPCs with FruBM overexpression than in control IPCs (Fig. 4, E and F), and thus this synaptic potentiation also contributes to enhanced coupling between the P1-GAL4 neurons and IPCs.

Concordant with the potentiated coupling between P1 neurons and IPCs, we found that some *D. melanogaster* males overexpressing FruBM in IPCs regurgitated during attempts to lick female genitals in courtship (Fig. 4, G and H). Our close observation of courting males revealed that a few wild-type *D. melanogaster* males in fact did regurgitate during attempts to lick (Fig. 4H). Thus, FruBM overexpression in the IPCs of *D. melanogaster* males enhances regurgitation during courtship. NGG occurs between wing display and copulation attempt in *D. subobscura*, a timing analogous to that of licking in *D. melanogaster*. These observations collectively suggest that FruBM-dependent coupling of IPCs with P1 neurons is pivotal for the execution of courtship-associated regurgitation. Nonetheless, P1 neurons were not found to be a candidate for the regurgitation-inducing neurons when clonally activated in *D. subobscura* (Fig. 2C). This was partly because we could obtain only two mosaic files carrying P1 neuron clones, and neither of them showed regurgitation upon thermogenetic activation. This apparently negative result is reminiscent of the clonal activation of P1 neurons in *D. melanogaster*, in which P1 neurons successfully triggered the earlier part of courtship, including singing, yet failed to initiate the later components such as licking (*9*, *17*). Overexpression of FruAM and FruEM did not increase the occurrence of NGG (Fig. 4H), and no discernible extension of dendrites was observed. We conclude that FruBM, but not FruAM or FruEM, functions to establish the P1-IPC connections critical for the NGG induction.

Motor pathways for NGG

Some neurons in the SG were labeled more often in regurgitating than in nonregurgitating flies. These neurons were grouped as L-pSG neurons, which may include heterogeneous populations of neurons, as mentioned above. Despite this complexity, we noted that neurons with large, laterally located somata with dendrites extending to the midline

of the SG were repeatedly labeled in different mosaic males that exhibited regurgitation during thermogenetic activation (Fig. 2C). The overall structure of L-pSG neurons resembled that of some proboscis-innervating motoneurons (Fig. 2A and fig. S10A) previously reported in *D. melanogaster* (*18*–*20*). Some L-pSG neurons have an axon that exits the brain-SG complex through a peripheral nerve, indicating that they are indeed motoneurons (fig. S10A). We therefore recalculated the A-scores after dividing the L-pSG into two subclasses: L-pSG motoneurons (L-pSG-Motor) and L-pSG non-motoneurons, and compared the A-scores for L-pSG-Motor between regurgitating and non-regurgitating mosaic flies. The mosaic flies carrying *dTrpA1*-positive clones in L-pSG-Motor were substantially more enriched in the group that exhibited regurgitation upon thermogenetic activation (A-score: 33.3; four of 12 flies) than in the group that did not exhibit regurgitation (A-score: 7.6; four of 52 flies) (fig. S10B). We noted that central arborizations of the L-pSG motoneurons were juxtaposed to IPC axon terminals when three-dimensional reconstitution of these two types of neurons was registered on a template brain (fig. S10C). This finding suggests that the proboscis-innervating motoneurons may constitute a downstream pathway of IPCs.

It was difficult to deduce the cellular identity of *D. subobscura* motoneurons by analogy with their *D. melanogaster* counterparts. We therefore turned to looking for *fru*-positive motoneurons that terminate on proboscis muscles. Among the muscles we examined, muscle 9 (m9), m10, m11, and m12 [fig. S10D, terminology after (*18*)], *fru*^{so}-*GAL4*–labeled axons had terminals only on m9 in *D. subobscura* (fig. S10E). A connectome-based computational model also predicted the involvement of m9-innervating motor units in inducing proboscis extension (*21*). We therefore focused on this muscle in subsequent analyses. It remains to be rigorously tested whether these *fru*^{so}-*GAL4*–labeled axons innervating m9 indeed contain axons of L-pSG motoneurons.

Insulin neurons modulate motor outputs

The m9 muscle fibers showed spontaneous electrical activities that were characterized by repetitive volleys of depolarizing potentials: a single volley of 1.36 ± 0.15 s (mean ± SD) in duration and 11.00 ± 7.17 mV (mean ± SD) in amplitude occurred with intervals of 6.67 ± 1.81 s (mean ± SD; n = 13; Fig. 5, A to C). A volley consisted of several types of EPSPs, each different in size, which collectively formed a large, depolarizing plateau (Fig. 5, B and C). Unilateral severing of the pharyngeal nerve eliminated phasic EPSP volleys and compromised contraction of the proboscis muscle m9 on the operated side while sparing these EPSPs and muscle contraction on the nerve-intact side (compare Fig. 5B for EPSPs). This observation

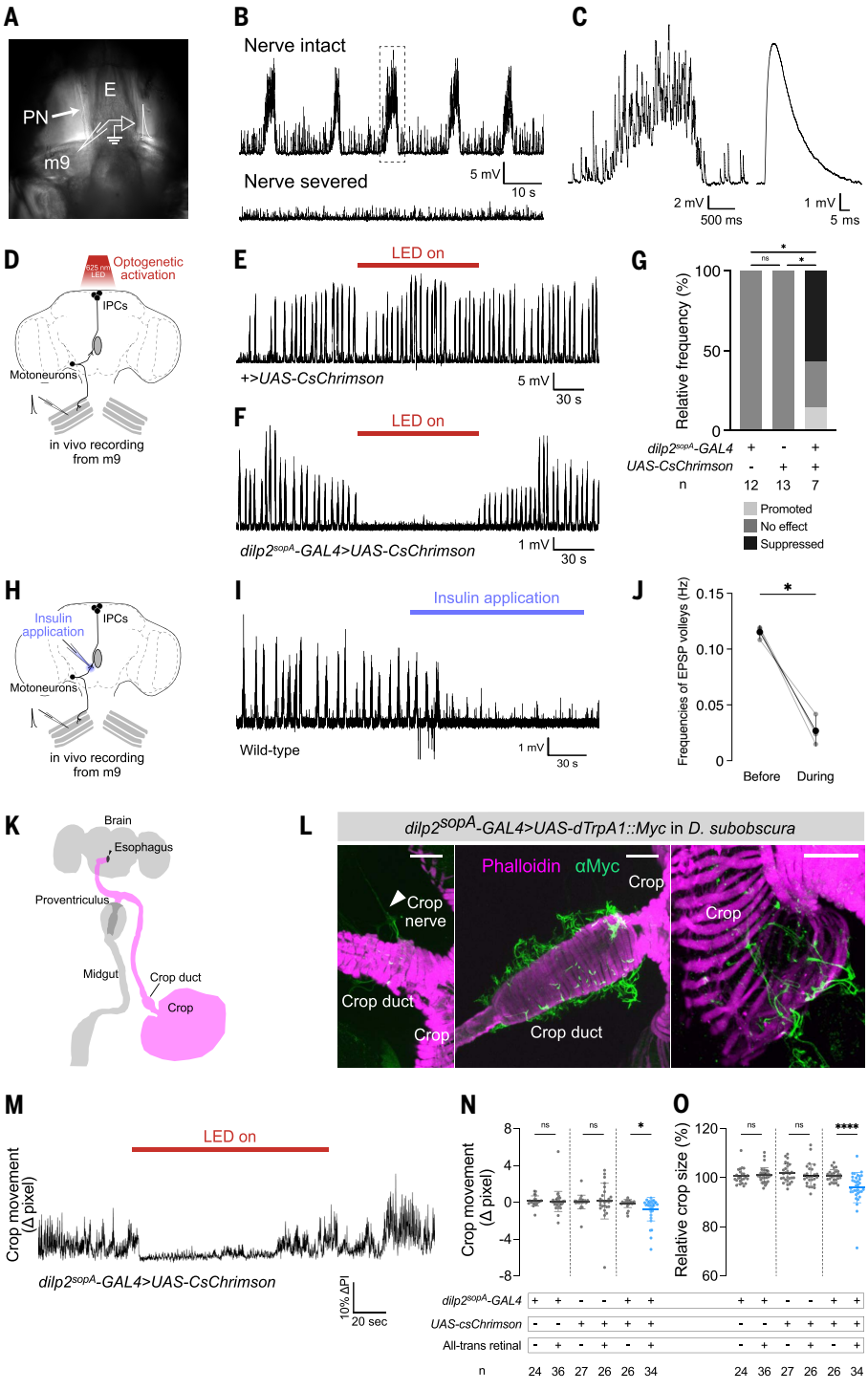

Fig. 5. IPCs suppress motor outputs in *D. subobscura* males. (**A**) Preparation for m9 electrophysiology. PN, pharyngeal nerve. E, esophagus. (**B**) Spontaneous activities in m9 when the PN is intact (top) or severed (bottom). (**C**) The boxed portion in (B) shown with two expanded time scales. (**D**) The recording system. (**E** to **G**) Effect of IPC activation (horizontal bars) on m9 activities in control (E) and test (F) flies and quantification of the effect (G). The proportions of flies in which EPSP volleys in m9 were promoted (pale gray), suppressed (black), or unaffected (gray) upon IPC activation is shown. (**H**) Schematic of an iontophoresis experiment. (**I** and **J**) Example (I) and quantification (J) of responses to insulin iontophoresis. (**K**) Schematic of the brain and digestive organs. (**L**) IPCs innervating the crop through the crop nerve (arrowhead). Scale bar, 50 μm. (**M**) Example of movement records showing the effect of IPC activation (horizontal bar). (**N**) Quantification of the crop movement (mean ± SD). (**O**) Quantification of the crop size. Error bars in (J), (N), and (O) represent the mean ± SD. Statistics are reported in table S6. ****P < 0.0001; **P < 0.01; *P < 0.05.

implies that m9 is controlled by the *fru*-positive motoneuron that innervates this muscle through the pharyngeal nerve. These electrical activities in m9 seem to be associated with spontaneously occurring partial extension of the proboscis: The average rate of volleys (0.161 ± 0.047 Hz, $n = 13$) was close to that of partial extension events (0.160 ± 0.124 Hz, $n = 4$). In most cases, optogenetic activation of IPCs immediately suppressed the occurrence of these EPSP volleys in m9 (Fig. 5, D to G). Likewise, iontophoretic application of insulin onto the SG neuropilar region where IPCs terminate almost immediately suppressed the generation of EPSP volleys (Fig. 5, H to J). The short latency of responses to a focally applied ligand suggests that insulin directly acted on the input synapses of motoneurons. Insulin has been shown to exert an acute inhibitory effect on excitatory transmission by reducing presynaptic release in the mouse hippocampus (*22*). McKeller *et al*. (*18*) showed in *D. melanogaster* that m9 acts as a protractor of the rostrum and at the same time as an extensor of the haustellum, leading to the downward extension of the proboscis upon activation of the innervating motoneuron mn9. The same authors also reported that the haustellum is flexed, rather than extended, when males perform licking, during which time the proboscis is extended anteriorly (*18*). In fact, they found that silencing mn9 inhibited the extension of the haustellum (*18*), which was thus kept flexed as in the case of courtship licking. We confirmed in *D. subobscura* that males extend their proboscis anteriorly for NGG and downwardly for feeding (movies S1 and S3). When IPCs were optogenetically activated during feeding, downward extension was interrupted by repetitive upward (and anteriorly directed) movements of the proboscis, resulting in spasms (fig. S11A and movie S4). By contrast, suppression of IPCs during courtship reduced the frequency of anterior proboscis extension (fig. S11B). Taking these results together, we postulate that IPCs modulate motor outputs to m9 within the central circuit that controls NGG. Close inspection of IPC morphology in *D. subobscura* revealed a prominent lateral extension of axon terminals, which overlapped with dendritic arbors of the L-pSG motoneurons, when two images of clonally labeled neurons were overlaid on a template brain (fig. S10C). The formation of extended terminals was abrogated by *fru* knockdown in *D. subobscura* IPCs (Fig. 3, I and K). In contrast to *D. subobscura* IPCs, *D. melanogaster* IPCs have no discernible lateral extension of terminals. We posit that the extended terminals could mediate the suppressive effect of IPC activation on motor output to m9 in *D. subobscura*.

IPC activity induces crop constriction

As in *D. melanogaster*, IPC axons form terminals on the crop in addition to the SG in *D. subobscura* (Fig. 5, K and L) (*23*). We found that optogenetic stimulation of IPCs with CsChrimson reduced crop movements in *D. subobscura* (Fig. 5, M and N). It is inferred that a reduced movement permits digested food to stay in the crop, and then this food can be allocated to produce a droplet as a nuptial gift. Furthermore, we found that IPC activation decreased the crop size in *D. subobscura* (Fig. 5O). This decrease in crop size could help to elicit regurgitation for NGG by increasing the internal pressure of the crop.

Discussion

IPCs appear to coordinate two important effectors operating for NGG, the proboscis and crop, through two distinct motor pathways. Our analysis favors a model in which IPCs are activated by P1 neurons, which strongly drives execution of species-specific male courtship behavior in *D. subobscura* (fig. S12). IPCs of *D. subobscura*, but not *D. melanogaster*, males express the male-specific *fru* product FruM. A tantalizing possibility is that the expression of specific adhesion molecules in *fru* neurons might promote their interconnection to establish the functional *fru* circuit for executing courtship behavior. Two established transcriptional targets of FruM, *robo1* (*24*) and *tei* (*25*), belong to the gene superfamily encoding immunoglobulin-like domain adhesion proteins, and many of the immunoglobulin superfamily members participate in neurite targeting (*26*, *27*). In fact, we found *D. subobscura*–specific extensions of IPC neurites that formed in *D. subobscura* in a FruM-dependent manner. These FruM-dependent extended neurites appeared to mediate connections of IPCs with courtship initiator P1 neurons and proboscis-innervating motoneurons, both of which express FruM. We presume that this expansion of FruM expression domains was a prerequisite for the recruitment of IPCs to the courtship circuit, which conferred on *D. subobscura* males the latent ability to perform NGG, in which regurgitation plays a central role.

REFERENCES AND NOTES

1. E. Immonen, A. Hoikkala, A. J. N. Kazem, M. G. Ritchie, *Behav. Ecol.* **20**, 289–295 (2009).
2. R. H. Steele, *Anim. Behav.* **34**, 1087–1098 (1986).
3. R. Tanaka, T. Higuchi, S. Kohatsu, K. Sato, D. Yamamoto, *J. Neurosci.* **37**, 11662–11674 (2017).
4. H. T. Spieth, *Bull. Am. Mus. Nat. Hist.* **99**, 395–474 (1952).
5. M. V. Hernández, C. C. Fabre, *J. Insect Behav.* **29**, 578–590 (2016).
6. H. Ito *et al.*, *Proc. Natl. Acad. Sci. U.S.A.* **93**, 9687–9692 (1996).
7. L. C. Ryner *et al.*, *Cell* **87**, 1079–1089 (1996).
8. S. Cachero, A. D. Ostrovsky, J. Y. Yu, B. J. Dickson, G. S. X. E. Jefferis, *Curr. Biol.* **20**, 1589–1601 (2010).
9. K. Kimura, T. Hachiya, M. Koganezawa, T. Tazawa, D. Yamamoto, *Neuron* **59**, 759–769 (2008).
10. J. Y. Yu, M. I. Kanai, E. Demir, G. S. X. E. Jefferis, B. J. Dickson, *Curr. Biol.* **20**, 1602–1614 (2010).
11. J. G. Stoffolano Jr., A. T. Haselton, *Annu. Rev. Entomol.* **58**, 205–225 (2013).
12. Y. D. Chen, S. Ahmad, K. Amin, A. Dahanukar, *J. Exp. Biol.* **222**, jeb210724 (2019).
13. D. R. Nässel, O. I. Kubrak, Y. Liu, J. Luo, O. V. Lushchak, *Front. Physiol.* **4**, 252 (2013).
14. L. F. Seeholzer, M. Seppo, D. L. Stern, V. Ruta, *Nature* **559**, 564–569 (2018).
15. F. A. Roemschied *et al.*, *Nature* **622**, 794–801 (2023).
16. L. Zhang, X. Guo, W. Zhang, *Sci. Adv.* **8**, eabl6121 (2022).
17. S. Kohatsu, D. Yamamoto, *Nat. Commun.* **6**, 6457 (2015).
18. C. E. McKellar, I. Siwanowicz, B. J. Dickson, J. H. Simpson, *eLife* **9**, e54978 (2020).
19. A. Manzo, M. Silies, D. M. Gohl, K. Scott, *Proc. Natl. Acad. Sci. U.S.A.* **109**, 6307–6312 (2012).
20. O. Schwarz *et al.*, *eLife* **6**, e19892 (2017).
21. P. K. Shiu *et al.*, *Nature* **634**, 210–219 (2024).
22. F. Zhao, J. J. Siu, W. Huang, C. Askwith, L. Cao, *Neuroscience* **411**, 237–254 (2019).
23. Y. Ohhara, S. Kobayashi, K. Yamakawa-Kobayashi, N. Yamanaka, *J. Comp. Neurol.* **526**, 1351–1367 (2018).
24. H. Ito, K. Sato, S. Kondo, R. Ueda, D. Yamamoto, *Curr. Biol.* **26**, 1532–1542 (2016).
25. K. Sato, H. Ito, D. Yamamoto, *Commun. Biol.* **3**, 598 (2020).
26. J. R. Sanes, S. L. Zipursky, *Cell* **181**, 536–556 (2020).
27. Q. Xie *et al.*, *Neuron* **110**, 2299–2314.e8 (2022).
28. S. D. Zhang, W. F. Odenwald, *Proc. Natl. Acad. Sci. U.S.A.* **92**, 5525–5529 (1995).

ACKNOWLEDGMENTS

We thank the Bloomington *Drosophila* Stock Center for fly stocks; M. Adachi for secretarial assistance; R. Nishimura at the Technical Center of Nagoya University for constructing the chambers used in the behavioral experiments; H. Toda for critical discussion; and Y.-J. Kim for a DNA plasmid. **Funding:** This work was supported by Grants-in-Aid for Scientific Research from the Ministry of Education, Culture, Sports, Science and Technology (grant 21H04790 to D.Y. and grants 19K16186, 21K15137, 22H05650, 23K05846, and 24H01433 to R.T.). **Author contributions:** Access to tools and facilities: T.A., A.K.; Conceptualization: R.T., D.Y.; Data analysis or interpretation; R.T., Y.H., S. Kohatsu, K.S., H.M., T.H., T.A., A.K., D.Y.; Funding acquisition: R.T., D.Y.; Genome sequence analysis and creation of the genome database: S. Kondo, A.T.; Investigation: R.T., Y.H., H.M., T.H.; Methodology: R.T., Y.H.; Project administration: R.T., D.Y.; Supervision: R.T., D.Y.; Visualization: R.T., Y.H.; Writing – original draft: D.Y.; Writing – review & editing: R.T., D.Y., Y.H. **Competing interests:** The authors declare no competing interests. **Data and materials availability:** All data are available in the main manuscript or the supplementary materials. The nucleotide sequence data reported are available in the DDBJ/EMBL/GenBank databases under accession numbers LC868266 and LC868267. All constructs, antibody, and transgenic fly strains developed in this study are available upon request.
License information: Copyright © 2025 the authors, some rights reserved; exclusive licensee American Association for the Advancement of Science. No claim to original US government works. https://www.science.org/about/science-licenses-journal-article-reuse

SUPPLEMENTARY MATERIALS

science.org/doi/10.1126/science.adp5831
Materials and Methods; Figs. S1 to S15; Tables S1 to S6; References (*29*–*42*); MDAR Reproducibility Checklist; Movies S1 to S4; Data S1 and S2

Submitted 2 April 2024; accepted 14 May 2025

10.1126/science.adp5831

Check for

Erratum

Post date 14 August 2025

Erratum for the Research Article "Flux-induced topological superconductivity in full-shell nanowires" by S. Vaitiekėnas *et al*.

The Research Article "Flux-induced topological superconductivity in full-shell nanowires" by S. Vaitiekėnas *et al*. did not originally include the definition of the tunneling regime, details of the device selection criteria and tuning procedure, or a catalog of measured devices. In response to the concerns of readers, the authors have provided this information. The definition of the tunneling regime has been added to the main text and supplementary materials. Section l, which discusses the device selection, the tuning procedure, and the determination of the tunneling regime, has been added to the supplementary materials, along with associated figures S25 to S36. A paragraph discussing the variability of growth batches and devices has been added to the main text, along with associated section m of the supplementary materials and tables S2 to S7. A comprehensive data catalog has been made available and cited as the last reference in the supplementary materials. These additions do not alter the main conclusions of the paper.

On 30 July 2021, *Science* posted an Editorial Expression of Concern alerting readers to concerns regarding data selection. This Erratum addresses those concerns. Therefore, the Editorial Expression of Concern has been removed from the paper.

10.1126/science.aea6837

Check for

Erratum

Post date 14 August 2025

Erratum for the Research Article "Improving metrology with quantum scrambling" by Z. Li *et al.*

In the Research Article "Improving metrology with quantum scrambling" (30 June 2023, 10.1126/science.adg9500), equation 3 defines the out-of-time-ordered correlation (OTOC) function as

$$\mathcal{I}(t) \equiv -\frac{1}{2}\frac{\partial^2 \mathcal{F}(t)}{(\partial \delta\phi)^2}\bigg|_{\delta\phi=0} = \left\langle \hat{S}_\alpha(t)\hat{\rho}(0)\hat{S}_\alpha(t)\hat{\rho}(0)\right\rangle$$

This expression is incorrect, and the correct expression is given by

$$\mathcal{I}(t) \equiv -\frac{1}{2}\frac{\partial^2 \mathcal{F}(t)}{(\partial \delta\phi)^2}\bigg|_{\delta\phi=0} = -\frac{1}{2}\left\langle \left[\rho(0), \hat{S}_\alpha(t)\right]^2\right\rangle = \frac{1}{2}C(t)$$

where $C(t)$ is called a squared commutator or double commutator (*1*, *2*):

$$\frac{1}{2}C(t) = \left\langle \hat{S}_\alpha(t)\hat{S}_\alpha(t)\hat{\rho}(0)\hat{\rho}(0)\right\rangle - \left\langle \hat{S}_\alpha(t)\hat{\rho}(0)\hat{S}_\alpha(t)\hat{\rho}(0)\right\rangle$$

and OTOC in the captions of Figs. 4 and 5 has been updated to "half squared commutator."

For the initial state considered in the experiment, the OTOC term in $\frac{1}{2}C(t)$, $\left\langle \hat{S}_\alpha(t)\hat{\rho}(0)\hat{S}_\alpha(t)\hat{\rho}(0)\right\rangle$, is strictly zero. This has two consequences. First, because there is no exponential growth of the out-of-time-ordered correlator, there is no clear relationship between the observed metrological gain and quantum information scrambling as quantified by the OTOC. Second, the experimentally observed exponential metrological gain arises from the time-ordered correlator (TOC) term in the half squared commutator, $\frac{1}{2}C(t)$. This also affects the abstract and main text, wherein the term "out-of-time-ordered correlator" or "OTOC" should be replaced by "time-ordered correlator" TOC. The protocol in this article is applicable to the quantum generalization of classical single-body chaotic trajectories.

The above correction does not affect any of the experimental results of the article, where metrological improvement over the standard quantum limit was demonstrated.

REFERENCES AND NOTES

1. J. Maldacena, S. H. Shenker, D. Stanford, A bound on chaos, *J. High Energy Phys.* **2016**, 1 (2016).
2. R. Lewis-Swan, A. Safavi-Naini, J. J. Bollinger, A. M. Rey, Unifying scrambling, thermalization and entanglement through measurement of fidelity out-of-time-order correlators in the Dicke model. *Nat. Commun.* **10**, 1581 (2019).

10.1126/science.aeb2349

Check for

How I learned to ride

Ehsan Hamzehpoor

I sat in my supervisor's office, red-faced and anxious, words tumbling out faster than I could control. For half an hour, I vented everything I had been holding in for months: the stress, the doubt, the sense that I didn't belong. I was in the third year of my Ph.D., and a creeping fear had taken root that I wasn't cut out for academia. I expected some kind of judgment or disappointment. Instead, my supervisor listened patiently, then calmly offered a line I'll never forget: "You are here to learn to ride a bicycle, not to invent a bicycle." That one sentence landed softly, but it cracked something open.

As a first-generation university graduate, I had always felt the pressure to lead the way, to live up to expectations no one else in my family had ever faced. To get into grad school, I focused on presenting myself not as a trainee ready to learn, but as an already successful, accomplished researcher, fully formed and self-sufficient. I internalized this mindset, too.

But after starting my Ph.D., I was hit by wave after wave of academic challenges—not to mention the culture shock and financial stress of being an international student. I barely passed my first-year classes. I had a string of scholarship applications rejected in my second and third years. My research group was full of productive postdocs and graduate students steadily publishing papers, but my research stalled. My attempts to generate and pursue fresh, innovative ideas hit wall after wall. I felt I was running an endless race with a late start, trailing far behind everyone else.

Friends and family encouraged me, reminding me how far I'd come and how many challenges I had already overcome. A professional adviser at the university urged me to stop comparing myself with others and helped me see that just being a Ph.D. candidate was already a meaningful achievement. But the shadows of self-doubt always returned. I still felt I was falling short in fundamental ways.

My supervisor had supported me from the very beginning. Still, I hesitated to share my struggles with him. I didn't want him to see me as a failure. But after 8 months of quietly carrying that weight, and repeated encouragement from my family, I finally spoke up.

My supervisor's words redefined graduate school for me. I realized that my focus on chasing productivity and conceiving new, groundbreaking projects was misguided. The competitive environment of academia had distracted me from the real reason I was a Ph.D. candidate: to learn how to do research and how to thrive.

Embracing that mindset helped me realize I could—and should—lean more on my supervisor and senior colleagues. I began to run my ideas by them and seek feedback early on, which helped me make progress. I worried less about publishing and productivity, and every project, whether it failed or succeeded, became a meaningful step forward and a story worth sharing in my presentations. Two years after that pivotal meeting, I completed my Ph.D. with loads of hard-earned experience, a strong network of supportive colleagues, and a CV I was proud of.

I went on to do a postdoc where—to borrow my supervisor's analogy—I mastered my riding skills while also gradually gathering the tools to ultimately invent my own bicycle. Instead of focusing solely on productivity, I worked closely with my postdoc adviser to develop and refine core skills such as lab techniques, grant writing, and leadership. Along the way, my research moved forward meaningfully, too. I made a discovery—the early framework of a new bicycle—that laid the foundation for the next generation of graduate students in the lab to improve their own riding.

Now, I'm about to establish my own research group. I feel ready to design and invent my own bicycle—or maybe even more than one. Just as important, I'll make sure to remind my trainees that their job, first and foremost, is to learn how to ride. □

Ehsan Hamzehpoor is an assistant professor at the University of Montreal.
Send your career story to SciCareerEditor@aaas.org.